

JUN 10 1980

NAS 160:1638

COMPLETED

NASA Technical Paper 1638

ORIGINAL

**Investigation of Axisymmetric
and Nonaxisymmetric Nozzles
Installed on a 0.10-Scale F-18
Prototype Airplane Model**

Francis J. Capone and Bobby L. Berrier

JUNE 1980

NASA

304

NASA Technical Paper 1638

**Investigation of Axisymmetric
and Nonaxisymmetric Nozzles
Installed on a 0.10-Scale F-18
Prototype Airplane Model**

Francis J. Capone and Bobby L. Berrier
Langley Research Center
Hampton, Virginia



National Aeronautics
and Space Administration

**Scientific and Technical
Information Office**

1980

A

SUMMARY

An investigation was conducted in the Langley 16-Foot Transonic Tunnel to determine afterbody/nozzle longitudinal aerodynamic characteristics of three different two-dimensional nozzles and a base-line axisymmetric nozzle installed on a 0.10-scale model of the F-18 airplane. The effects of thrust vectoring and in-flight thrust reversing were also studied. Horizontal-tail deflections of 0° , -2° , and -5° were tested. Test data were obtained at static conditions and at Mach numbers from 0.60 to 1.20 over an angle-of-attack range from -2° to 10° . Nozzle pressure ratio was varied from jet off to about 10.

At forward speeds, the single expansion ramp nozzle (SERN) and two-dimensional convergent-divergent (2-D C-D) nozzle installations generally provide higher thrust-minus-drag performance (untrimmed) than the base-line axisymmetric nozzle installation. Thrust-minus-drag performance of the wedge nozzle installation was inferior to that of the base-line configuration. Although the SERN suffers much larger thrust losses during vectored operation than the 2-D C-D nozzles, for comparable resultant thrust-vector angles at static conditions, it benefits from favorable external flow effects such that it generally provides the same thrust-minus-drag performance as the 2-D C-D nozzle at forward speeds. In addition, at dry power, the SERN generally provides the highest gain factors (induced lift) and total aft-end lift during vectored operation. The 2-D C-D and wedge nozzle (sideplates off) reversers generally provided comparable levels of reverse thrust at static conditions. However, at forward speeds, the wedge reverser provides 35 to 60 percent more reverse thrust than the 2-D C-D nozzle reverser, probably because of its larger base area and attendant base drag. Full deployment of the reversers at forward speeds caused severe losses in horizontal-tail pitch effectiveness and control reversal at small tail deflections at some conditions. Addition of sideplates to the wedge nozzle reverser panels provided up to 37.5 percent improvement in reverse thrust performance and also tended to increase horizontal-tail pitch effectiveness during reverse operation.

INTRODUCTION

Since the advent of the turbojet engine, exhaust nozzles have traditionally been circular in cross section to facilitate integration with the engine. Extensive development of the "round" nozzle concept has resulted in structurally and thermally efficient exhaust

systems with high internal performance. However, experimental investigations (refs. 1 to 3) on current, twin-engine fighter airplanes have shown that sizable airplane performance penalties are associated with the installation of the exhaust system into the airframe. For multiengine airplanes, most of the external installation penalty probably results from the integration of "round" nozzles into a "rectangular" afterbody. (See ref. 4.) These configurations inherently have boattailed "gutter" interfairings or base regions on the afterbody.

Recent studies on twin-engine fighter airplanes (refs. 5 to 13) have identified potential benefits for a new nozzle concept, the nonaxisymmetric or two-dimensional (2-D) nozzle. This new nozzle concept is geometrically amenable to improvements in nozzle/airframe integration to achieve installed drag reduction; thrust vectoring for maneuver enhancement and short-field take-off and landing; and thrust reversing for increased agility, ground handling, and reduced landing ground roll. Development of the nonaxisymmetric nozzle has concentrated primarily on three nozzle types: the single expansion ramp (refs. 8 and 13 to 20), the convergent-divergent (refs. 7, 10 to 12, 14, 19, and 20), and the wedge (refs. 4, 7, 10 to 12, 14, and 19 to 26).

As part of a coordinated government technology program (ref. 9), three nonaxisymmetric nozzles and a base-line axisymmetric nozzle were tested on a 0.10-scale F-18 prototype airplane model in the Langley 16-Foot Transonic Tunnel. These nonaxisymmetric nozzles included a single expansion ramp nozzle (SERN), a two-dimensional convergent-divergent (2-D C-D) nozzle, and a wedge nozzle. The F-18 airplane is a lightweight, highly maneuverable, twin-engine fighter with a relatively clean afterbody for nozzle installation. No control surface support structure (booms, fairings, etc.) is located adjacent to or ahead of the nozzles, and the vertical tails are located well forward of the nozzle/airframe juncture.

This paper presents F-18 model afterbody/nozzle longitudinal aerodynamic characteristics for three different 2-D nozzle installations and a base-line axisymmetric nozzle installation. Each nozzle type was investigated in both dry and afterburner power operating modes with varying nozzle expansion ratios. In addition to normal forward flight operating conditions, each 2-D nozzle was also investigated in vectored thrust operating modes; the 2-D C-D and wedge nozzles were also investigated in reverse thrust operating modes. Full reverser deployment was simulated on the 2-D C-D nozzle, and 50-percent and full reverser deployment were simulated on the wedge nozzle. The effect of reverser sideplates on reverser performance was investigated on the wedge nozzle. This investigation was conducted in the Langley 16-Foot Transonic Tunnel at static conditions and at Mach numbers from 0.60 to 1.20. Angle of attack was varied from -2° to a maximum of 10° , depending on Mach number, and nozzle pressure ratio was varied from jet off to a maximum of 10, depending on nozzle power setting and Mach number.

Horizontal-tail deflections of 0° , -2° , and -5° were tested. The results of this investigation are summarized in references 27 and 28.

SYMBOLS

All forces and moments, with the exception of body axis thrust F_j , jet normal force $F_{N,j}$, and resultant gross thrust F_g , are referenced to the stability axis system. The moment reference center was located at fuselage station 116.47.

A_e	nozzle-exit area, cm^2
A_t	nozzle-throat area, cm^2
$C_{D,aft}$	aft-end drag coefficient, $\frac{D}{q_{\infty} S}$
$C_{(F-D)}$	thrust-minus-aft-end drag coefficient, $\frac{F - D}{q_{\infty} S}$
$C_{F,i}$	ideal isentropic gross thrust coefficient, $\frac{F_i}{q_{\infty} S}$
C_L	total aft-end lift coefficient (including thrust component), $\frac{\text{Total lift}}{q_{\infty} S}$
$C_{L,aft}$	aft-end lift coefficient with static thrust component removed, $\frac{\text{Lift}}{q_{\infty} S}$
$C_{L,j}$	jet lift coefficient, $\frac{F_g}{q_{\infty} S} \sin (\alpha + \delta)$
$C_{L,o}$	jet-off lift coefficient
$C_{L,\Gamma}$	jet-induced supercirculation lift coefficient
C_m	total aft-end pitching-moment coefficient (including thrust component), <u>Total pitching moment</u> $\frac{q_{\infty} S \bar{c}}{}$
$C_{m,aft}$	aft-end pitching-moment coefficient with static thrust component removed, <u>Pitching moment</u> $\frac{q_{\infty} S \bar{c}}{}$

\bar{c}	wing mean geometric chord, 35.12 cm
D	aft-end drag, N
F	thrust along stability axis, N
F_g	resultant gross thrust, $\sqrt{F_j^2 + F_{N,j}^2}$, N
F_i	ideal isentropic gross thrust, $\dot{m} \sqrt{RT_{t,j} \frac{2\gamma}{\gamma - 1} \left[1 - \left(\frac{p_\infty}{p_{t,j}} \right)^{(\gamma-1)/\gamma} \right]}$, N
F_j	thrust along body axis, N
$F_{N,j}$	jet normal force, N
G	lift gain factor, $\frac{C_{L,\Gamma} + C_{L,j}}{C_{L,j}}$
M	free-stream Mach number
\dot{m}	measured mass-flow rate, kg/sec
\dot{m}_i	ideal mass-flow rate, kg/sec
p_a	ambient pressure, Pa
$p_{t,j}$	average jet total pressure, Pa
p_∞	free-stream static pressure, Pa
q_∞	free-stream dynamic pressure, Pa
R	gas constant (for $\gamma = 1.3997$), 287.3 J/kg-K
r	vertical distance from nozzle reference line to nozzle flap internal surface, positive up (fig. 8), cm

S	wing reference area, 3716.2 cm ²
T _{t,j}	jet total temperature, K
x	axial distance along nozzle reference line from nozzle connect station, positive downstream, cm
y ₁ ,y ₂	vertical distances from wedge center line (fig. 16), cm
α	angle of attack, deg
β	thrust deflection angle of second panel on wedge reverser with respect to nozzle reference line (fig. 20), deg
γ	ratio of specific heats, 1.3997 for air
δ	resultant thrust vector angle at $M = 0$, $\tan^{-1}\left(\frac{F_{N,j}}{F_j}\right)$, deg
δ_h	horizontal-tail deflection, positive leading edge up, deg
δ_v	geometric thrust vector angle, deg
θ	thrust deflection angle of first panel on wedge reverser with respect to nozzle reference line (fig. 20), deg
ϕ	thrust deflection angle of third panel on wedge reverser with respect to nozzle reference line (fig. 20), deg

Subscripts:

F	forward thrust mode
R	reverse thrust mode
V	vectored thrust mode

Abbreviations:

A/B	afterburning
ASME	American Society of Mechanical Engineers
BL	butt line, cm
C-D	convergent-divergent
FRP	fuselage reference plane
FS	fuselage station, cm
N.A.	not applicable
SERN	single expansion ramp nozzle
2-D	two-dimensional (nonaxisymmetric)

APPARATUS AND METHODS

Wind Tunnel

The experimental investigation was conducted in the Langley 16-Foot Transonic Tunnel. This tunnel is a single-return, atmospheric tunnel with a slotted, octagonal test section and continuous air exchange. The wind tunnel has a variable airspeed up to a Mach number of 1.30. Test-section plenum suction is used for speeds above a Mach number of 1.10. A complete description of this facility and operating characteristics can be found in reference 29.

Model and Support System

A 0.10-scale F-18 afterbody jet-effects model was employed for this investigation and is shown in the sketch of figure 1 and the photograph of figure 2. The F-18 airplane is a lightweight, highly maneuverable fighter with a relatively clean afterbody for nozzle installation. As shown by figures 1 and 2, the configuration is characterized by nose strakes, a straight wing, inlet diverter bleed slots through the wing, twin vertical tails located well forward on the afterbody and close-spaced twin engines. The 0.10-scale model reproduced F-18 airplane lines except for faired-over inlets (required for

power-model tests and located on the forebody well forward of the afterbody) and wing alterations required for the model support system. The term afterbody, as used in this paper, refers to the metric portion of the model on which forces and moments are measured. The metric break, or seal station, begins at FS 144.78 and includes the aft fuselage, nozzles (including internal thrust hardware), and empennage surfaces. The model forebody and wing were nonmetric. A 0.064-cm gap in the external skin at the metric-break station prevented fouling between the nonmetric forebody/wing and metric afterbody. A flexible rubber strip located in the metric-break gap was used as a seal to prevent internal flow in the model. The metric afterbody was attached to a six-component strain-gage balance which was grounded to the nonmetric forebody.

As shown in figures 1 and 2, the model was supported at the wing tips in the tunnel. The model FRP was located 7.13 cm below the tunnel center line. The outer wing panels, from 65 percent of the semispan to the tip, were modified from airplane lines to accommodate the wing-tip support system and air supply system. The two wing-tip booms were attached to the normal tunnel support system with V-struts as shown in figure 2. High-pressure air and instrumentation lines were routed through the V-struts and wing-tip booms entering the model fuselage through gun-drilled passages in both wings. The high-pressure air was dumped into a common high-pressure air plenum contained in the center section of the model.

Propulsion Simulation System

An external high-pressure air system provided a continuous flow of clean, dry air at a controlled temperature of about 294 K at the nozzles. This high-pressure air is transferred from a common high-pressure plenum in the model center section into the metric portion of the model by means of two flow-transfer assemblies. A sketch showing details of one of these assemblies is presented in figure 3. These flow-transfer devices have been used in several previous investigations (refs. 14, 20, 23, and 30) and are described in reference 30. Flexible metal bellows are located in each end of the flow-transfer assemblies and act to minimize pressurization tares and provide a lead-free assembly.

Transition and instrumentation sections, including 17.9-percent-open choke plates, were attached to each of the flow-transfer assemblies and terminated at FS 169.32 cm, which was the common connect station for all nozzles.

Nozzle Designs

The base-line F-18 axisymmetric nozzle and three nonaxisymmetric or 2-D nozzles were tested. The 2-D nozzles represent three generically different types: (1) single

expansion ramp nozzle (SERN), (2) two-dimensional convergent-divergent (2-D C-D), and (3) wedge. Each 2-D nozzle type was integrated into the F-18 model so that realistic external lines were established which were expected to minimize the potential for external flow separation in the transonic speed range. Internal clearance between the engine and airframe skin needed for structural frames, engine installation and removal, engine-bay cooling air, nozzle actuation equipment, and other required accessories within the airplane afterbody were considered in establishing these realistic external lines.

Each afterbody/nozzle combination was then tested in the Northrop diagnostic water tunnel in order to determine and fix regions of separated flow. The configuration with the base-line axisymmetric nozzles was used as a calibration standard to adjust test-section velocity. Test-section velocity was adjusted to give the same nozzle flow separation at the angle of attack known from tests previously conducted in transonic wind tunnels. A further discussion of the rationale for operating this tunnel can be found in reference 31.

For installation of the 2-D nozzles, modifications were made to the model afterbody starting at about FS 152.40 cm. This modification consisted of filling in the engine/nozzle interfairing that began at this fuselage station and adding filler at the fuselage corners for smooth transition to the rectangular shaped 2-D nozzles. Figure 4 presents a sketch showing both a profile view of all nozzles tested and typical afterbody cross sections to illustrate afterbody modification. All nozzles were attached to the model at FS 169.32 cm.

Two power settings were investigated for each nozzle type and represented a dry or cruise power setting with a model throat area of 16.13 cm^2 and an afterburning (A/B) power setting with a throat area of 25.81 cm^2 . The three nonaxisymmetric nozzles had an exhaust-duct aspect ratio of 1.00 upstream of the nozzle throat. The SERN and 2-D C-D nozzles had throat aspect ratios (ratio of throat width to height) of 3.71 and 2.32 for dry and A/B power settings, respectively. The wedge nozzle had an exhaust-duct aspect ratio (includes wedge thickness) at the throat of 1.00 for both power settings. Based on an effective throat height (sum of upper and lower throat heights), the wedge nozzle had a throat aspect ratio of 3.26 at dry power setting and 2.03 at A/B power setting. Thrust vectoring was investigated for all 2-D nozzle types and thrust reversing was investigated for the 2-D C-D and wedge nozzles only. Nozzle parameters varied during this investigation are summarized in table I.

TABLE I. - NOZZLE PARAMETERS

Nozzle	A_e/A_t	δ_v , deg	Reverser deployment, percent
Axisymmetric			
Dry power	1.28	0	0
A/B power	1.56	0	0
SERN			
Dry power	1.06	0, 20	0
Dry power	1.15	-7, 0, 7, 20	0
A/B power	1.19	-7, 0, 7, 20	0
A/B power	1.36	0, 20	0
2-D C-D			
Dry power	1.15	-7, 0, 7, 20	0, 100
Dry power	1.65	0	0
A/B power	1.15	-7, 0, 7, 20	0
Wedge			
Dry power	1.10	0	0, 50, 100
Dry power	1.30	0	0
Dry power	1.50	0	0
A/B power	1.20	-10, 0, 10, 20	0
A/B power	1.40	0	0

Base-line axisymmetric nozzle. - The base-line axisymmetric nozzles installed on the F-18 model are shown in the photographs of figure 5. A sketch of the nozzle showing both the dry and A/B power configurations is given in figure 6. This axisymmetric exhaust nozzle represents a hinged-flap, variable-position, convergent-divergent nozzle. Both the convergent and divergent portions of the nozzle are conical. On full-scale hardware, a single actuation system controls the nozzle-throat area; the nozzle-exit area A_e is controlled by an adjustable linkage rod and is a unique function of throat area. Thus, for a set linkage rod length/hinge location, the nozzle area ratio A_e/A_t is a unique function of A_t . Nozzle area ratios of 1.28 and 1.56 that represented dry and A/B power settings, respectively, were tested.

Single expansion ramp nozzles. - SERN nozzles installed on the F-18 model are shown in the photograph of figure 7. Figure 8 presents sketches of the nozzle configuration that simulated both power settings at the nozzle area ratios and vector angles tested.

The SERN nozzle is a 2-D, variable-area, internal/external expansion exhaust system. Basic components consist of (1) a transition section from a round cross section at the tail-pipe connect flange to a 2-D cross section at the nozzle throat; (2) a 2-D variable-geometry convergent-divergent upper flap assembly used to vary power setting (throat area); (3) a 2-D variable ventral flap used to vary nozzle area ratio A_e/A_t ; and (4) a 2-D external expansion ramp which can be fixed for nonvectoring applications or varied for vectoring applications. Note that the throat is forward of the ventral flap, so that the power setting A_t is independent of the ventral flap position or area ratio A_e/A_t . The model was tested with nozzle area ratios of 1.06 and 1.15 for the dry power throat area and with nozzle area ratios of 1.19 and 1.36 for the A/B power throat area. In addition, several vector angles δ_v were investigated for each nozzle area ratio, as shown in table I. Photographs of a vectored SERN nozzle installed on the model are shown in figure 9.

The SERN nozzle shape blends well with airframe contours. In addition, during full-scale nozzle design, sidewall thickness was minimized by locating actuation hardware in the available area on top of the exhaust duct. The result is a nozzle installation that minimizes drag-producing base regions.

Two-dimensional convergent-divergent nozzle. - The 2-D C-D nozzles installed on the F-18 model are shown in the photographs of figures 10 and 11. Sketches of the nozzle representing configurations with both power settings and for several vector angles are shown in figure 12. A photograph showing the 2-D C-D reverser installed on the model is shown in figure 13, and a sketch giving important reverser dimensions is presented in figure 14.

The 2-D C-D nozzle is a variable-area internal-expansion exhaust system which is a three-flap design between fixed sidewalls. The 2-D convergent flap controls nozzle-throat area. The 2-D variable-position divergent flap and external boattail flap assembly controls both nozzle-exit area and thrust vector angle independently of throat area. The model was tested with a nozzle area ratio A_e/A_t of 1.15 for both power-setting throat areas. A nozzle area ratio of 1.65 was tested with the dry power throat area only.

Thrust vectoring would be achieved on the full-scale nozzle by differential positioning of the upper and lower flap assemblies. The range of vector angles tested with each configuration is shown in table I. Thrust reversing is provided by a two-dimensional clamshell blocker and outer door combination. The reverser is located immediately downstream of the transition section that changes the exhaust duct from a round to a rectangular cross section. This reverser was designed for 30-percent reverse

thrust ($F_g/F_i = -0.3$). Thrust reversing was tested on the model for the dry power nozzle only, $A_e/A_t = 1.15$.

Initially, the exit of the 2-D C-D nozzle was fixed at the same fuselage station as the axisymmetric nozzle. However, tests conducted in the Northrop water tunnel indicated a flow separation problem at about FS 169.32 due to locally higher afterbody slopes. This flow separation was eliminated in the water tunnel tests by extending the nozzle exit 3.02 cm aft.

Wedge nozzle.- Figure 15 presents a photograph of the wedge nozzle installed on the F-18 model, and figure 16 presents sketches of the nozzle showing representations of both power settings and all nozzle area ratios tested. The wedge nozzle investigated is a 2-D, variable-area, internal/external expansion exhaust system. Results on a similar nozzle are reported in reference 23. The nozzle has a collapsing wedge centerbody and a fixed external nozzle flap or boattail. The wedge geometry for a flight nozzle can be varied by unique scissor-type linkages and hinges which allow nozzle-exit area and area ratio to be varied independently of the throat area (ref. 24). For A/B power, the wedge is collapsed to obtain the desired throat area. Nozzle area ratios of 1.10, 1.30, and 1.50 were tested with the dry power throat area, and nozzle area ratios of 1.20 and 1.40 were tested with the A/B power throat area.

The wedge is divided into three segments, and to obtain thrust vectoring, the two aft segments are deflected to effectively camber the wedge. The same mechanisms used for varying full-scale nozzle throat and exit area would be employed to camber the wedge. Photographs of a vectored wedge nozzle are shown in figure 17, and a sketch of the vectored wedge is presented in figure 18. The model was tested with vector angles from -10° to 20° for the A/B power nozzle with $A_e/A_t = 1.20$, as indicated in table I. As shown in figures 17 and 18, the aft portions of the nozzle sidewalls were attached rigidly to the aft wedge segment and thus rotated as the wedge vector angle varied. The use of rotating sidewalls is considered an alternative to the use of seals to prevent flow leakage between the aft portion of the wedge and a fixed sidewall. Provision for this type of seal is complicated by the fact that with fixed sidewalls, the wedge would unport during vectoring. To determine the effect of sidewall rotation on vectoring performance, straight (nonrotating) sidewalls were also tested at $\delta_v = 20^\circ$.

Thrust reversing is obtained on the wedge nozzle by variable-geometry, three-segment flaps located in the upper and lower wedge surfaces. Figure 19 presents photographs of the wedge nozzle thrust reverser, and figure 20 presents a sketch showing details of the reverser design. For flight hardware, this reverser is designed to operate in flight as well as on the ground. During this investigation, two deployment positions were tested on the dry power nozzle with $A_e/A_t = 1.10$. One reverser position repre-

presented a nominal 50-percent deployment, which symmetrically directed the thrust 63° from the horizontal plane, as shown in figure 20. The other position represented a nominal 100-percent deployment, which directed the flow forward at an angle of 135° from the horizontal. The reverser with 100-percent deployment was designed for 50-percent reversed thrust ($F_g/F_i = -0.5$). The 50-percent reverser simulated a thrust-spoiler position. To determine the effect of reverser flap sideplates (see fig. 20) on reverse thrust performance, the reverser was also tested in each deployment position with the sideplates off.

Instrumentation

External afterbody aerodynamic and internal nozzle thrust forces and moments were measured with an internal six-component strain-gage balance. Ten pressure orifices in the metric-break gap at FS 144.78 cm were used to measure pressures for tare corrections. Internal cavity pressure, also used for pressure-area force tares, was measured at 10 locations in the afterbody cavity. Model angle of attack, relative to gravity, was measured by a calibrated attitude indicator mounted in the nose.

Mass-flow rate in each nozzle was determined from total pressure and temperature measurements in the flow transfer assemblies (fig. 3) and by constants determined from calibrations with ASME standard nozzles. Total mass-flow rate (both nozzles) was also measured by a turbine flowmeter (external to tunnel) and used as a backup to the flow-transfer assembly measurements. Flow conditions in each nozzle were determined from two total pressure rakes and one total temperature probe located in the instrumentation section aft of the transition section and choke plate (fig. 3). Each rake, one from the top and one from the side of both instrumentation sections, contained three total pressure probes. All pressures were measured with individual pressure transducers.

Tests

Tests were conducted in the Langley 16-Foot Transonic Tunnel at Mach numbers from 0.60 to 1.20. Angle of attack was varied from -2° to 10°, depending upon Mach number; nozzle pressure ratio was varied from jet off to 10.0, depending upon Mach number and nozzle power setting. Basic data were obtained by holding the nozzle pressure ratio constant and varying the angle of attack; nozzle pressure ratio sweeps were conducted at selected, constant angles of attack. All configurations were tested with the horizontal-tail incidence at 0°, and selected configurations were also tested at -2° and -5°. Reynolds number based on the wing mean geometric chord varied from about 3.4×10^6 to 4.8×10^6 .

All tests were conducted with 0.25-cm-wide boundary-layer transition strips consisting of No. 100 silicon carbide grit sparsely distributed in a thin film of lacquer. These strips were located 3.81 cm from the tip of the nose and 2.54 cm aft (streamwise) of all lifting surface and inlet (imaginary) leading edges.

Data Reduction

All data for both the model and the wind-tunnel facility were recorded simultaneously on magnetic tape. Approximately 50 frames of data, taken at a rate of 10 frames per second, were used for each data point; average values were used in computations. The recorded data were used to compute standard force and moment coefficients using wing area and mean geometric chord for reference area and length, respectively.

Because the center line of the balance was located below the flow transfer assembly (bellows) center line, a force and moment interaction (tare) between the bellows and balance existed. In addition, although the bellows were designed to minimize momentum and pressurization tares, small bellows tares still existed with the jet on. These tares result from small pressure differences between the ends of the bellows when internal velocities are high and also from small differences in the forward and aft bellows spring constants when the bellows are pressurized. The bellows/balance interaction tares were determined by single and combined calibration loadings on the balance, with and without the jet operating with the ASME calibration nozzles installed. These tare forces and moments were then removed from the appropriate balance component data. A more detailed description of this procedure can be found in references 14 and 30. In addition, balance corrections were also made to account for metric-break gap and internal cavity pressure/area tares.

The angle of attack of the nonmetric wing and forebody was determined from a calibrated attitude indicator located in the model nose. Angle of attack α , which is the angle between the afterbody center line and the relative wind, was determined by applying deflection terms caused by model and balance bending under aerodynamic load and a flow angularity term to the angle measured by the attitude indicator. A flow angularity adjustment of 0.1° was applied, which is the average angle measured in the 16-Foot Transonic Tunnel.

Since the choke plate and nozzle flow instrumentation were downstream of the round-to-rectangular duct transition section (see fig. 3), nozzle performance parameters were independent of duct transition effects. Total pressure profiles were determined for the ASME calibration nozzles and for the 2-D C-D nozzle at A/B power with the divergent flaps removed. Thus, total pressure profiles were measured at the throat of a con-

vergent 2-D nozzle. Each internal total pressure probe was then corrected to the integrated value of jet total pressure at the nozzle throat.

Thrust-removed coefficients are obtained by determining the components of thrust in the axial and normal direction and subtracting these values from the measured after-body forces. These thrust components at forward speeds are determined from measured static data and are a function of the free-stream static and dynamic pressure. As such, thrust-removed coefficients at nozzle pressure ratios greater than that measured at static conditions are calculated by extrapolating the static data. These results are shown in part of the data presentation as dashed lines.

The lift gain factor G resulting from thrust vectoring was computed for each nozzle type at $\delta_v = 20^\circ$. Jet-induced lift coefficient plus jet lift coefficient was obtained from the following relation:

$$C_{L,\Gamma} + C_{L,j} = C_L - C_{L,0}$$

Jet lift coefficient was calculated by using the resultant thrust vector angle measured at static conditions and the following relation:

$$C_{L,j} = \frac{F_g}{q_\infty S} \sin(\alpha + \delta)$$

Model balance arrangement made it necessary to use static resultant thrust vector angle in this relation, since resultant thrust vector angle could not be determined for conditions at forward speeds. Lift gain factor is then defined as

$$G = \frac{C_{L,\Gamma} + C_{L,j}}{C_{L,j}}$$

PRESENTATION OF RESULTS

The results of this investigation are presented in plotted coefficient and ratio form in the following figures:

Static ($M = 0$) data:

Figure	Nozzle	Power setting	$\frac{A_e}{A_t}$	Vectorized thrust		Reverse thrust	
				δ_v , deg	Sidewalls	Deployment, percent	Sideplates
21	Axisymmetric	Dry	1.28	N.A.	N.A.	N.A.	N.A.
		A/B	1.56	N.A.	N.A.	N.A.	N.A.
22	SERN	Dry	1.15	0 -7 7 20	N.A.	N.A.	N.A.
		A/B	1.19	0 -7 7 20			
23	SERN	Dry	1.06 1.06 1.15 1.15 A/B	0 20 0 20 0 20 0 20	N.A.	N.A.	N.A.
			1.19 1.19 1.36 1.36				
24	2-D C-D	Dry	1.15	0 -7 7 20	N.A.	0	N.A.
		A/B	1.15	0 -7 7 20			
25	2-D C-D	Dry	1.15	0	N.A.	0	N.A.
	2-D C-D	Dry	1.65	0	N.A.	0	N.A.
26	Wedge	A/B	1.20	0 -10 10 20	Vectorized	0	N.A.
27	Wedge	Dry	1.10 1.30 1.50	0 10 20	N.A.	0	N.A.
		A/B	1.20				
		A/B	1.40				
28	Wedge	A/B	1.20	20	Straight	0	N.A.
	Wedge	A/B	1.20	20	Vectorized	0	N.A.
29	2-D C-D	Dry	N.A.	0	N.A.	0	N.A.
	2-D C-D	Dry	N.A.	0	N.A.	100	N.A.
30	Wedge	Dry	1.10	0	N.A.	0	N.A.
						50	On
						50	Off
						100	On
						100	Off

Figure

Ideal thrust coefficient:

Static ($M = 0$) conditions	31
Conditions at forward speeds	32

Longitudinal afterbody aerodynamic characteristics:

Figure	Nozzle	Power setting	$\frac{A_e}{A_t}$	δ_h , deg	δ_v , deg	Remarks
33	Axisymmetric	Dry	1.28	0	0	
34				-2		
35				-5		
36	Axisymmetric	A/B	1.56	0	0	
37				-2		
38				-5		
39	SERN	Dry	1.15	0	0	
40				-2	0	
41				-5	0	
42				0	-7	
43				0	7	
44				0	20	
45				-2	20	
46				-5	20	
47	SERN	A/B	1.19	0	0	
48				-2	0	
49				-5	0	
50				0	-7	
51				0	7	
52				0	20	
53				-2	20	
54				-5	20	
55	2-D C-D	Dry	1.15	0	0	
56				-2	0	
57				-5	0	
58				0	-7	
59				0	7	
60				0	20	

Figure	Nozzle	Power setting	$\frac{A_e}{A_t}$	δ_h , deg	δ_v , deg	Remarks
61	2-D C-D	Dry	1.15	-2	20	
62	2-D C-D	Dry	1.15	-5	20	
63	2-D C-D	A/B	1.15	0	0	
64				-2	0	
65				-5	0	
66				0	-7	
67				0	7	
68				0	20	
69				-2	20	
70				-5	20	
71	Wedge	Dry	1.10	0	0	
72				-2	0	
73				-5	0	
74	Wedge	A/B	1.20	0	0	
75				-2	0	
76				-5	0	
77				0	-10	Vectorized sidewalls
78				-2	-10	
79				0	10	
80				-2	10	
81				0	20	
82	Wedge	A/B	1.20	0	20	Straight sidewalls
83	Wedge	A/B	1.40	0	0	

Figure

Afterbody performance ($\delta_v = 0^0$):

Effect of area ratio; SERN nozzle, dry and A/B power	84
Effect of area ratio; 2-D C-D nozzle, dry power	85
Effect of tails; 2-D C-D nozzle, A/B power (tails off and on)	86
Effect of area ratio; wedge nozzle, dry and A/B power	87

Effect of vectoring on measured afterbody forces:

SERN nozzle, dry power	88
SERN nozzle, A/B power	89

Figure

2-D C-D nozzle, dry power	90
2-D C-D nozzle, A/B power	91
Wedge nozzle, A/B power	92
Effect of vectoring on thrust-removed afterbody forces:	
SERN nozzle, dry power	93
SERN nozzle, A/B power	94
2-D C-D nozzle, dry power	95
2-D C-D nozzle, A/B power	96
Wedge nozzle, A/B power	97
Effect of area ratio and vectoring on measured afterbody forces ($\delta_v \geq 0^\circ$):	
SERN nozzle, dry power	98
SERN nozzle, A/B power	99
Effect of area ratio and vectoring on thrust-removed afterbody forces ($\delta_v \geq 0^\circ$):	
SERN nozzle, dry power	100
SERN nozzle, A/B power	101
Effect of tails and/or sidewalls on measured afterbody forces ($\delta_v \geq 0^\circ$):	
2-D C-D nozzle, A/B power	102
Wedge nozzle, A/B power	103
Effect of tails and/or sidewalls on thrust-removed afterbody forces ($\delta_v \geq 0^\circ$):	
2-D C-D nozzle, A/B power	104
Wedge nozzle, A/B power	105
Effect of reverser on thrust-minus-drag ratio:	
2-D C-D nozzle	106
Wedge nozzle	107
Effect of thrust reversing on afterbody lift and pitching-moment coefficients:	
2-D C-D nozzle; $\delta_h = 0^\circ$	108
2-D C-D nozzle; $\delta_h = -2^\circ$	109
2-D C-D nozzle; $\delta_h = -5^\circ$	110
Wedge nozzle; $\delta_h = 0^\circ$	111
Wedge nozzle; $\delta_h = -2^\circ$	112
Wedge nozzle; $\delta_h = -5^\circ$	113

Figure

Summary figures:

Forward thrust mode:

Comparison of unvectored static nozzle performance	114
Comparison of longitudinal aerodynamic characteristics	115

Vectored thrust mode:

Comparison of static nozzle performance	116
Comparison of lift, thrust, and drag characteristics	117
Comparison of incremental lift and lift gain factors	118

Reverse thrust mode:

Comparison of static nozzle performance	119
Comparison of reverser performances at forward speeds	120
Effect on horizontal-tail pitch effectiveness	121

RESULTS AND DISCUSSION

Basic Data

Static (M = 0) performance. - Static performance of all nozzle types tested in forward thrust mode, vectored thrust mode, and reverse thrust mode is shown in figures 21 to 30. Forward thrust performance (F_g/F_i) of all nozzle types was similar in magnitude and trends to that reported in previous investigations. (See refs. 14 and 19.) Nozzle types with all internal exhaust flow expansion, namely the axisymmetric and 2-D C-D nozzles, are characterized by a single performance peak which occurs near the nozzle pressure ratio required for fully expanded exhaust flow. As expected, peak internal performance shifted to higher nozzle pressure ratios as nozzle area ratio A_e/A_t increased. (See fig. 25.) Nozzle types with both internal and external exhaust flow expansion, namely the SERN and wedge nozzles, are characterized by two performance peaks. The nozzle pressure ratio at which each of these peaks occurs is a function of the nozzle area ratio at the exit (values given in this paper) and also of the area ratio at the end of the external flap or wedge expansion surface. (See ref. 19.) It should be noted that internal performance of nozzles with external expansion surfaces will be sensitive to external flow effects during forward flight.

The SERN nozzles (see fig. 22) produce measured resultant thrust vector angles δ which are a strong function of nozzle pressure ratio at all geometric vector angles δ_v tested, including the cruise $\delta_v = 0$ condition. For example, measured resultant thrust vector angle varied from about -4° to 4° at dry power and from about -2° to 6° at A/B power for the $\delta_v = 0^\circ$ case. These results, which are caused by changing wave patterns impinging upon the expansion ramp, are typical for SERN nozzles, as reported

in references 14 and 19. Measured resultant thrust vector angles for the 2-D C-D and wedge nozzle types were not as dependent on nozzle pressure ratio as the SERN nozzle. (Compare figs. 24 and 26 with fig. 22.) However, both the 2-D C-D and wedge nozzles produced small positive resultant thrust vector angles (1° to 4°) for the $\delta_v = 0^{\circ}$ case. These small angles may be caused by model misalignment during construction and/or assembly. Another possible explanation for this phenomenon could be an asymmetric pressure profile in the nozzle exhaust flow pitch plane. At static conditions ($M = 0$), all three 2-D nozzles produced incremental resultant thrust vector angles $(\delta)_v - (\delta)_F$ which were approximately equal to the geometric vector angle δ_v . Flow turning effectiveness generally decreased with increasing nozzle pressure ratio, particularly for the SERN.

Nozzle efficiency (resultant gross thrust ratio F_g/F_i) generally decreased with increasing positive values of geometric thrust vector angle. (See figs. 22, 24, and 26.) Since thrust losses resulting from turning the jet flow away from the body axis have been accounted for by computing a resultant thrust term (see F_g in "Symbols"), any reductions in nozzle efficiency shown for vectored thrust operation result from flow-turning losses in the nozzles. Negative geometric vector angles generally increased resultant gross thrust ratio for all three 2-D nozzle types. A possible explanation for this phenomenon is that negative geometric vector angles helped to offset losses associated with the small, positive resultant thrust vector angles which were measured at $\delta_v = 0^{\circ}$ and discussed previously. In addition, asymmetric pressure profiles, which may be present at $\delta_v = 0^{\circ}$, could perhaps be improved by negative vector angles.

Two nozzle area ratios were tested on the SERN nozzle at $\delta_v = 0^{\circ}$ and 20° . As shown by figure 23, nozzle area ratio had little effect on nozzle vectoring performance.

Static reverse thrust performance is presented in figures 29 and 30 for the 2-D C-D and wedge nozzles, respectively. The 2-D C-D nozzle was designed to produce 30-percent reverse dry power thrust when fully deployed at static conditions. Results from this investigation indicate that this goal was exceeded for $p_{t,j}/p_a < 3.6$. (See fig. 29.) However, the operating nozzle pressure ratio at static conditions for most current engines is generally less than 3.6. Two reverser deployment positions were tested on the wedge nozzle, namely, 50 and 100 percent. The 50-percent deployment represents a thrust-spoiler position and the 100-percent deployment was designed to produce reverse thrust. Both deployment positions were tested with and without sideplates (see fig. 20), which were designed to prevent spillage of the exhaust flow around the sides of the reverser panels. On the wedge nozzle, reverser efficiency increased with increasing nozzle pressure ratio. (See fig. 30.) With sideplates off, the reverser with 50-percent deployment achieved dry power static thrust levels of 0.34 to 0.44, while the 100-percent reverser deployment produced thrust levels of -0.30 to -0.42. Addition of the sideplates

improved reverser performance by about 16.5 percent when partially deployed and by about 37.5 percent when fully deployed.

Performance at forward speeds. - Basic data for most configurations investigated are presented as aerodynamic coefficients in figures 32 to 83. Total coefficients, including thrust contributions, are shown at the top of each figure; thrust-removed coefficients are shown at the bottom of each figure. The variation of the aeropropulsion performance parameter $(F - D)/F_i$ with nozzle pressure ratio $p_{t,j}/p_\infty$ is presented in figures 84 to 87 for each nozzle type and expansion ratio A_e/A_t investigated in the forward thrust mode. The effects of area ratio, vectoring, reversing, and several configuration variables on aerodynamic coefficients (total and thrust removed) are presented in figures 88 to 113.

As expected, because of increased drag, the aeropropulsion performance of all configurations tested decreased with increasing Mach number and/or model angle of attack. (See figs. 84 to 87.) Consistent trends with nozzle area ratio are not evident from the data obtained with SERN and wedge nozzle installations. Both these nozzles have external expansion surfaces which would be affected by external flow effects and thus have internal performance which depends on Mach number, angle of attack, nozzle pressure ratio, and configuration external geometry. On the other hand, the 2-D C-D nozzle, which has no external expansion surfaces, has internal performance independent of external flow effects as long as the nozzle exhaust flow does not separate from the nozzle divergent flaps. Thus, the variation of wind-on 2-D C-D nozzle performance with nozzle area ratio shown in figure 85 follows trends indicated at static conditions. (See fig. 25.) That is, low nozzle area ratios generally produce higher performance at low nozzle pressure ratios, and high nozzle area ratios generally produce higher performance at high nozzle pressure ratios. Since actual nozzle flight hardware would be continuously variable within mechanical constraints, nozzle area ratio would be programmed, as closely as possible, for optimum performance over the operating range of nozzle pressure ratio.

Vectorized thrust operation at positive geometric thrust vector angles typically increased lift and decreased thrust minus drag, particularly at high geometric thrust vector angles. (See fig. 88, for example.) As expected, vectored thrust operation at negative geometric thrust vector angles produced negative lift-coefficient increments. The magnitude of the lift-coefficient increments produced by thrust vectoring generally decreased with increasing Mach number. (Compare figs. 88(a) to 88(c).) Comparison of total aft-end coefficients (includes thrust component), shown in figures 88 to 92, with the thrust removed aft-end lift coefficients, shown in figures 93 to 97, indicates that most of the lift increment obtained during vectored thrust operation results from the component of thrust in the lift direction. Significant increases in aft-end drag are associated with large geometric thrust vector angles. (See figs. 93(b) and 94(b).)

Nozzle expansion ratio affected vectored thrust performance only slightly, as indicated in figures 98 to 101. As expected, removing the horizontal tails reduced lift and increased thrust minus drag at both vectored and unvectored thrust conditions. (See fig. 102.)

The wedge nozzle was investigated both with a fixed straight sidewall and a simulated variable sidewall which moved with the wedge during vectored operation. (See figs. 17 and 18.) As shown in figure 103, wedge sidewall angle had little effect on vectored thrust performance.

The effect of Mach number on thrust reverser performance is presented in figures 106 and 107. At forward speeds, thrust reverser effectiveness significantly exceeds that obtained at static ($M = 0$) design conditions and increases with increasing Mach number. As indicated in reference 23, improved reverser effectiveness at forward speeds probably results from a significant base drag on the rear face of deployed reverser panels. For the wedge nozzle, reverser effectiveness is significantly improved by adding sideplates (see fig. 19) to the reverser panel, as shown in figure 107. These sideplates probably prevent exhaust flow spillage out the sides of the reverser and thus direct more of the exhaust flow in the forward (reverse) direction.

Configuration Comparisons

Forward thrust mode. - Static internal performance of the 2-D C-D nozzle throughout the nozzle pressure ratio range and of the SERN at $p_{t,j}/p_a > 6.0$ is competitive with the axisymmetric convergent-divergent nozzle at dry power setting. (See fig. 114.) Performance of the wedge nozzle and of the SERN at $p_{t,j}/p_a < 6.0$ generally is 2 to 4 percent below the axisymmetric nozzle at dry power setting. Both the SERN and wedge nozzles, however, have external expansion surfaces; thus internal performance will be altered by external flow effects at forward speeds. At A/B power, all three nonaxisymmetric nozzles have higher performance than the axisymmetric nozzle, with the 2-D C-D nozzle exhibiting the highest performance. However, it should be noted that the axisymmetric nozzle expansion ratio tested at A/B power is much higher than the nozzle expansion ratios tested for the nonaxisymmetric nozzles. A lower nozzle expansion ratio for the axisymmetric nozzle should produce internal performance levels similar to that obtained for the 2-D C-D nozzle.

At forward speeds and dry power setting (fig. 115(a)), the 2-D C-D and SERN nozzles have higher or equal thrust-minus-drag performance than the axisymmetric base-line configuration, and the wedge nozzle generally has lower performance than the base line. All three nonaxisymmetric nozzles had lower aft-end drag than the axisymmetric nozzle base-line configuration at the dry power setting. At A/B power setting (fig. 115(b)), the nonaxisymmetric nozzles, particularly the SERN, generally produced higher aft-end

drag than the axisymmetric nozzle base-line configuration. Even so, the nonaxisymmetric nozzles produced higher thrust-minus-drag performance (one exception is noted at $M = 0.60$ for the 2-D C-D nozzle) than the axisymmetric base-line configuration. The overexpansion losses resulting from the too high nozzle expansion ratio (1.56) tested for the axisymmetric nozzle at A/B power partially explain this performance. In addition, an examination of the static and forward-speed data clearly indicates that the SERN also benefits from favorable external flow effects on internal performance.

In summary, for the test conditions of this investigation, the SERN and 2-D C-D nozzles generally produce higher and the wedge nozzle generally produces lower thrust-minus-drag performance than the axisymmetric nozzle base-line configuration.

Nozzle type generally affected aft-end lift and pitching-moment characteristics only slightly. The SERN, because of its asymmetric geometry in the pitch plane, had the largest effect, particularly at A/B power. This fact indicates that the SERN nozzle will also have the largest impact on trimmed aerodynamic data and thus greater care must be exercised when integrating nozzles of this type into the airframe.

Vectorized thrust mode. - A comparison of thrust vectoring capabilities for the non-axisymmetric nozzles at static ($M = 0$) conditions is presented in figure 116. All three nozzle types have good flow-turning capabilities, as evidenced by measured resultant thrust vector angles nearly equal to geometric thrust vector angles. At $p_{t,j}/p_{\infty} > 2.0$, the 2-D C-D nozzle produced resultant thrust vector angles greater than 20° while losing less than 2 percent of its internal performance. The SERN nozzle generally lost 4 to 8 percent of its internal performance in achieving similar resultant thrust vector angles. The loss associated with turning the thrust away from the axial direction is given as a dashed line in figure 116. As can be seen from this figure, the entire 2-D C-D nozzle thrust loss due to thrust vectoring results from turning the thrust away from the axial direction. Because of the efficient internal flow-turning characteristics of 2-D C-D nozzles (ref. 32) no additional turning losses are incurred. However, the SERN nozzle, which utilizes external, supersonic-flow deflection turning for positive vector angles (ref. 14), suffers from additional flow-turning losses due to shock-induced momentum losses above those expected from geometric considerations.

Although the SERN nozzle suffers large thrust losses due to thrust vectoring at static conditions, it benefits from favorable external flow effects at forward speeds. During dry power vectored thrust operation at forward speeds, the SERN nozzle produces the most lift (fig. 117(a)), thrust minus drag comparable to that achieved with the 2-D C-D nozzle (fig. 117(b)), and the largest gain (induced lift) factors (fig. 118) of all configurations tested.

Reverse thrust mode. - During reverse thrust operation, the 2-D C-D and wedge nozzles (without reverser sideplates) produce comparable levels of reverse thrust at

static conditions (fig. 119). However, opposite trends with increasing nozzle pressure ratio were determined for each nozzle. Reverser efficiency of the 2-D C-D nozzle decreases and reverser efficiency of the wedge nozzle increases with increasing nozzle pressure ratio. Addition of reverser sideplates on the wedge nozzle increases reverser efficiency by about 37.5 percent (more negative values of F_g/F_i).

As discussed previously, reverser efficiency increases with increasing Mach number (fig. 120) because of base drag on the reverser panels. Reverser performance obtained during the current investigation is compared in figure 120 with that reported for other nonaxisymmetric nozzles in references 14 and 23 and for an axisymmetric nozzle described in reference 33. Comparison of the 2-D C-D and wedge nozzle reversers (reverser sideplates off) can be made only at 100-percent deployment. Although at $M = 0$ both reversers have almost identical performance (fig. 120(a)), at forward speeds (fig. 120(b) and (c)), the wedge reverser provides from 0.25 to 0.45 more reverse thrust than the 2-D C-D reverser. That is, the change in $(F - D)_R/(F - D)_F$ was 0.25 to 0.45, with the wedge reverser having more negative values. This higher performance results from a larger base area on the wedge reverser than the one on the 2-D C-D reverser at 100-percent deployment. (Compare figs. 14 and 20.) This area also acts as a conventional speed brake. The performance of the axisymmetric nozzle reverser is similar to that of the wedge nozzle at 100-percent deployment but provides 0.30 to 0.40 more reverse thrust (35 to 60 percent) than the 2-D C-D nozzle at forward speeds.

At 50-percent deployment, the wedge nozzle reverser (thrust spoiler) is significantly more effective than the axisymmetric nozzle reverser. Addition of sideplates to the wedge nozzle reverser panels improves wedge nozzle reverser performance at all test conditions.

Operation of an in-flight thrust reverser can cause severe stability and control problems at forward speeds. Data on an axisymmetric nozzle reverser reported in reference 34 indicate severe nose-down pitching moment at large deployments and 30- to 40-percent reduction in horizontal-tail effectiveness. Results for a wedge nozzle reverser (ref. 23) also showed not only losses in tail lift, but also significant losses in rudder effectiveness for a configuration with both single and twin vertical tails. The effect of 2-D C-D and wedge nozzle reversers on horizontal-tail pitch effectiveness is presented in figure 121. Severe losses in horizontal-tail pitch effectiveness are shown for 100-percent deployment of both nonaxisymmetric nozzle reversers. At some conditions, control reversal is indicated for small tail deflections. Addition of sideplates to the wedge reverser appeared to improve horizontal-tail pitch effectiveness at $M = 0.60$. A possible explanation for this is that the sideplates prevent lateral spillage of the exhaust flow and thus tend to isolate the horizontal tails from the reverser flow. Although severe

problems are noted for in-flight reverser operation, they can probably be eliminated or minimized to an acceptable level by proper design and by integration of the reverser into the airframe. However, since these problems are probably highly configuration dependent, no attempt at fixes were studied during the current investigation.

CONCLUSIONS

An investigation was conducted in the Langley 16-Foot Transonic Tunnel to determine afterbody/nozzle longitudinal aerodynamic characteristics of three different two-dimensional nozzles and a base-line axisymmetric nozzle installed on a 0.10-scale model of the prototype F-18 airplane. The effects of thrust vectoring and in-flight thrust reversing were also studied. Horizontal-tail deflections of 0° , -2° , and -5° were tested. Test data were obtained at static conditions and at Mach numbers from 0.60 to 1.20 and over an angle-of-attack range from -2° to 10° . Nozzle pressure ratio was varied from jet off to about 10. Results from this study indicate the following conclusions:

1. At forward speeds, the single expansion ramp nozzle (SERN) and two-dimensional convergent-divergent (2-D C-D) nozzle installations generally provide higher thrust-minus-drag performance (untrimmed) than the base-line axisymmetric nozzle installation. The thrust-minus-drag performance of the wedge nozzle installation was inferior to that of the base-line configuration.
2. Although for comparable resultant thrust vector angles at static conditions the SERN suffers much larger thrust losses during vectored operation than the 2-D C-D nozzle, it benefits from favorable external flow effects so that it generally provides the same thrust-minus-drag performance as the 2-D C-D nozzle at forward speeds. In addition, at dry power, the SERN generally provides the highest gain factors (induced lift) and total aft-end lift during vectored operation.
3. The 2-D C-D and wedge nozzle (sideplates off) reversers generally provided comparable levels of reverse thrust at static conditions. However, at forward speeds, the wedge reverser provides 35 to 60 percent more reverse thrust than the 2-D C-D nozzle reverser, probably because of its larger base area and attendant base drag.
4. Full deployment of the reversers at forward speeds caused severe losses in horizontal-tail pitch effectiveness and control reversal at small tail deflections at some conditions.

5. Addition of sideplates to the wedge nozzle reverser panels provided up to 37.5-percent improvement in reverse thrust performance and also tended to increase horizontal-tail pitch effectiveness during reverse operation.

Langley Research Center
National Aeronautics and Space Administration
Hampton, VA 23665
February 29, 1980

REFERENCES

1. Schmeer, James W.; Lauer, Rodney F., Jr.; and Berrier, Bobby L.: Performance of Blow-in-Door Ejector Nozzles Installed on a Twin-Jet Variable-Wing-Sweep Fighter Airplane Model. NASA TM X-1383, 1967.
2. Reubush, David E.; and Mercer, Charles E.: Effects of Nozzle Interfairing Modifications on Longitudinal Aerodynamic Characteristics of a Twin-Jet, Variable-Wing-Sweep Fighter Model. NASA TN D-7817, 1975.
3. Maiden, Donald L.; and Berrier, Bobby L.: Effect of Airframe Modifications on Longitudinal Aerodynamic Characteristics of a Fixed-Wing, Twin-Jet Fighter Airplane Model. NASA TM X-2523, 1972.
4. Maiden, Donald L.; and Petit, John E.: Investigation of Two-Dimensional Wedge Exhaust Nozzles for Advanced Aircraft. *J. Aircr.*, vol. 13, no. 10, Oct. 1976, pp. 809-816.
5. Martens, Richard E.: F-15 Nozzle/Afterbody Integration. *J. Aircr.*, vol. 13, no. 5, May 1976, pp. 327-333.
6. Capone, Francis J.: The Nonaxisymmetric Nozzle - It Is for Real. AIAA Paper 79-1810, Aug. 1979.
7. Hiley, P. E.; Wallace, H. W.; and Booz, D. E.: Nonaxisymmetric Nozzles Installed in Advanced Fighter Aircraft. *J. Aircr.*, vol. 13, no. 12, Dec. 1976, pp. 1000-1006.
8. Sedgwick, T. E.: Investigation of Nonaxisymmetric Two-Dimensional Nozzles Installed in Twin-Engine Tactical Aircraft. AIAA Paper No. 75-1319, Sept.-Oct. 1975.
9. Berrier, Bobby L.; Palcza, J. Lawrence; and Richey, G. Keith: Nonaxisymmetric Nozzle Technology Program - An Overview. AIAA Paper 77-1225, Aug. 1977.
10. F-15 2-D Nozzle System Integration Study. Volume I - Technical Report. NASA CR-145295, 1978.
11. Stevens, H. L.: F-15/Nonaxisymmetric Nozzle System Integration Study Support Program. NASA CR-135252, 1978.
12. Bergman, D.; Mace, J. L.; and Thayer, E. B.: Non-Axisymmetric Nozzle Concepts for an F-111 Test Bed. AIAA Paper No. 77-841, July 1977.
13. Wasson, H. R.; Hall, G. R.; and Palcza, J. L.: Results of a Feasibility Study to Add Canards and ADEN Nozzle to the YF-17. AIAA Paper 77-1227, Aug. 1977.
14. Capone, Francis J.: Static Performance of Five Twin-Engine Nonaxisymmetric Nozzles With Vectoring and Reversing Capability. NASA TP-1224, 1978.

15. Lander, J. A.; and Palcza, J. Lawrence: Exhaust Nozzle Deflector Systems for V/STOL Fighter Aircraft. AIAA Paper No. 74-1169, Oct. 1974.
16. Lander, J. A.; Nash, D. O.; and Palcza, J. Lawrence: Augmented Deflector Exhaust Nozzle (ADEN) Design for Future Fighters. AIAA Paper No. 75-1318, Sept.-Oct. 1975.
17. Nash, D. O.; Wakeman, T. G.; and Palcza, J. L.: Structural and Cooling Aspects of the ADEN Nonaxisymmetric Exhaust Nozzle. Paper No. 77-GT-110, American Soc. Mech. Eng., Mar. 1977.
18. Schnell, W. C.; Grossman, R. L.; and Hoff, G. E.: Comparison of Non-Axisymmetric & Axisymmetric Nozzles Installed on a V/STOL Fighter Model. [Preprint] 770983, Soc. Automot. Eng., Nov. 1977.
19. Berrier, Bobby L.; and Re, Richard J.: Effect of Several Geometric Parameters on the Static Internal Performance of Three Nonaxisymmetric Nozzle Concepts. NASA TP-1468, 1979.
20. Hiley, P. E.; Kitzmiller, D. E.; and Willard, C. M.: Installed Performance of Vectoring/Reversing Nonaxisymmetric Nozzles. J. Aircr., vol. 16, no. 3, Aug. 1979, pp. 532-538.
21. Maiden, Donald L.: Performance of an Isolated Two-Dimensional Variable-Geometry Wedge Nozzle With Translating Shroud and Collapsing Wedge at Speeds Up to Mach 2.01. NASA TN D-7906, 1975.
22. Maiden, Donald L.: Performance of an Isolated Two-Dimensional Wedge Nozzle With Fixed Cowl and Variable Wedge Centerbody at Mach Numbers Up to 2.01. NASA TN D-8218, 1976.
23. Capone, Francis J.; and Maiden, Donald L.: Performance of Twin Two-Dimensional Wedge Nozzles Including Thrust Vectoring and Reversing Effects at Speeds Up to Mach 2.20. NASA TN D-8449, 1977.
24. Goetz, Gerald F.; Young, John H.; and Palcza, J. Lawrence: A Two-Dimensional Airframe Integrated Nozzle Design With Inflight Thrust Vectoring and Reversing Capabilities for Advanced Fighter Aircraft. AIAA Paper No. 76-626, July 1976.
25. Pendergraft, O. C.: Comparison of Axisymmetric and Nonaxisymmetric Nozzles Installed on the F-15 Configuration. AIAA Paper 77-842, July 1977.
26. Carson, George T., Jr.; and Mason, Mary L.: Experimental and Analytical Investigation of a Nonaxisymmetric Wedge Nozzle at Static Conditions. NASA TP-1188, 1978.

27. Capone, Francis J.; Gowadia, Noshir S.; and Wooten, W. H.: Performance Characteristics of Nonaxisymmetric Nozzles Installed on the F-18 Aircraft. AIAA Paper 79-0101, Jan. 1979.
28. Petit, John E.; and Capone, Francis J.: Performance Characteristics of a Wedge Nozzle Installed on an F-18 Propulsion Wind Tunnel Model. AIAA Paper 79-1164, June 1979.
29. Corson, Blake W., Jr.; Runckel, Jack F.; and Igoe, William B.: Calibration of the Langley 16-Foot Transonic Tunnel With Test Section Air Removal. NASA TR R-423, 1974.
30. Capone, Francis J.: The Effects on Propulsion-Induced Aerodynamic Forces of Vectoring a Partial-Span Rectangular Jet at Mach Numbers From 0.40 to 1.20. NASA TN D-8039, 1975.
31. Lorincz, Dale J.: A Water Tunnel Flow Visualization Study of the F-15. NASA CR-144878, 1978.
32. Berrier, Bobby L.; and Re, Richard J.: A Review of Thrust-Vectoring Schemes for Fighter Applications. AIAA Paper 78-1023, July 1978.
33. Maiden, Donald L.; and Mercer, Charles E.: Performance Characteristics of a Single-Engine Fighter Model Fitted With an In-Flight Thrust Reverser. NASA TN D-6460, 1971.
34. Mercer, Charles E.; and Maiden, Donald L.: Effects of an In-Flight Thrust Reverser on the Stability and Control Characteristics of a Single-Engine Fighter Airplane Model. NASA TN D-6886, 1972.

30

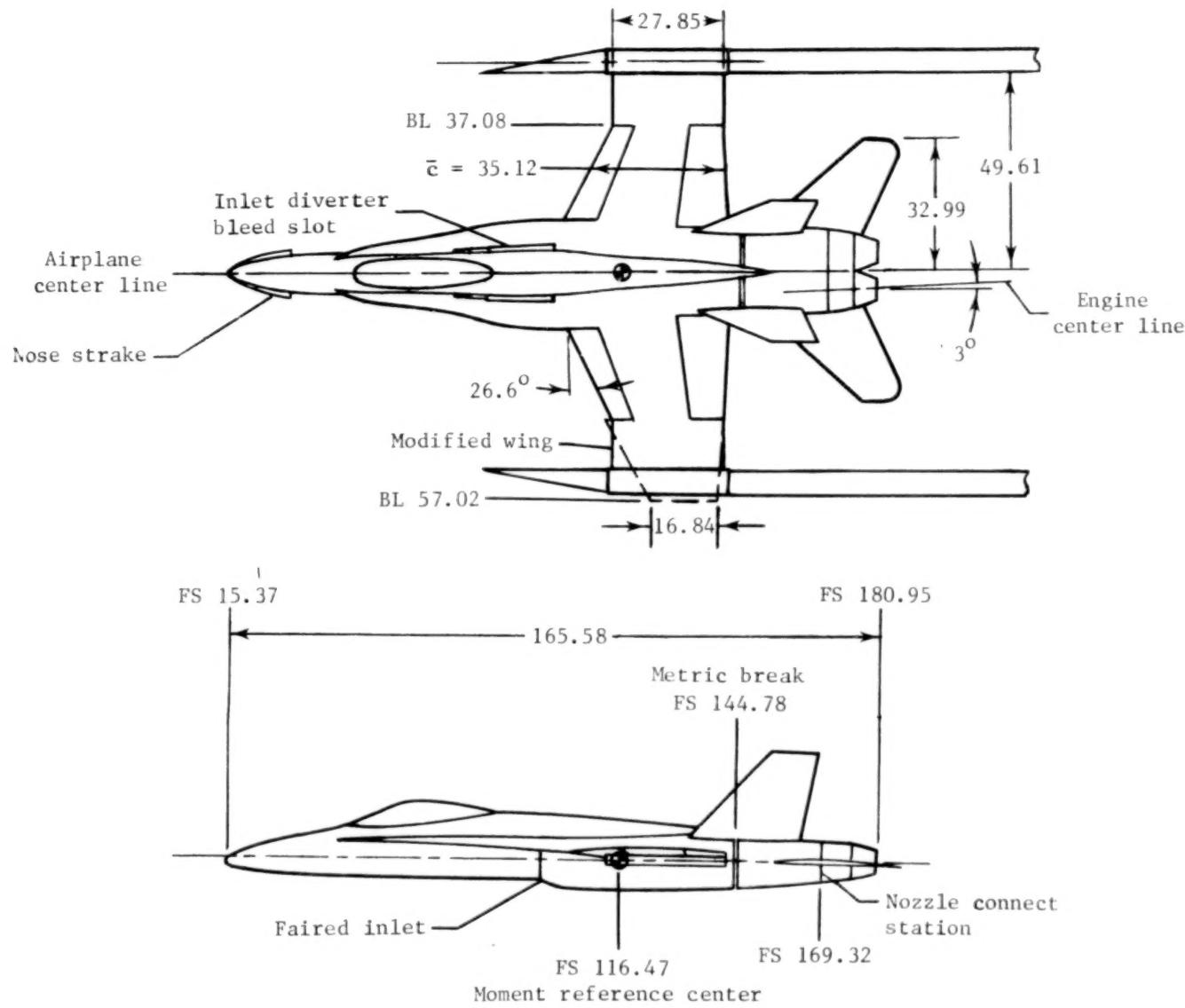
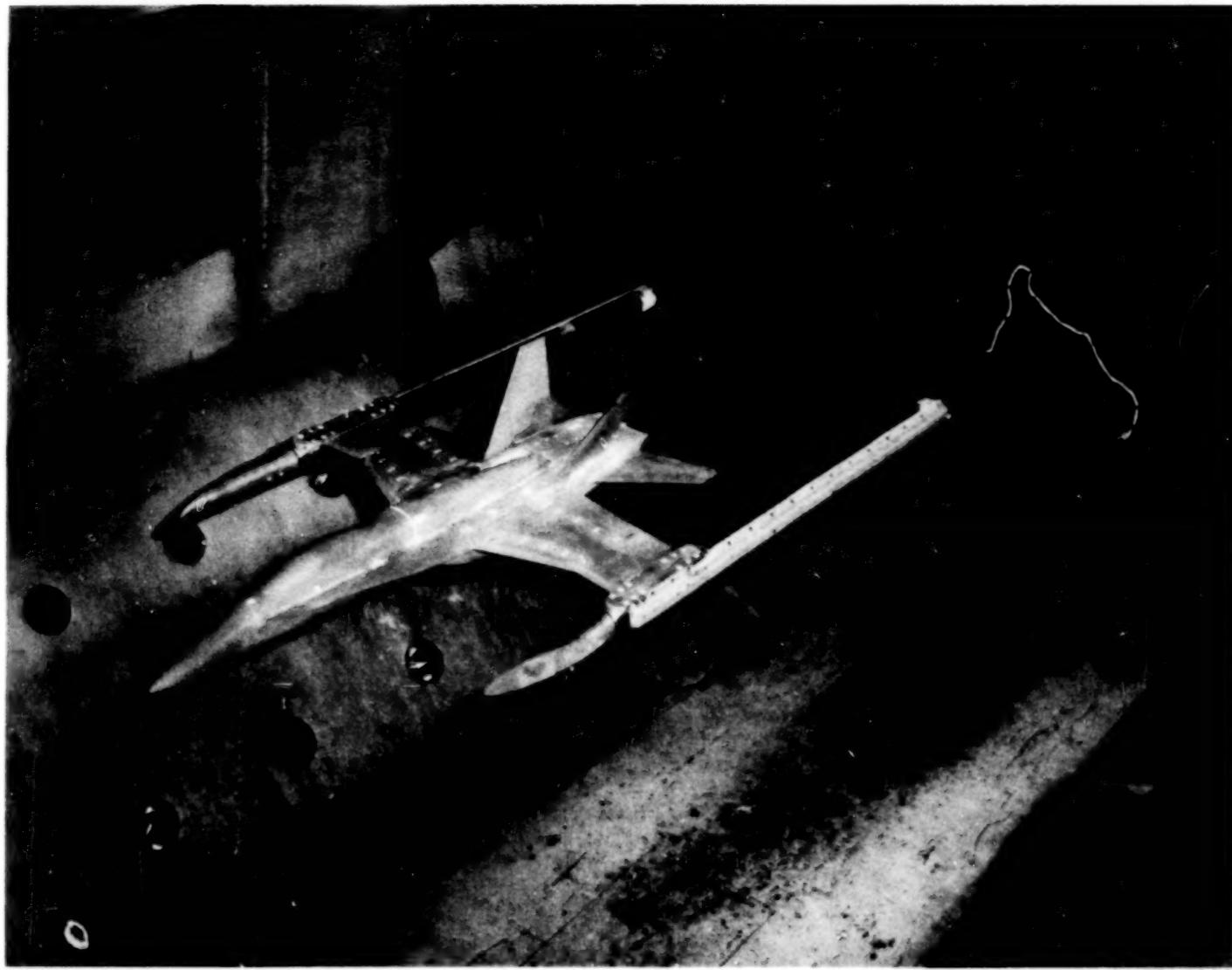


Figure 1.- Sketch of model. All dimensions are in centimeters.



L-78-1908

Figure 2.- Installation of F-18 model in Langley 16-Foot Transonic Tunnel.

30

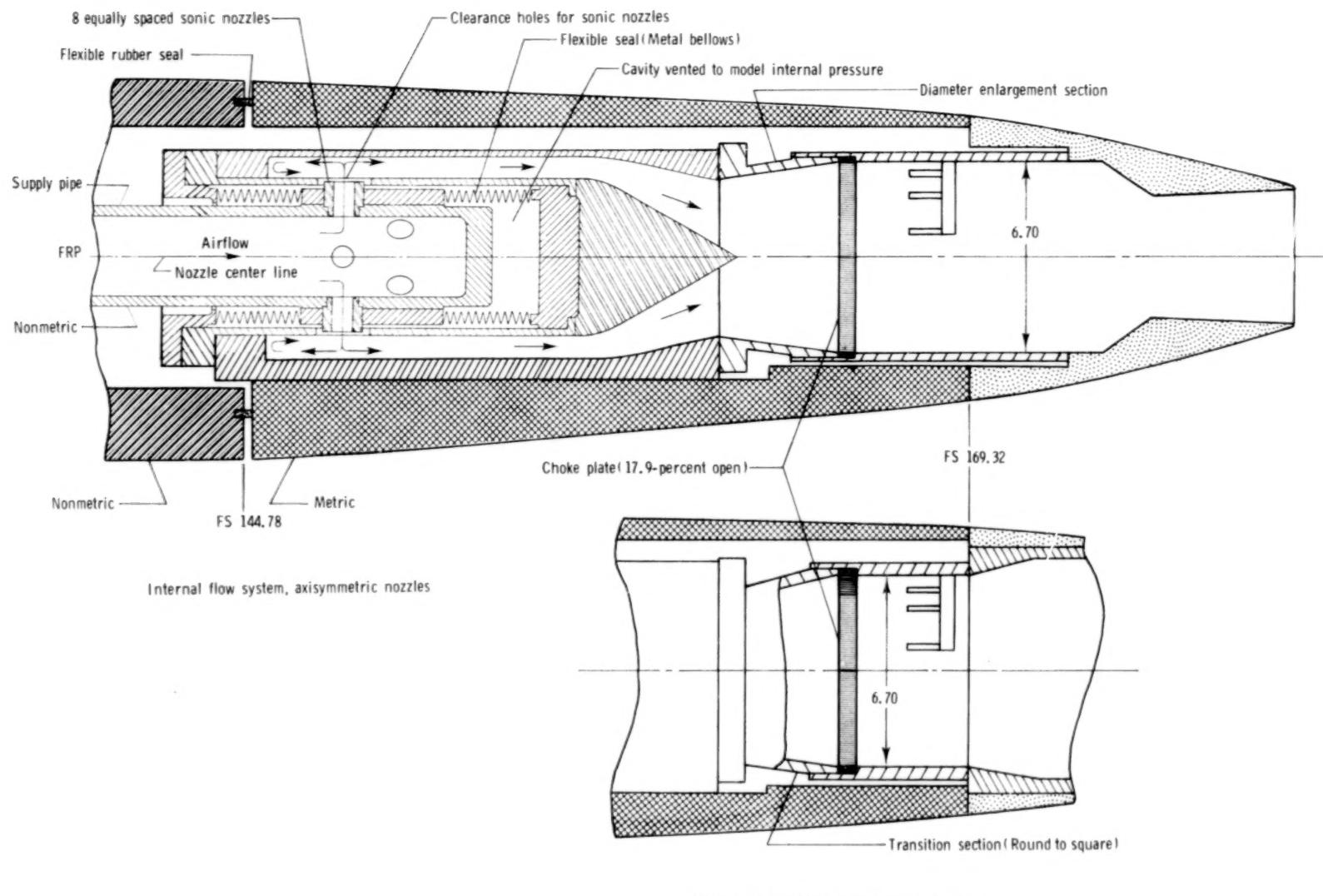
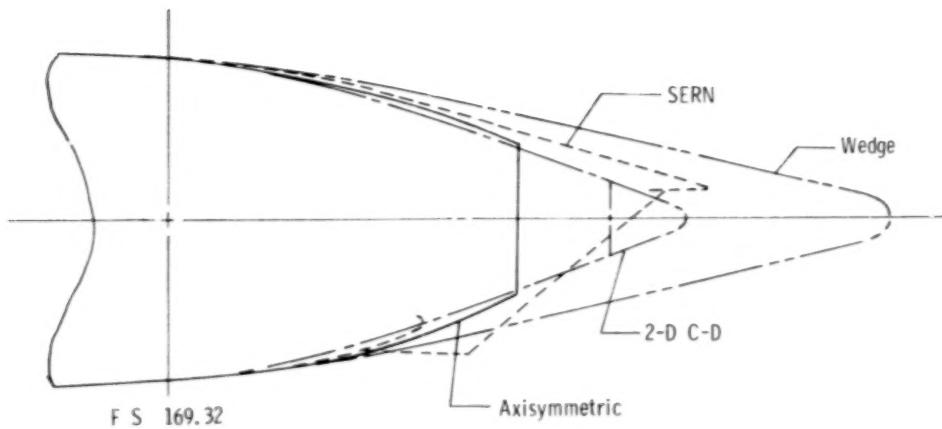
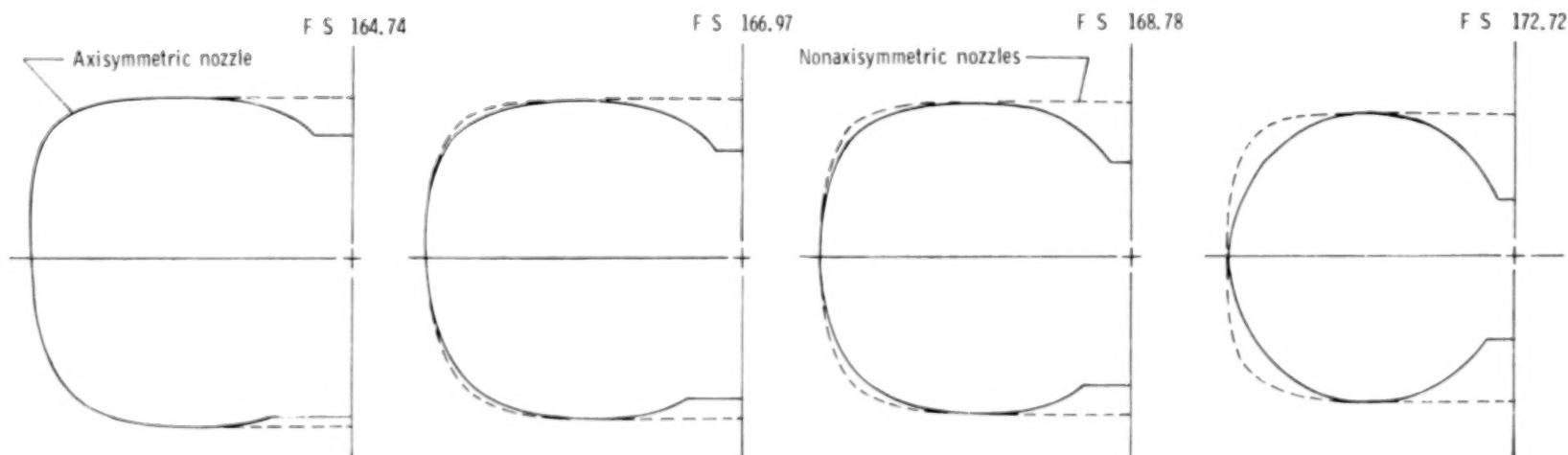


Figure 3.- Details of internal flow systems showing flow transfer assemblies. All dimensions in centimeters unless otherwise noted.

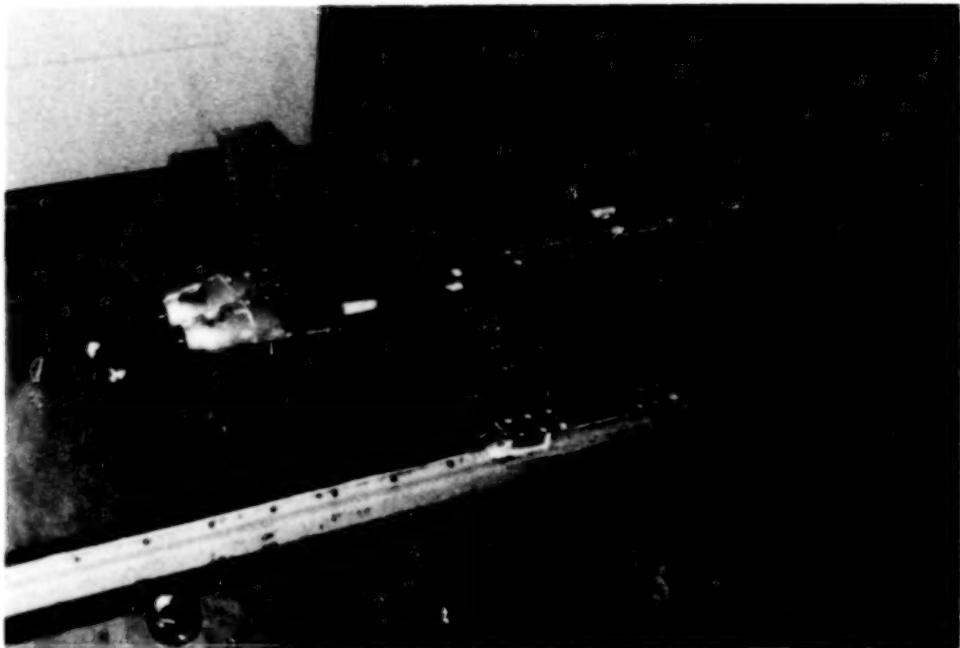


Composite profile view of nozzles tested

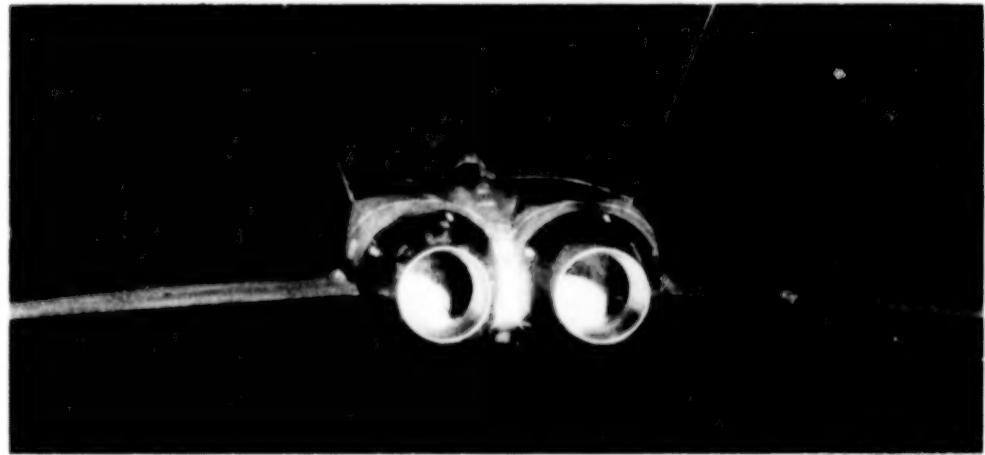


Typical afterbody cross sections

Figure 4.- Sketch showing composite view of nozzles tested and some afterbody cross sections.
All dimensions in centimeters unless otherwise noted.



L-78-1648



L-78-1646

Figure 5.- Base-line axisymmetric nozzle, dry power, installed on F-18 model.

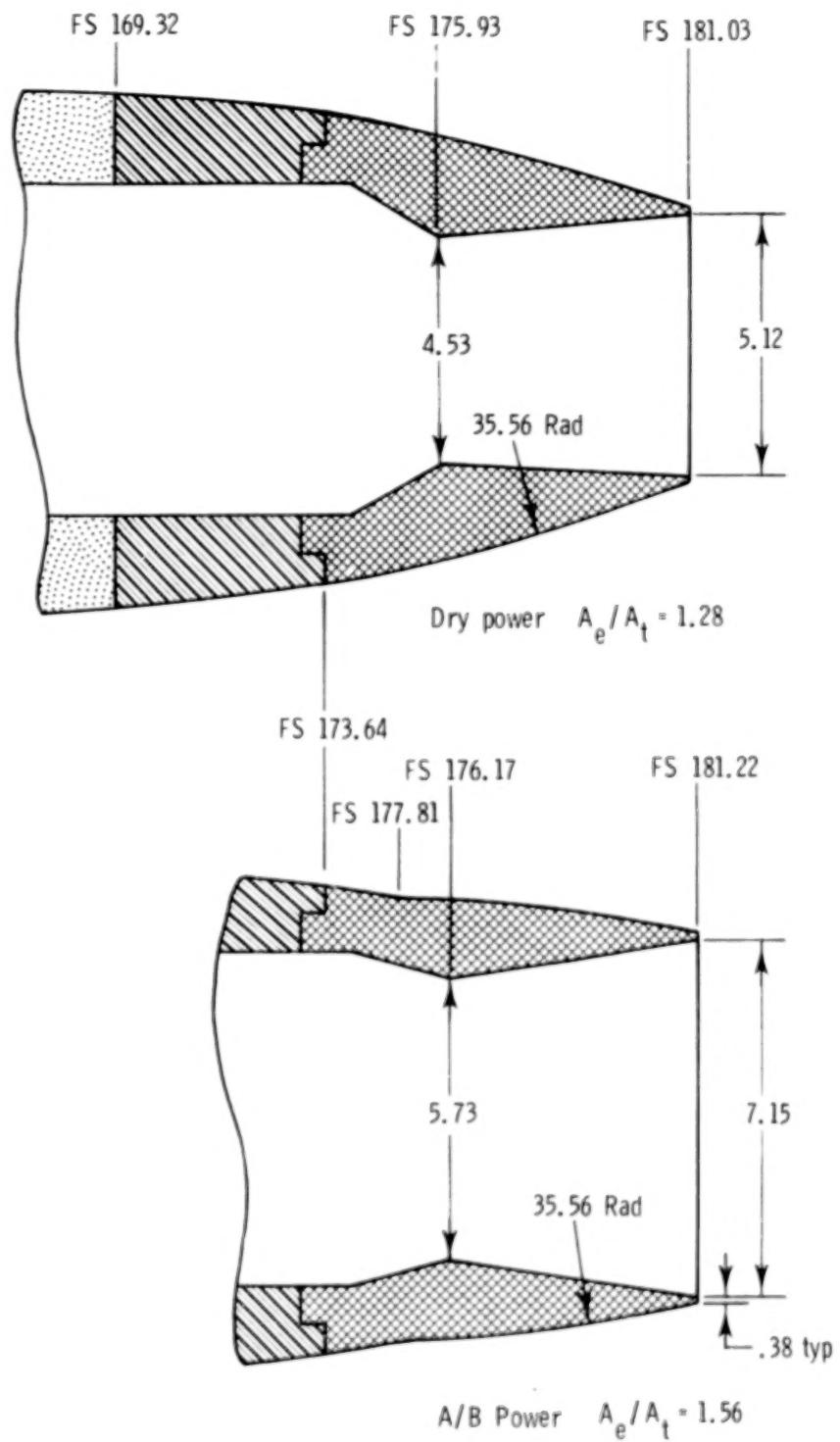
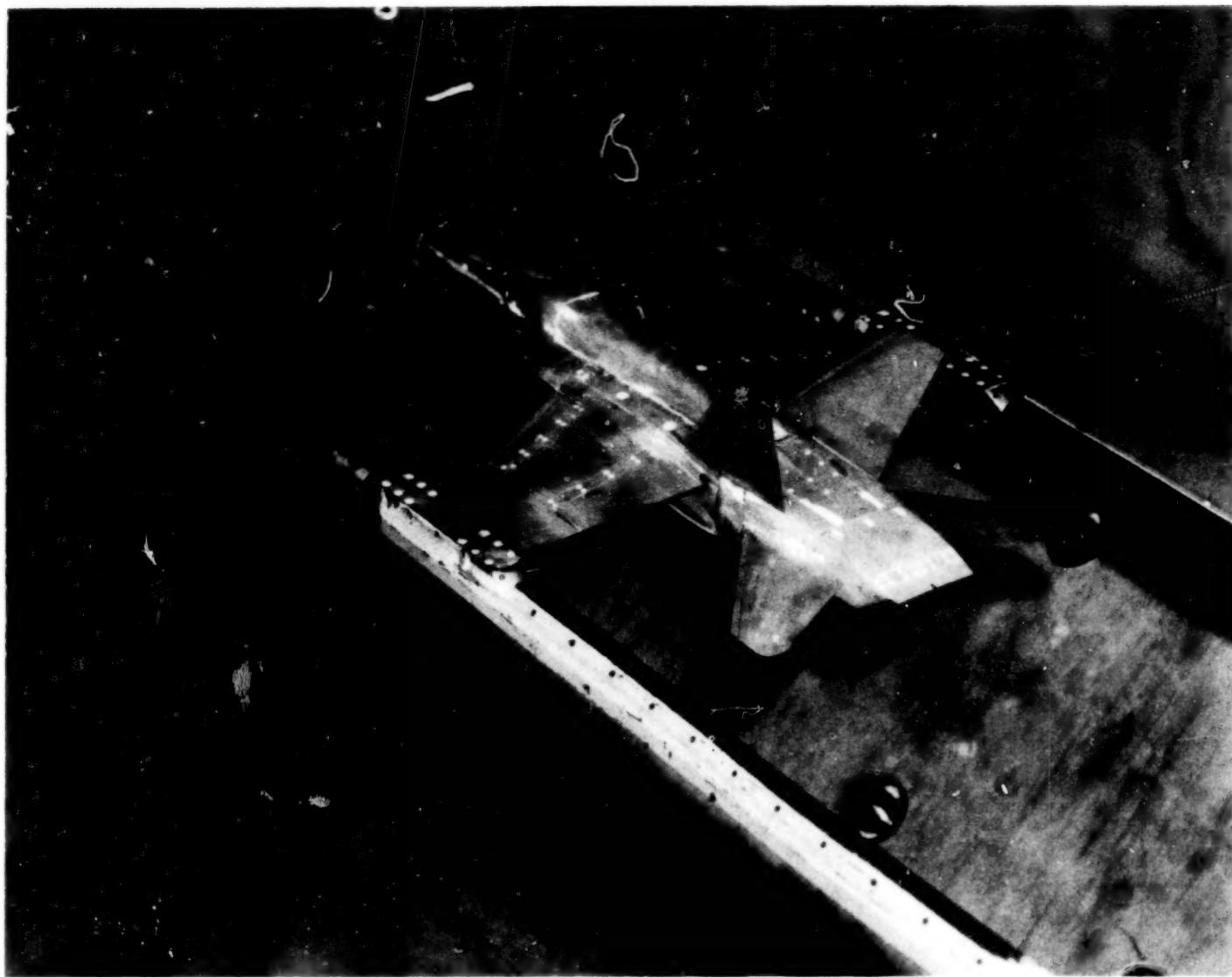


Figure 6.- Sketch of axisymmetric nozzle. All dimensions in centimeters unless otherwise noted.

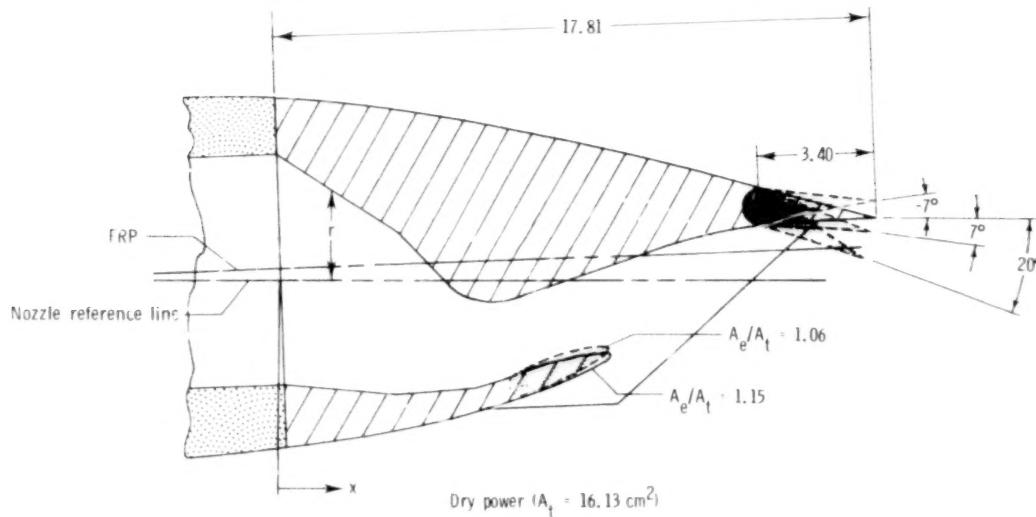
36



L-78-2024

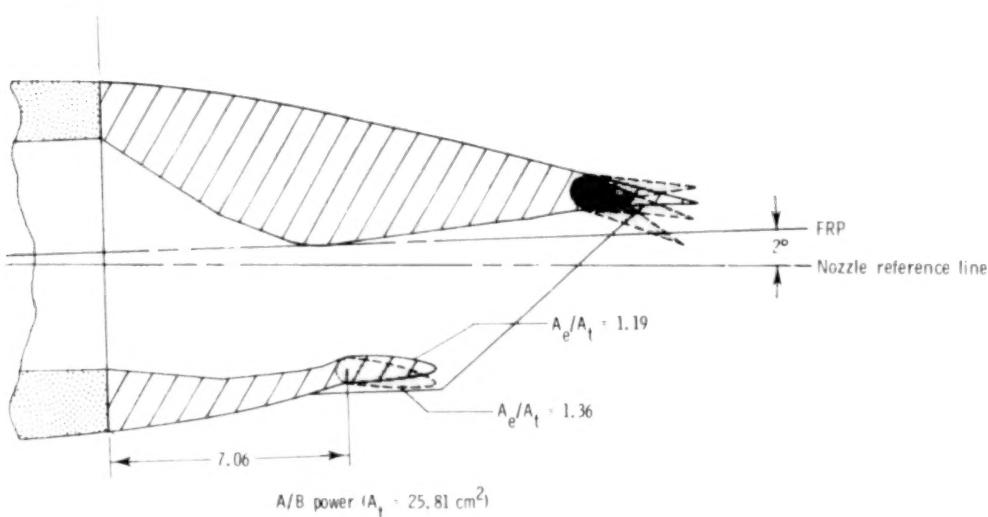
Figure 7.- Overall view of SERN nozzle installed on F-18 model.

FS 169.32



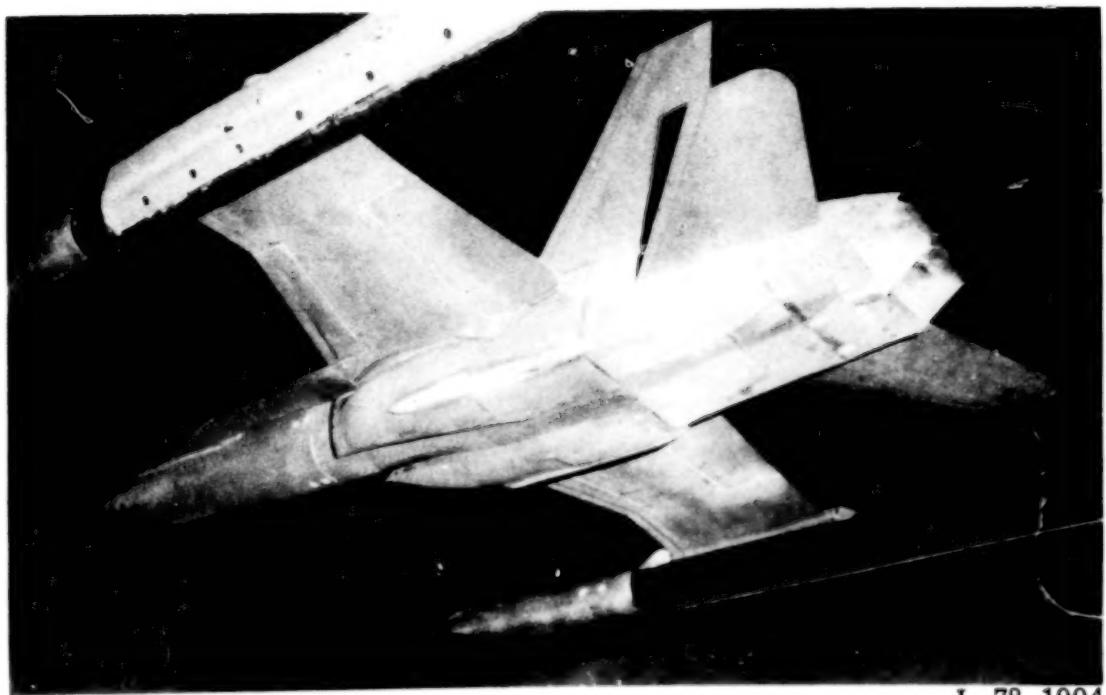
Upper flap geometry ($\delta_v = 0^\circ$)		
x	Dry power r	A/B power r
3.48	1.41	1.41
5.04	-0.18	st. line
5.44	-0.44	
5.73	-0.53	0.64
5.99	-0.60	0.59
6.62		0.57
6.84	-0.55	
7.12	-0.48	st. line
10.79	st. line	1.16
11.36	0.97	1.22
11.92	1.14	1.26
12.20	1.22	1.27
12.48	1.26	1.26
12.77	1.35	1.35
13.05	1.41	1.41
13.61	1.52	1.52
14.18	1.60	1.60
14.75	1.67	1.67
15.32	1.71	1.71
17.81	1.82	1.82

FS 169.32

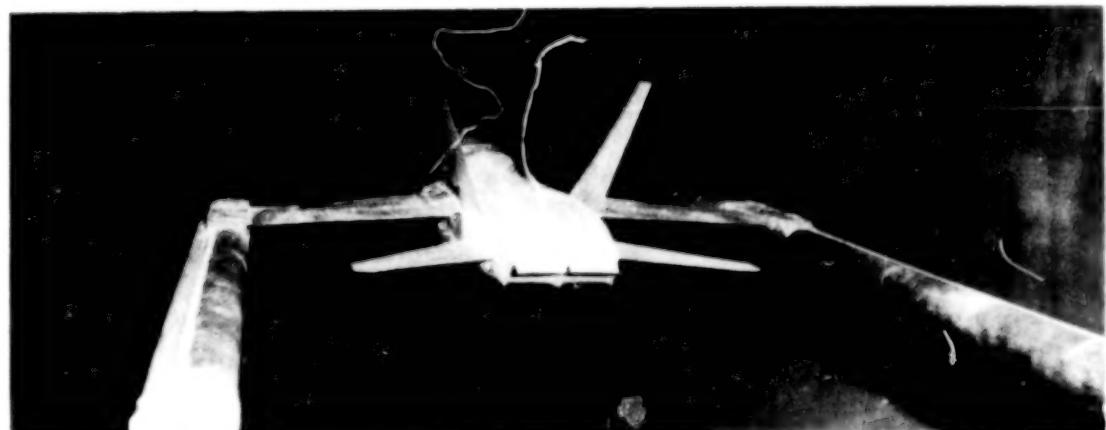


Lower flap geometry ($A_e/A_t = 1.15$)	
x	r
3.48	-3.32
5.85	-3.12
6.66	-2.92
6.92	-2.80
7.40	-2.61
7.68	-2.52
8.25	-2.35
8.81	-2.23
9.38	-2.14
9.78	-2.11

Figure 8.- Sketches of SERN nozzle. Nozzle has diverging sidewalls from FS 169.32 to FS 171.86; nozzle width from FS 171.86 to exit is 7.73 cm. All dimensions in centimeters unless otherwise specified.

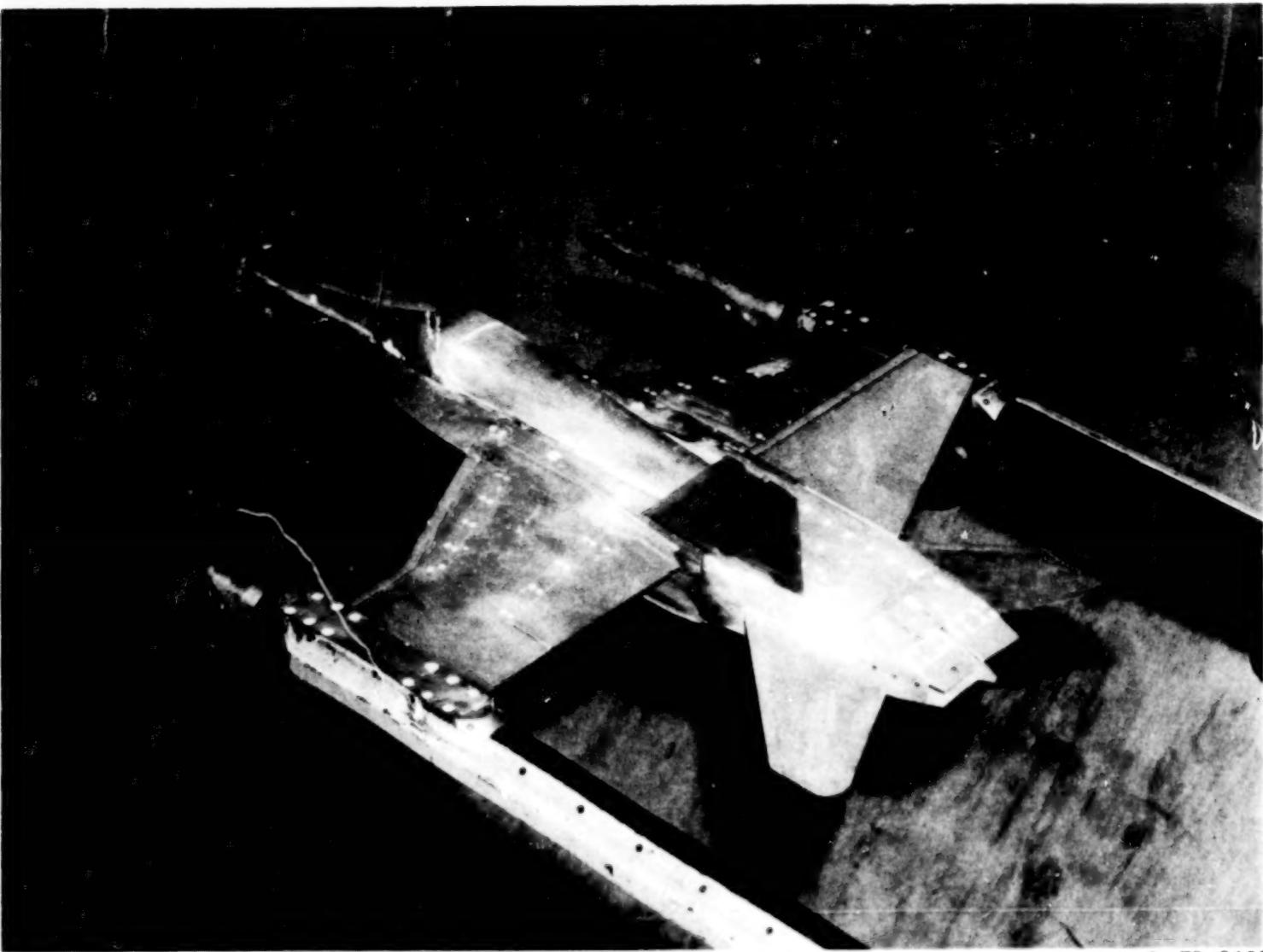


L-78-1904



L-78-1903

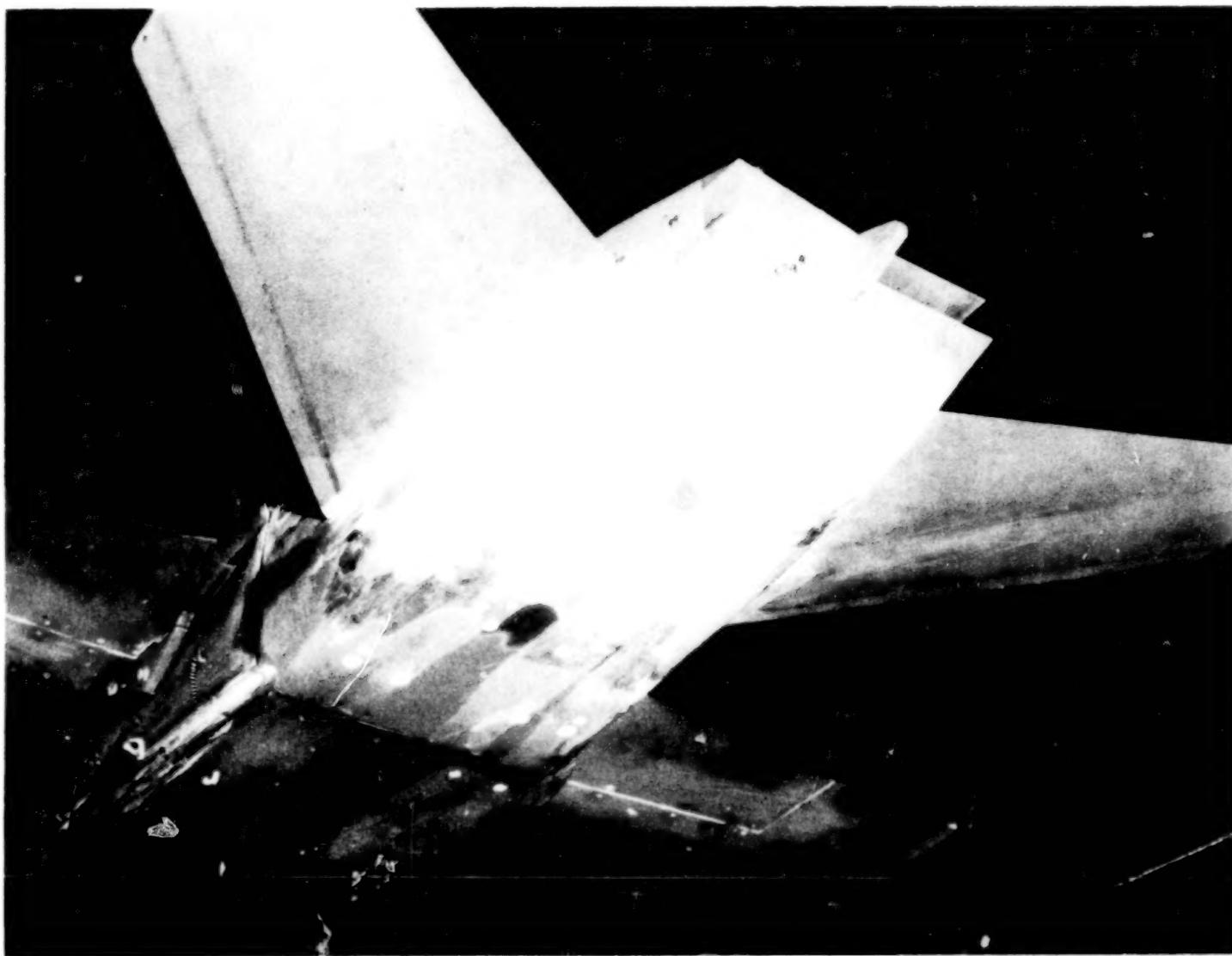
Figure 9. - SERN model installed on F-18 model with $\delta_v = 20^\circ$.



L-78-2105

Figure 10.- Overall view of 2-D C-D nozzle installed on F-18 model.

40



L-78-4817

Figure 11.- 2-D C-D nozzle, dry power, installed on F-18 model.

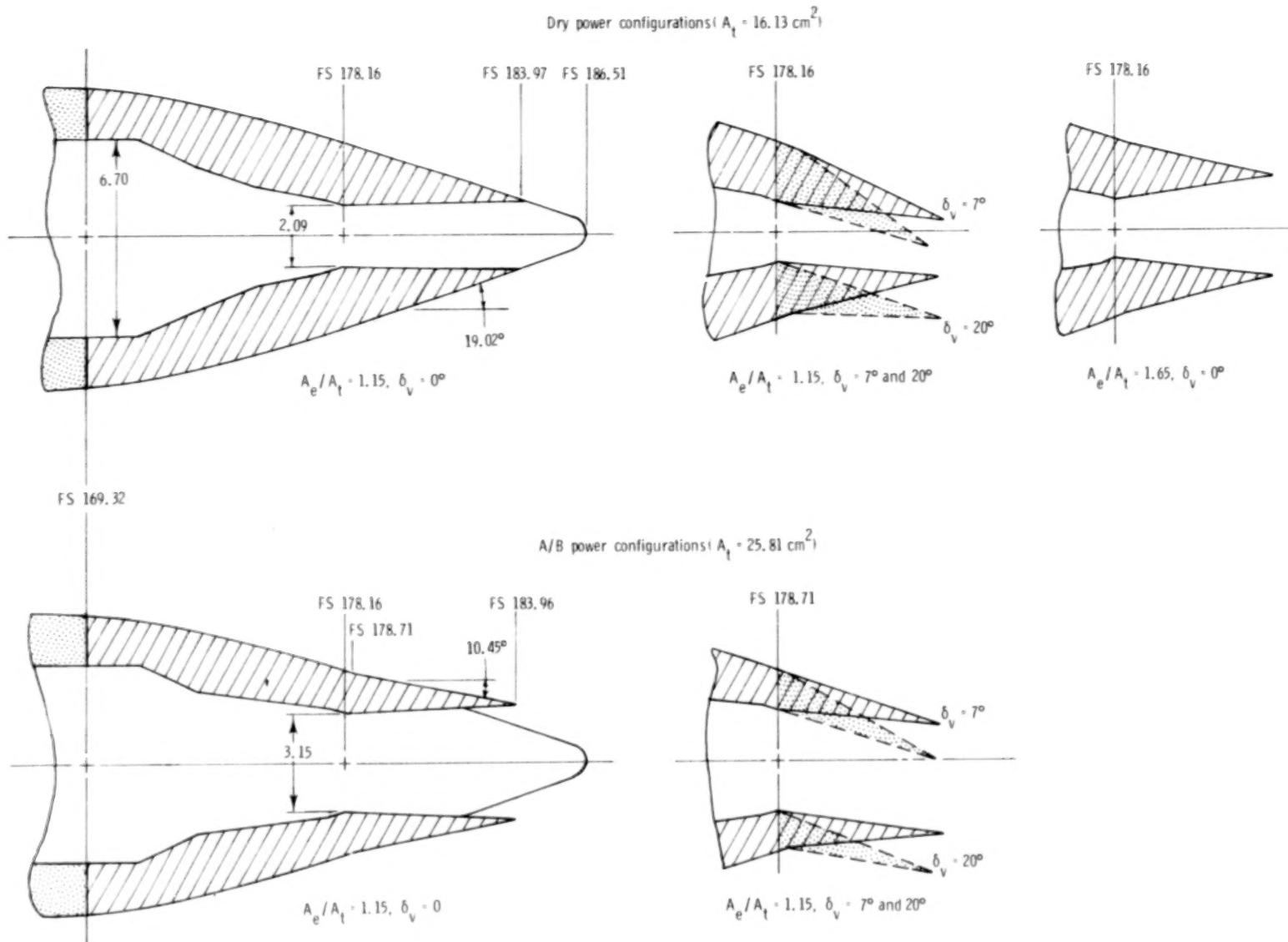
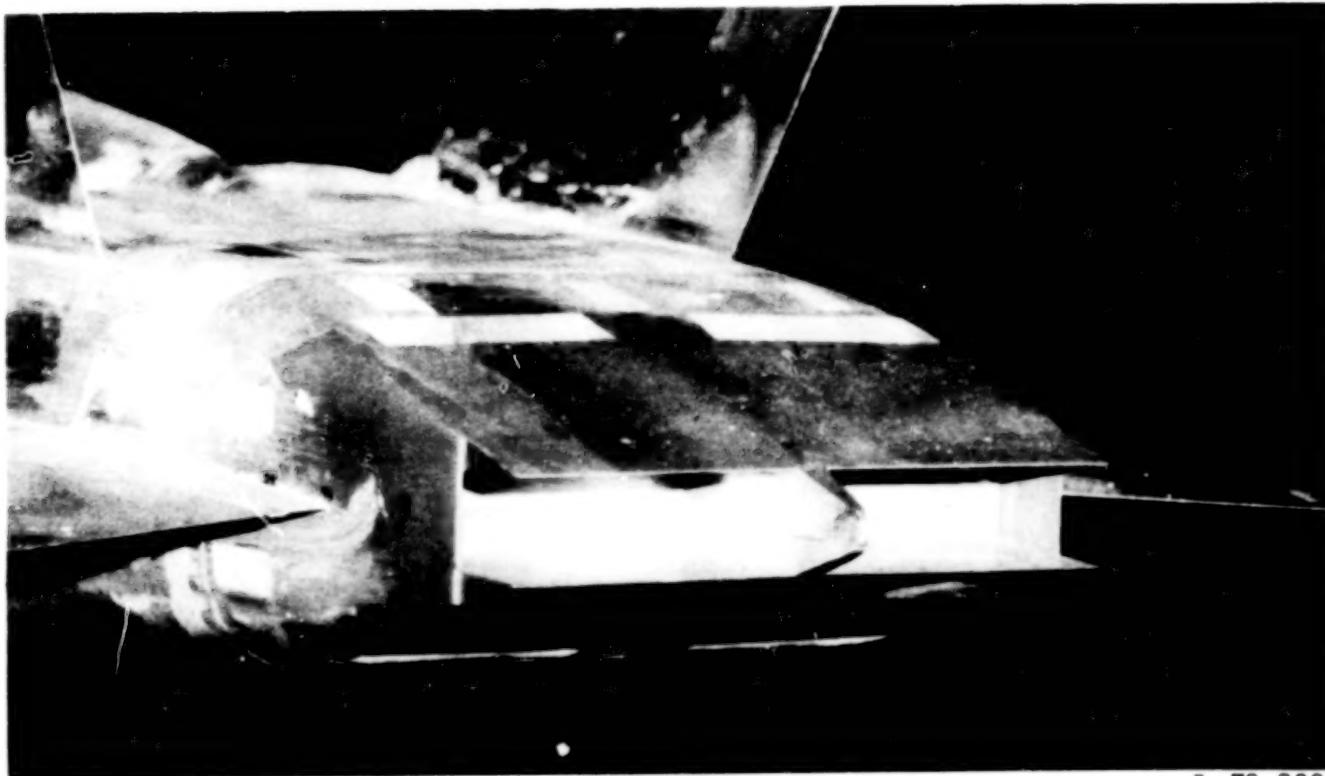


Figure 12. - Sketch of 2-D C-D nozzle. Nozzle has diverging sidewalls from FS 171.09 to FS 173.09; nozzle width from FS 173.09 to exit is 7.74 cm. All dimensions in centimeters unless otherwise specified.

42



L-78-8001

Figure 13.- 2-D C-D thrust reverser.

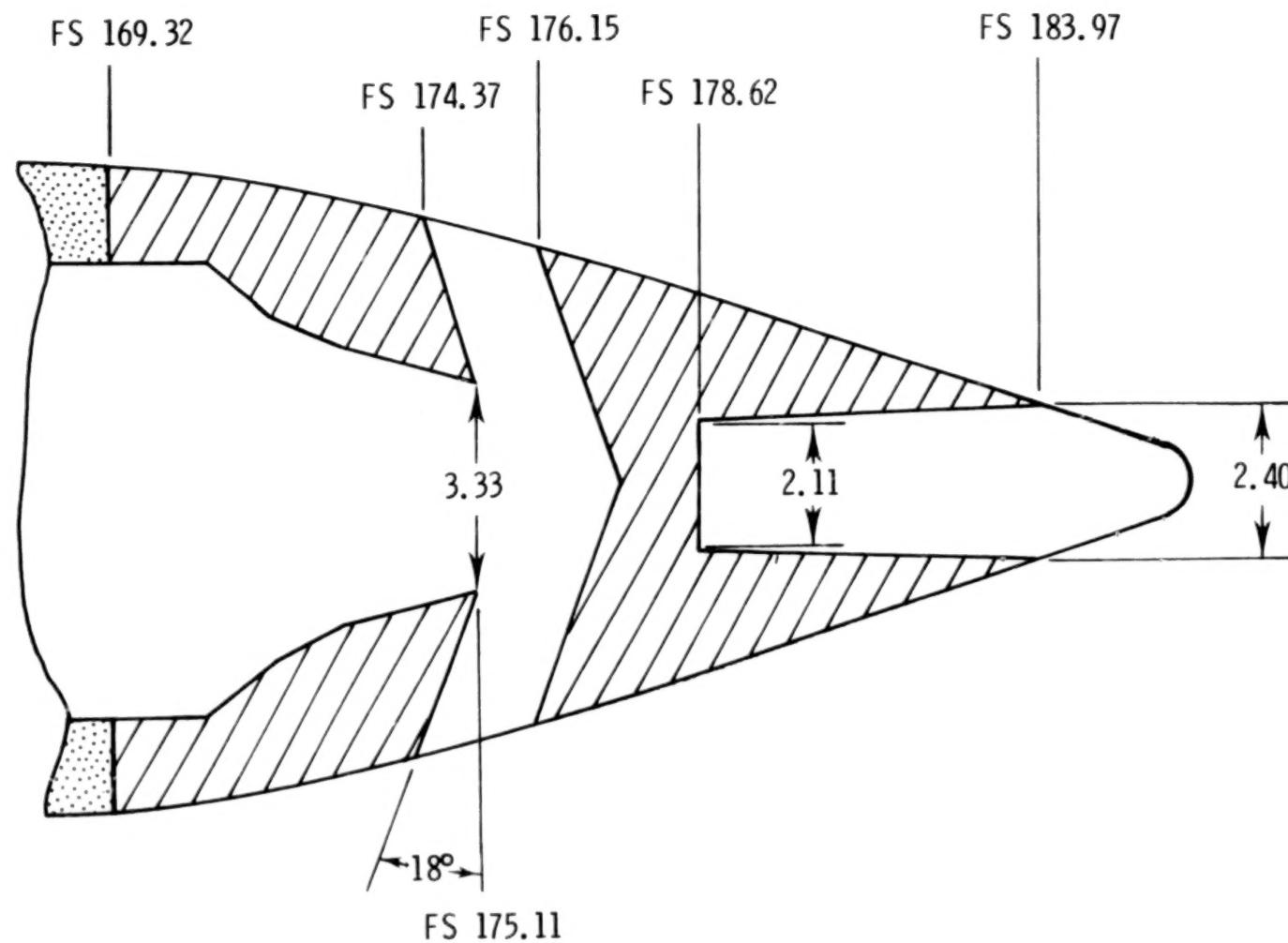
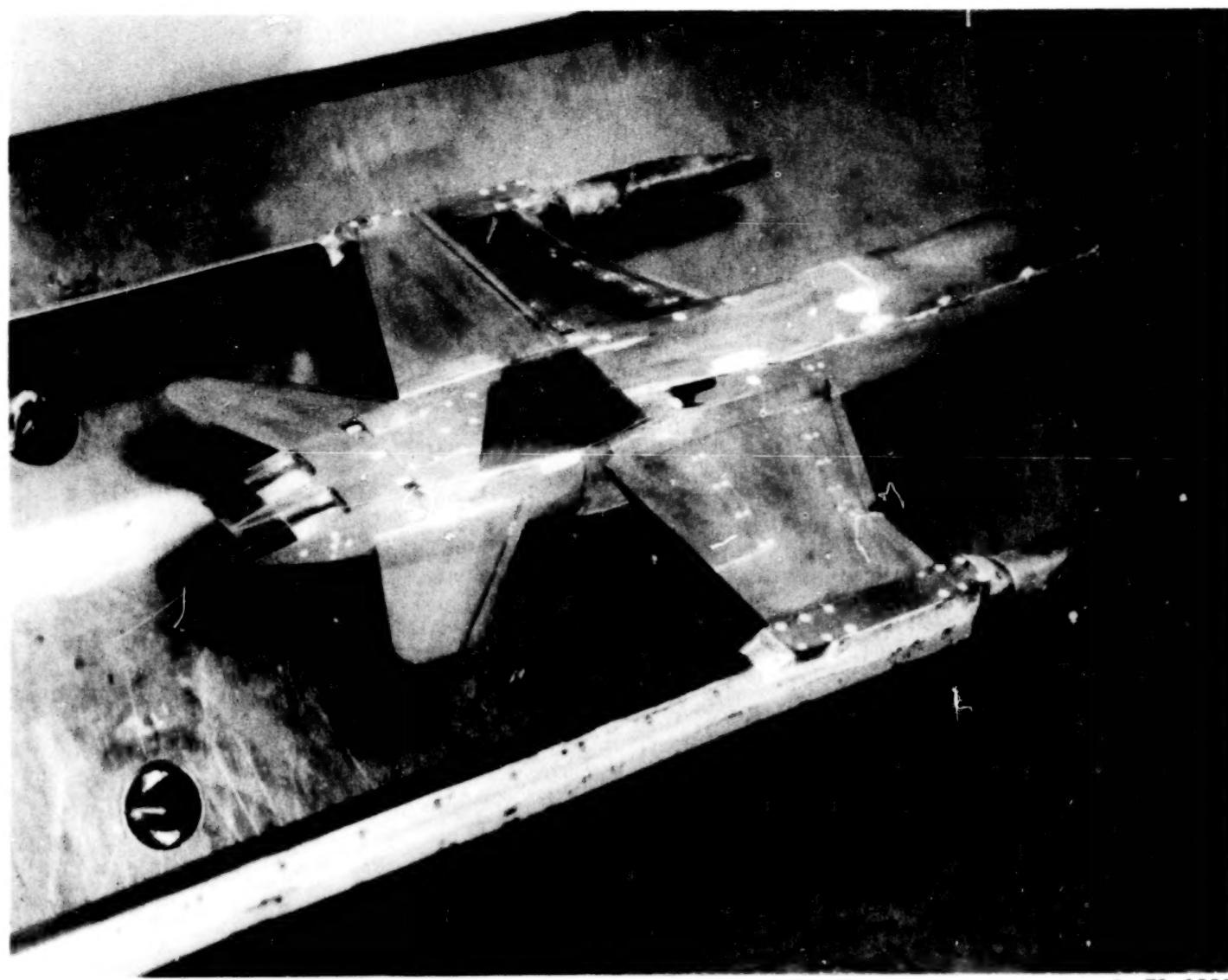


Figure 14.- Sketch of 2-D C-D thrust reverser. All dimensions in centimeters unless otherwise specified.

44



L-78-2555

Figure 15.- Overall view of wedge nozzle installed on F-18 model.

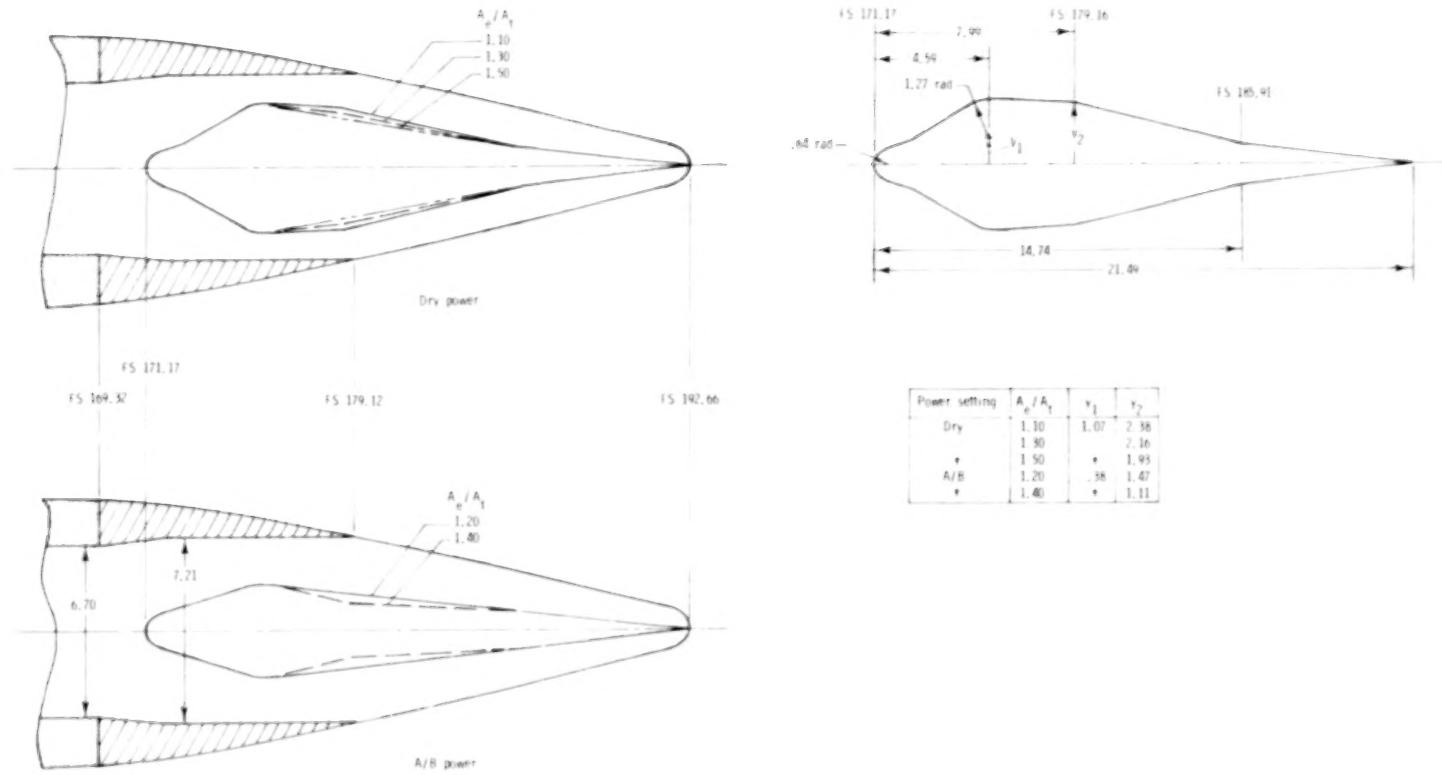
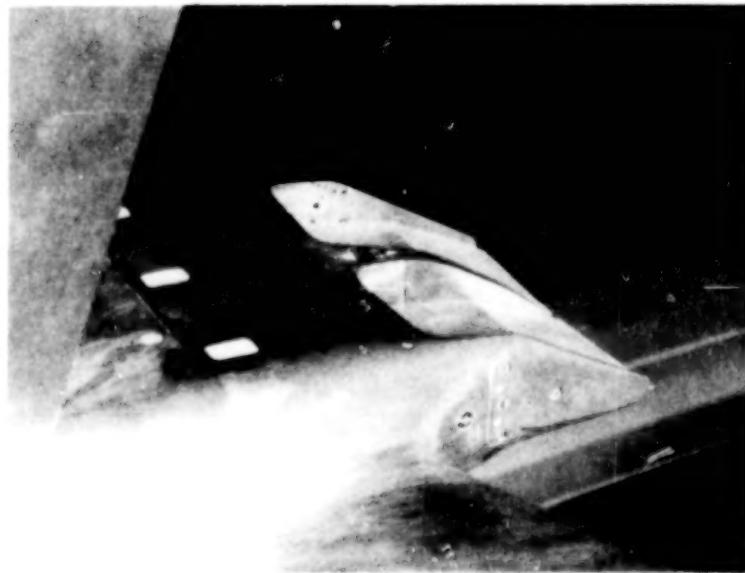


Figure 16.- Sketch of wedge nozzle. Nozzle has diverging sidewalls from FS 169.32 to FS 171.86; nozzle width from FS 171.86 to exit is 7.21 cm. All dimensions in centimeters unless otherwise specified.



L-78-2858



L-78-2856

Figure 17. - Vectored sidewalls of wedge nozzle with $\delta_v = 20^{\circ}$.

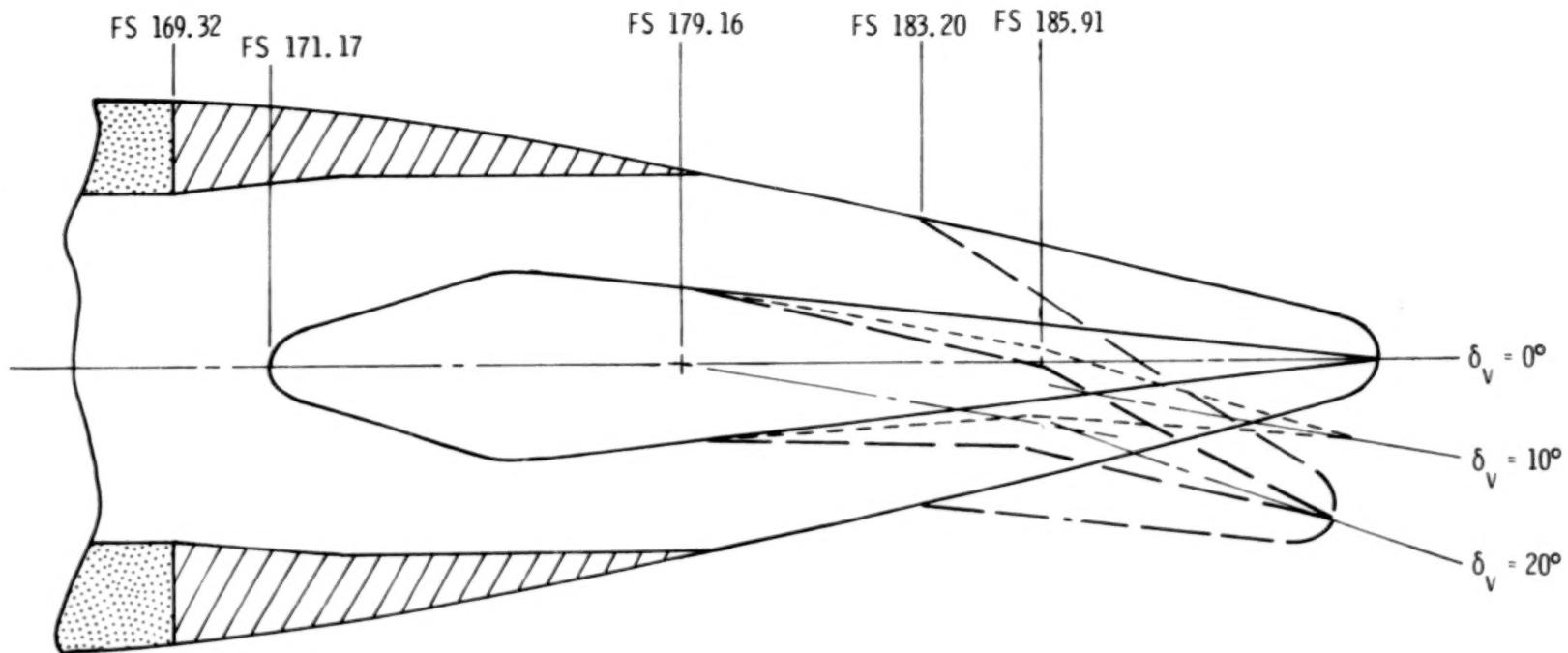


Figure 18.- Sketch showing positive vectoring modes of wedge nozzle. Vectored sidewall shown only for $\delta_v = 20^\circ$. All dimensions in centimeters unless otherwise noted.



50% deployed, no sideplates



100% deployed, no sideplates



50% deployed, sideplates



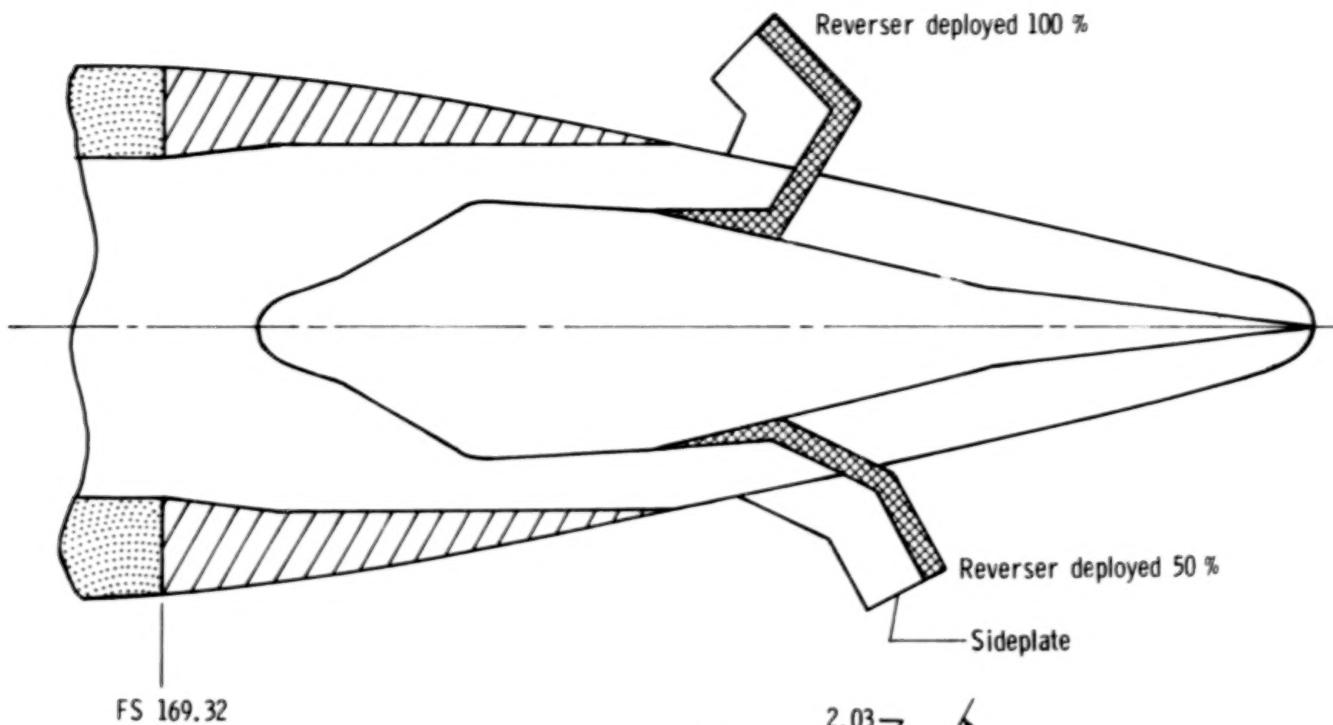
100% deployed, sideplates



Overall view, 100% deployed, sideplates

L-80-112

Figure 19.- Details of wedge nozzle thrust reverser.



Reverser, %	θ , deg	β , deg	ϕ , deg
50	4.5	25.5	63.0
100	0.0	60.0	135.0

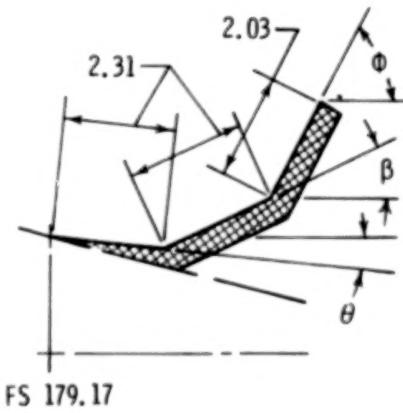


Figure 20.- Sketch showing thrust reversing modes of wedge nozzle. All dimensions in centimeters unless otherwise specified.

50

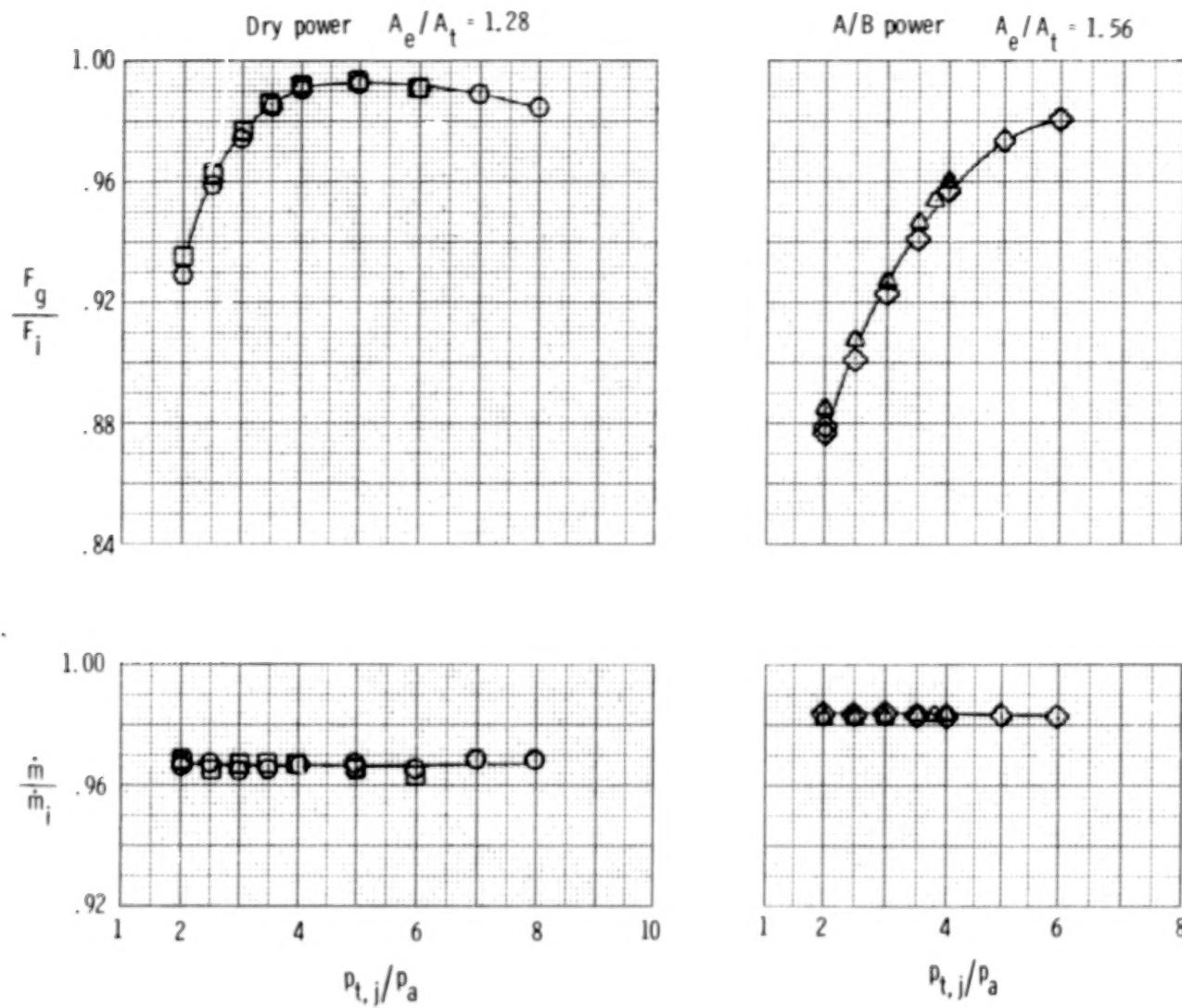


Figure 21.- Unvectored static performance for axisymmetric nozzle.
Different symbols represent repeat runs.

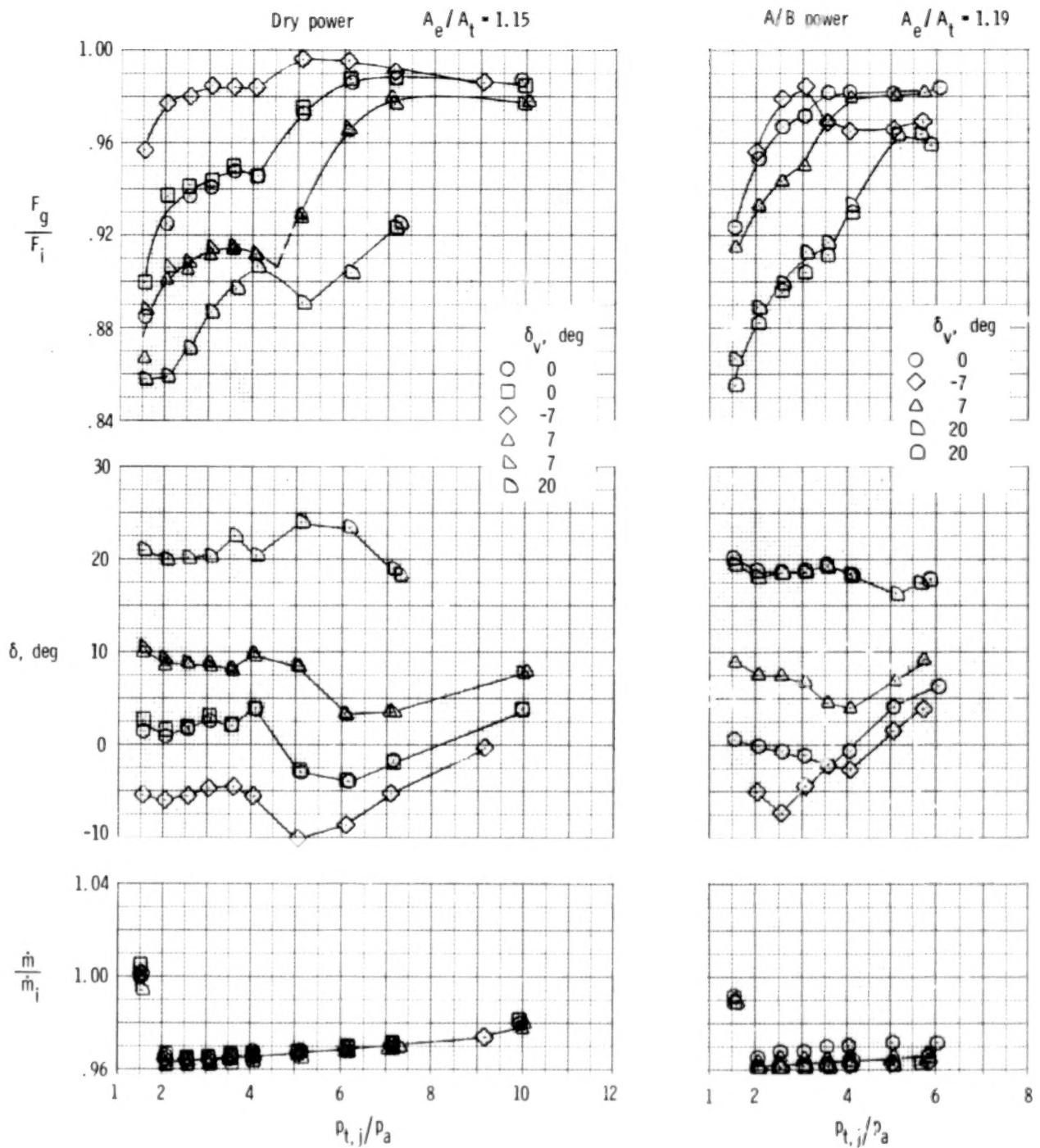


Figure 22.- Static vectoring performance for SERN nozzle.

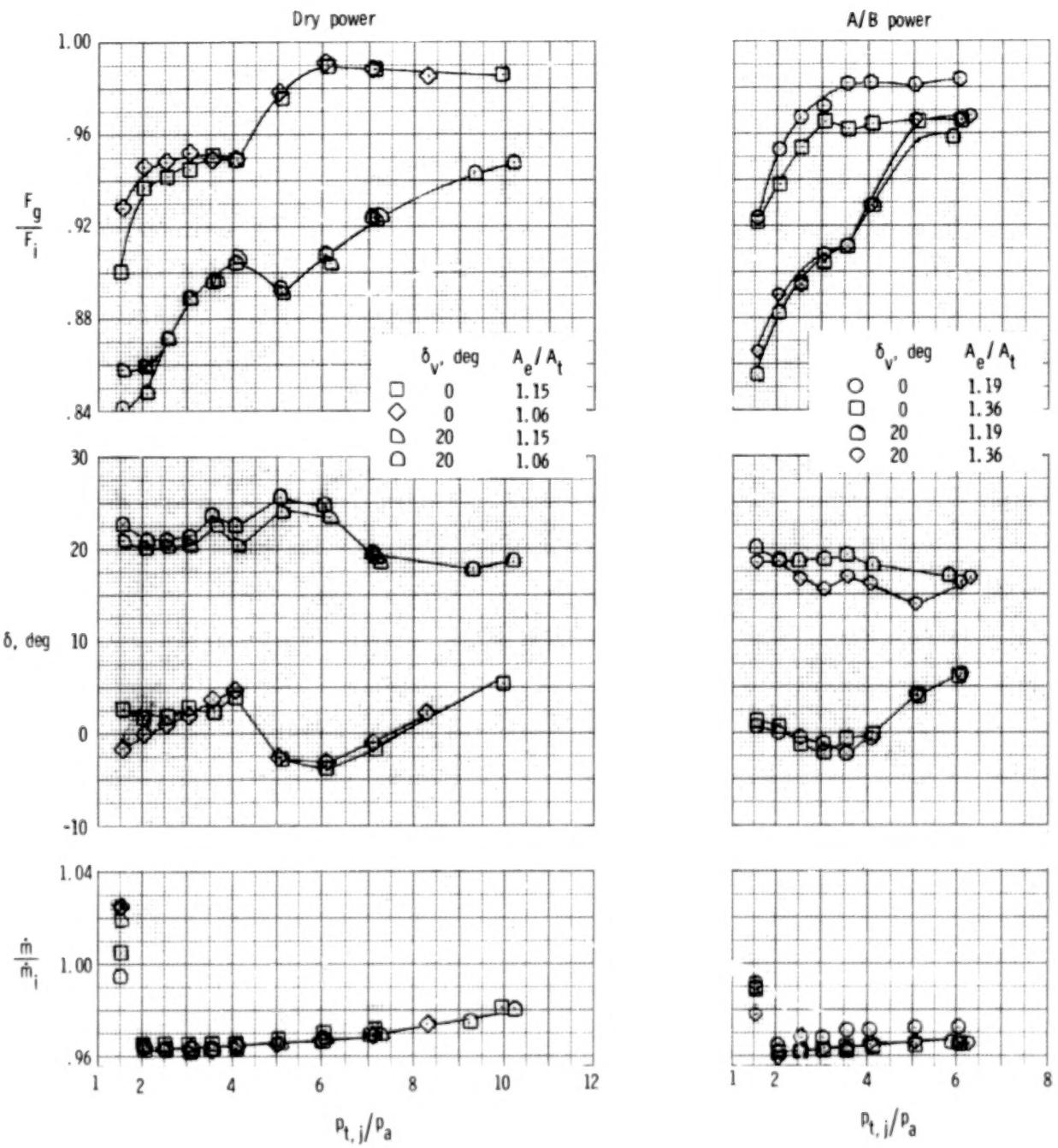


Figure 23.- Effect of area ratio on static vectoring performance of SERN nozzle.

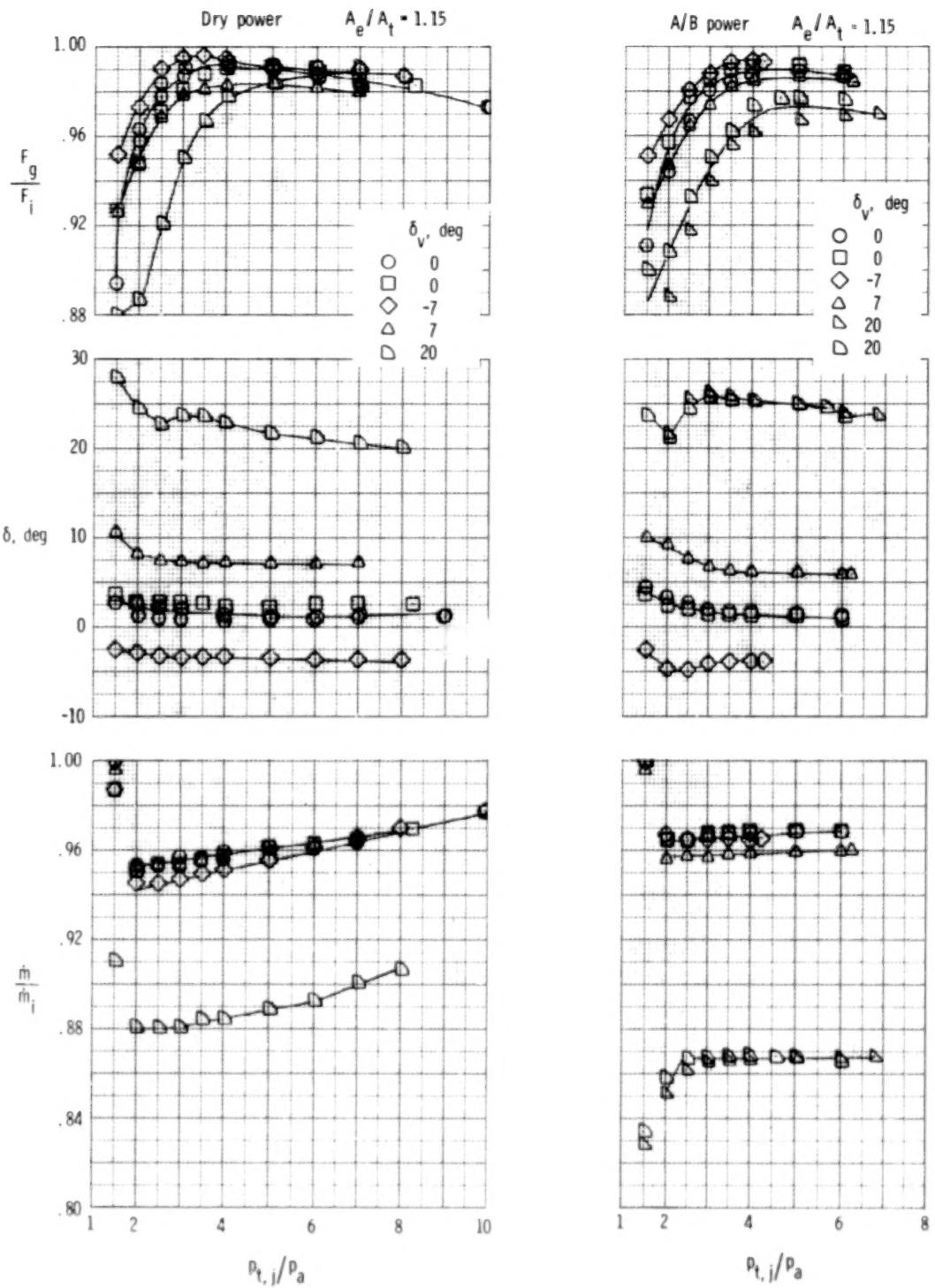


Figure 24.- Static vectoring performance for 2-D C-D nozzle.

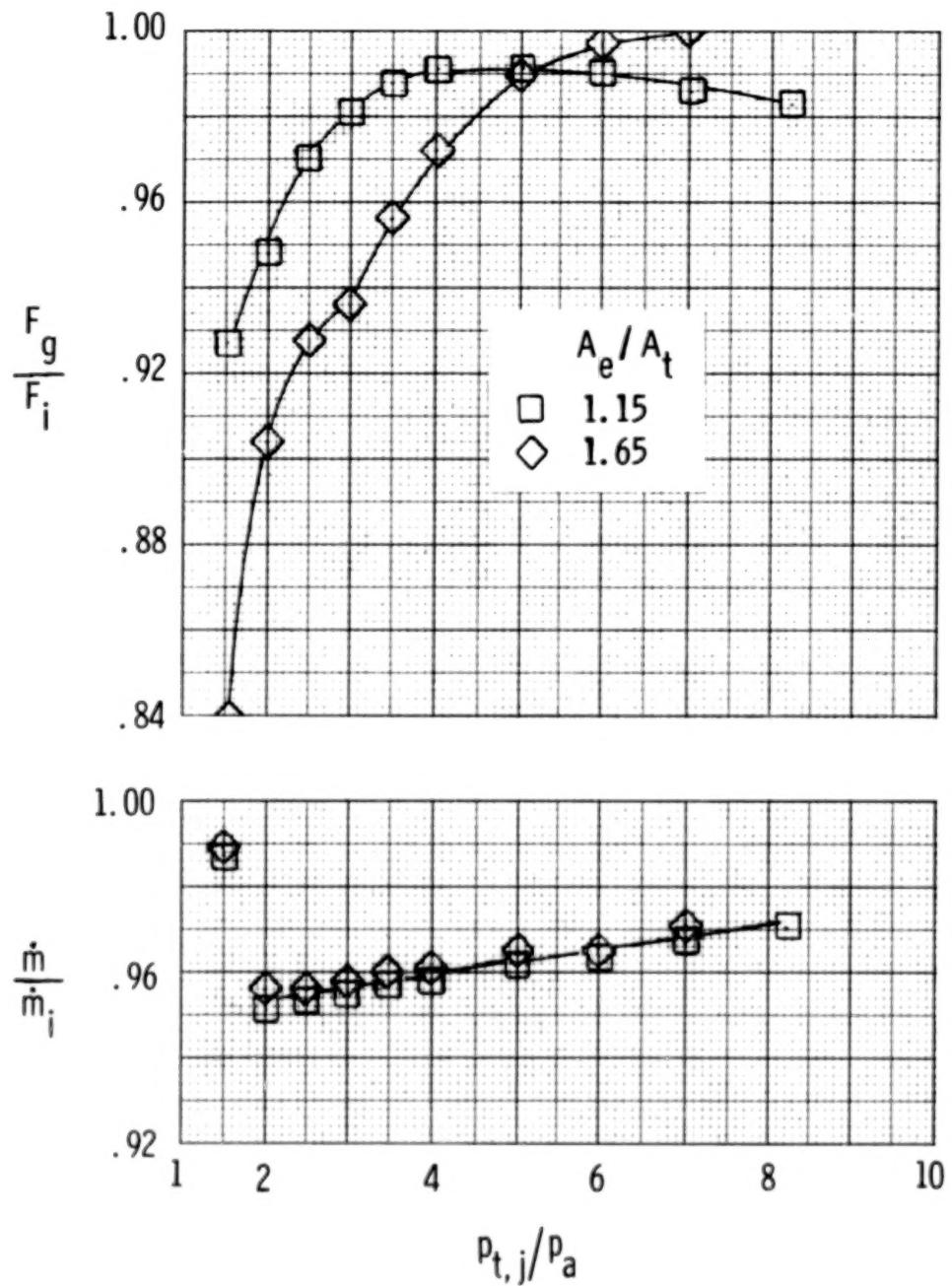


Figure 25. - Effect of area ratio on static unvectored performance for 2-D C-D nozzle, dry power.

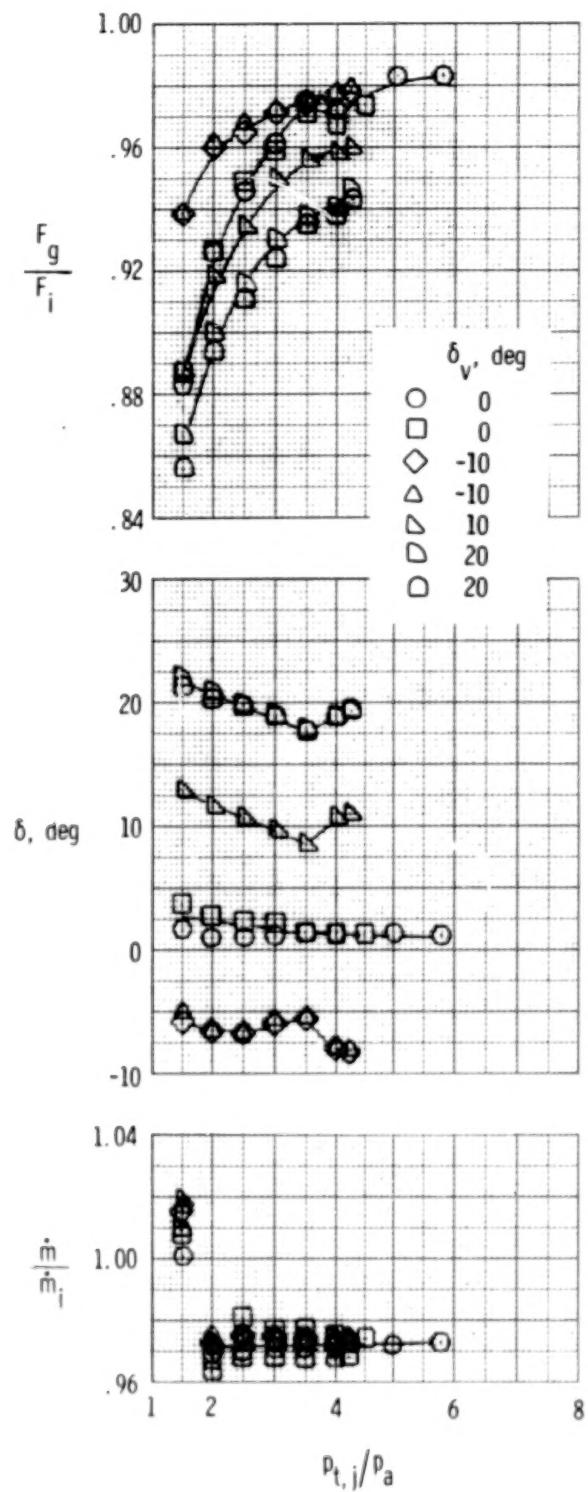


Figure 26.- Static vectoring performance for wedge nozzle, A/B power. $A_e/A_t = 1.20$.

56

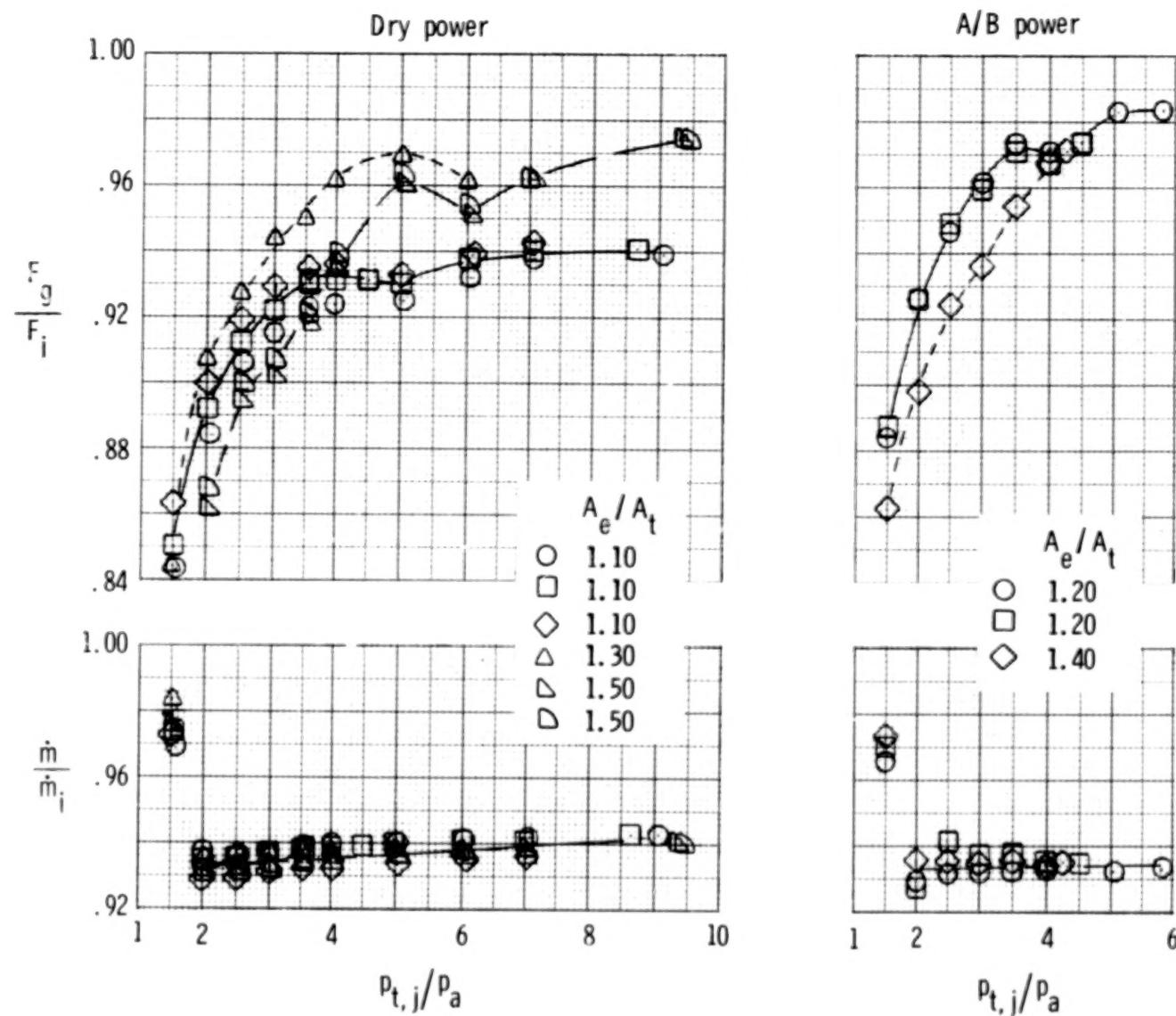


Figure 27.- Effect of area ratio on static unvectored performance for wedge nozzle.

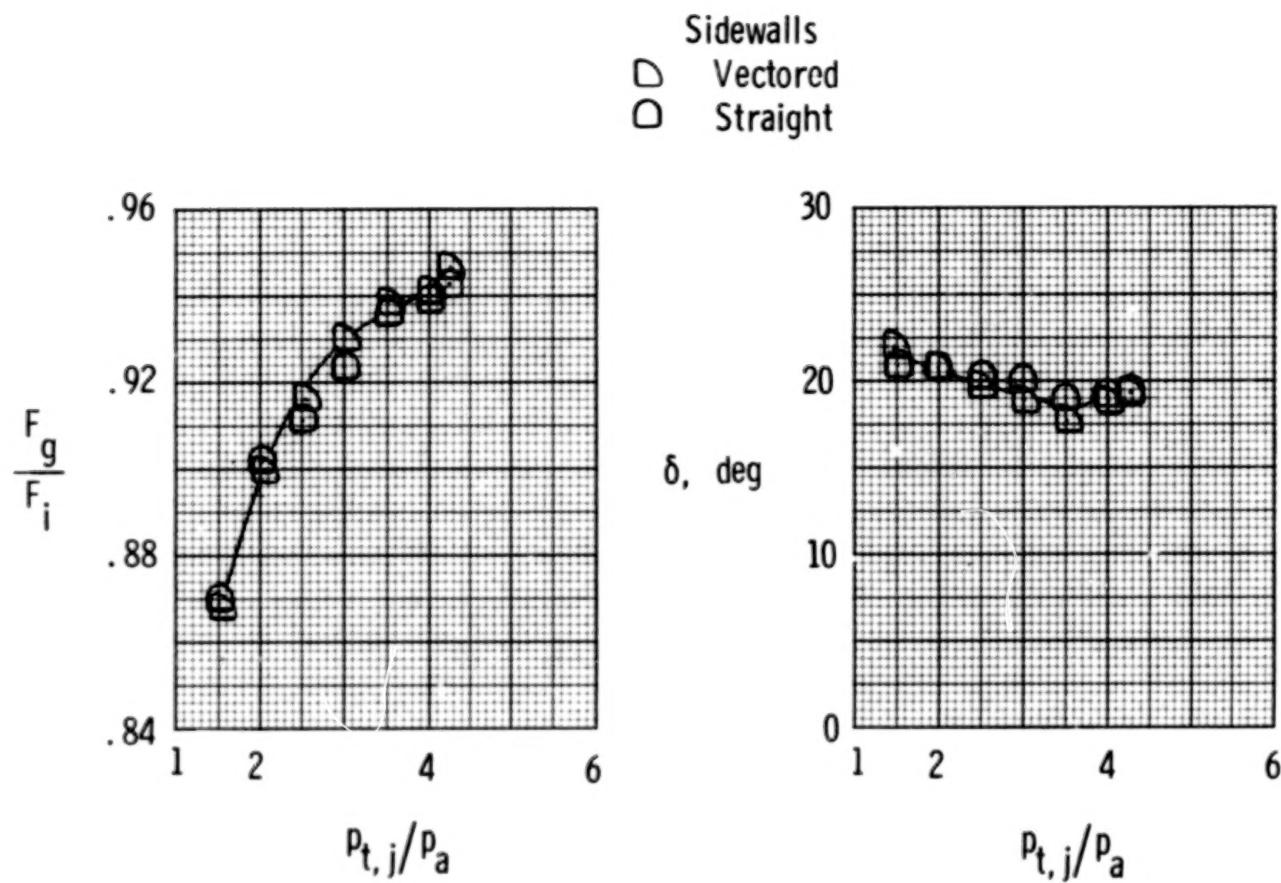


Figure 28.- Effect of sidewall geometry on wedge nozzle static performance.

$\delta_v = 20^\circ$; A/B power; $A_e/A_t = 1.20$.

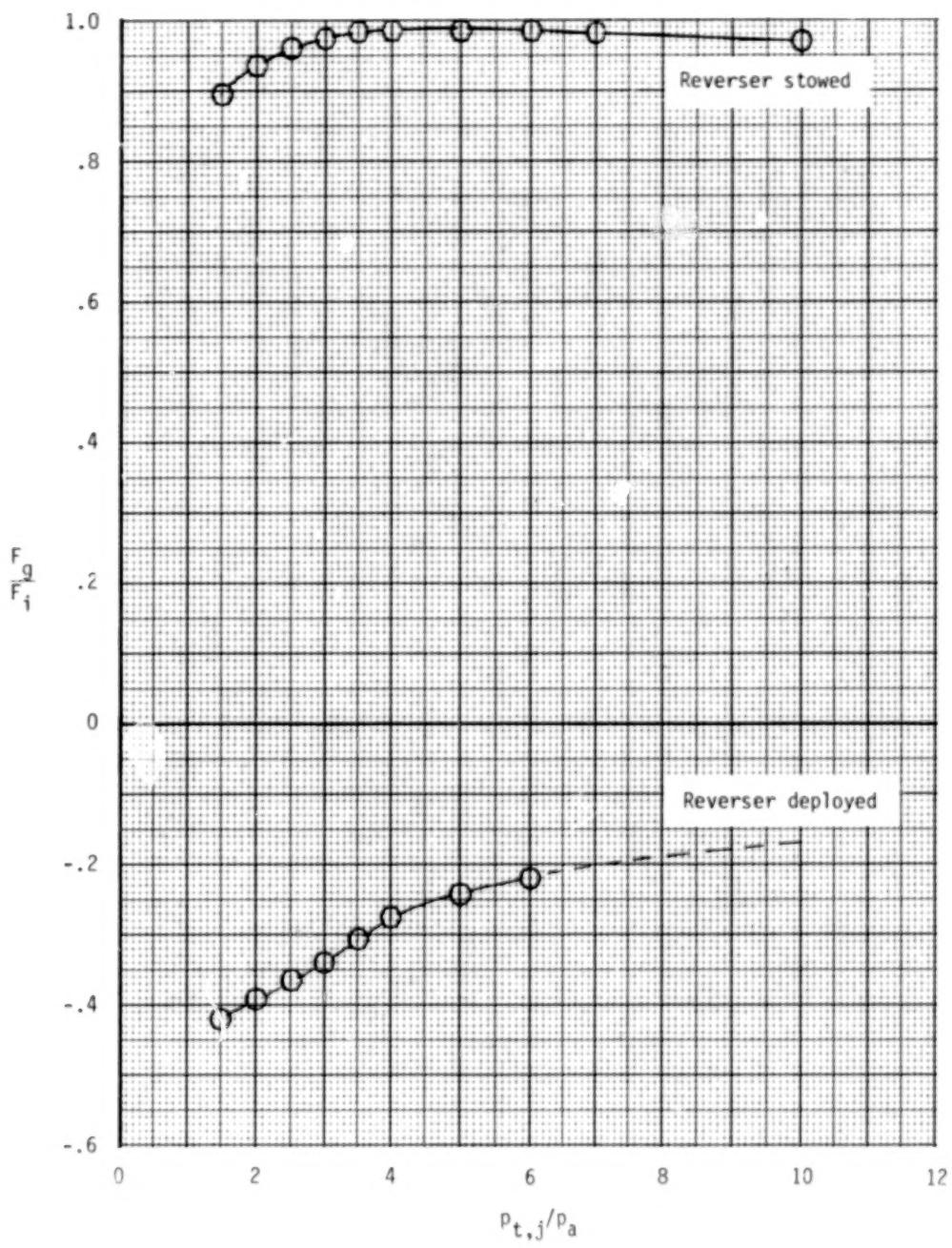


Figure 29.- Static reverse thrust performance for 2-D C-D nozzle, dry power. Dashed line indicates extrapolated data.

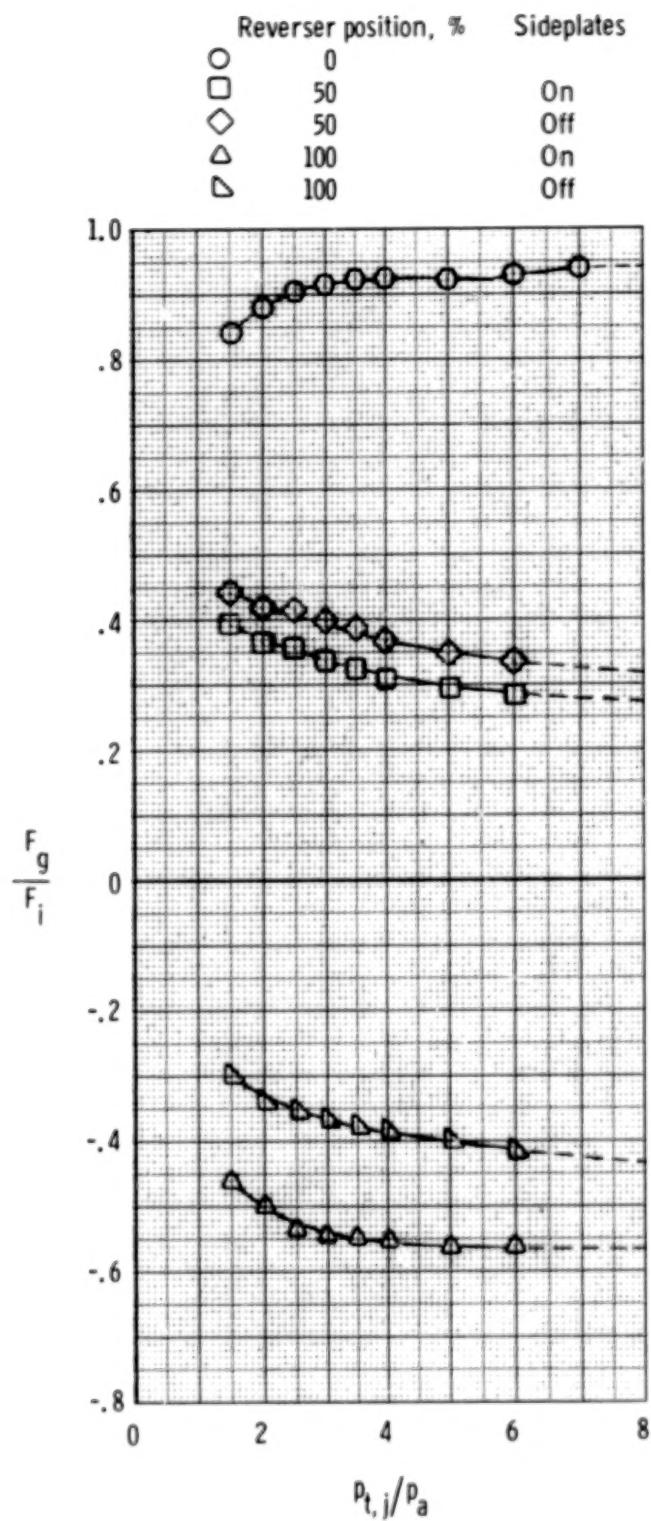


Figure 30.- Static reverse thrust performance for wedge nozzle, dry power. Dashed line indicates extrapolated data. $A_e/A_t = 1.10$.

60

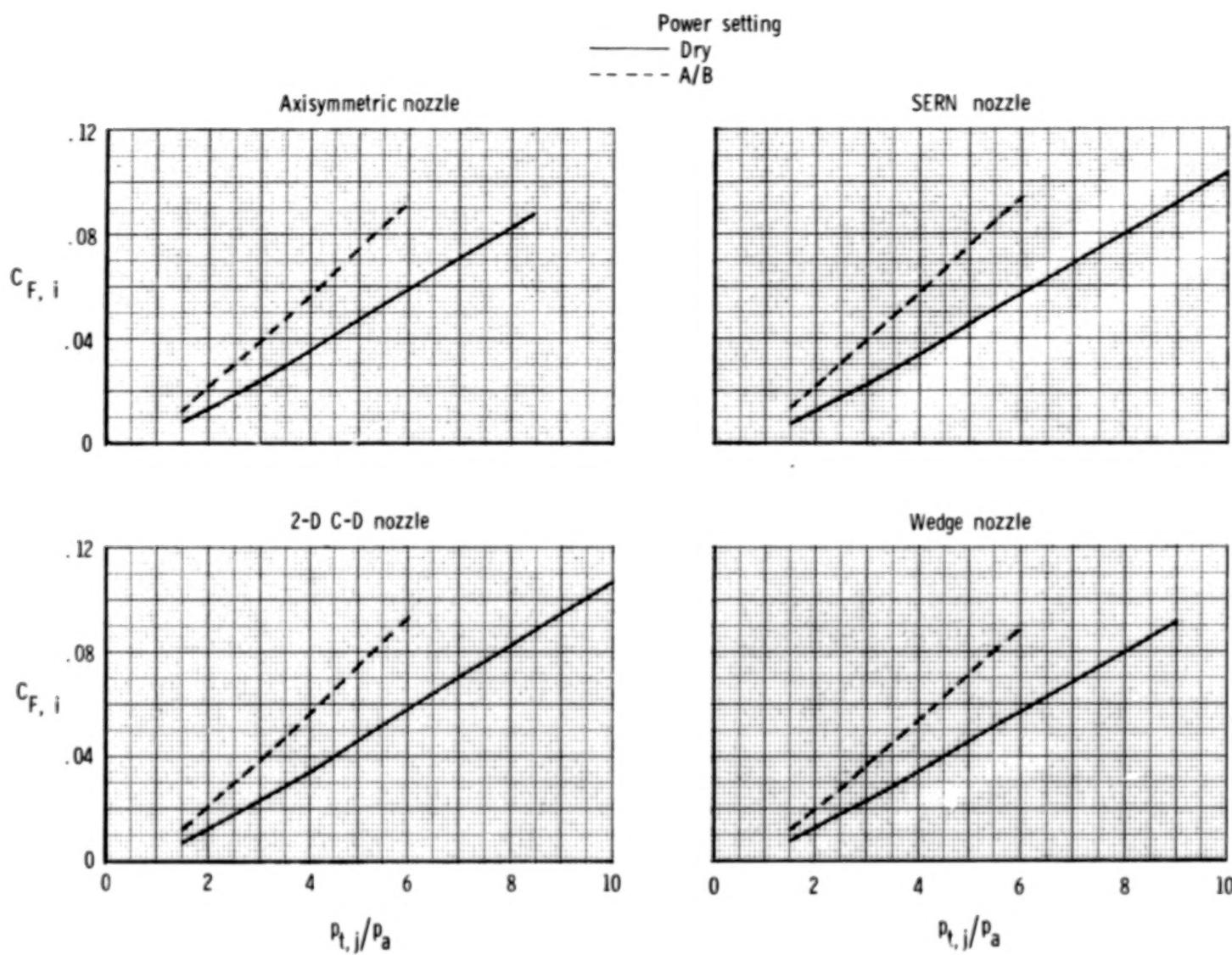
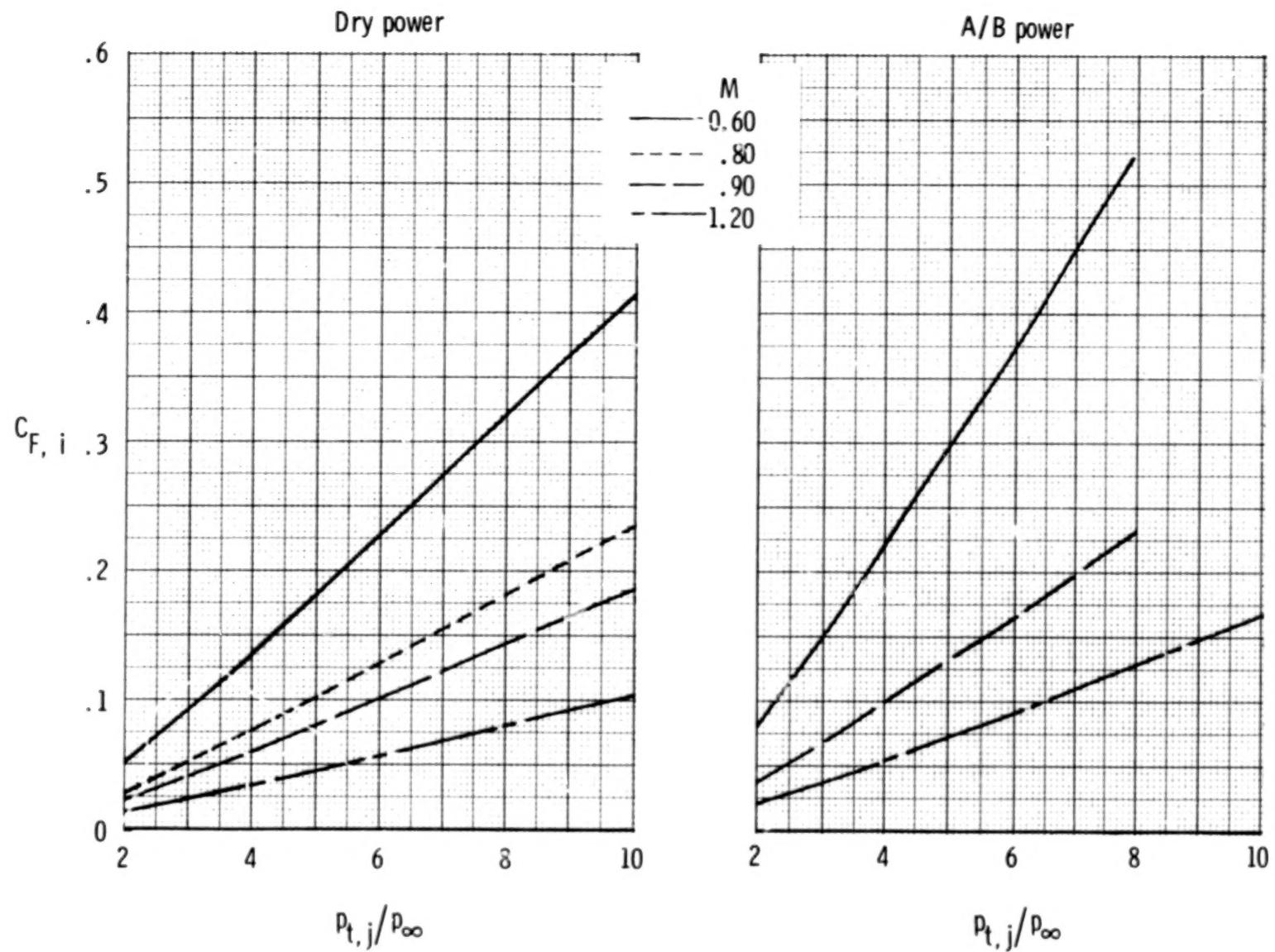


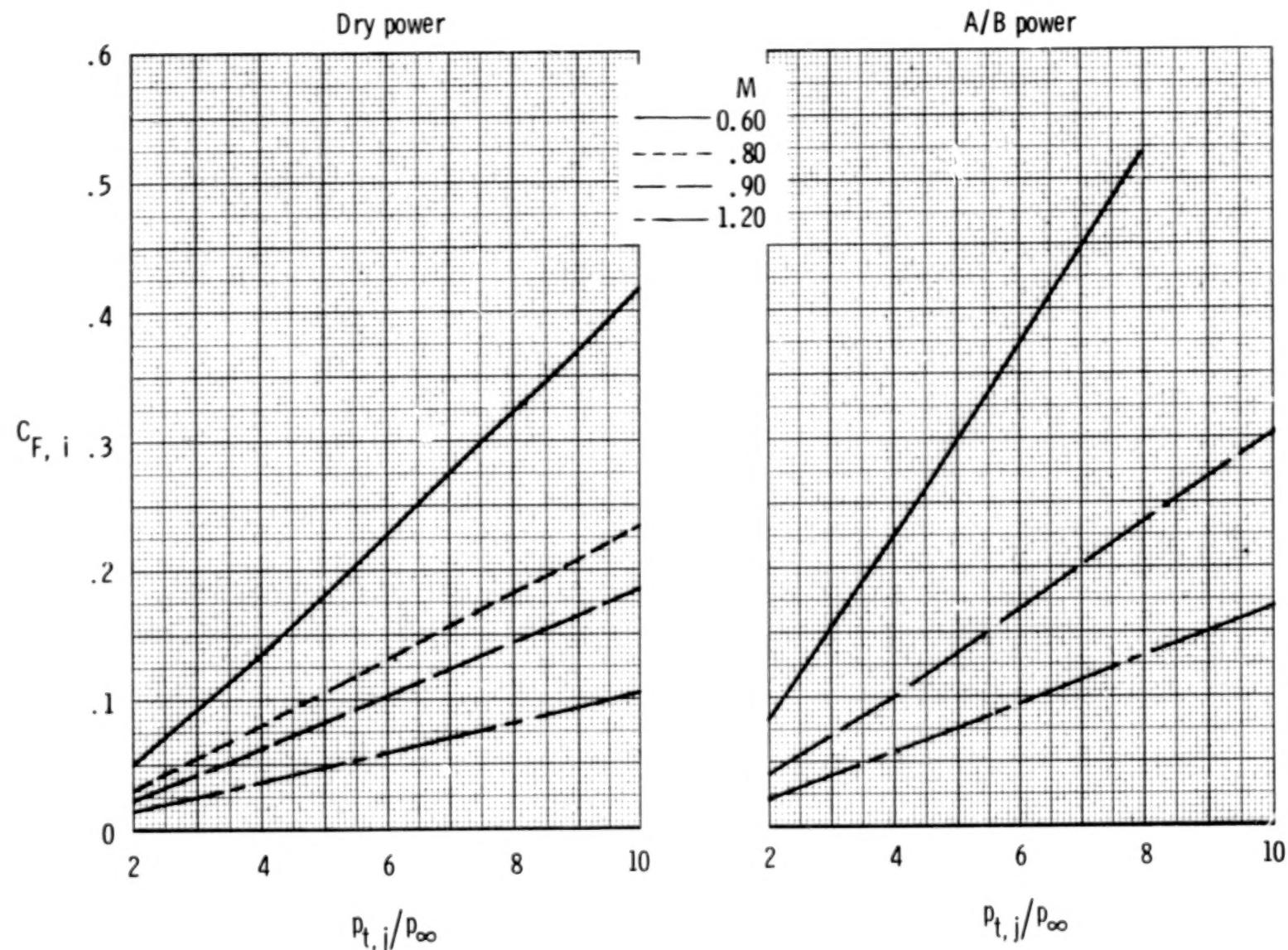
Figure 31.- Variation of ideal thrust coefficient with nozzle pressure ratio for various nozzles tested. $M = 0$.



(a) Axisymmetric nozzle.

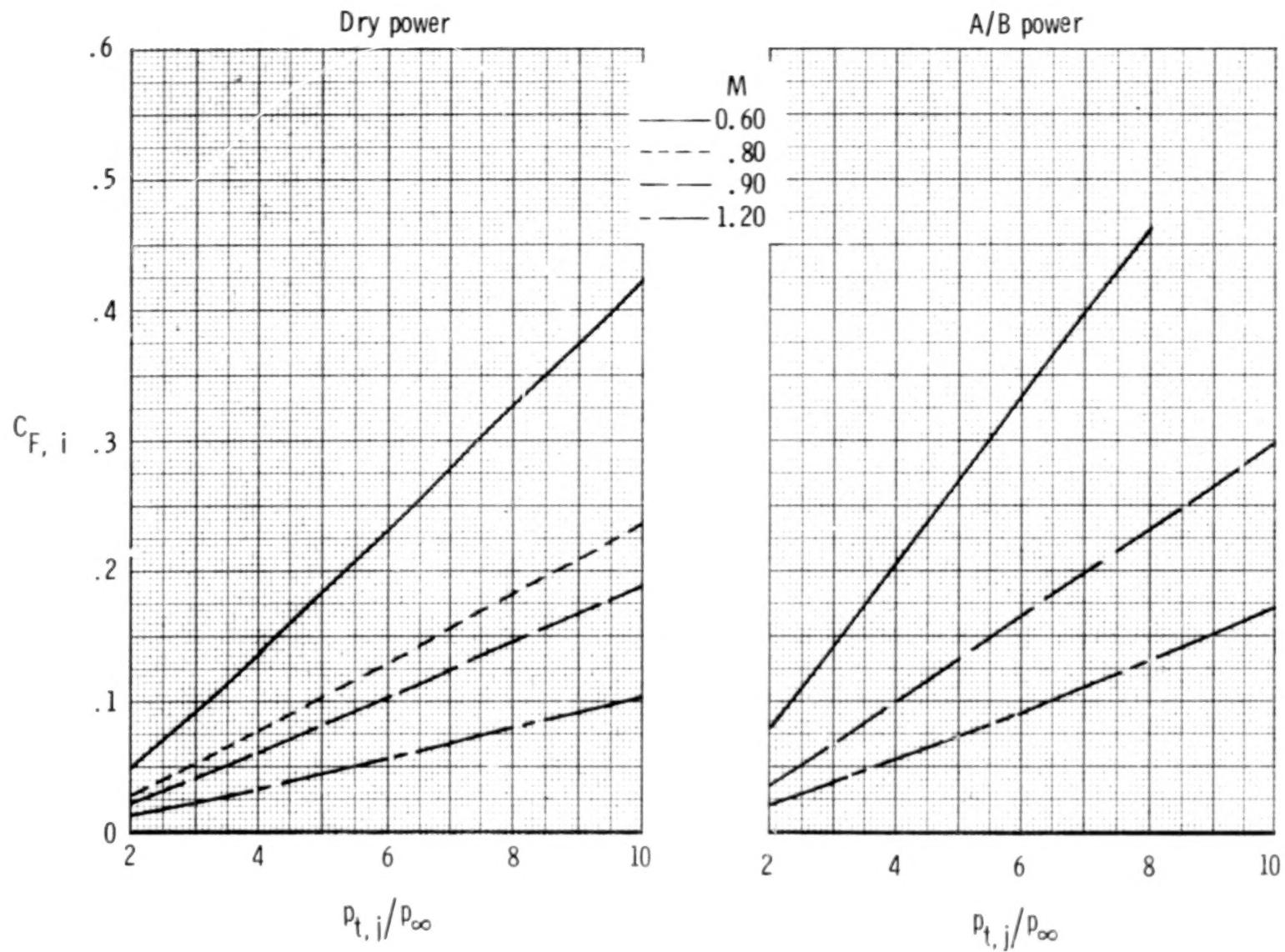
Figure 32.- Variation of aerodynamic ideal thrust coefficient with nozzle pressure for various nozzles tested.

62



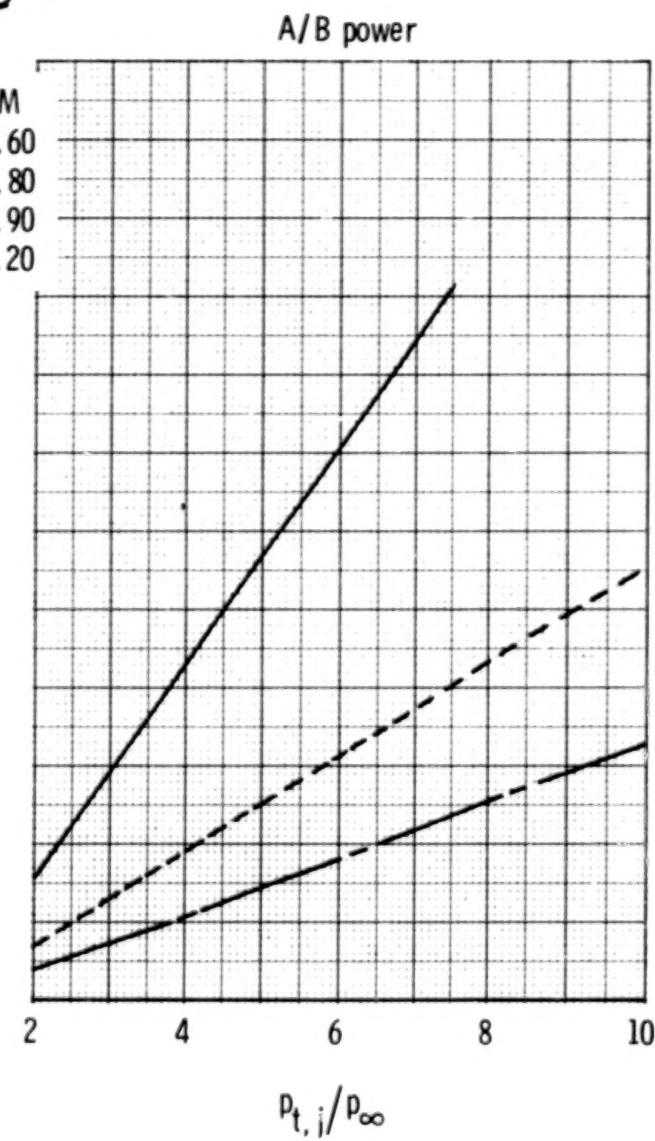
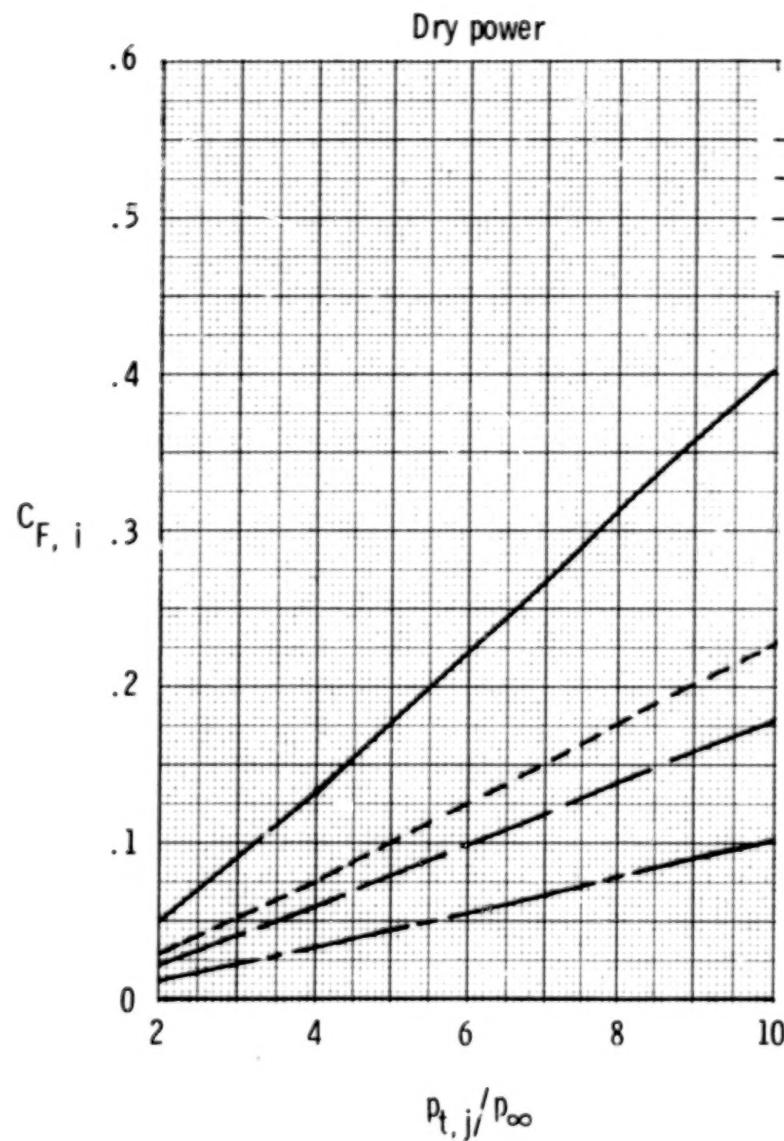
(b) SERN nozzle.

Figure 32. - Continued.



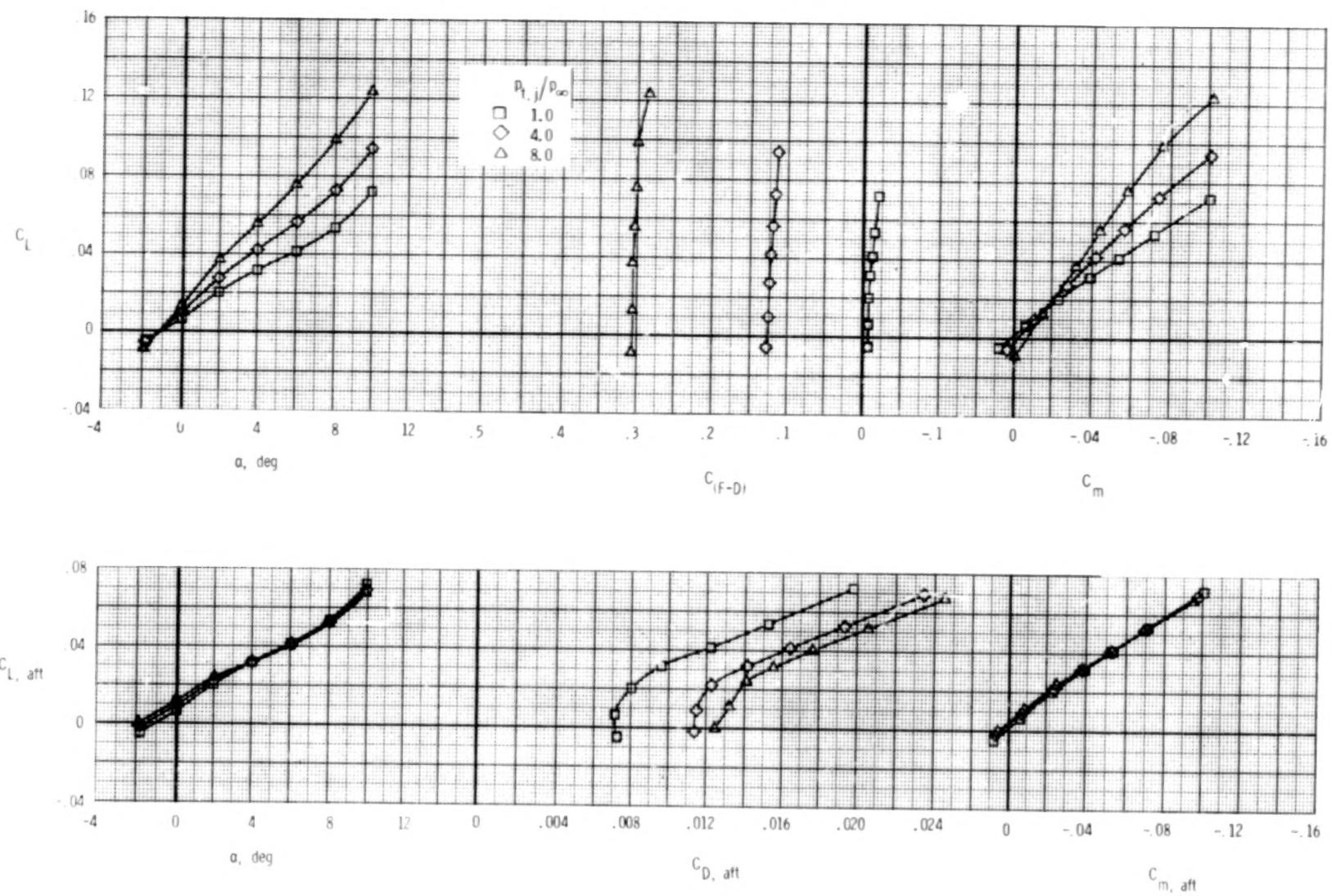
(c) 2-D C-D nozzle.

Figure 32.- Continued.



(d) Wedge nozzle.

Figure 32.- Concluded.



(a) $M = 0.60$.

Figure 33.- Longitudinal afterbody aerodynamic characteristics, axisymmetric nozzles, dry power.

$$\delta_h = 0^\circ; \quad \delta_v = 0^\circ; \quad A_e/A_t = 1.28.$$

66

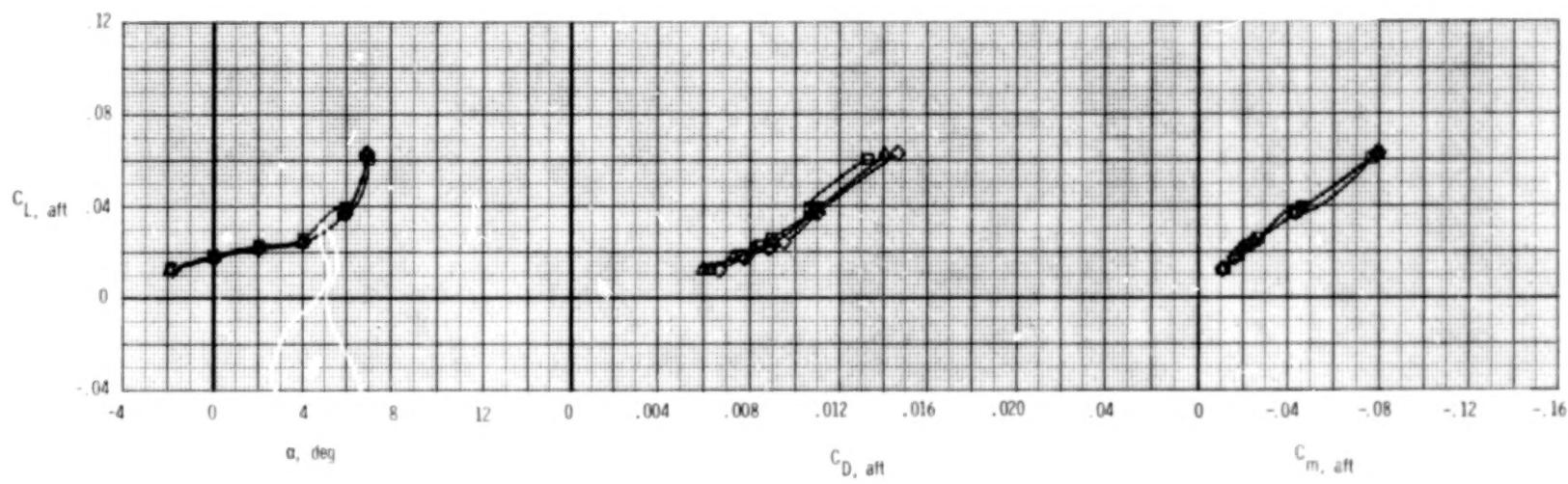
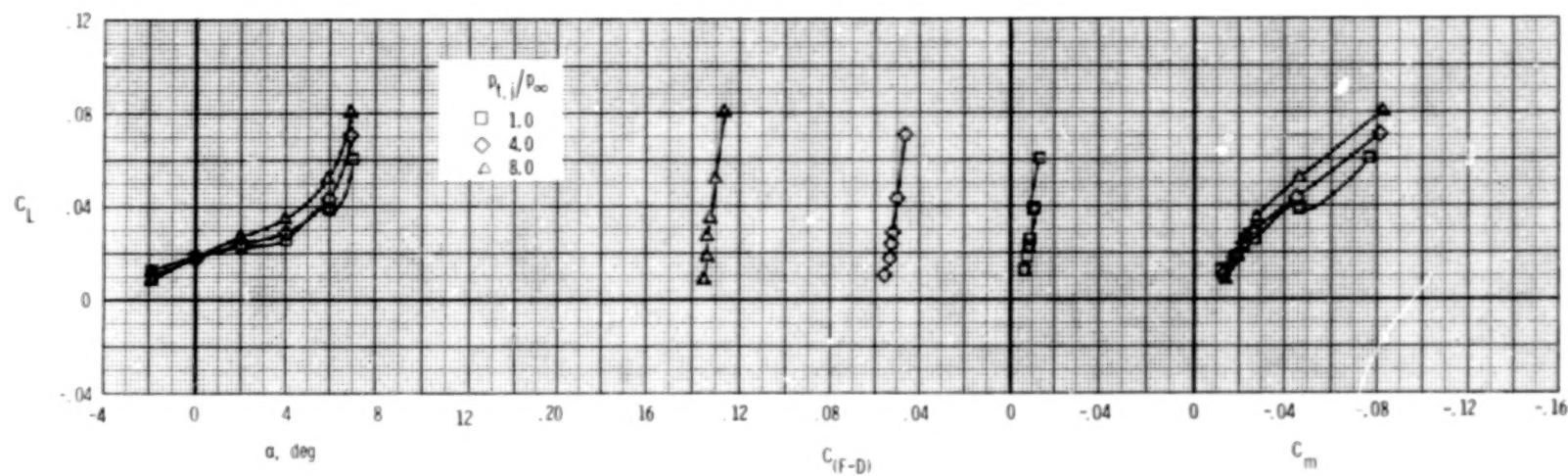
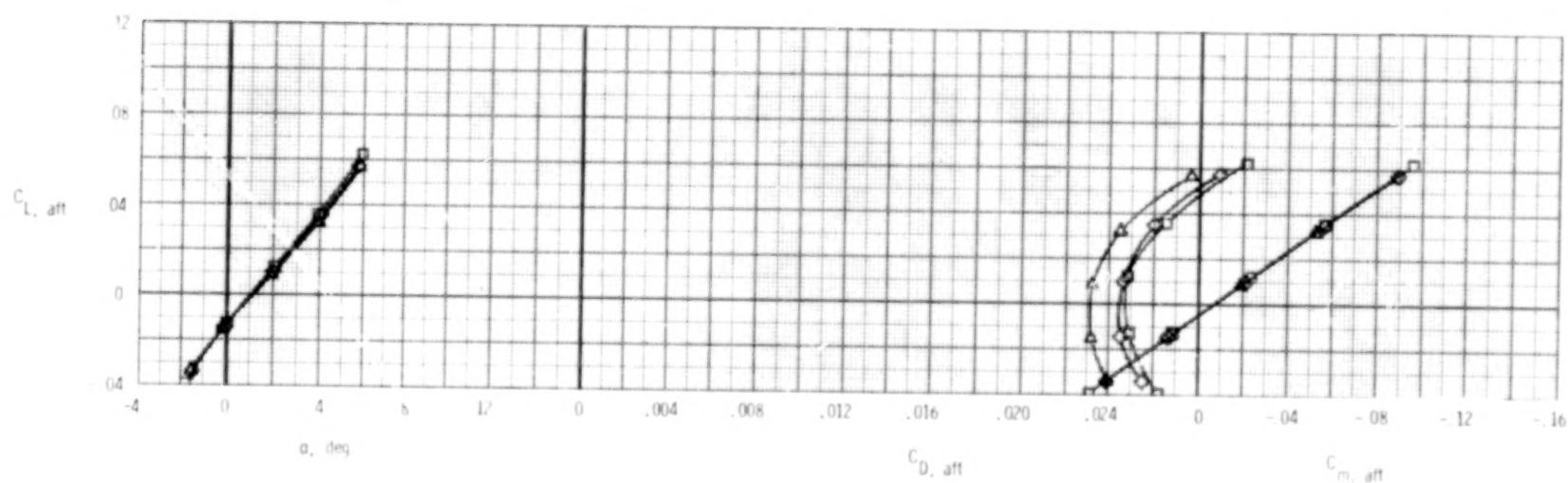
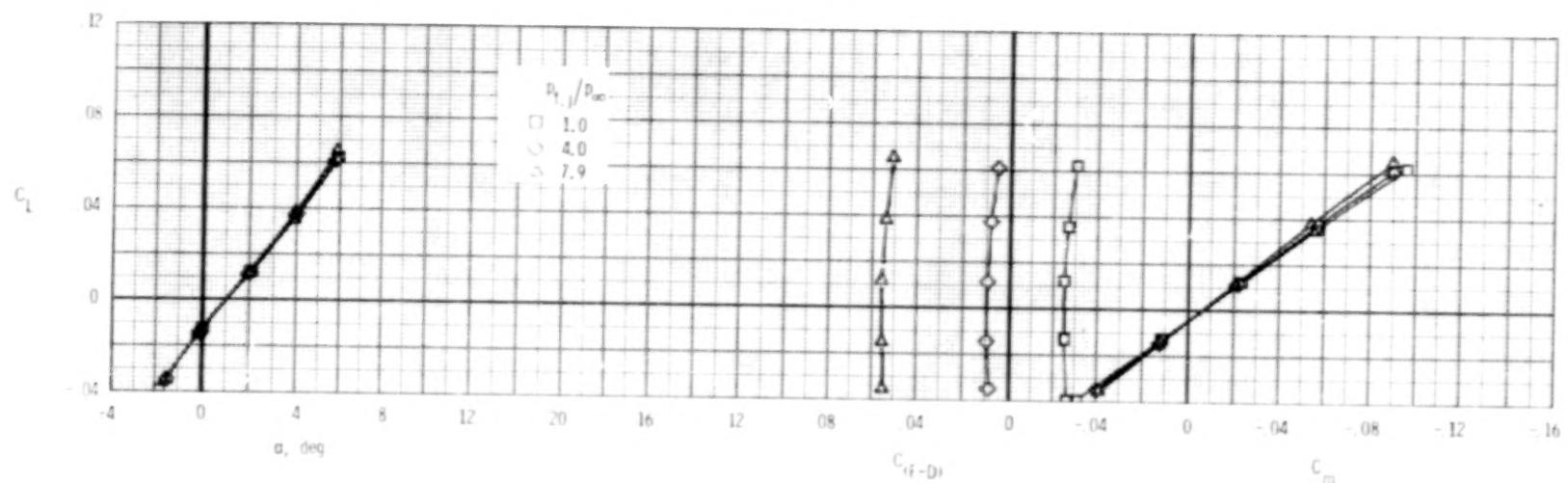
(b) $M = 0.90$.

Figure 33.- Continued.



(c) $M = 1.20$.

Figure 33. - Concluded.

68

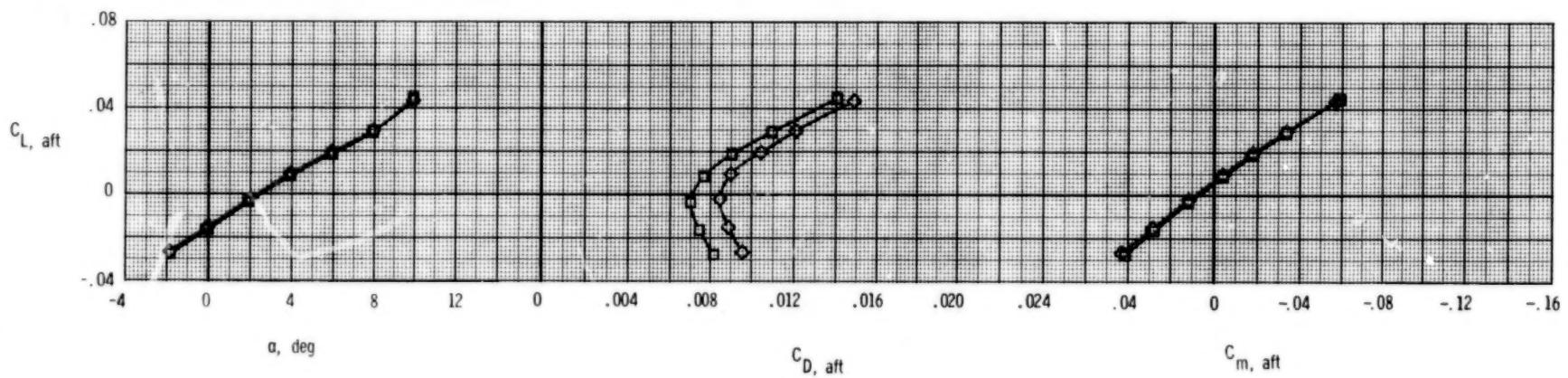
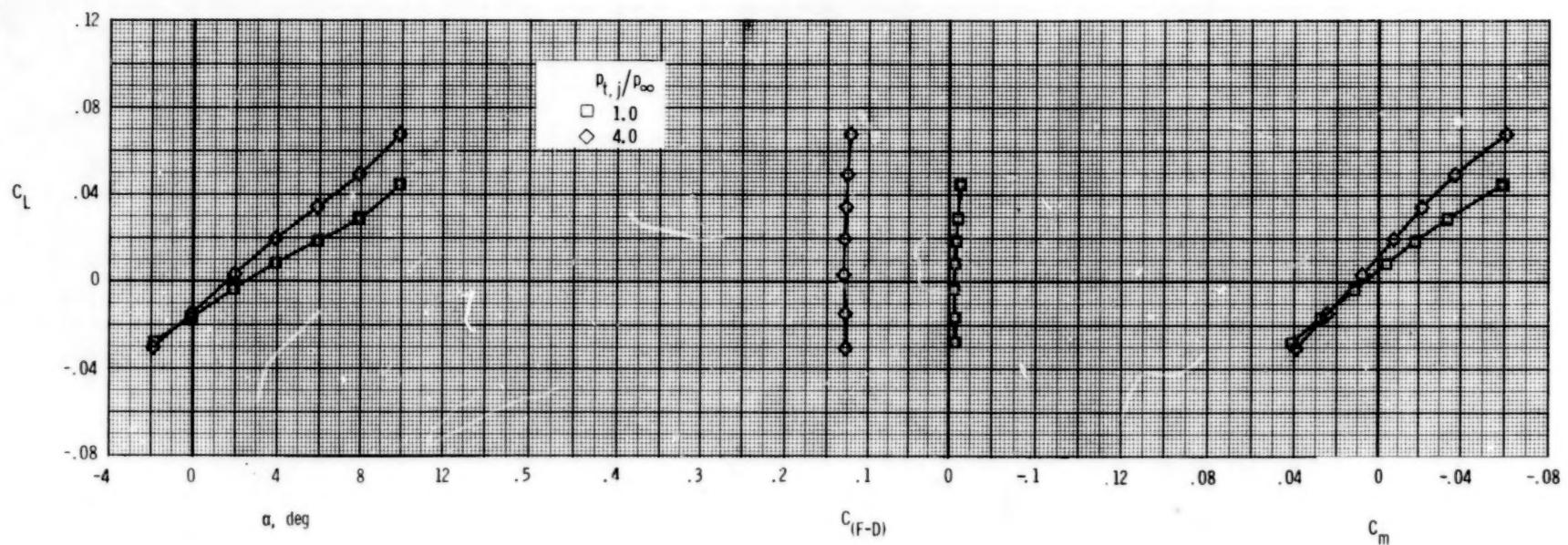
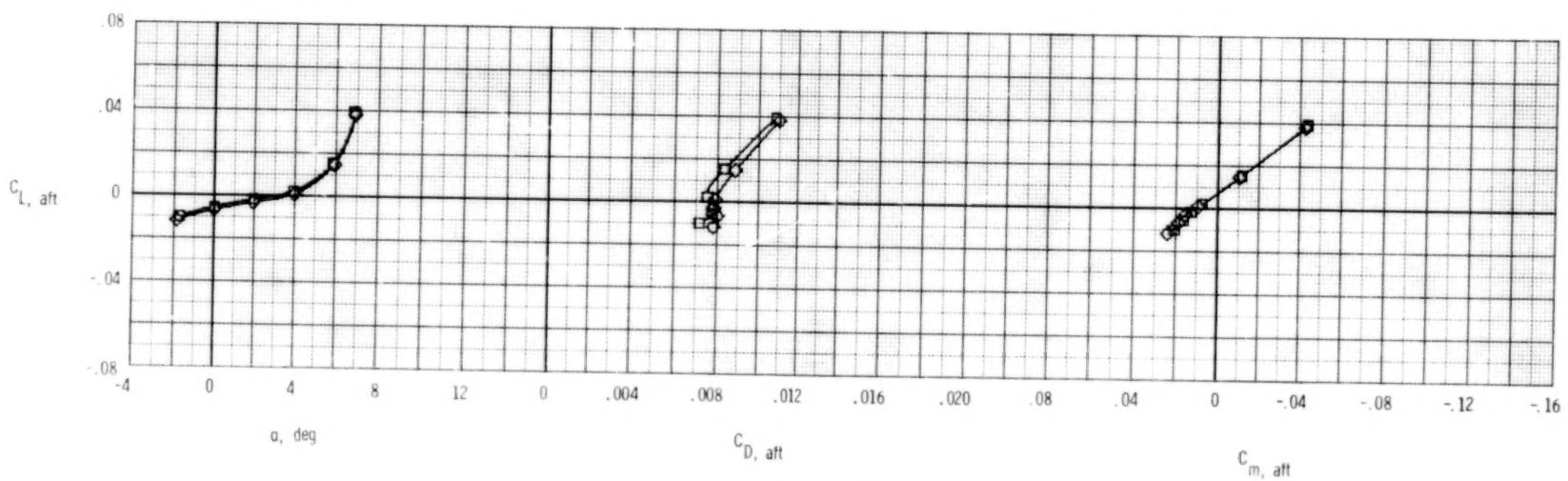
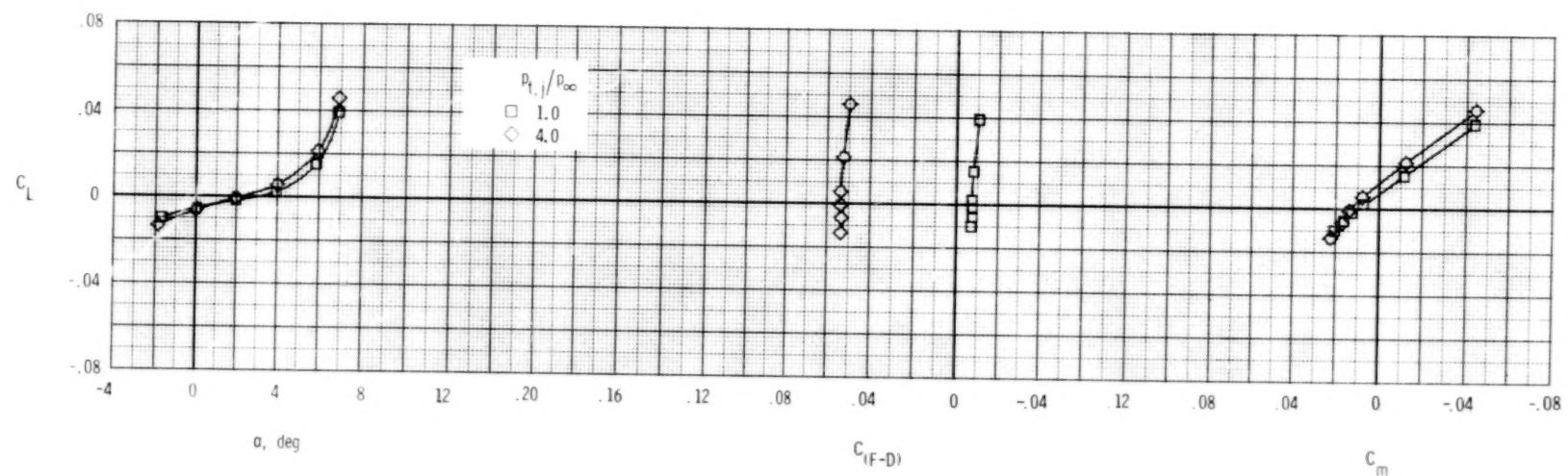
(a) $M = 0.60$.

Figure 34.- Longitudinal afterbody aerodynamic characteristics, axisymmetric nozzles, dry power.

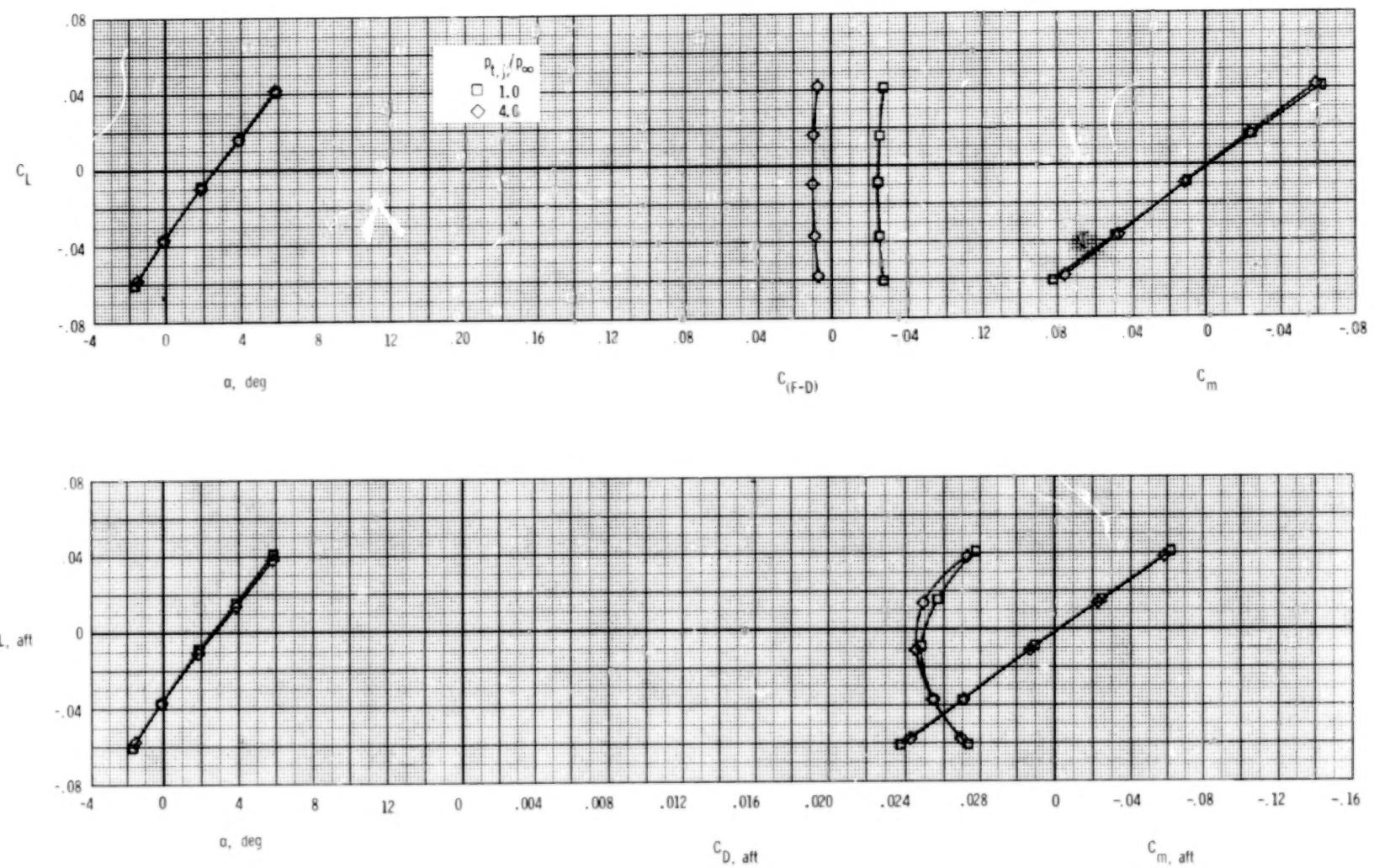
$$\delta_h = -2^\circ; \quad \delta_v = 0^\circ; \quad A_e/A_t = 1.28.$$



(b) $M = 0.90$.

Figure 34.- Continued.

70



(c) $M = 1.20.$

Figure 34.- Concluded.

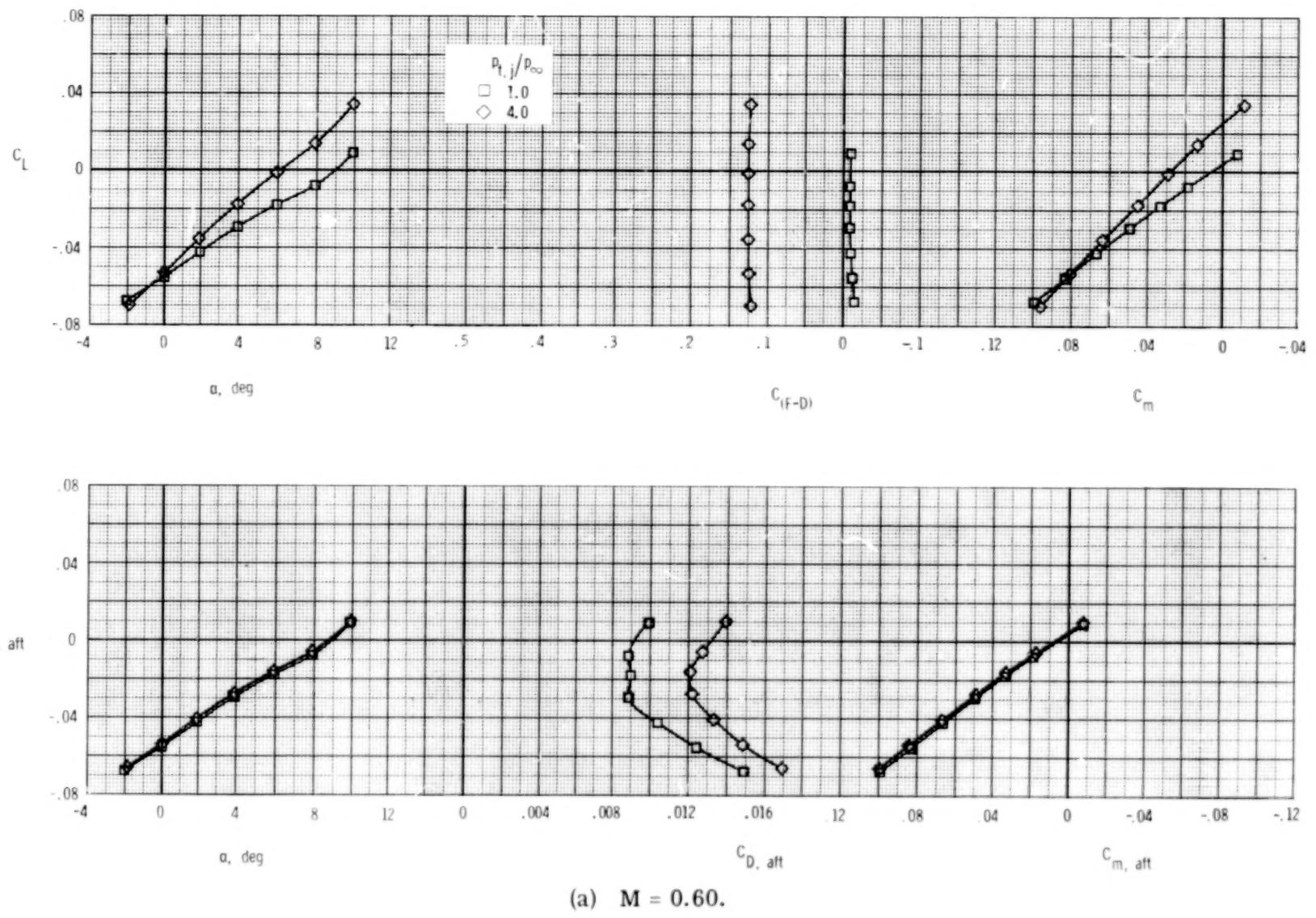
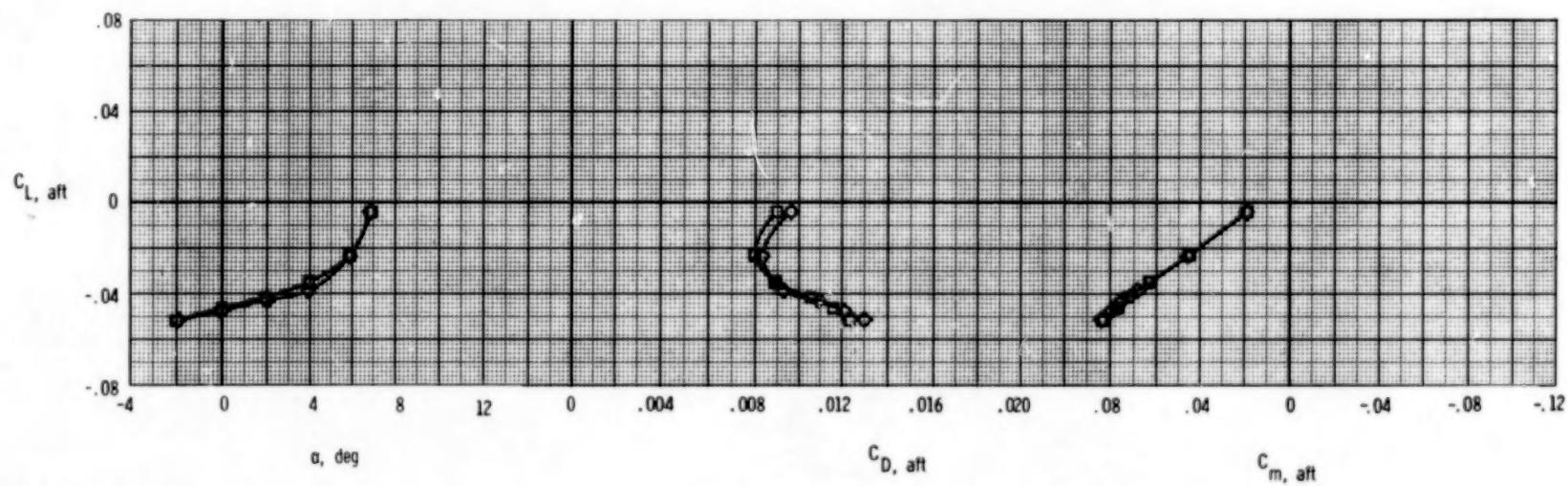
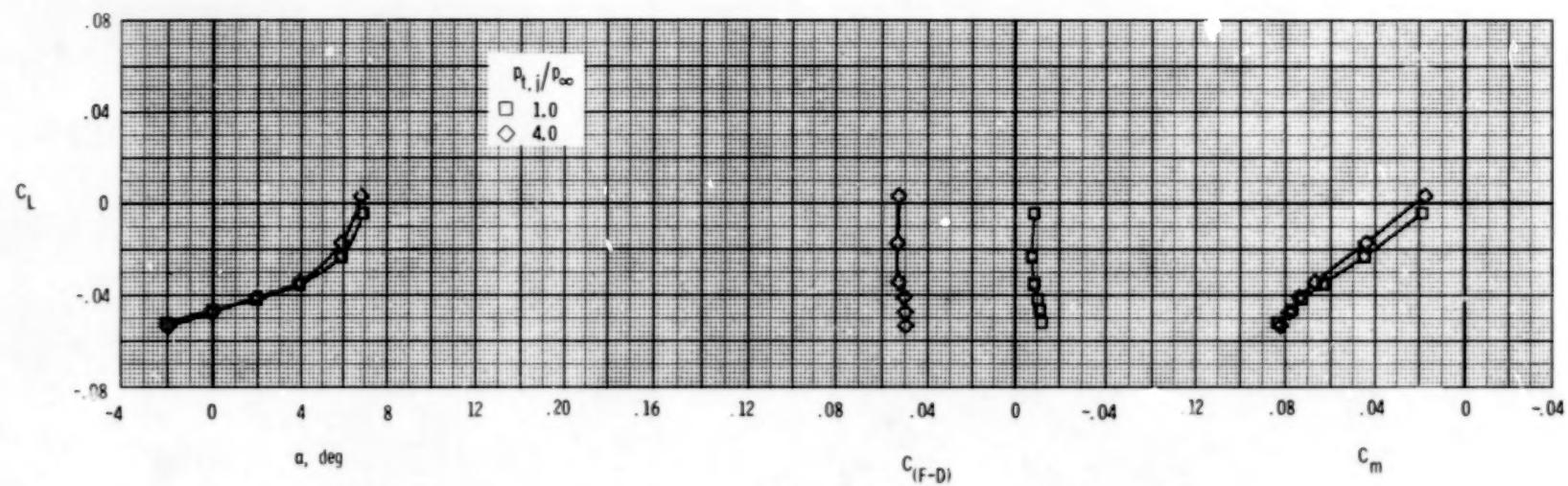


Figure 35.- Longitudinal afterbody aerodynamic characteristics, axisymmetric nozzles, dry power.

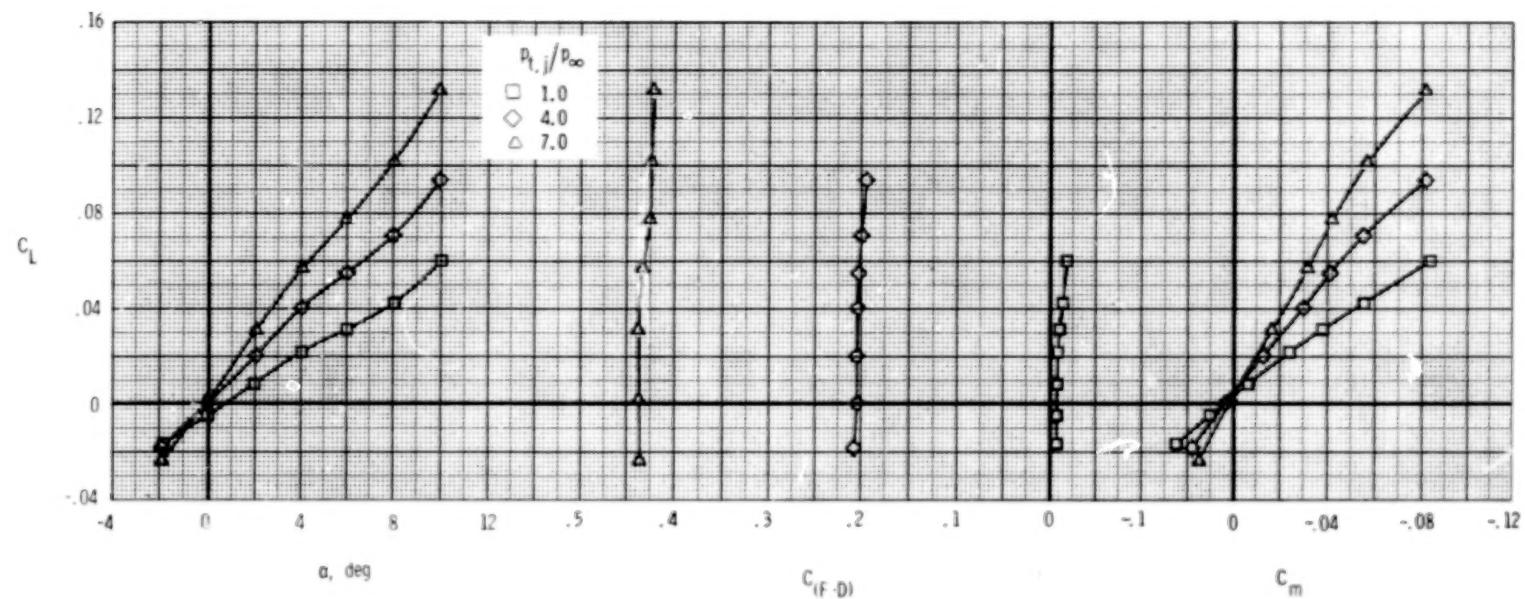
$$\delta_h = -5^\circ; \quad \delta_v = 0^\circ; \quad A_e/A_t = 1.28.$$

62



(b) $M = 0.90.$

Figure 35.- Concluded.



(a) $M = 0.60$.

Figure 36. - Longitudinal afterbody aerodynamic characteristics, axisymmetric nozzles, A/B power.

$$\delta_h = 0^\circ; \quad \delta_v = 0^\circ; \quad A_e/A_t = 1.56.$$

74

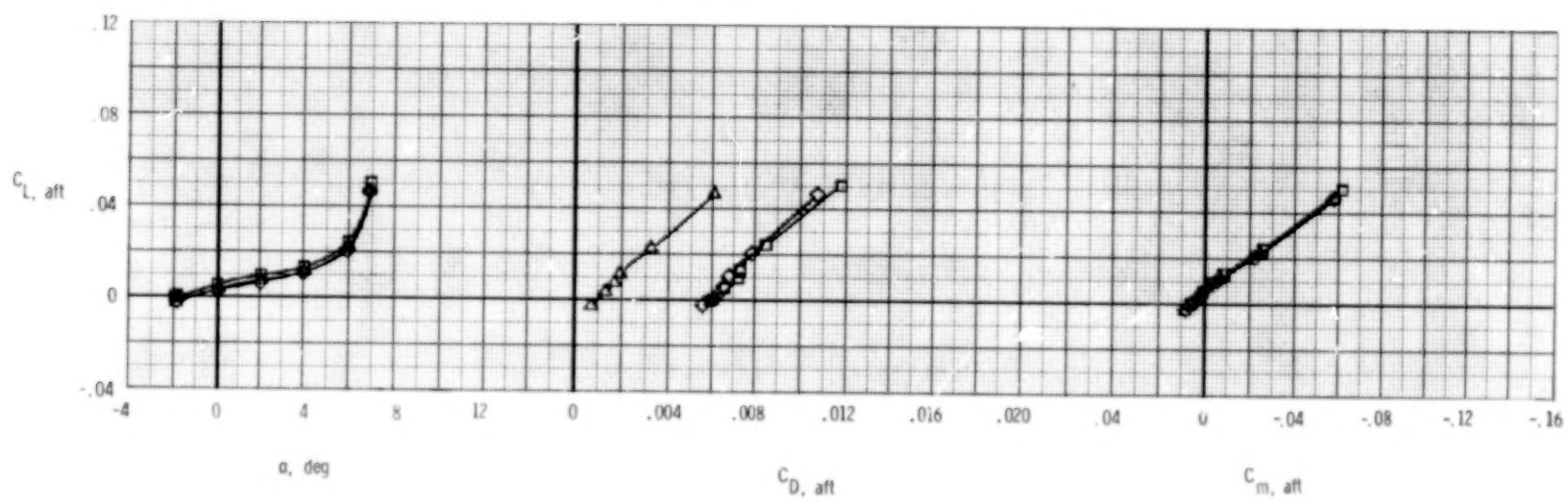
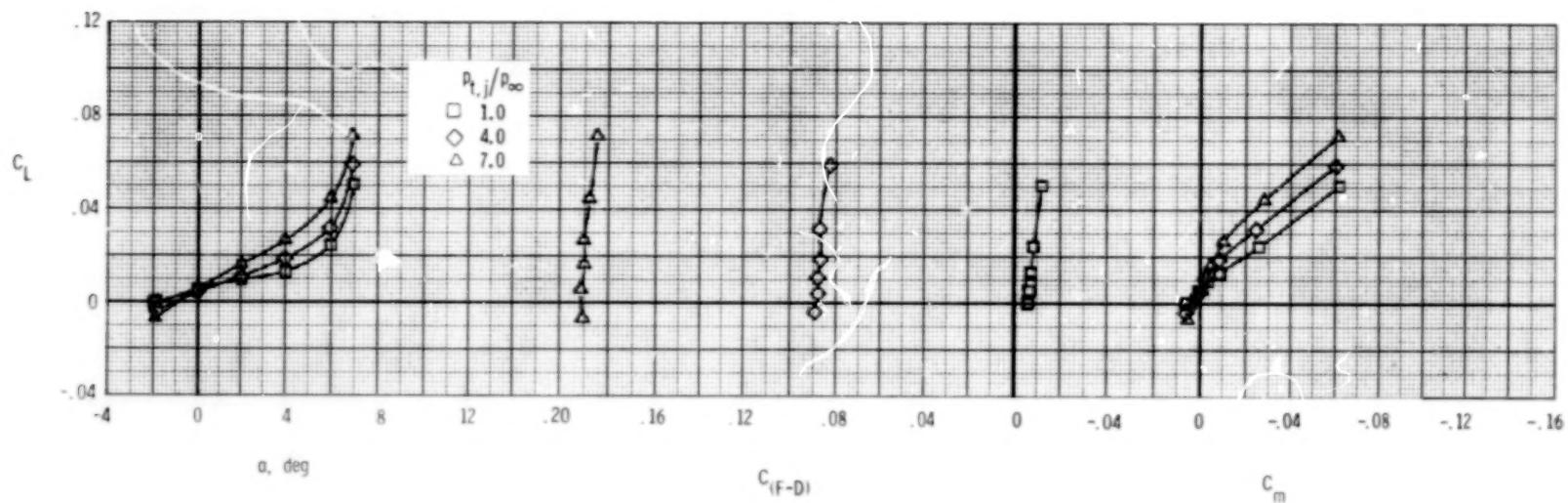
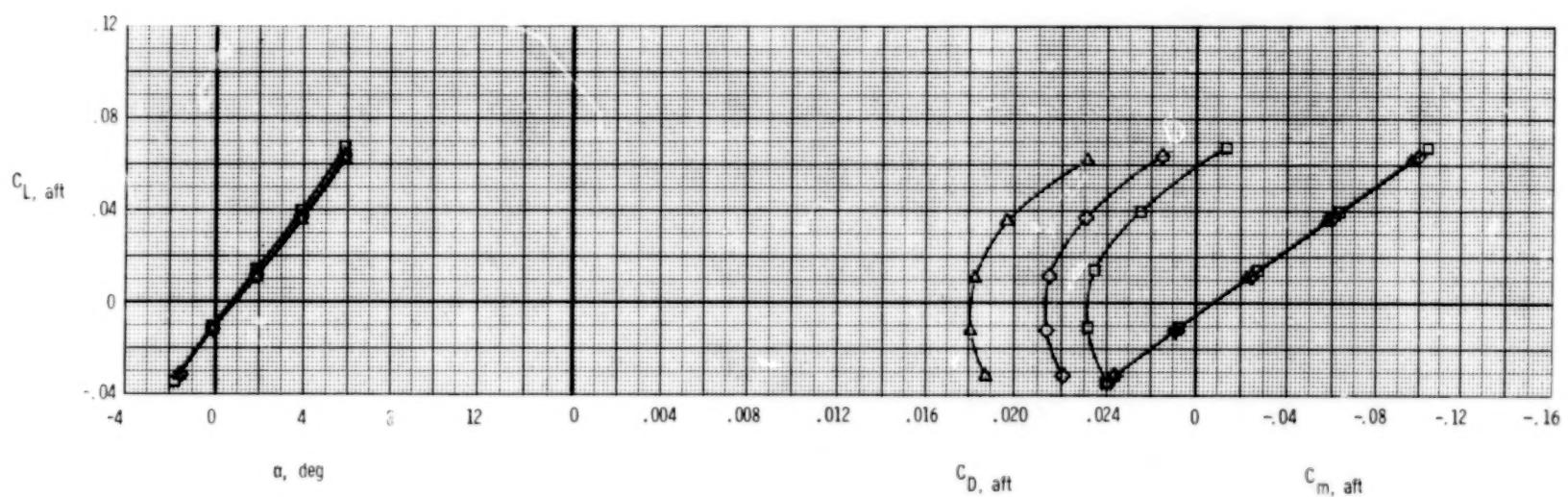
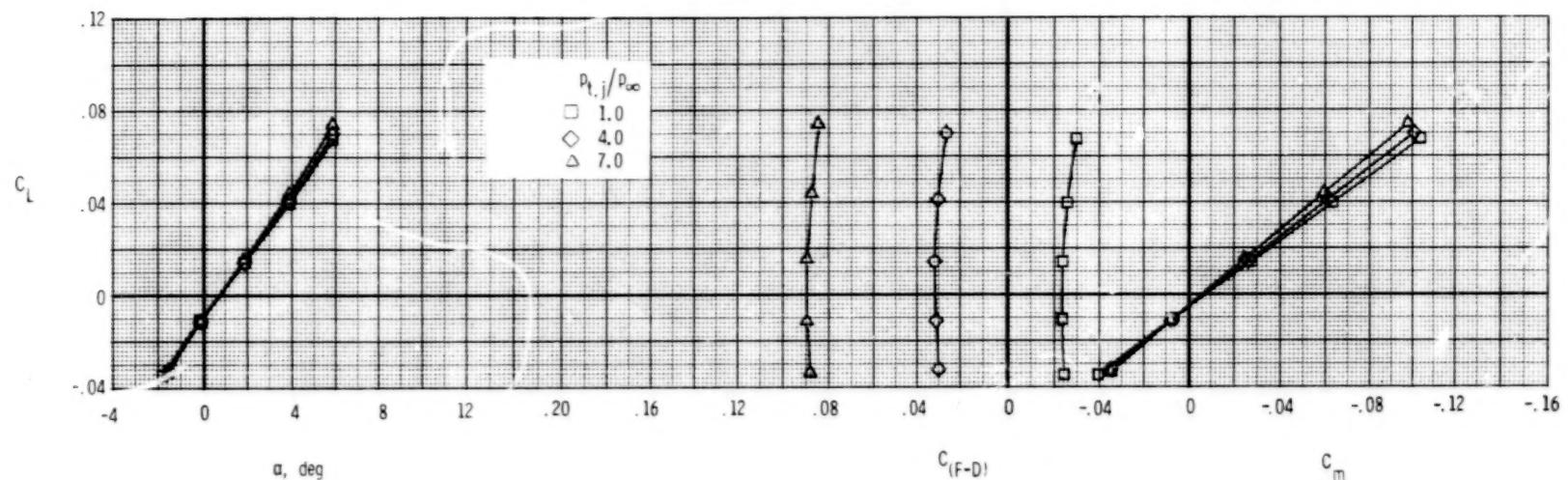
(b) $M = 0.90$.

Figure 36.- Continued.



(c) $M = 1.20$.

Figure 36.- Concluded.

76

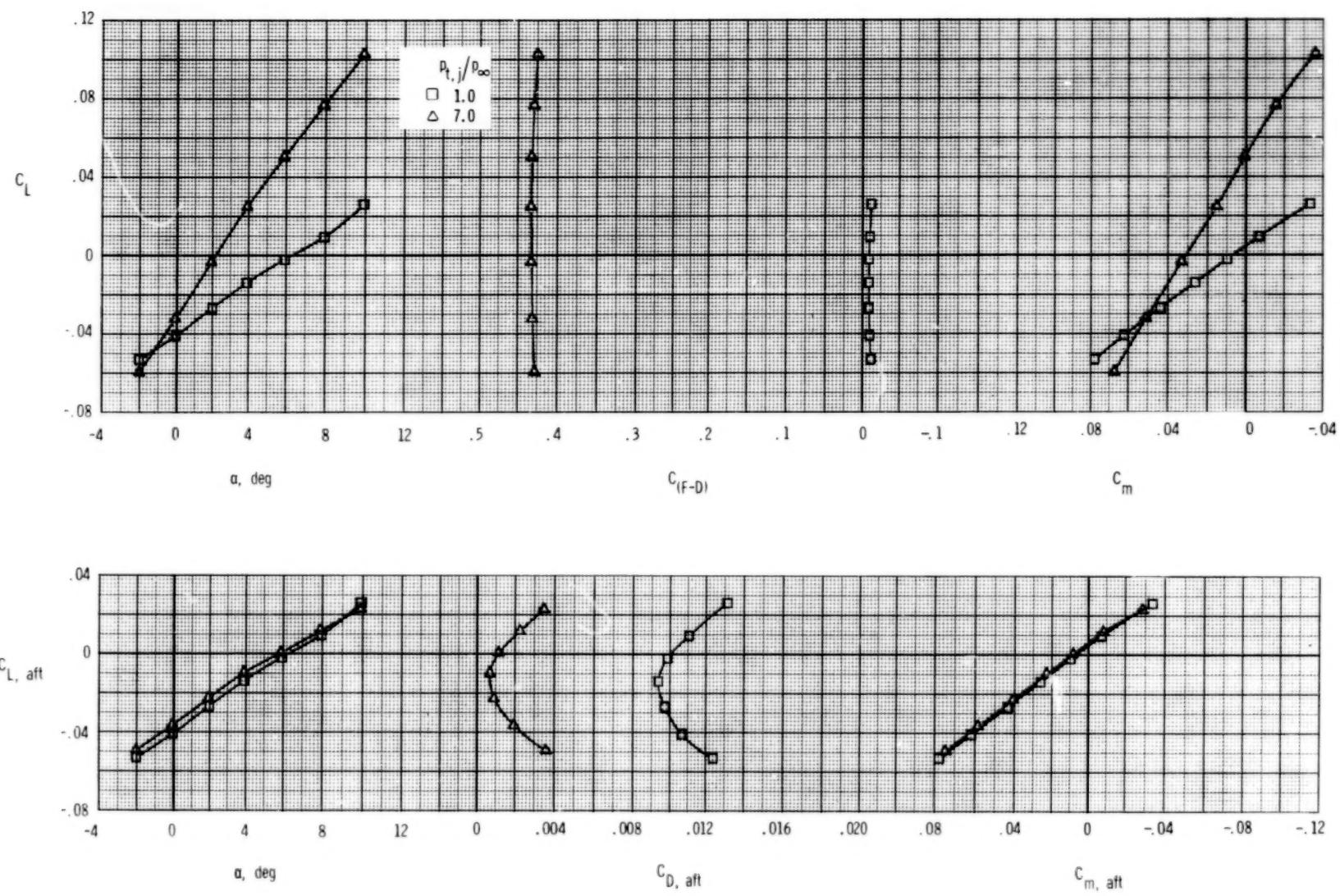
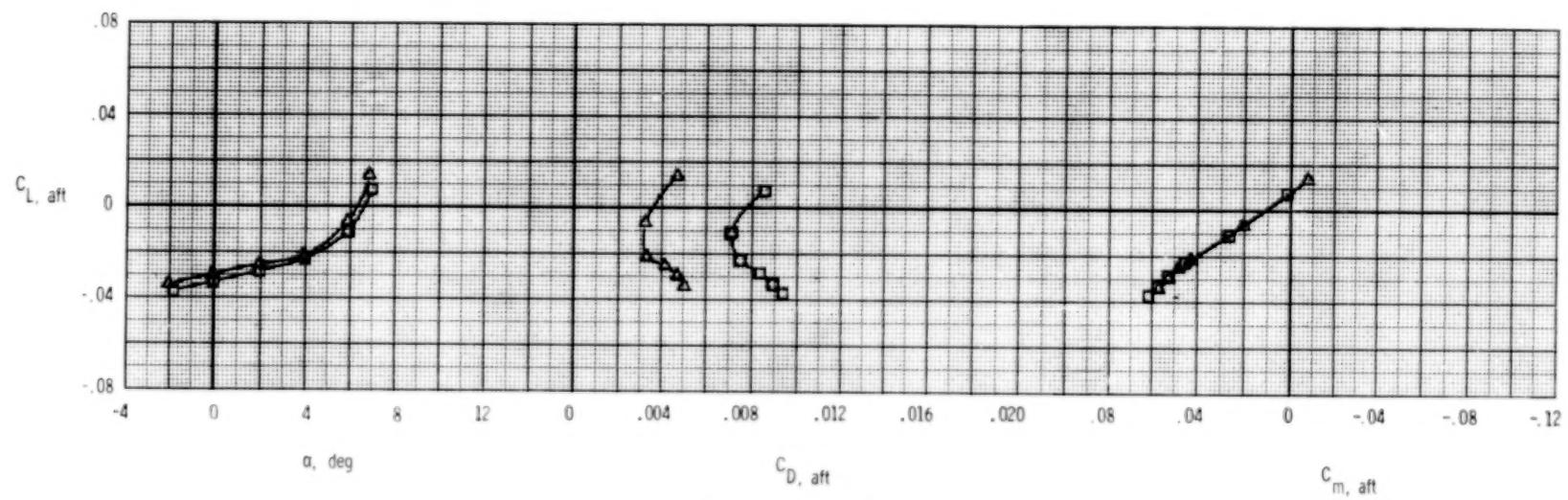
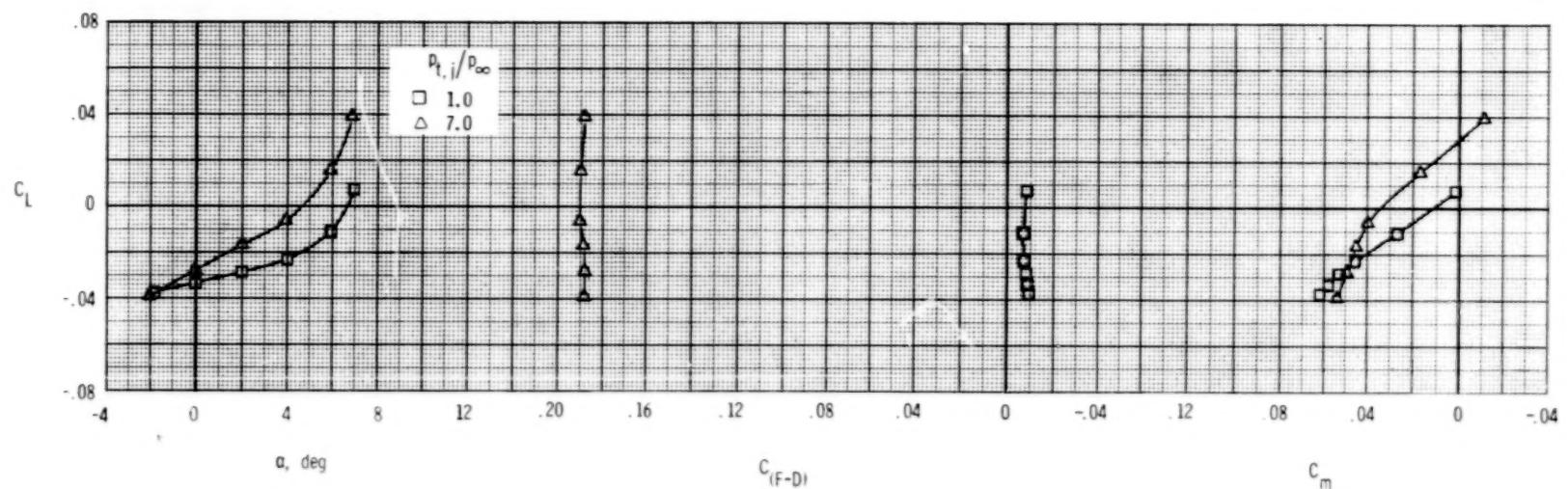
(a) $M = 0.60$.

Figure 37.- Longitudinal afterbody aerodynamic characteristics, axisymmetric nozzles, A/B power.

$$\delta_h = -2^\circ; \quad \delta_v = 0^\circ; \quad A_e/A_t = 1.56.$$



(b) $M = 0.90.$

Figure 37.- Continued.

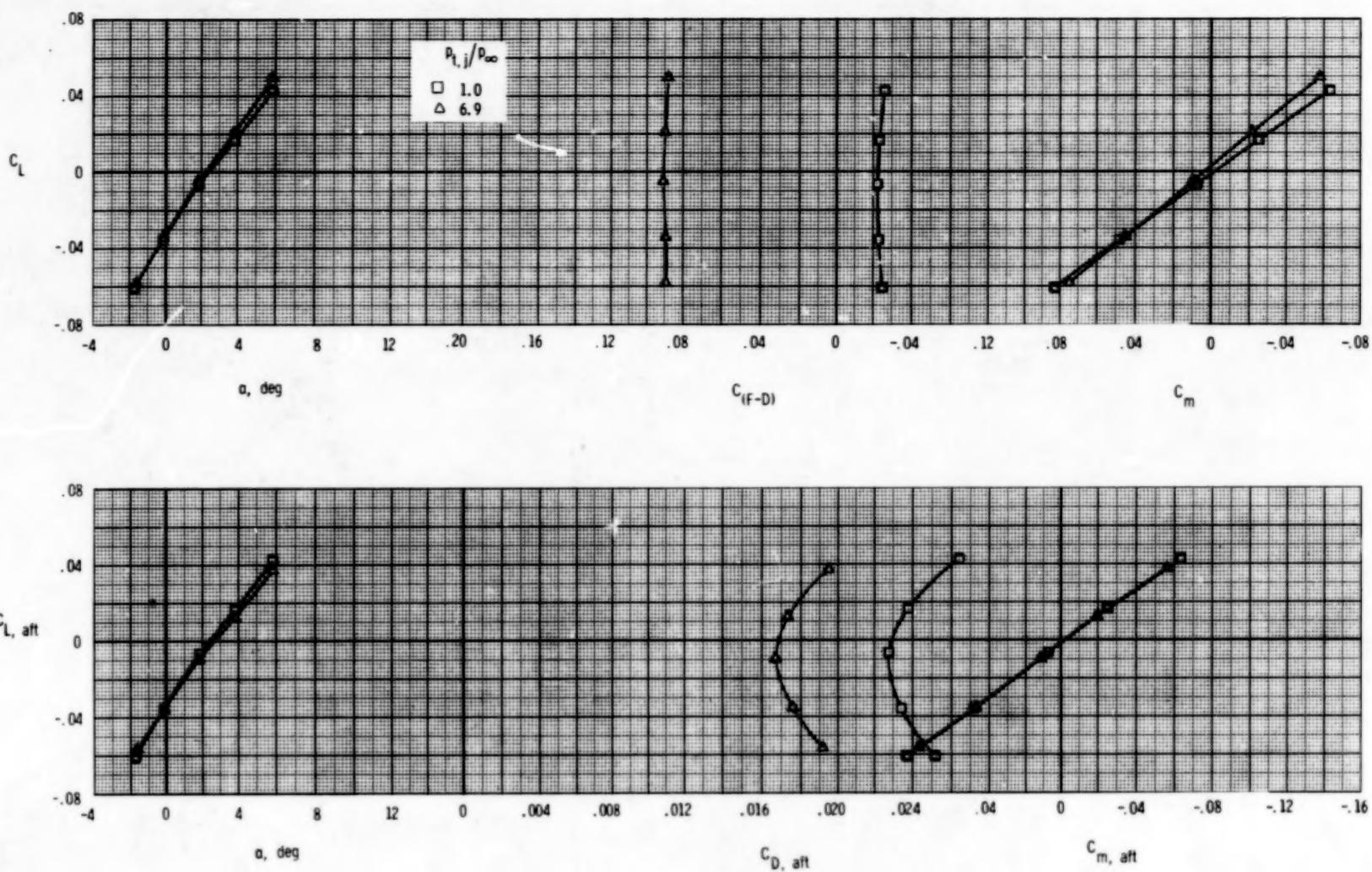
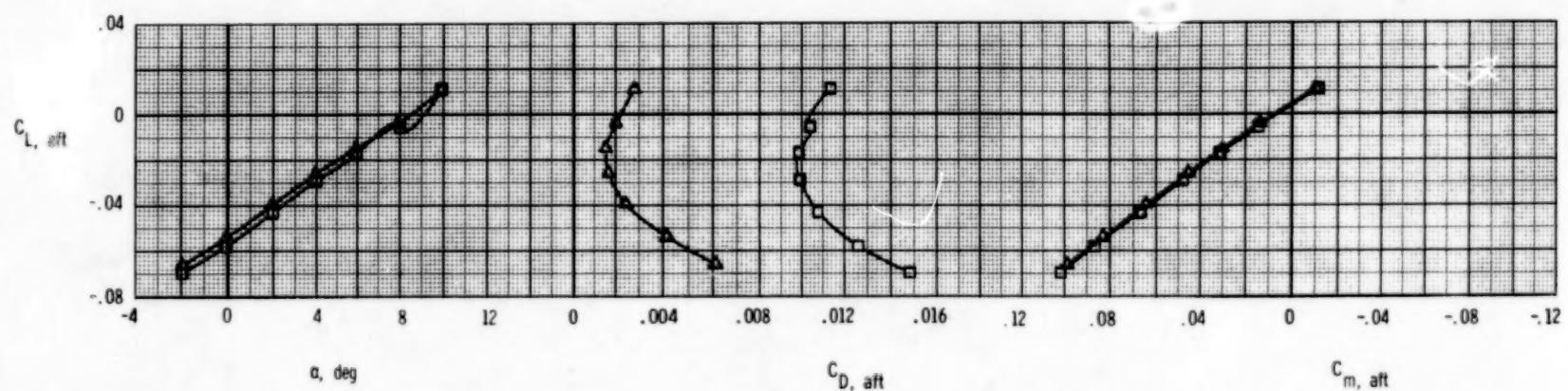
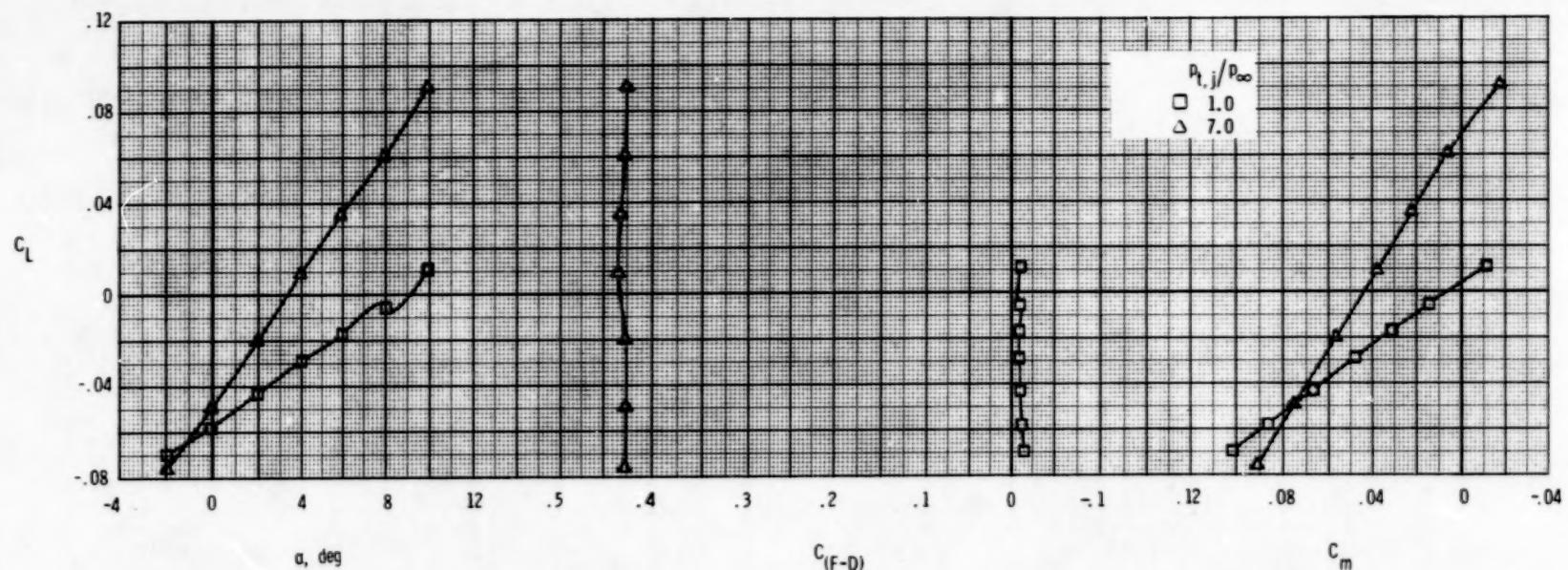
(c) $M = 1.20$.

Figure 37.- Concluded.



(a) $M = 0.60$.

Figure 38.- Longitudinal afterbody aerodynamic characteristics, axisymmetric nozzles, A/B power.

$$\delta_h = -5^\circ; \quad \delta_v = 0^\circ; \quad A_e/A_t = 1.56.$$

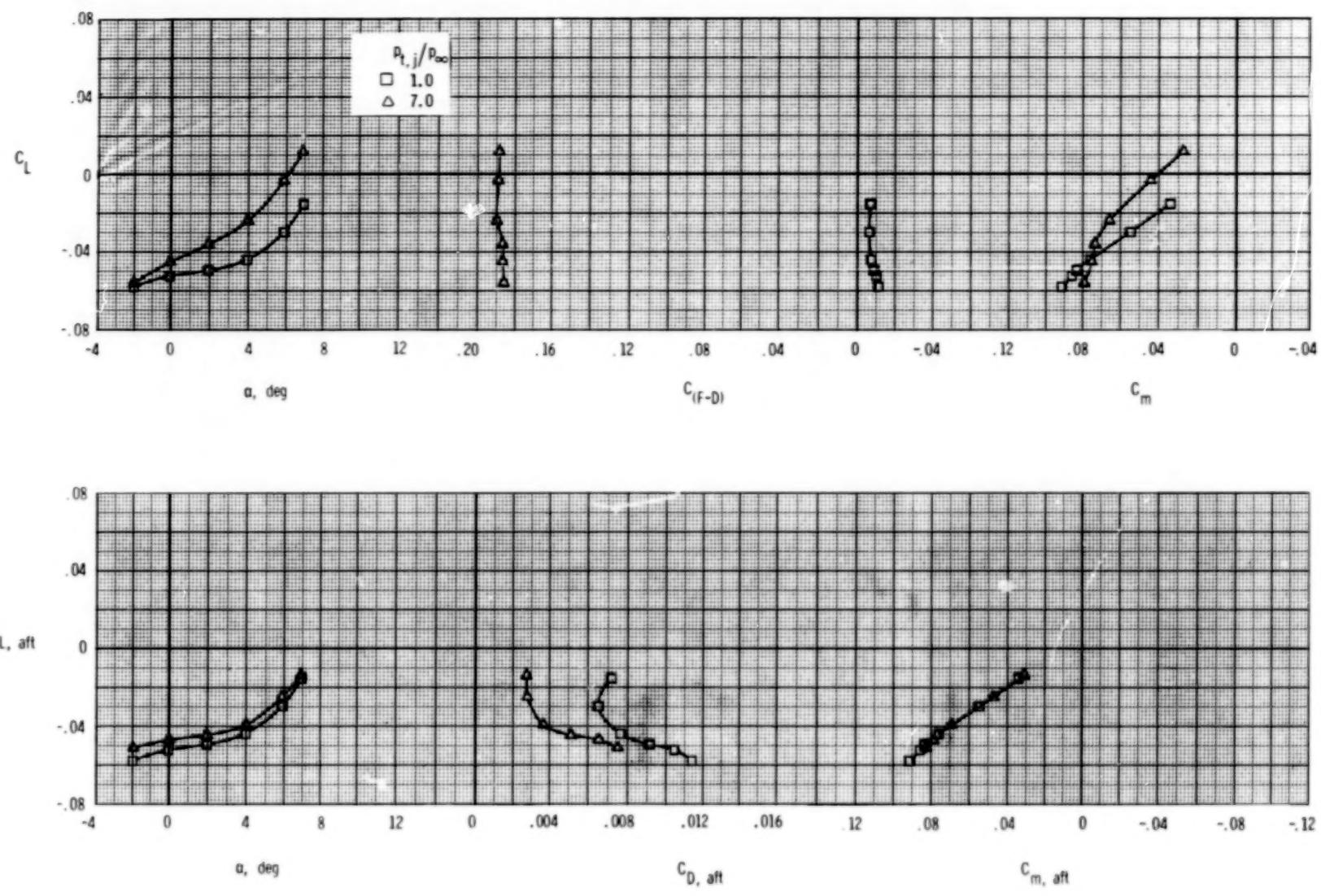
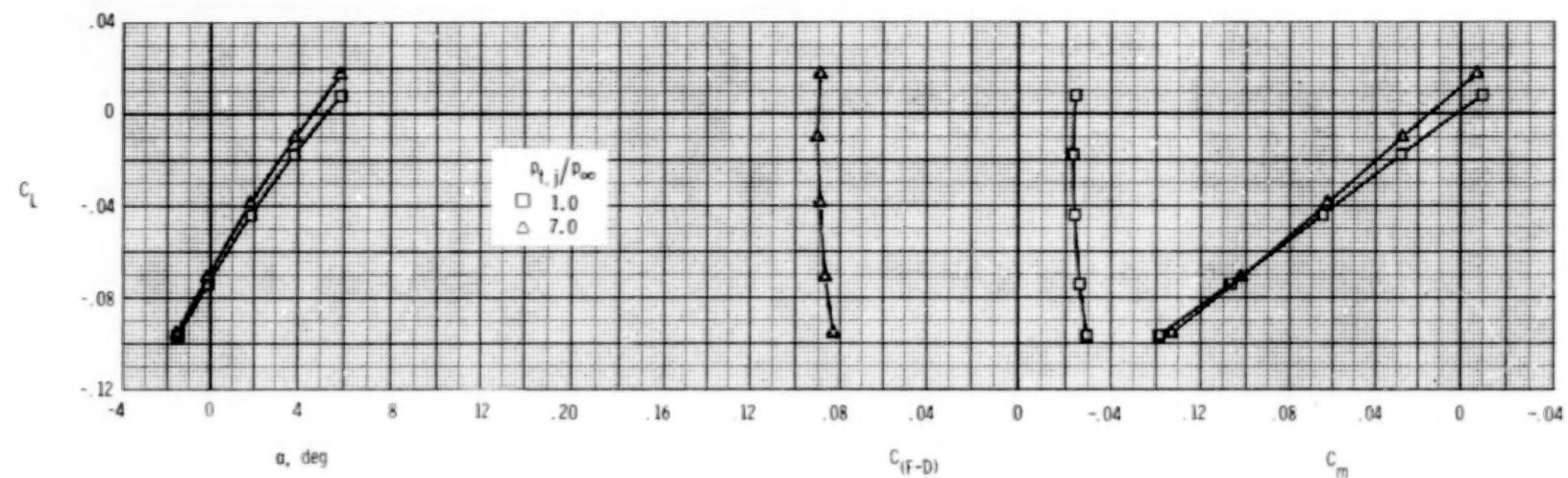
(b) $M = 0.90$.

Figure 38.- Continued.



(c) $M = 1.20$.

Figure 38.- Concluded.

82

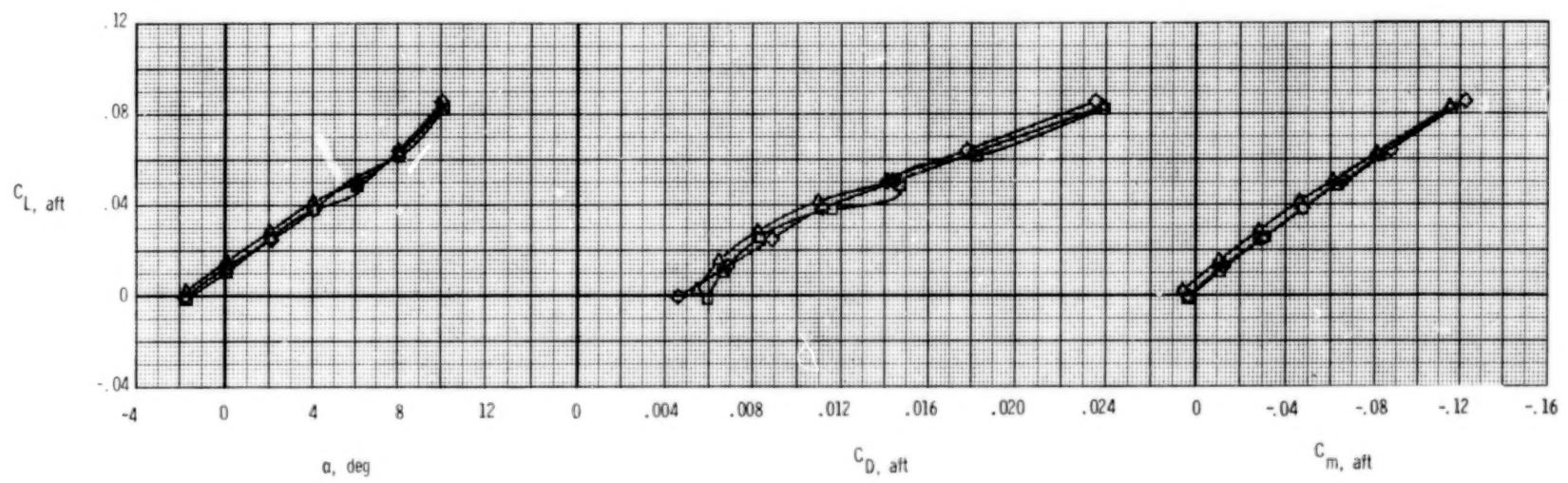
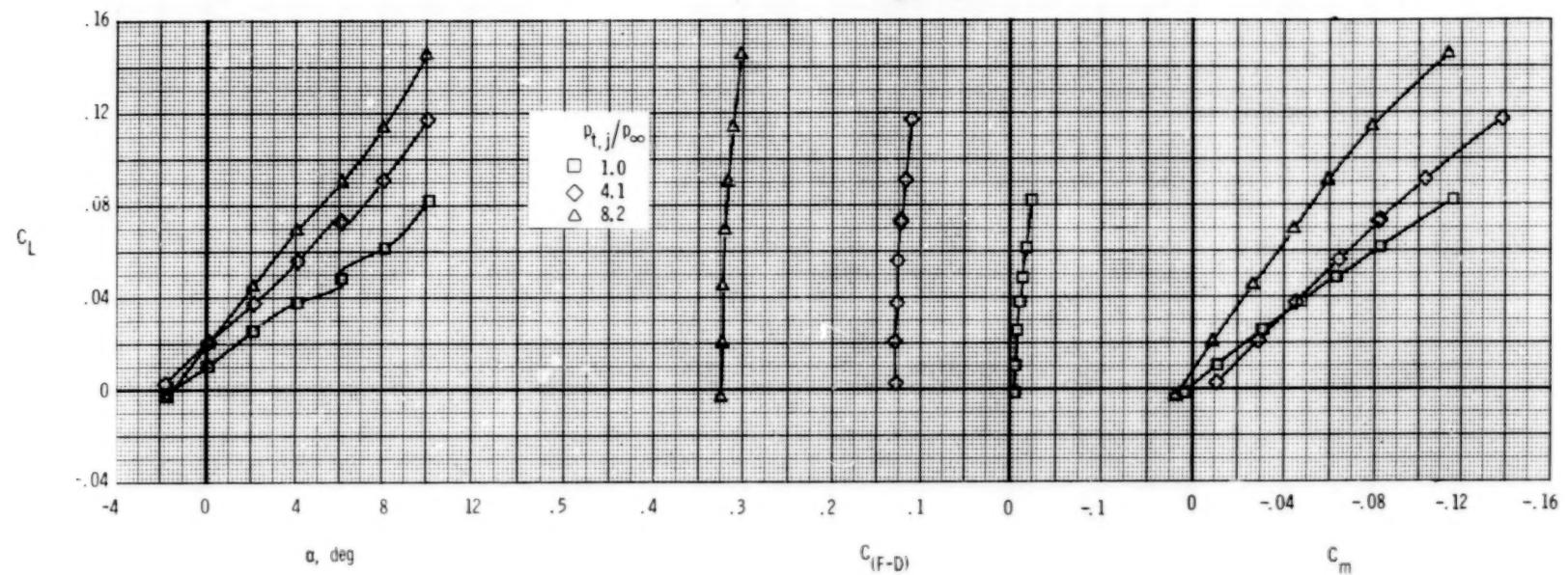
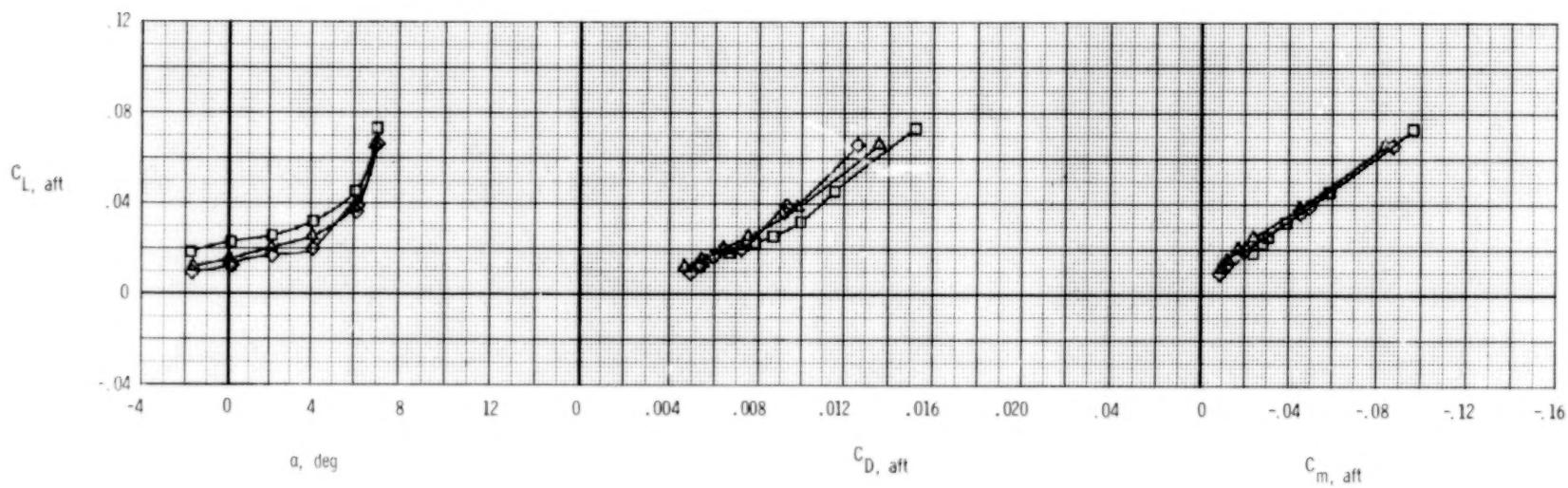
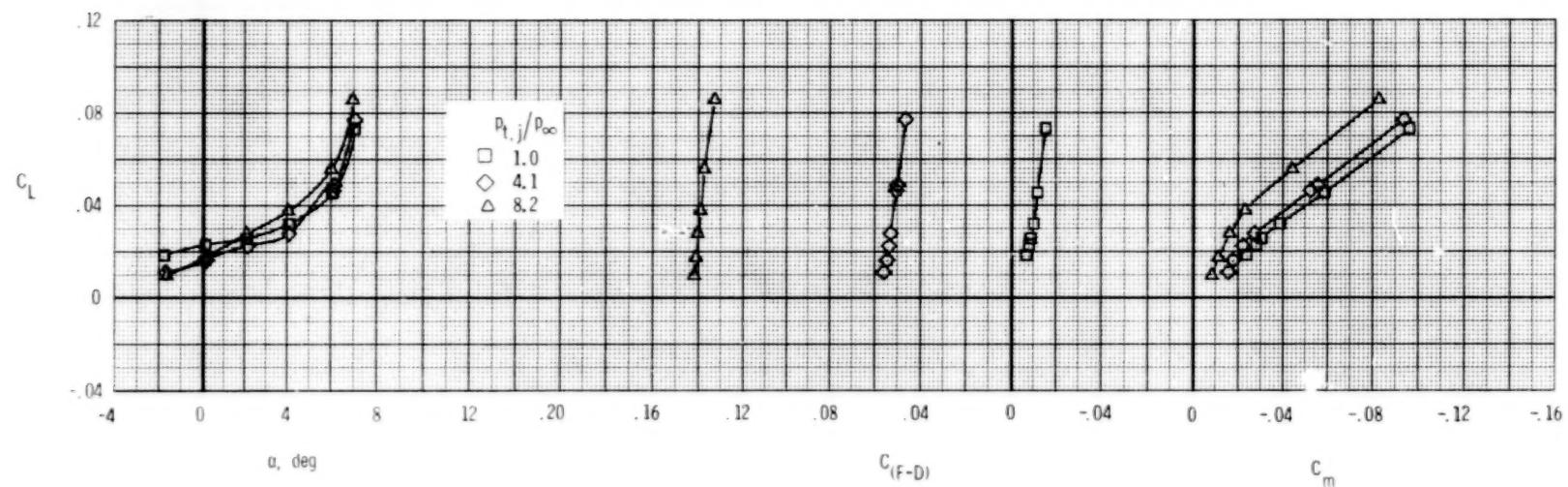
(a) $M = 0.60.$

Figure 39.- Longitudinal afterbody aerodynamic characteristics, SERN nozzle, dry power.

$$\delta_h = 0^0; \quad \delta_v = 0^0; \quad A_e/A_t = 1.15.$$



(b) $M = 0.90$.

Figure 39.- Continued.

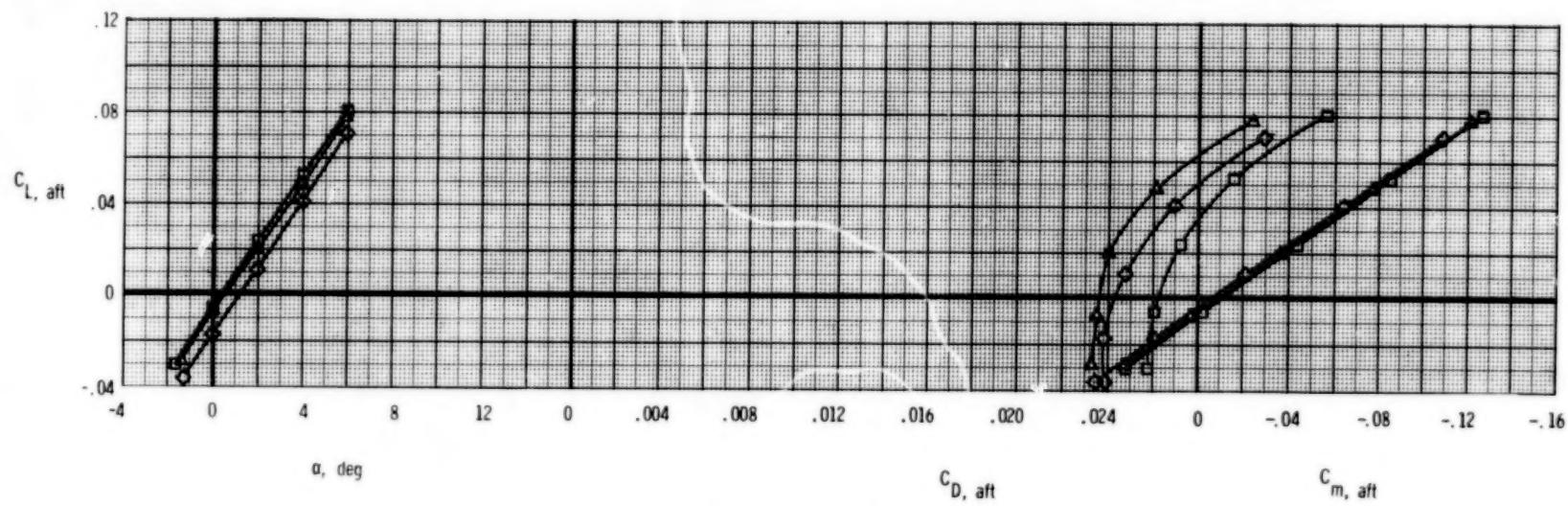
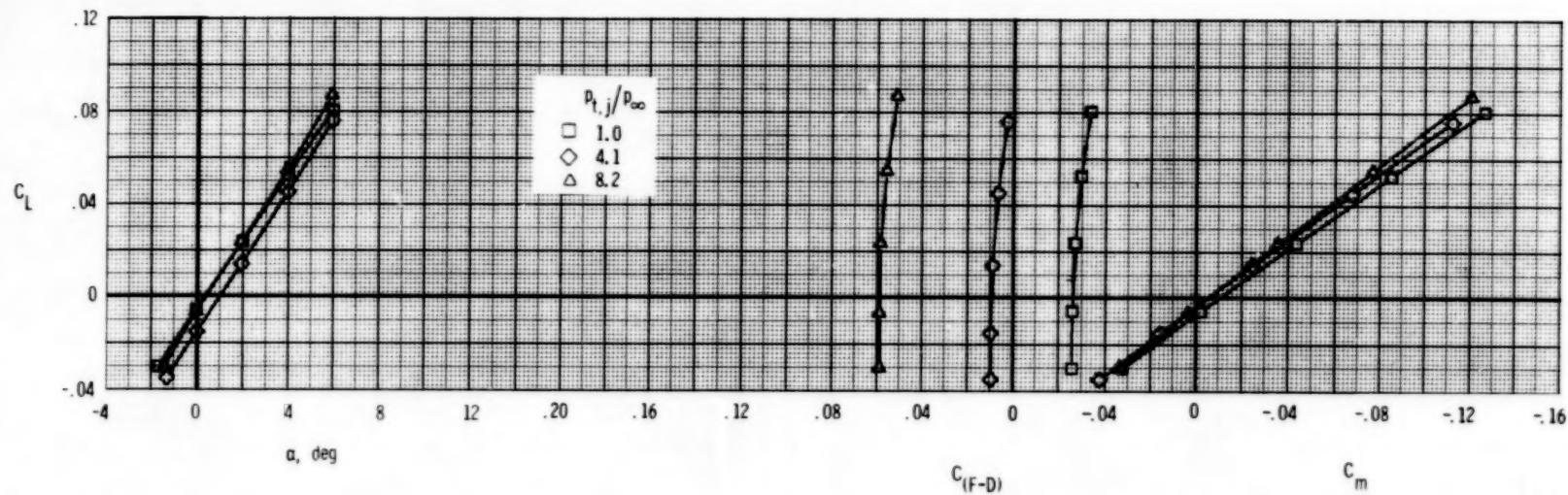
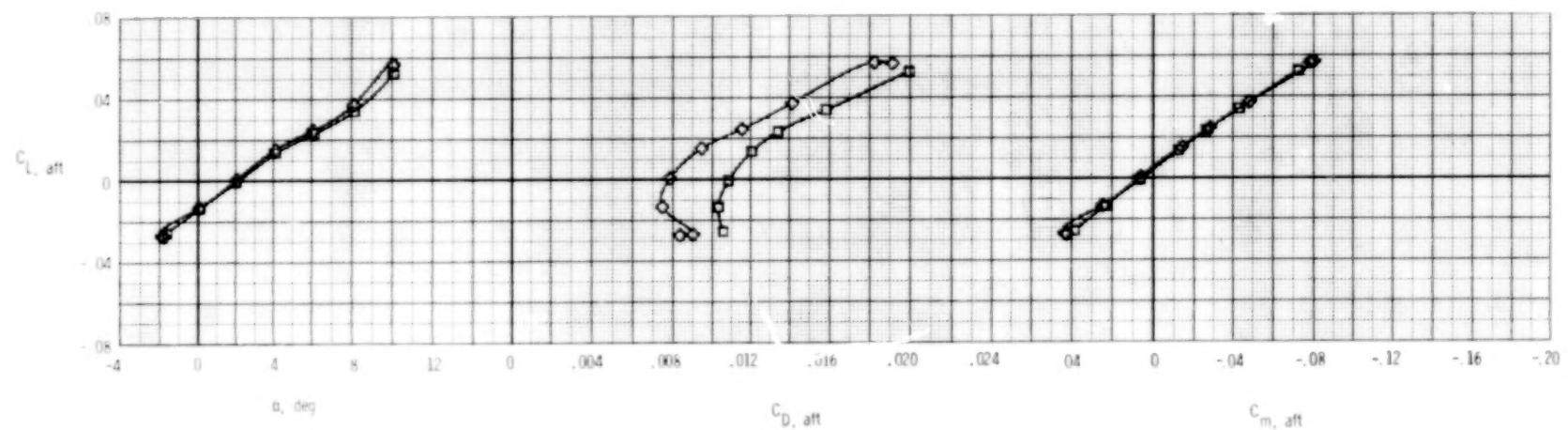
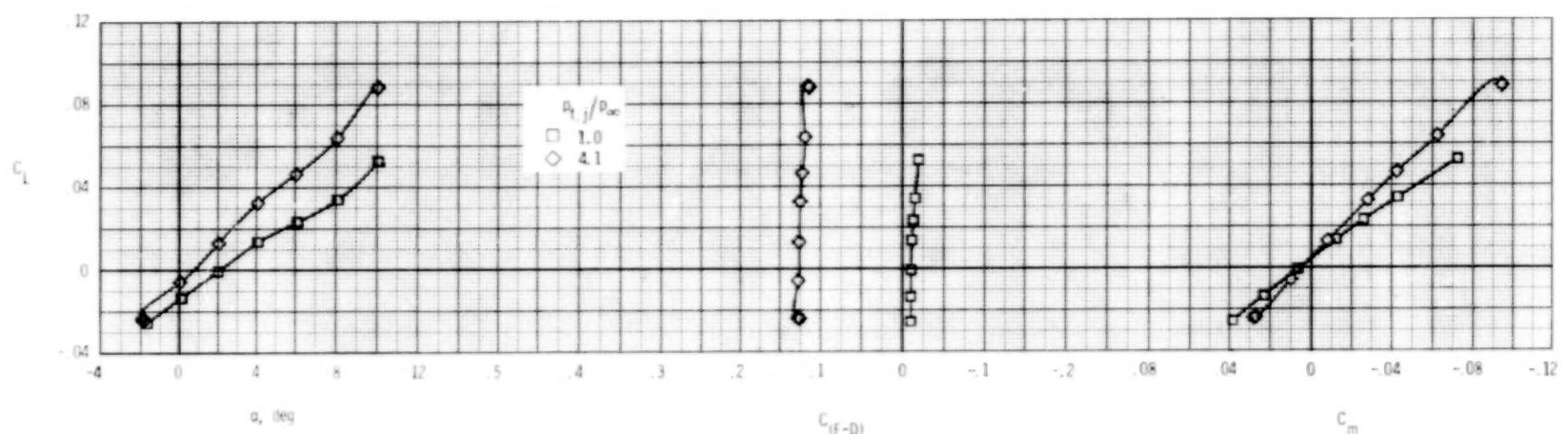
(c) $M = 1.20$.

Figure 39.- Concluded.



(a) $M = 0.60$.

Figure 40.- Longitudinal afterbody aerodynamic characteristics, SERN nozzle, dry power.

$$\delta_h = -2^\circ; \quad \delta_v = 0^\circ; \quad A_e/A_t = 1.15.$$

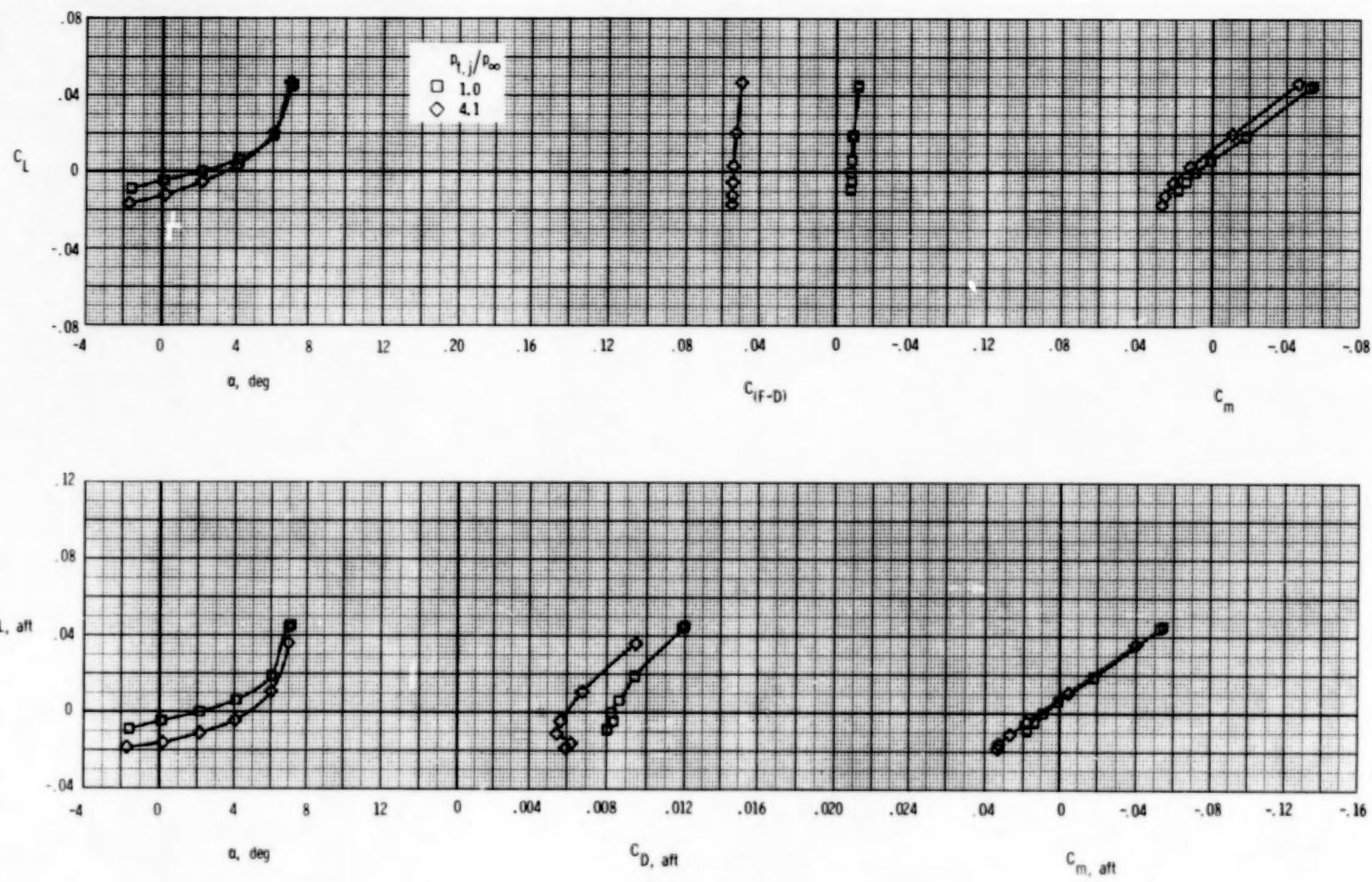
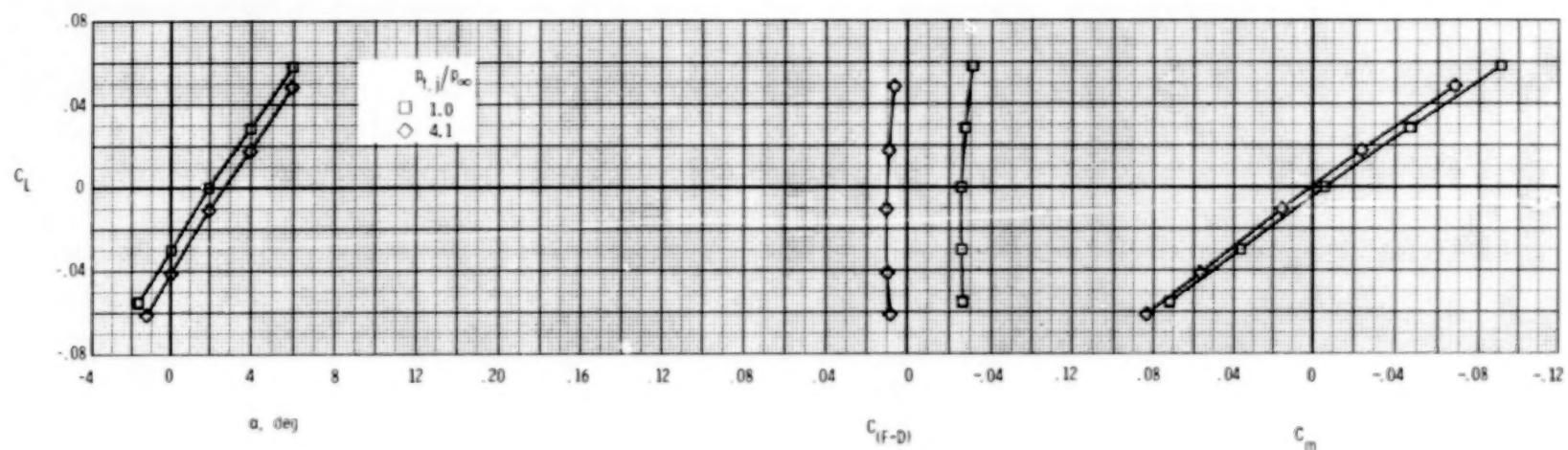
(b) $M = 0.90.$

Figure 40.- Continued.



(c) $M = 1.20$.

Figure 40.- Concluded.

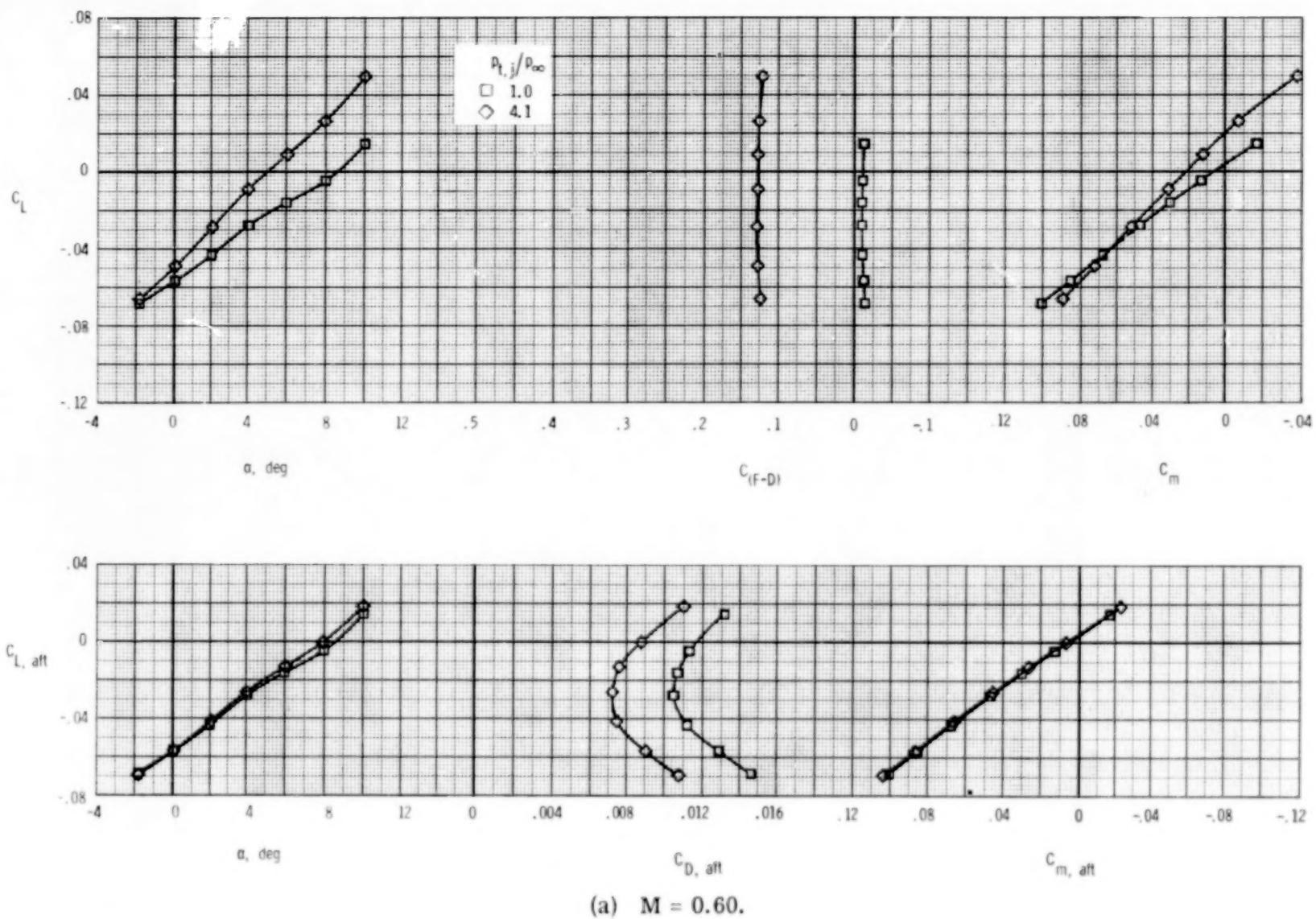
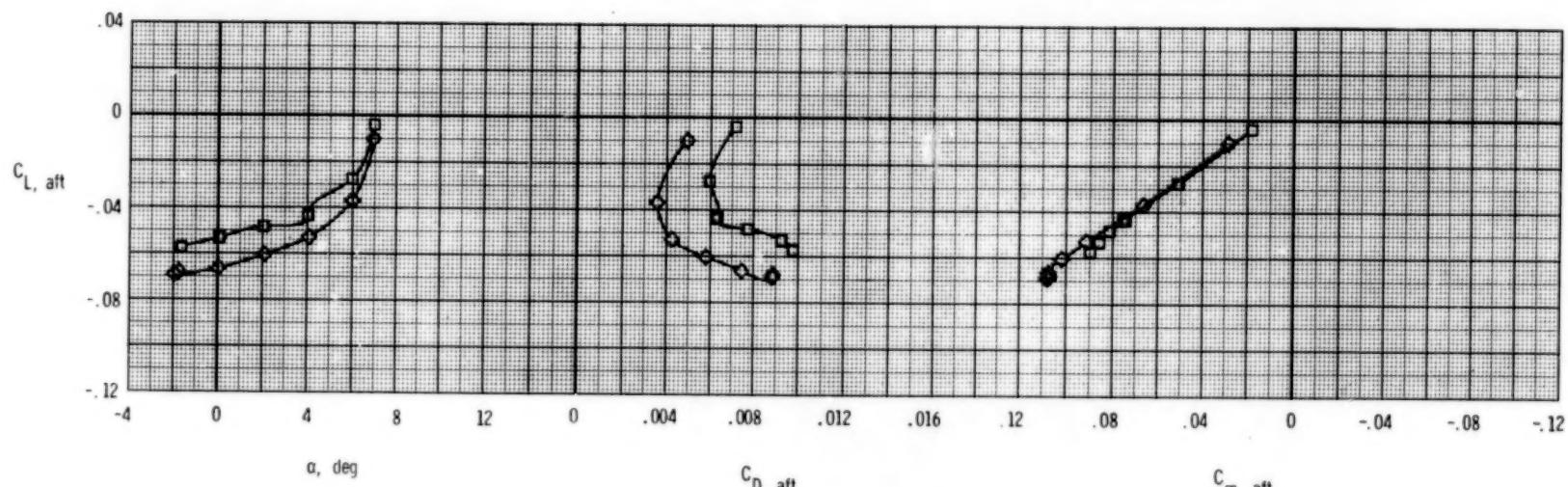
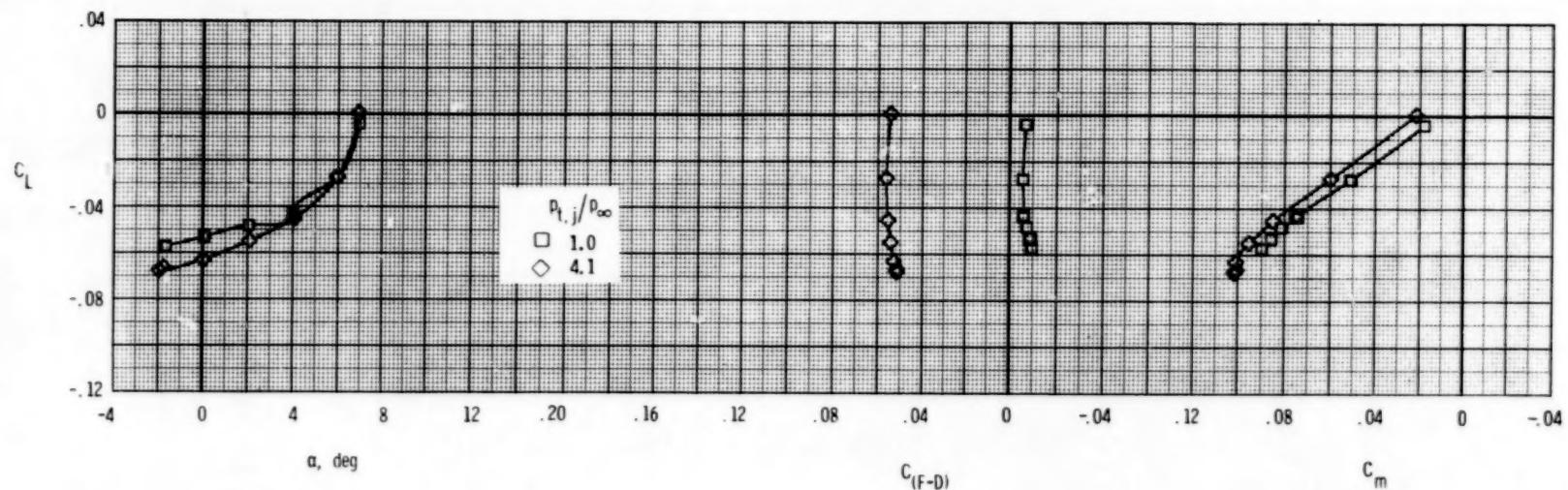
(a) $M = 0.60$.

Figure 41.- Longitudinal afterbody aerodynamic characteristics, SERN nozzle, dry power.

$$\delta_h = -5^\circ; \quad \delta_v = 0^\circ; \quad A_e/A_t = 1.15.$$



(b) $M = 0.90$.

Figure 41.- Concluded.

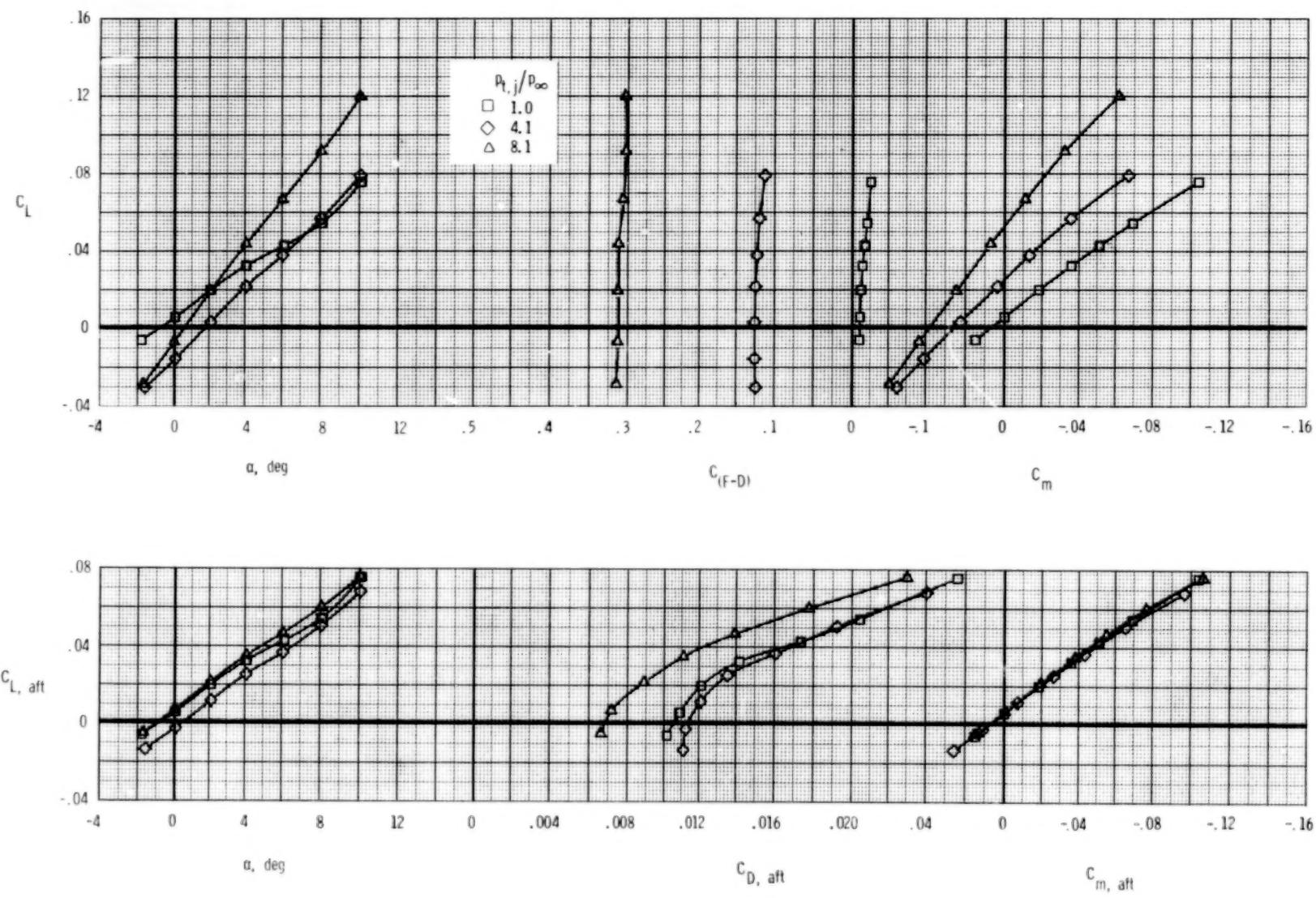
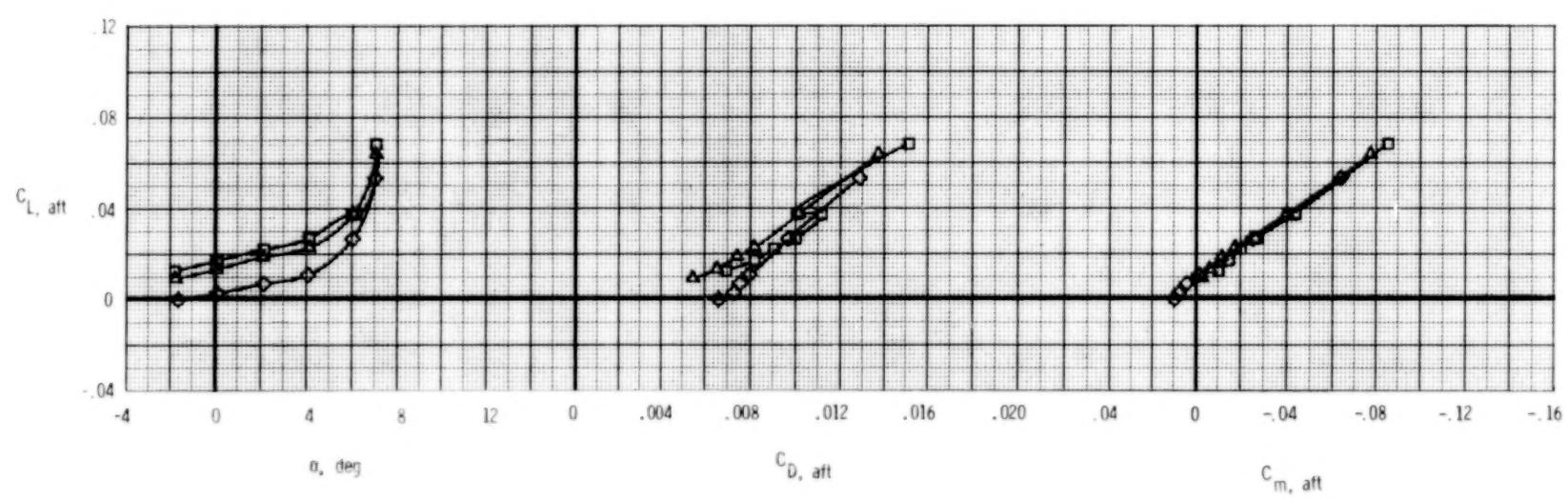
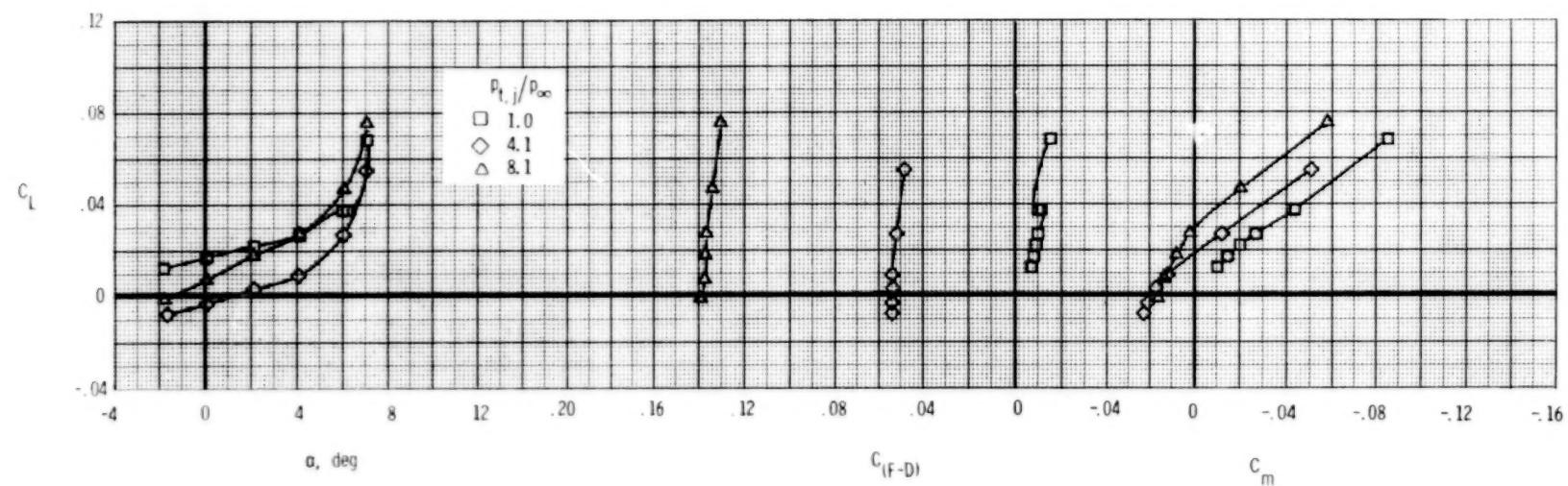
(a) $M = 0.60$.

Figure 42.- Longitudinal afterbody aerodynamic characteristics, SERN nozzle, dry power.

$$\delta_h = 0^\circ; \quad \delta_v = -7^\circ; \quad A_e/A_t = 1.15.$$



(b) $M = 0.90$.

Figure 42.- Continued.

92

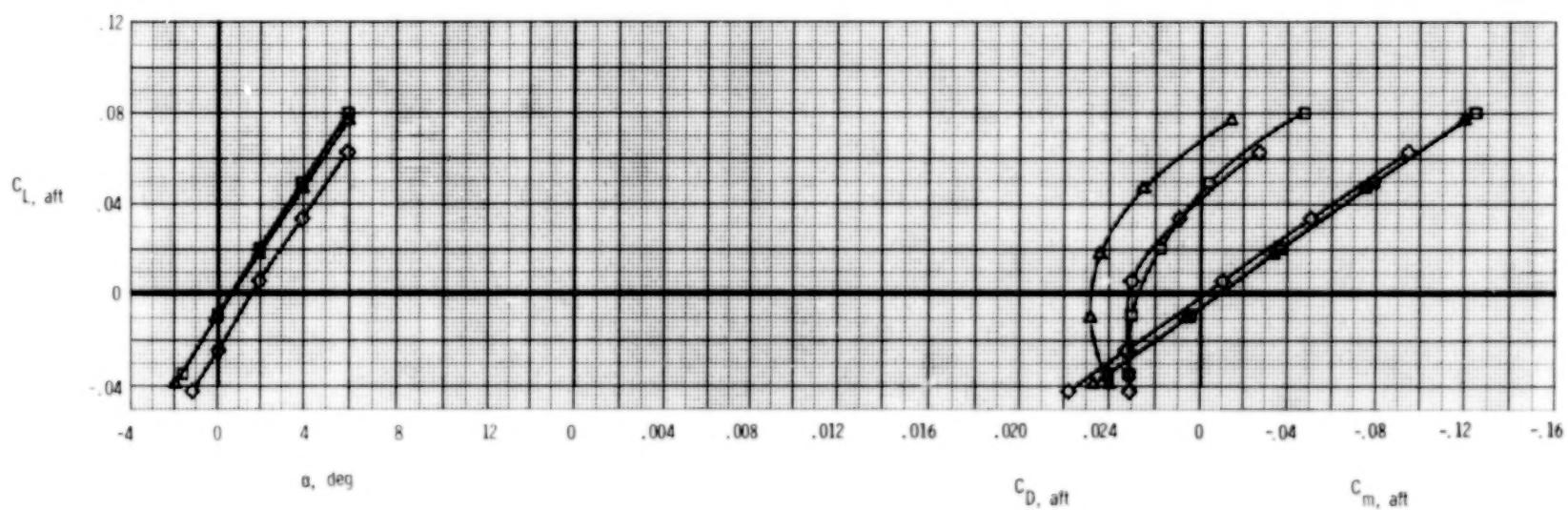
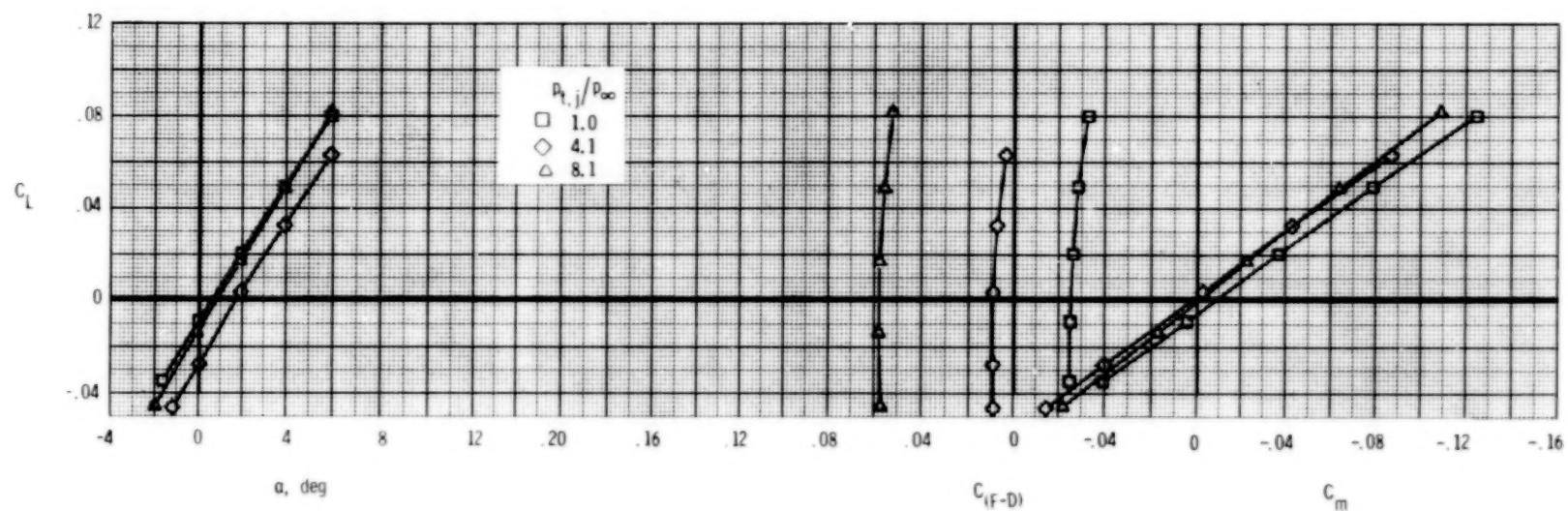
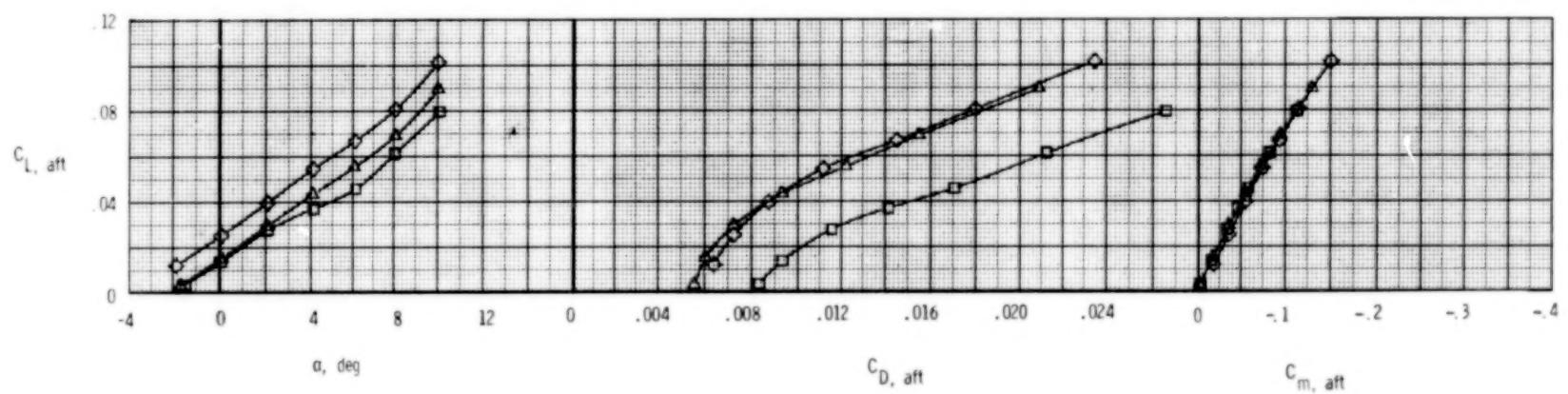
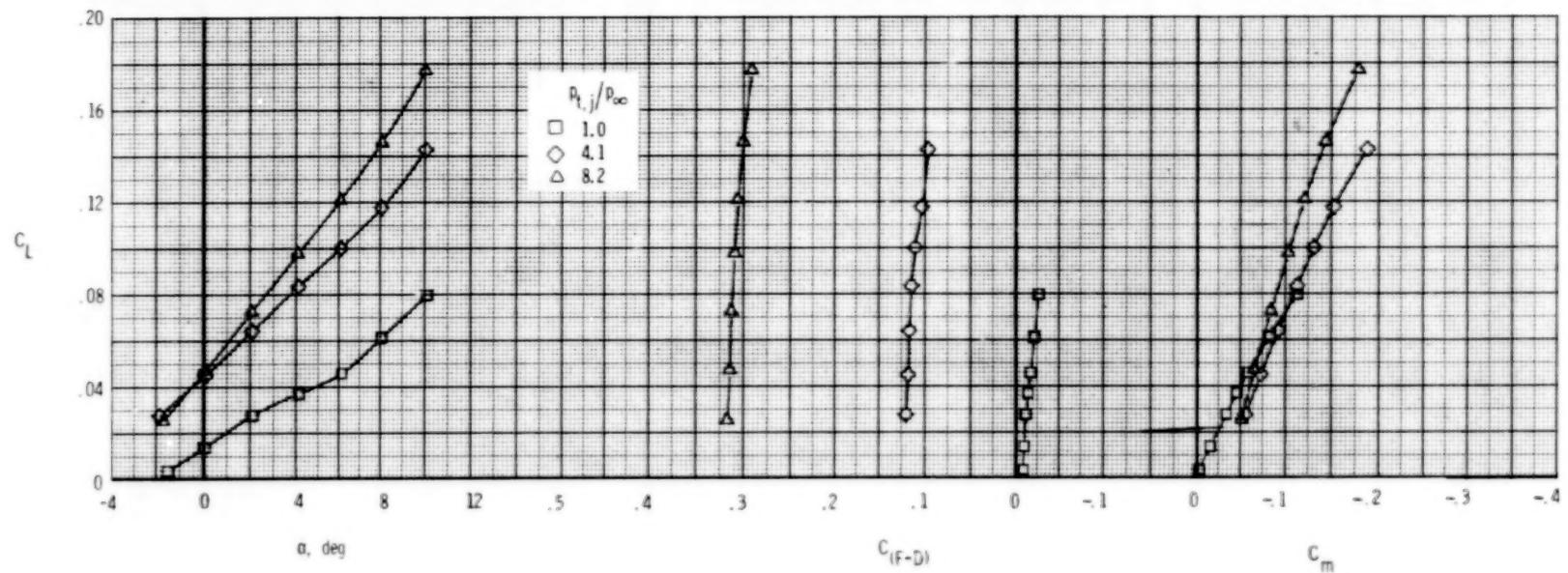
(c) $M = 1.20$.

Figure 42.- Concluded.



(a) $M = 0.60$.

Figure 43.- Longitudinal afterbody aerodynamic characteristics, SERN nozzle, dry power.

$$\delta_h = 0^\circ; \quad \delta_v = 7^\circ; \quad A_e/A_t = 1.15.$$

94

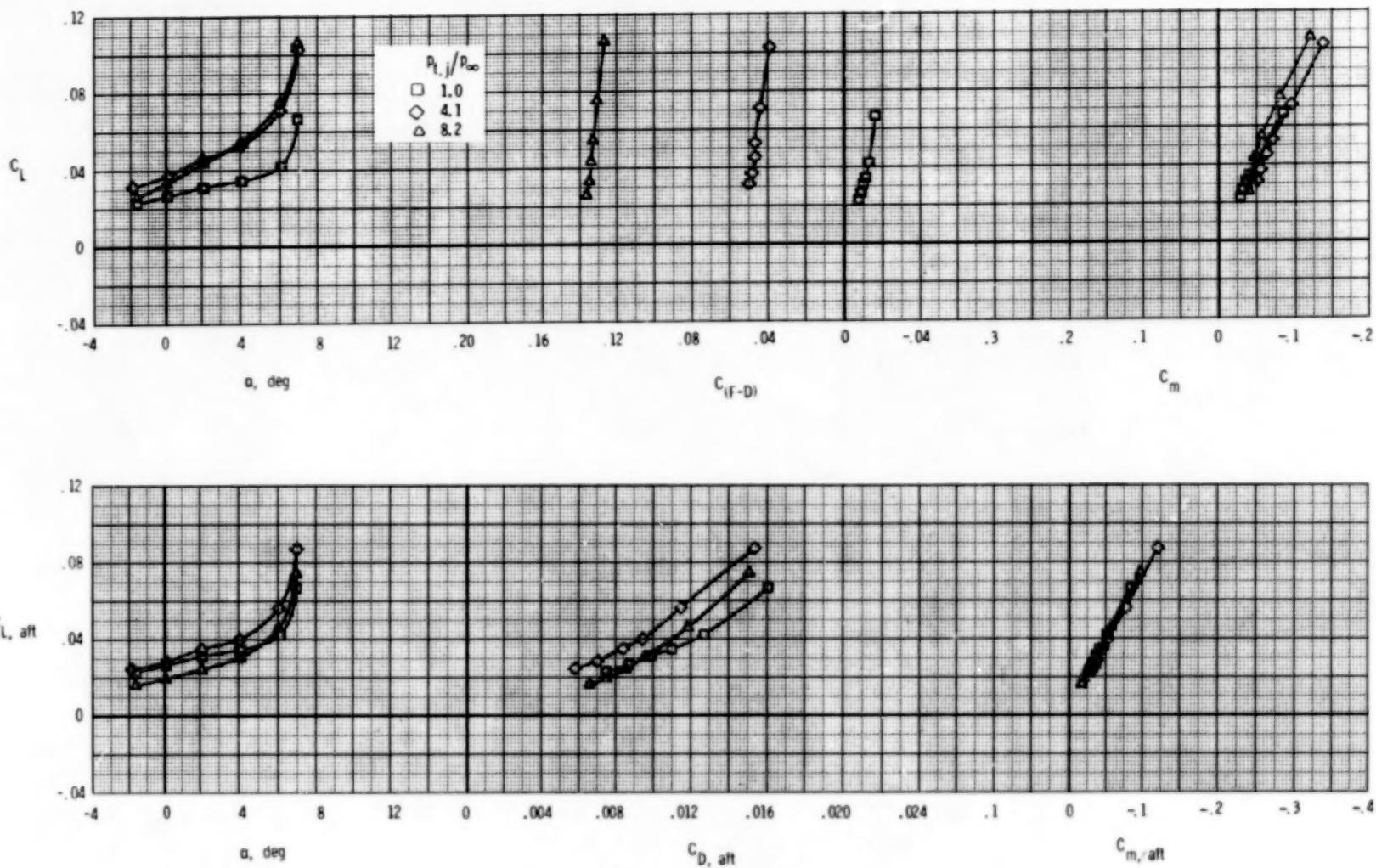
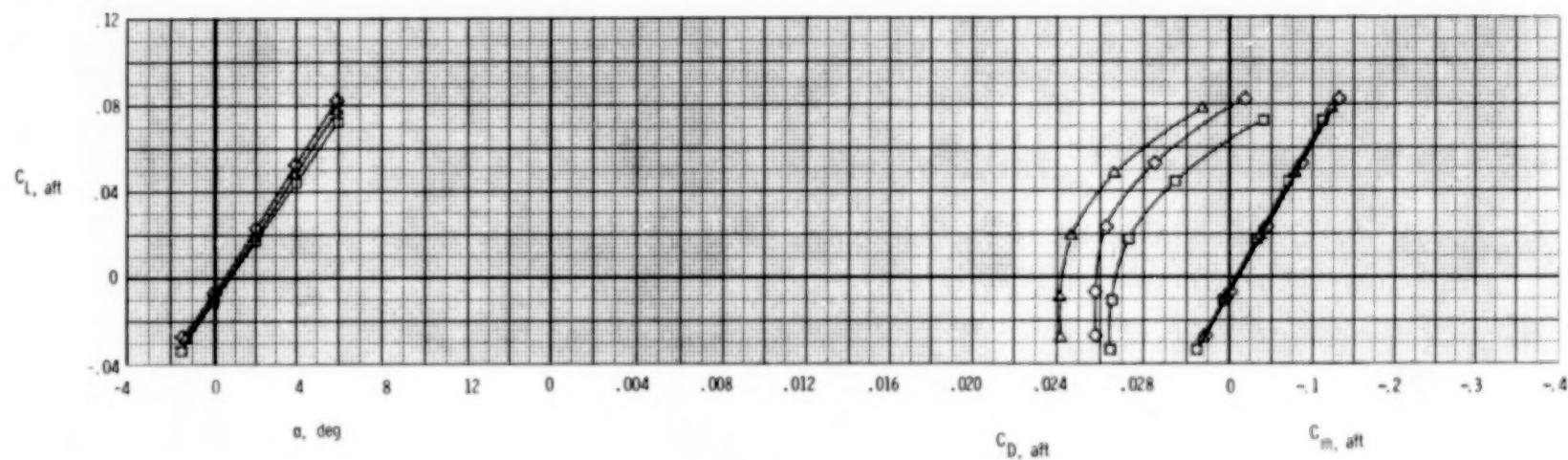
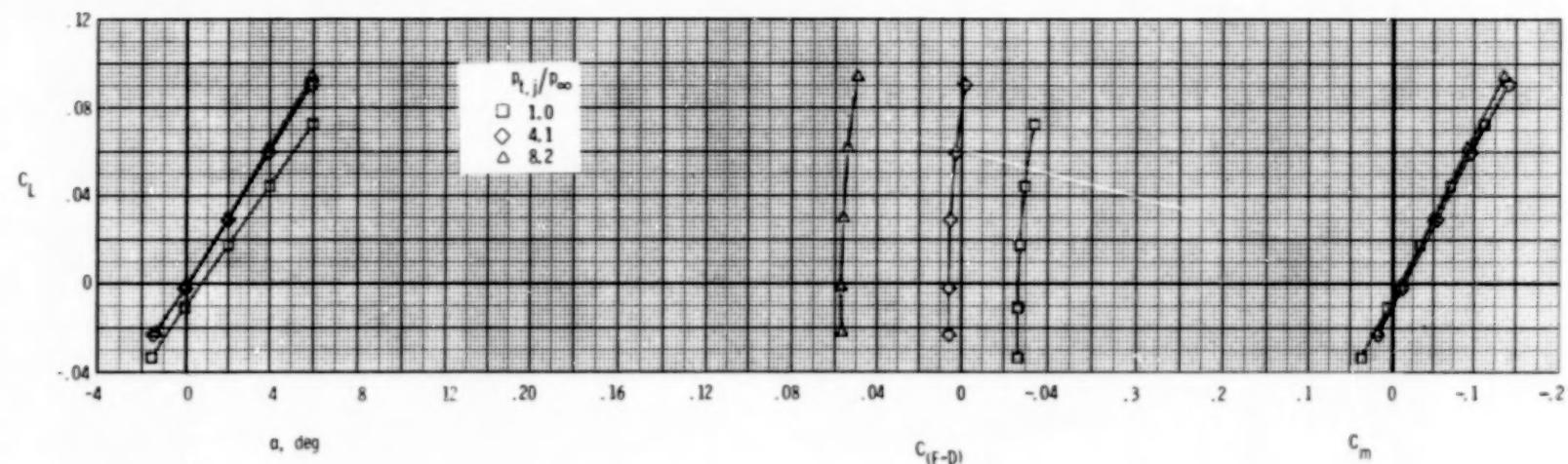
(b) $M = 0.90$.

Figure 43.- Continued.



(c) $M = 1.20$.

Figure 43.- Concluded.

96

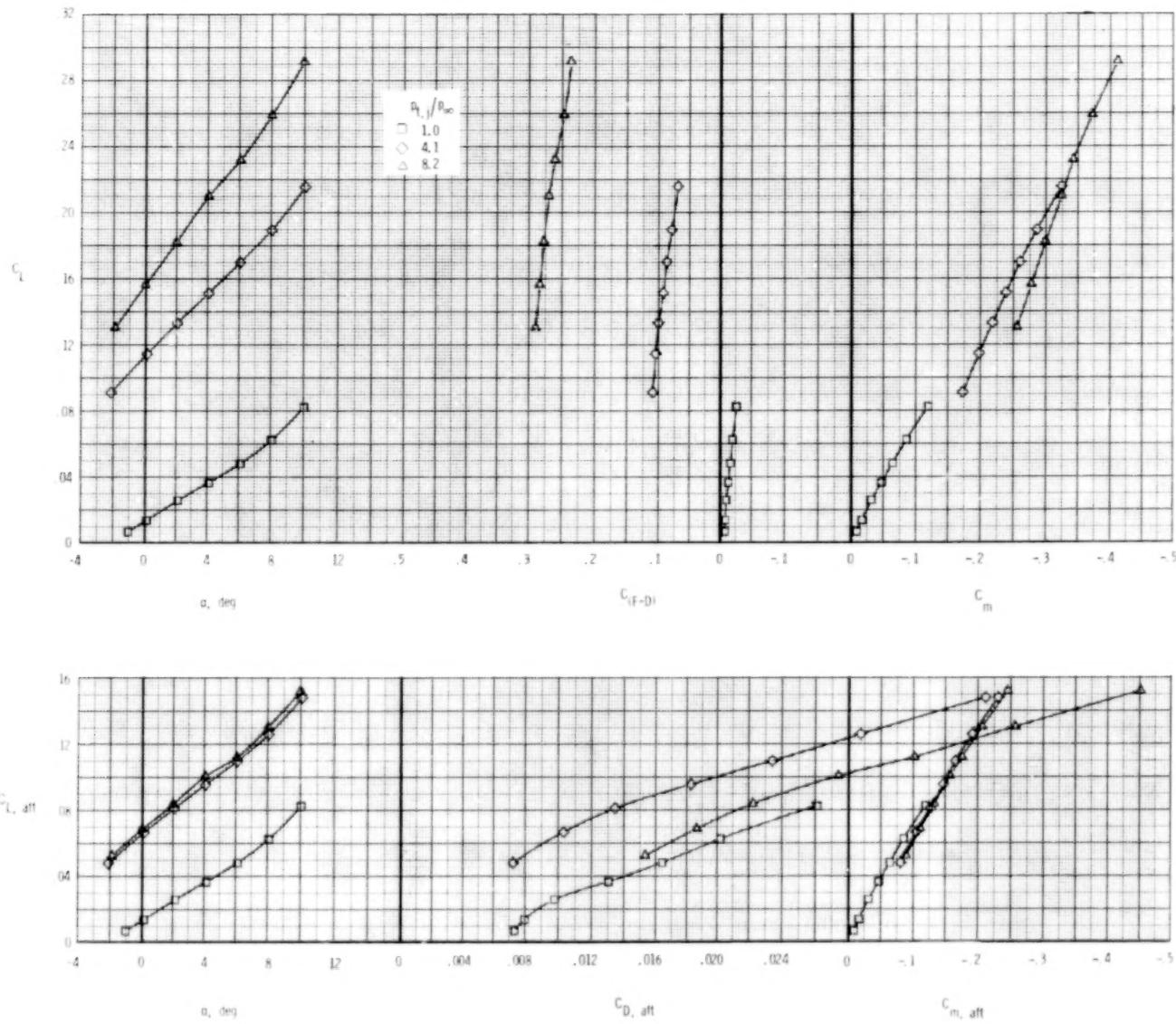
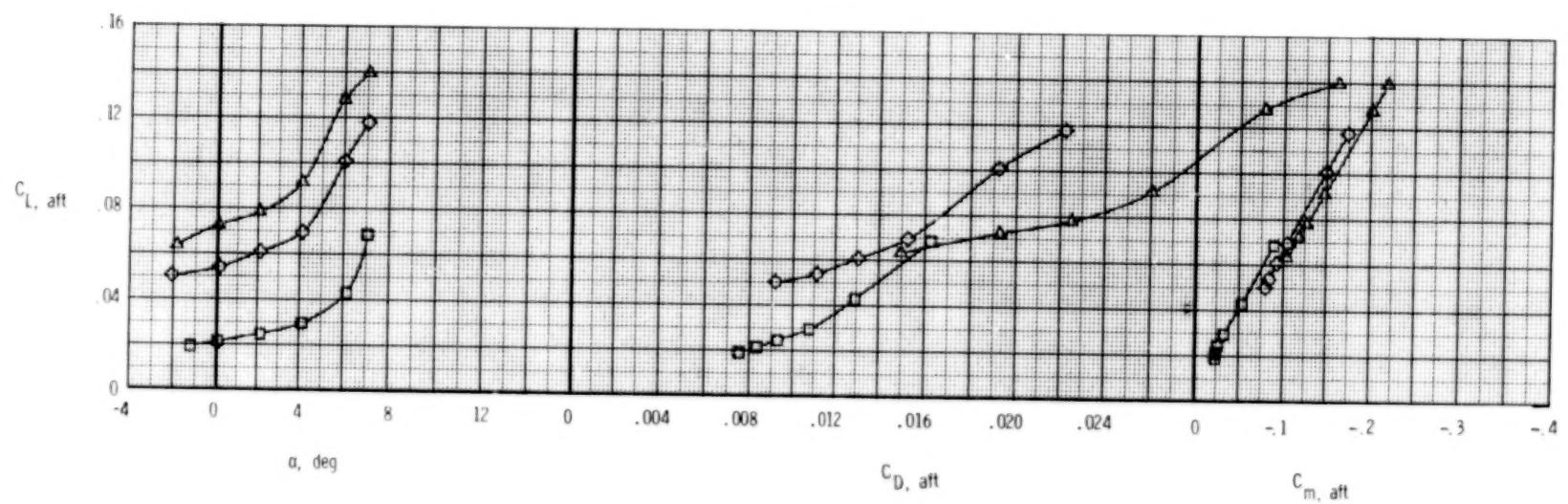
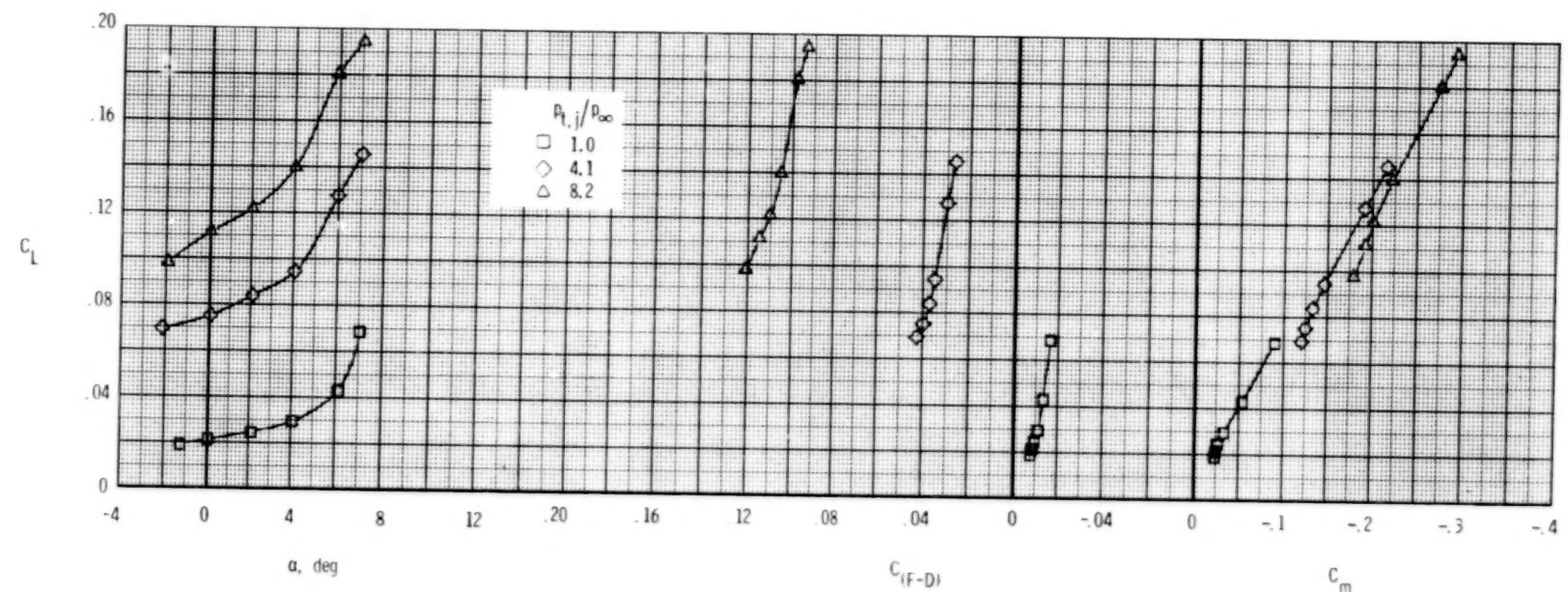
(a) $M = 0.60.$

Figure 44.- Longitudinal afterbody aerodynamic characteristics, SERN nozzle, dry power.

$$\delta_h = 0^\circ; \quad \delta_v = 20^\circ; \quad A_e/A_t = 1.15.$$



(b) $M = 0.90$.

Figure 44.- Continued.

98

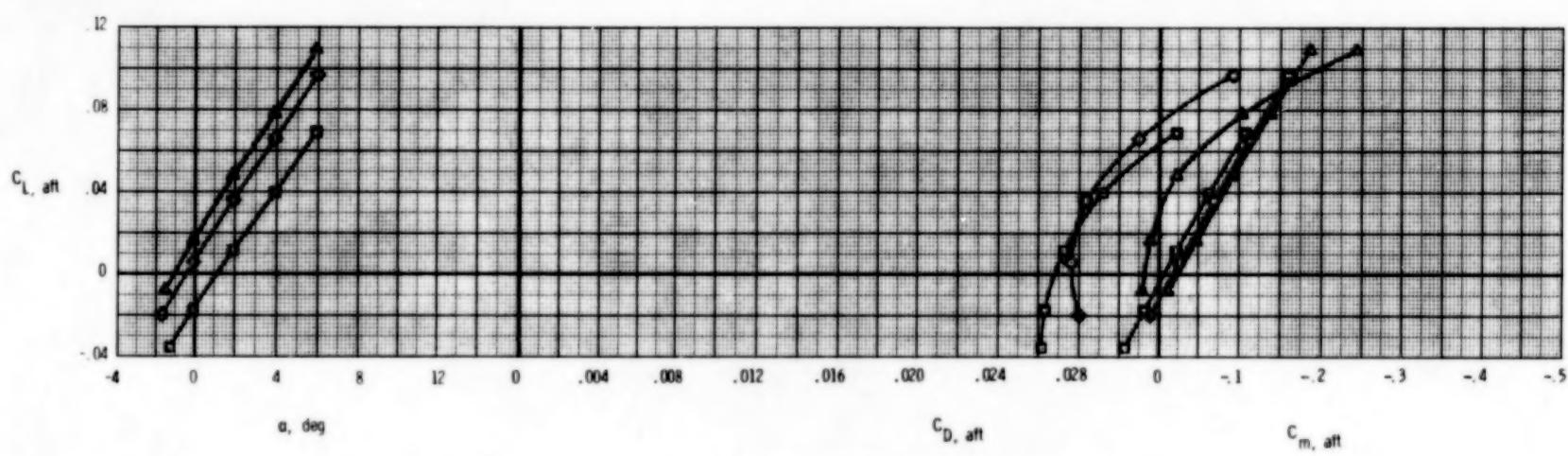
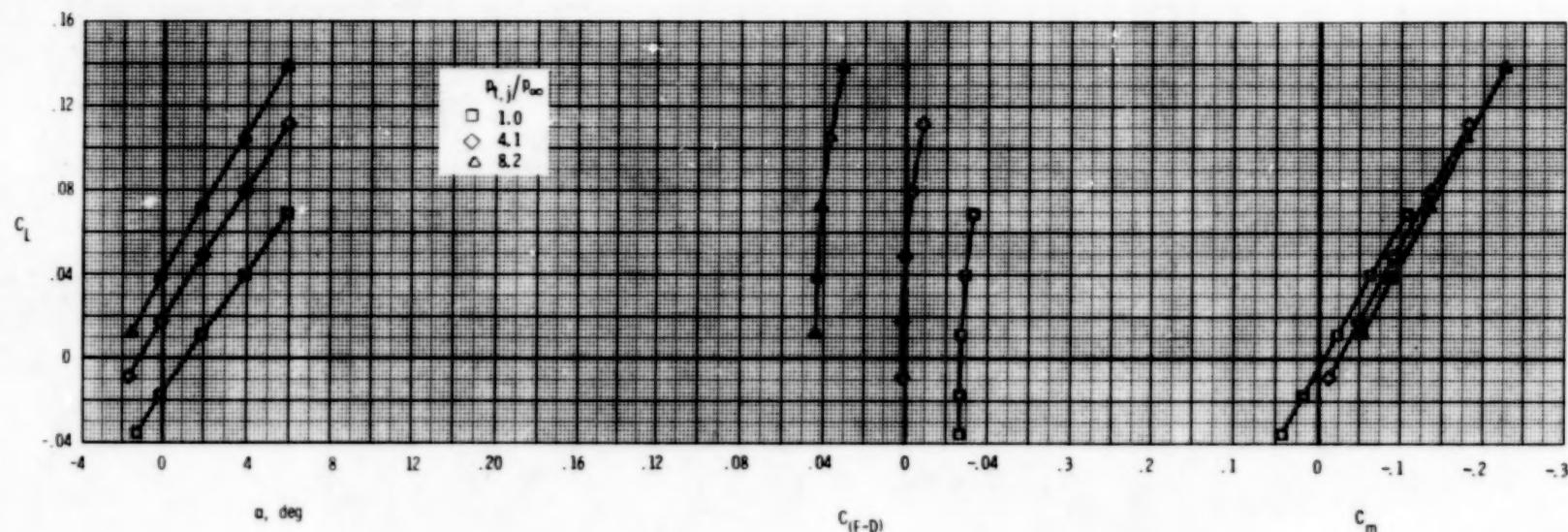
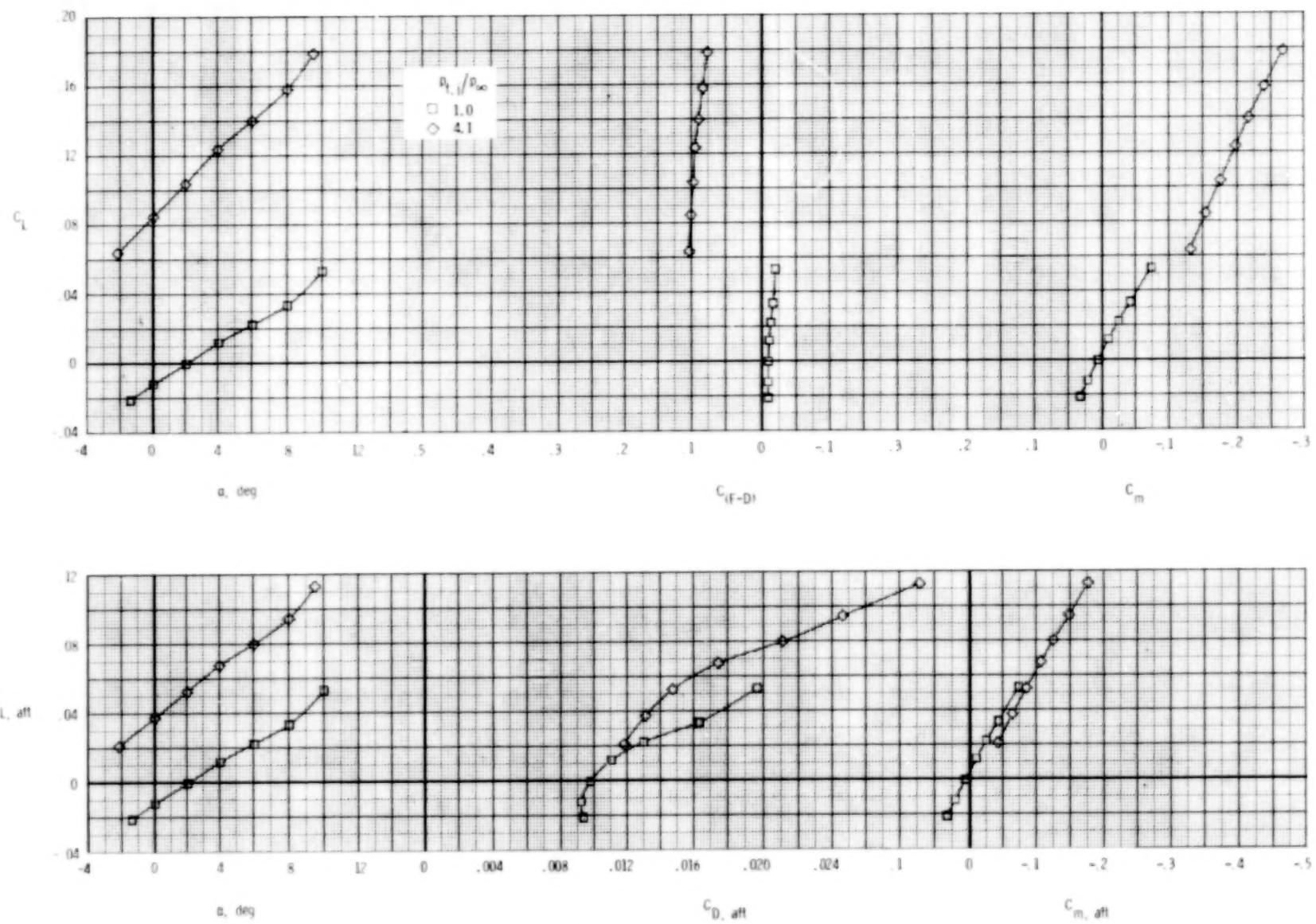
(c) $M = 1.20$.

Figure 44.- Concluded.



(a) $M = 0.60$.

Figure 45.- Longitudinal afterbody aerodynamic characteristics, SERN nozzle, dry power.

$$\delta_h = -2^0; \quad \delta_v = 20^0; \quad A_e/A_t = 1.15.$$

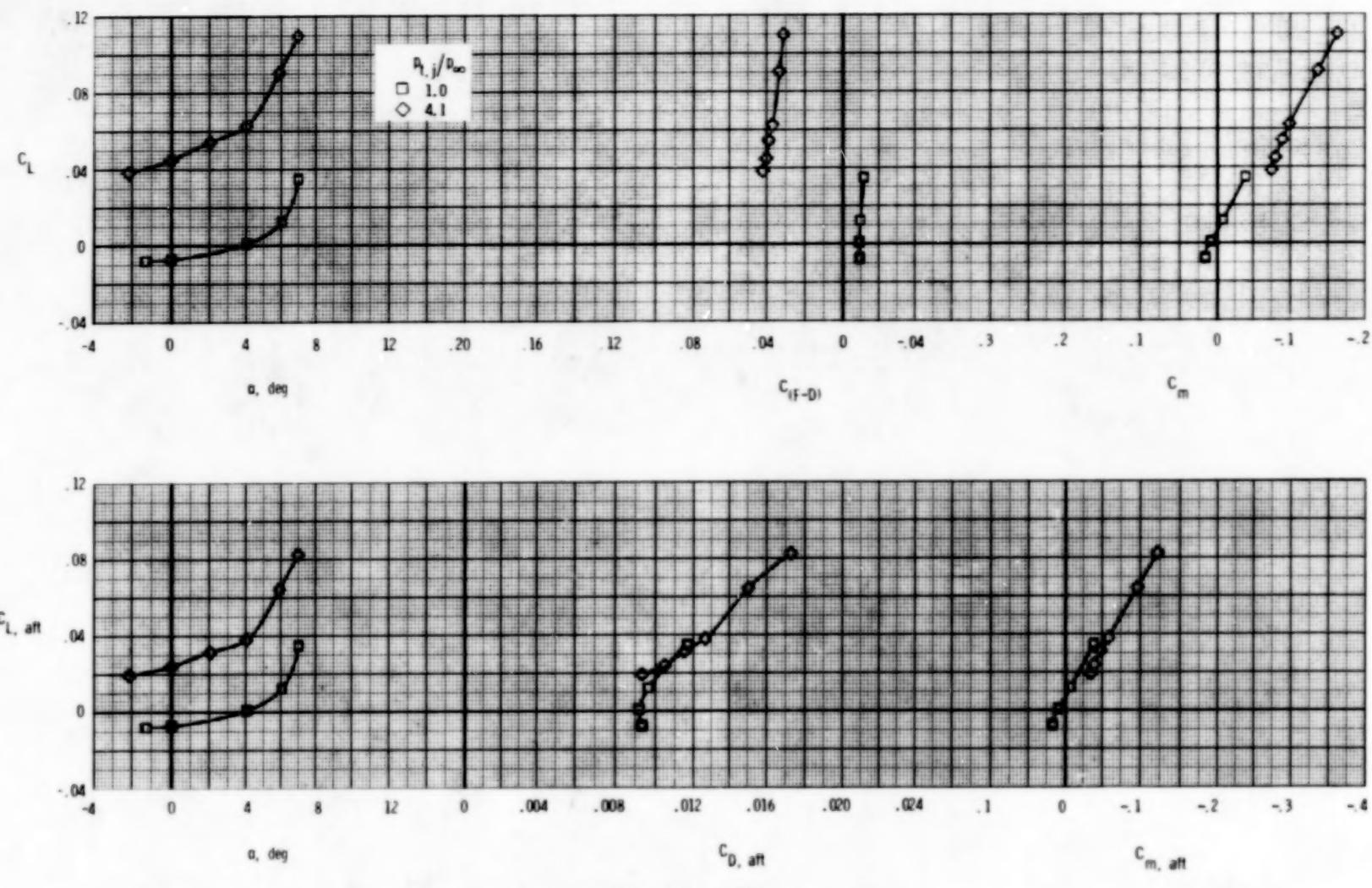
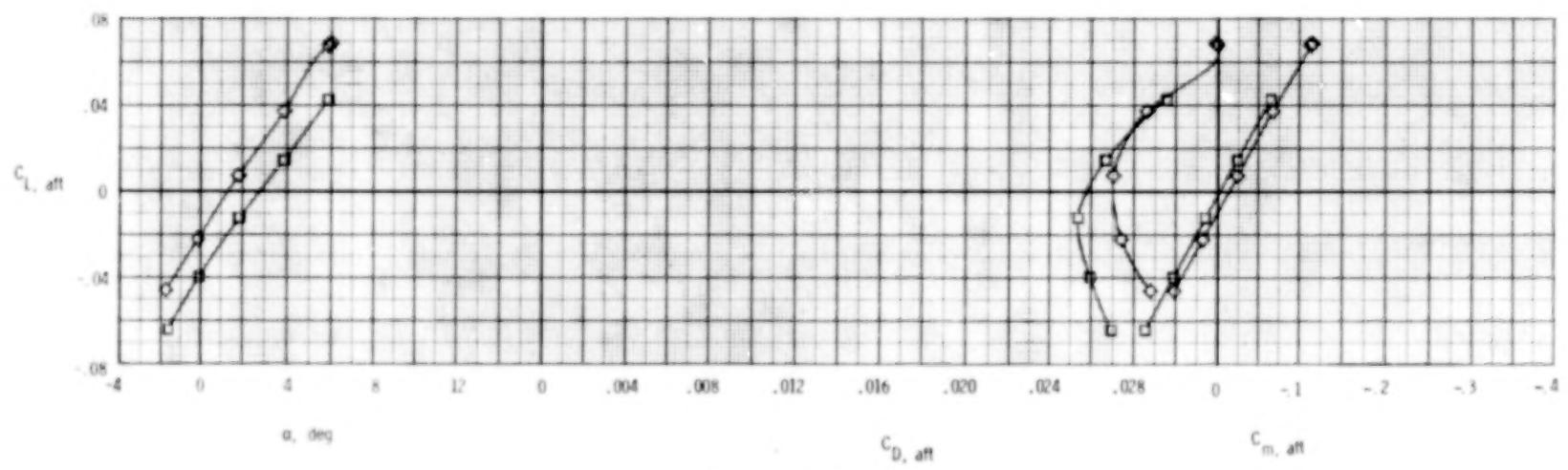
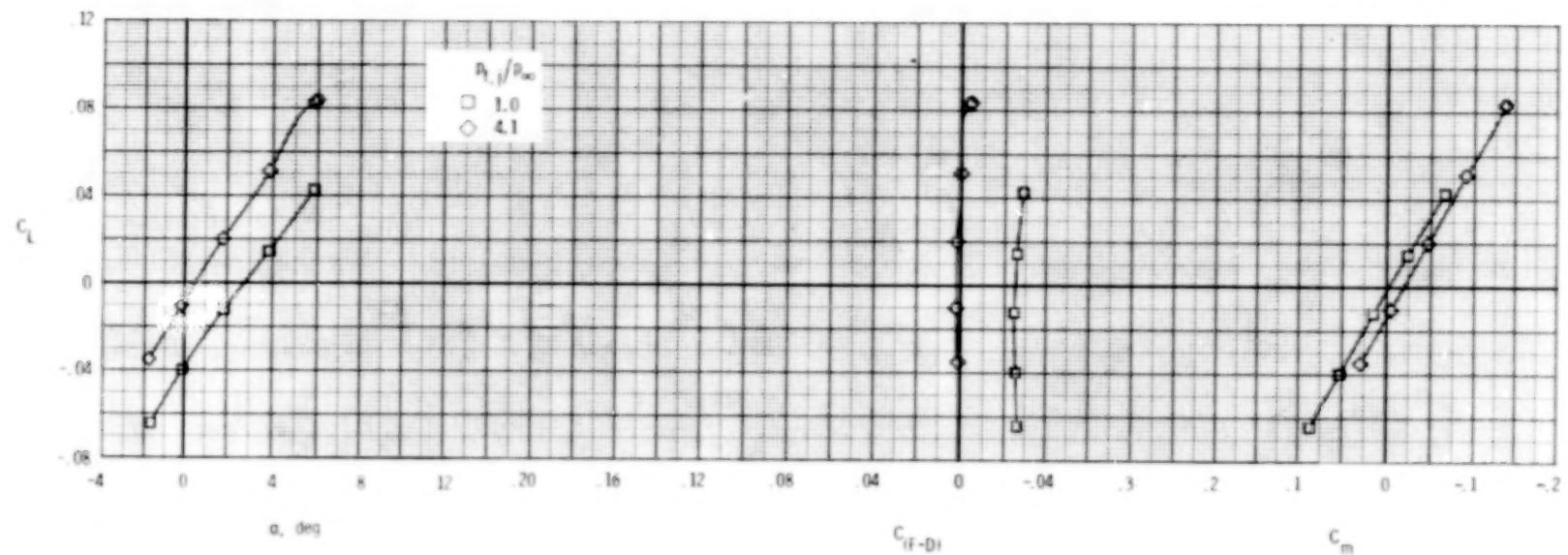
(b) $M = 0.90$.

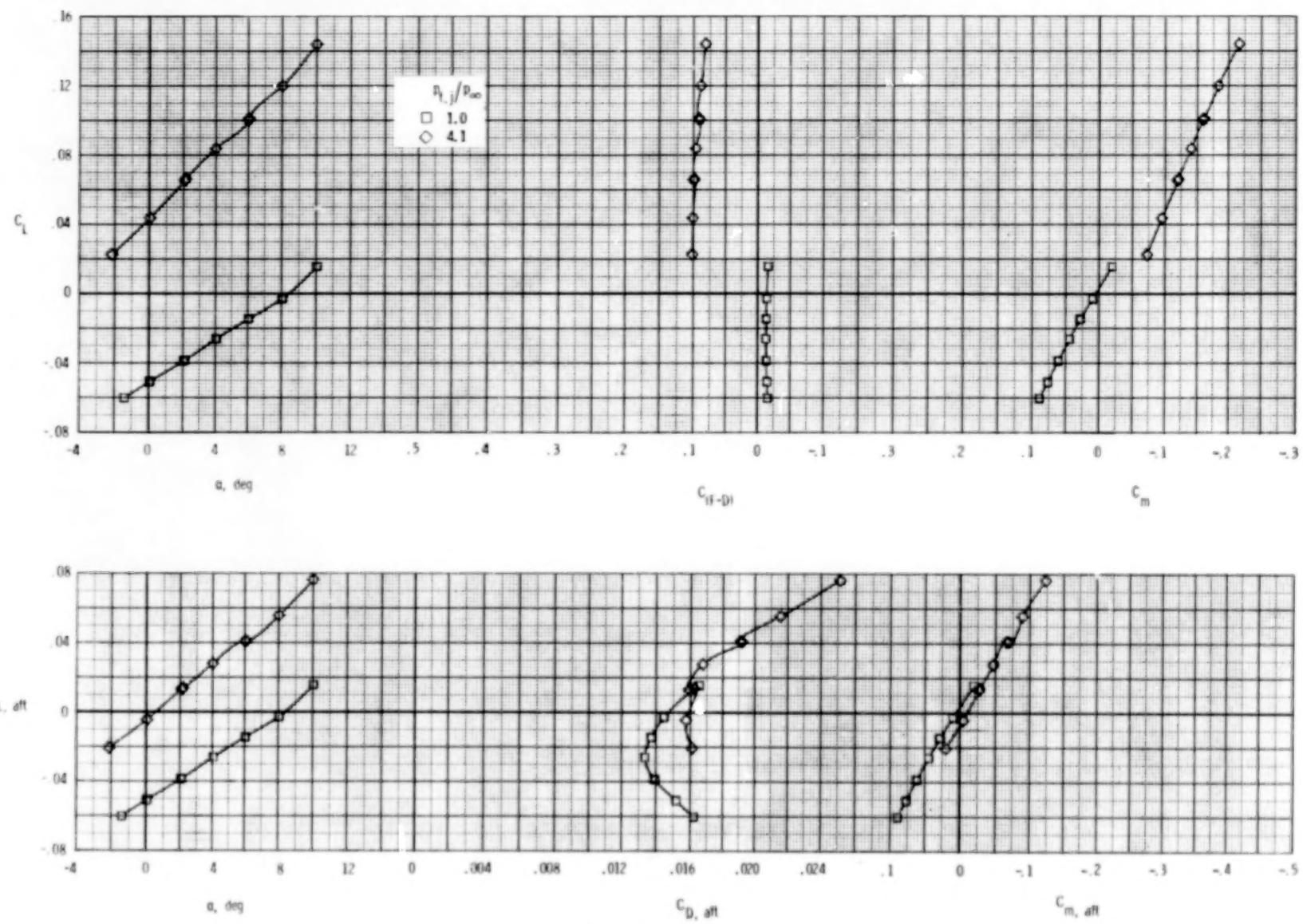
Figure 45.- Continued.



(c) $M = 1.20$.

Figure 45.- Concluded.

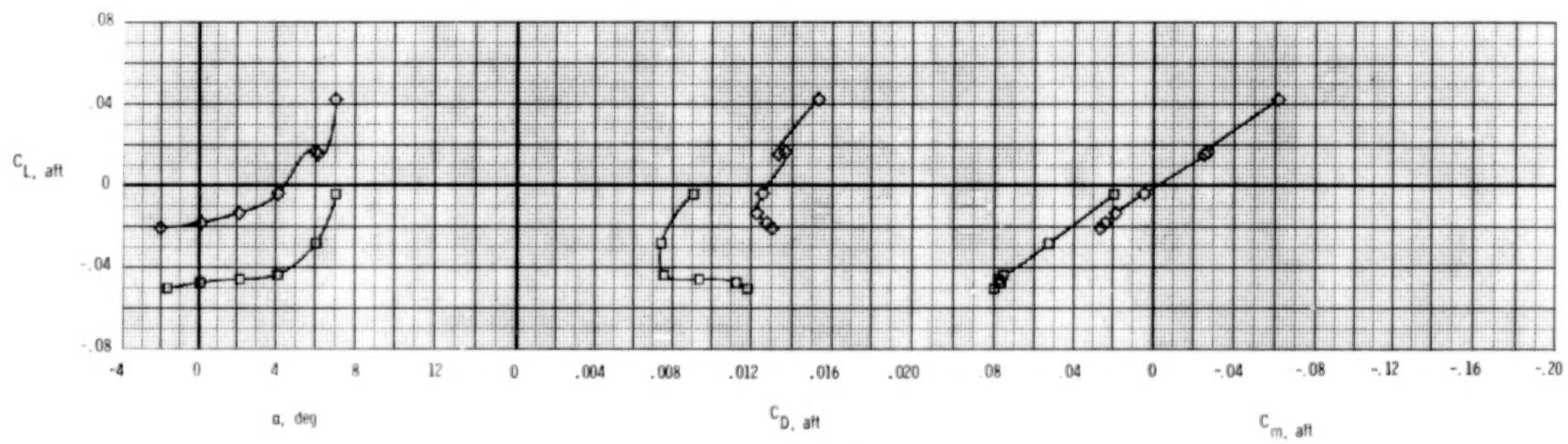
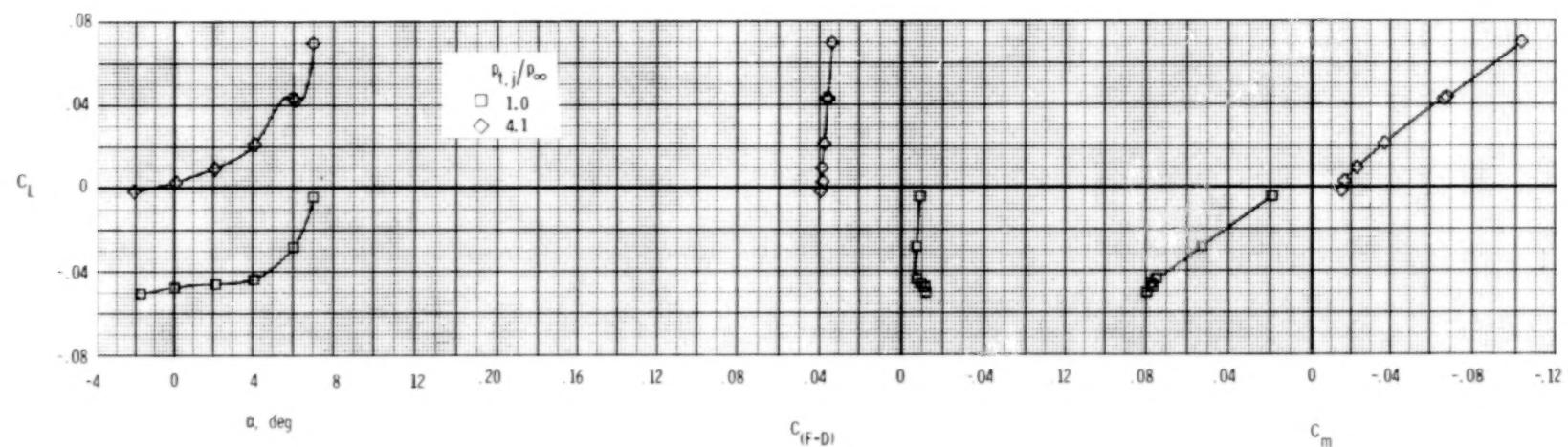
102



(a) $M = 0.60$.

Figure 46. - Longitudinal afterbody aerodynamic characteristics, SERN nozzle, dry power.

$$\delta_h = -5^\circ; \quad \delta_v = 20^\circ; \quad A_e/A_t = 1.15.$$



(b) $M = 0.90$.

Figure 46.- Concluded.

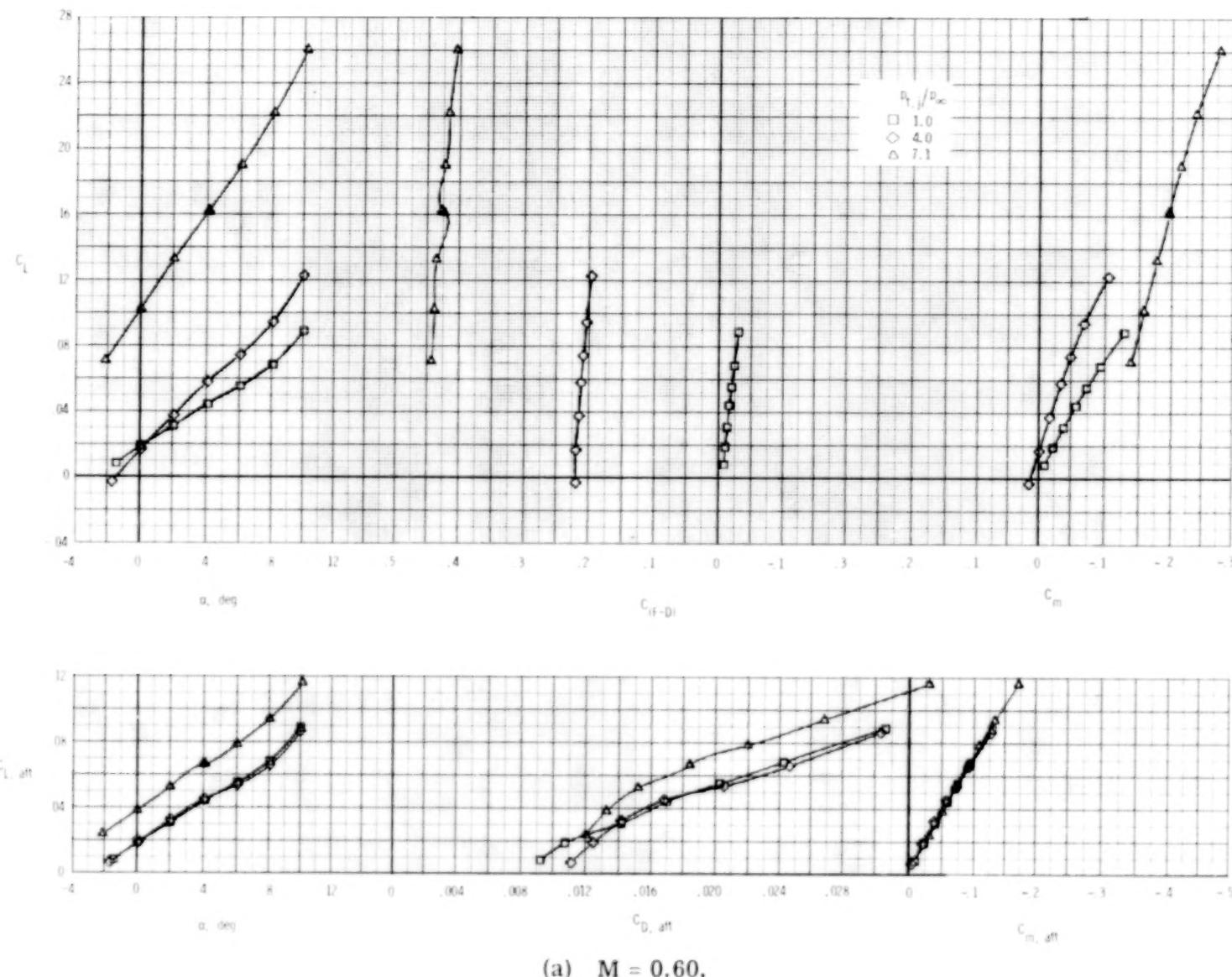
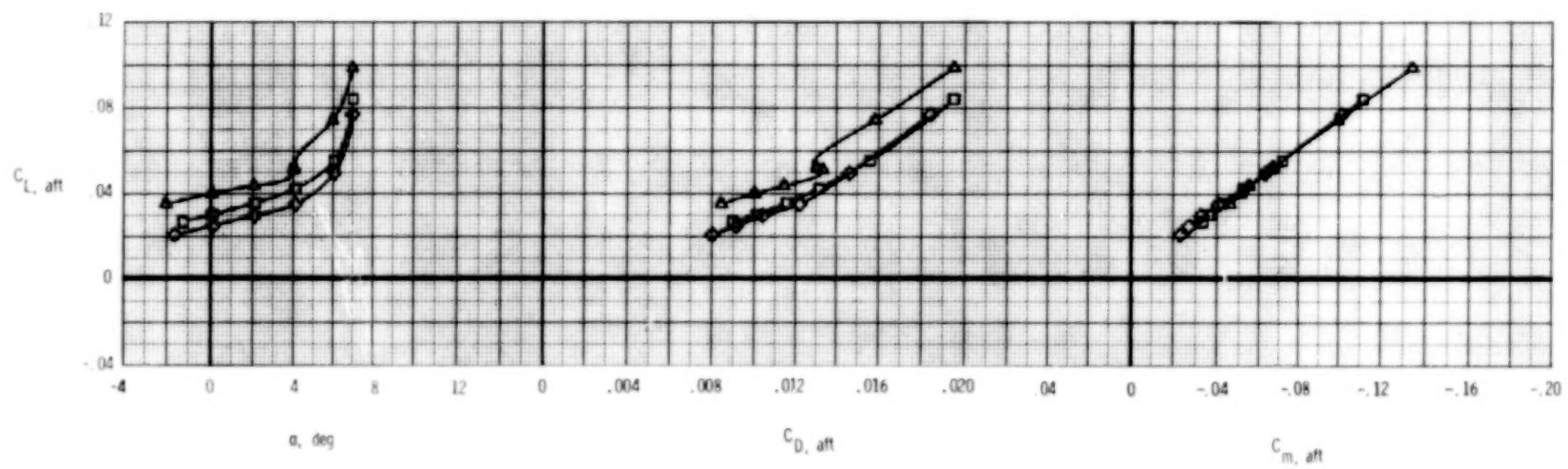
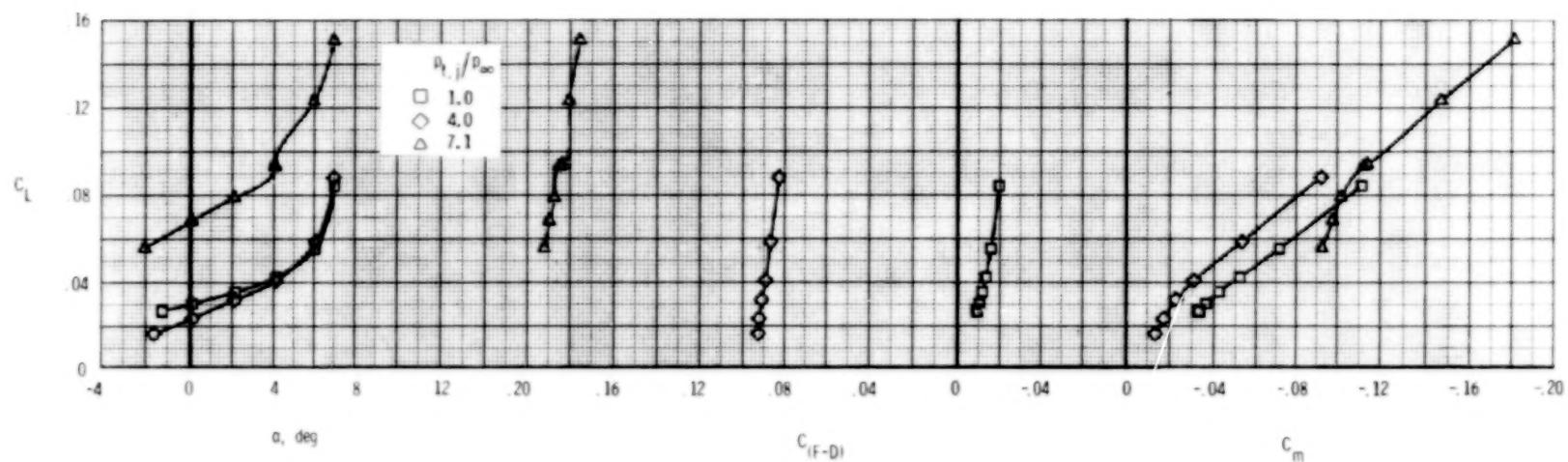
(a) $M = 0.60$.

Figure 47.- Longitudinal afterbody aerodynamic characteristics, SERN nozzle, A/B power.

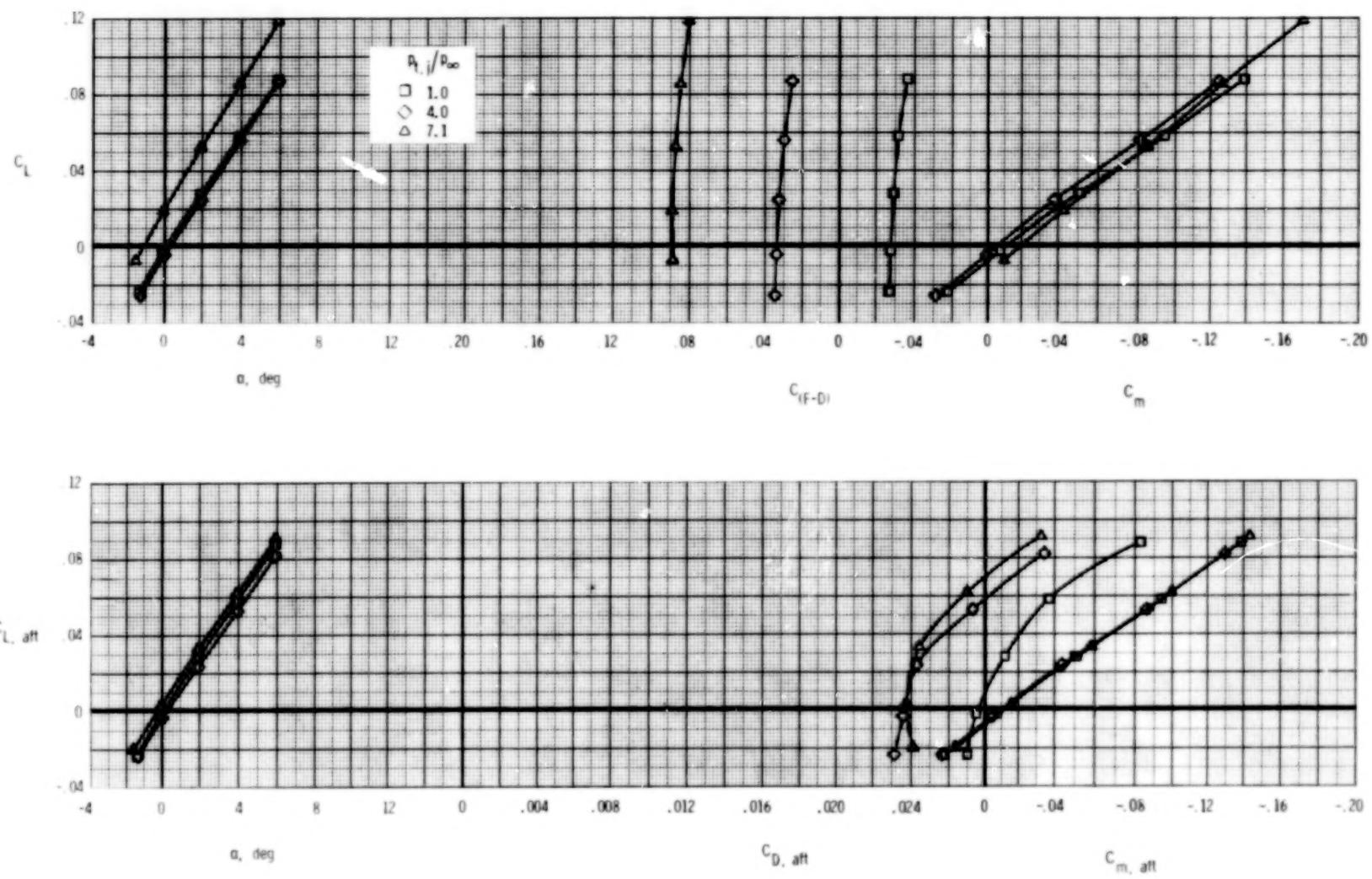
$$\delta_h = 0^\circ; \quad \delta_v = 0^\circ; \quad A_e/A_t = 1.19.$$



(b) $M = 0.90$.

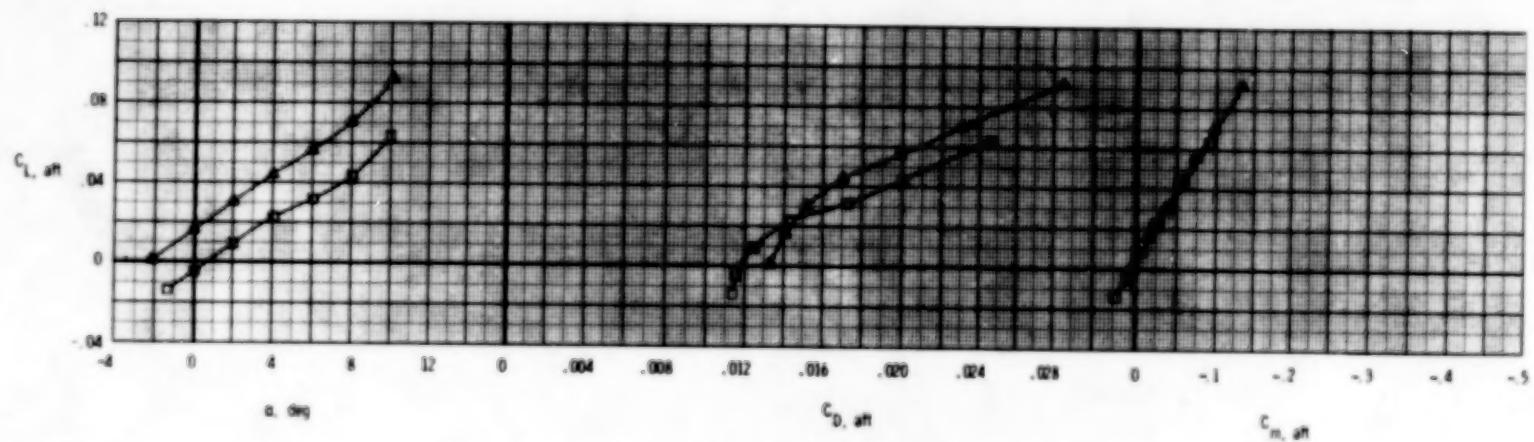
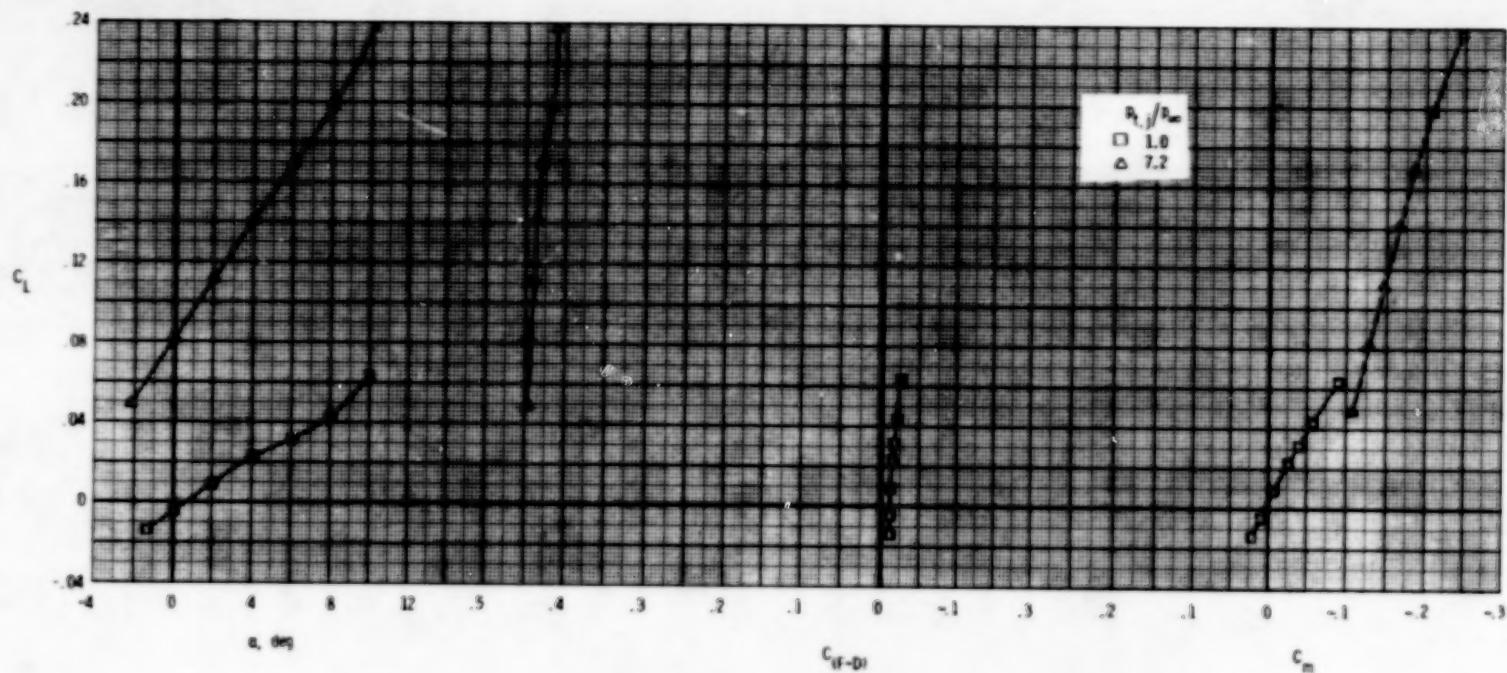
Figure 47.- Continued.

106



(c) $M = 1.20$.

Figure 47.- Concluded.



(a) $M = 0.60$.

Figure 18.- Longitudinal afterbody aerodynamic characteristics, SERN nozzle, A/B power.

$$\delta_h = -2^\circ; \quad \delta_v = 0^\circ; \quad A_e/A_t = 1.19.$$

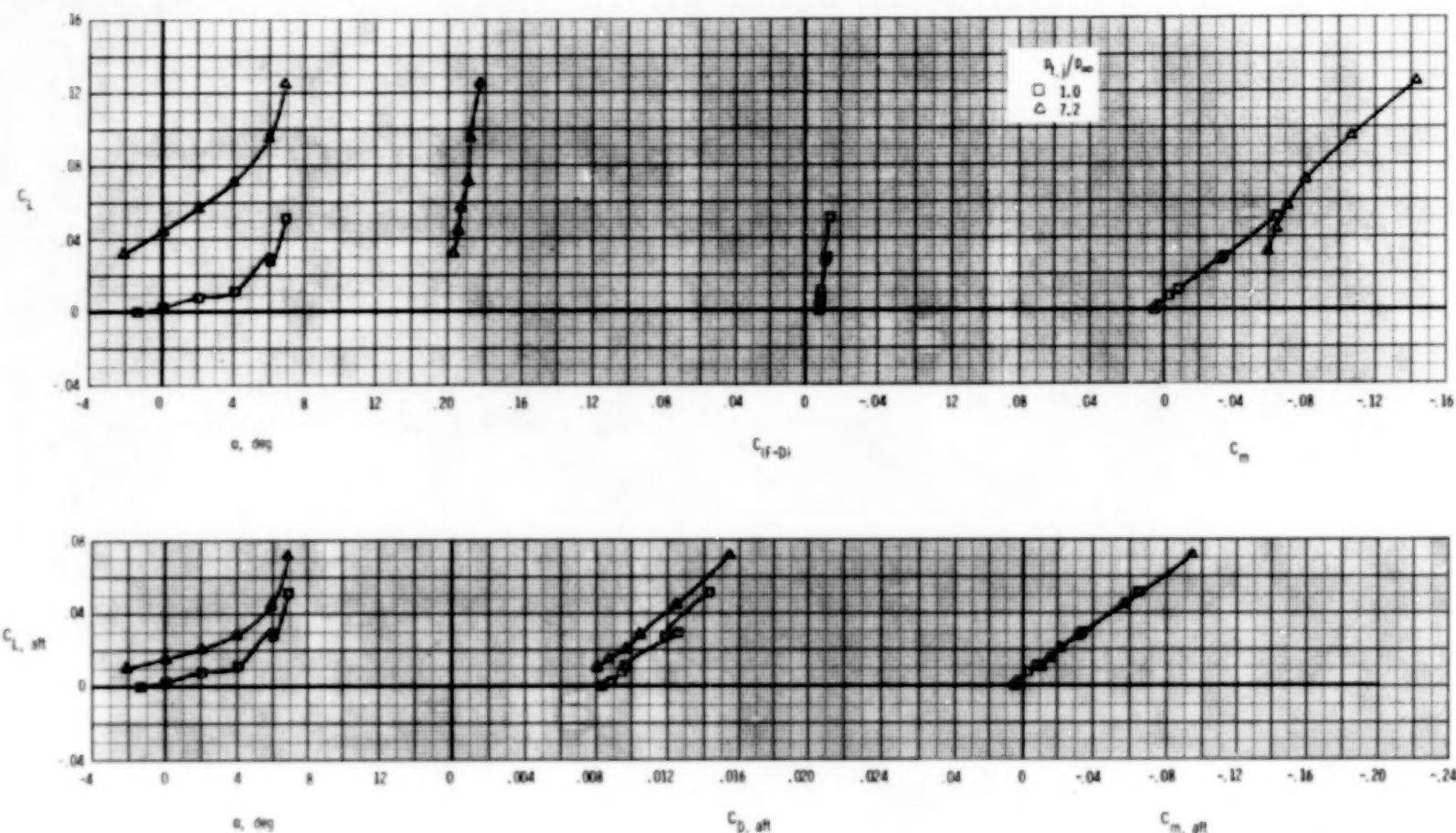
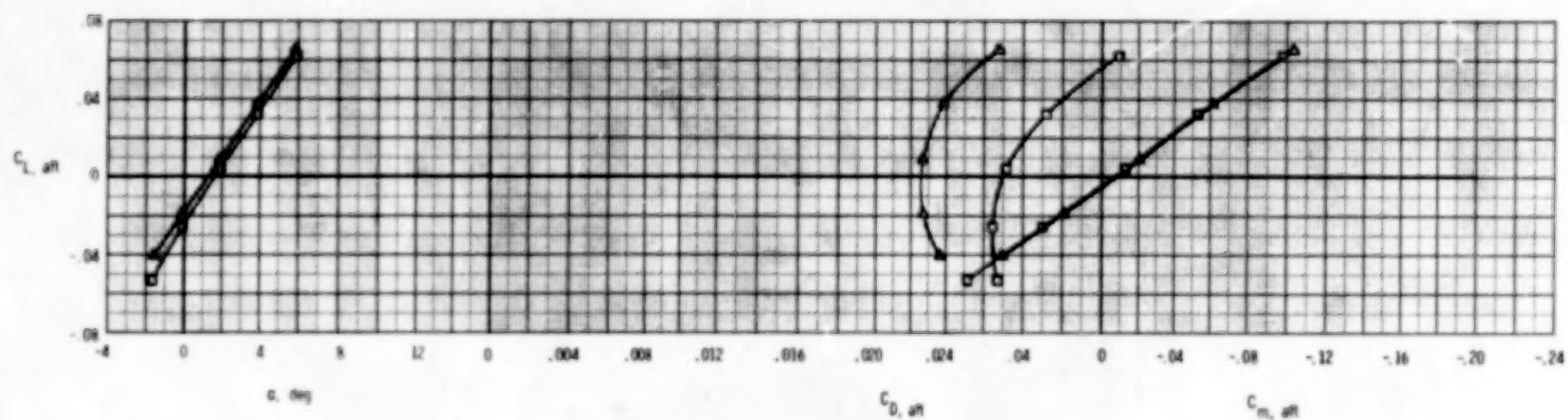
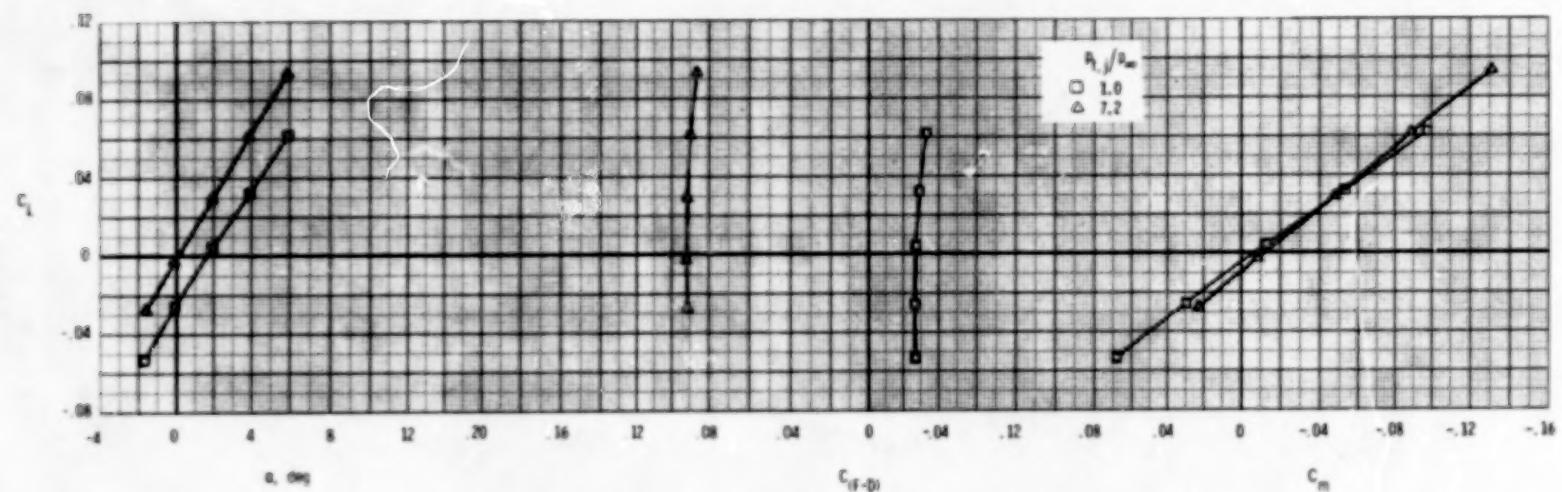
(b) $M = 0.90$.

Figure 48.- Continued.



(c) $M = 1.20$.

Figure 48.- Concluded.

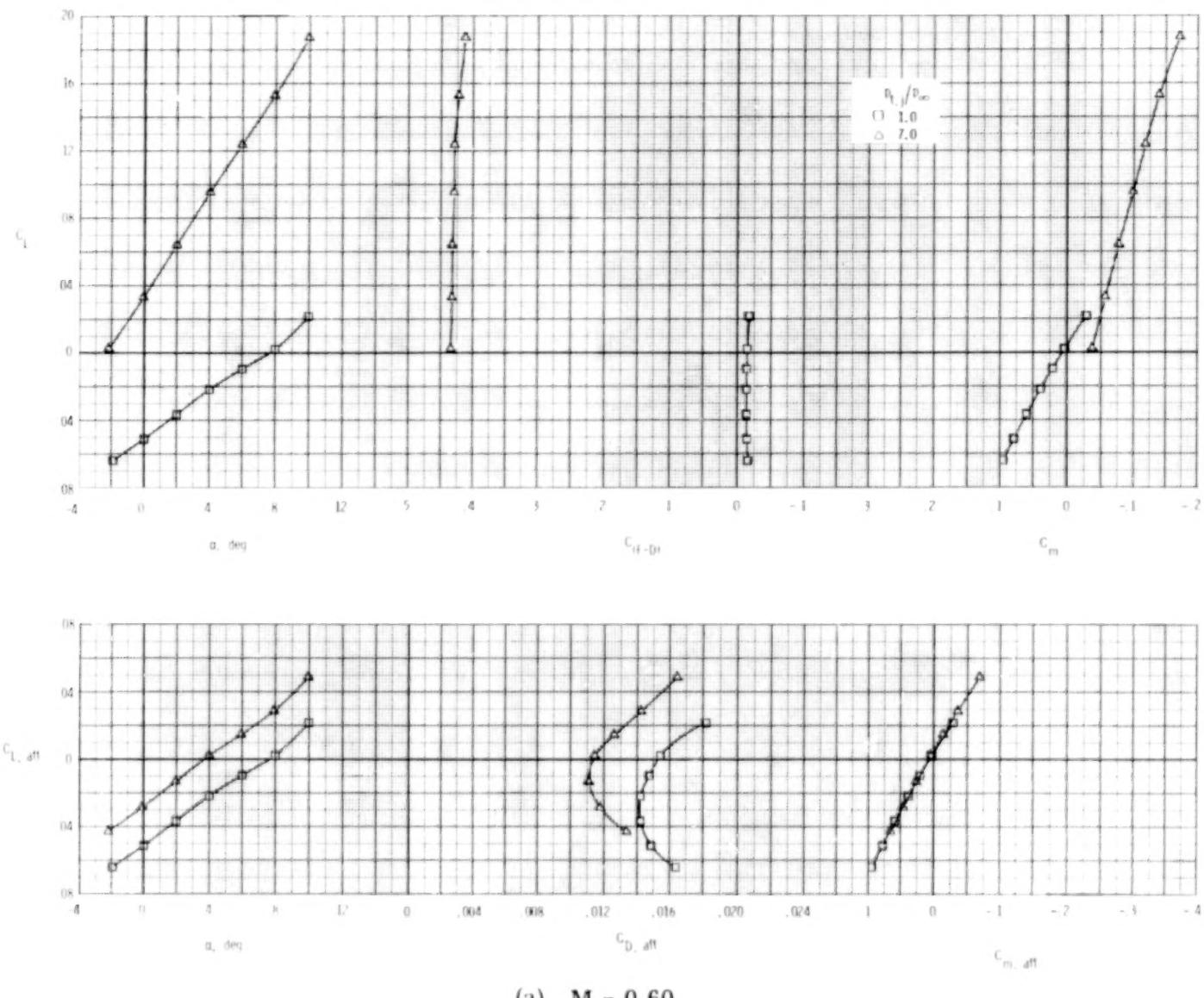
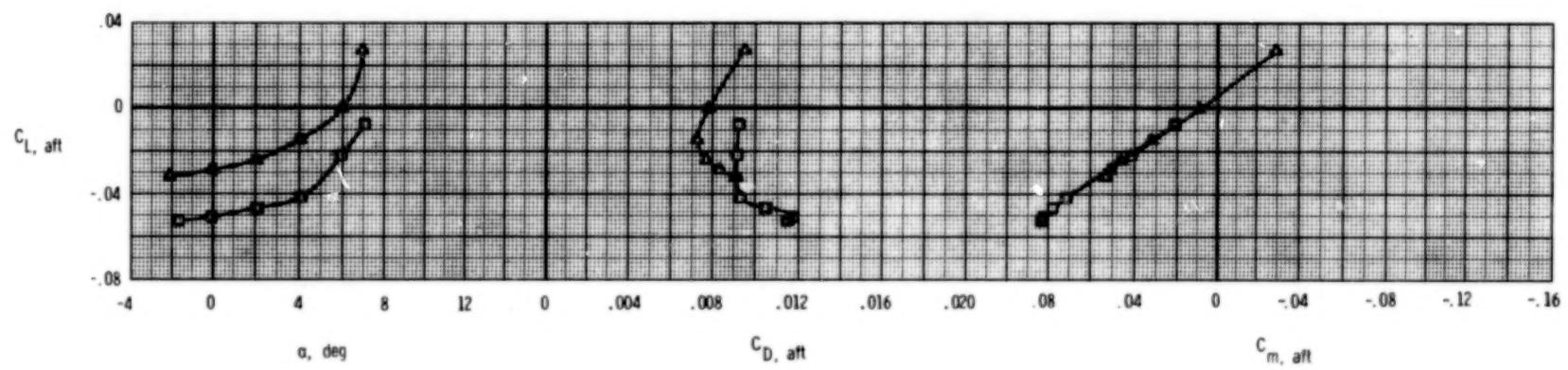
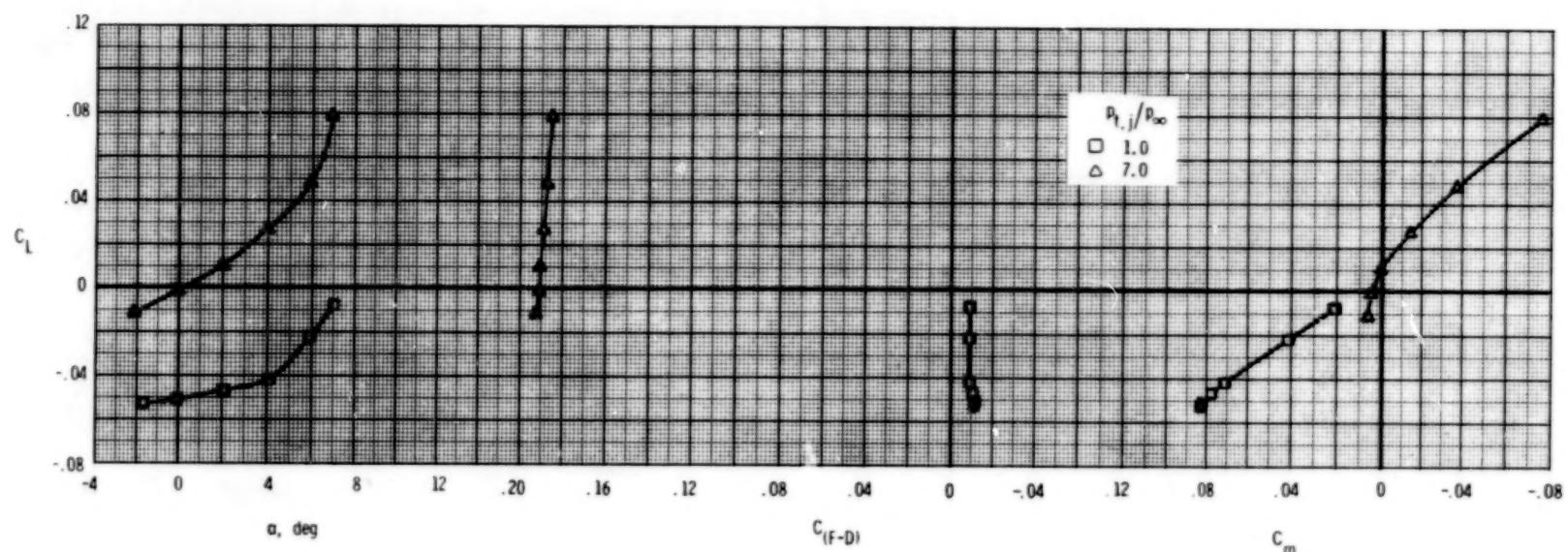
(a) $M = 0.60$.

Figure 49.- Longitudinal afterbody aerodynamic characteristics, SERN nozzle, A/B power.

$$\delta_h = -5^\circ; \quad \delta_v = 0^\circ; \quad A_e/A_t = 1.19.$$



(b) $M = 0.90.$

Figure 49.- Continued.

112

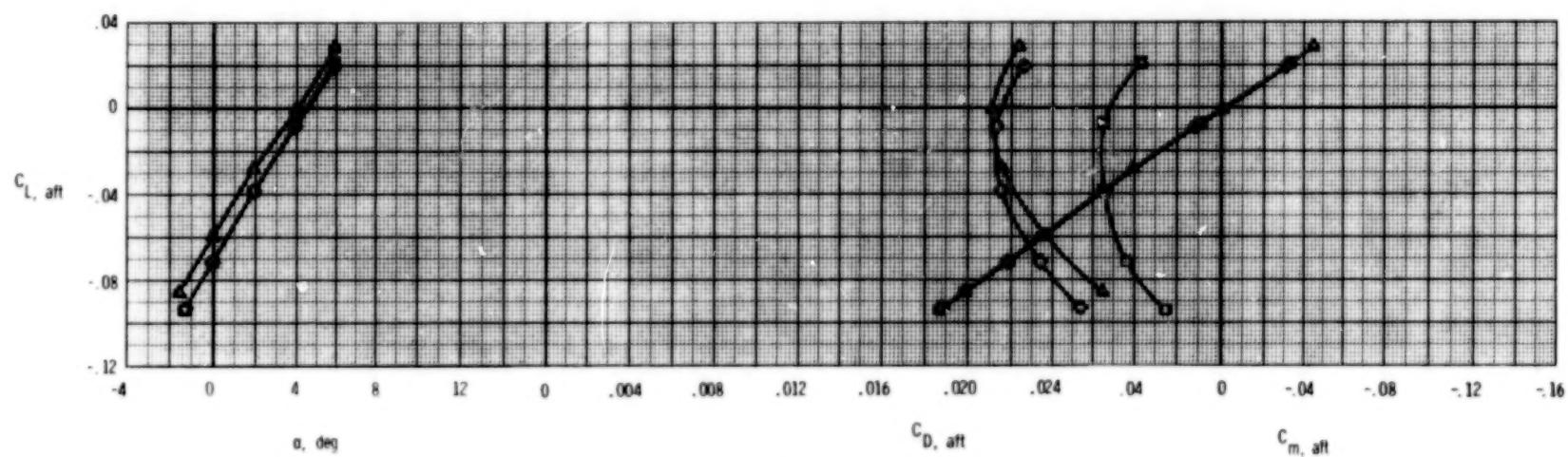
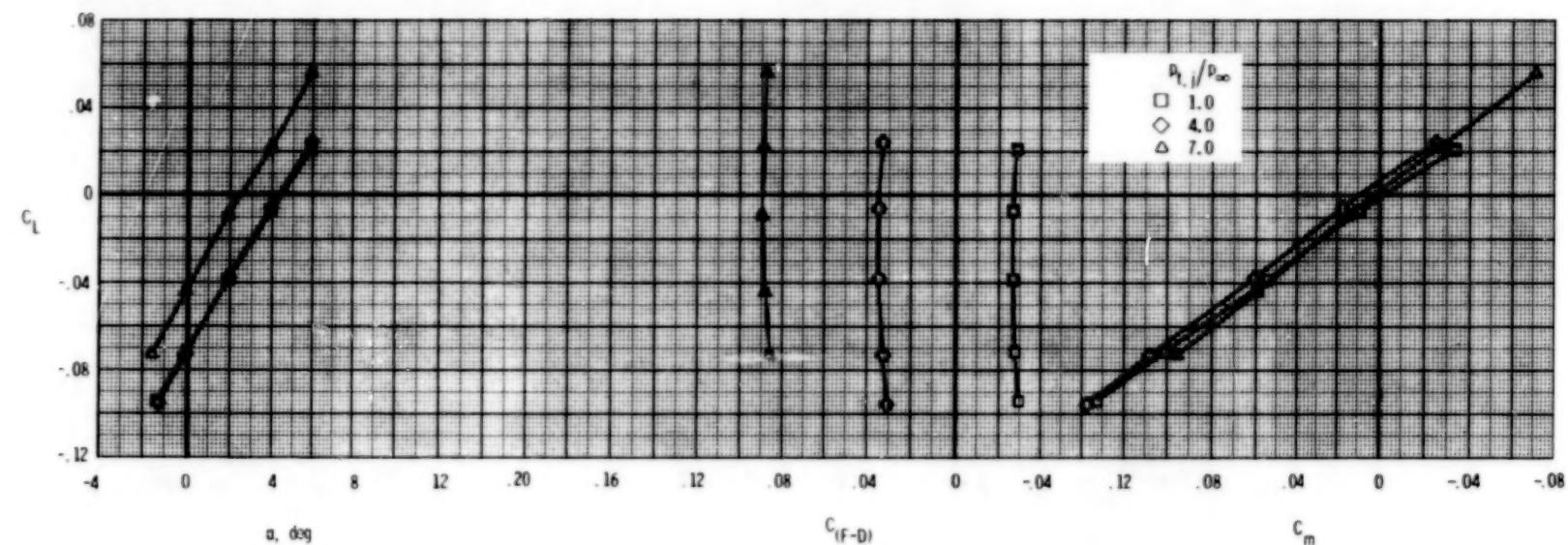
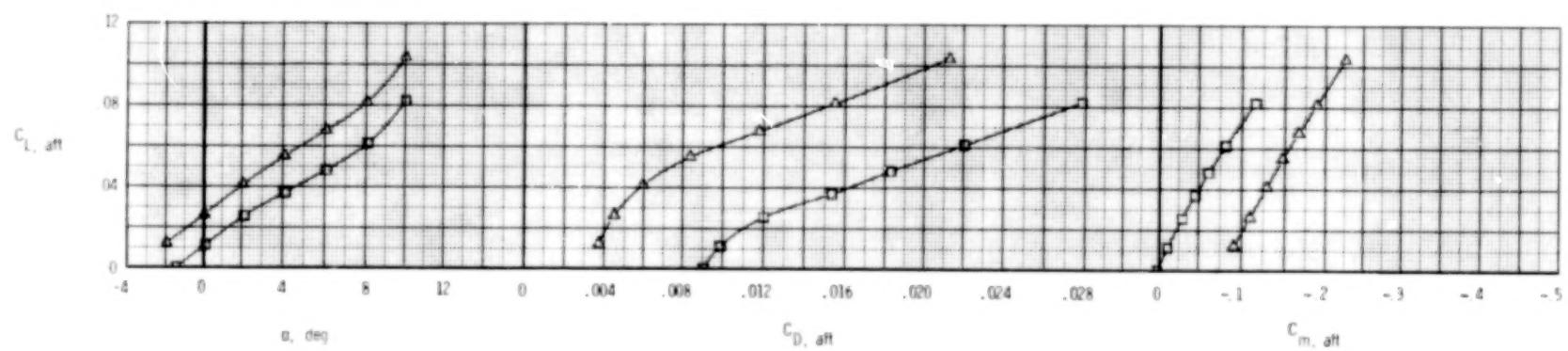
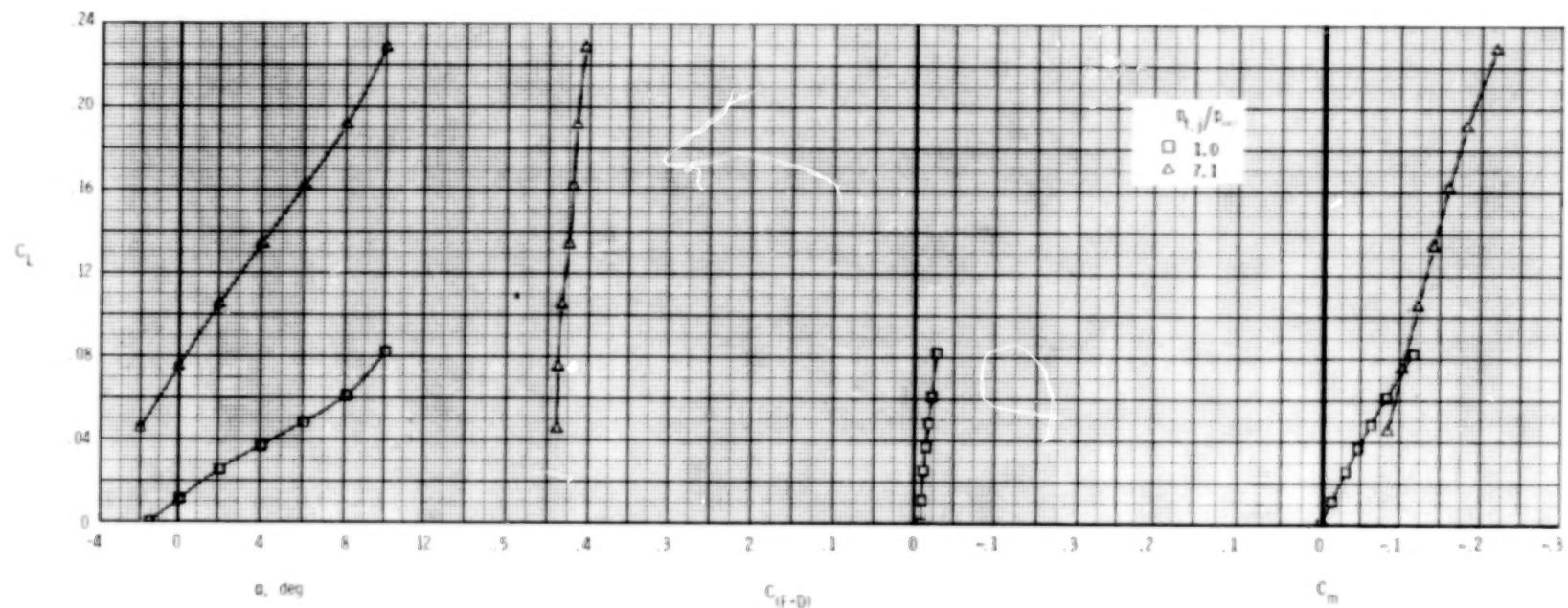
(c) $M = 1.20$.

Figure 49.- Concluded.



(a) $M = 0.60$.

Figure 50.- Longitudinal afterbody aerodynamic characteristics, SERN nozzle, A/B power.

$$\delta_h = 0^\circ; \quad \delta_v = -7^\circ; \quad A_e/A_t = 1.19.$$

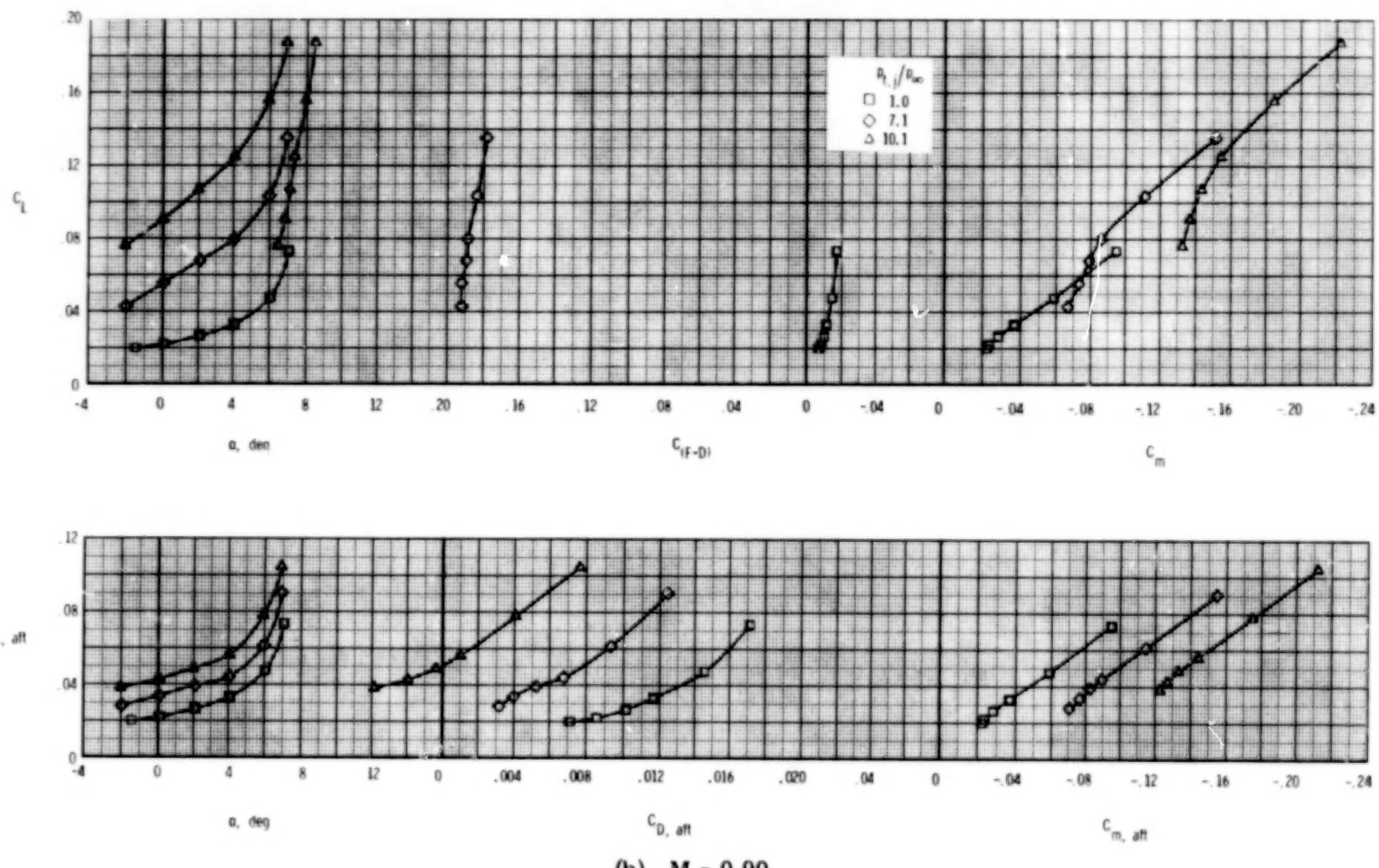
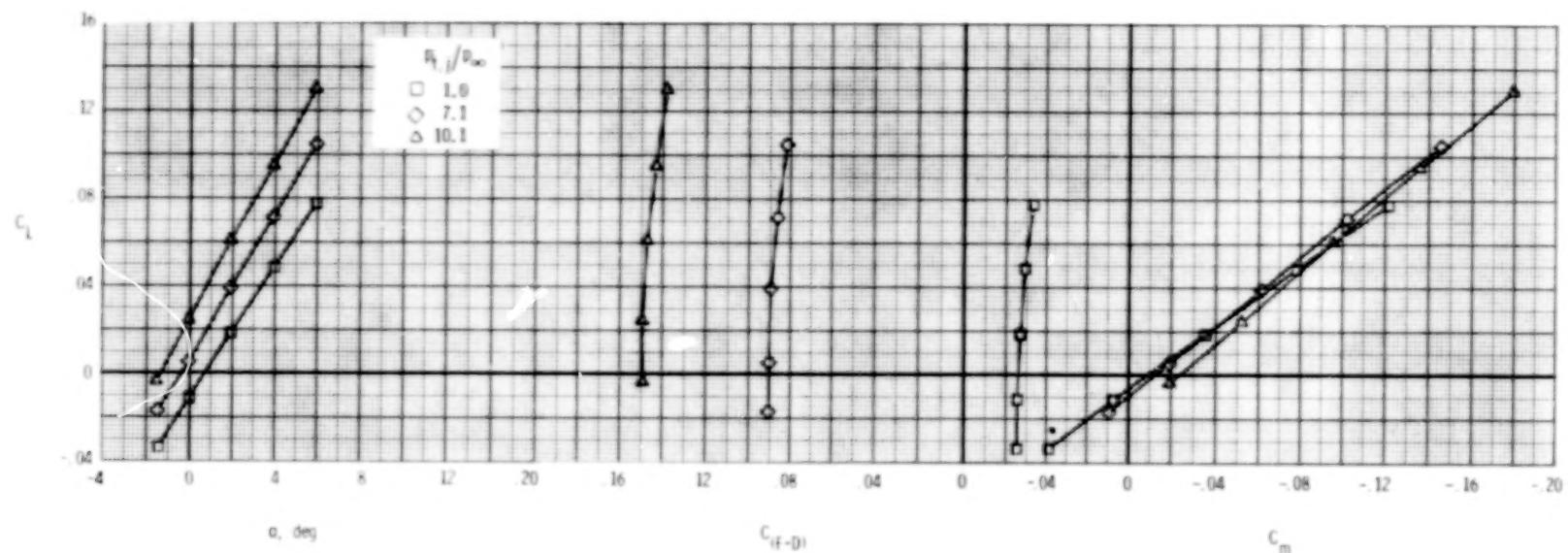
(b) $M = 0.90$.

Figure 50.- Continued.



(c) $M = 1.20$.

Figure 50.- Concluded.

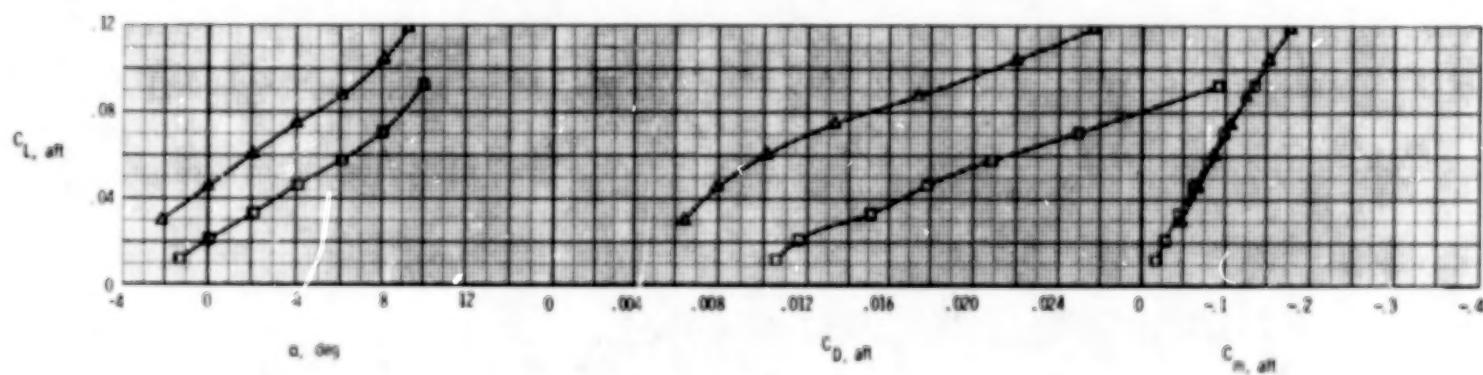
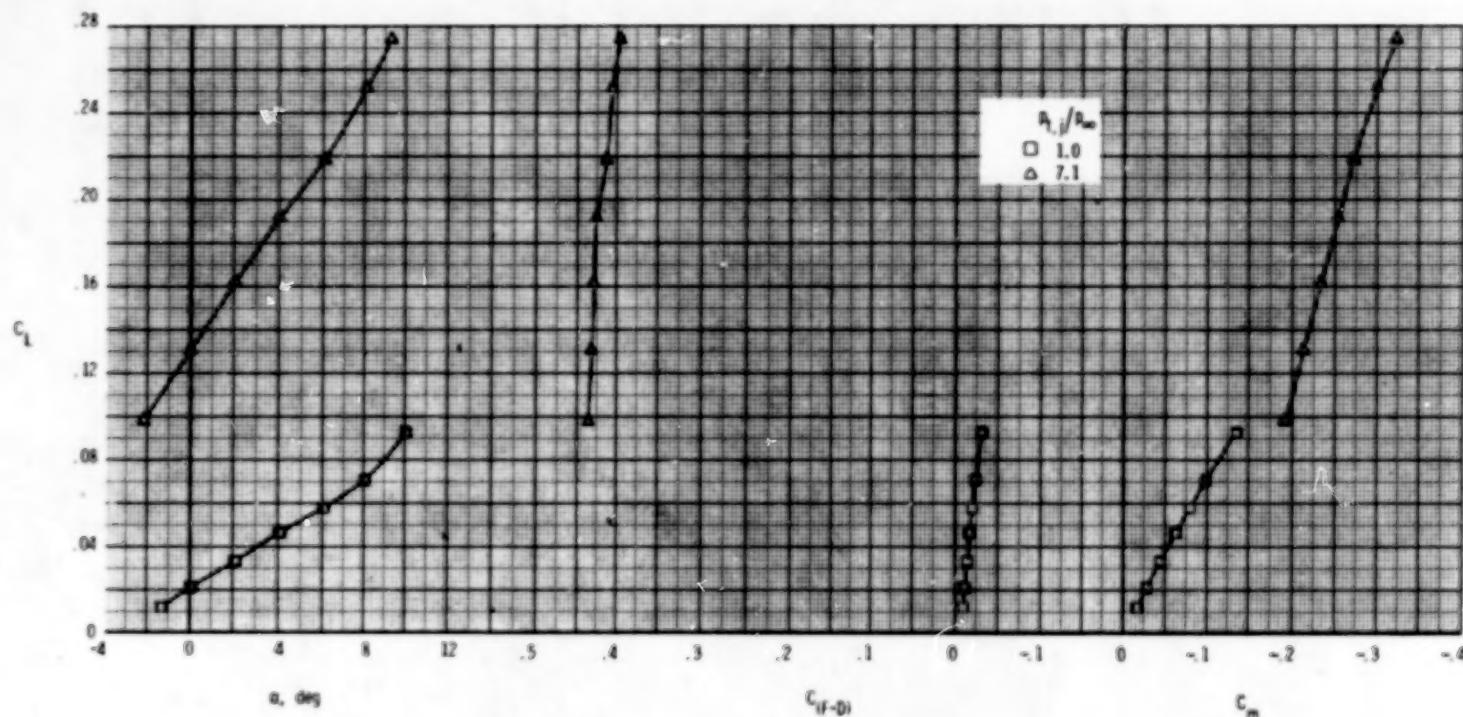
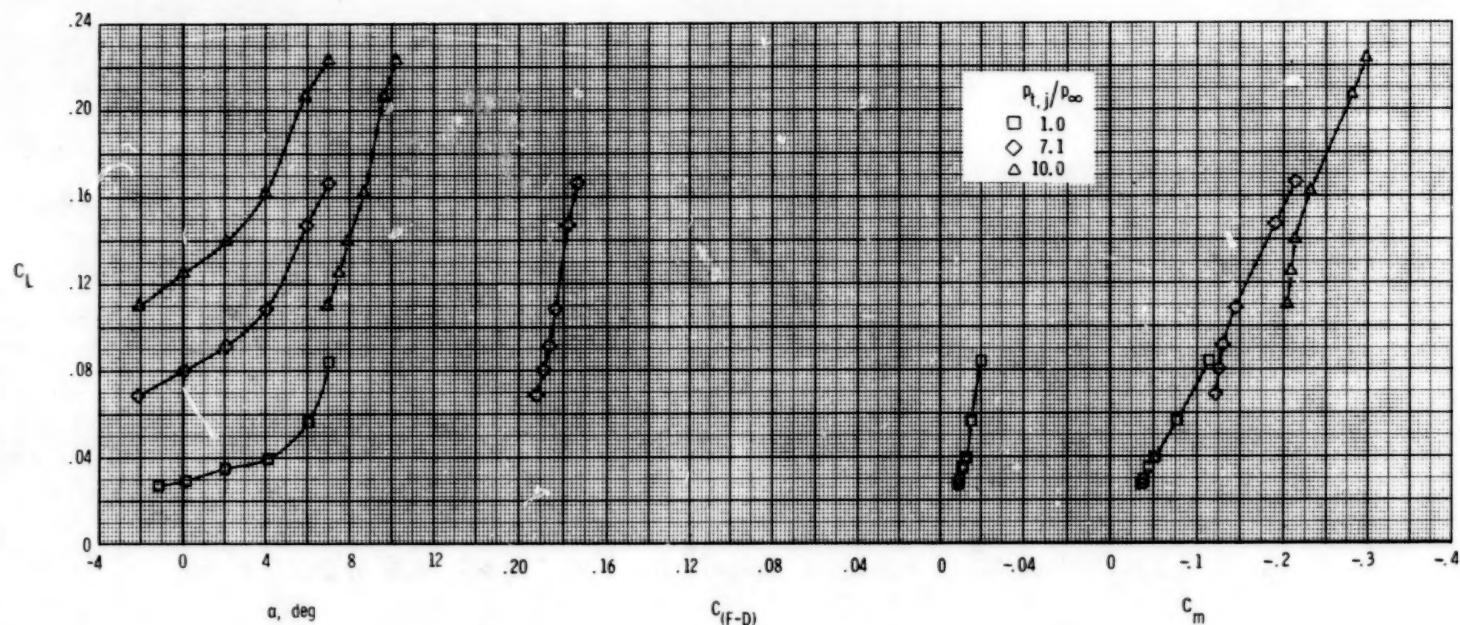
(a) $M = 0.60$.

Figure 51.- Longitudinal afterbody aerodynamic characteristics, SERN nozzle, A/B power.

$$\delta_h = 0^\circ; \quad \delta_v = 7^\circ; \quad A_e/A_t = 1.19.$$



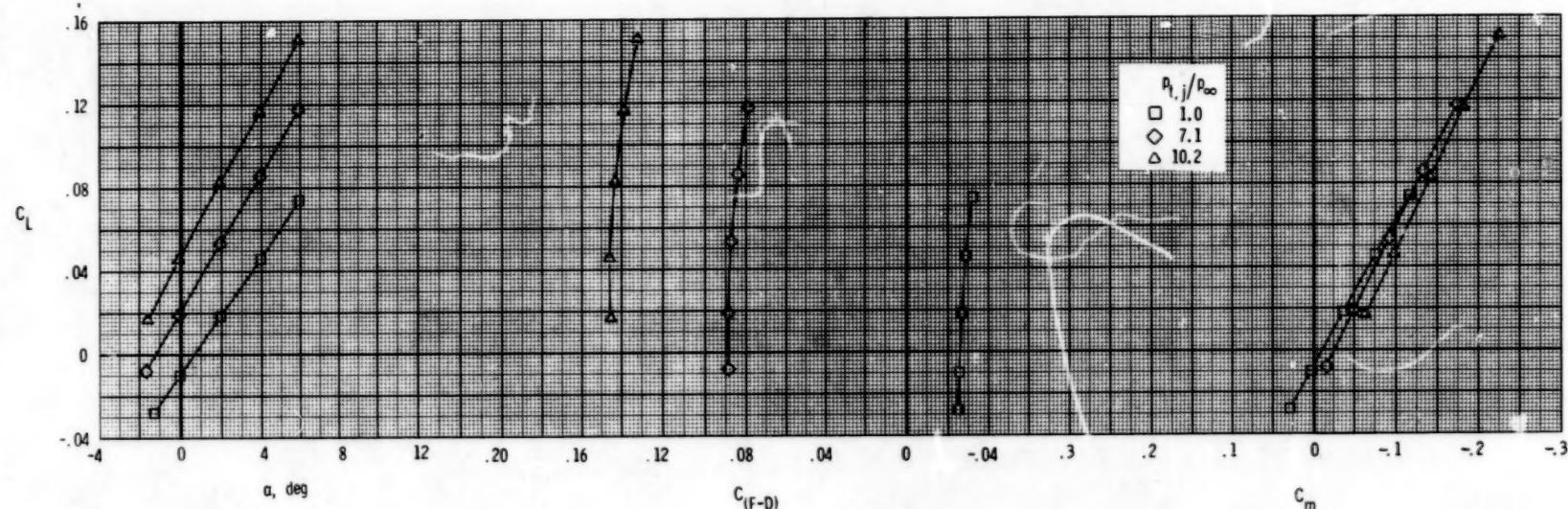
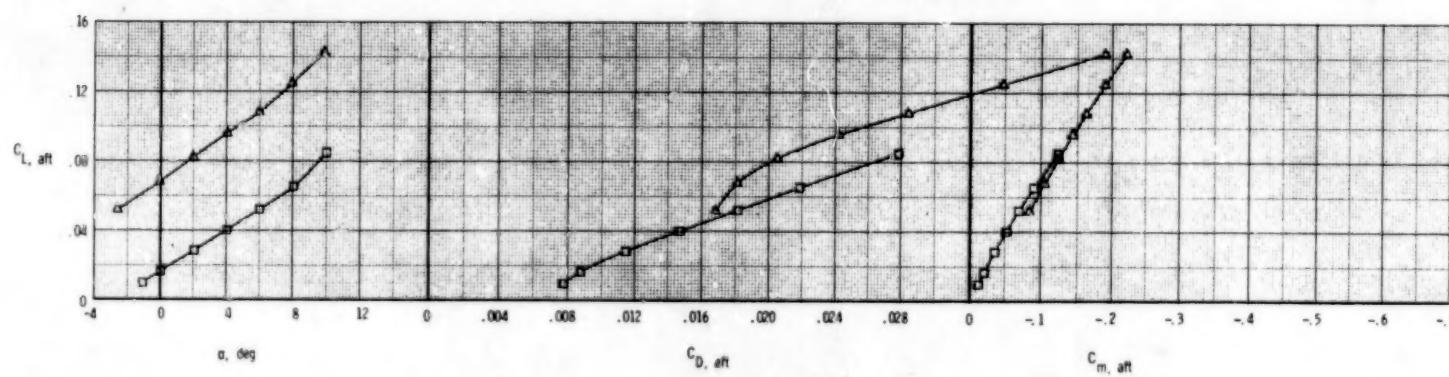
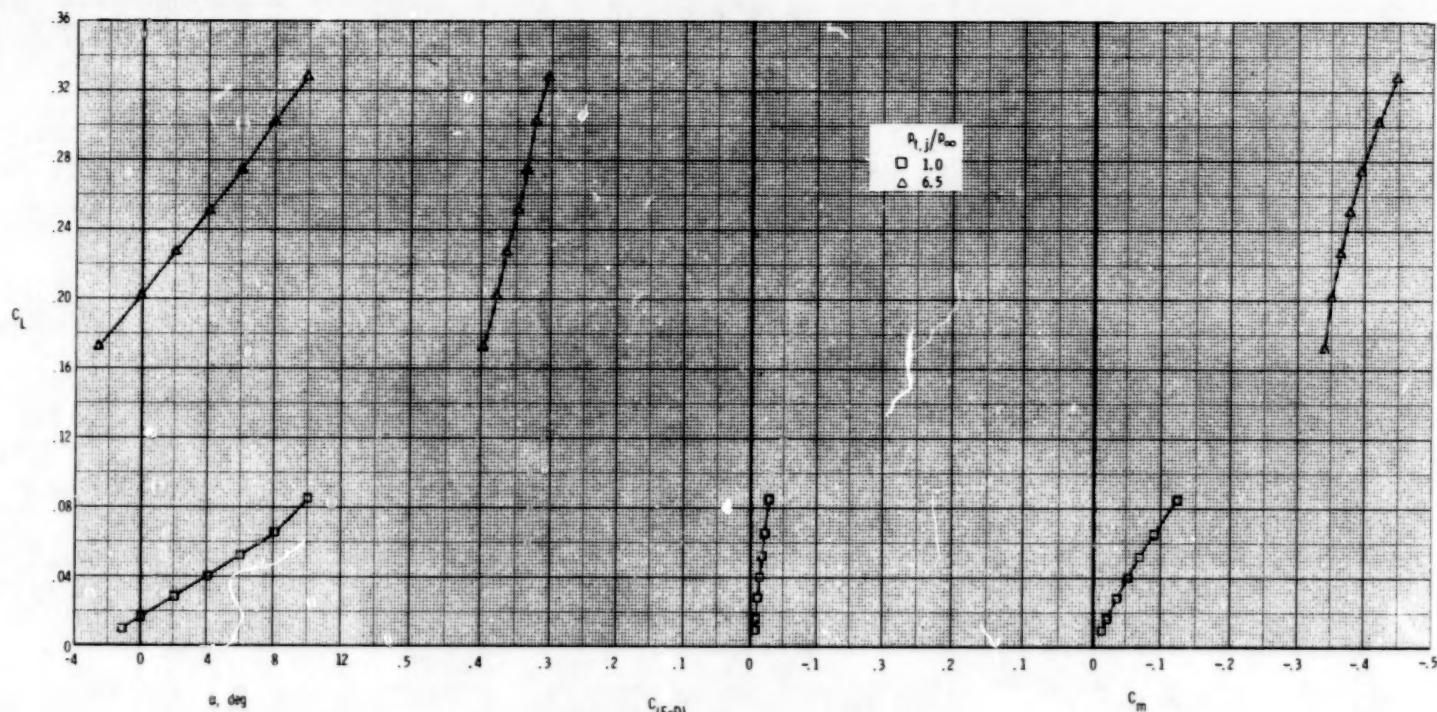
(c) $M = 1.20$.

Figure 51.- Concluded.



(a) $M = 0.60$.

Figure 52. - Longitudinal afterbody aerodynamic characteristics, SERN nozzle, A/B power.

$$\delta_h = 0^\circ; \quad \delta_v = 20^\circ; \quad A_e/A_t = 1.19.$$

120

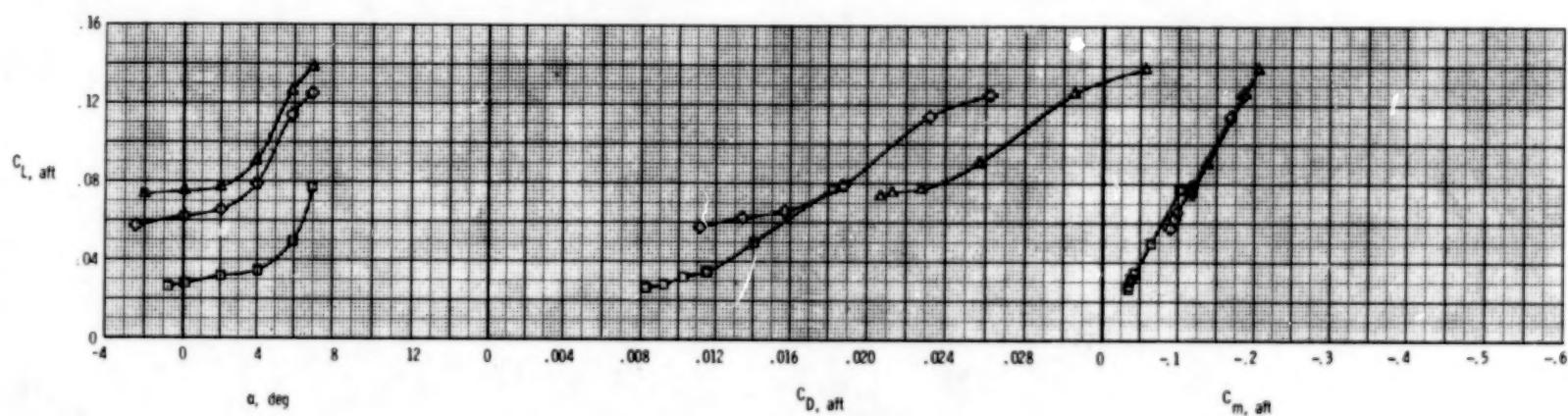
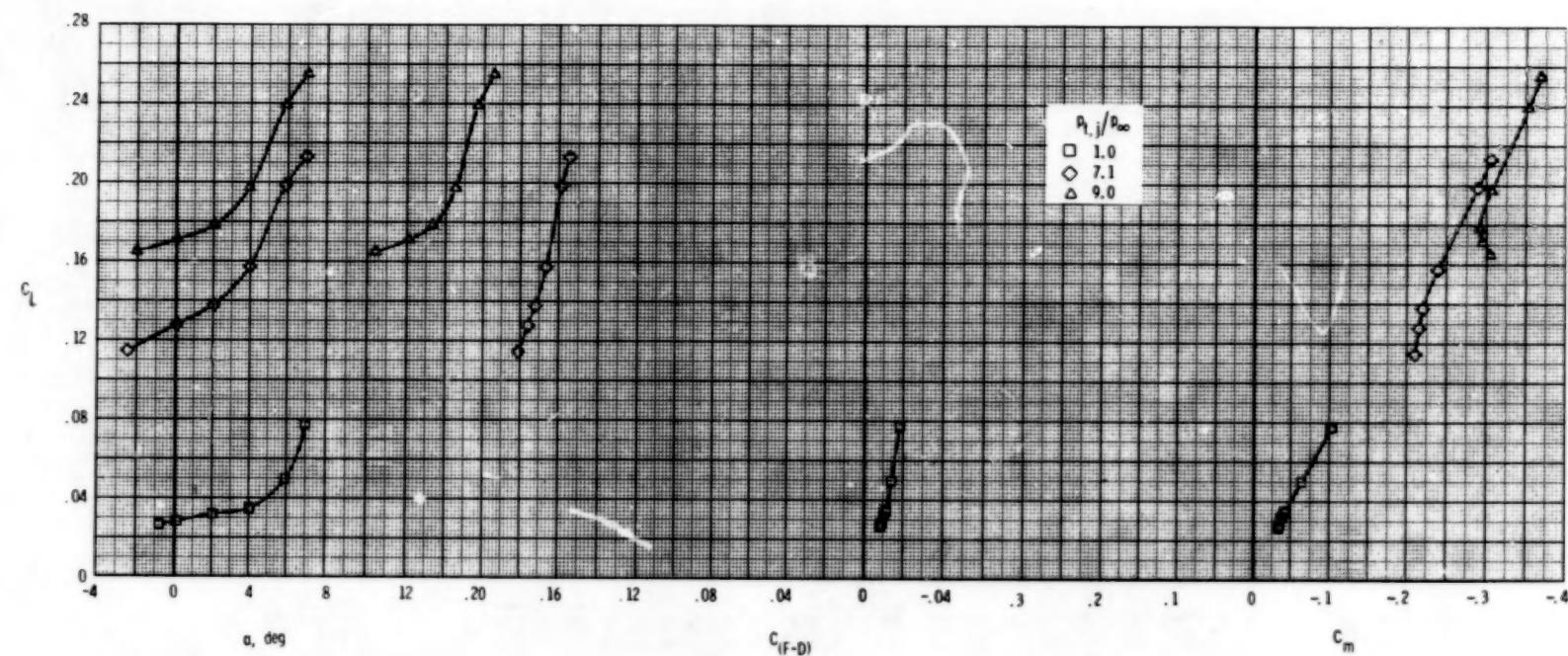
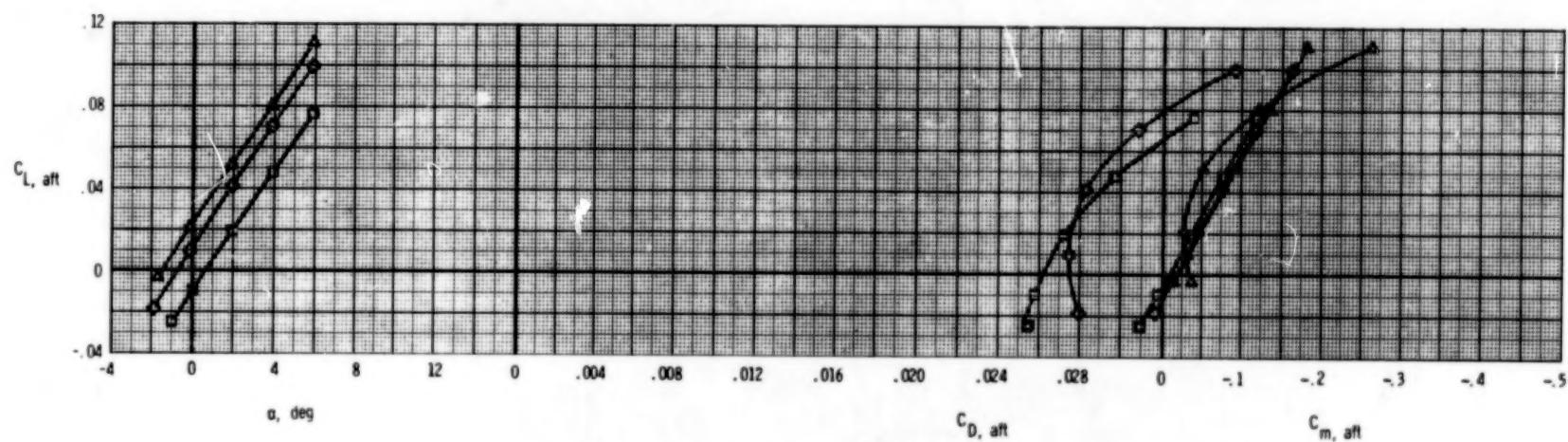
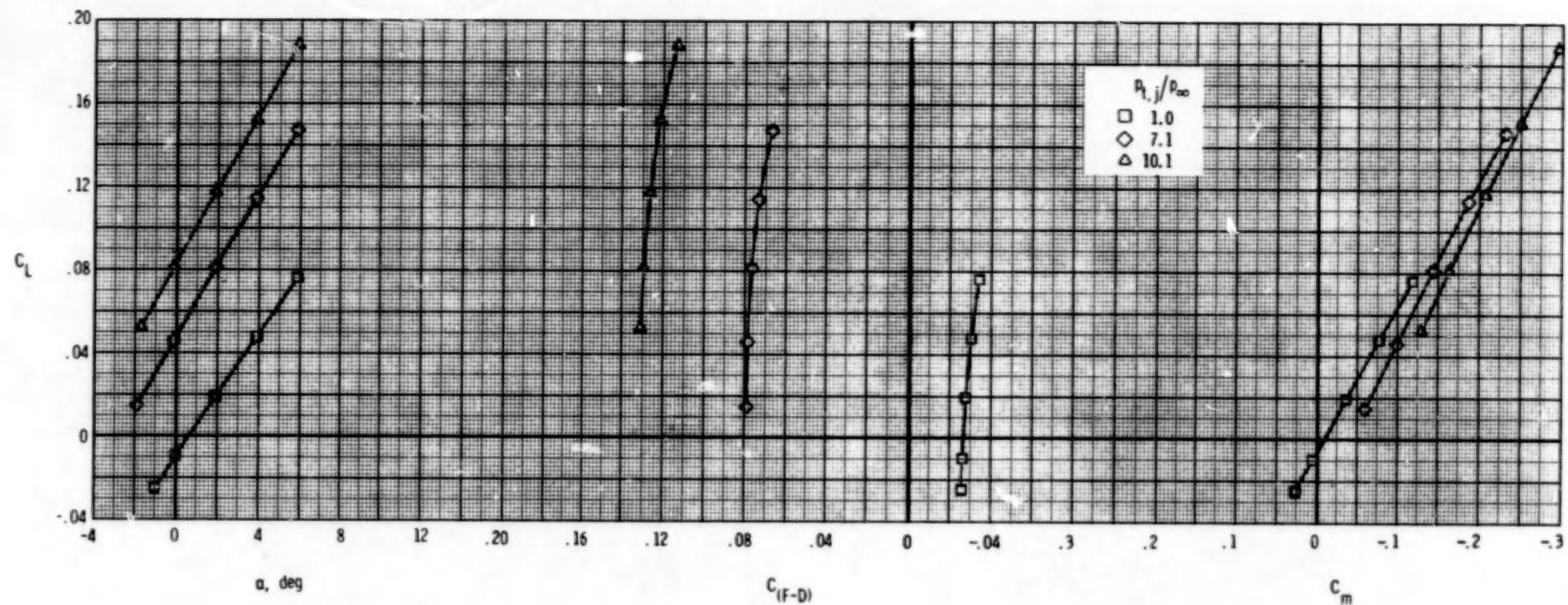
(b) $M = 0.90$.

Figure 52.- Continued.



(c) $M = 1.20$.

Figure 52.- Concluded.

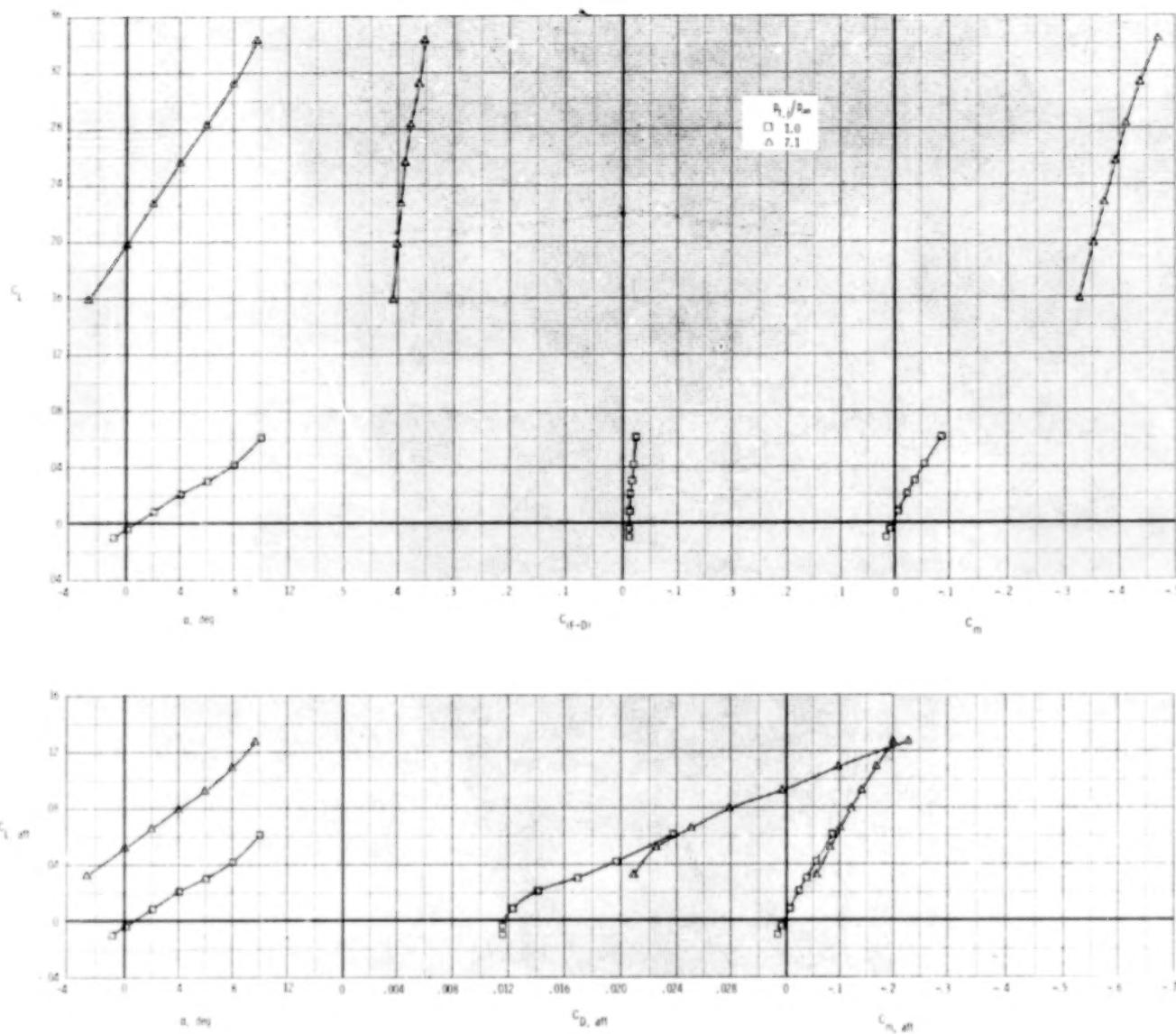
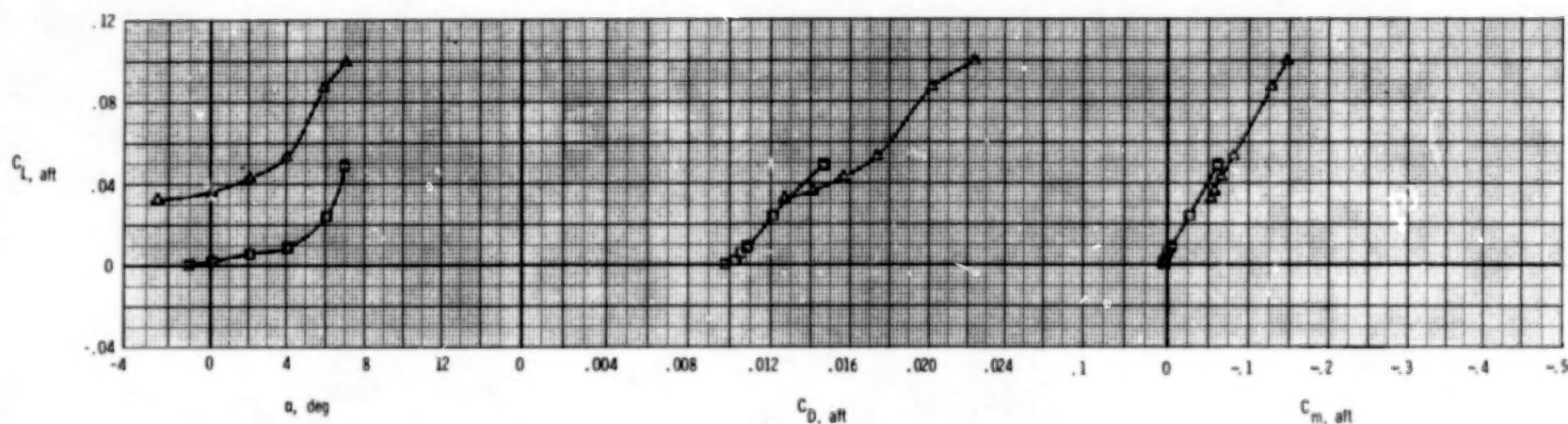
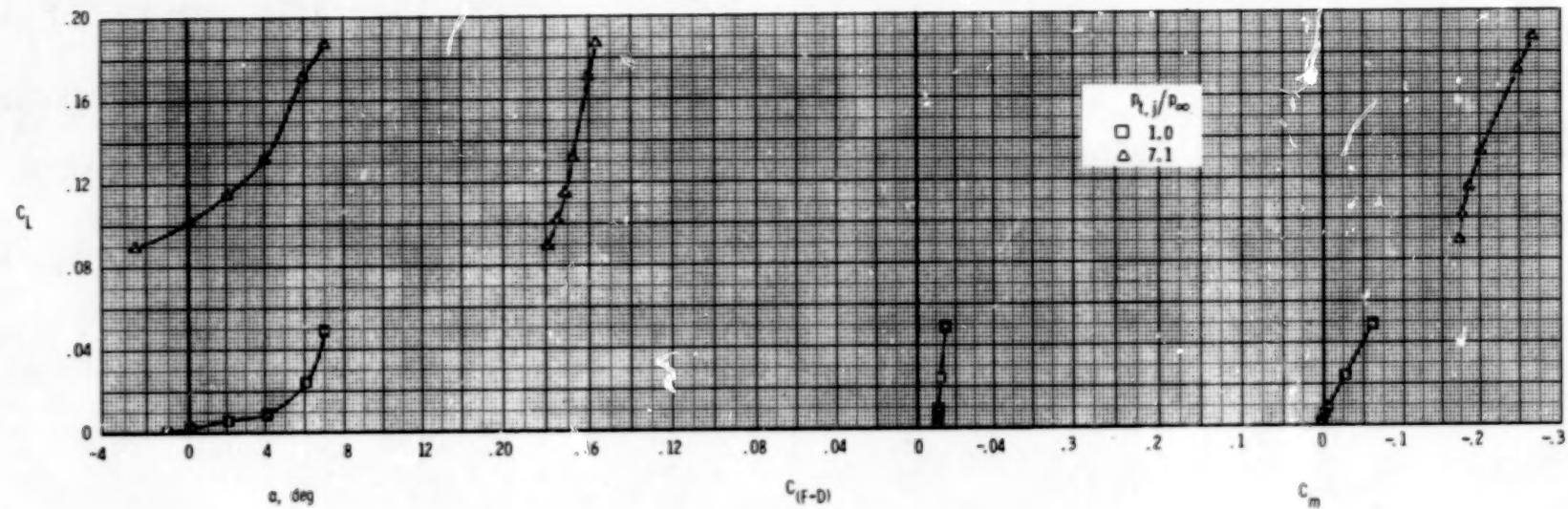
(a) $M = 0.60.$

Figure 53.- Longitudinal afterbody aerodynamic characteristics, SERN nozzle, A/B power.
 $\delta_h = -2^0$; $\delta_v = 20^0$; $A_e/A_t = 1.19$.



(b) $M = 0.90$.

Figure 53.- Continued.

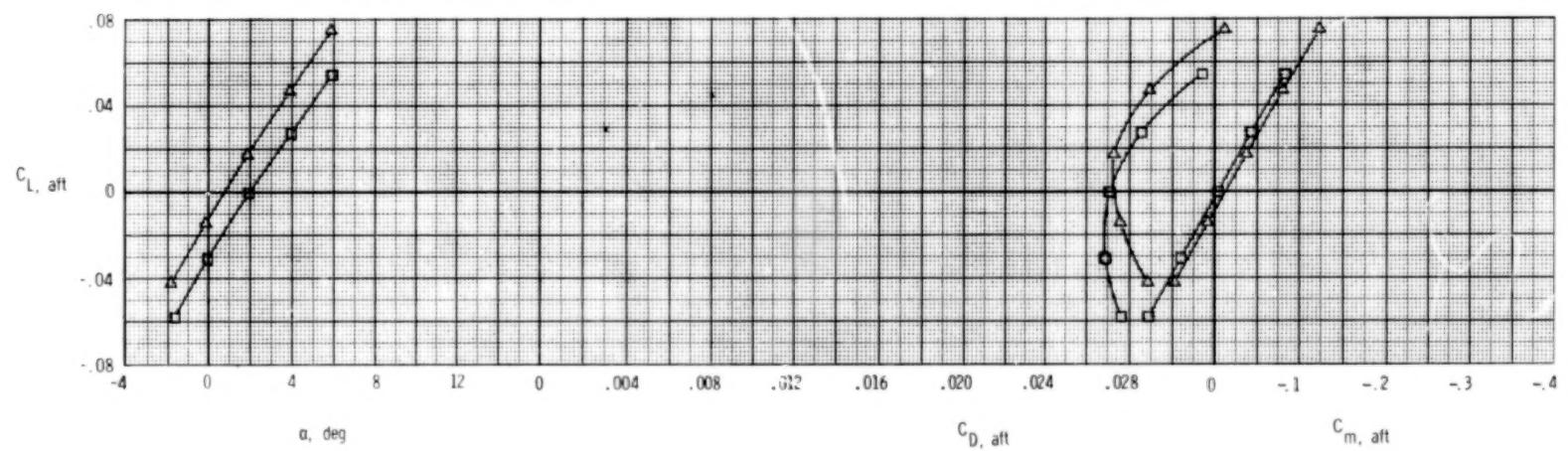
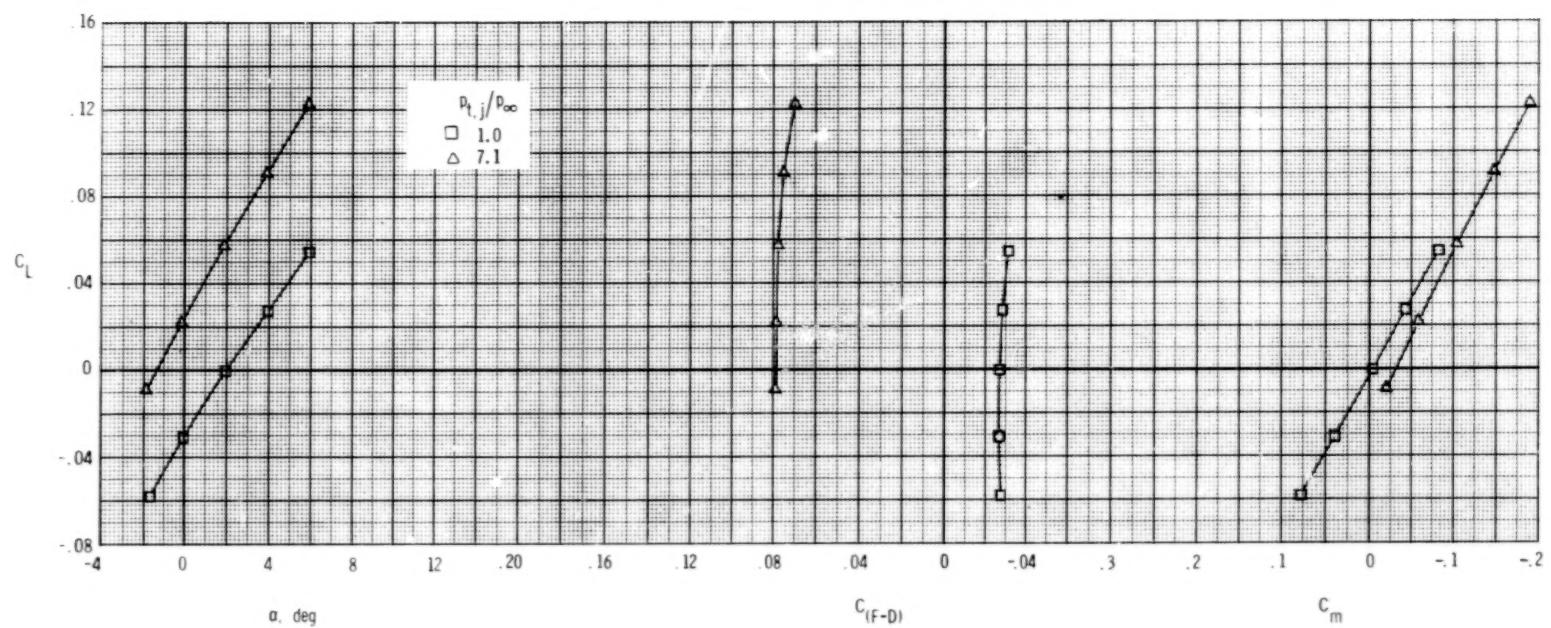
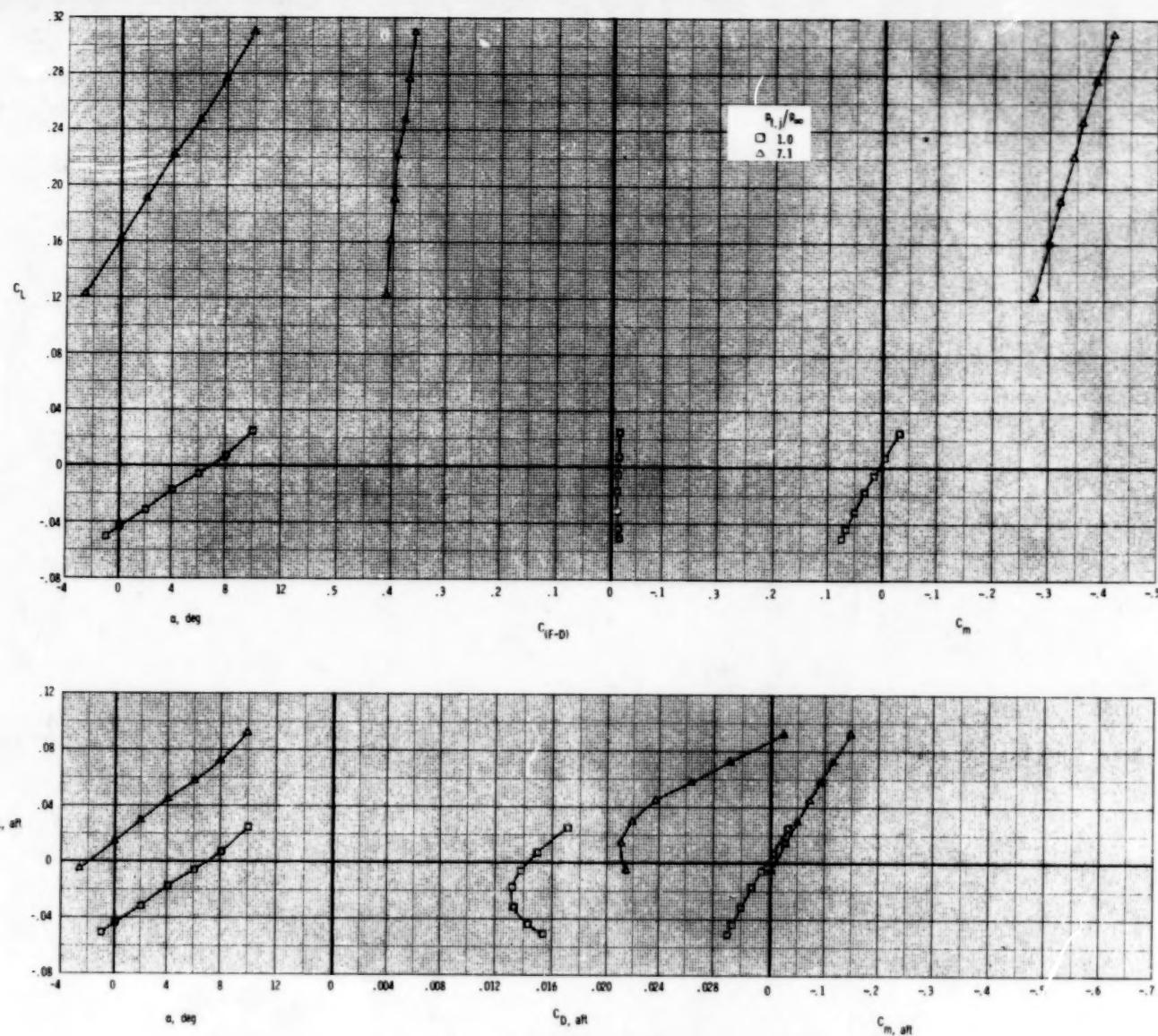
(c) $M = 1.20$.

Figure 53.- Concluded.



(a) $M = 0.60.$

Figure 54.- Longitudinal afterbody aerodynamic characteristics, SERN nozzle, A/B power.

$$\delta_h = -5^0; \quad \delta_v = 20^0; \quad A_e/A_t = 1.19.$$

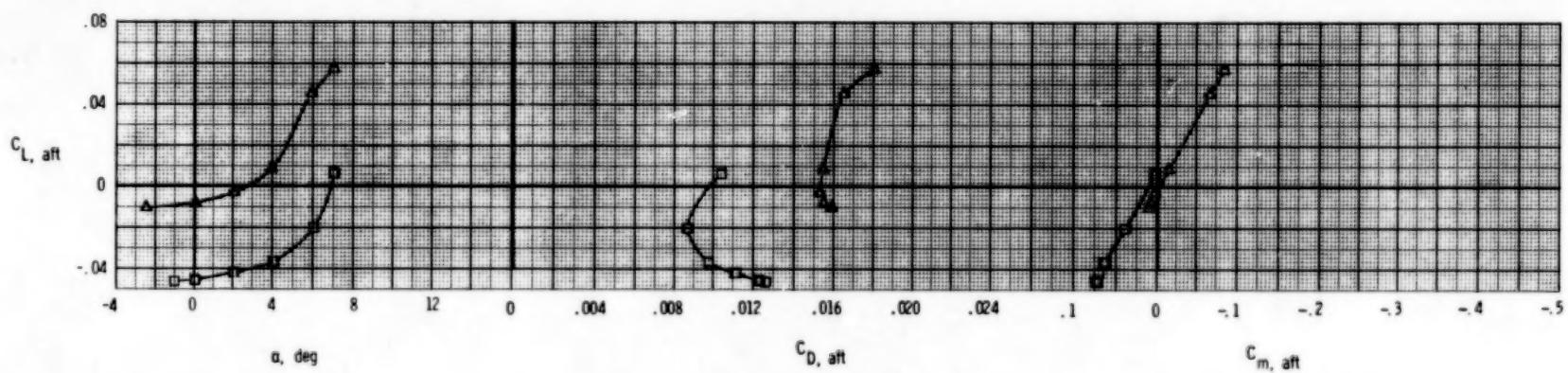
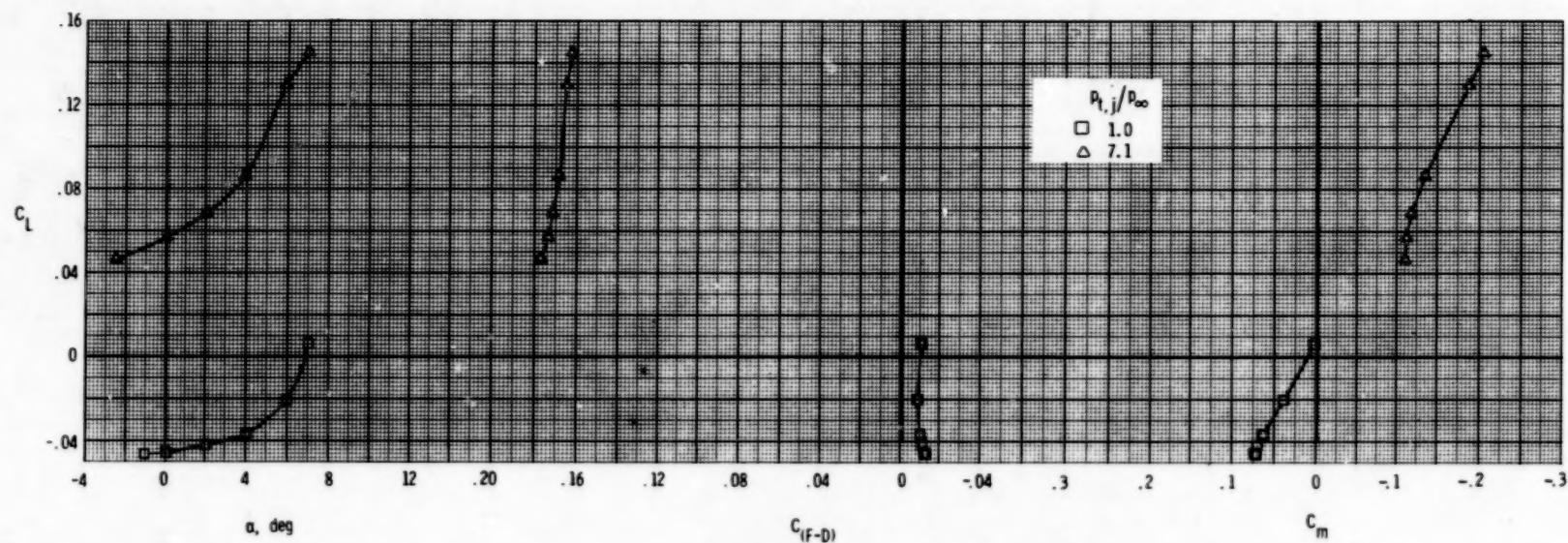
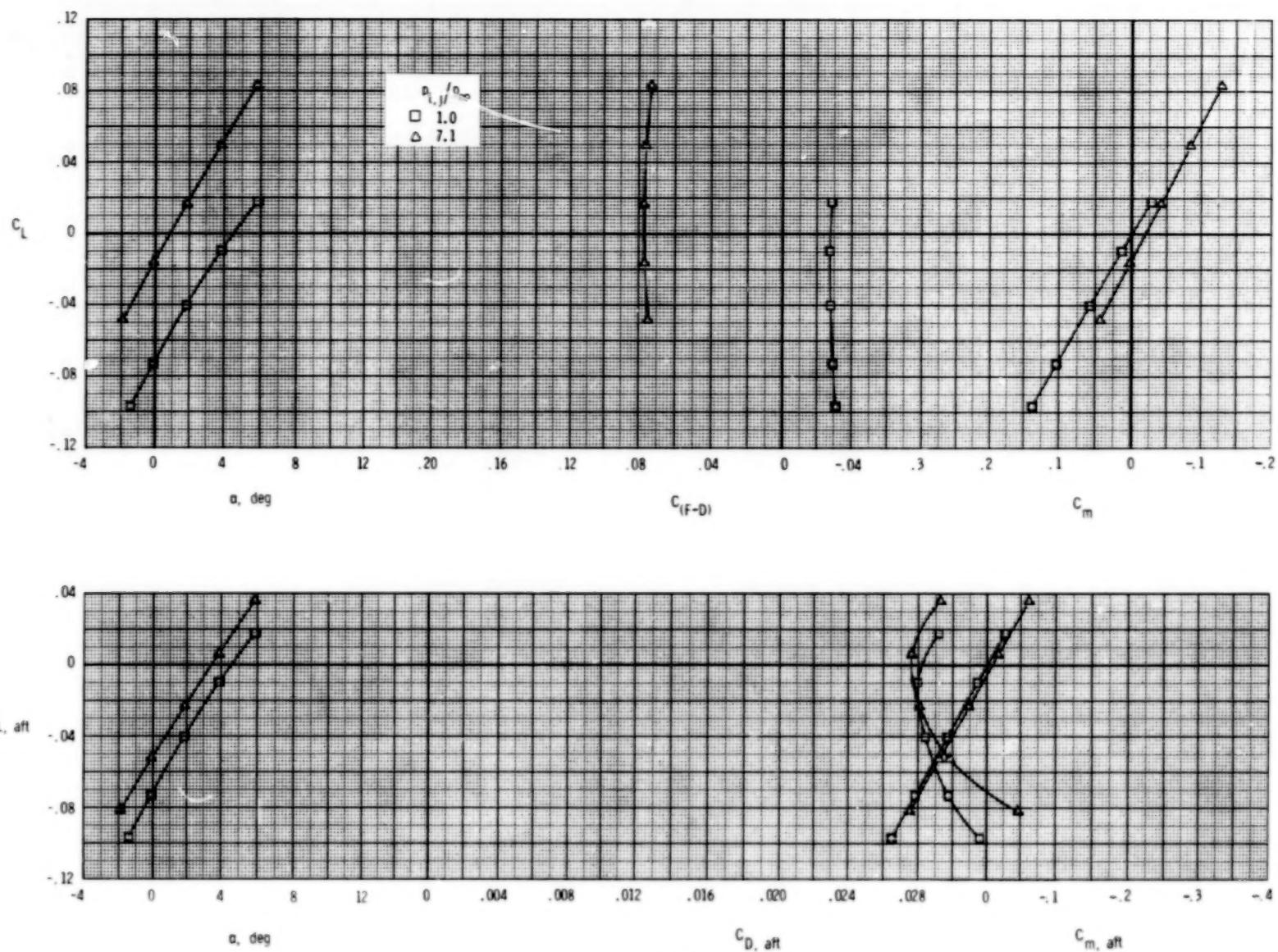
(b) $M = 0.90$.

Figure 54. - Continued.



(c) $M = 1.20$.

Figure 54.- Concluded.

128

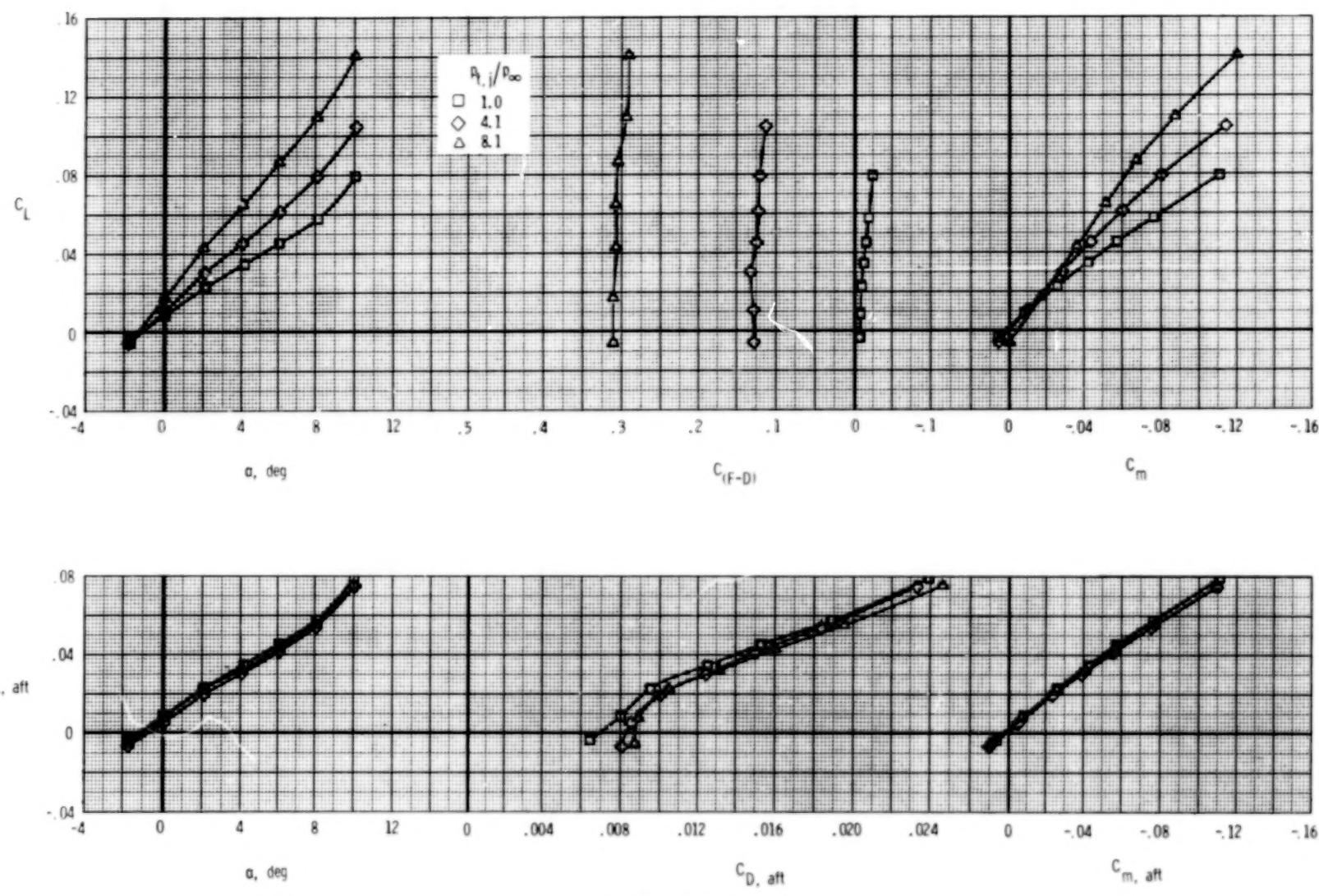
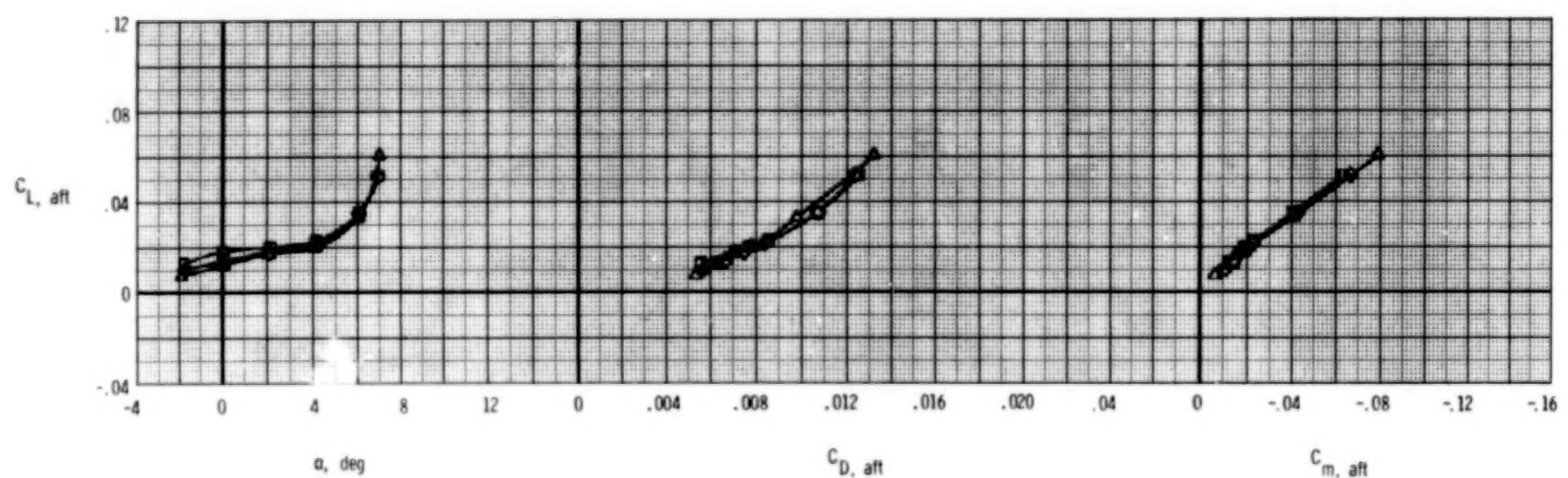
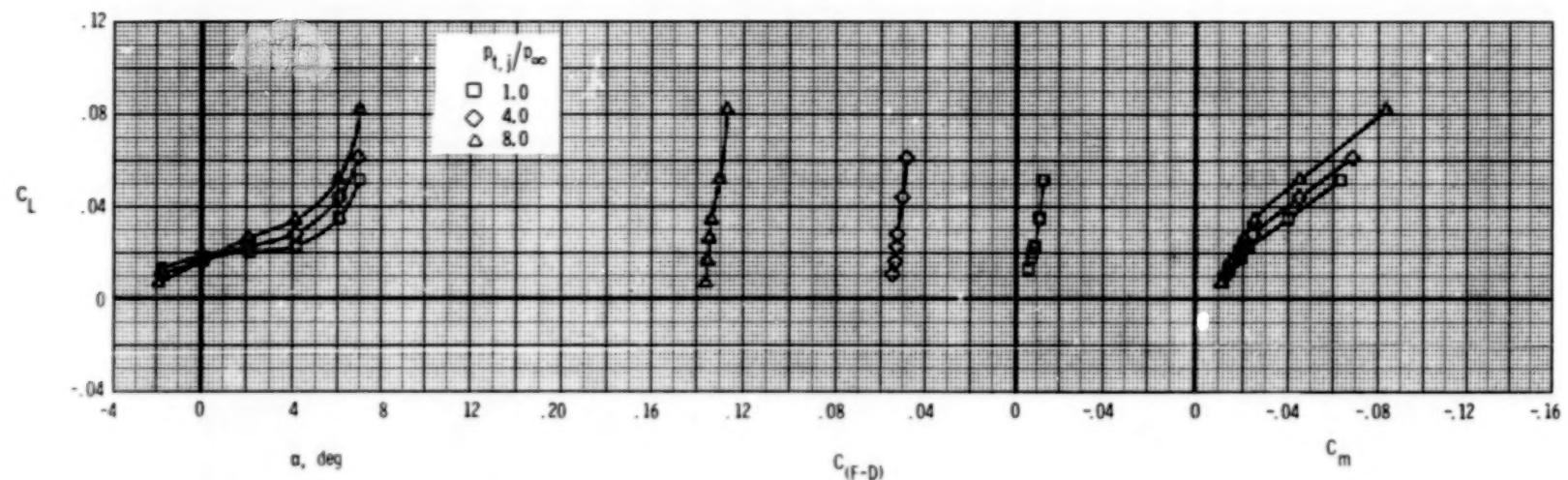
(a) $M = 0.60$.

Figure 55.- Longitudinal afterbody aerodynamic characteristics, 2-D C-D nozzle, dry power.

$$\delta_h = 0^0; \quad \delta_v = 0^0; \quad A_e/A_t = 1.15.$$



(b) $M = 0.90$.

Figure 55.- Continued.

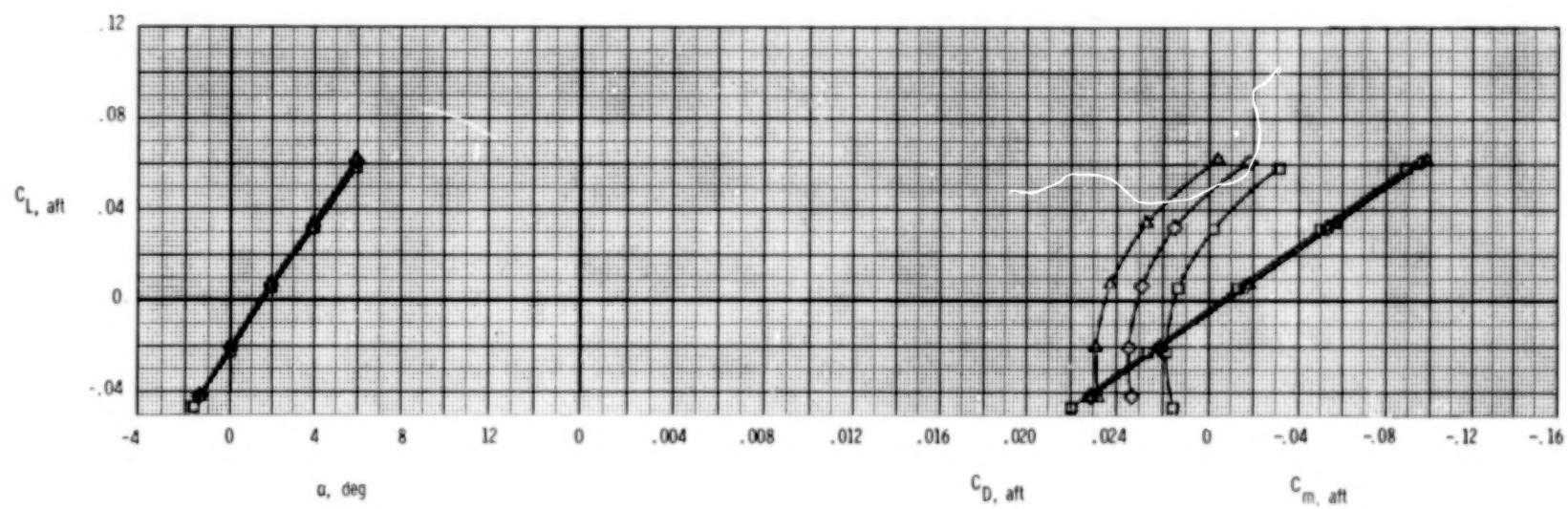
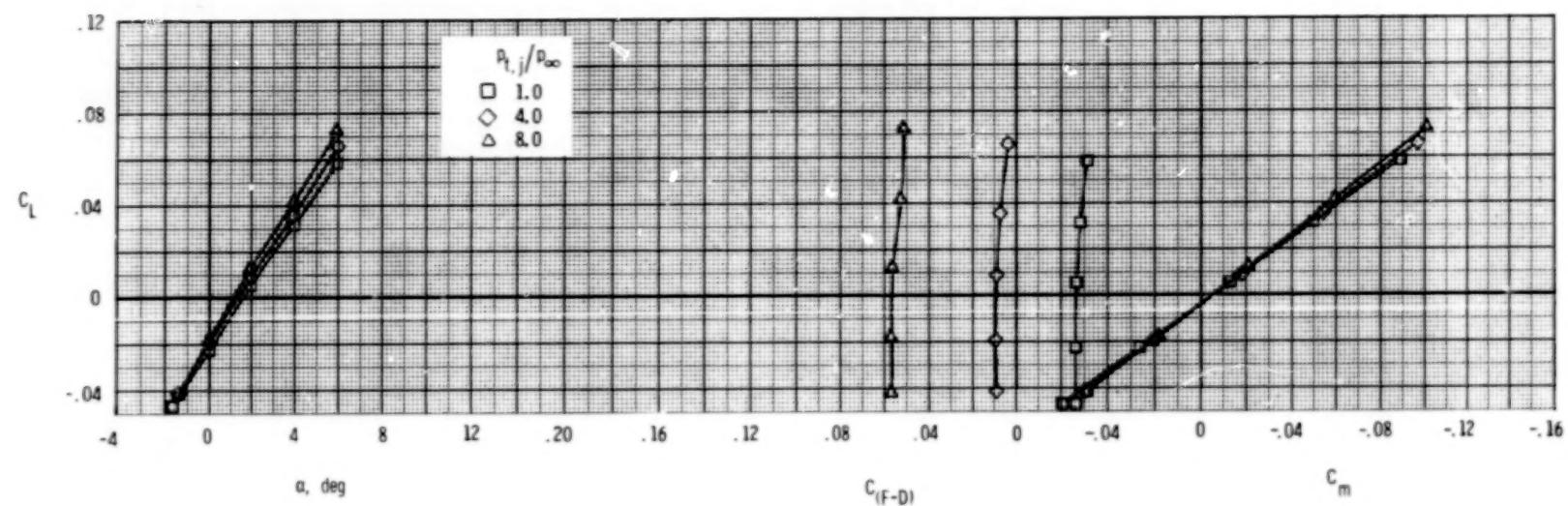
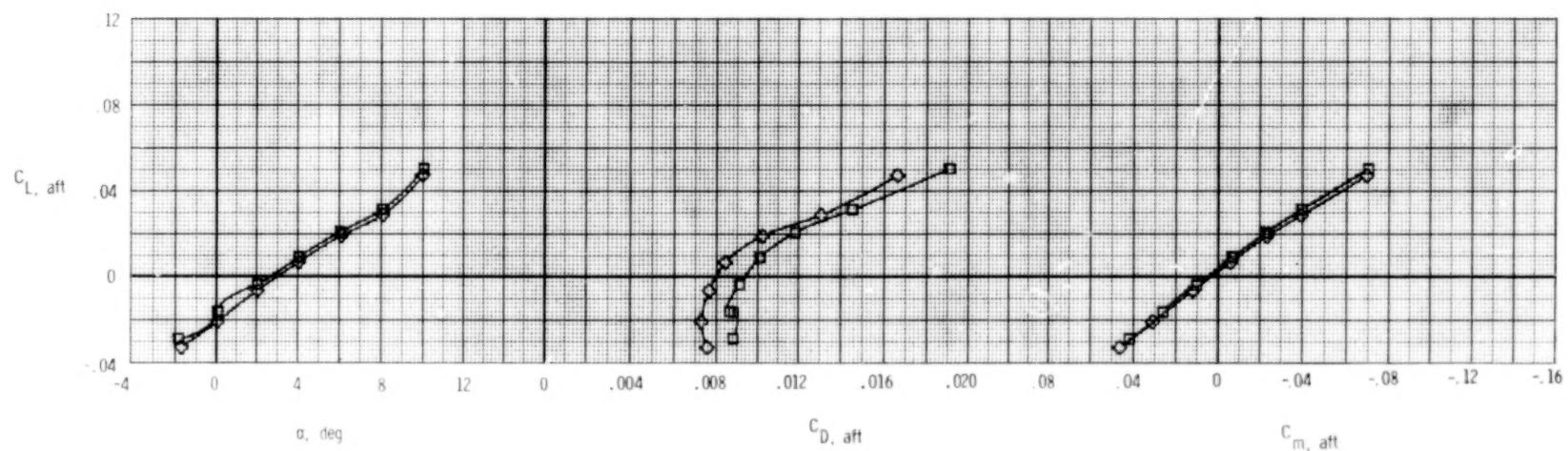
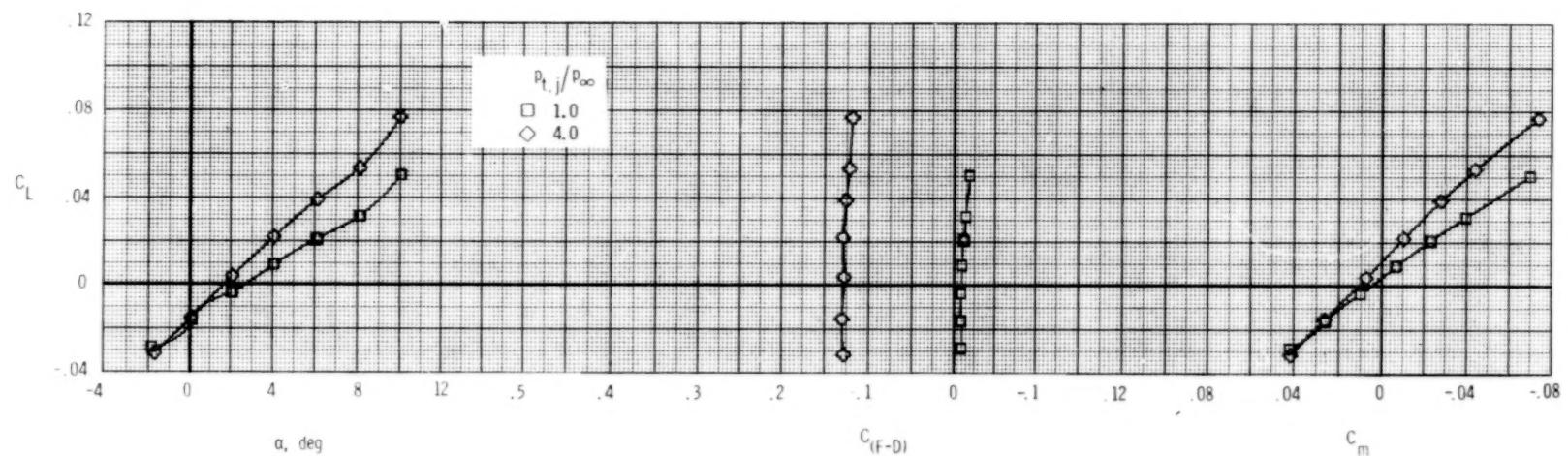
(c) $M = 1.20$.

Figure 55.- Concluded.

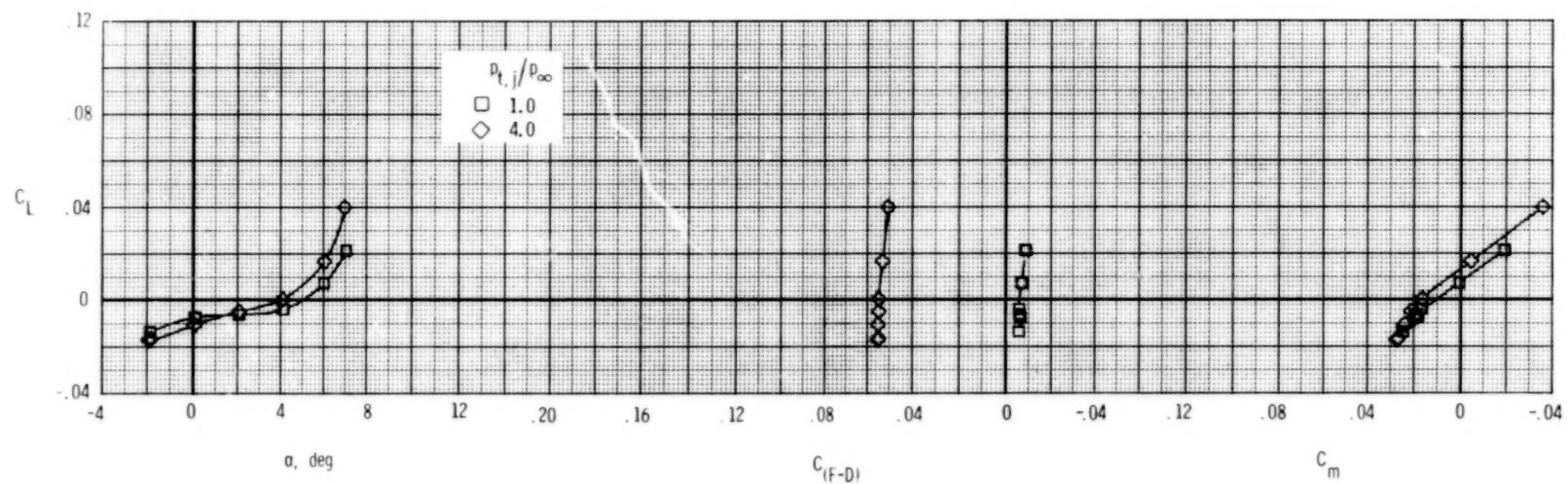


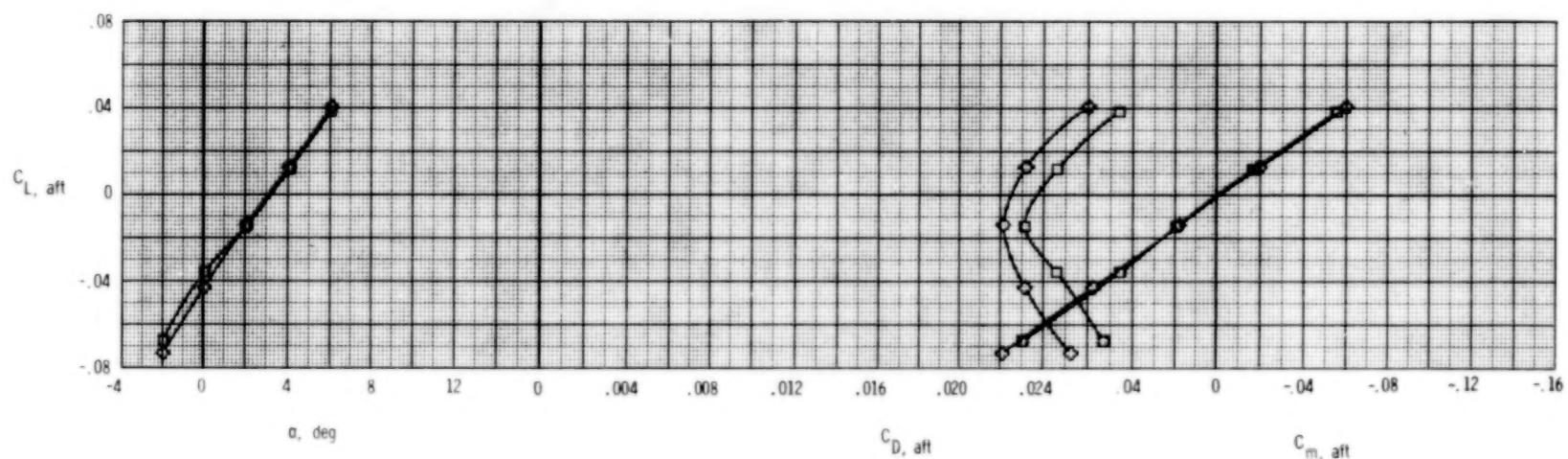
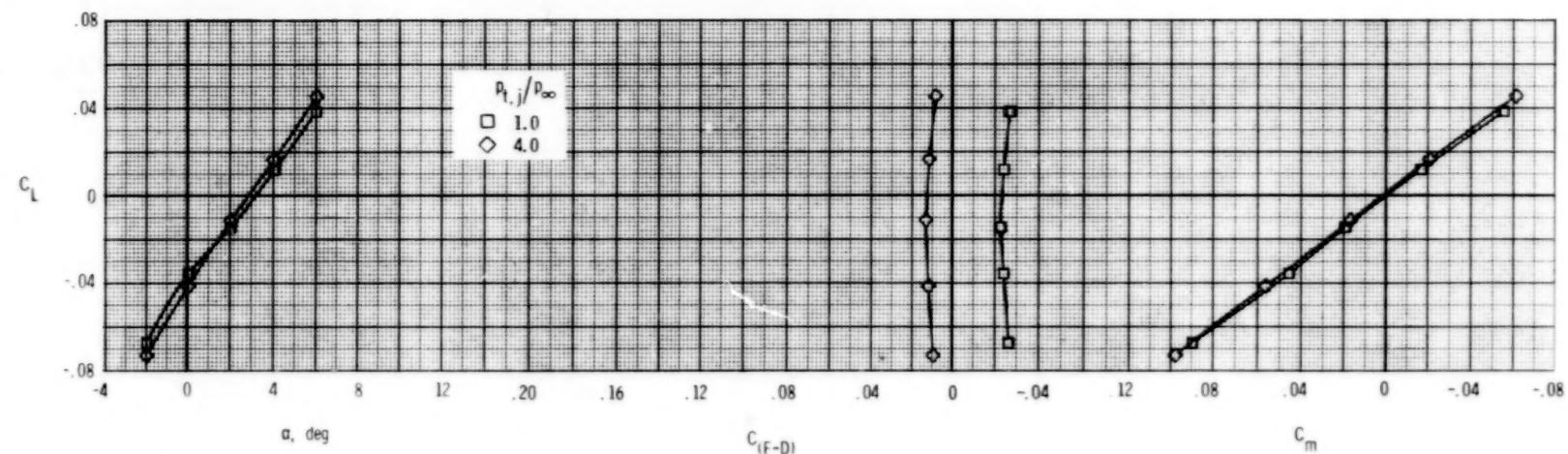
(a) $M = 0.60$.

Figure 56.- Longitudinal afterbody aerodynamic characteristics, 2-D C-D nozzle, dry power.

$$\delta_h = -2^\circ; \quad \delta_v = 0^\circ; \quad A_e/A_t = 1.15.$$

132





(c) $M = 1.20$.

Figure 56.- Concluded.

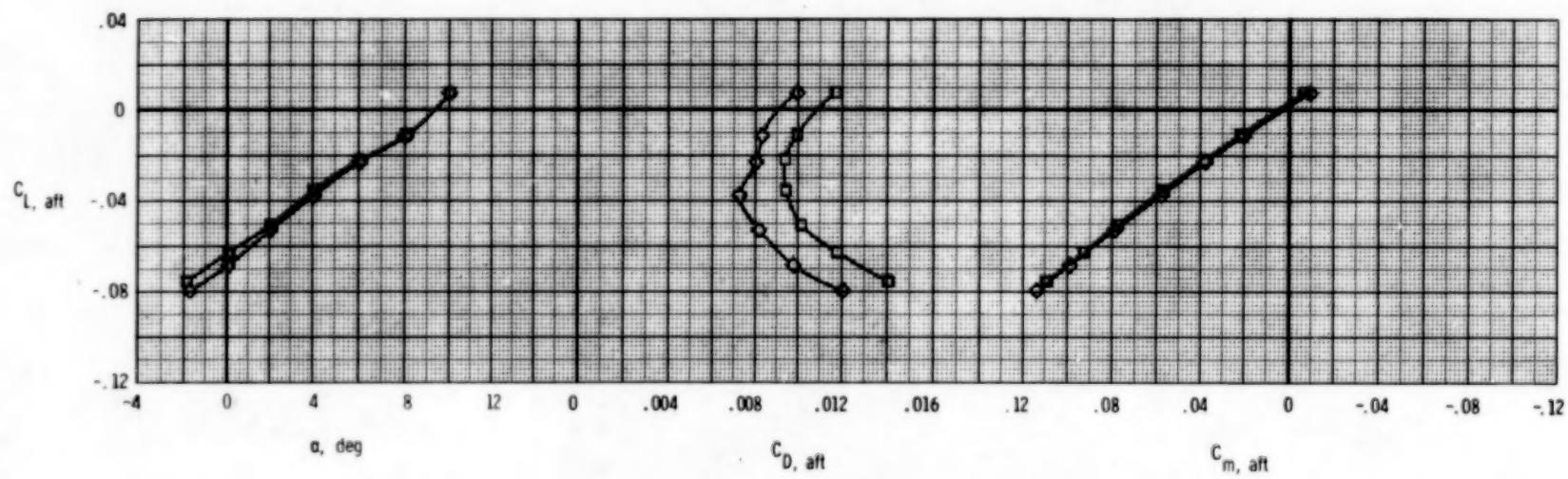
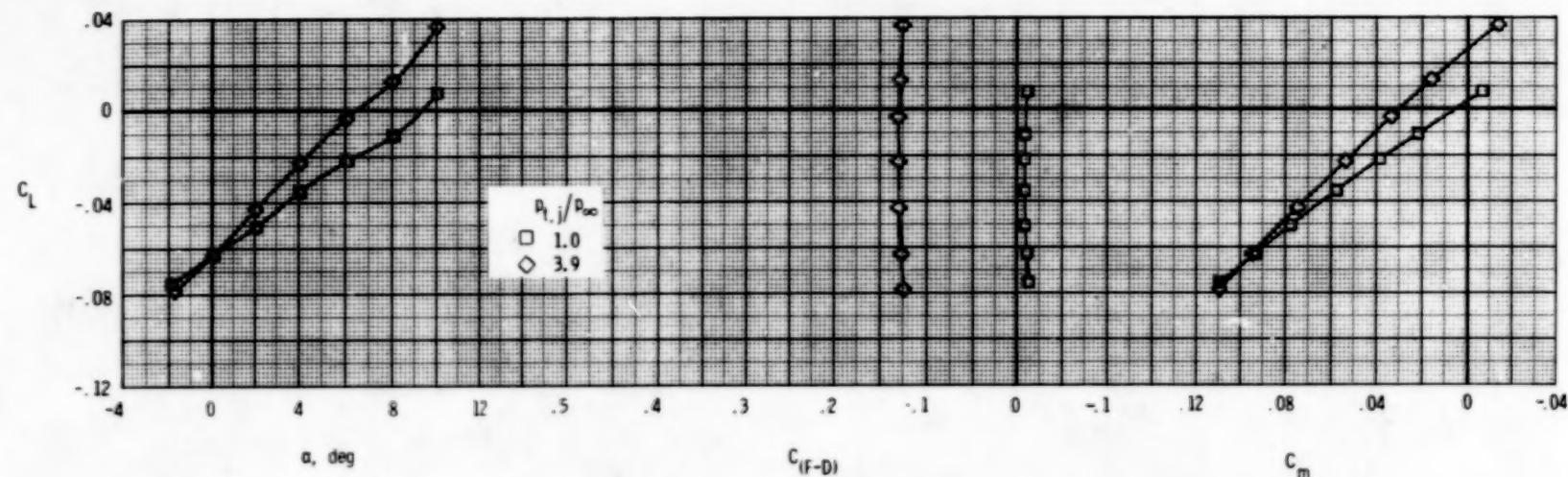
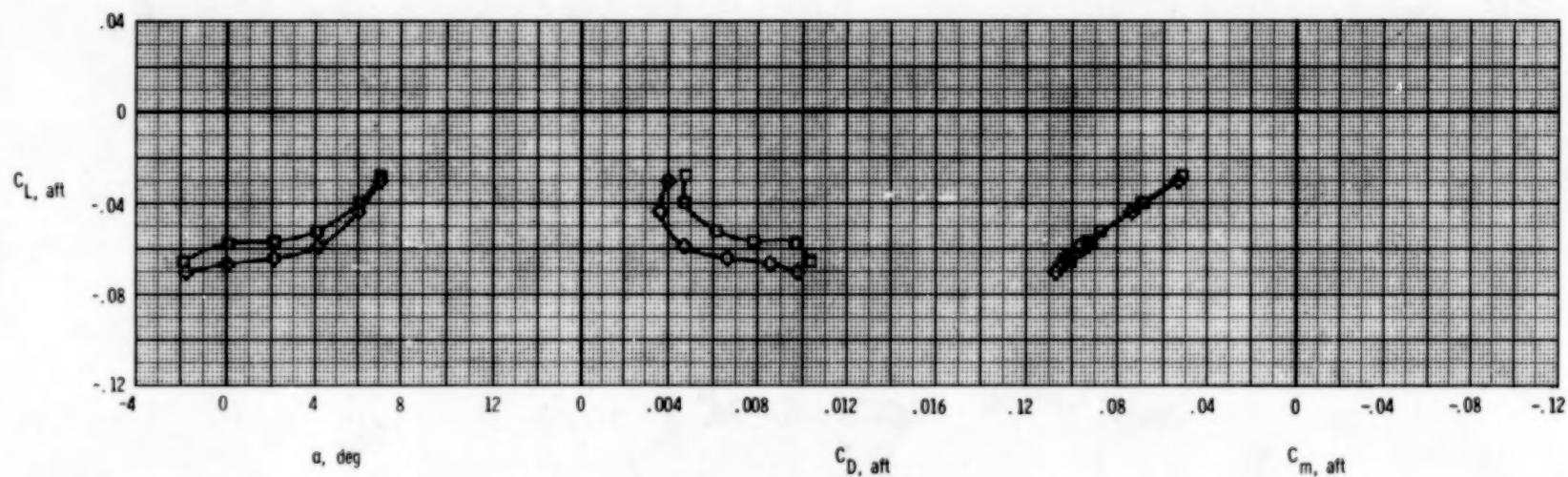
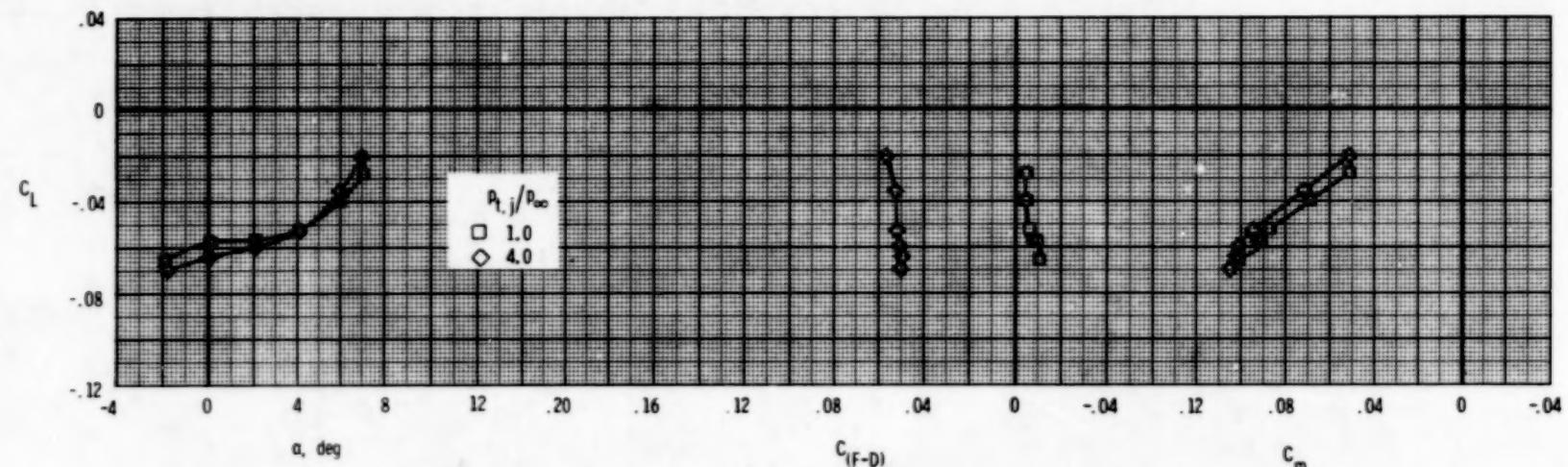
(a) $M = 0.60$.

Figure 57.- Longitudinal afterbody aerodynamic characteristics, 2-D C-D nozzle, dry power.

$$\delta_h = -5^\circ; \quad \delta_v = 0^\circ; \quad A_e/A_t = 1.15.$$



(b) $M = 0.90$.

Figure 57.- Concluded.

136

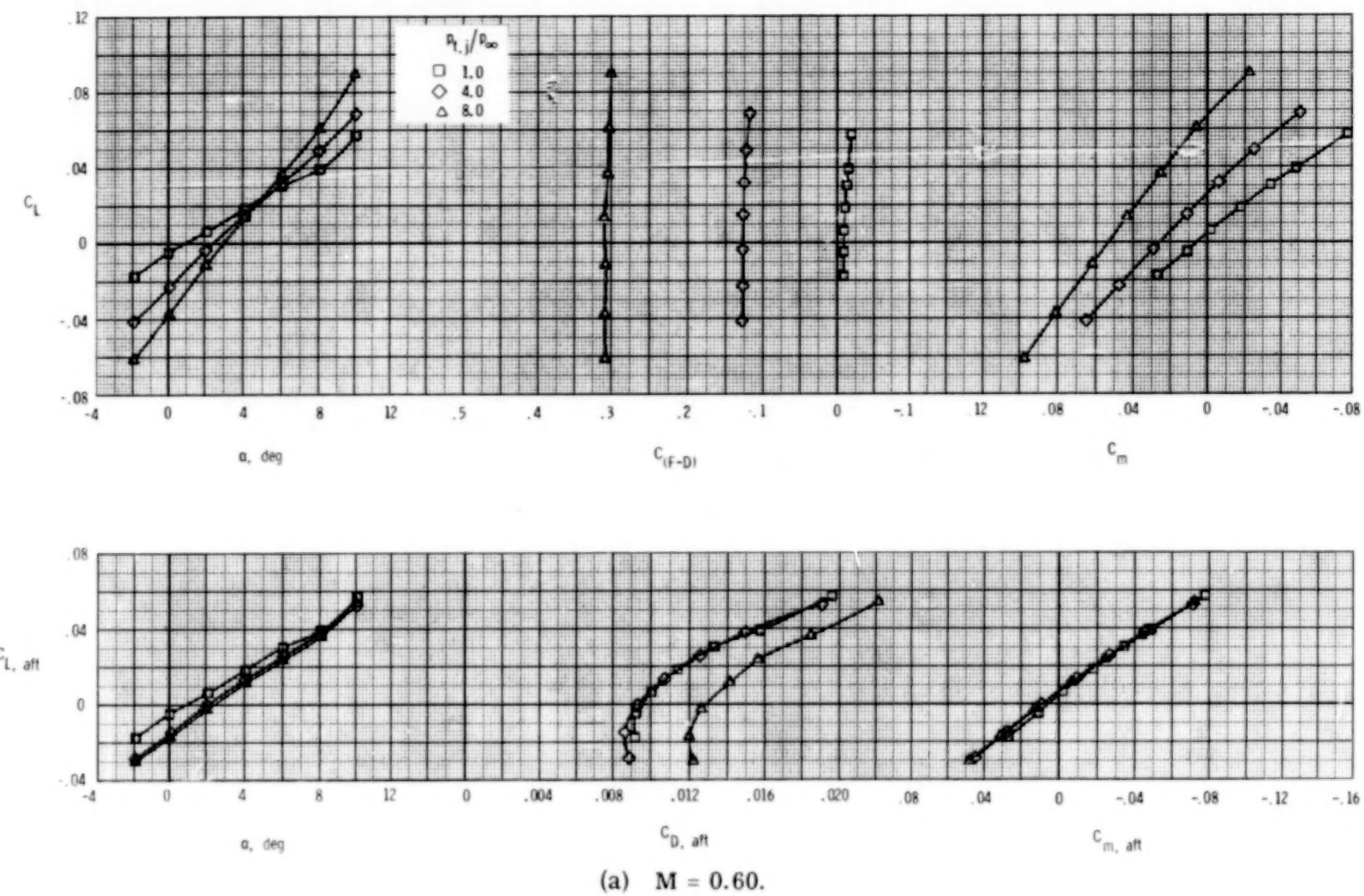
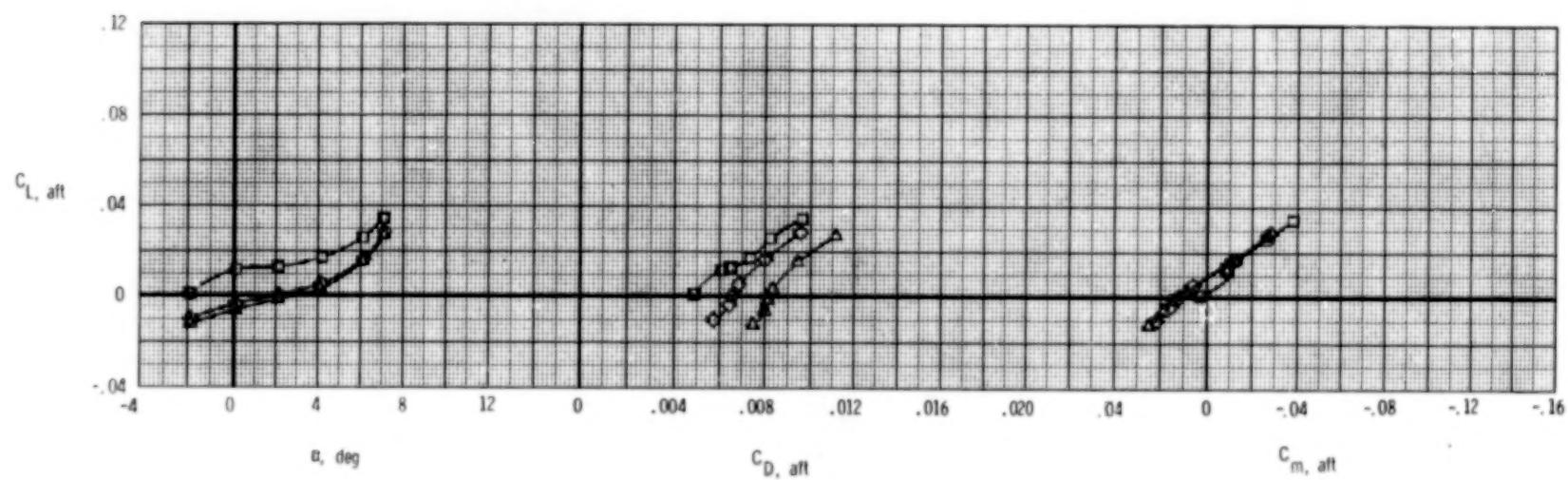
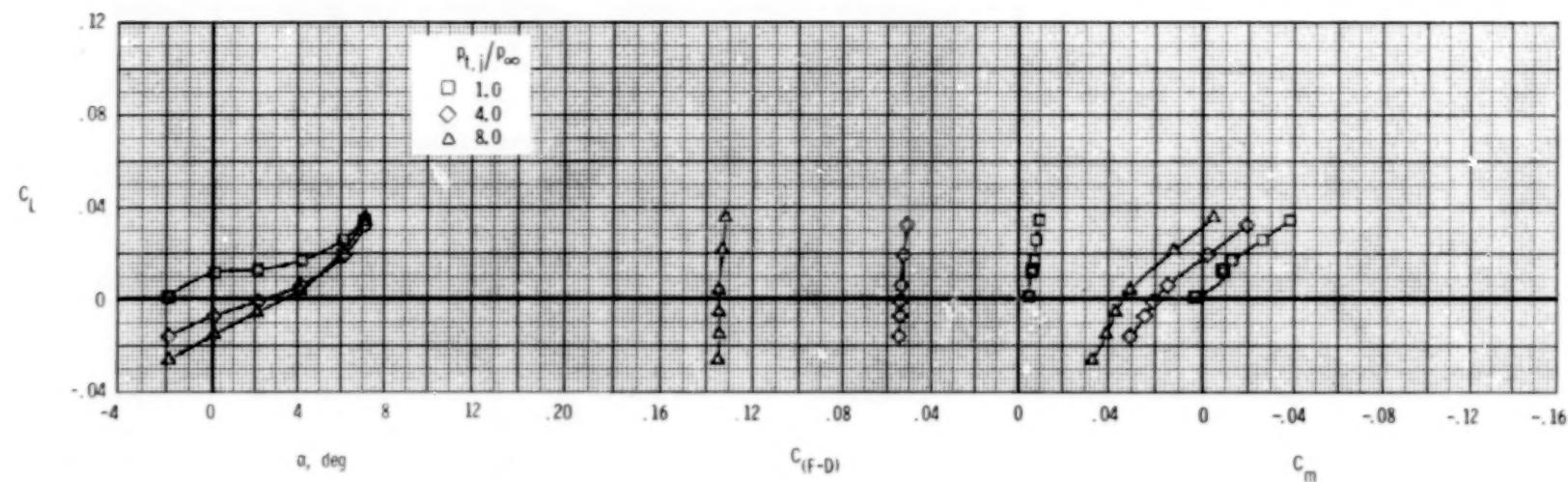
(a) $M = 0.60$.

Figure 58.- Longitudinal afterbody aerodynamic characteristics, 2-D C-D nozzle, dry power.

$$\delta_h = 0^\circ; \quad \delta_v = -7^\circ; \quad A_e/A_t = 1.15.$$



(b) $M = 0.90$.

Figure 58.- Continued.

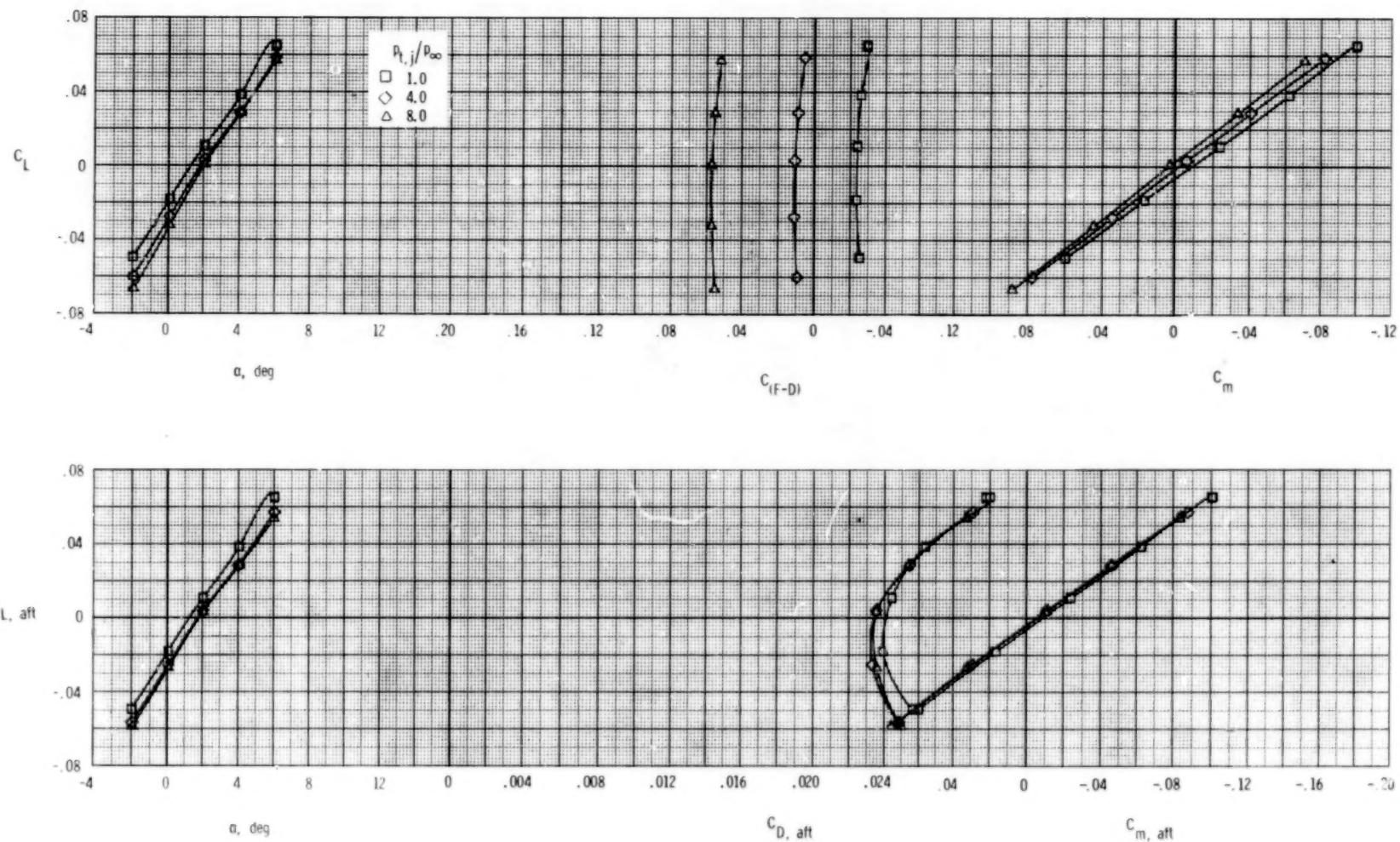
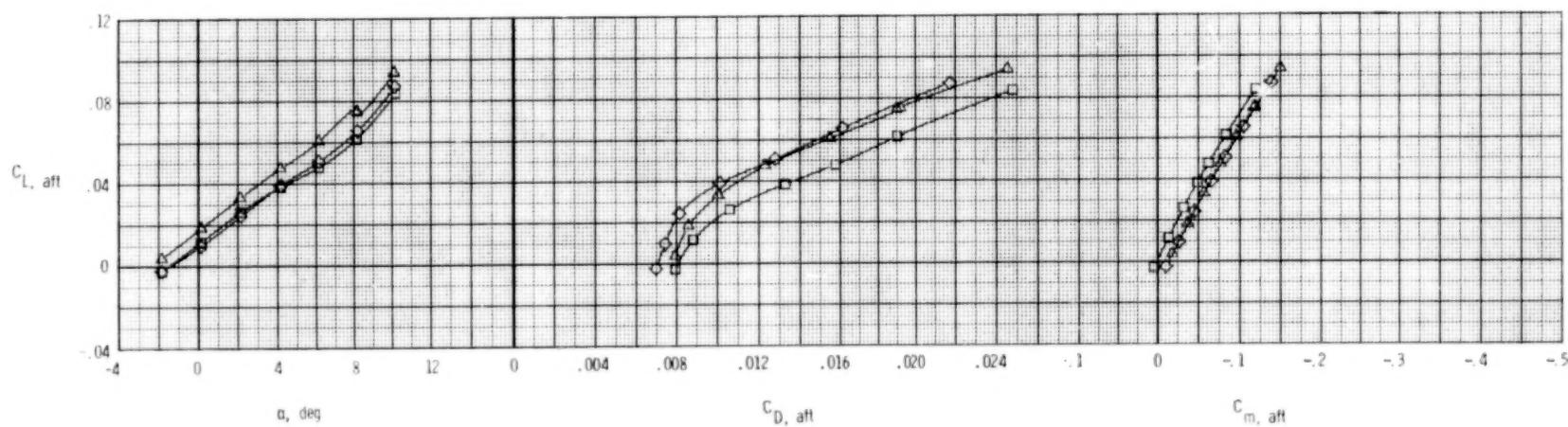
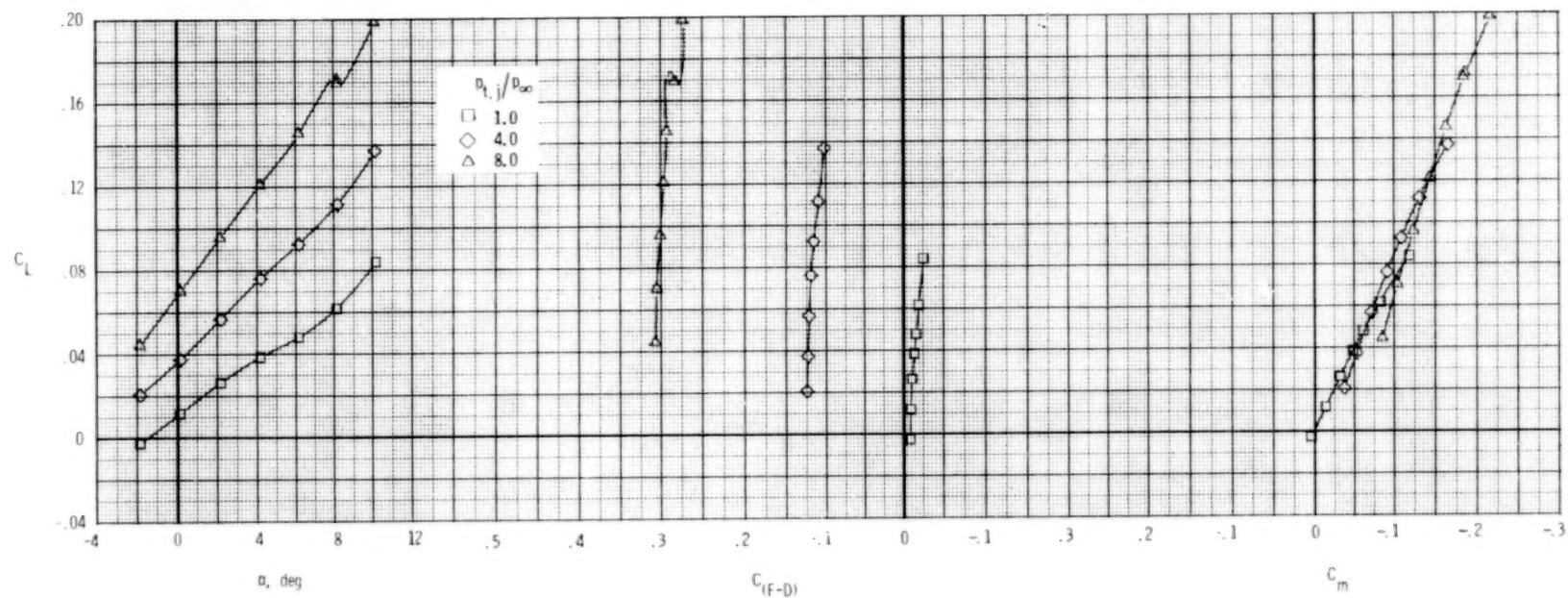
(c) $M = 1.20$.

Figure 58.- Concluded.



(a) $M = 0.60$.

Figure 59.- Longitudinal afterbody aerodynamic characteristics, 2-D C-D nozzle, dry power.

$$\delta_h = 0^\circ; \quad \delta_v = 7^\circ; \quad A_e/A_t = 1.15.$$

140

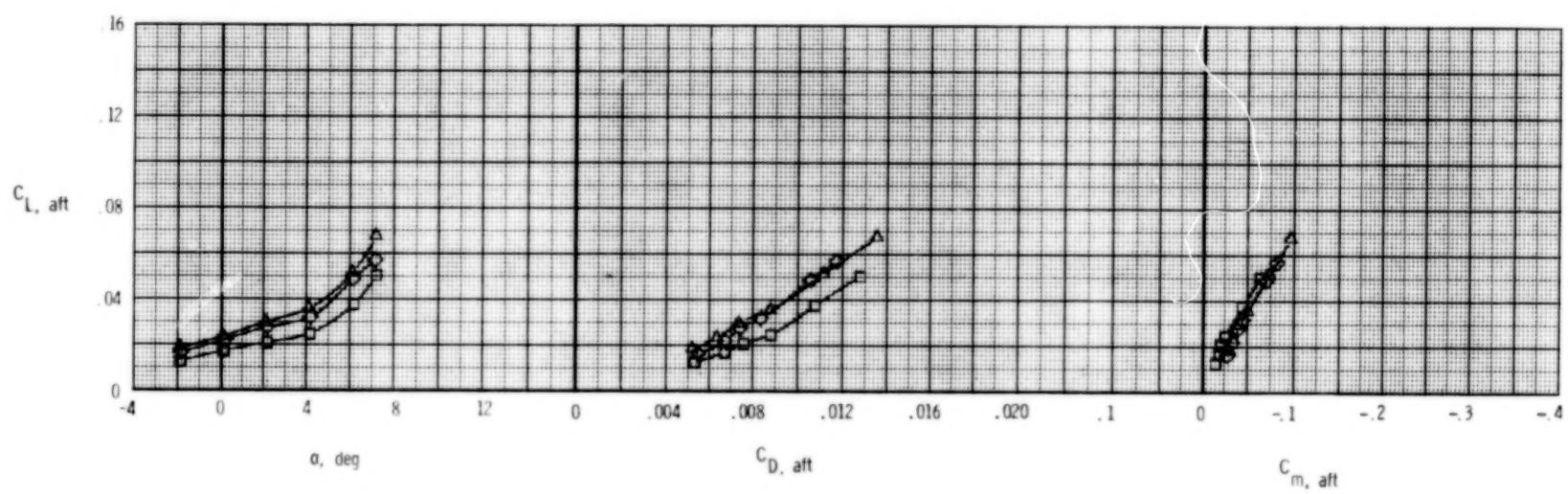
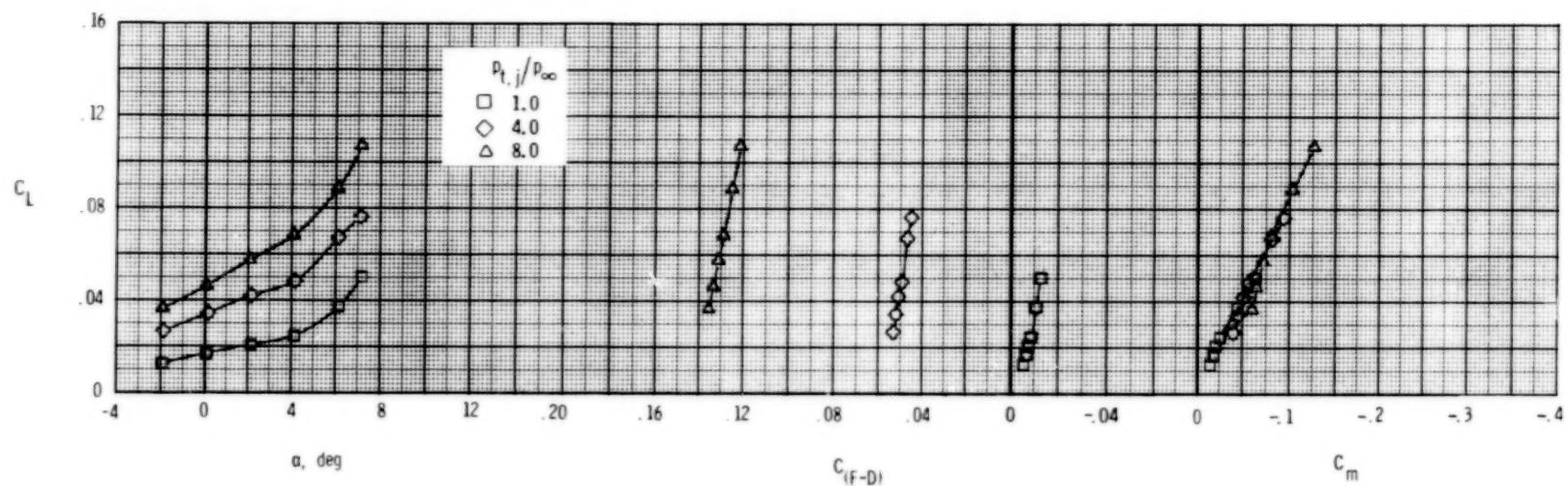
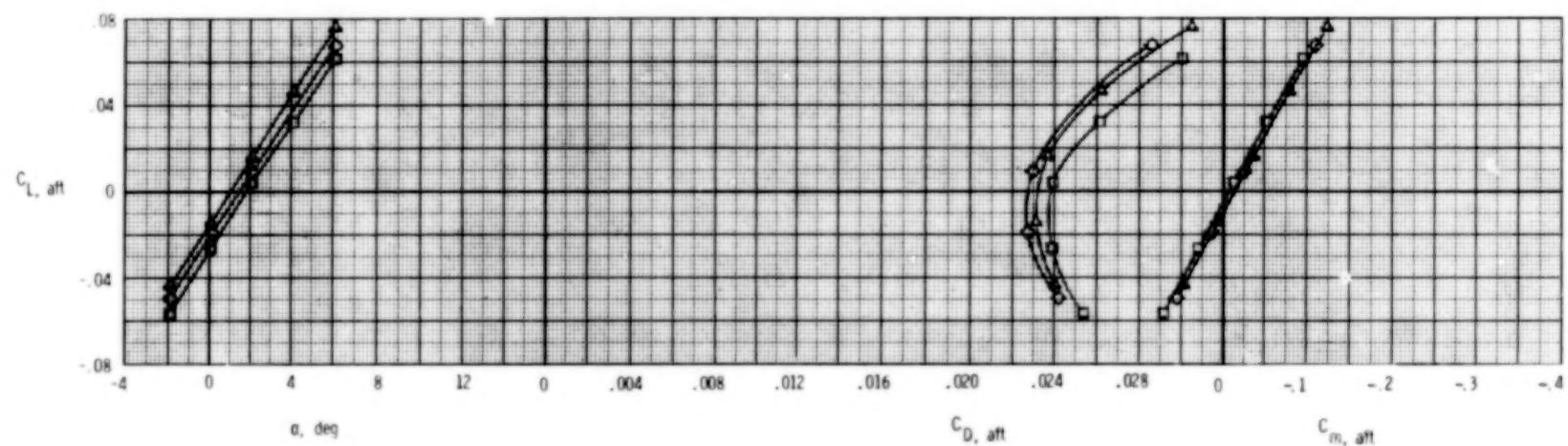
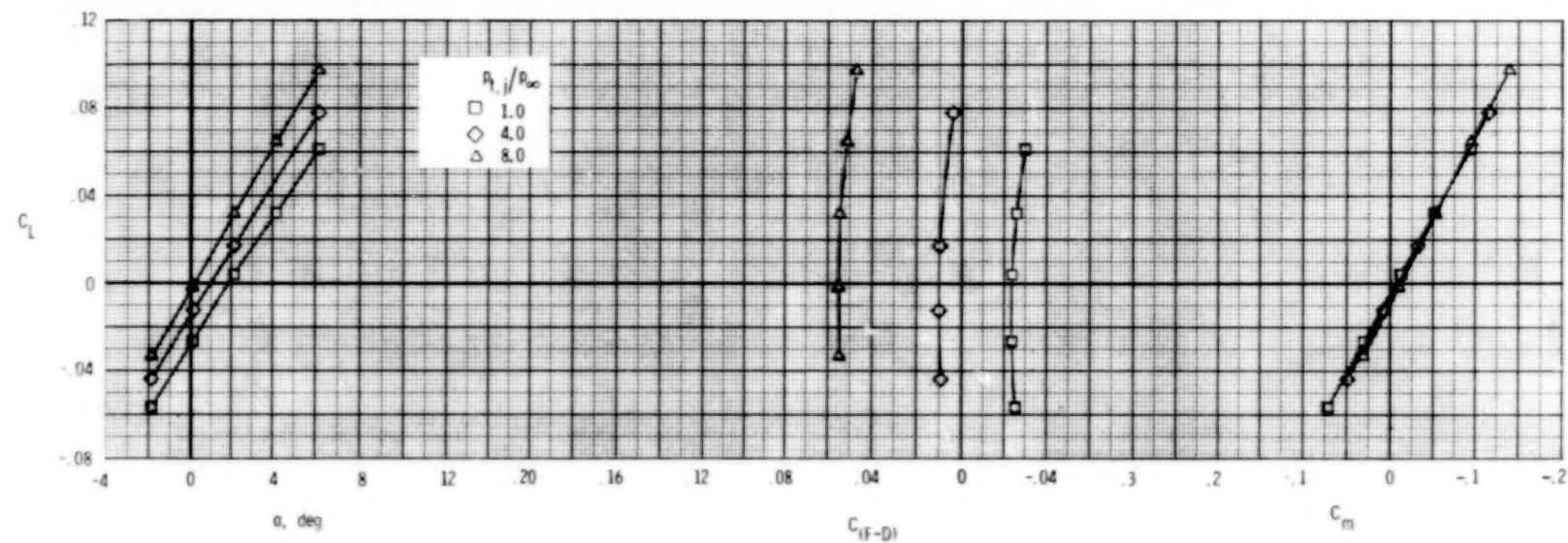
(b) $M = 0.90$.

Figure 59.- Continued.



(c) $M = 1.20$.

Figure 59.- Concluded.

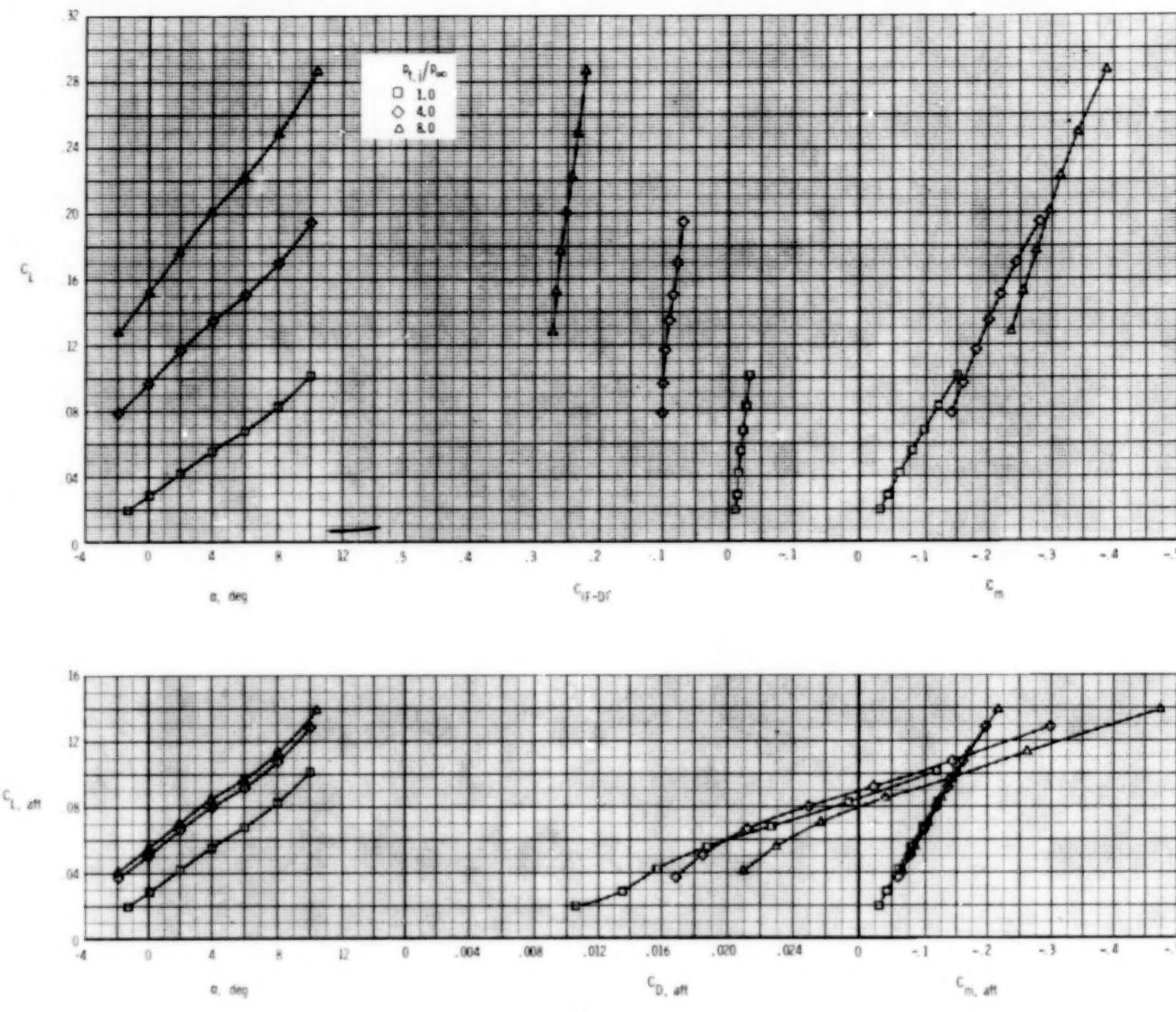
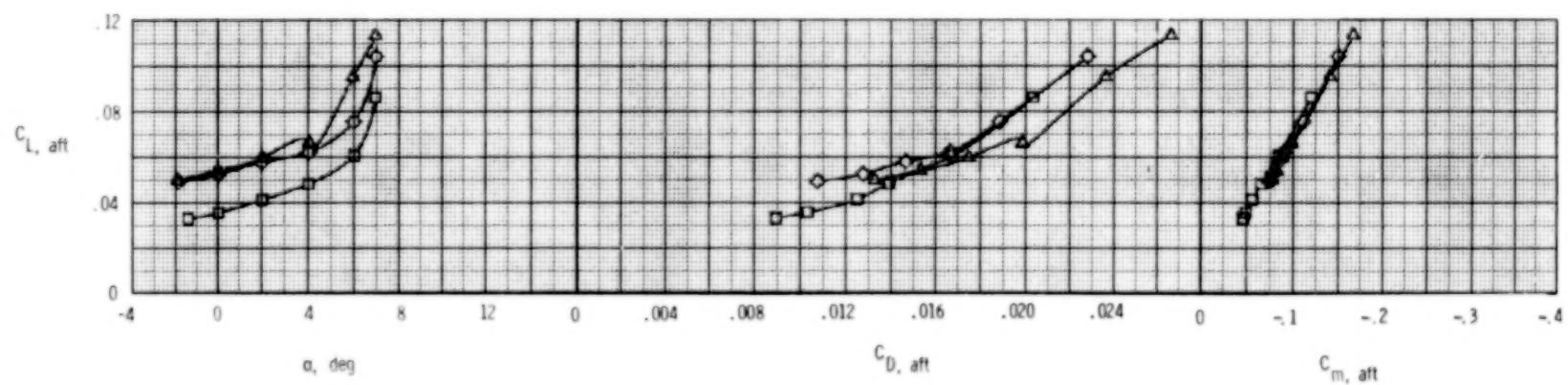
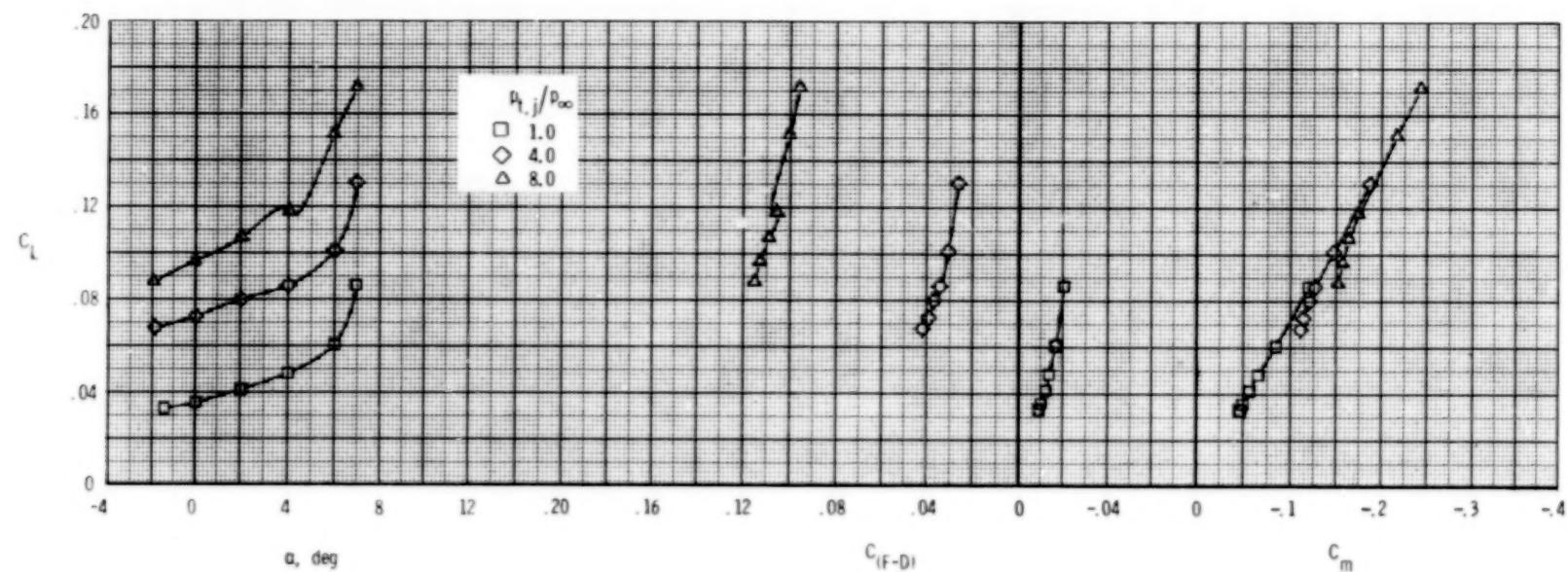
(a) $M = 0.60$.

Figure 60.- Longitudinal afterbody aerodynamic characteristics, 2-D C-D nozzle, dry power.
 $\delta_h = 0^0$; $\delta_v = 20^0$; $A_e/A_t = 1.15$.



(b) $M = 0.90$.

Figure 60.- Continued.

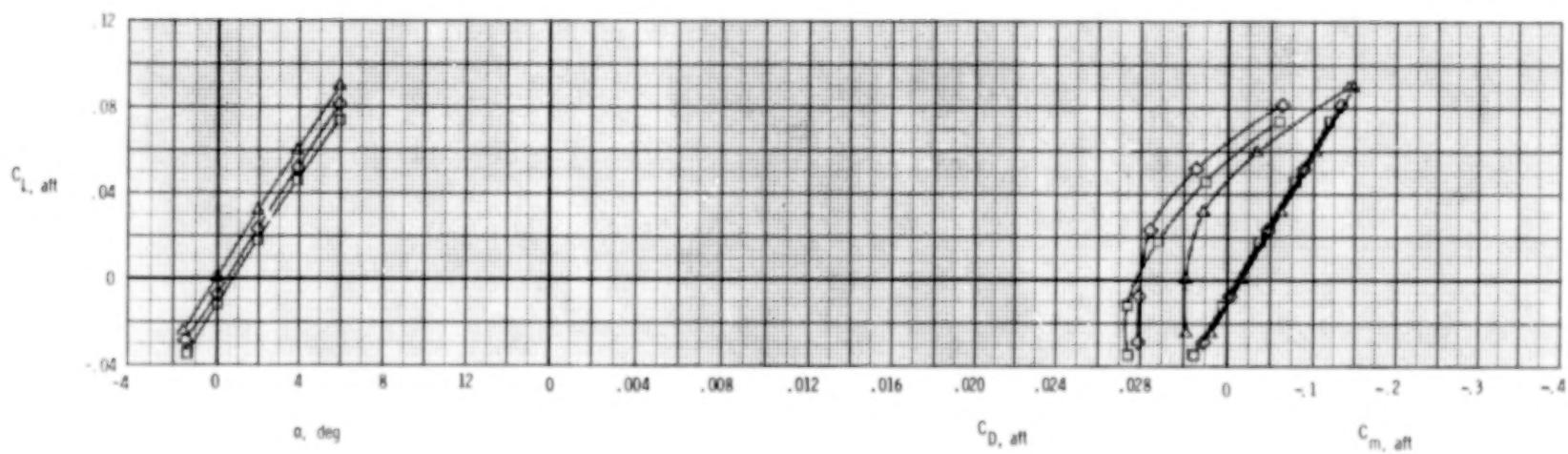
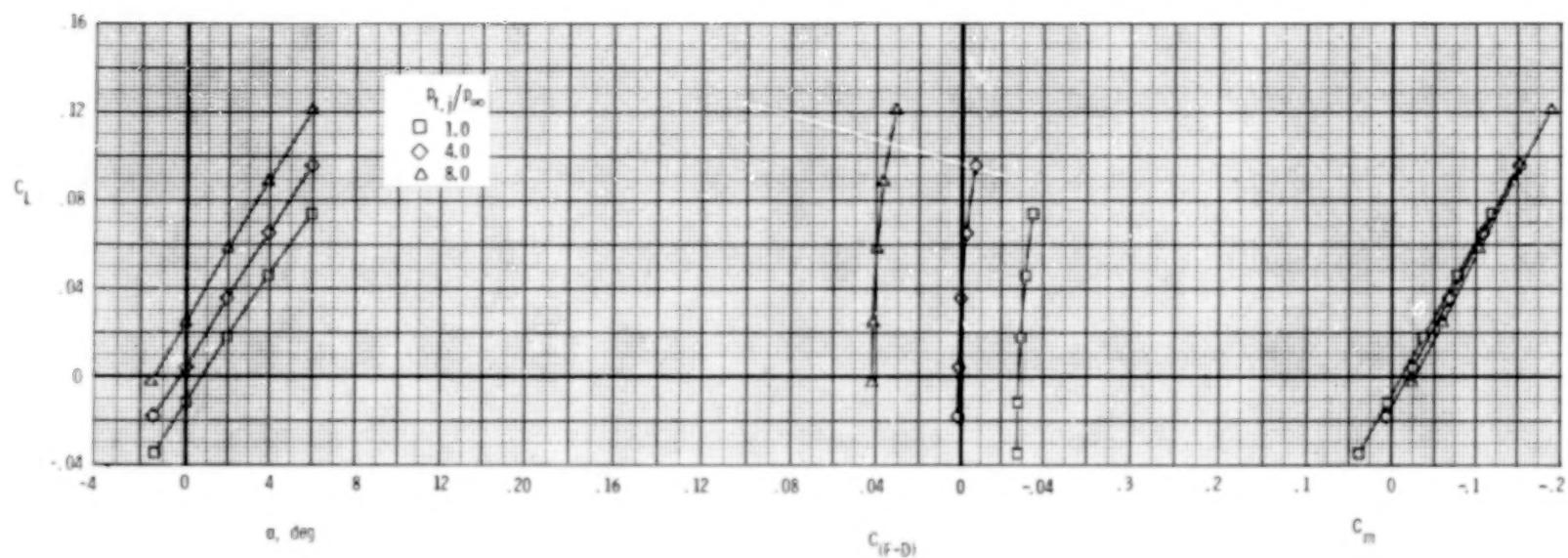
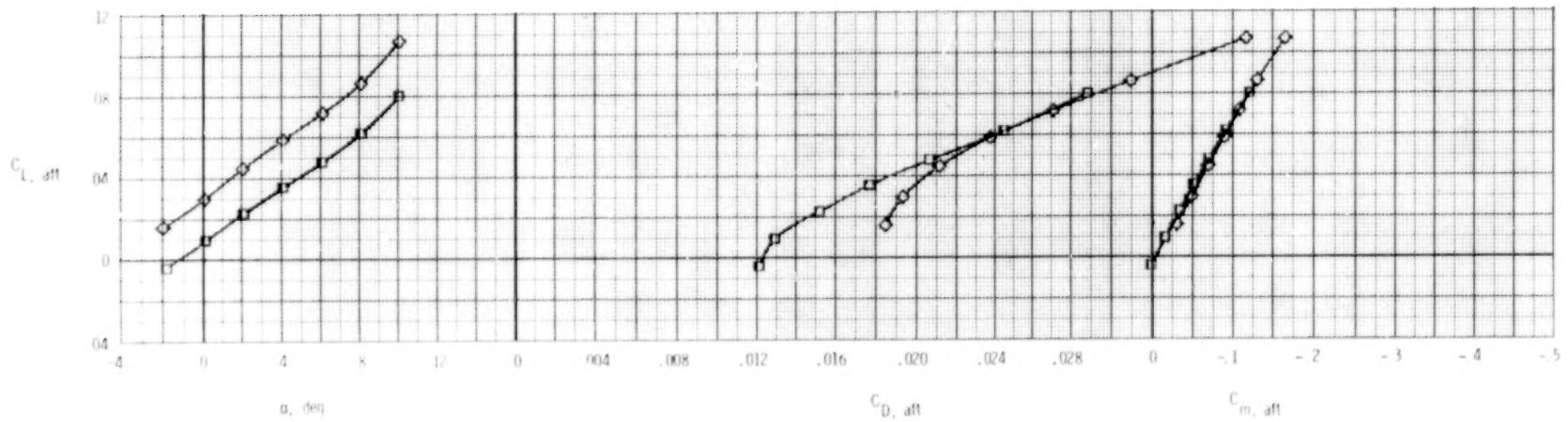
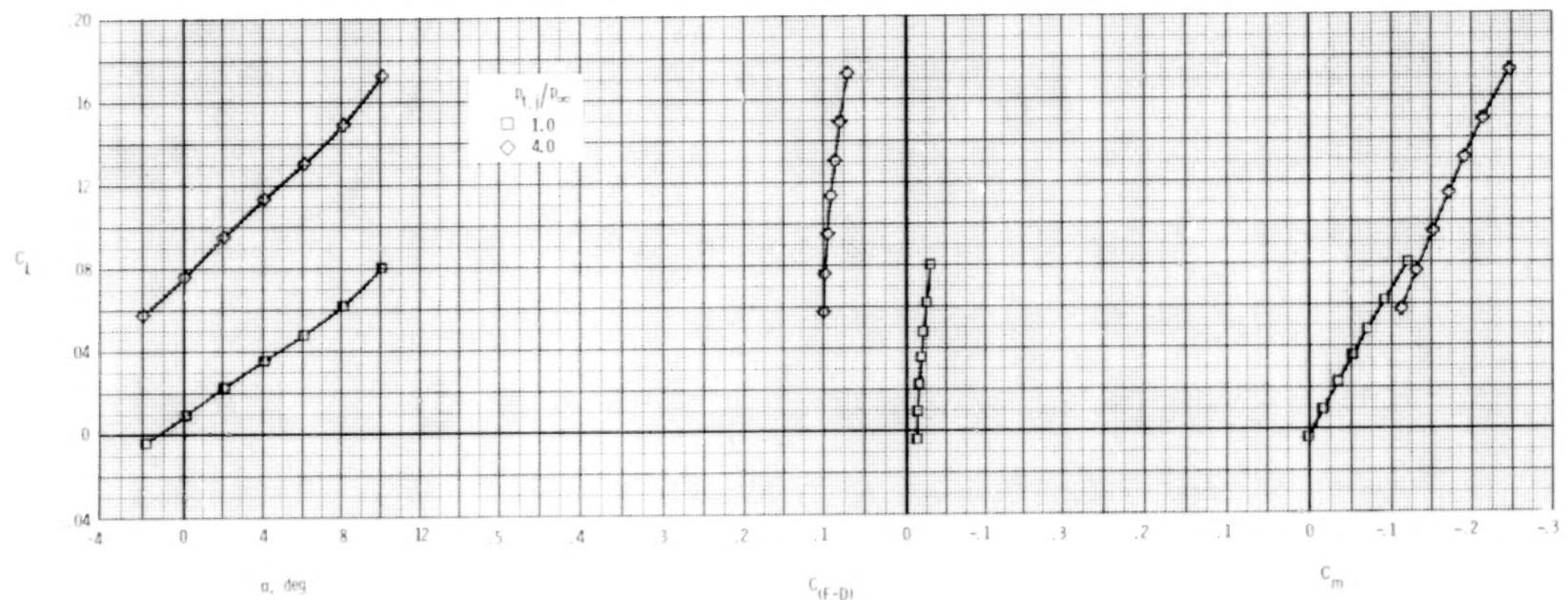
(c) $M = 1.20$.

Figure 60.- Concluded.



(a) $M = 0.60$.

Figure 61.- Longitudinal afterbody aerodynamic characteristics, 2-D C-D nozzle, dry power.

$$\delta_h = -2^\circ; \quad \delta_v = 20^\circ; \quad A_e/A_t = 1.15.$$

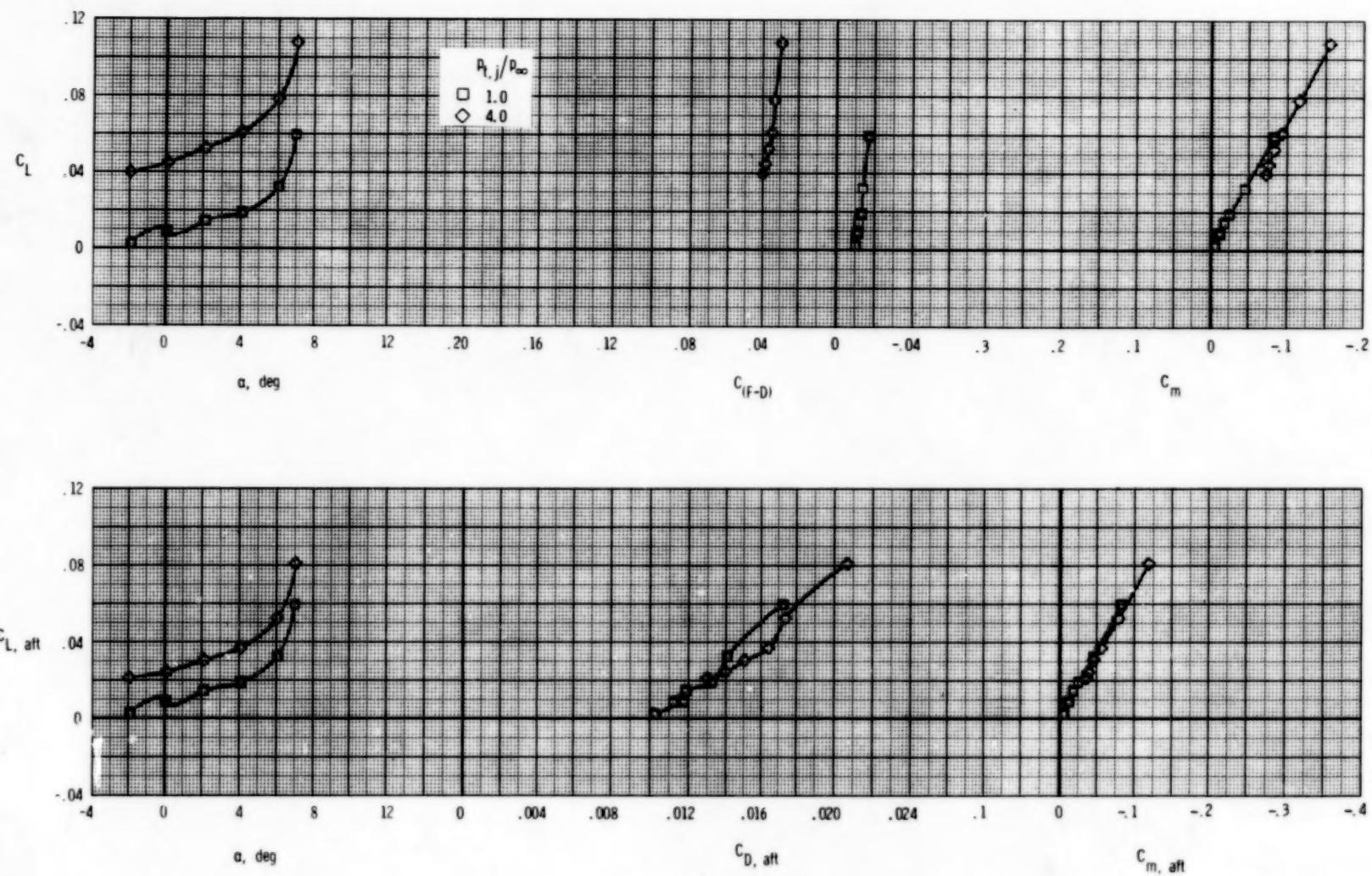
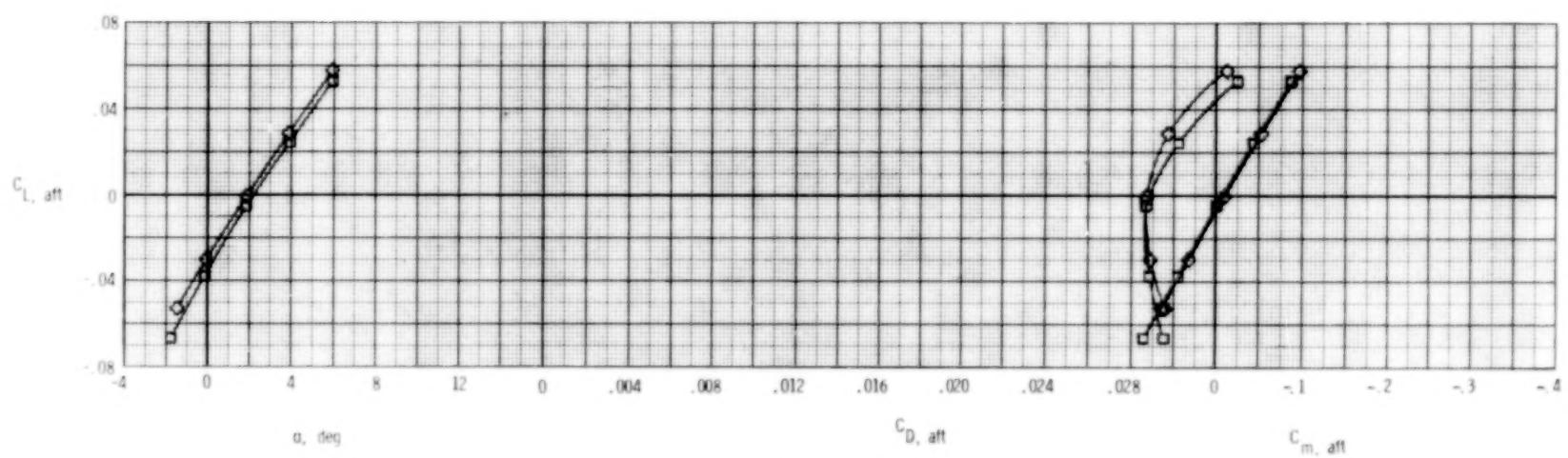
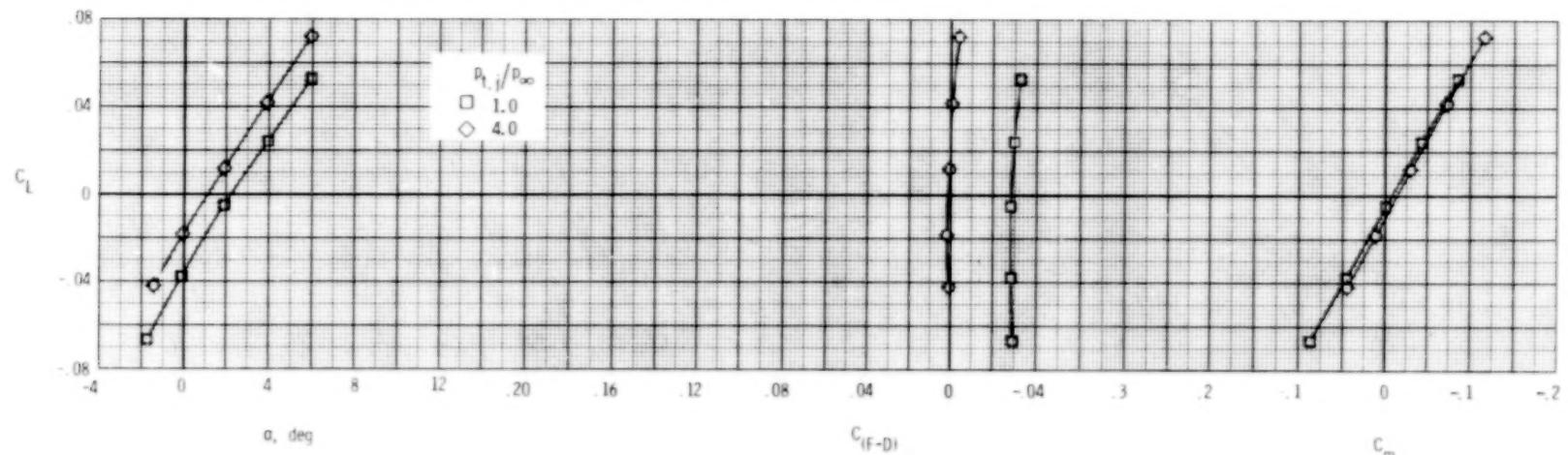
(b) $M = 0.90$.

Figure 61.- Continued.



(c) $M = 1.20$.

Figure 61.- Concluded.

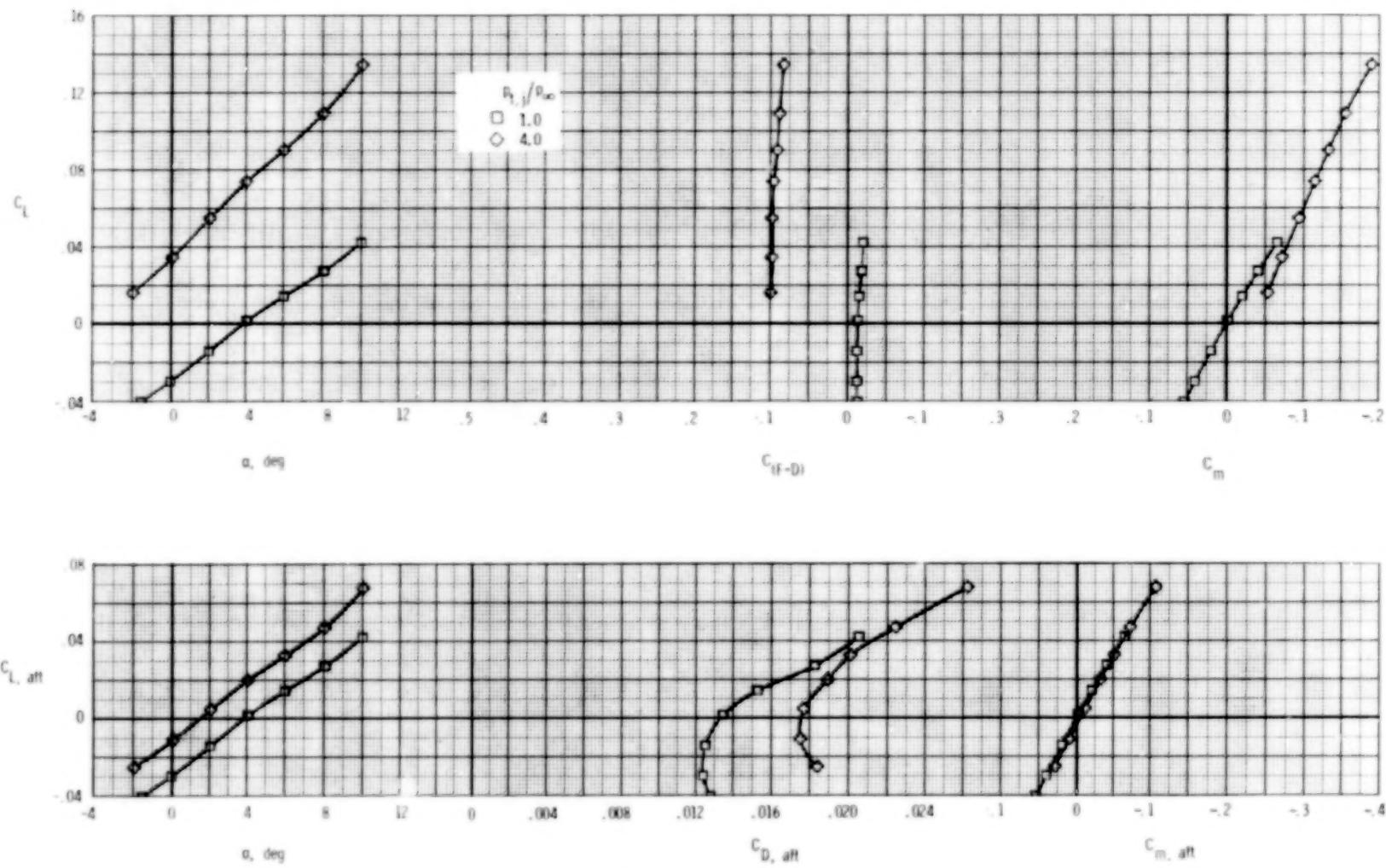
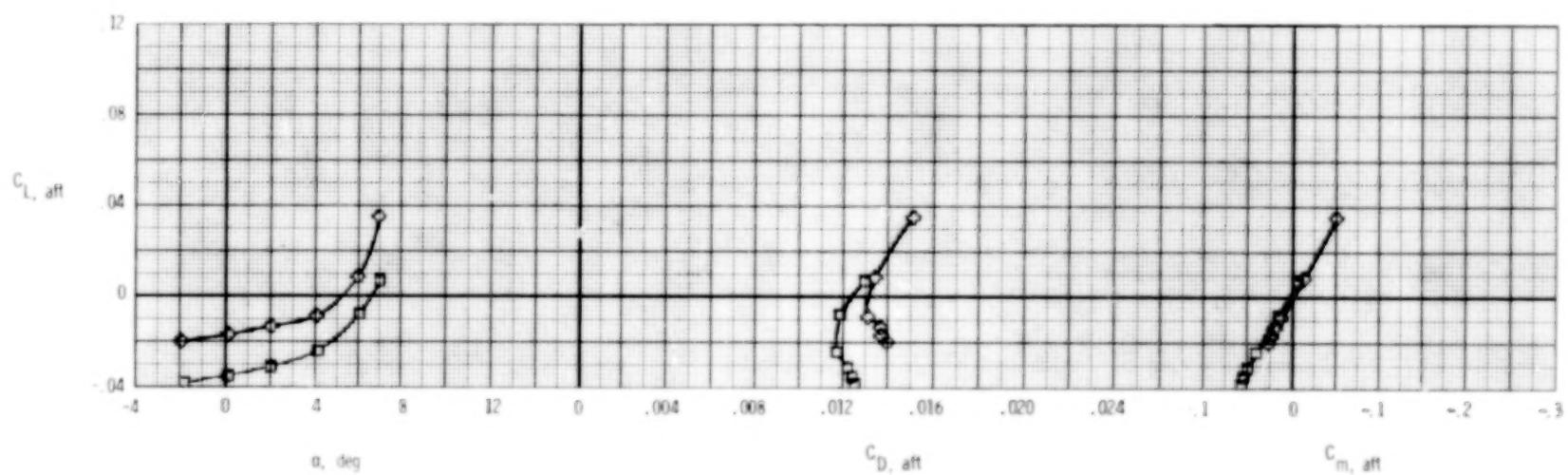
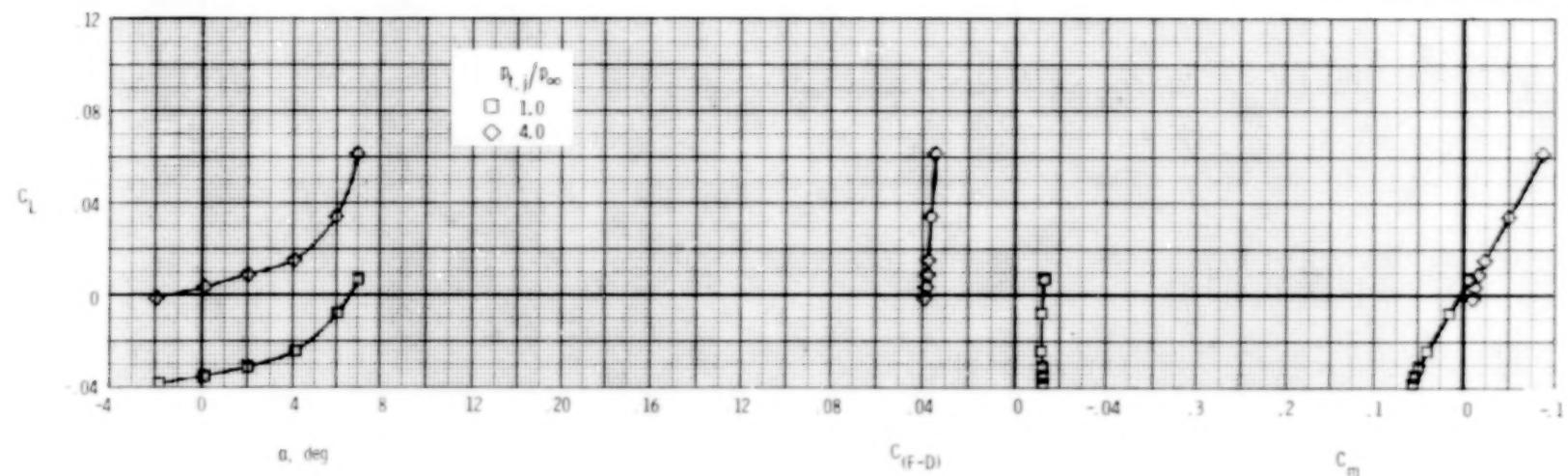
(a) $M = 0.60$.

Figure 62.- Longitudinal afterbody aerodynamic characteristics, 2-D C-D nozzle, dry power.

$$\delta_h = -5^\circ; \quad \delta_v = 20^\circ; \quad A_e/A_t = 1.15.$$



(b) $M = 0.90$.

Figure 62.- Concluded.

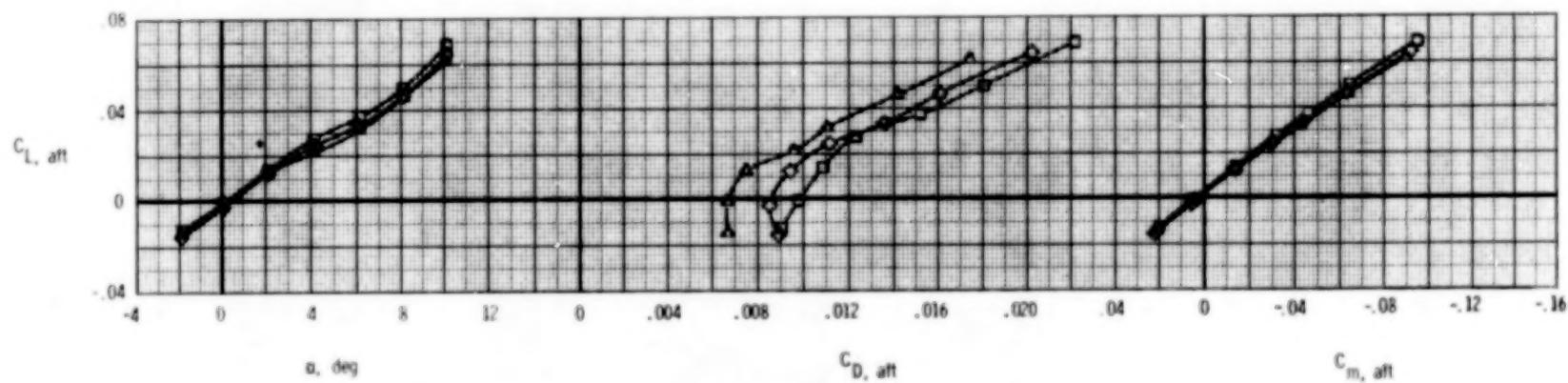
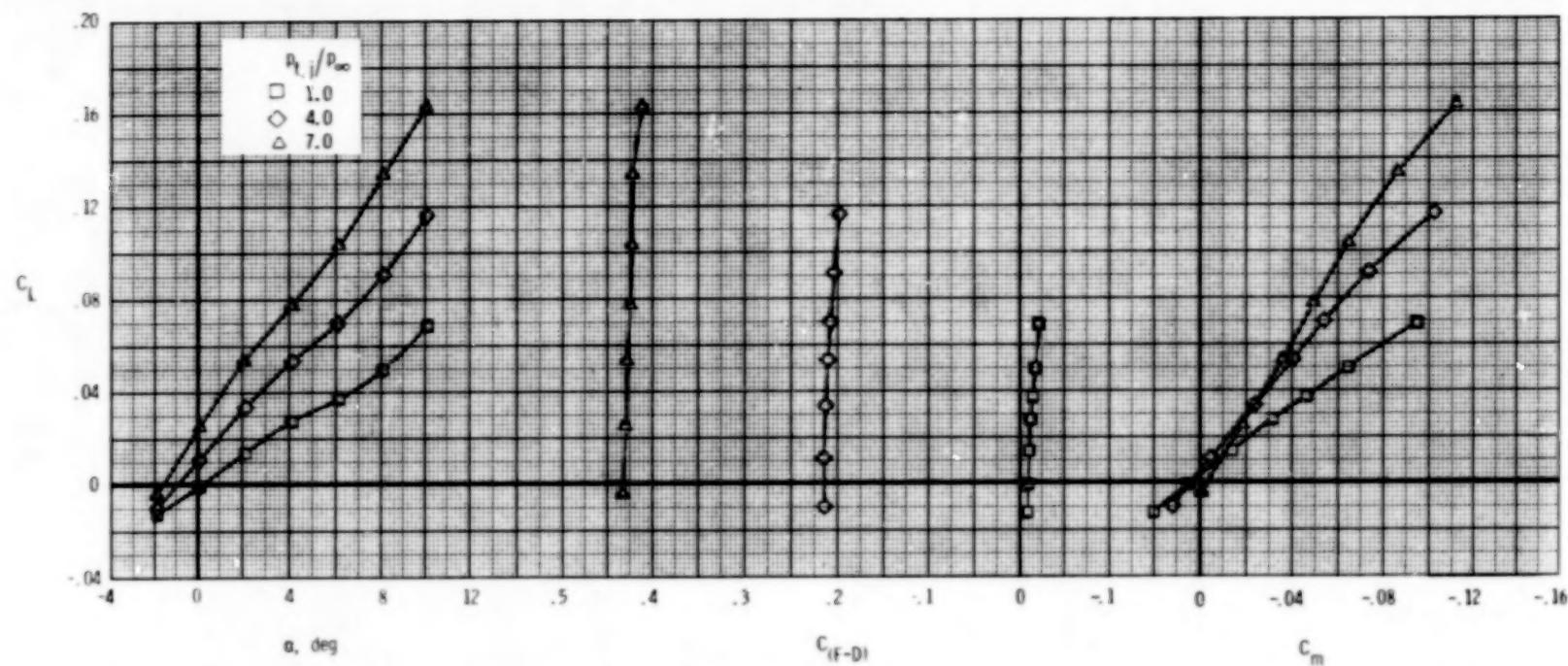
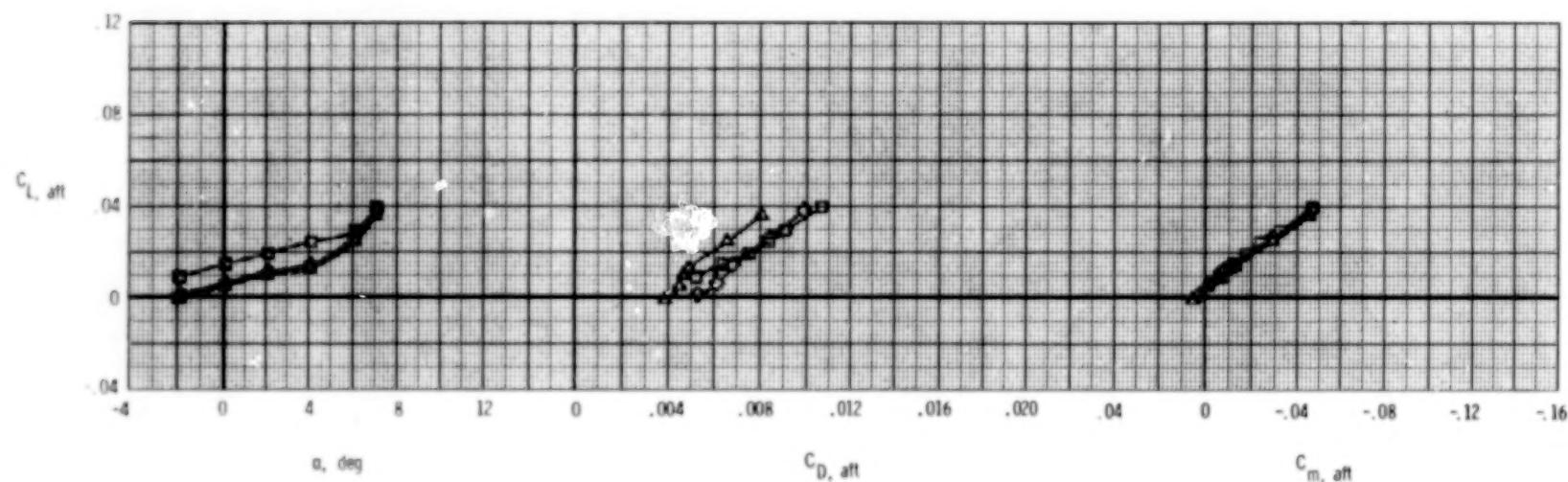
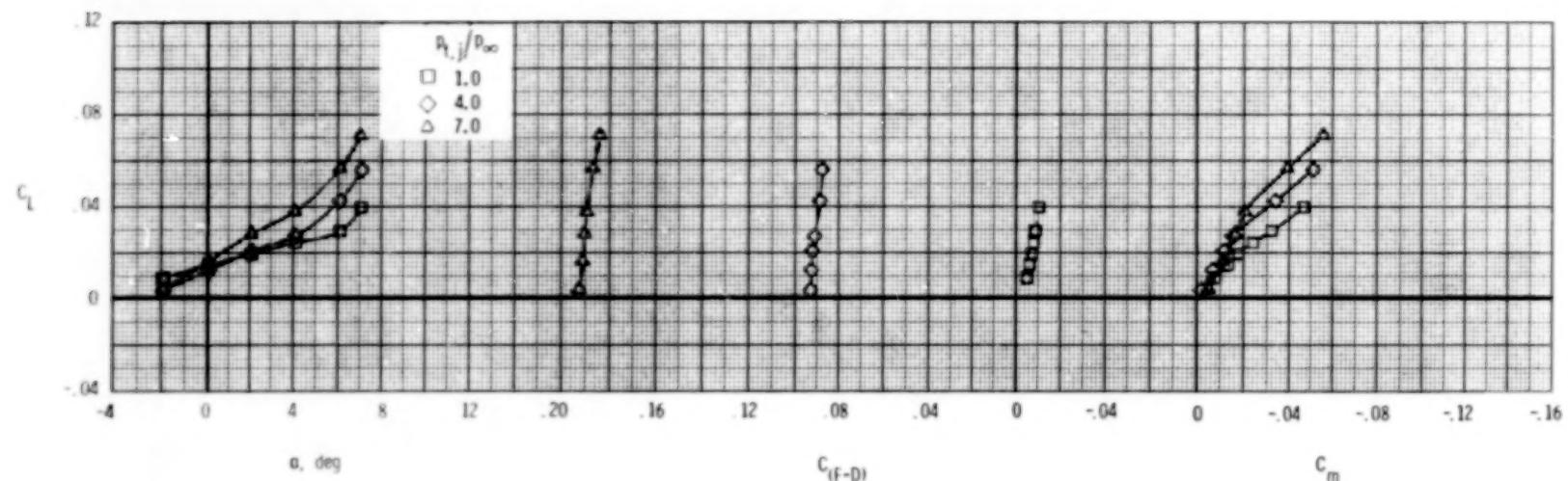
(a) $M = 0.60$.

Figure 63.- Longitudinal afterbody aerodynamic characteristics, 2-D C-D nozzle, A/B power.

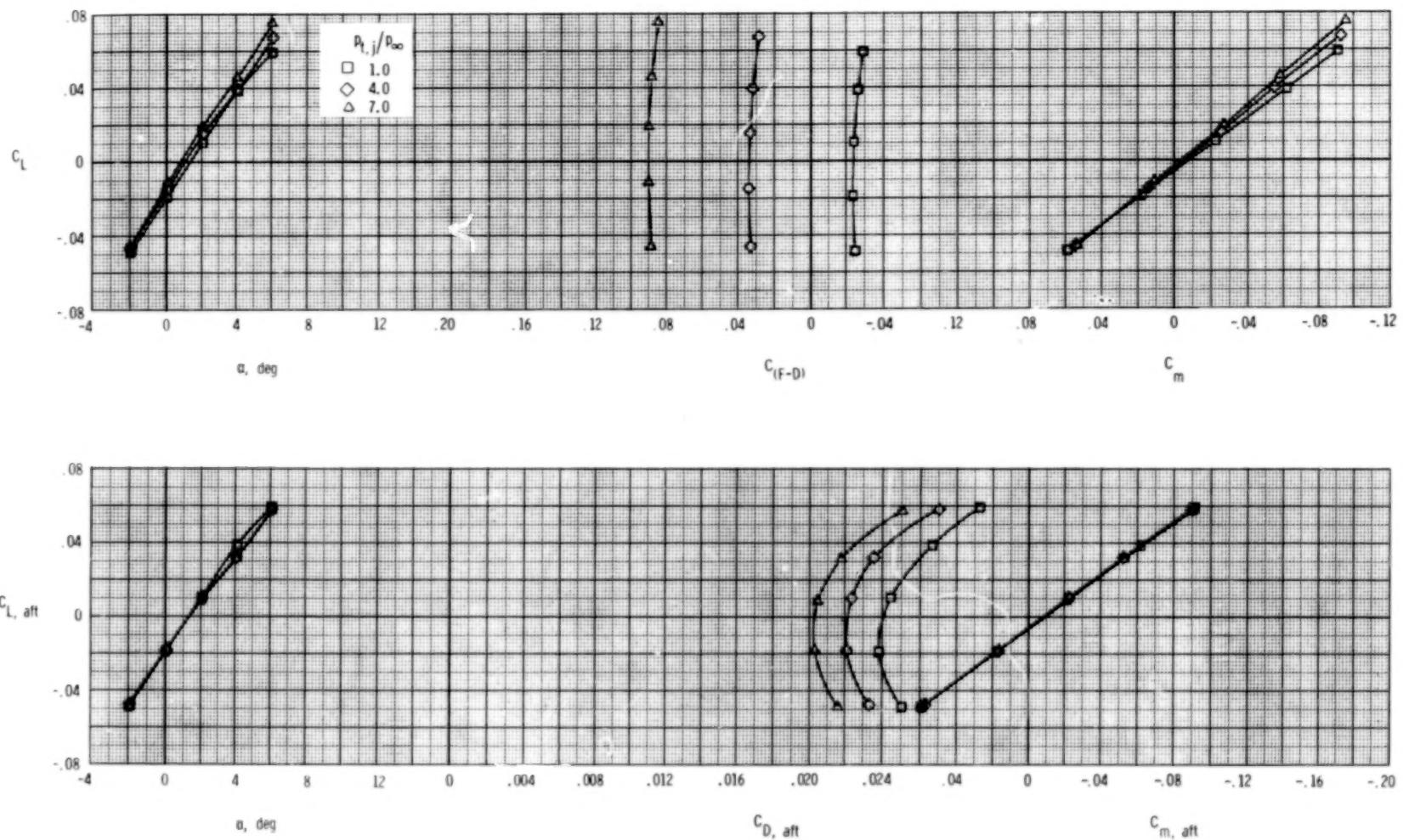
$$\delta_h = 0^\circ; \delta_v = 0^\circ; A_e/A_t = 1.15.$$



(b) $M = 0.90$.

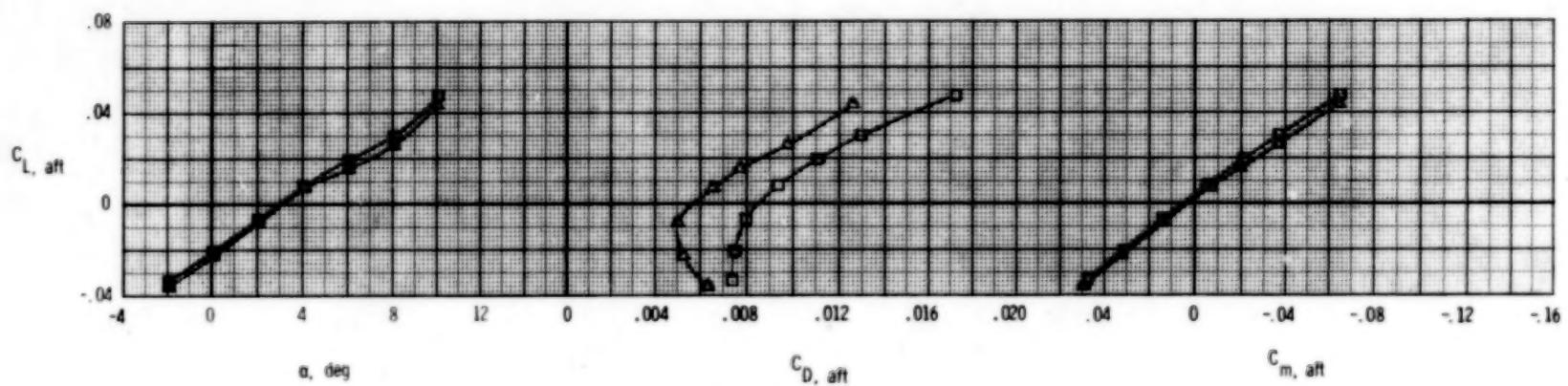
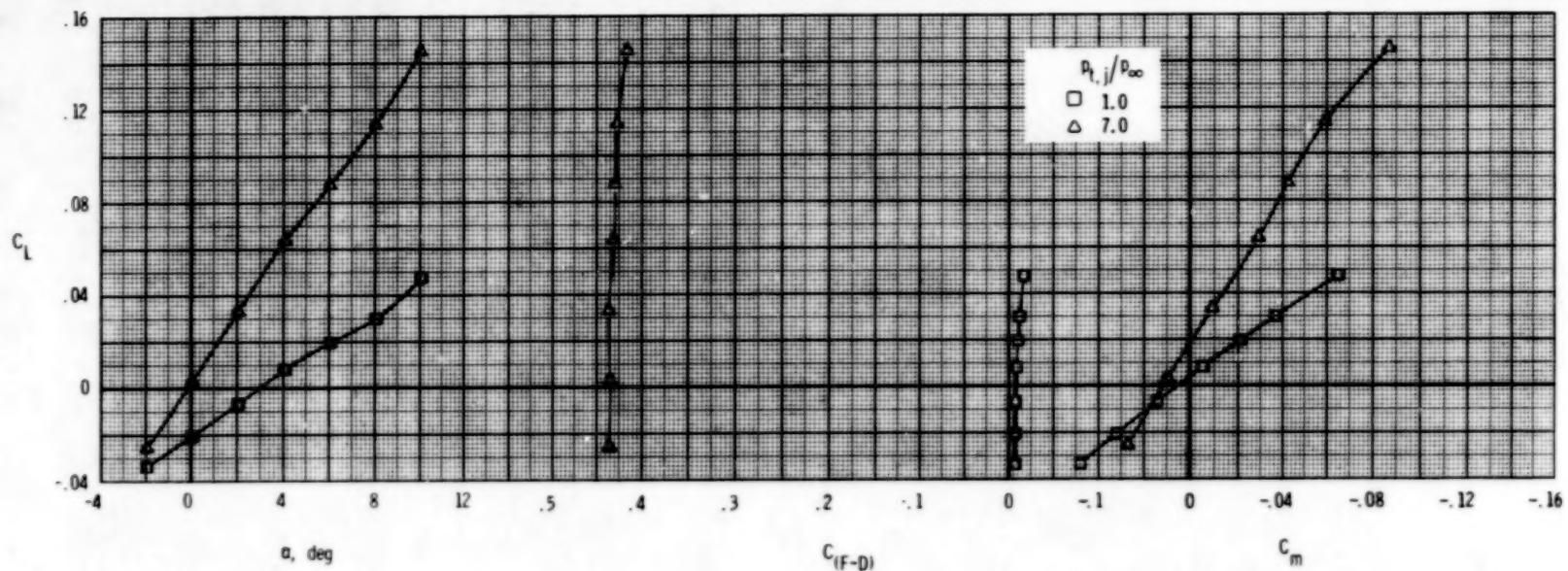
Figure 63.- Continued.

152



(c) $M = 1.20.$

Figure 63.- Concluded.



(a) $M = 0.60$.

Figure 64.- Longitudinal afterbody aerodynamic characteristics, 2-D C-D nozzle, A/B power.

$$\delta_h = -2^\circ; \quad \delta_v = 0^\circ; \quad A_e/A_t = 1.15.$$

154

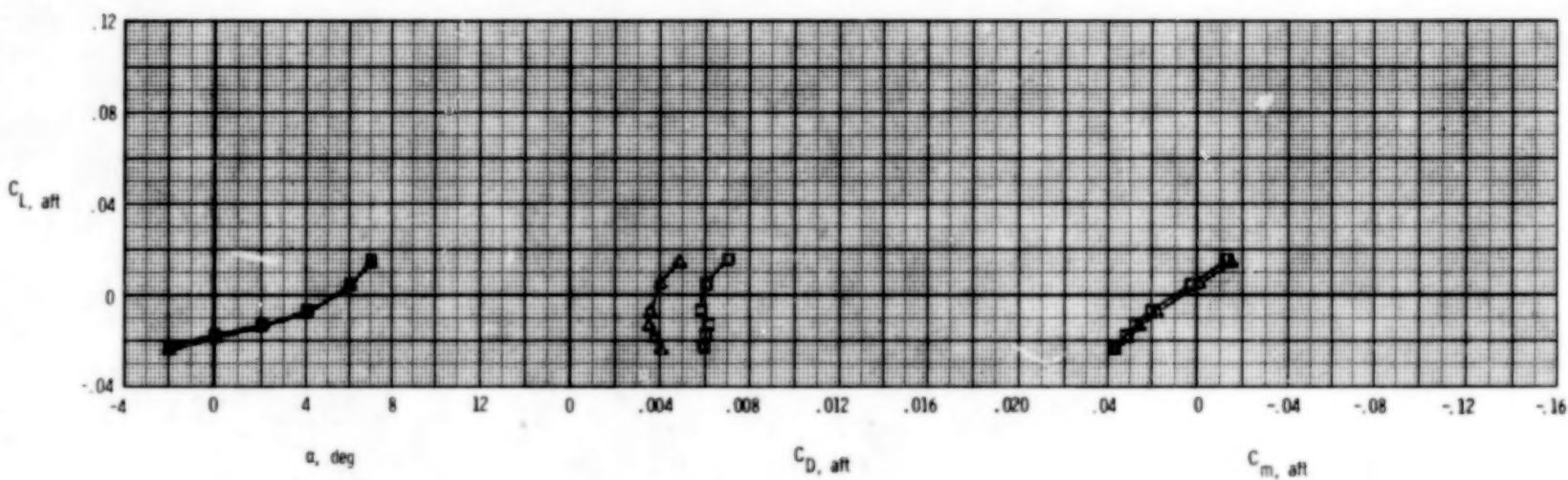
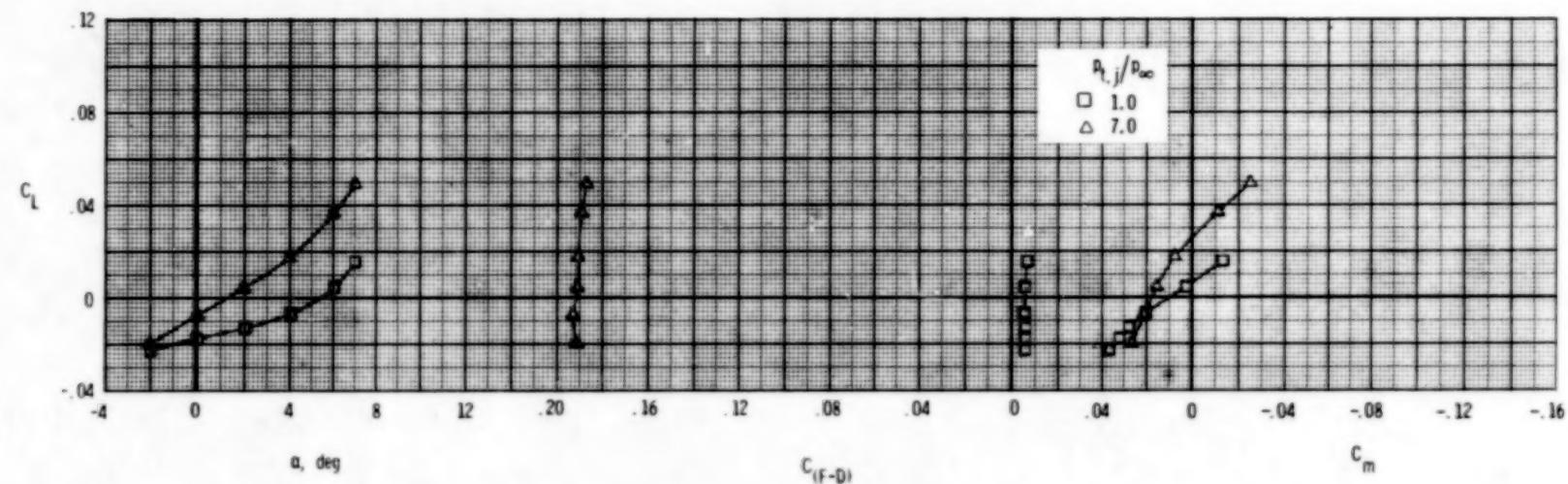
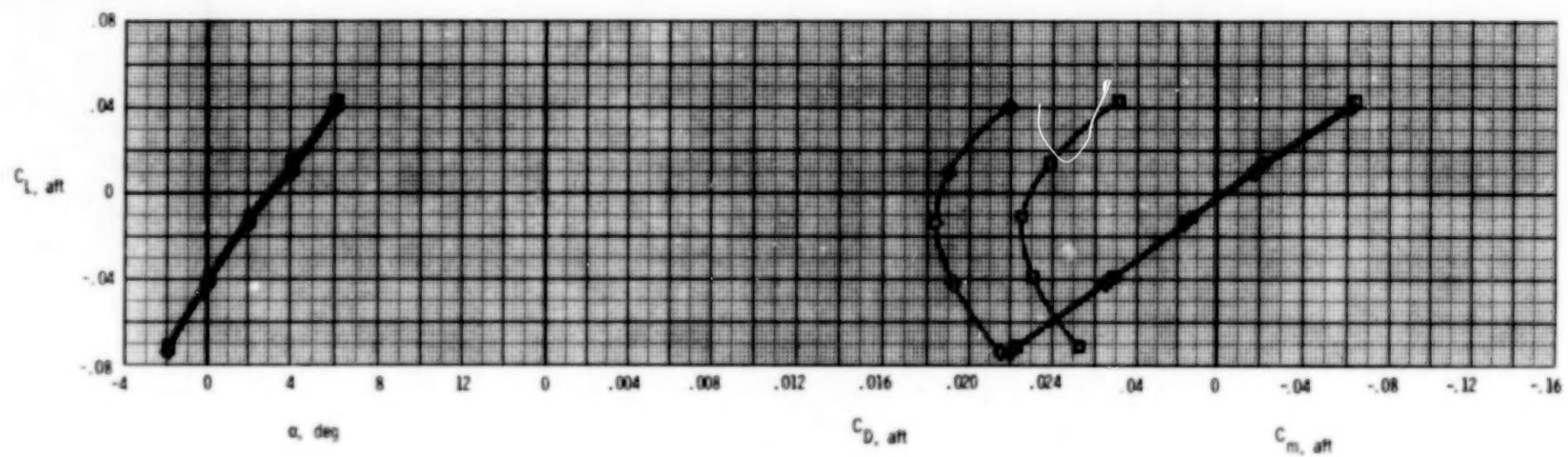
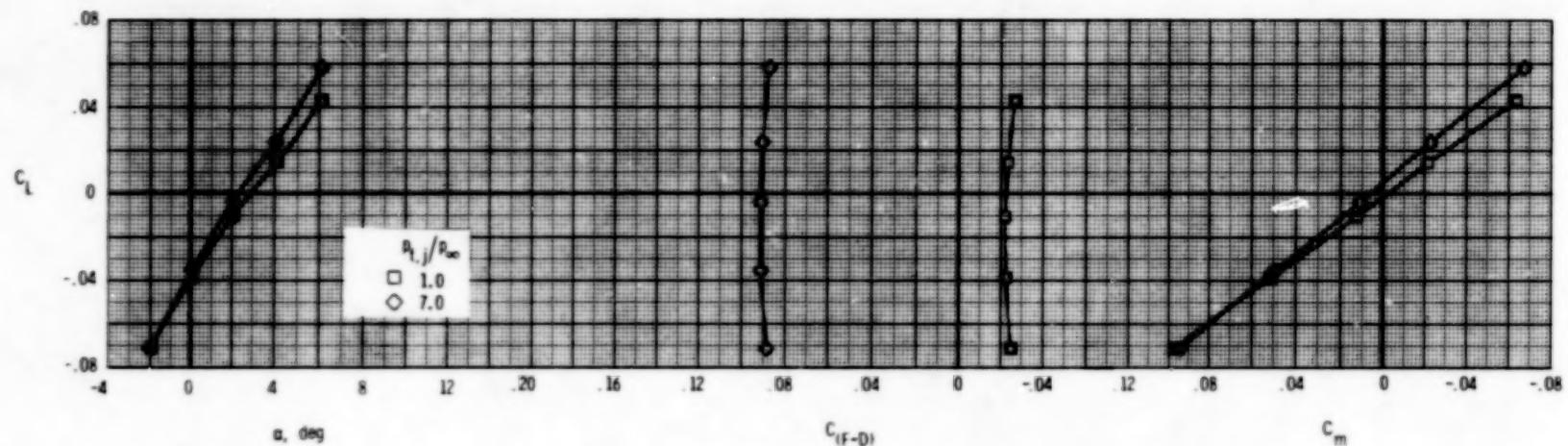
(b) $M = 0.90$.

Figure 64. - Continued.



(c) $M = 1.20$.

Figure 64.- Concluded.

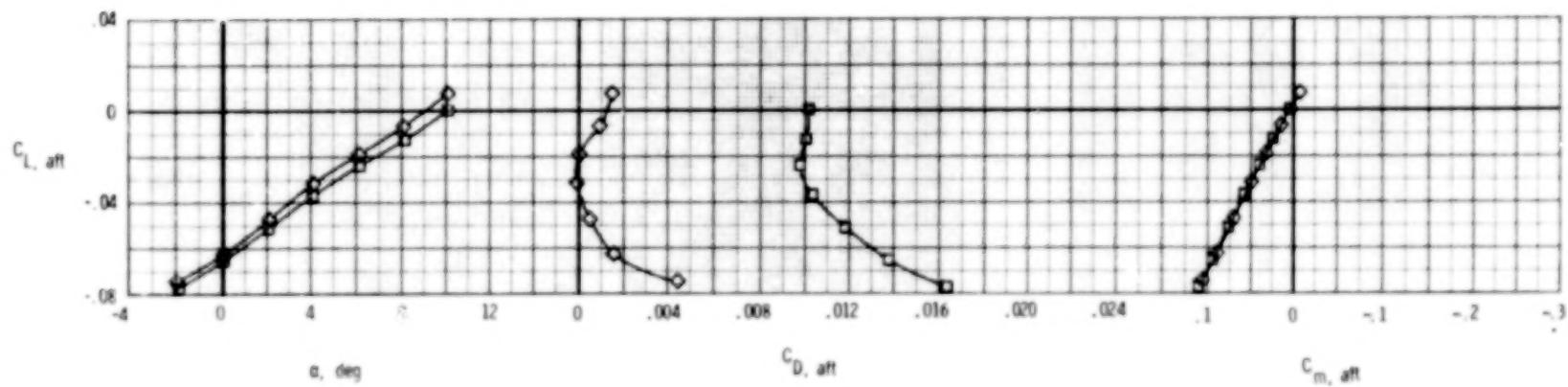
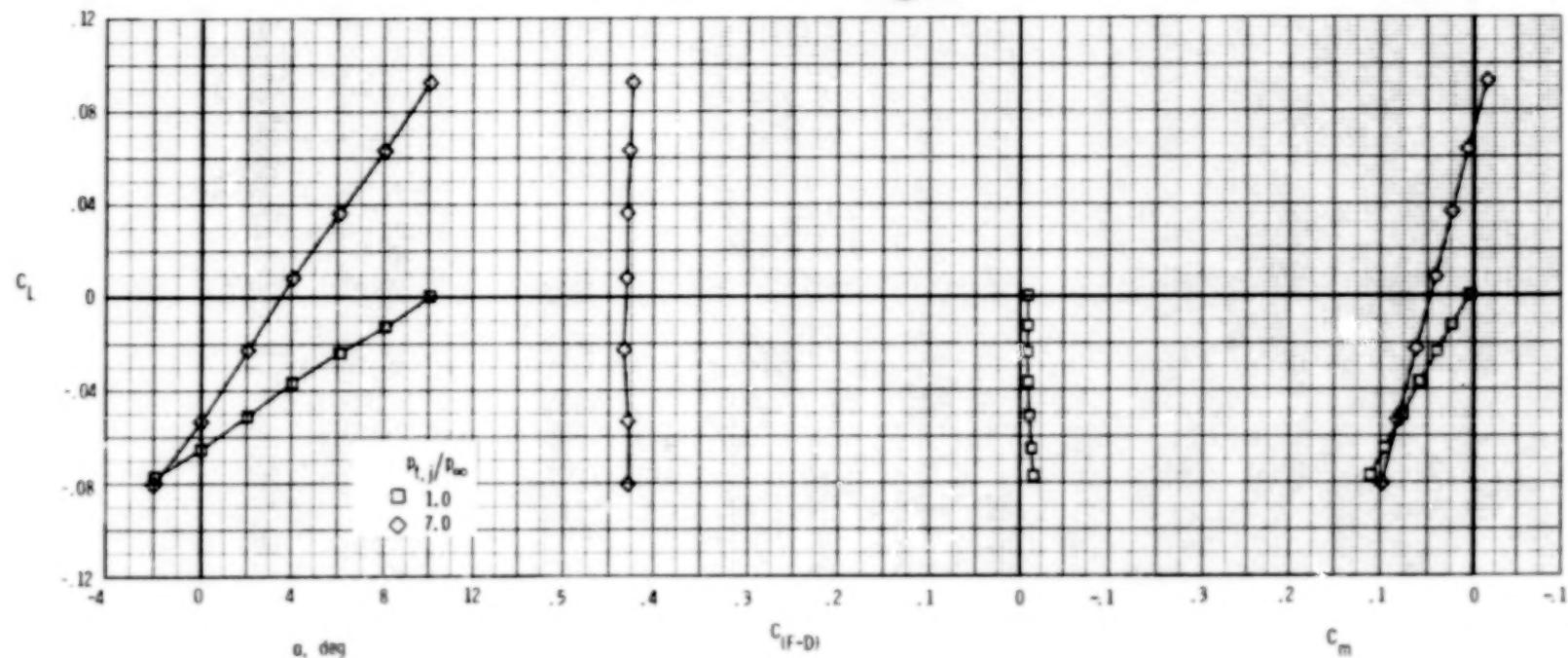
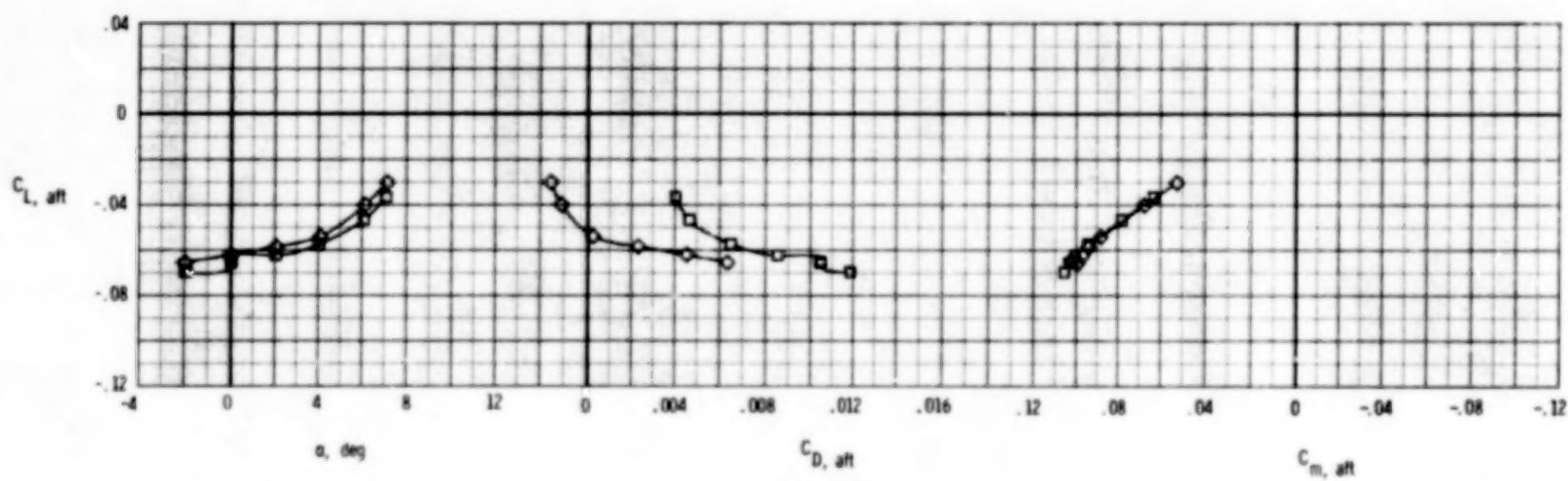
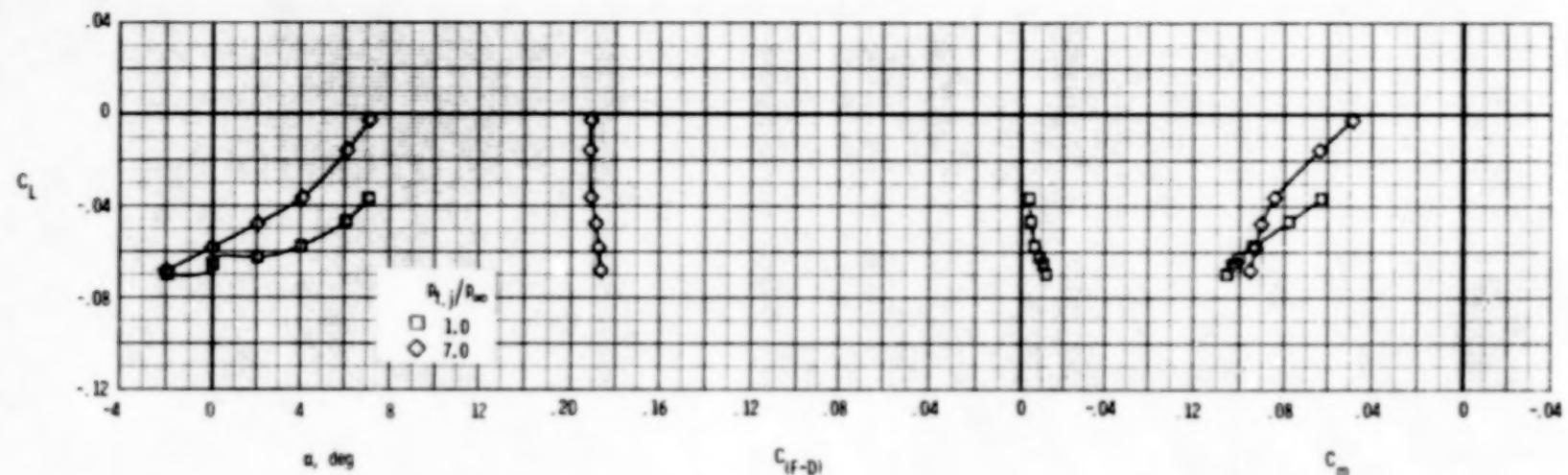
(a) $M = 0.60$.

Figure 65.- Longitudinal afterbody aerodynamic characteristics, 2-D C-D nozzle, A/B power.

$$\delta_h = -5^\circ; \quad \delta_v = 0^\circ; \quad A_e/A_t = 1.15.$$



(b) $M = 0.90$.

Figure 65.- Continued.

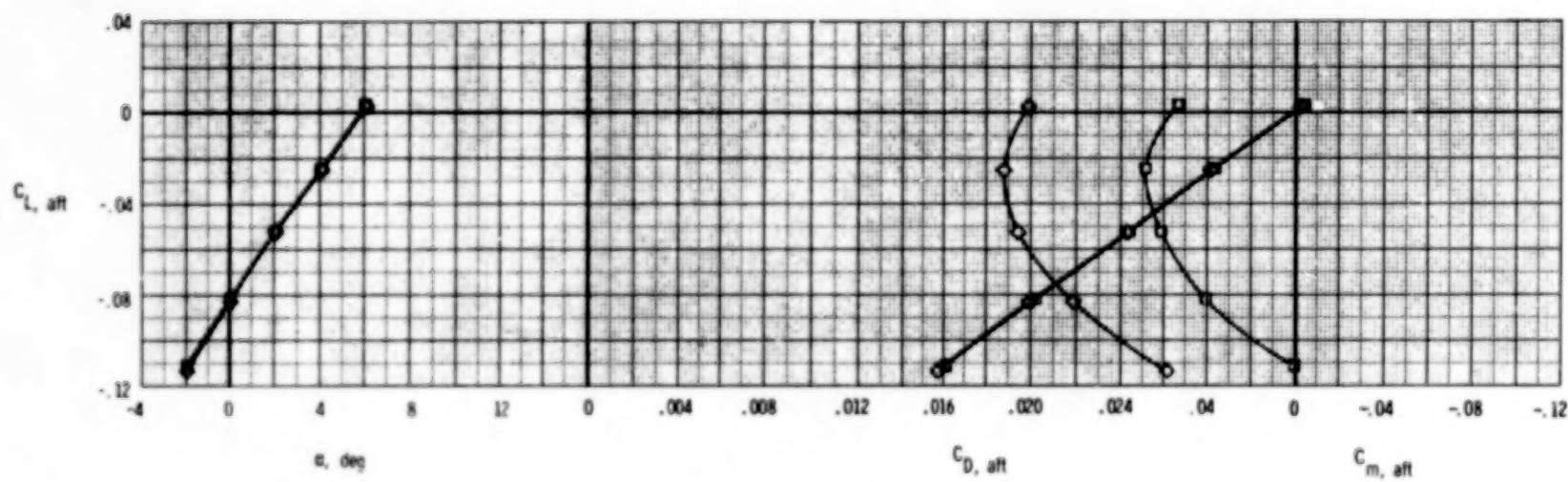
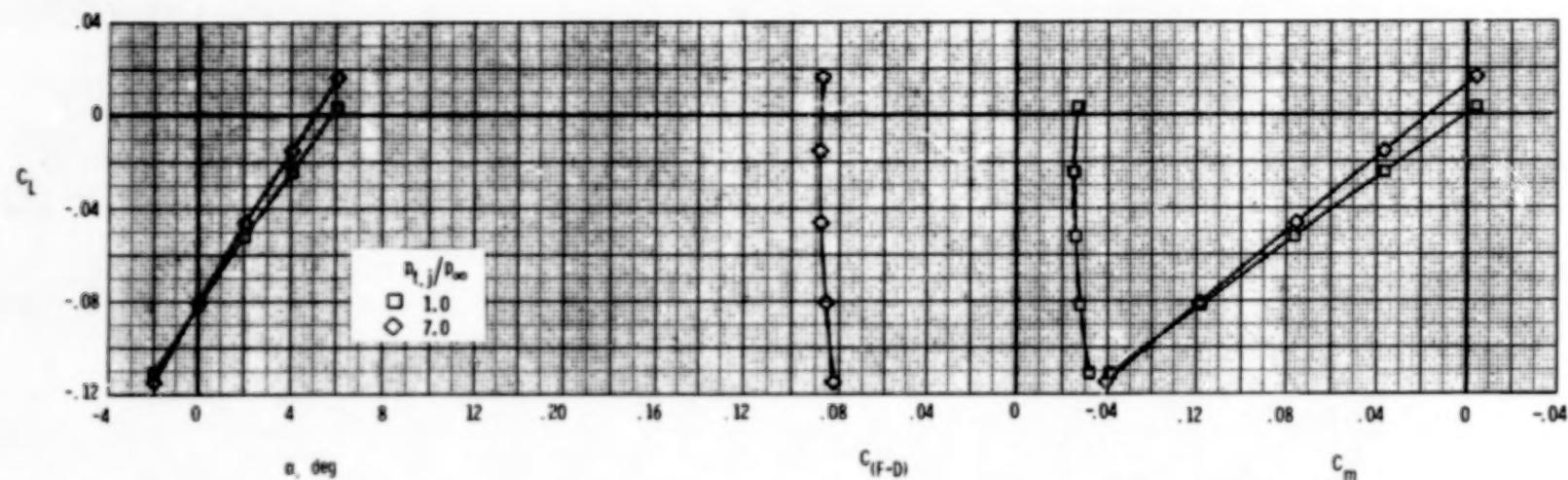
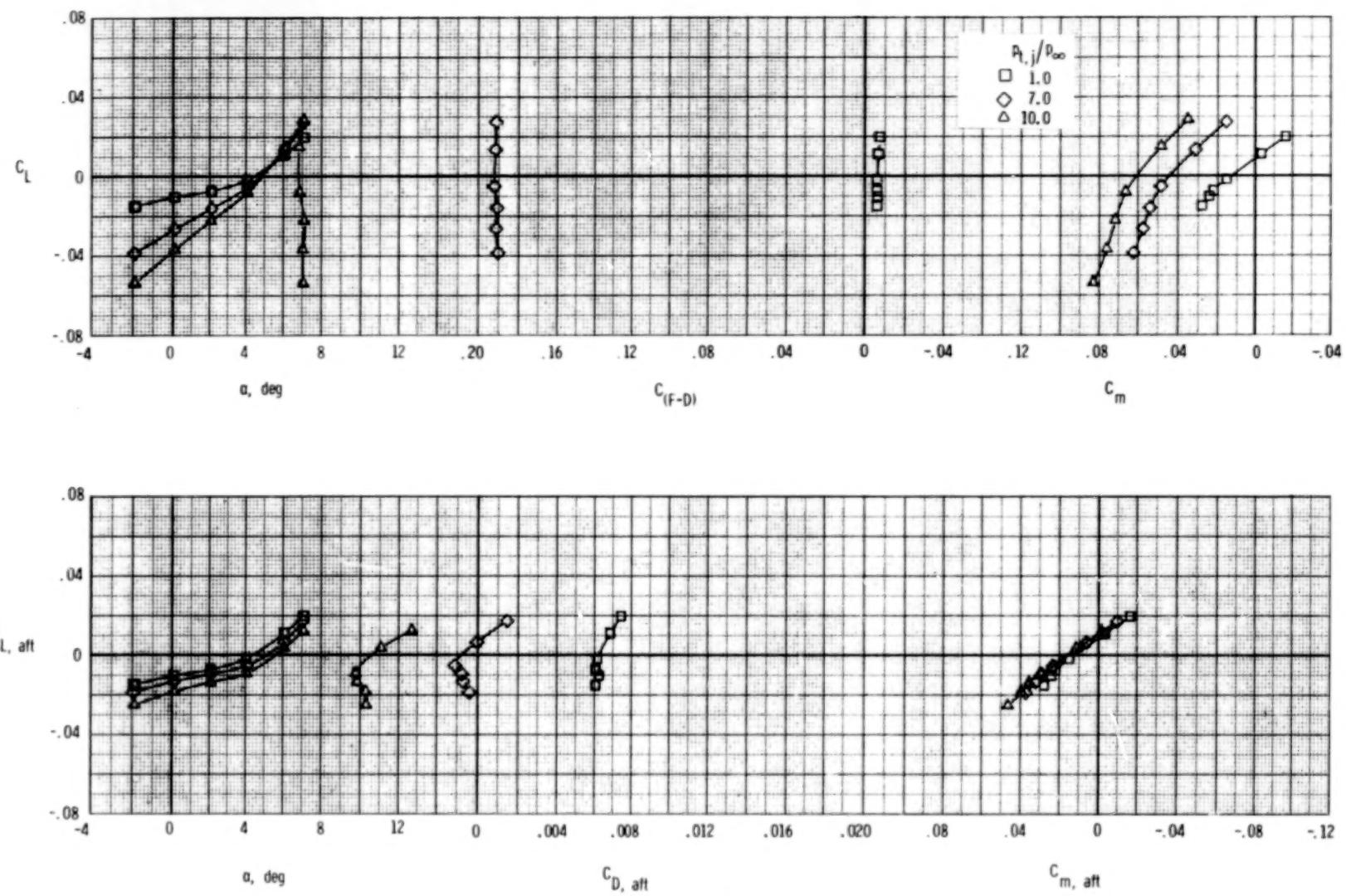
(c) $M = 1.20$.

Figure 65.- Concluded.



(a) $M = 0.90$.

Figure 66.- Longitudinal afterbody aerodynamic characteristics, 2-D C-D nozzle, A/B power.

$$\delta_h = 0^\circ; \quad \delta_v = -7^\circ; \quad A_e/A_t = 1.15.$$

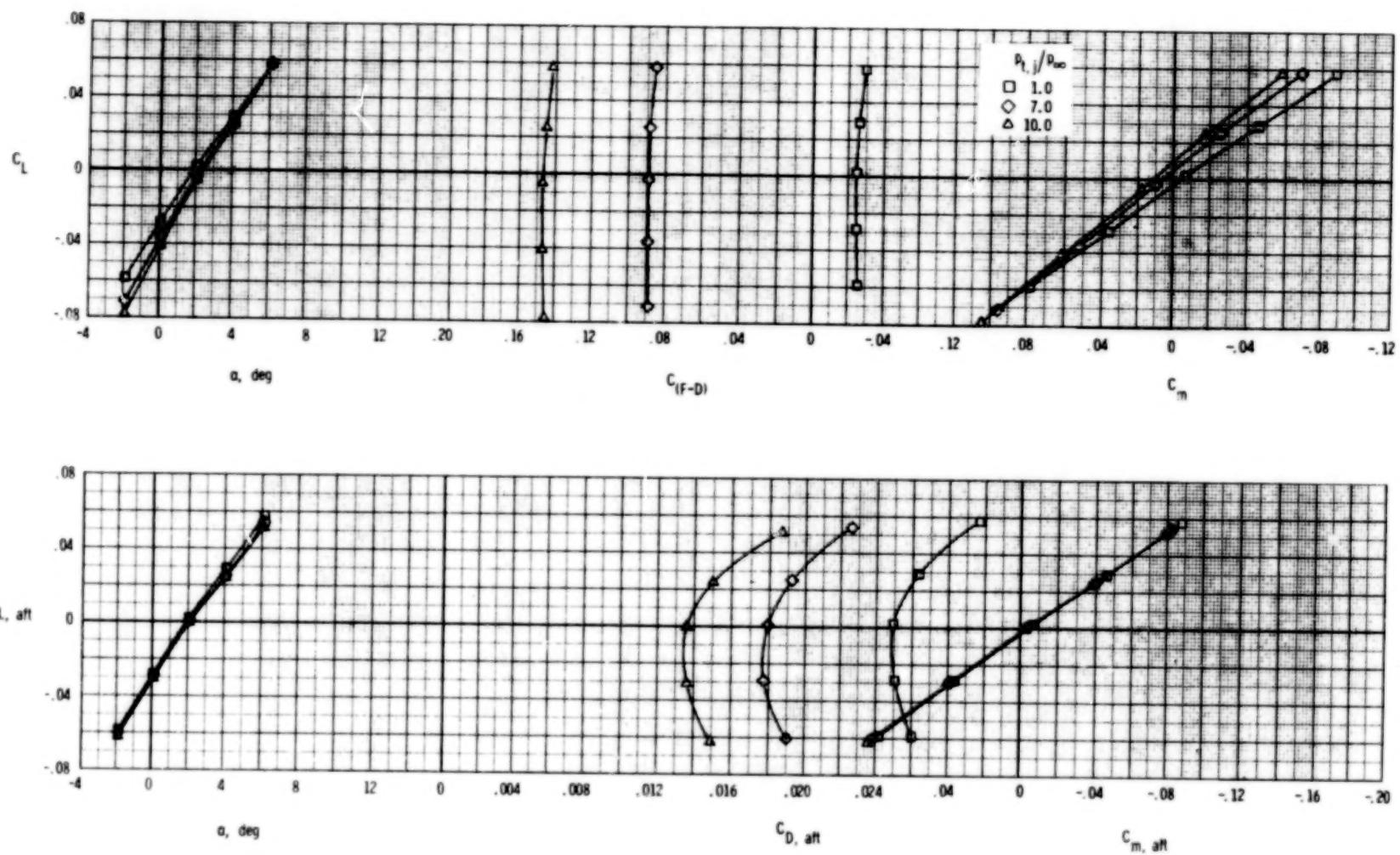
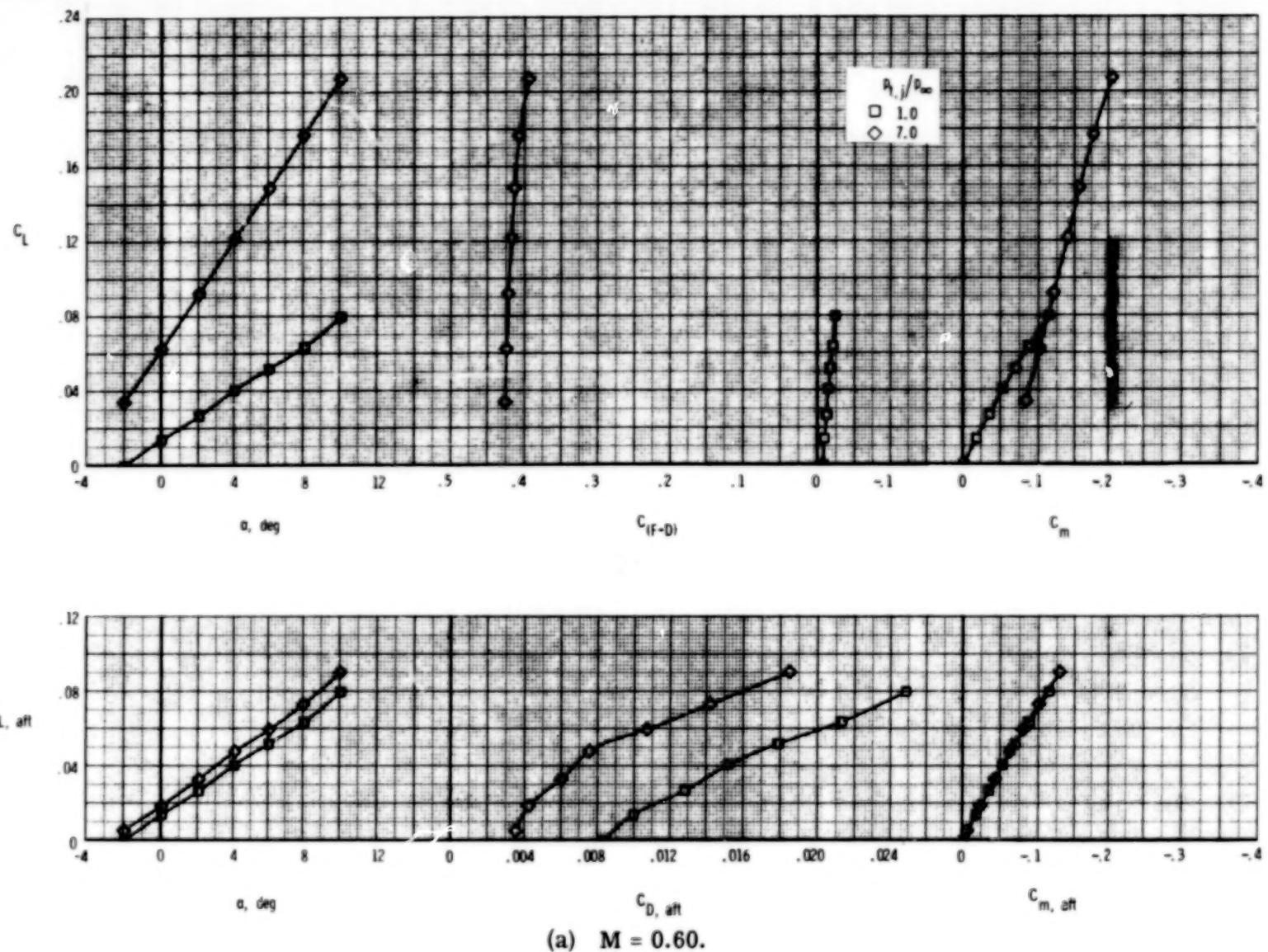
(b) $M = 1.20$.

Figure 66.- Concluded.



(a) $M = 0.60$.

Figure 67.- Longitudinal afterbody aerodynamic characteristics, 2-D C-D nozzle, A/B power.

$$\delta_h = 0^\circ; \quad \delta_v = 7^\circ; \quad A_e/A_t = 1.15.$$

162

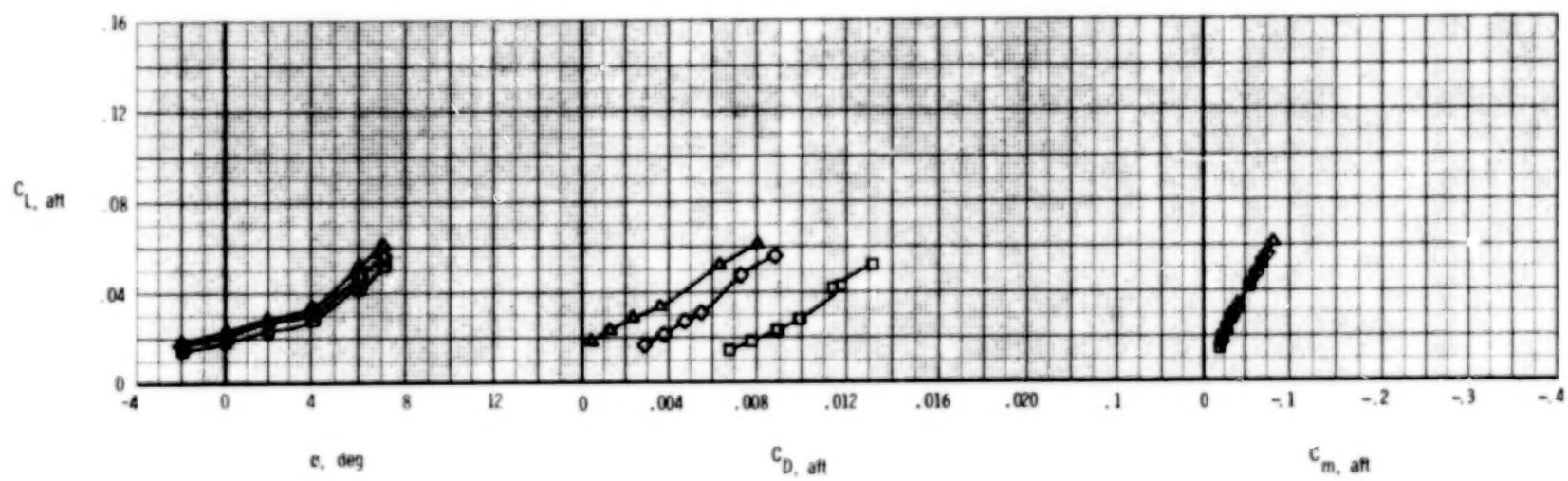
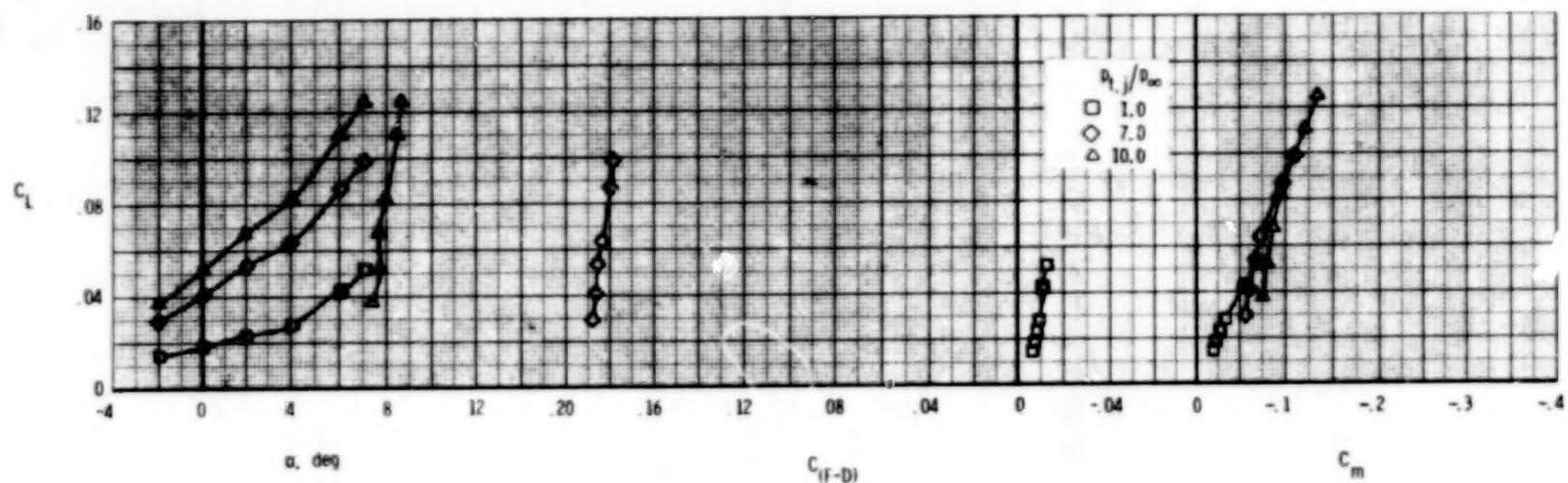
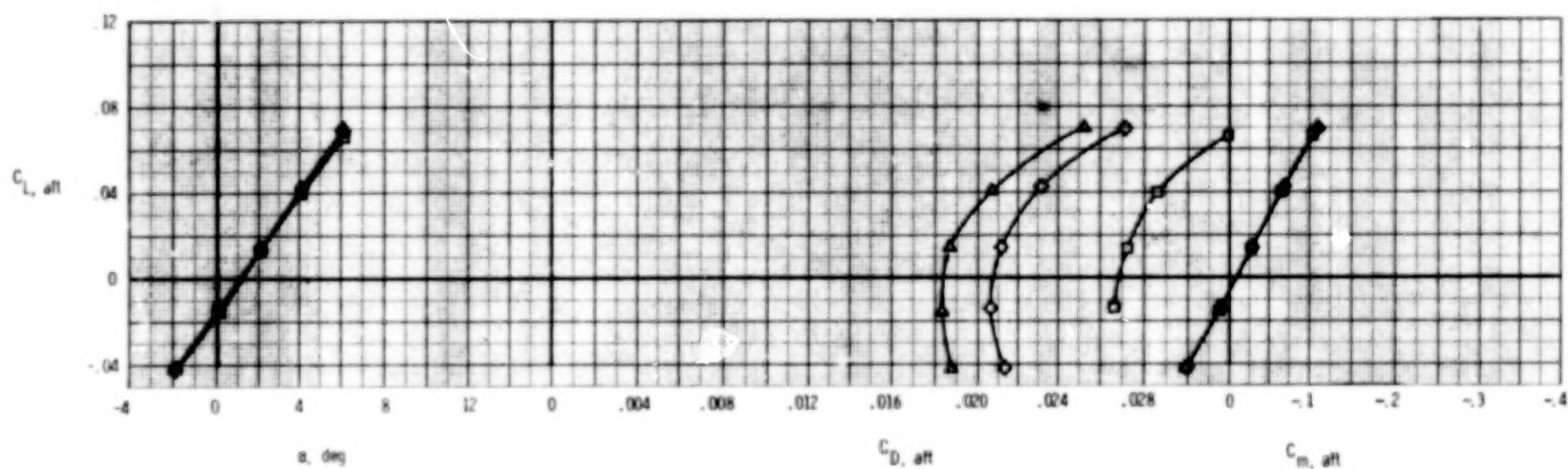
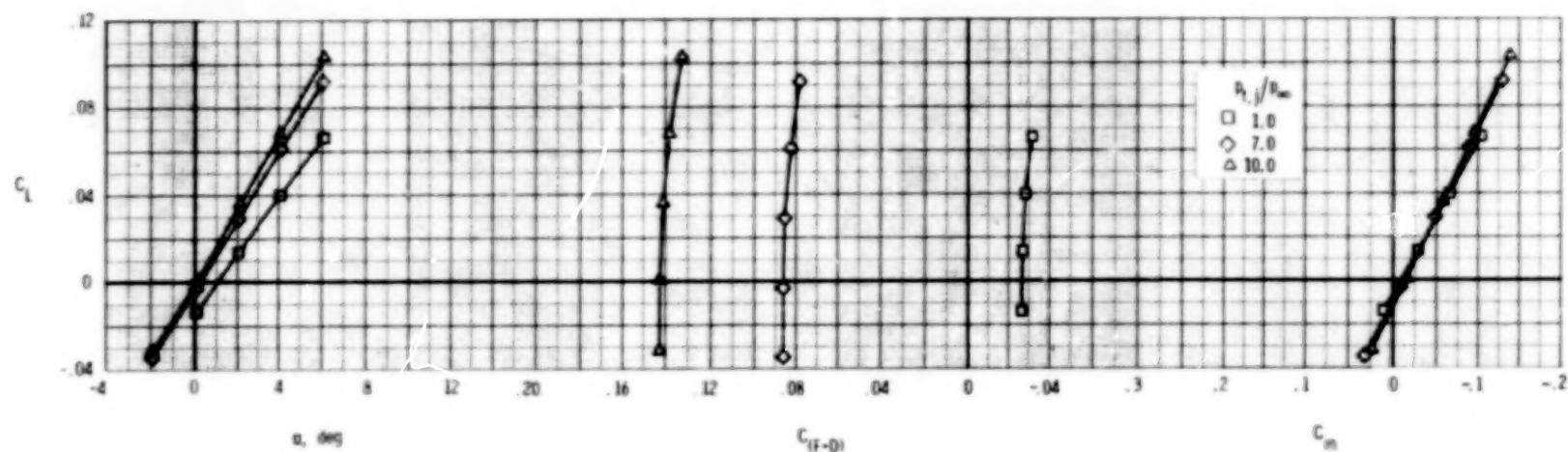
(b) $M = 0.90$.

Figure 67.- Continued.



(c) $M = 1.20$.

Figure 67.- Concluded.

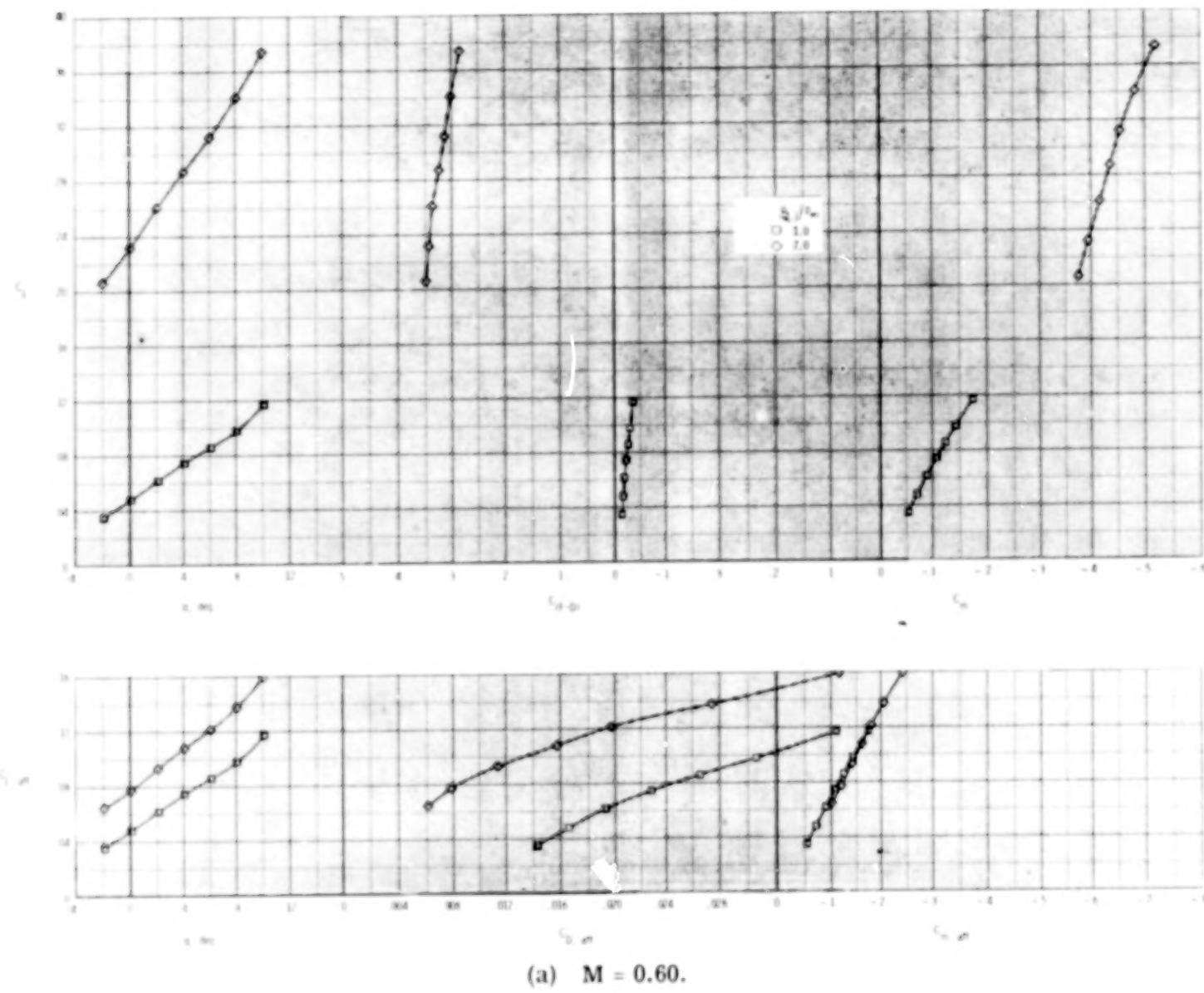
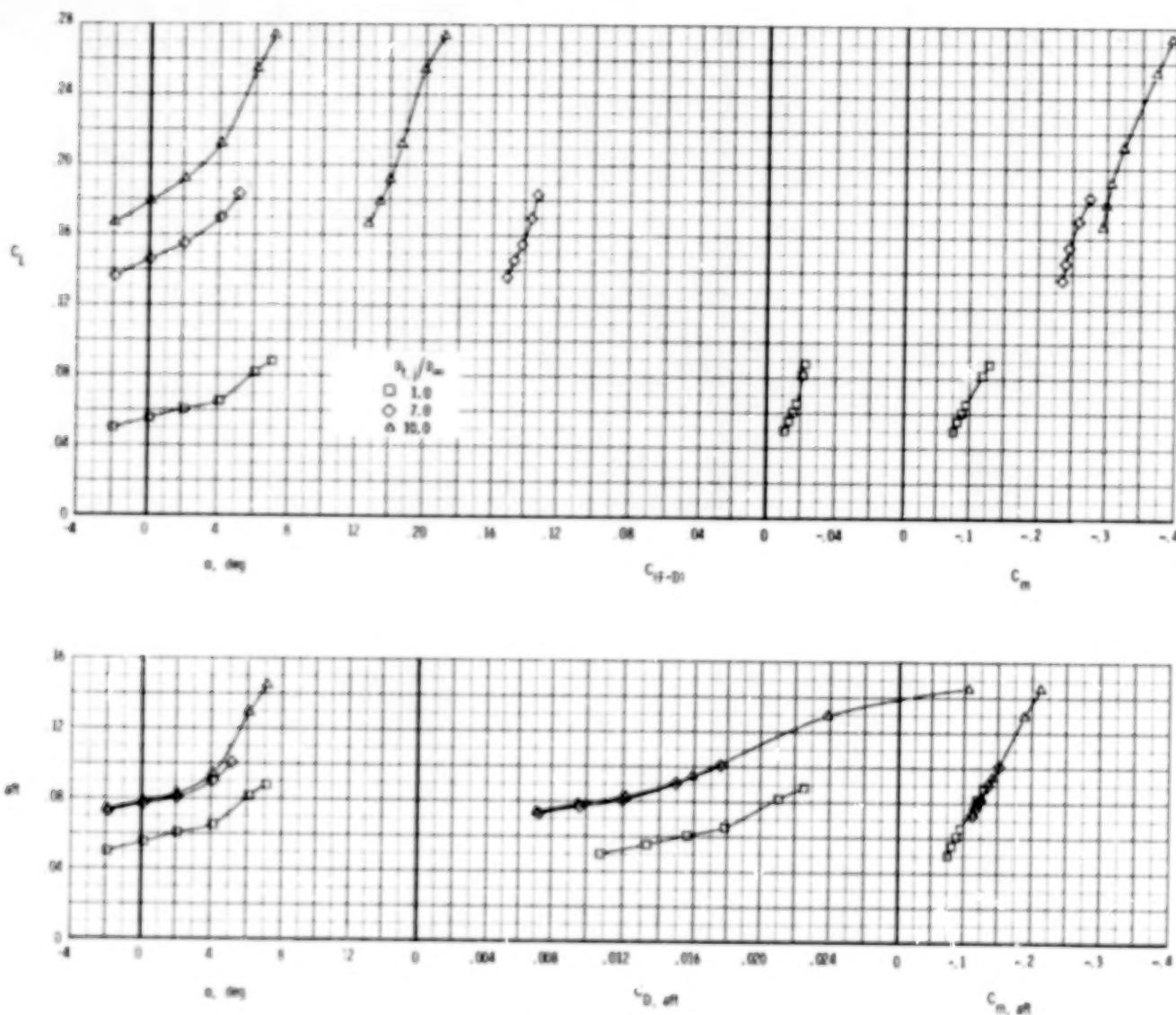
(a) $M = 0.60$.

Figure 68.- Longitudinal afterbody aerodynamic characteristics, 2-D C-D nozzle, A/B power.

$$\delta_h = 0^\circ; \quad \delta_v = 20^\circ; \quad A_e/A_t = 1.15.$$



(b) $M = 0.90$.

Figure 68.- Continued.

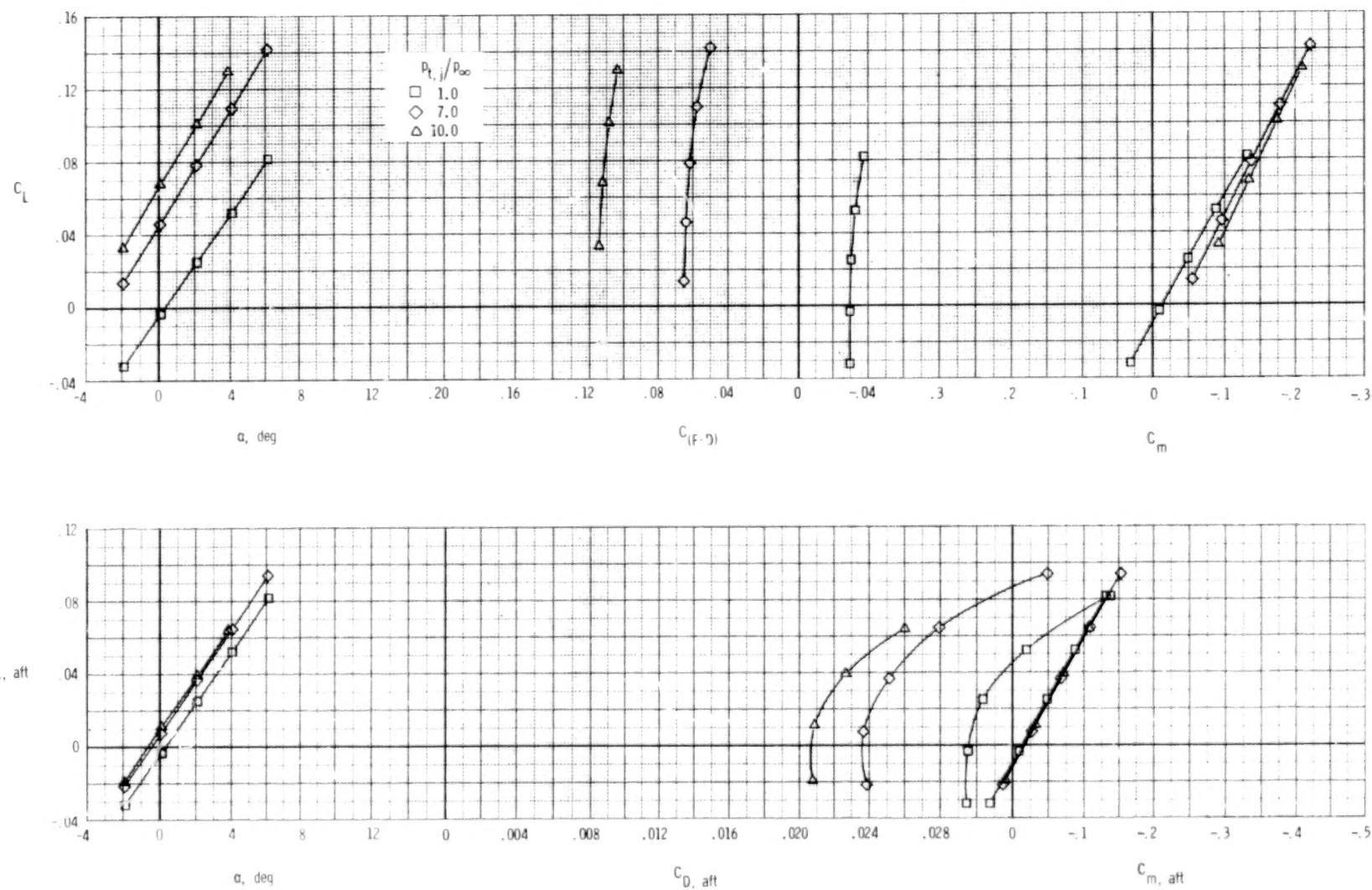
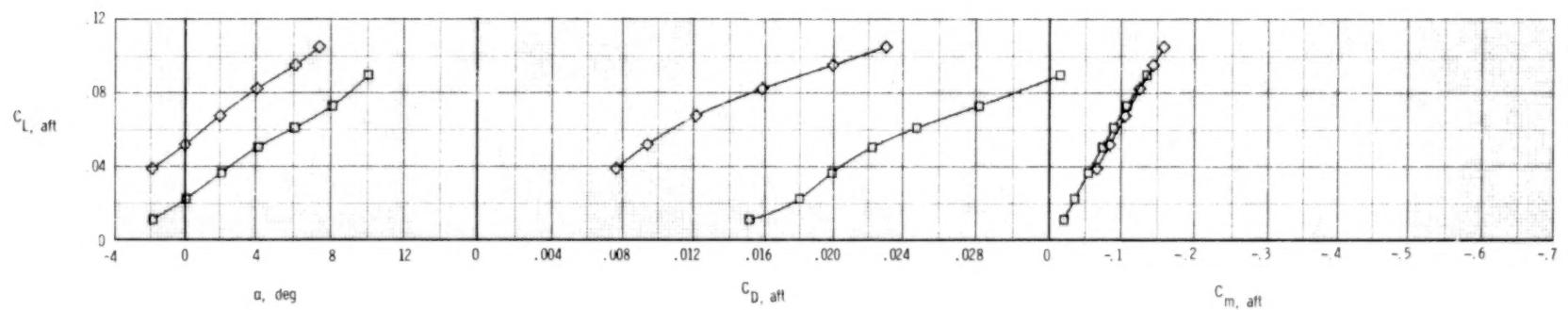
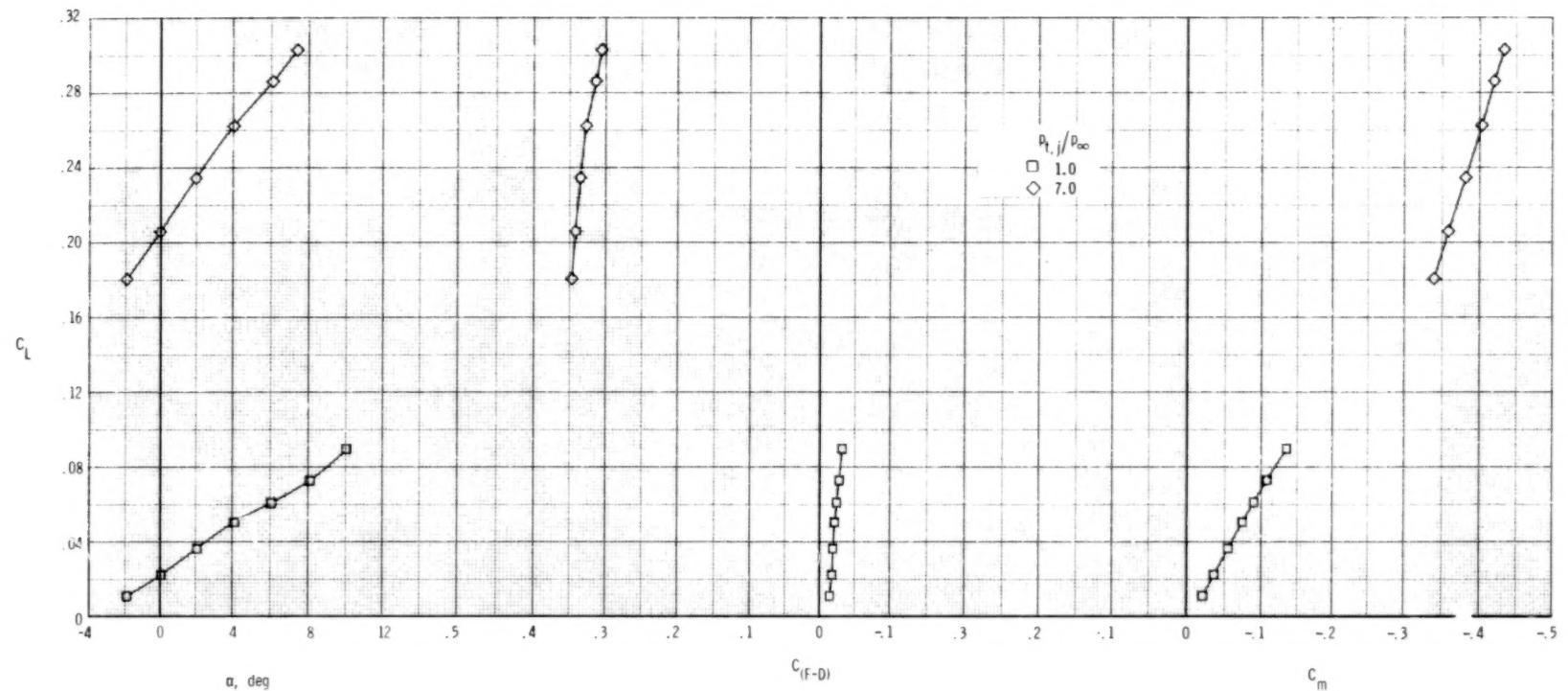
(c) $M = 1.20$.

Figure 68.- Concluded.



(a) $M = 0.60$.

Figure 69.- Longitudinal afterbody aerodynamic characteristics, 2-D C-D nozzle, A/B power.

$$\delta_h = -2^0; \quad \delta_v = 20^0; \quad A_e/A_t = 1.15.$$

168

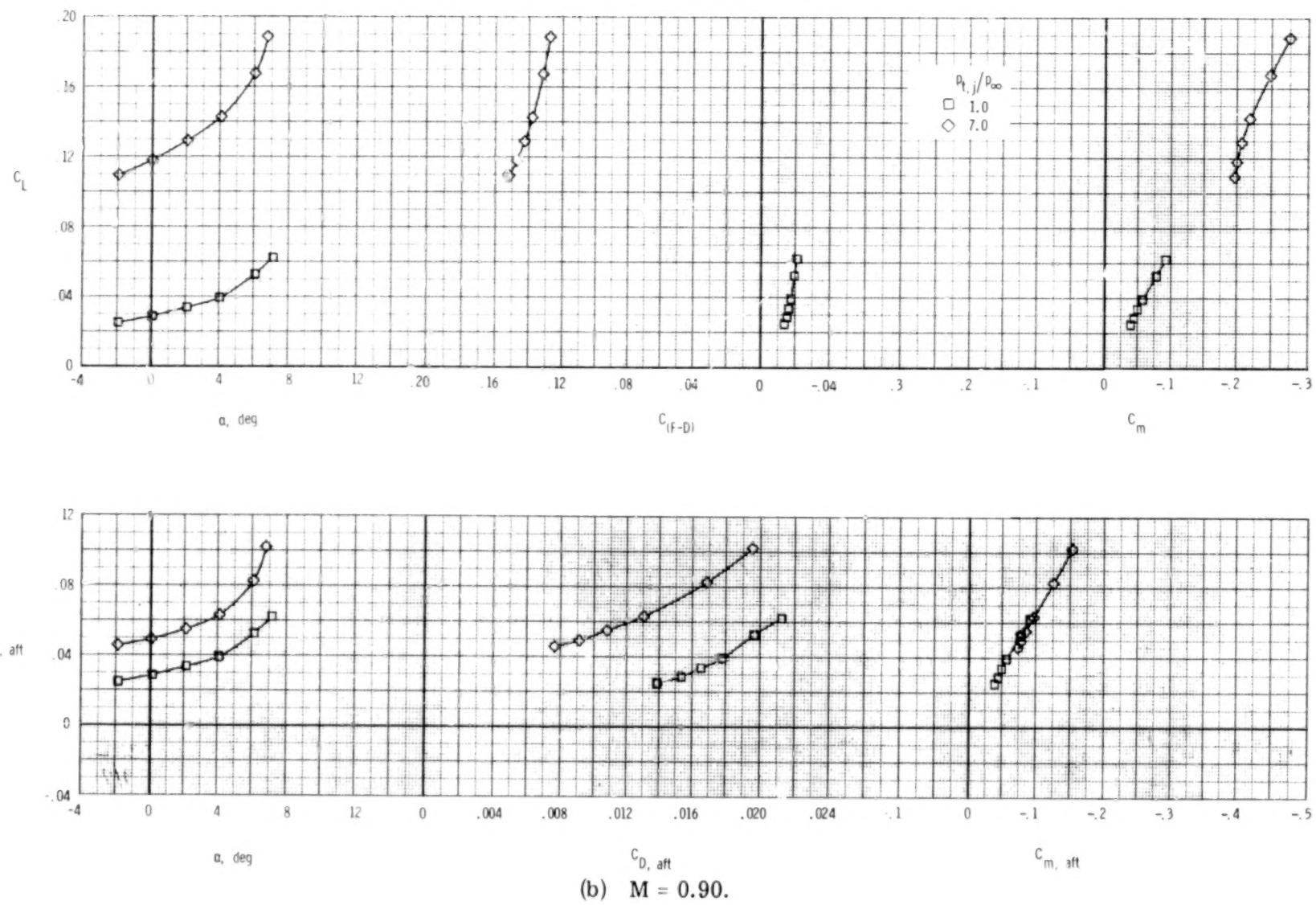
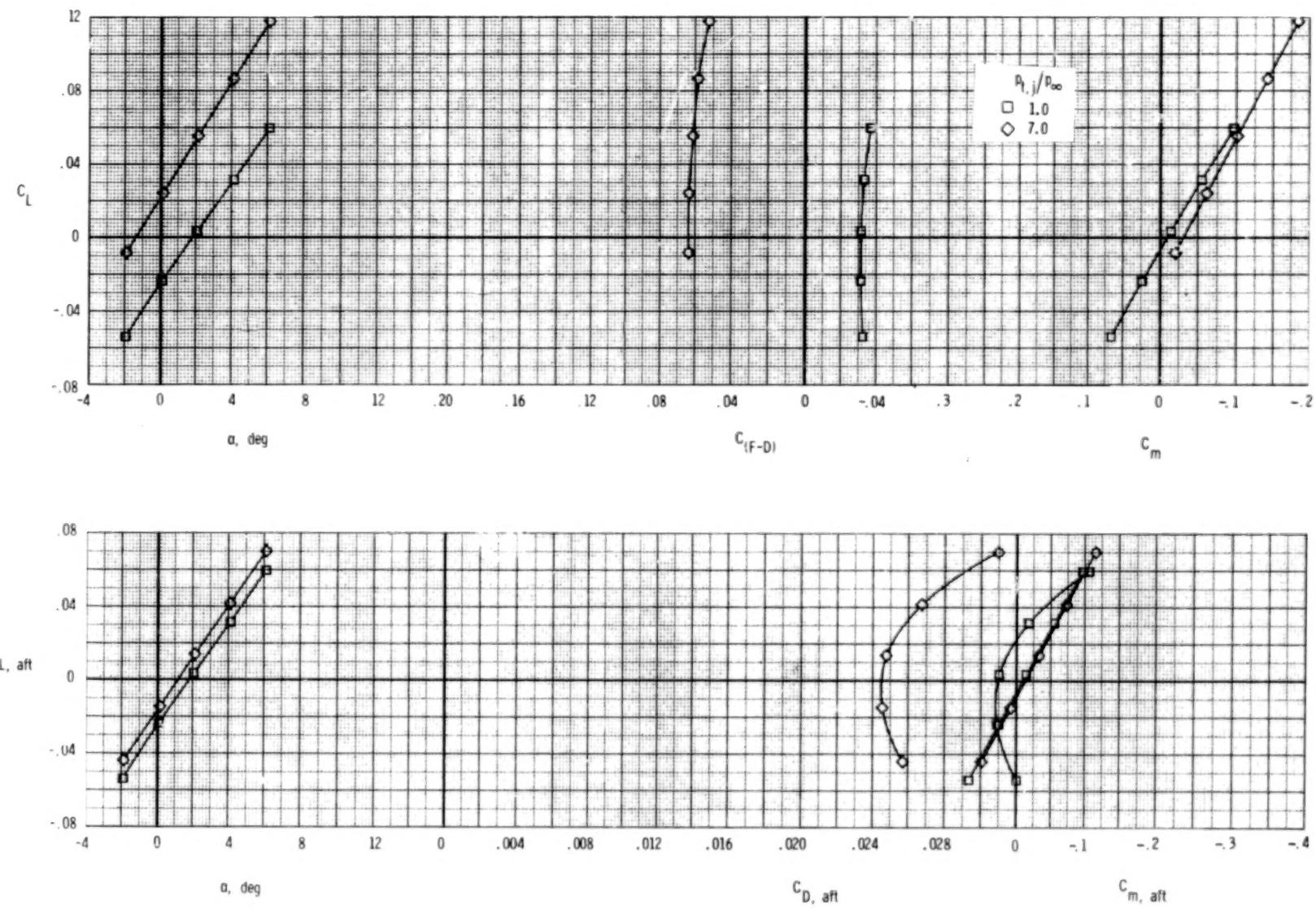
(b) $M = 0.90$.

Figure 69.- Continued.



(c) $M = 1.20.$

Figure 69.- Concluded.

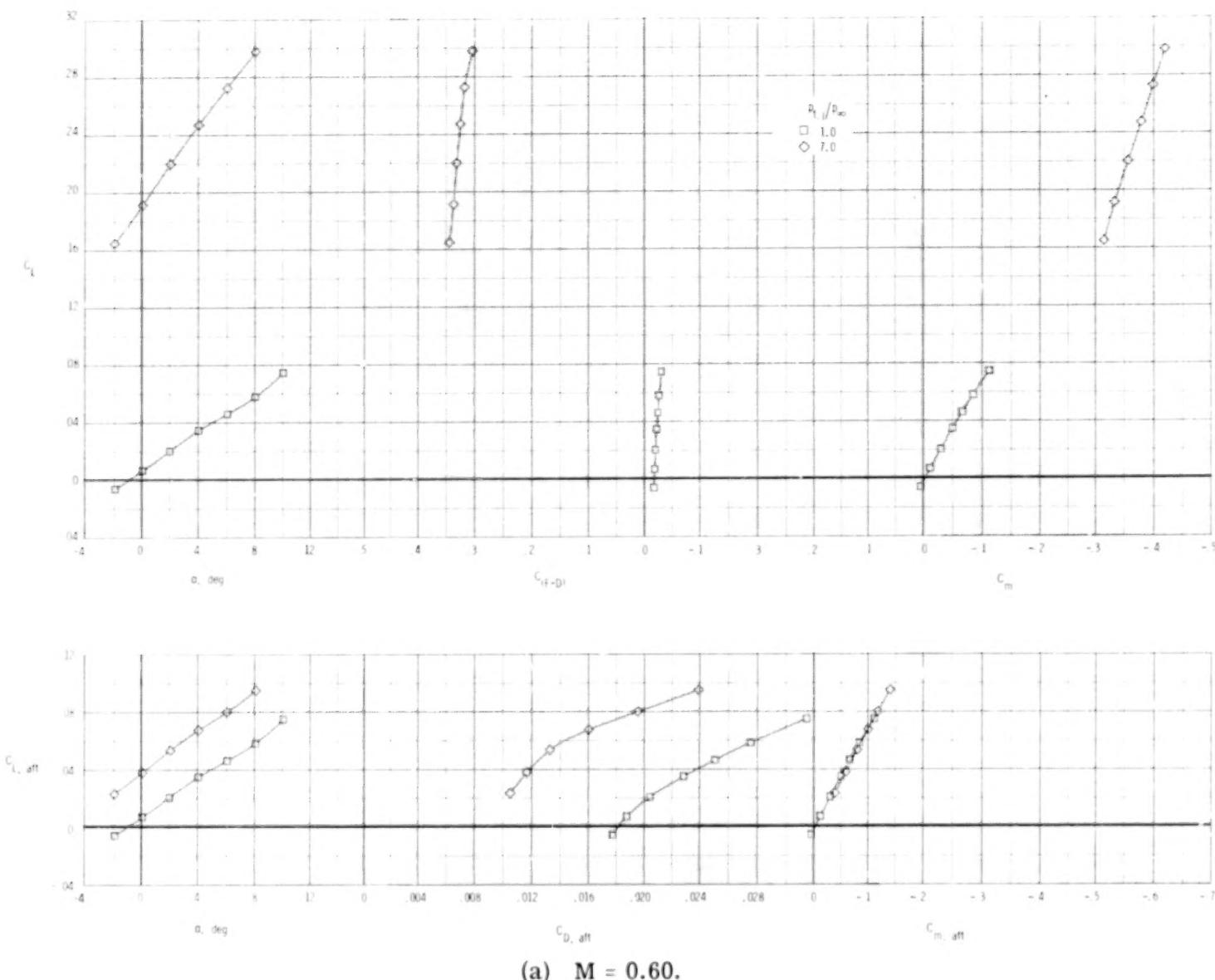
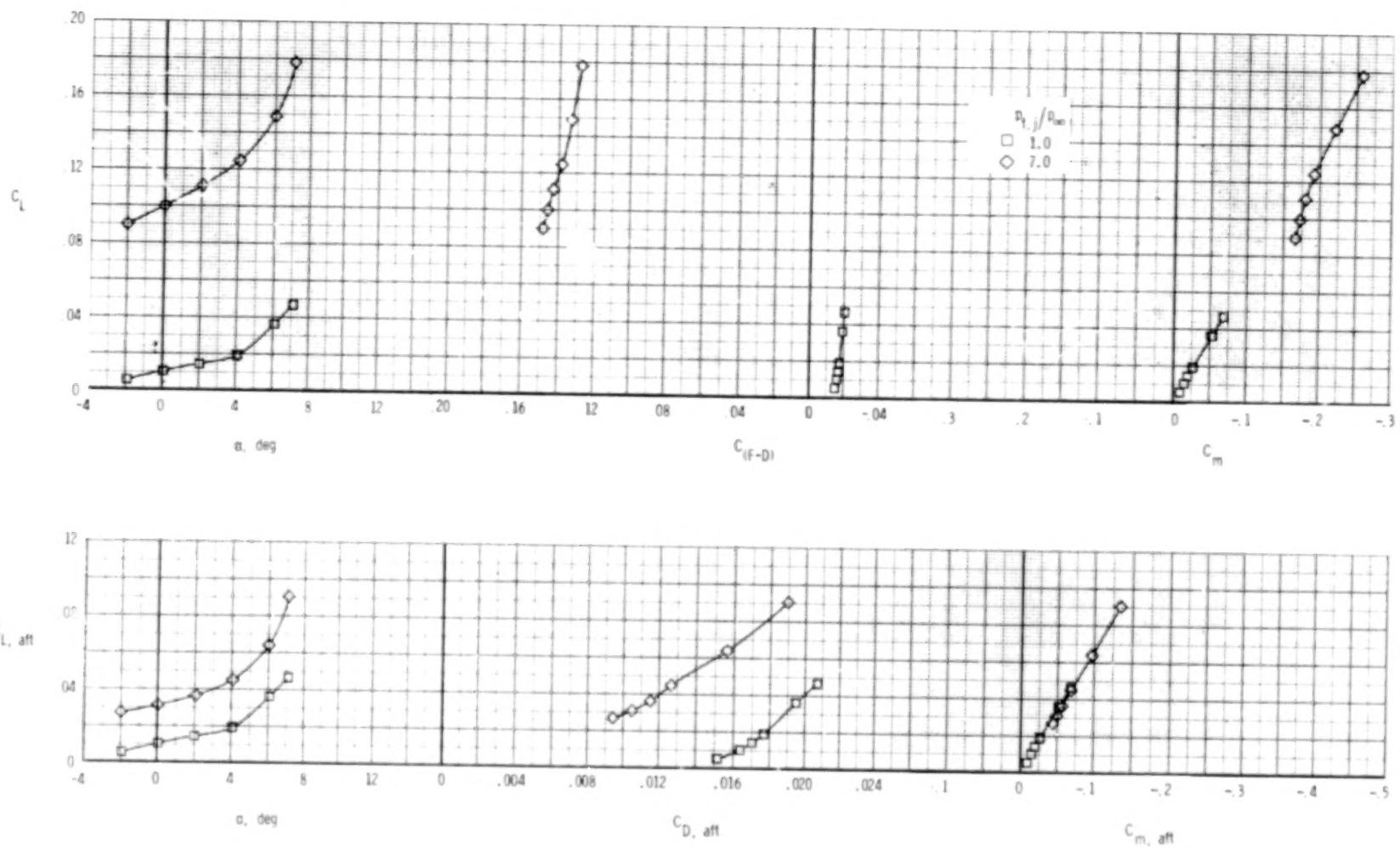
(a) $M = 0.60$.

Figure 70.- Longitudinal afterbody aerodynamic characteristics, 2-D C-D nozzle, A/B power.

$$\delta_h = -5^\circ; \quad \delta_v = 20^\circ; \quad A_e/A_t = 1.15.$$



(b) $M = 0.90$.

Figure 70.- Continued.

171

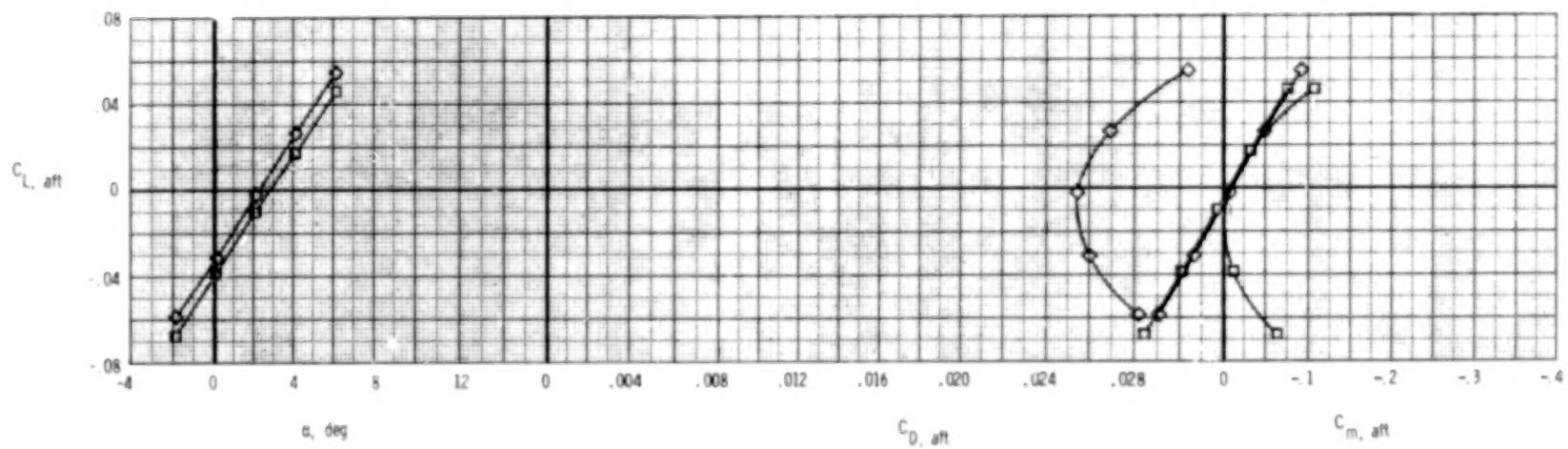
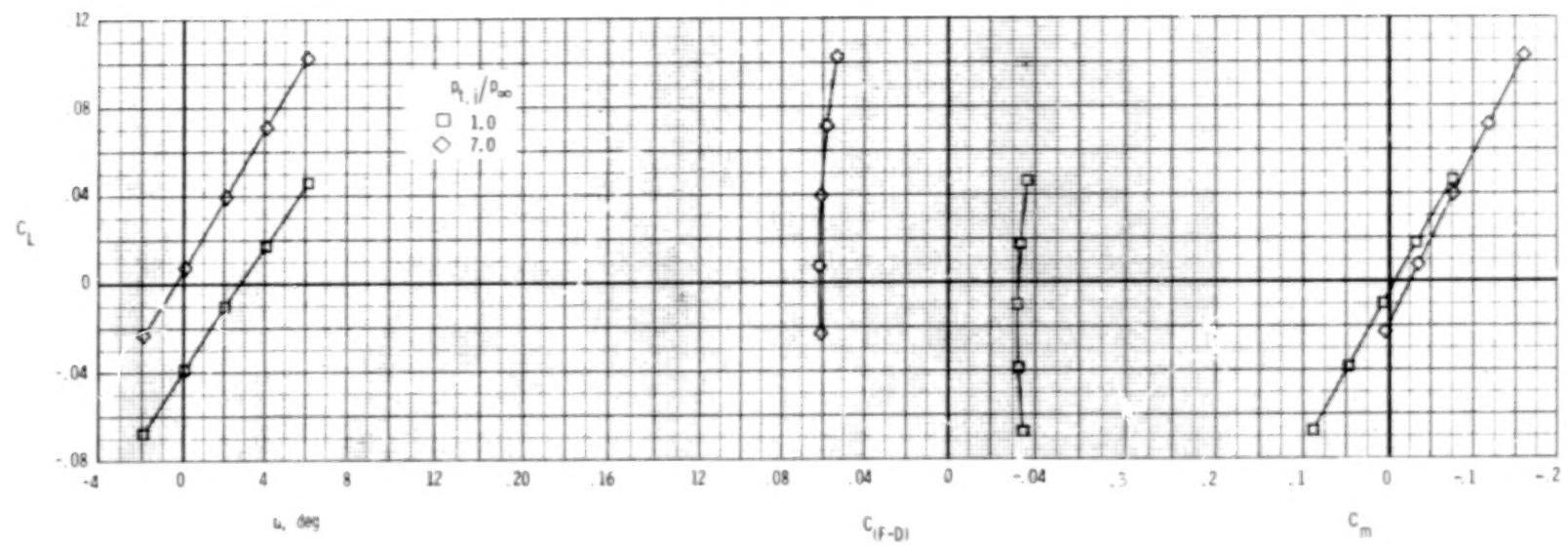
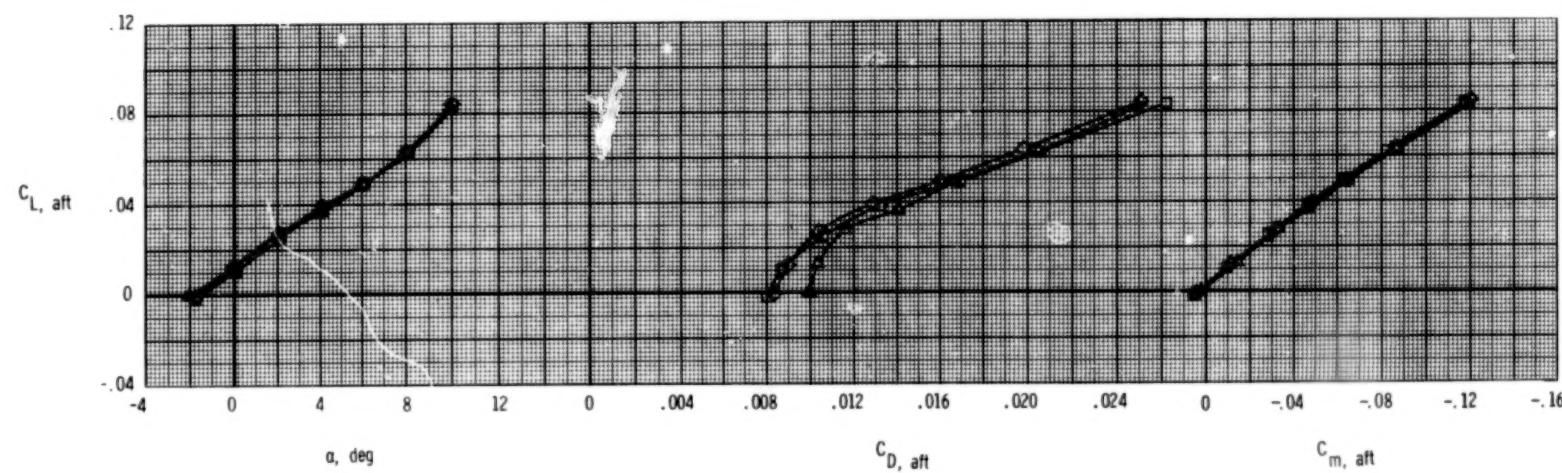
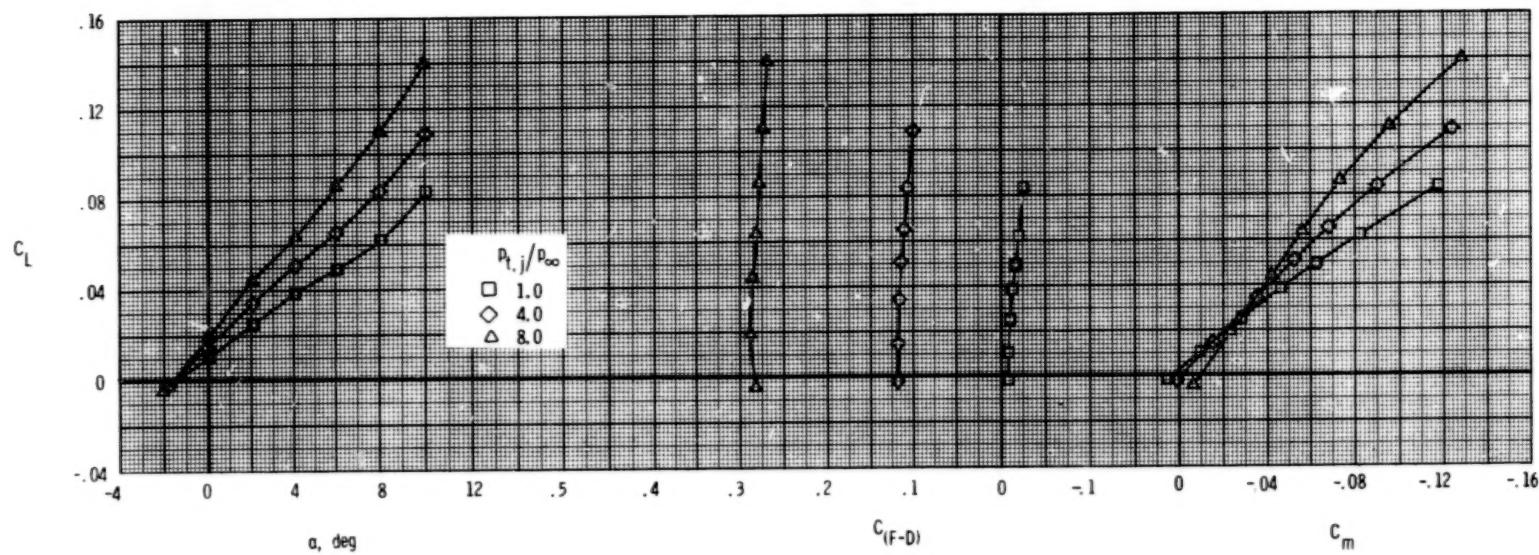
(c) $M = 1.20$.

Figure 170. - Concluded.



(a) $M = 0.60.$

Figure 71.- Longitudinal afterbody aerodynamic characteristics, wedge nozzle, dry power.

$$\delta_h = 0^\circ; \quad \delta_v = 0^\circ; \quad A_e/A_t = 1.10.$$

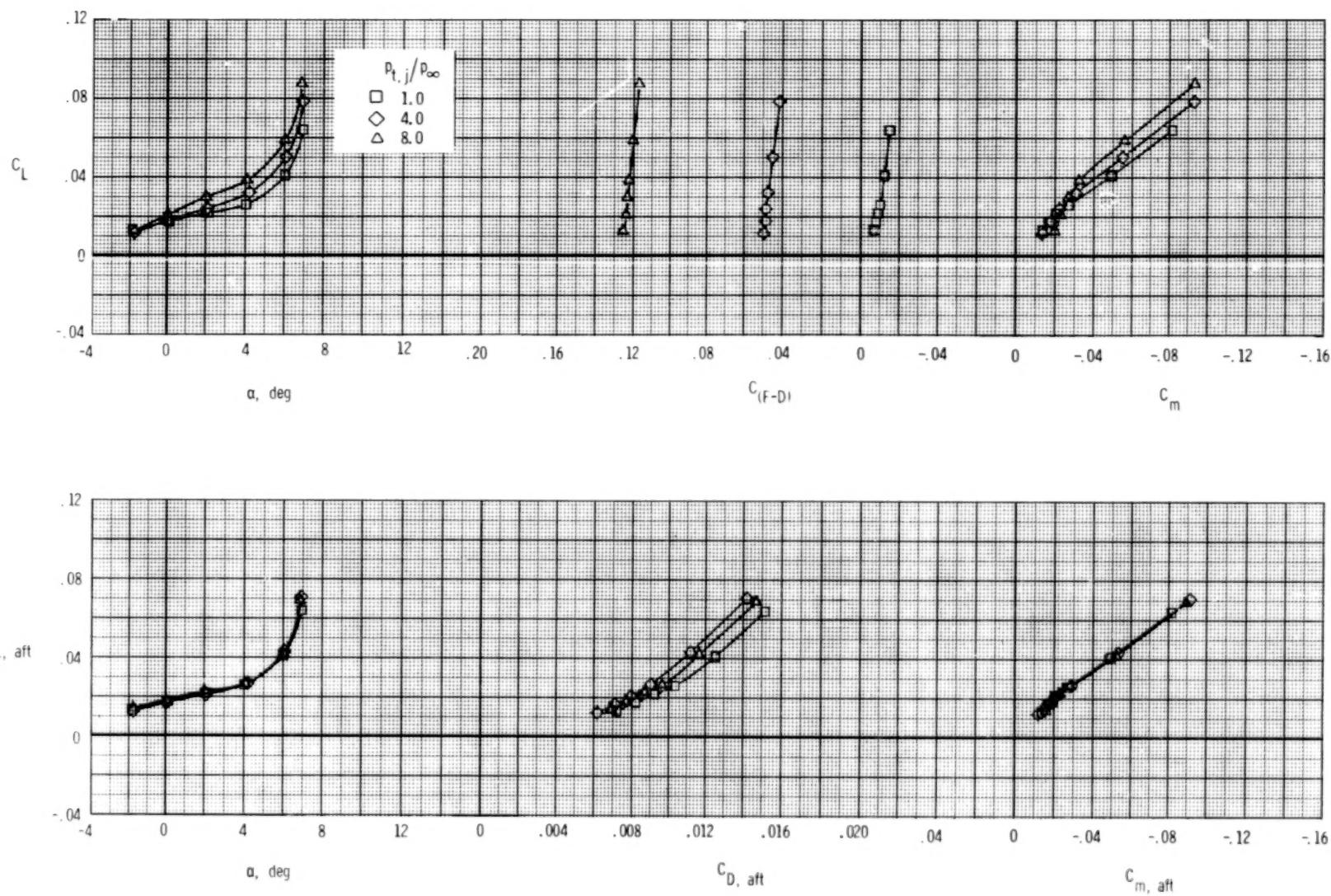
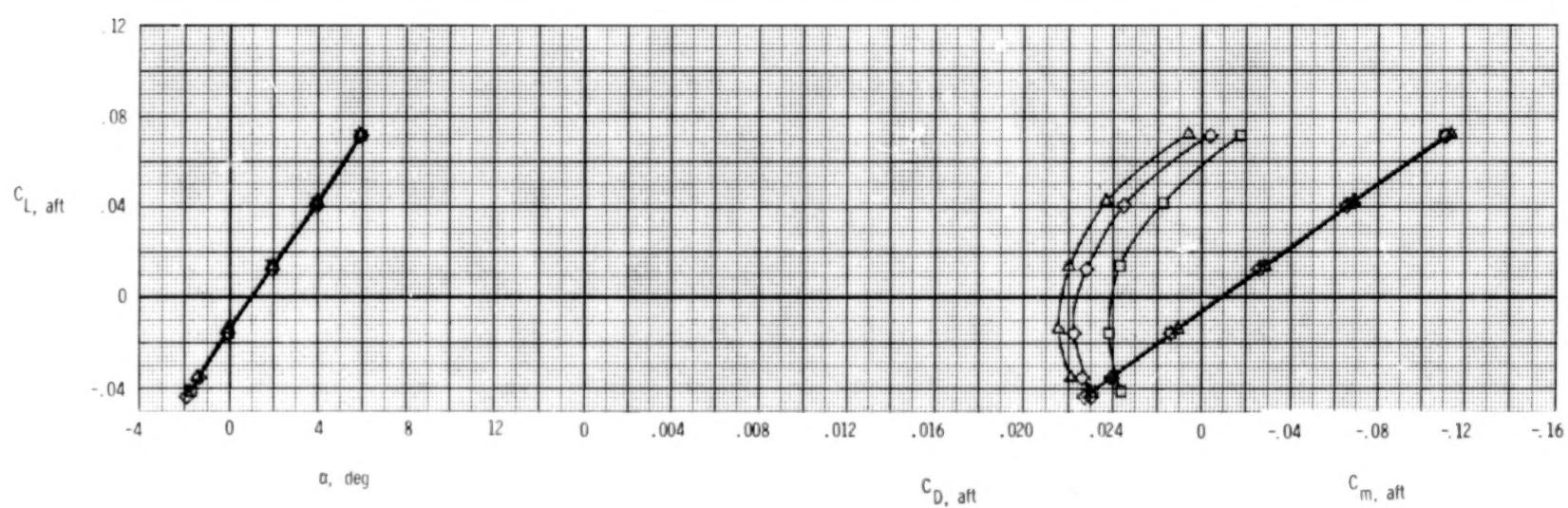
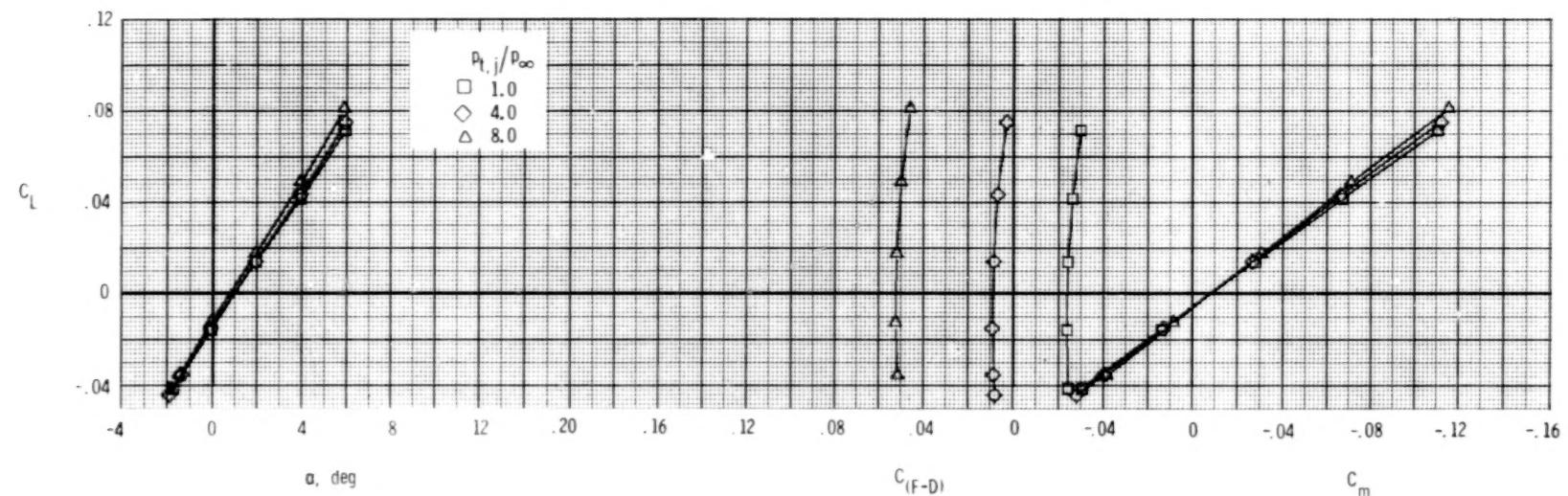
(b) $M = 0.90$.

Figure 71.- Continued.



(c) $M = 1.20$.

Figure 71.- Concluded.

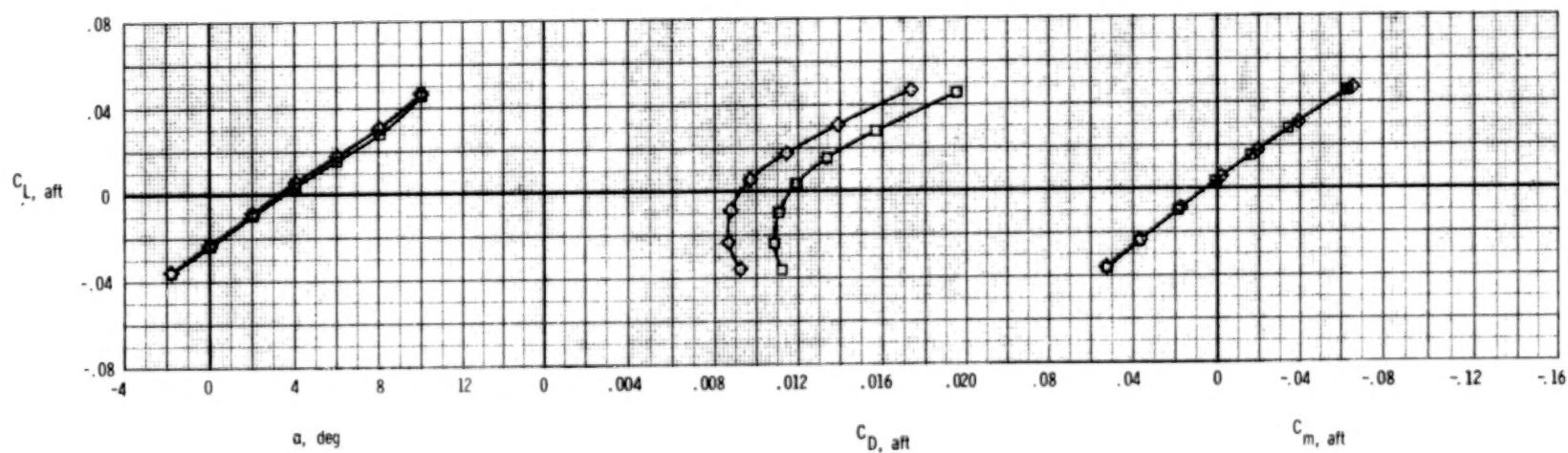
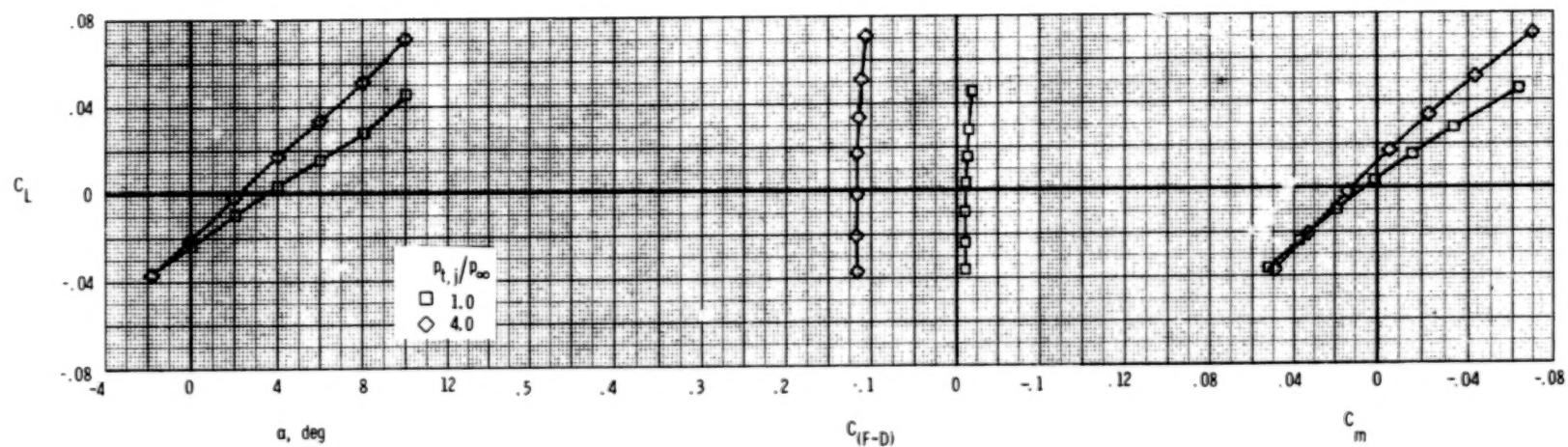
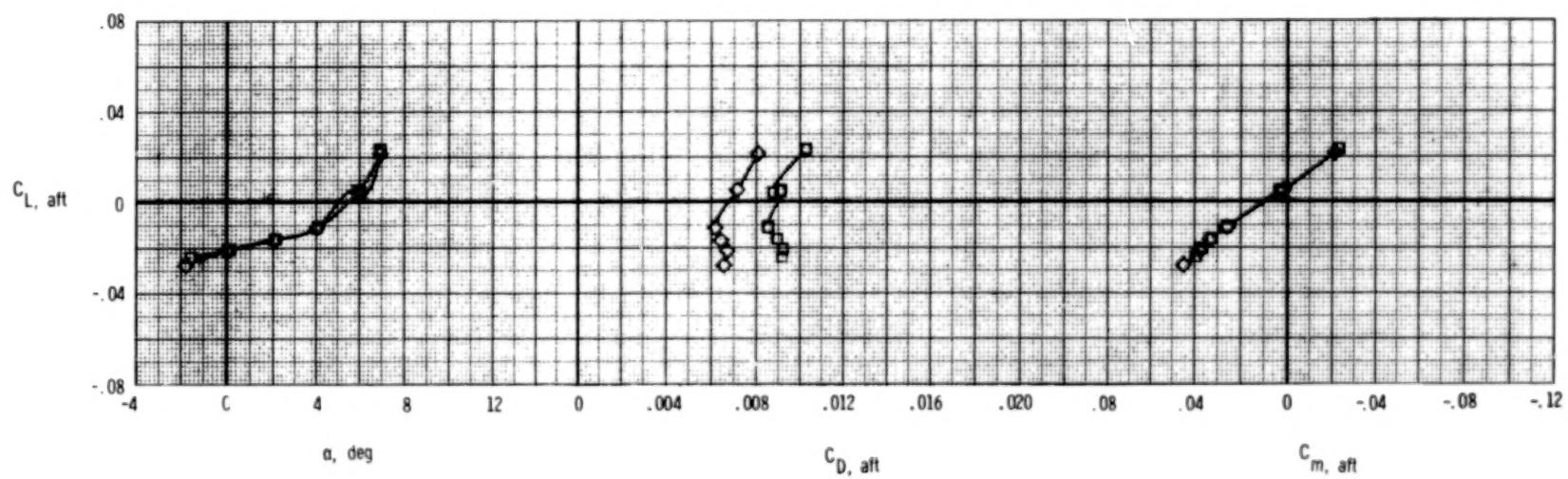
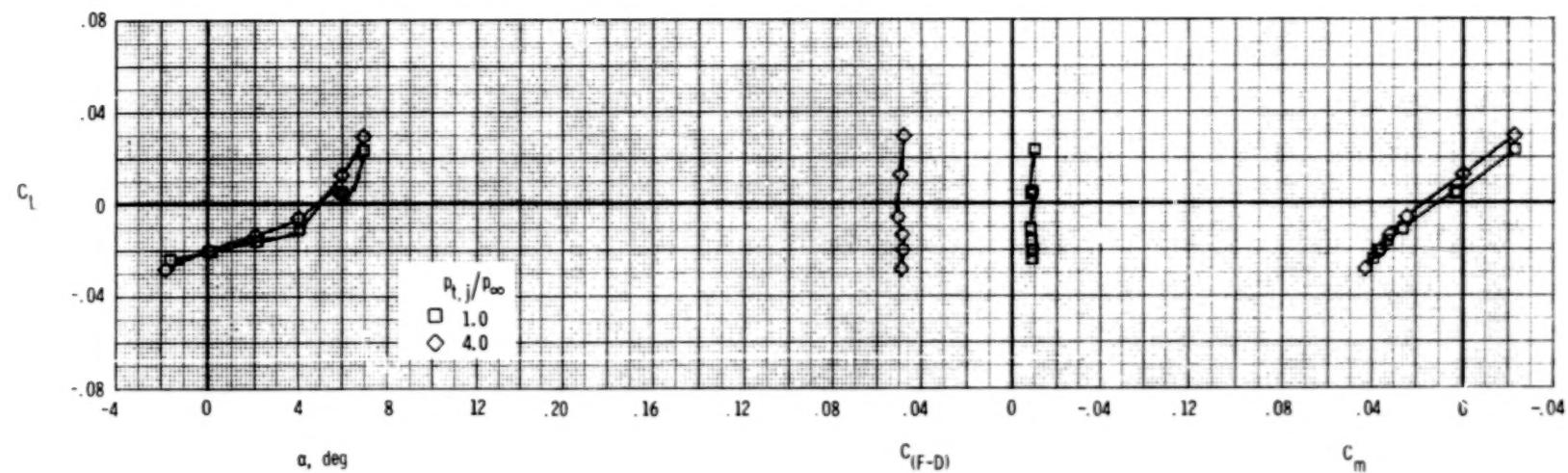
(a) $M = 0.60$.

Figure 72.- Longitudinal afterbody aerodynamic characteristics, wedge nozzle, dry power.

$$\delta_h = -2^\circ; \quad \delta_v = 0^\circ; \quad A_e/A_t = 1.10.$$



(b) $M = 0.90$.

Figure 72.- Continued.

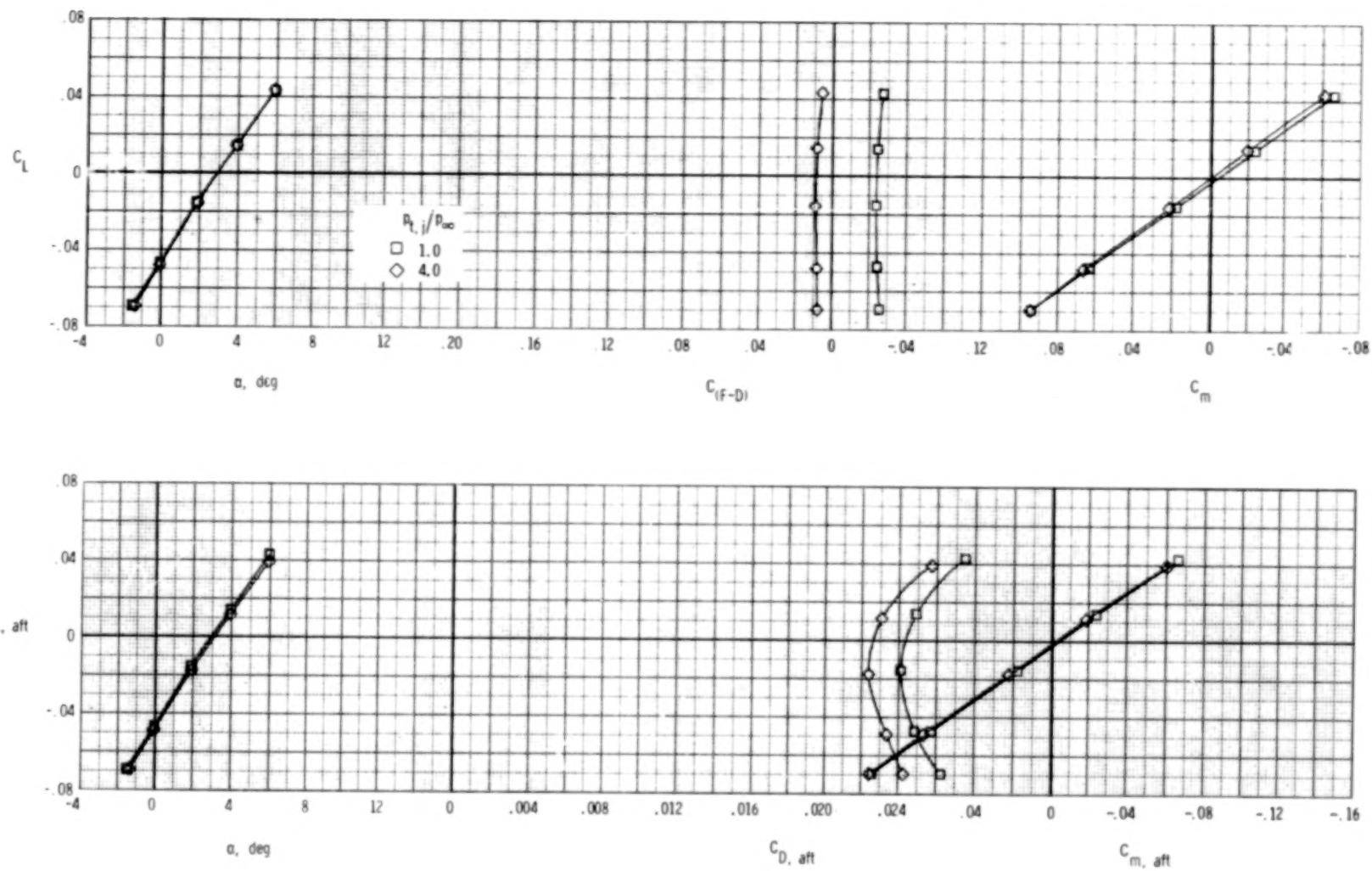
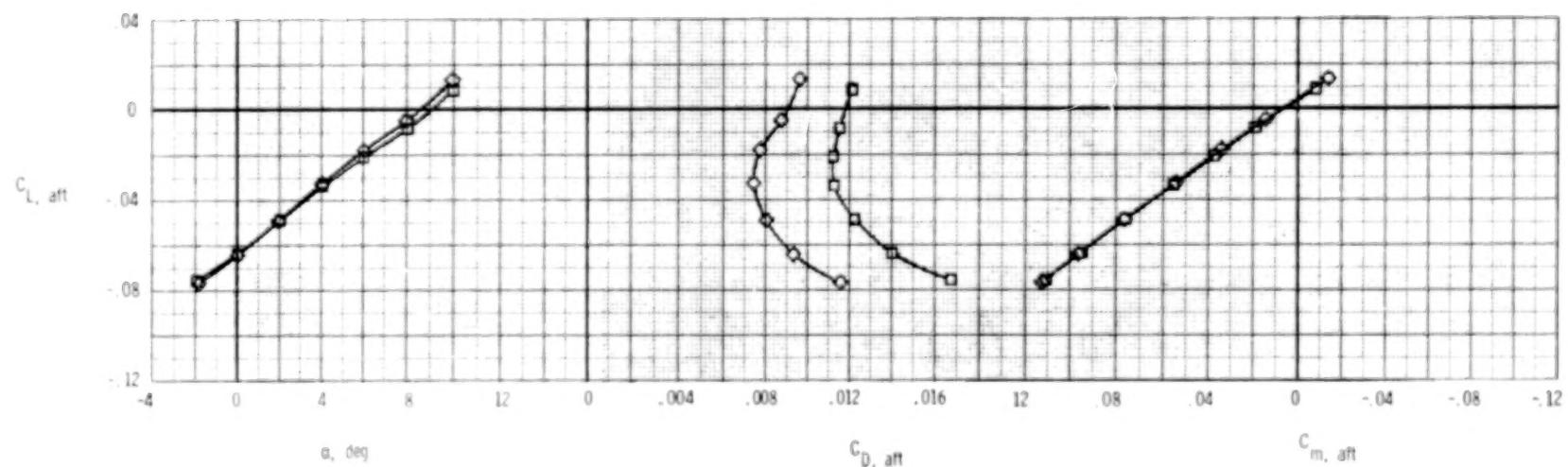
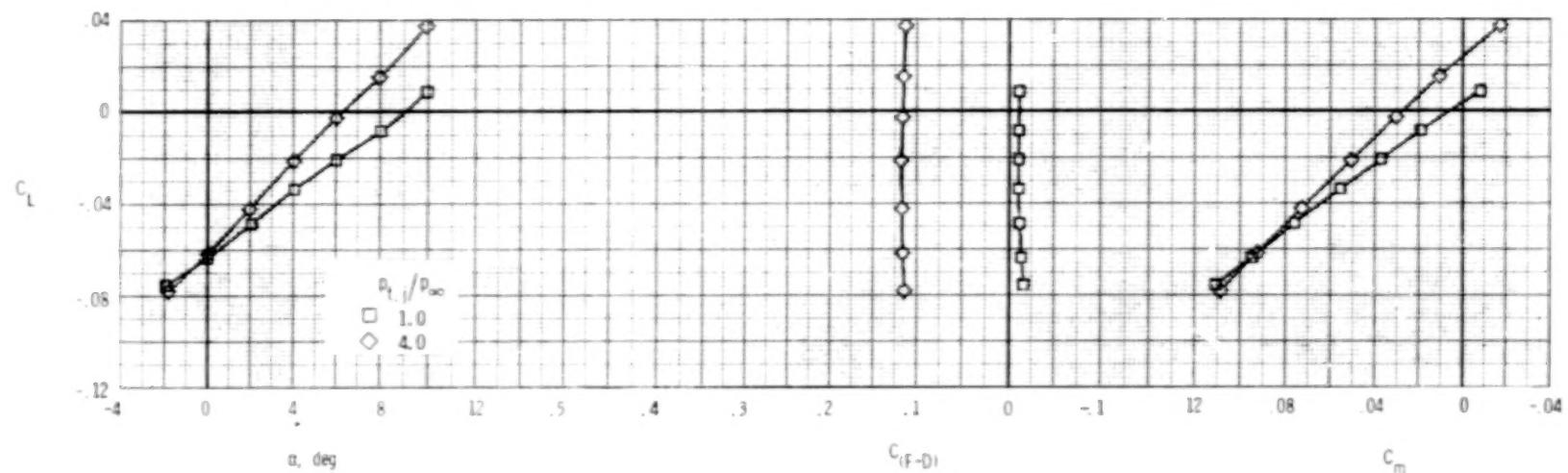
(c) $M = 1.20.$

Figure 72.- Concluded.

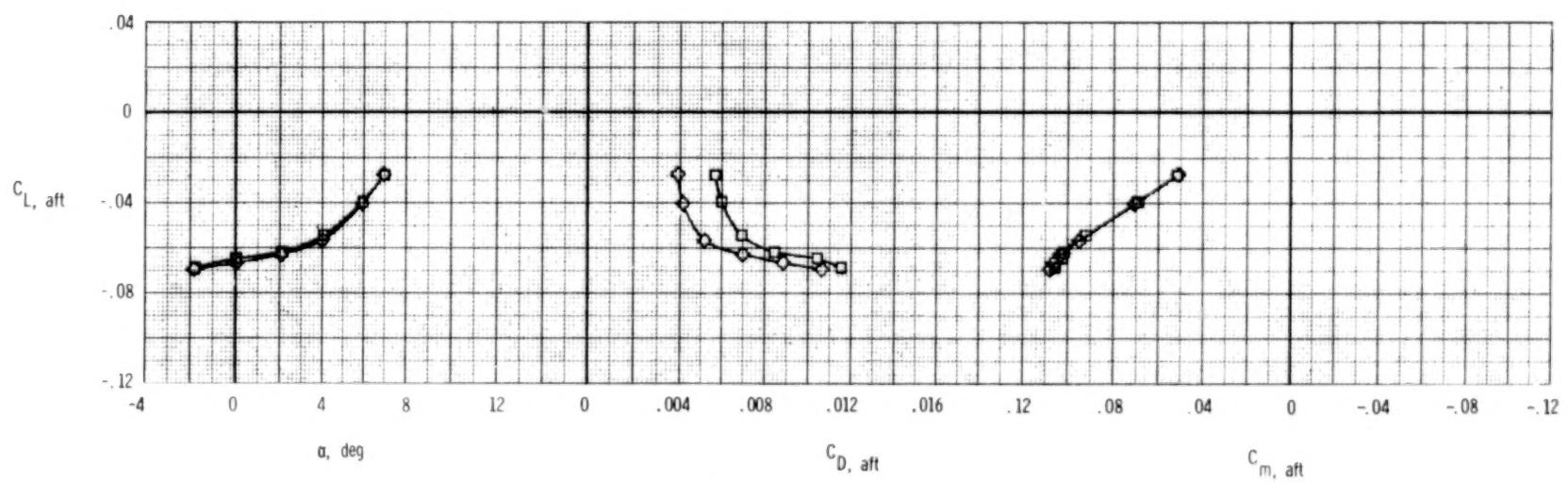
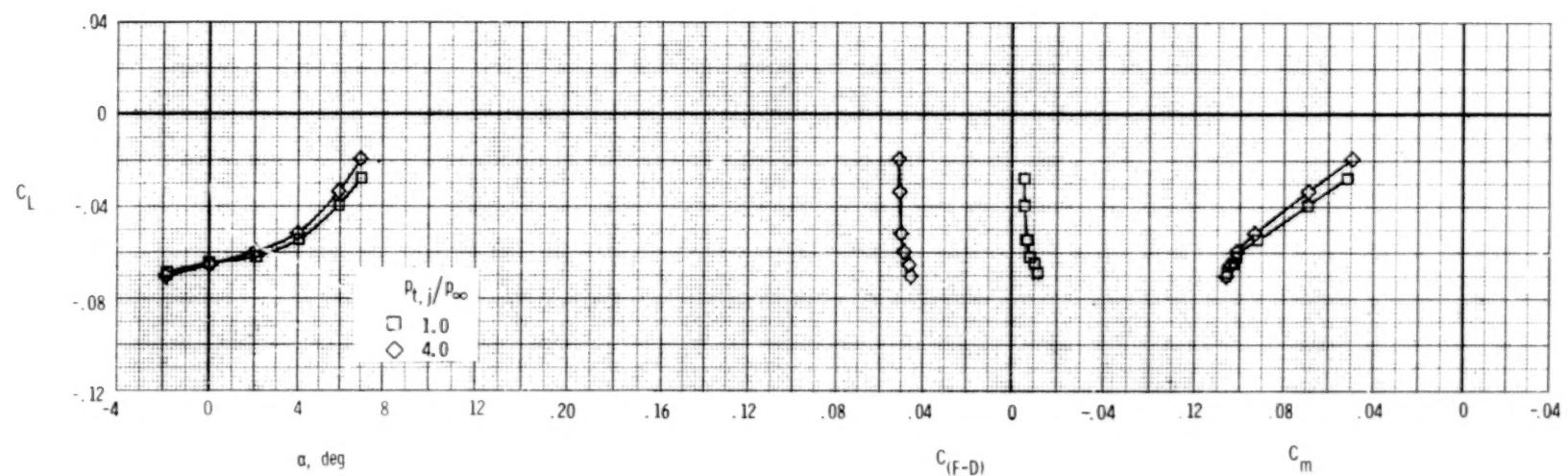


(a) $M = 0.60$.

Figure 73.- Longitudinal afterbody aerodynamic characteristics, wedge nozzle, dry power.

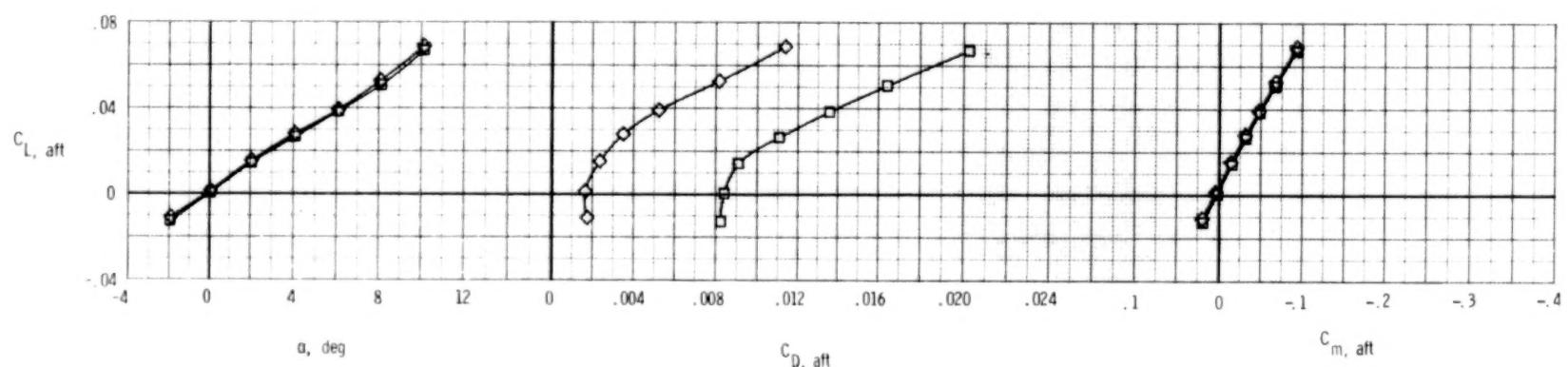
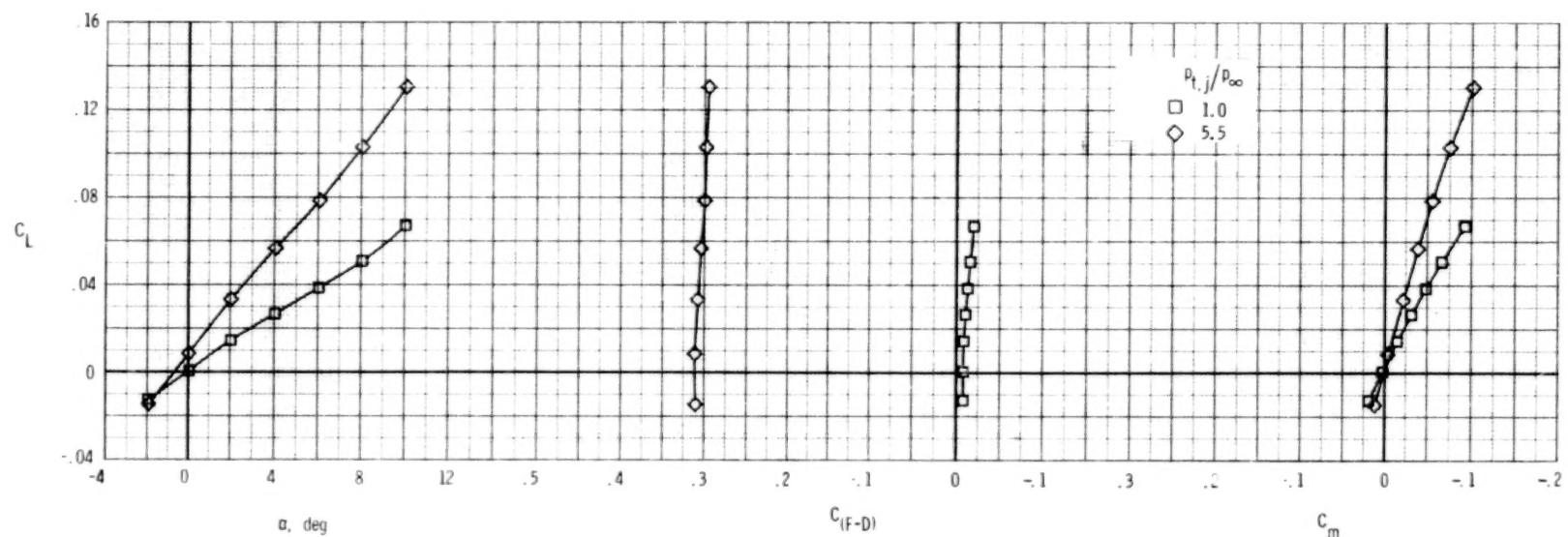
$$\delta_h = -5^\circ; \quad \delta_v = 0^\circ; \quad A_e/A_t = 1.10.$$

180



(b) $M = 0.90$.

Figure 73.- Concluded.

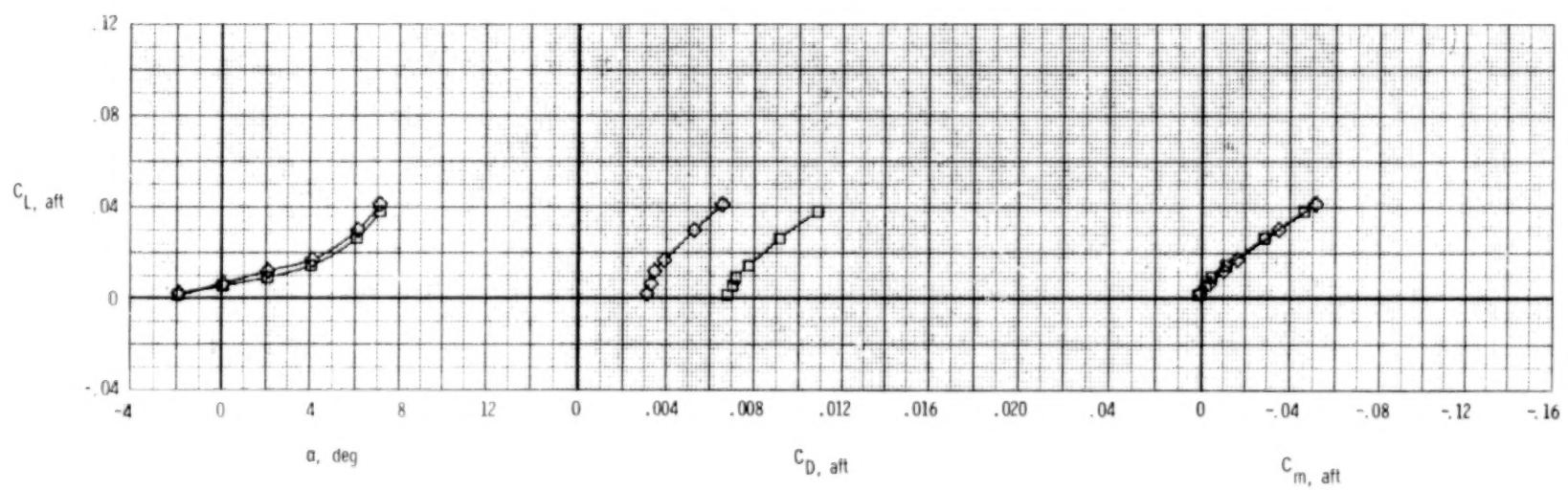
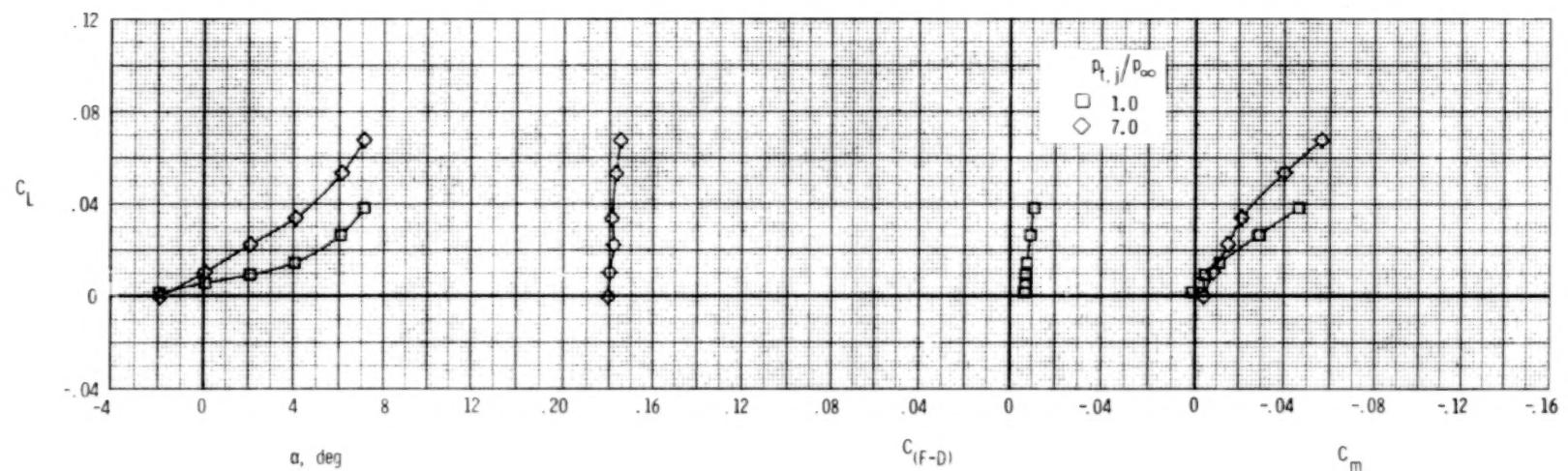


(a) $M = 0.60$.

Figure 74.- Longitudinal afterbody aerodynamic characteristics, wedge nozzle, A/B power.

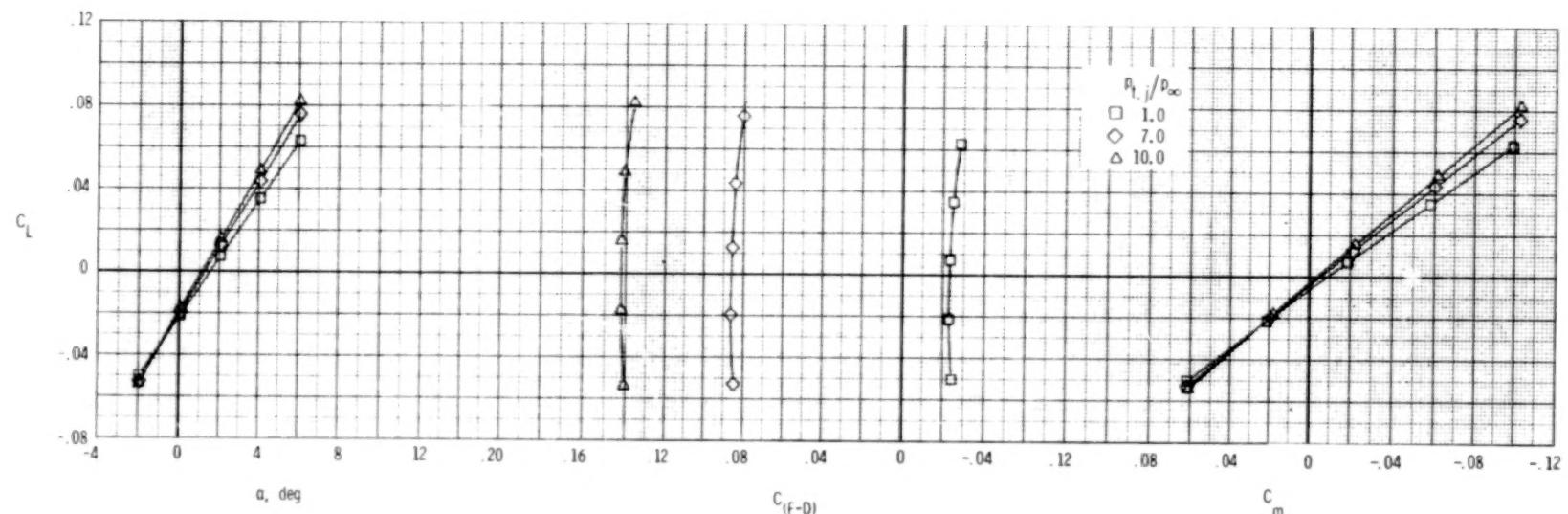
$$\delta_h = 0^\circ; \quad \delta_v = 0^\circ; \quad A_e/A_t = 1.20.$$

182



(b) $M = 0.90$.

Figure 74.- Continued.



(c) $M = 1.20$.

Figure 74.- Concluded.

184

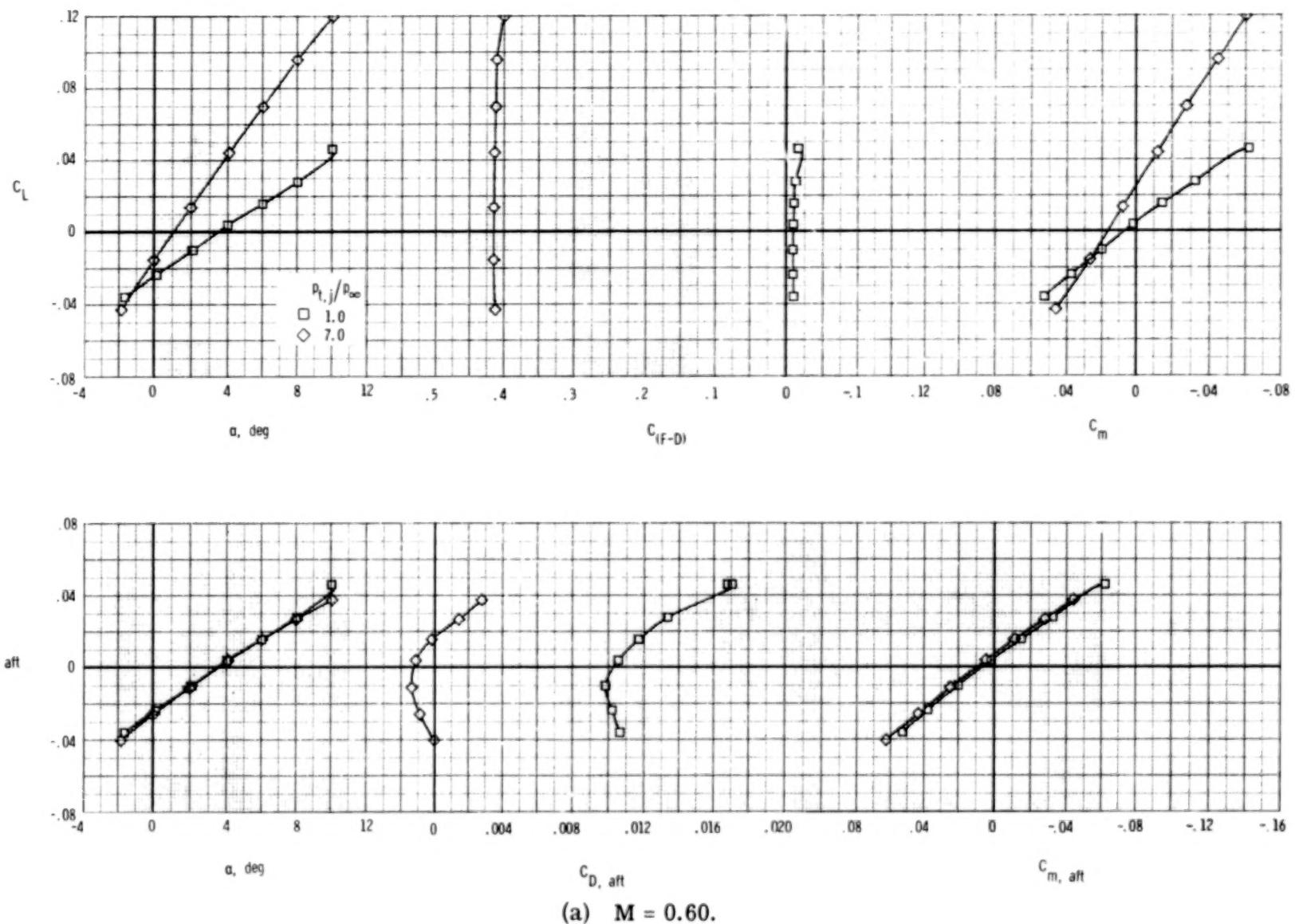
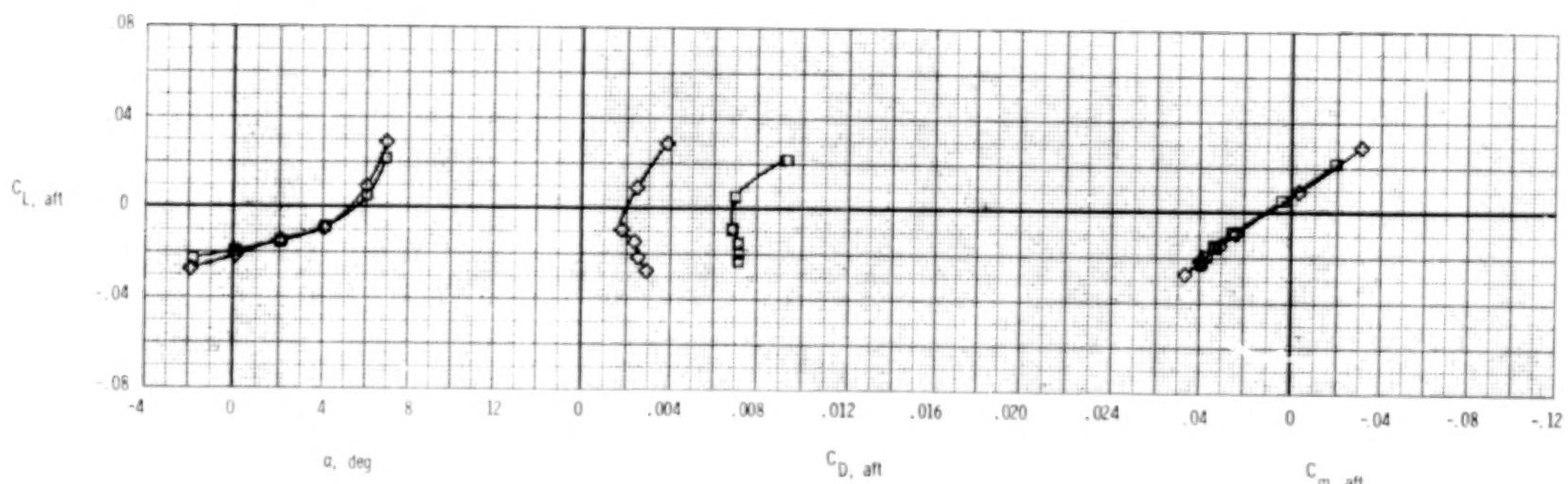
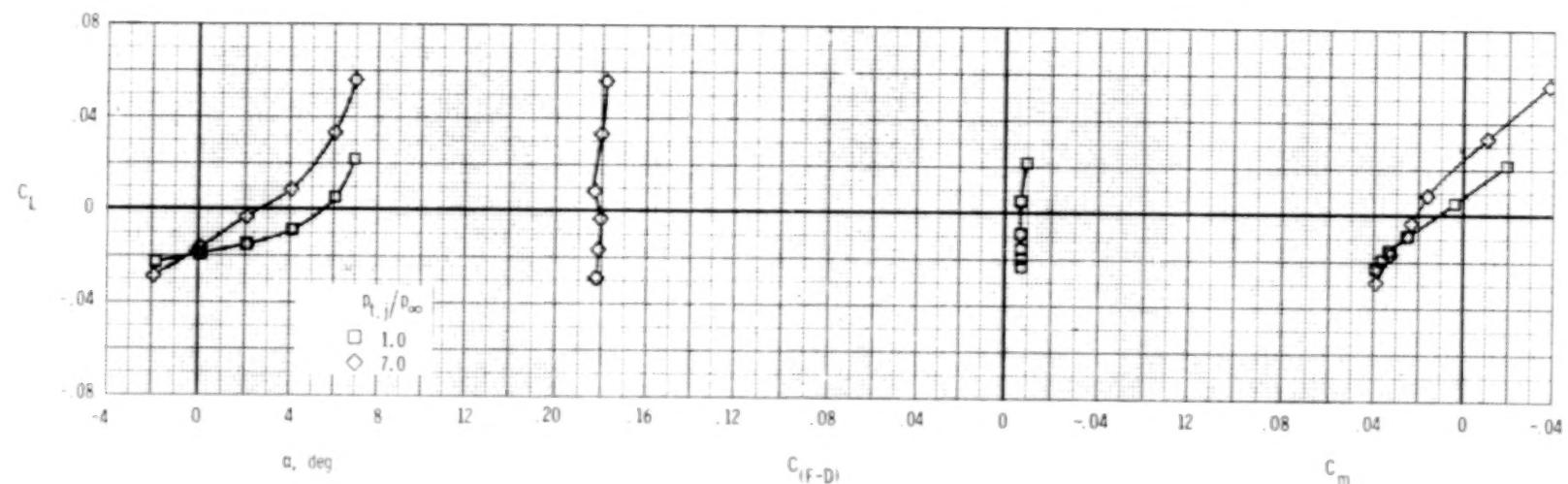
(a) $M = 0.60$.

Figure 75.- Longitudinal afterbody aerodynamic characteristics, wedge nozzle, A/B power.
 $\delta_h = -2^0$; $\delta_v = 0^0$; $A_e/A_t = 1.20$.



(b) $M = 0.90$.

Figure 75.- Concluded.

186

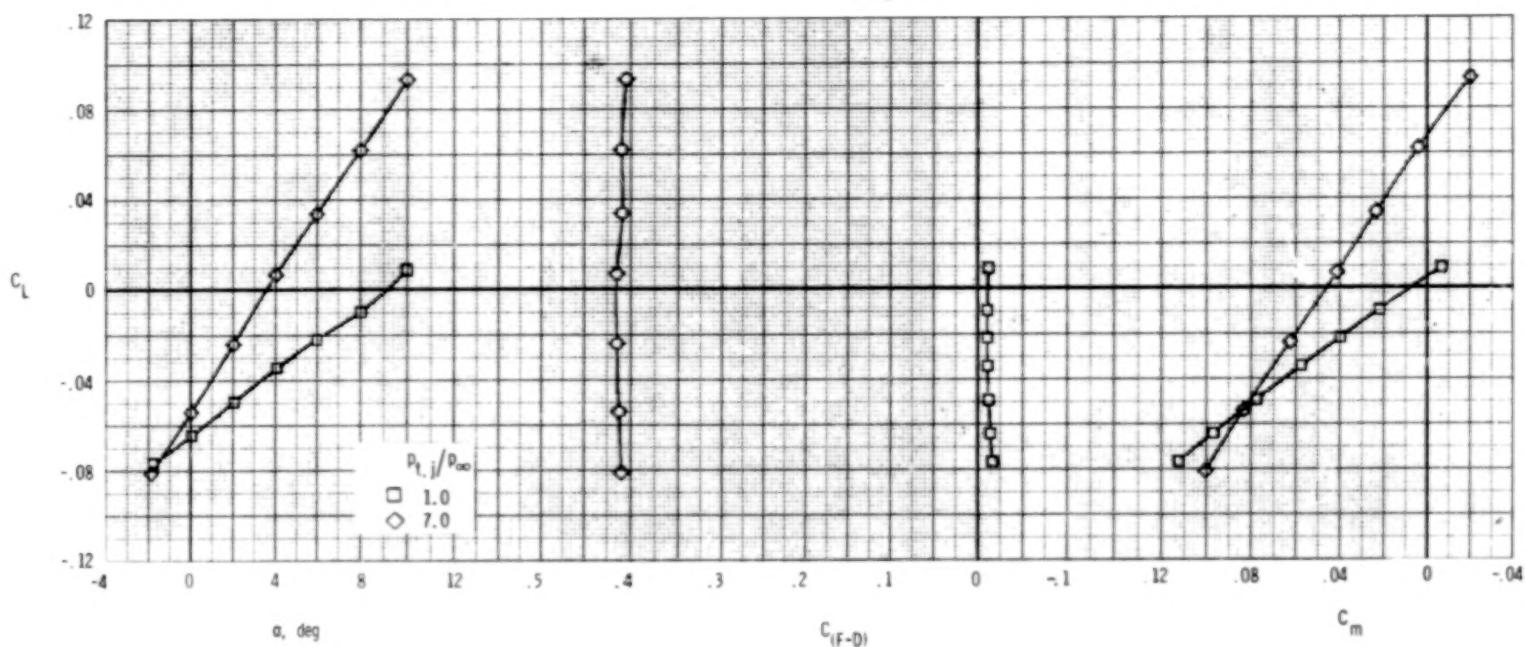
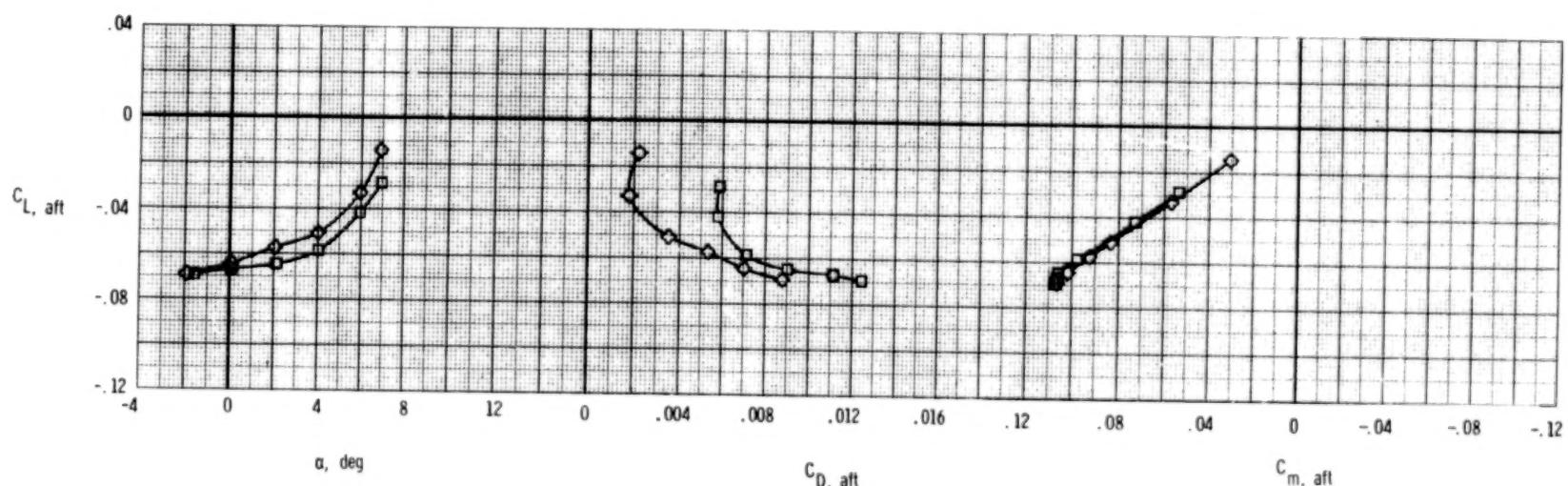
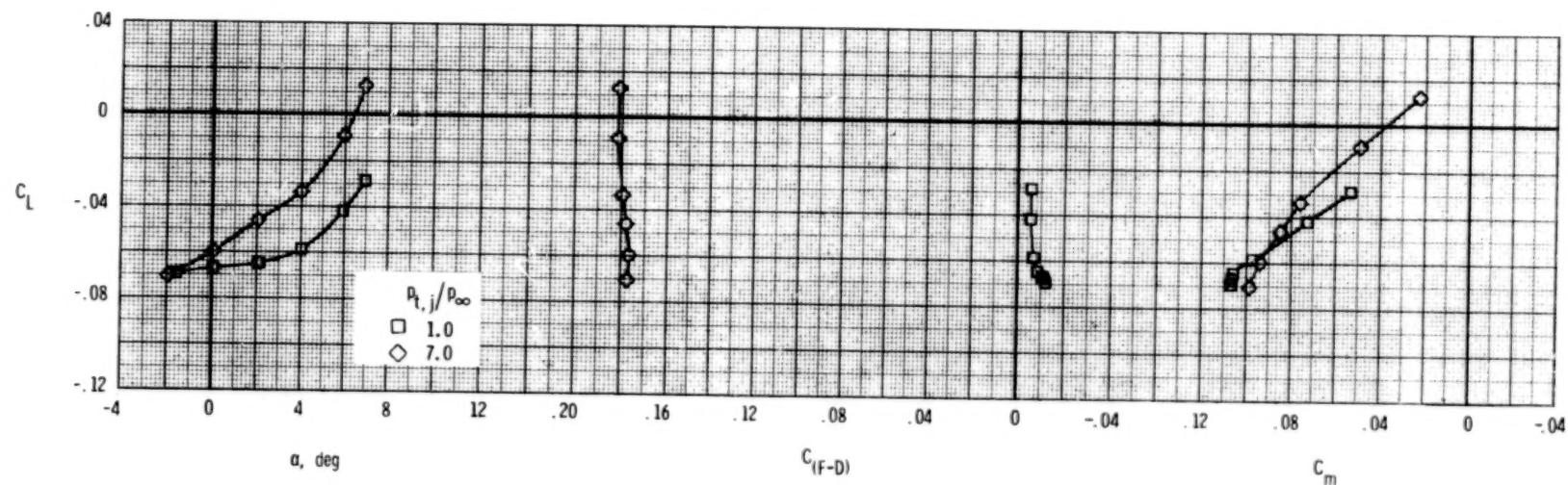
(a) $M = 0.60$.

Figure 76.- Longitudinal afterbody aerodynamic characteristics, wedge nozzle, A/B power.

$$\delta_h = -5^\circ; \quad \delta_v = 0^\circ; \quad A_e/A_t = 1.20.$$



(b) $M = 0.90$.

Figure 76.- Continued.

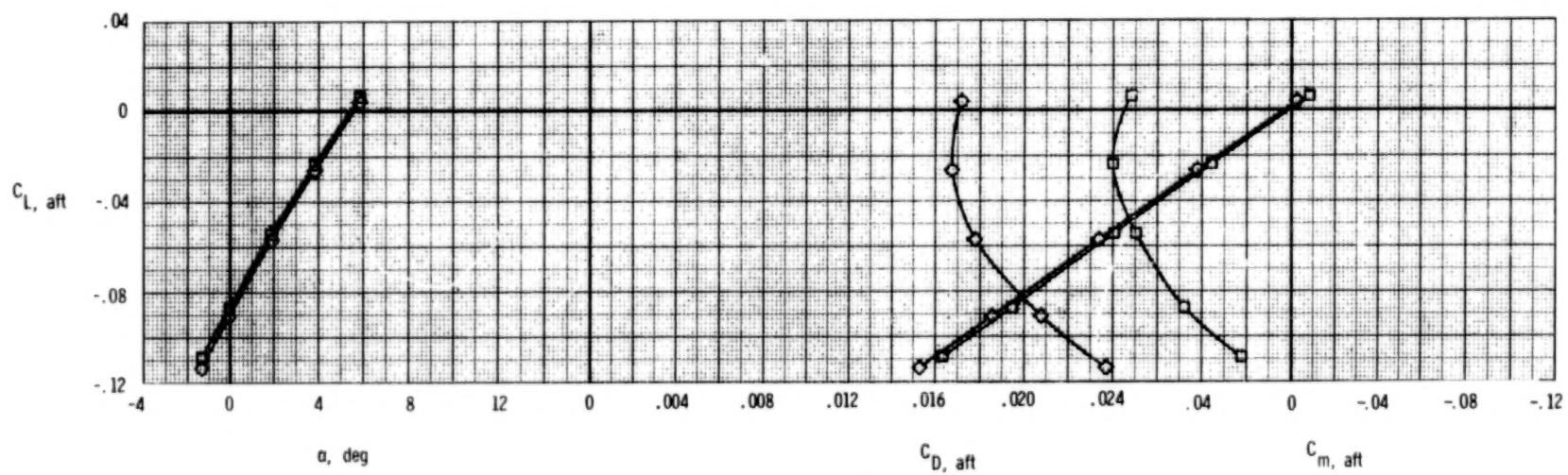
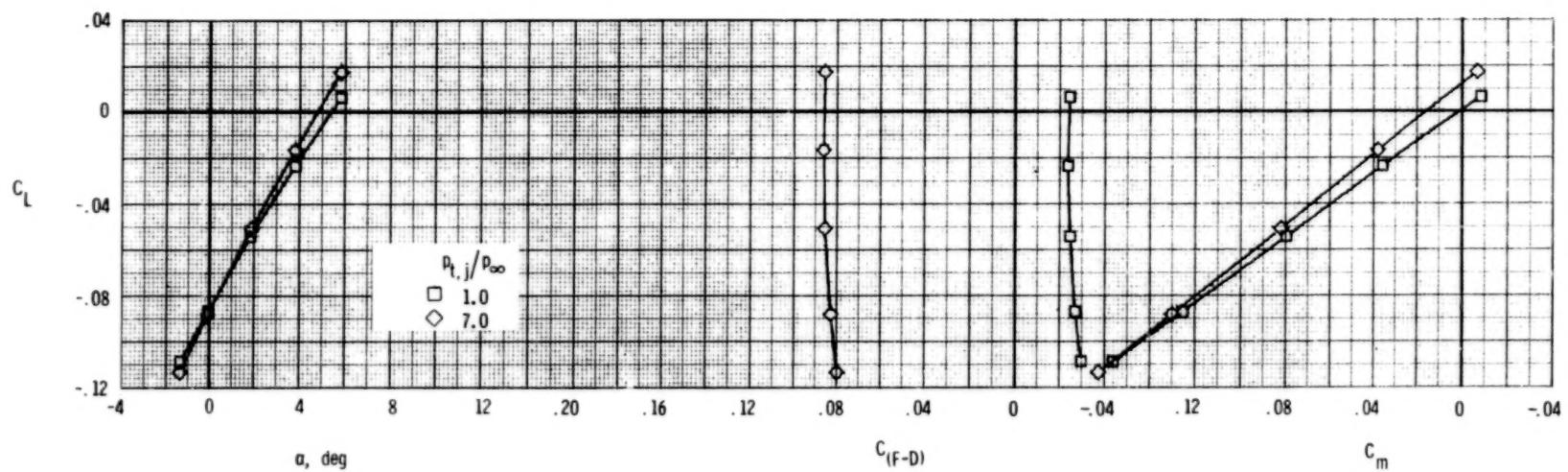
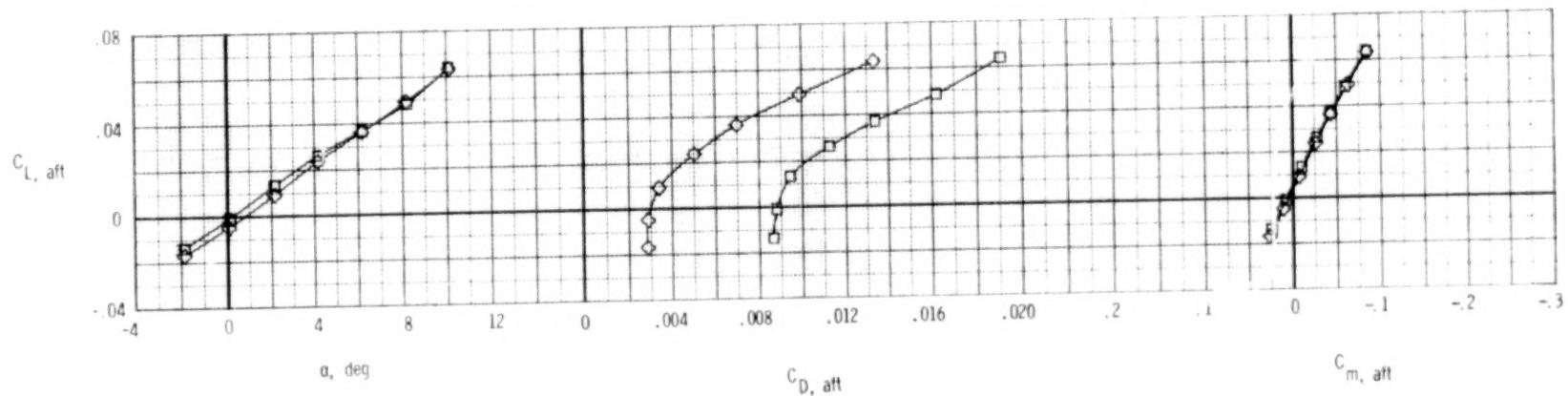
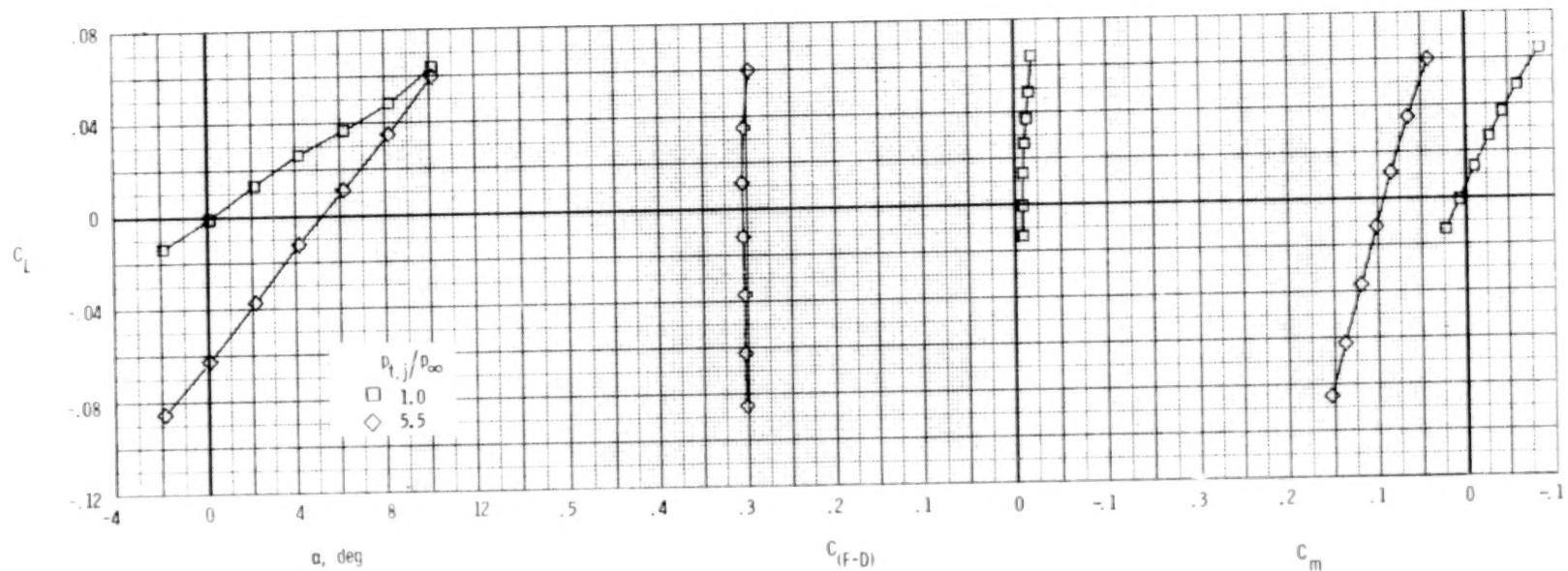
(c) $M = 1.20.$

Figure 76.- Concluded.



(a) $M = 0.60$.

Figure 77.- Longitudinal afterbody aerodynamic characteristics, wedge nozzle, A/B power.

$\delta_h = 0^\circ$; $\delta_v = -10^\circ$; vectored sidewalls; $A_e/A_t = 1.20$.

190

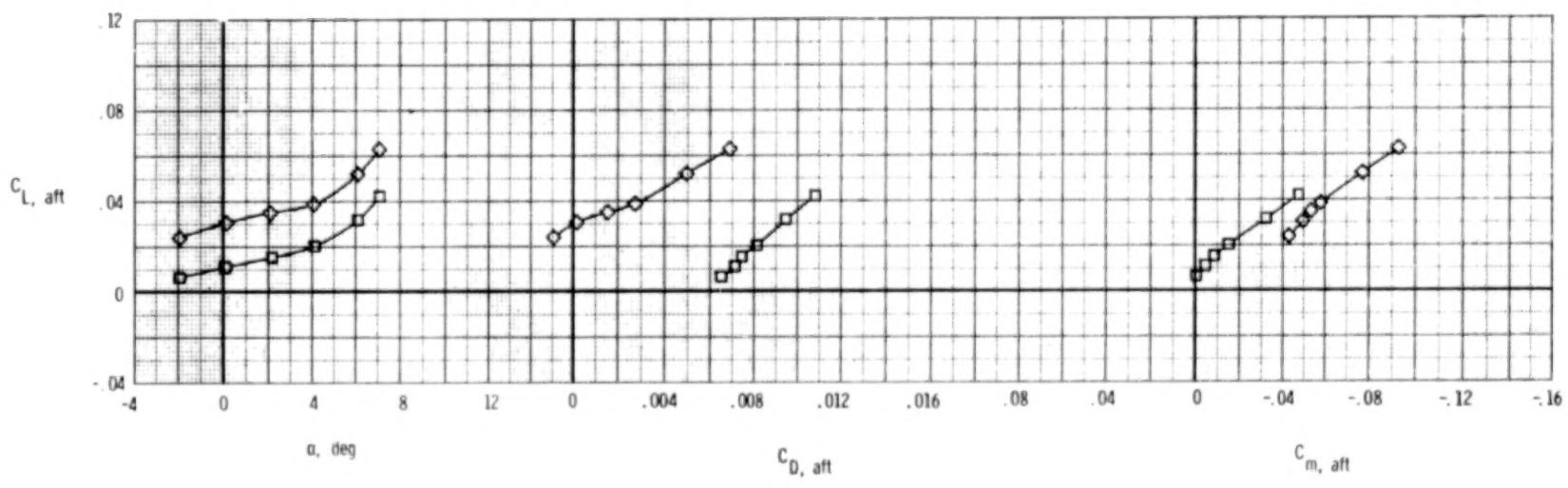
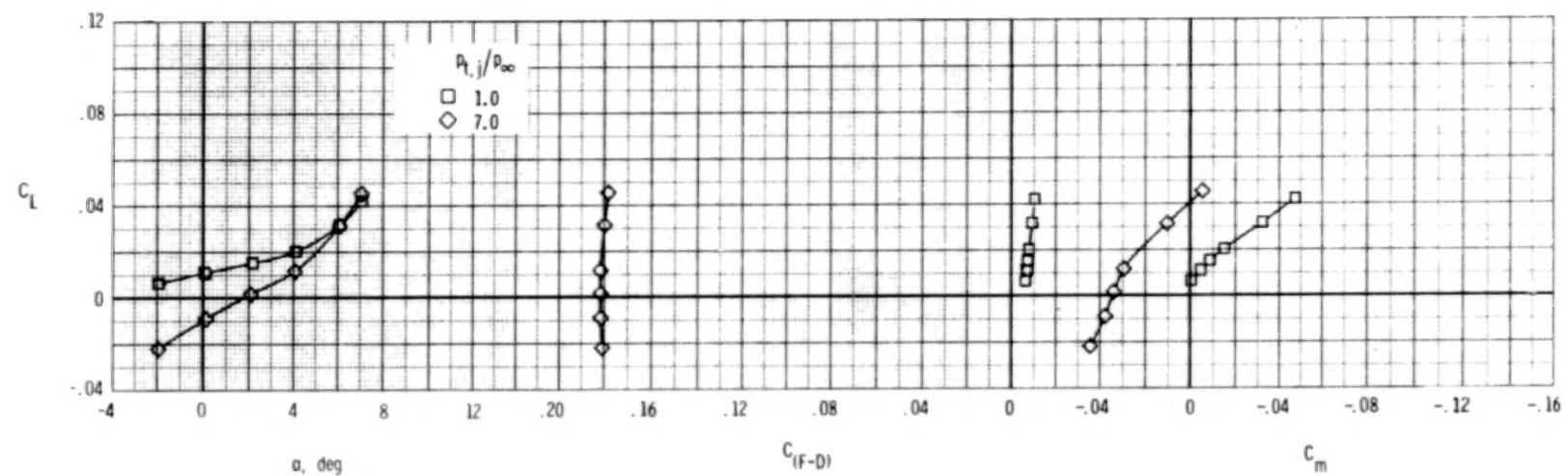
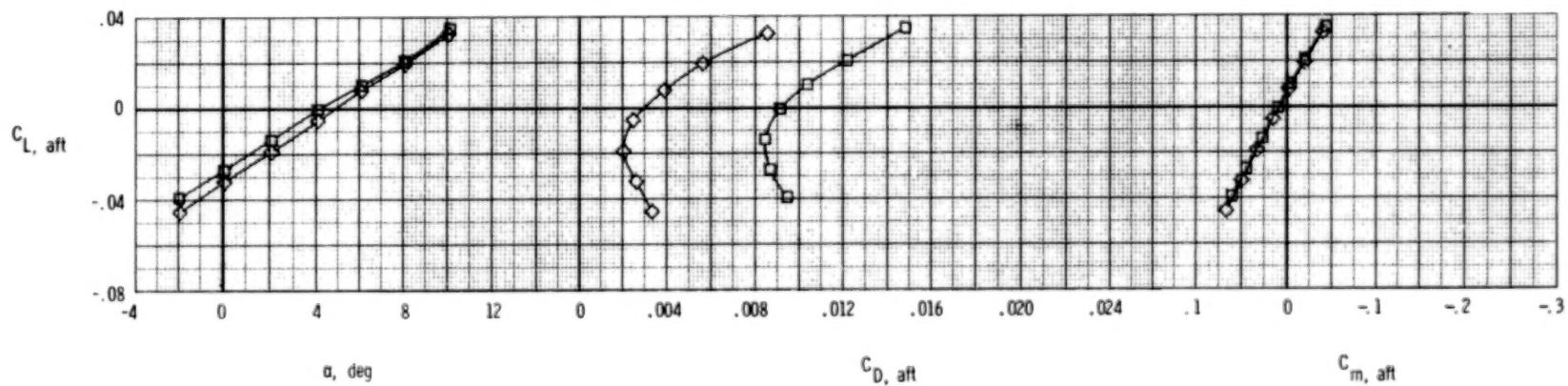
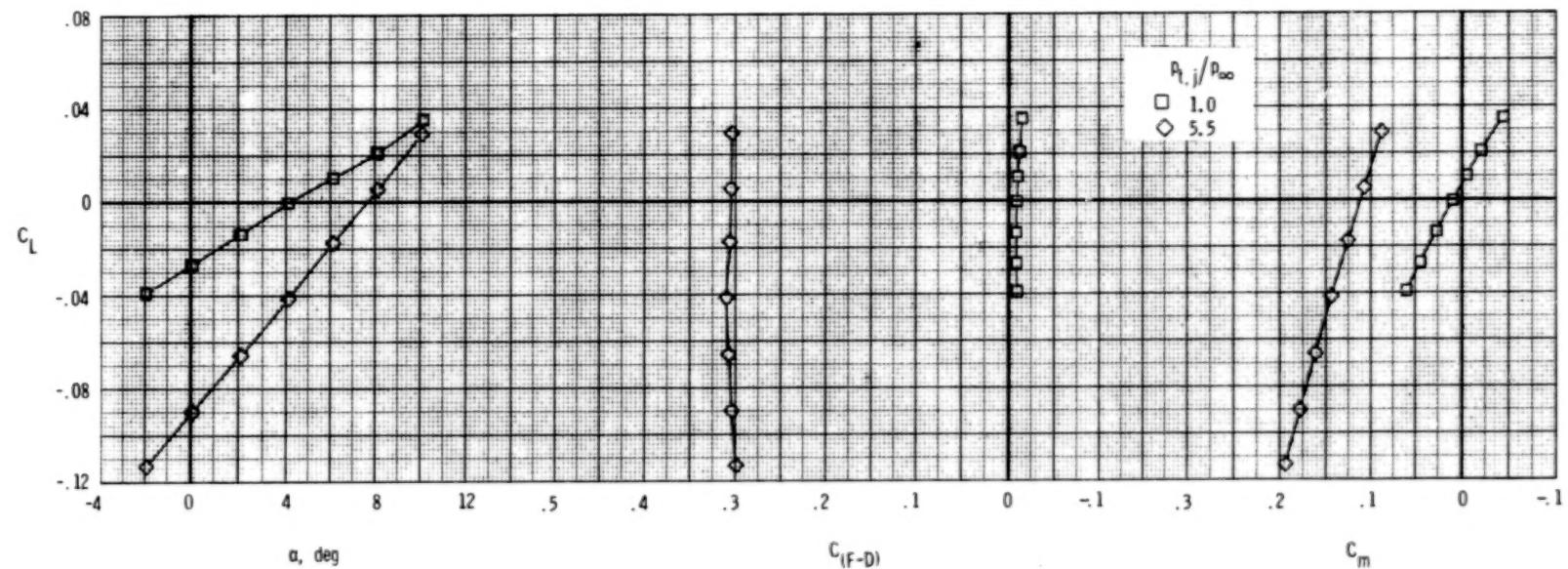
(b) $M = 0.90.$

Figure 77.- Concluded.



(a) $M = 0.60$.

Figure 78.- Longitudinal afterbody aerodynamic characteristics, wedge nozzle, A/B power.

$\delta_h = -2^\circ$; $\delta_v = -10^\circ$; vectored sidewalls; $A_e/A_t = 1.20$.

192

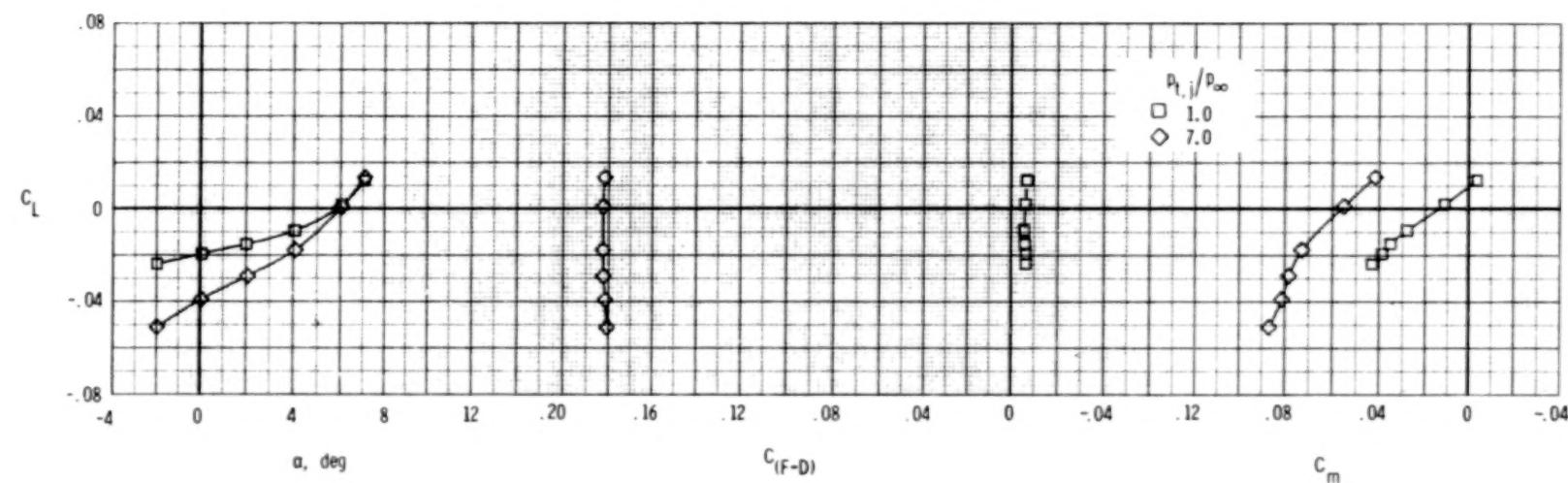
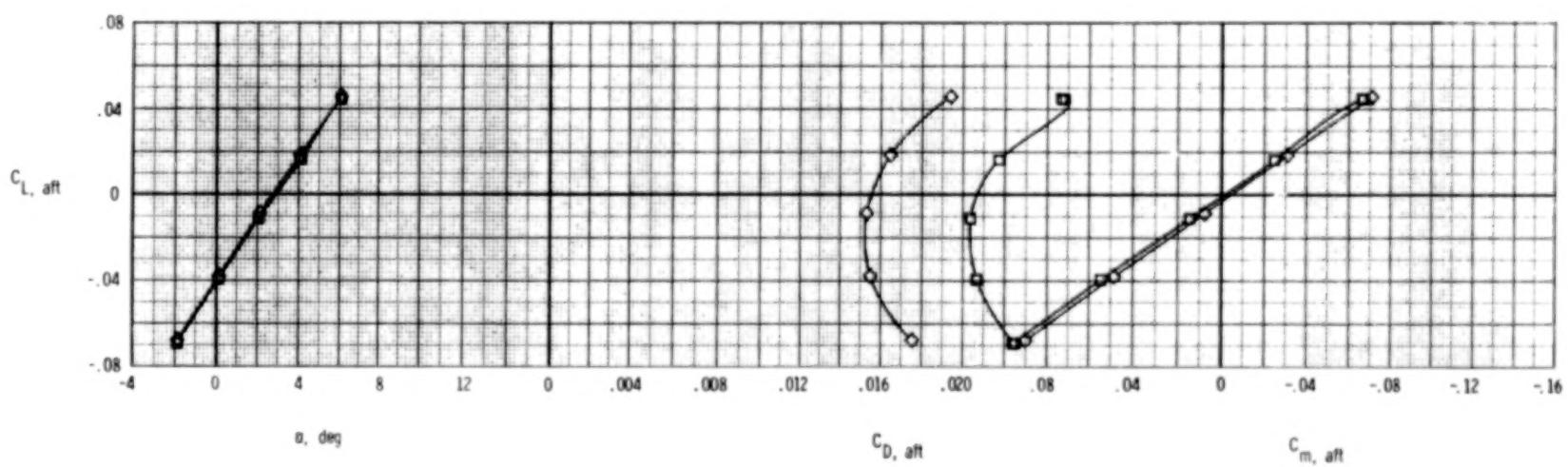
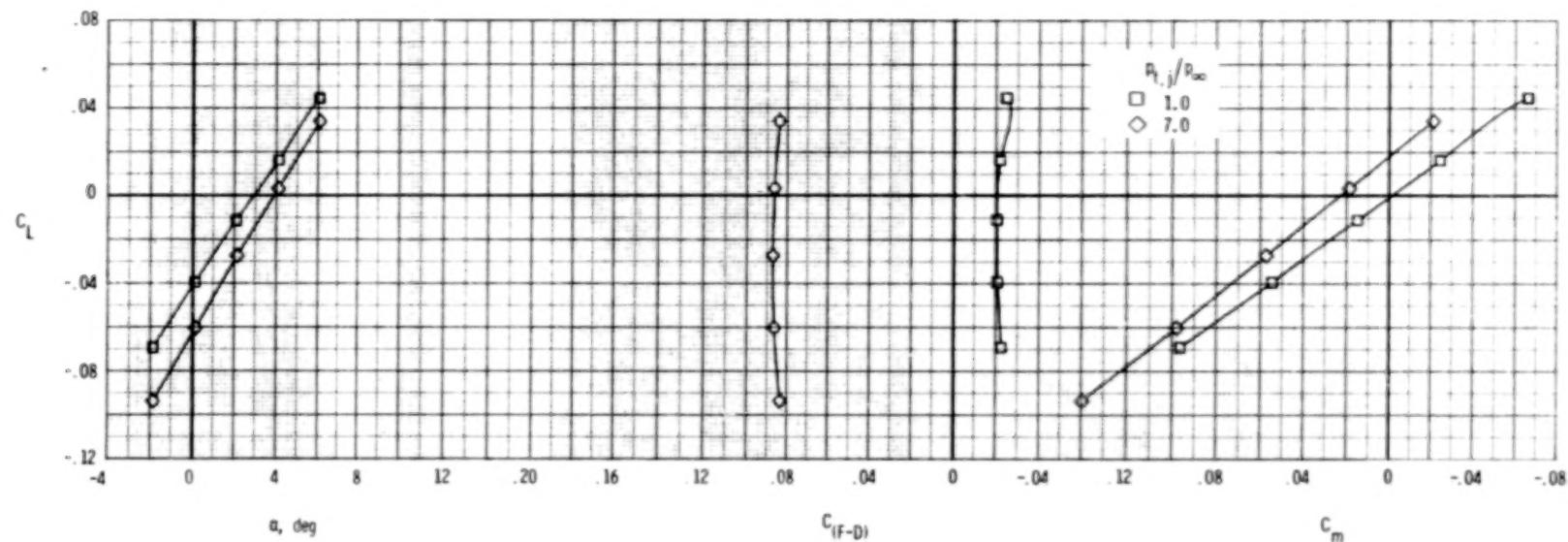
(b) $M = 0.90$.

Figure 78.- Continued.



(c) $M = 1.20$.

Figure 78.- Concluded.

194

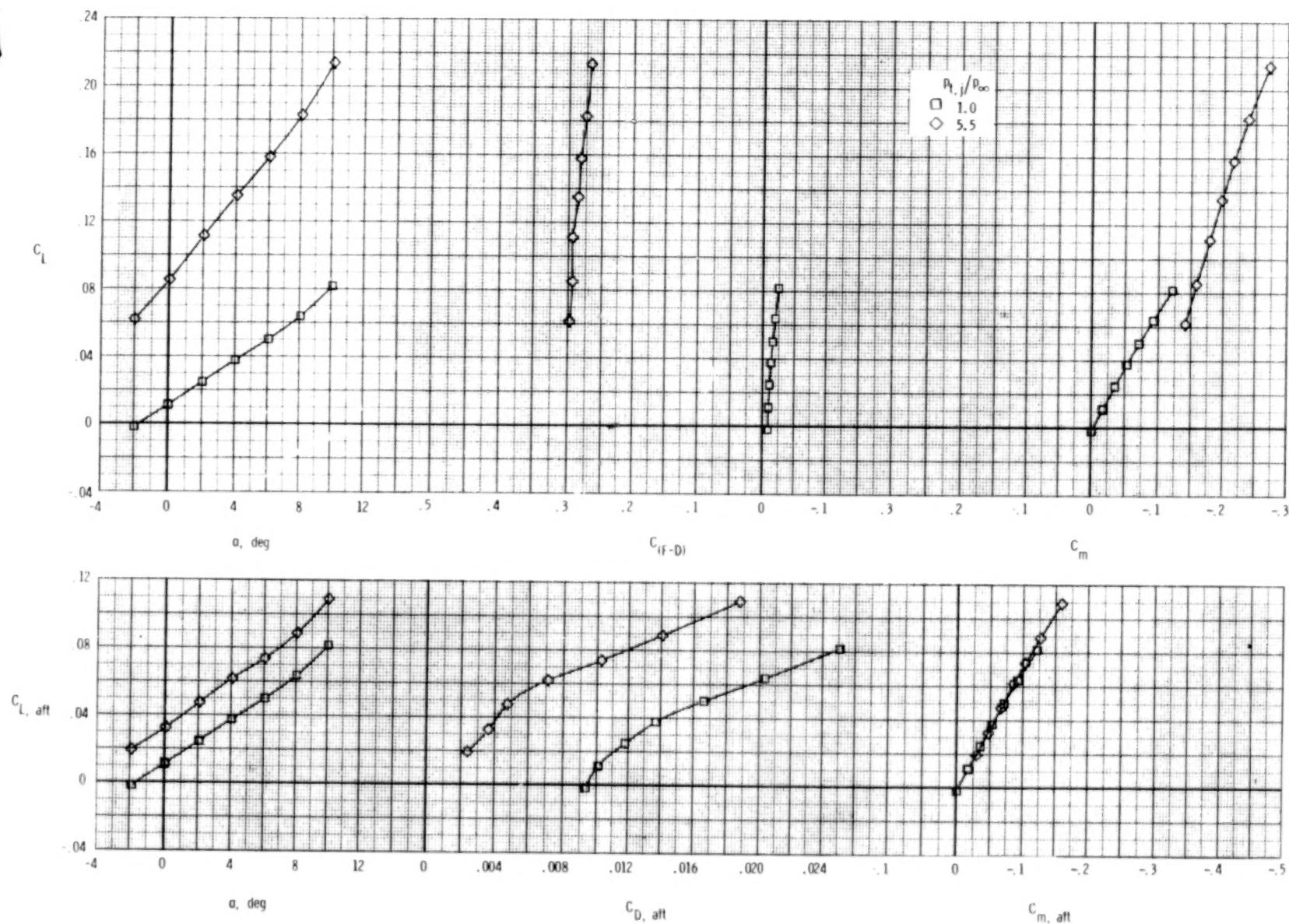
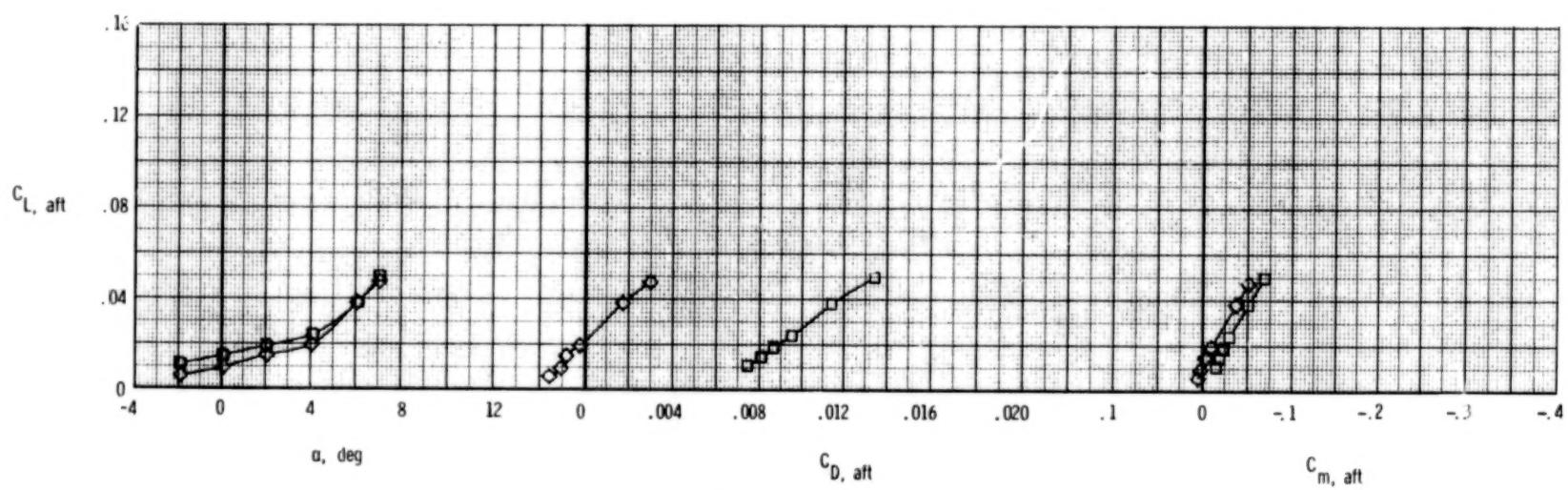
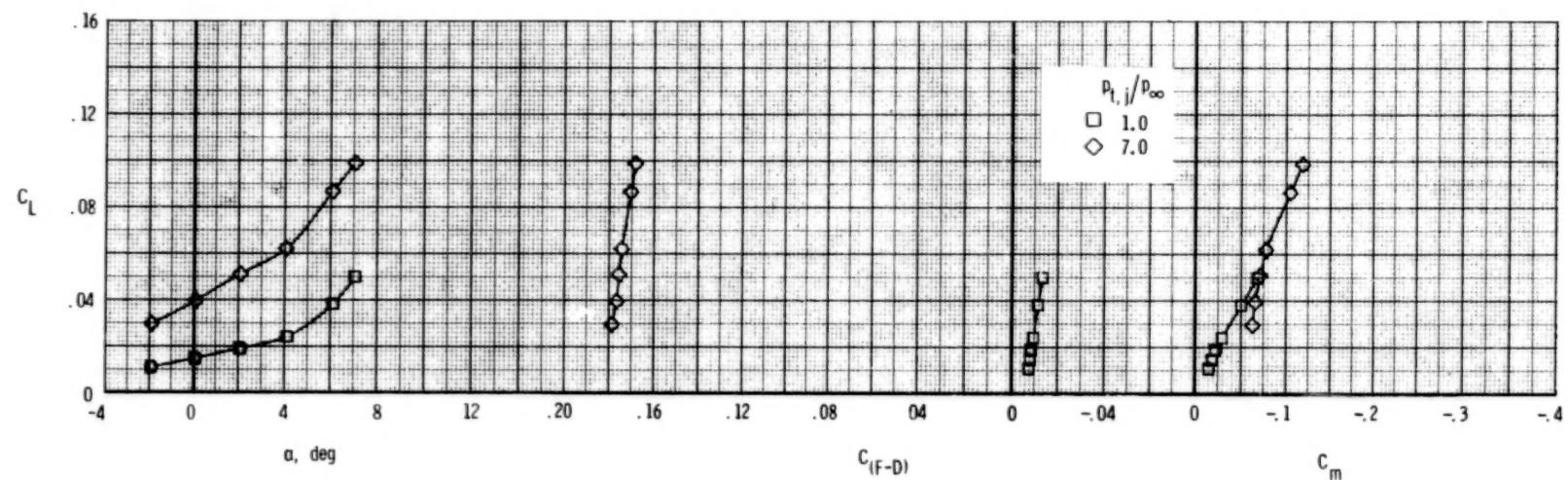
(a) $M = 0.60$.

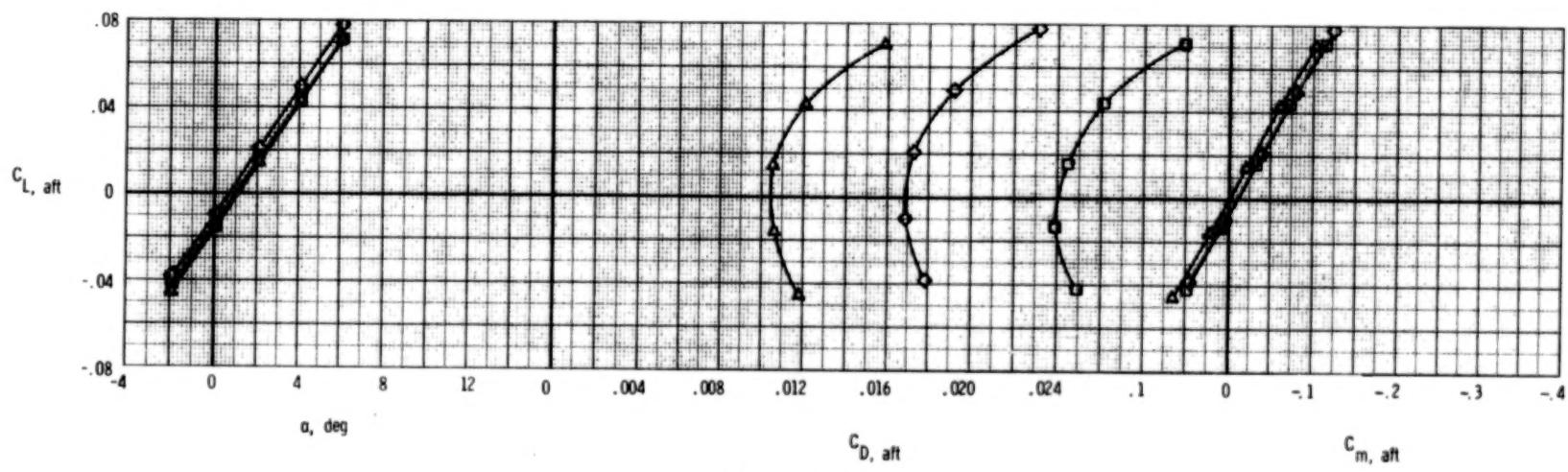
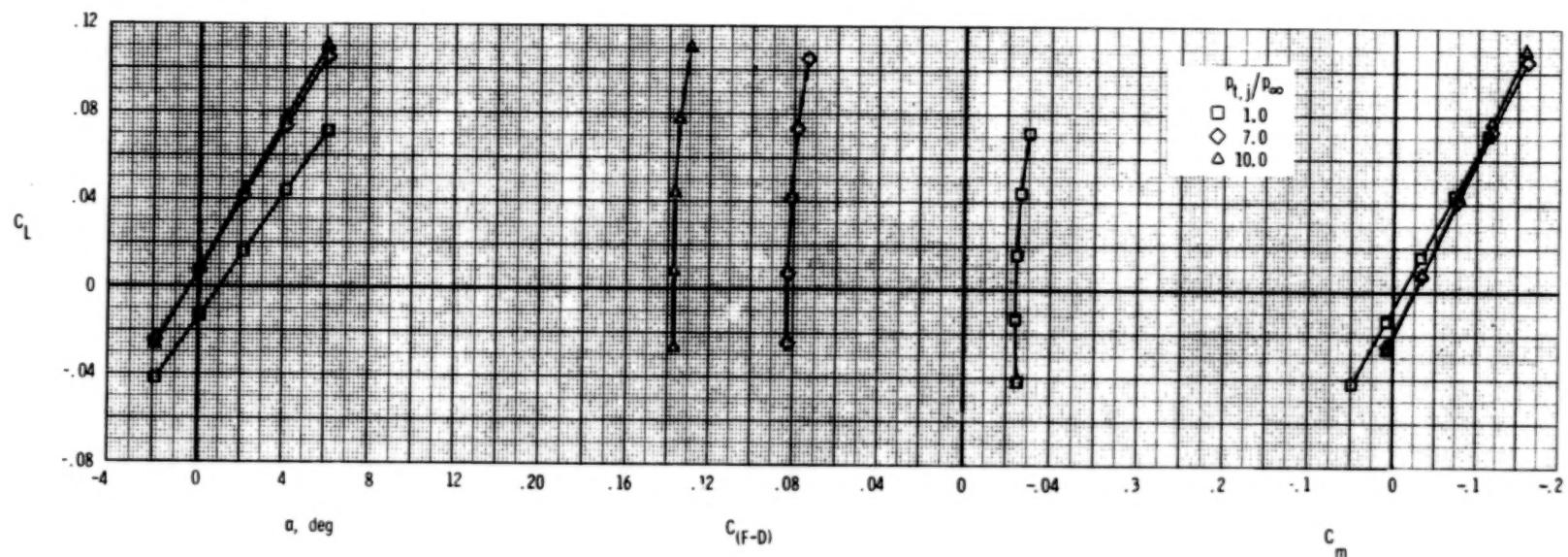
Figure 79.- Longitudinal afterbody aerodynamic characteristics, wedge nozzle, A/B power.
 $\delta_h = 0^\circ$; $\delta_v = 10^\circ$; vectored sidewalls; $A_e/A_t = 1.20$.



(b) $M = 0.90$.

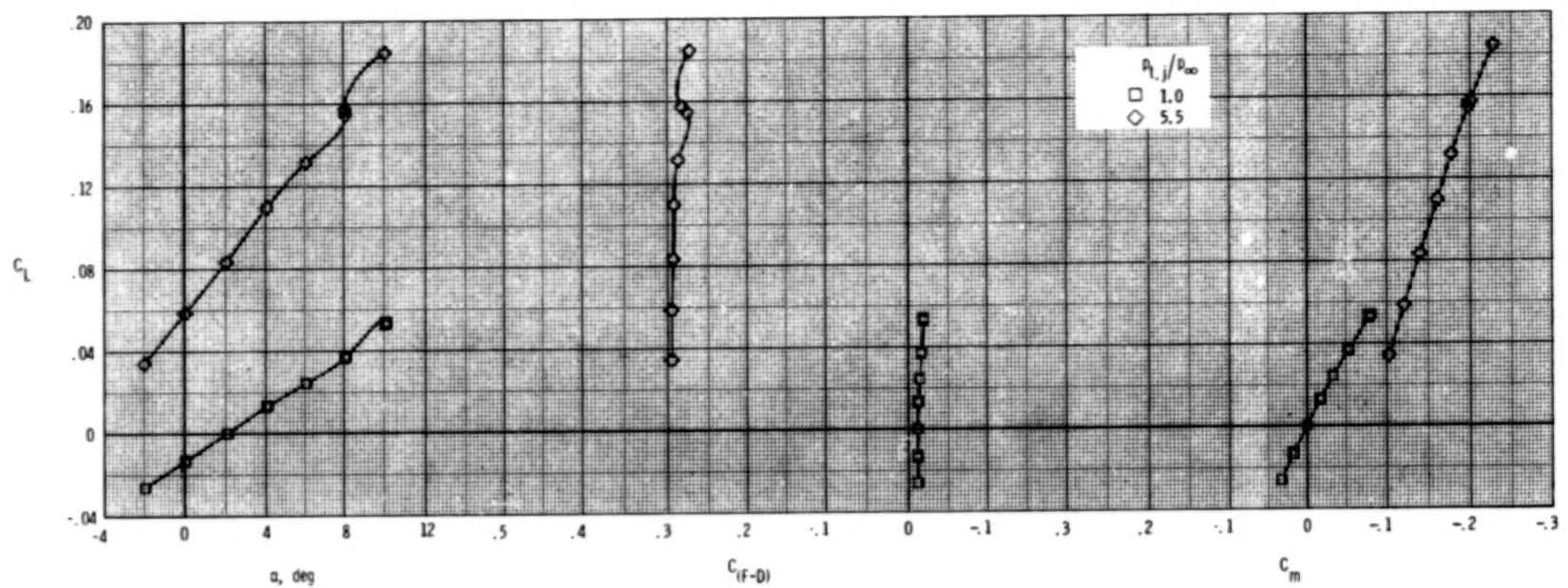
Figure 79.- Continued.

196



(c) $M = 1.20$.

Figure 79.- Concluded.



(a) $M = 0.60$.

Figure 80.- Longitudinal afterbody aerodynamic characteristics, wedge nozzle, A/B power.

$\delta_h = -2^\circ$; $\delta_v = 10^\circ$; vectored sidewalls; $A_e/A_t = 1.20$.

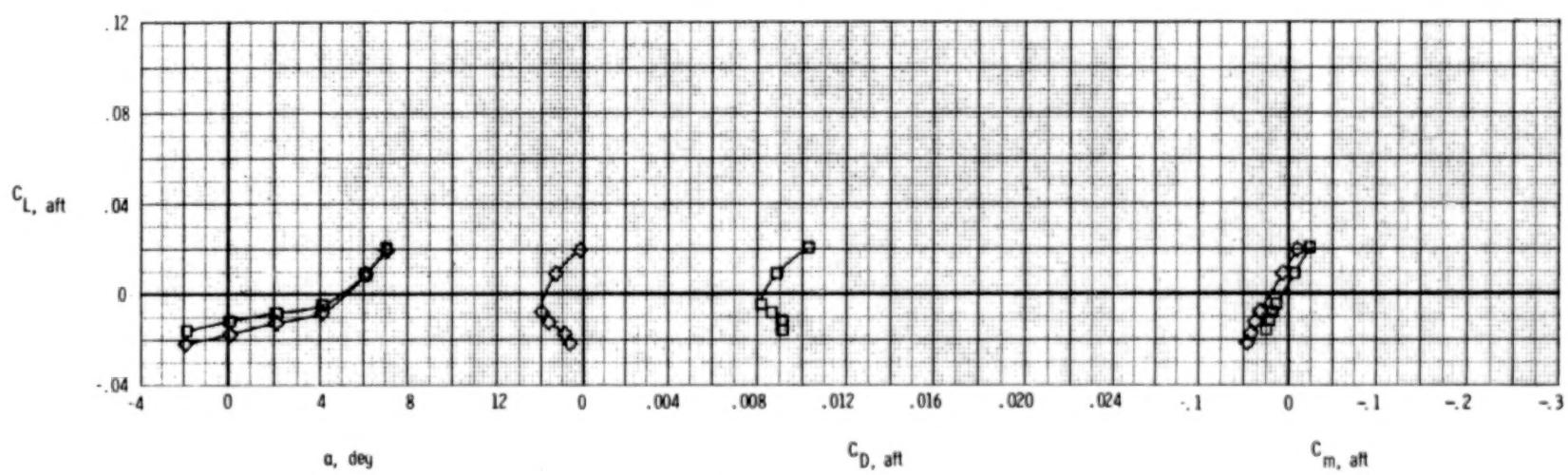
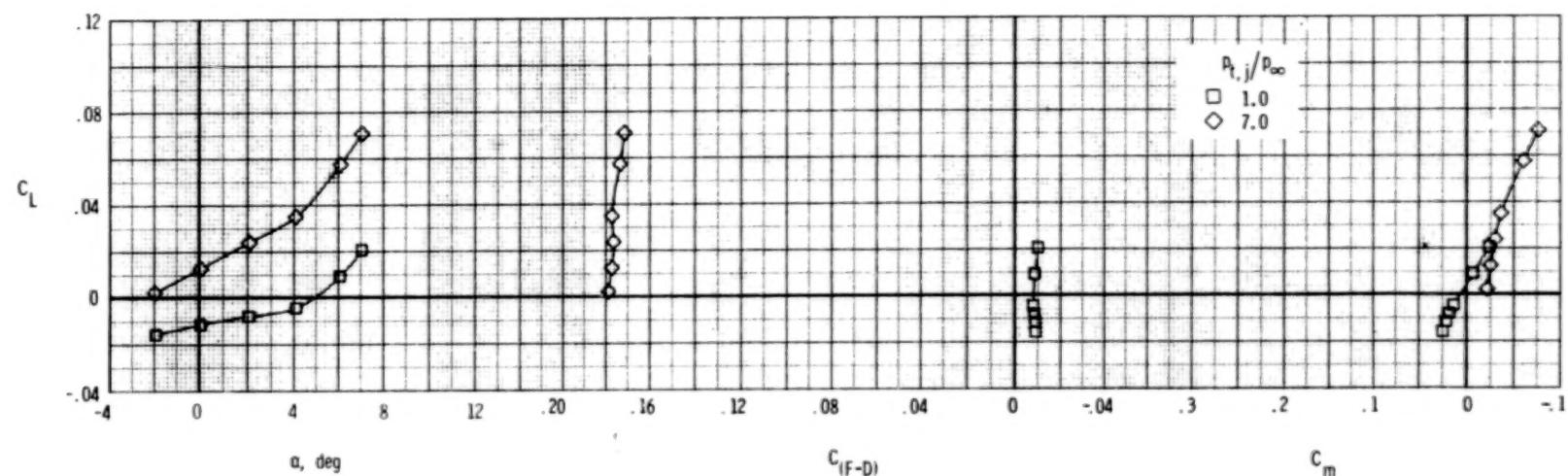
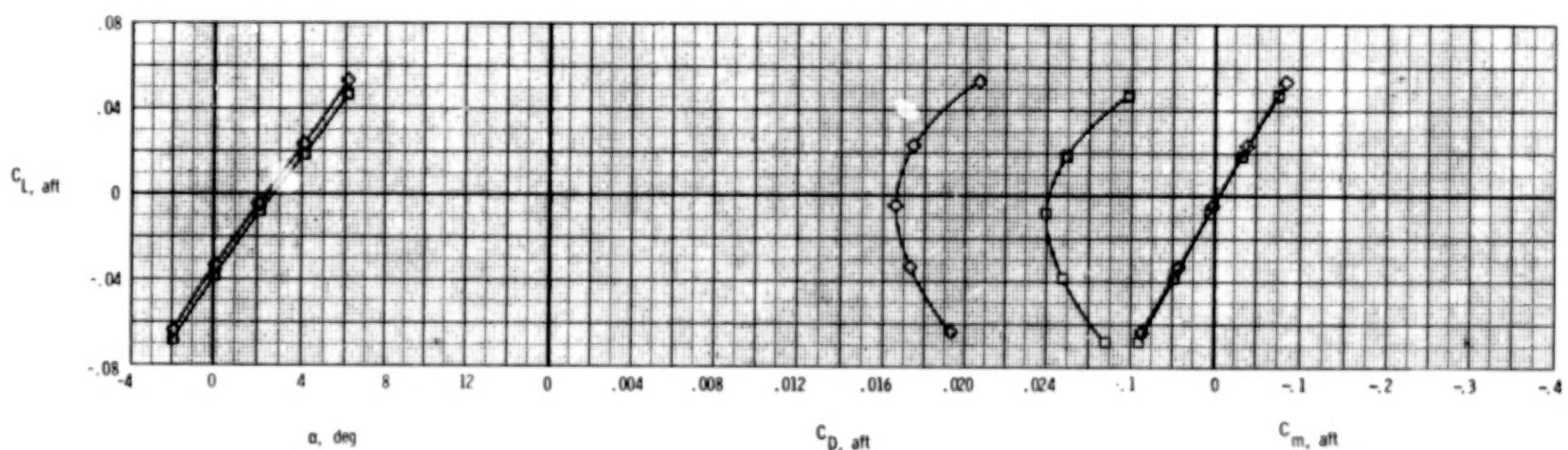
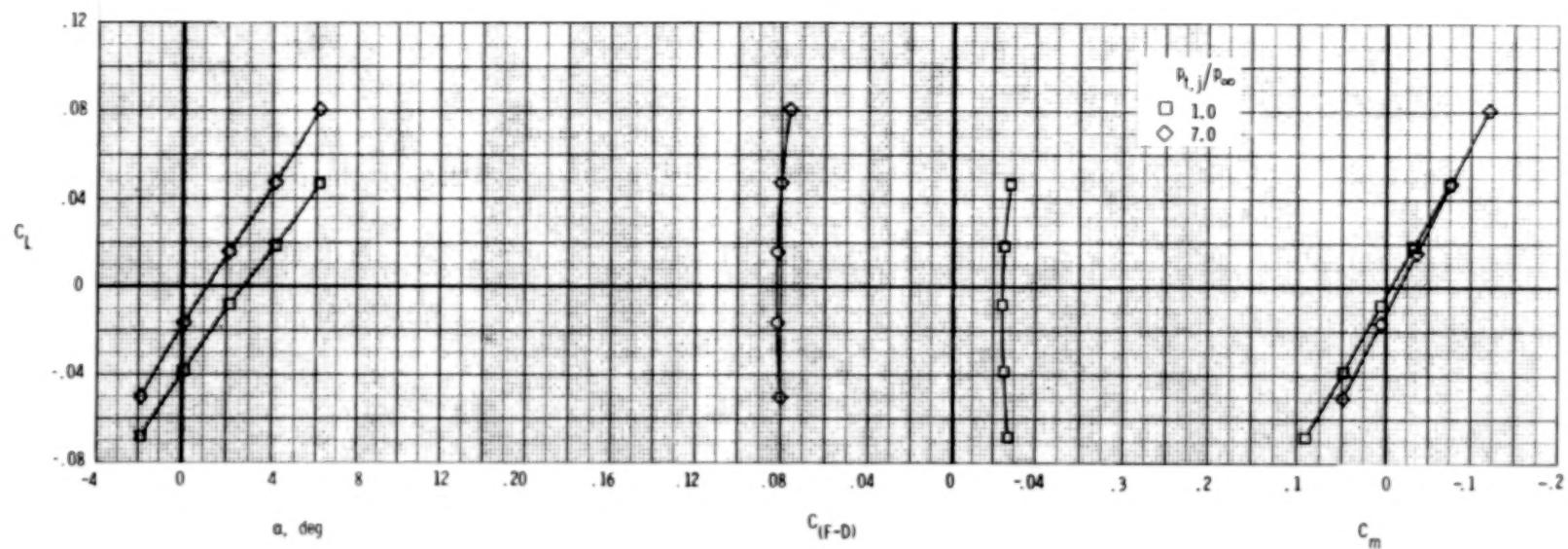
(b) $M = 0.90$.

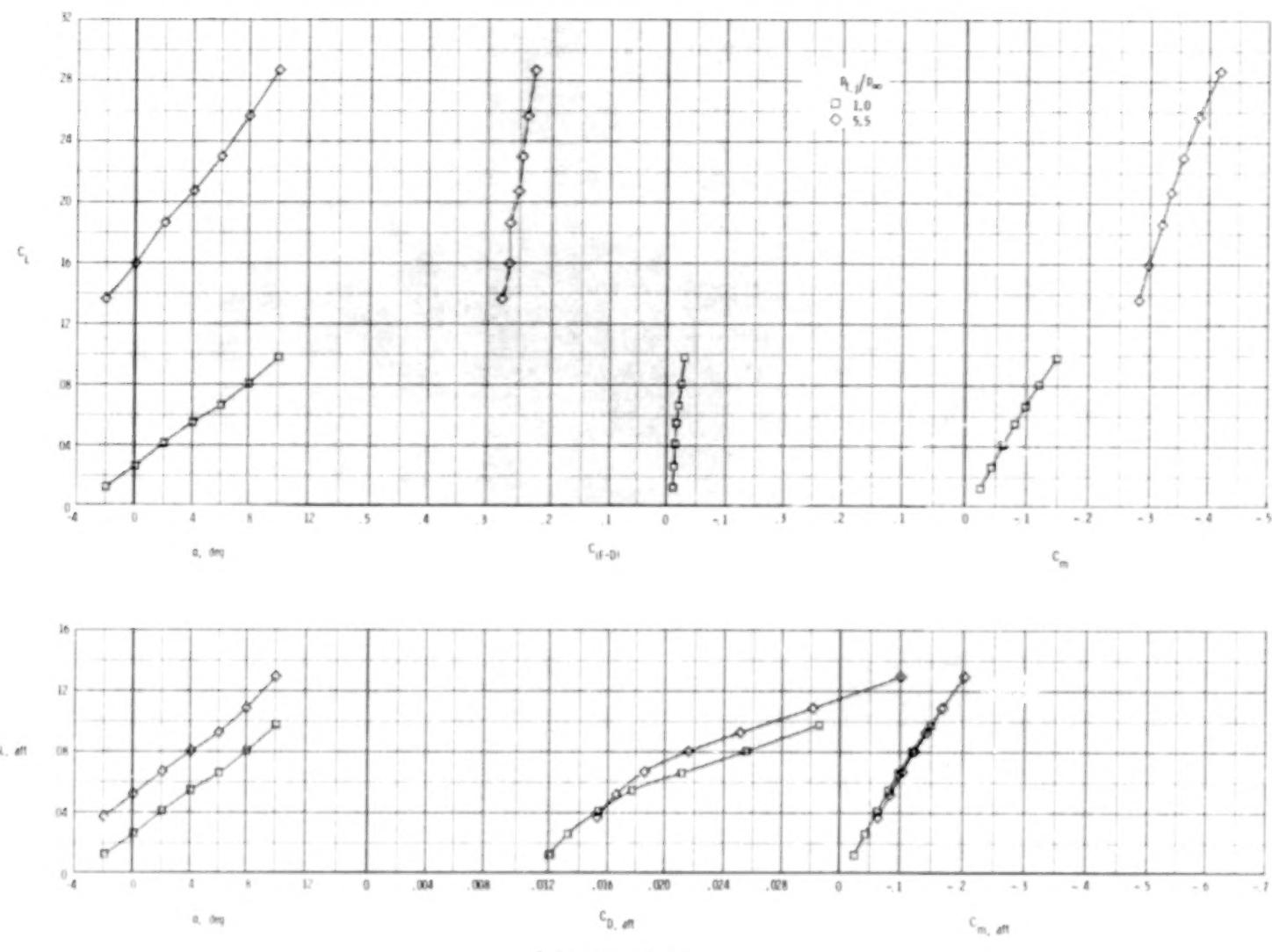
Figure 80.- Continued.



(c) $M = 1.20$.

Figure 80.- Concluded.

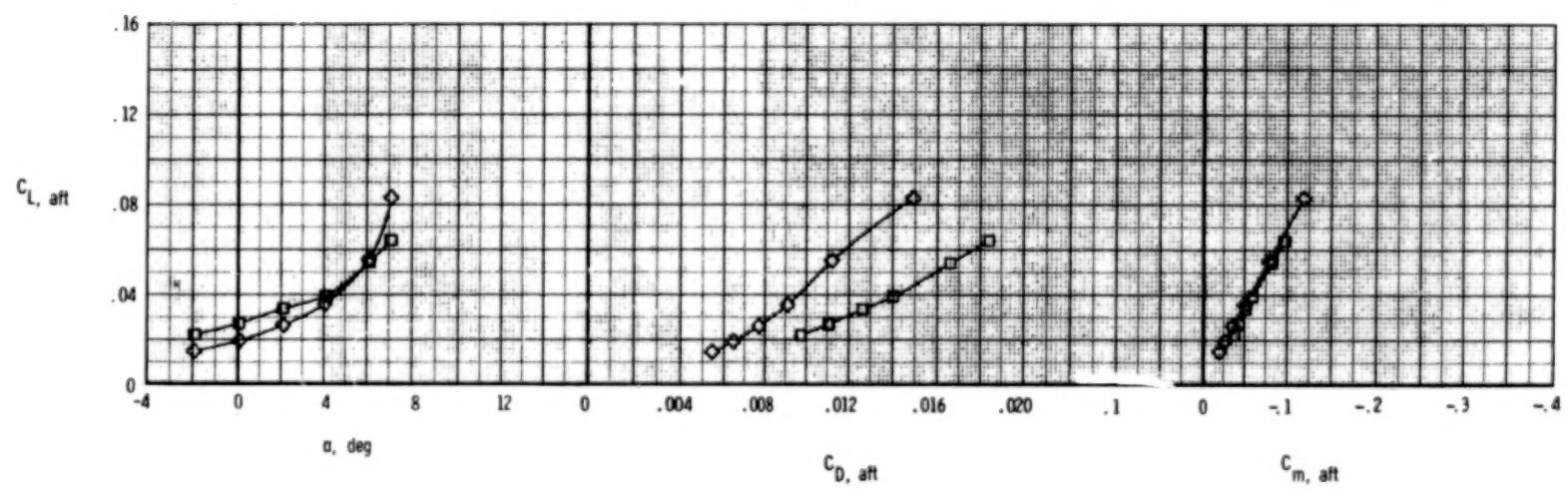
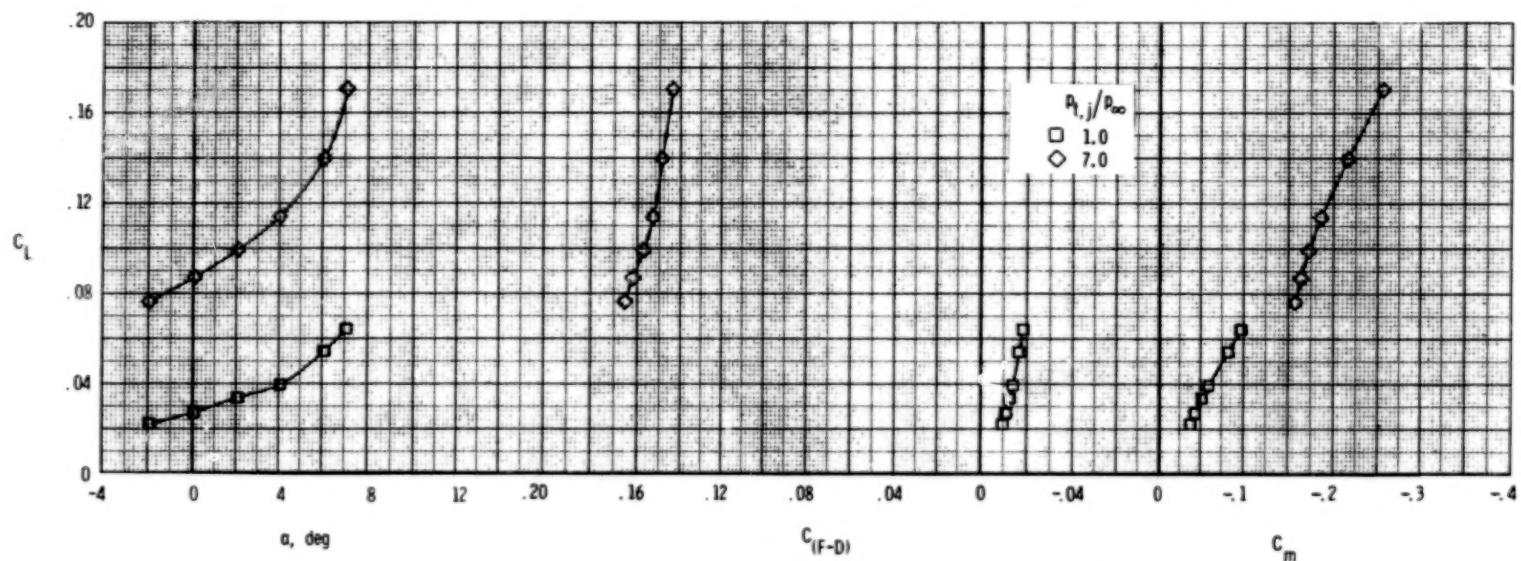
200



(a) $M = 0.60$.

Figure 81.- Longitudinal afterbody aerodynamic characteristics, wedge nozzle, A/B power.

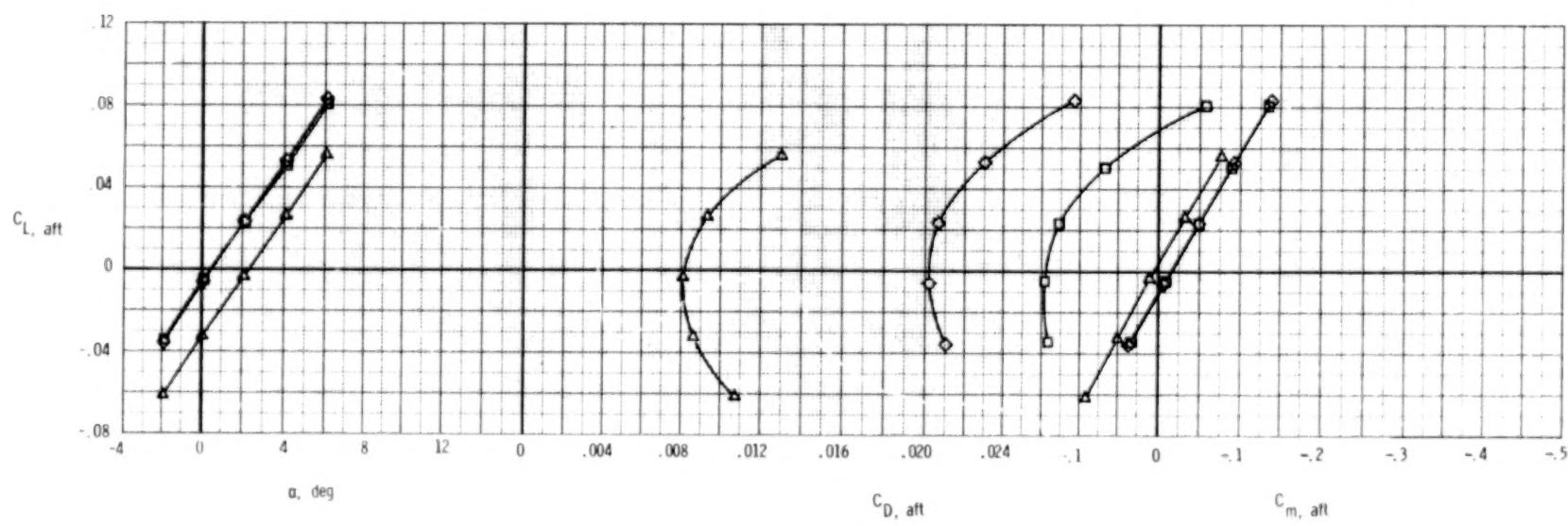
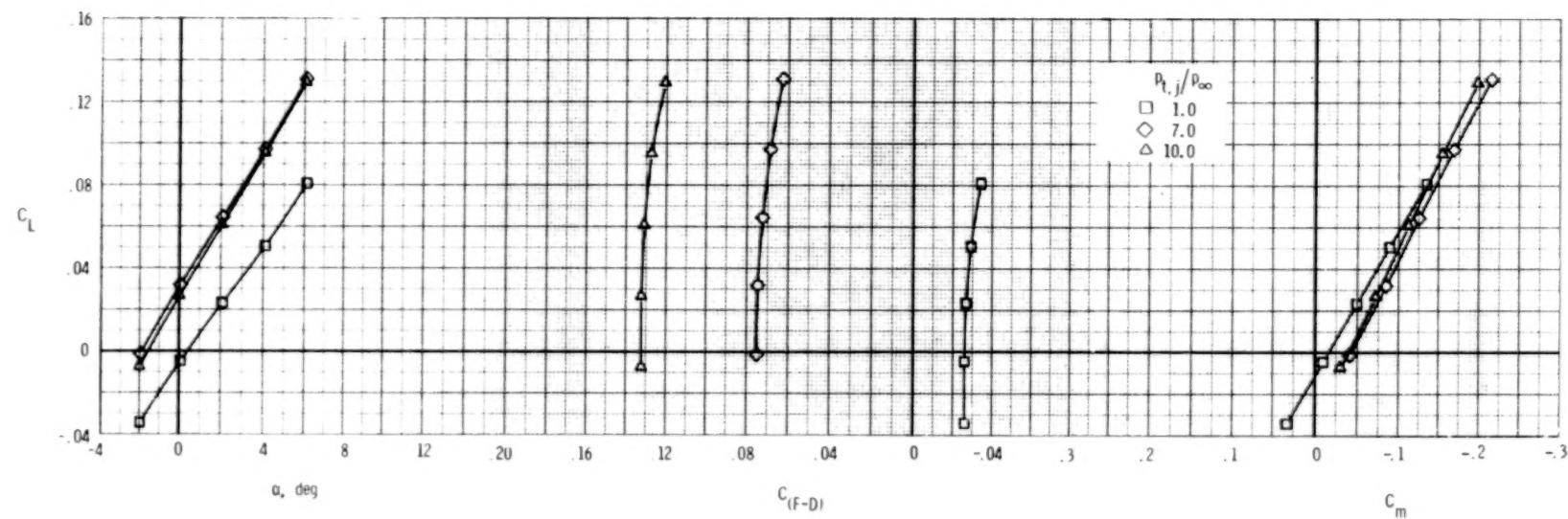
$\delta_h = 0^\circ$; $\delta_v = 20^\circ$; vectored sidewalls; $A_e/A_t = 1.20$.



(b) $M = 0.90$.

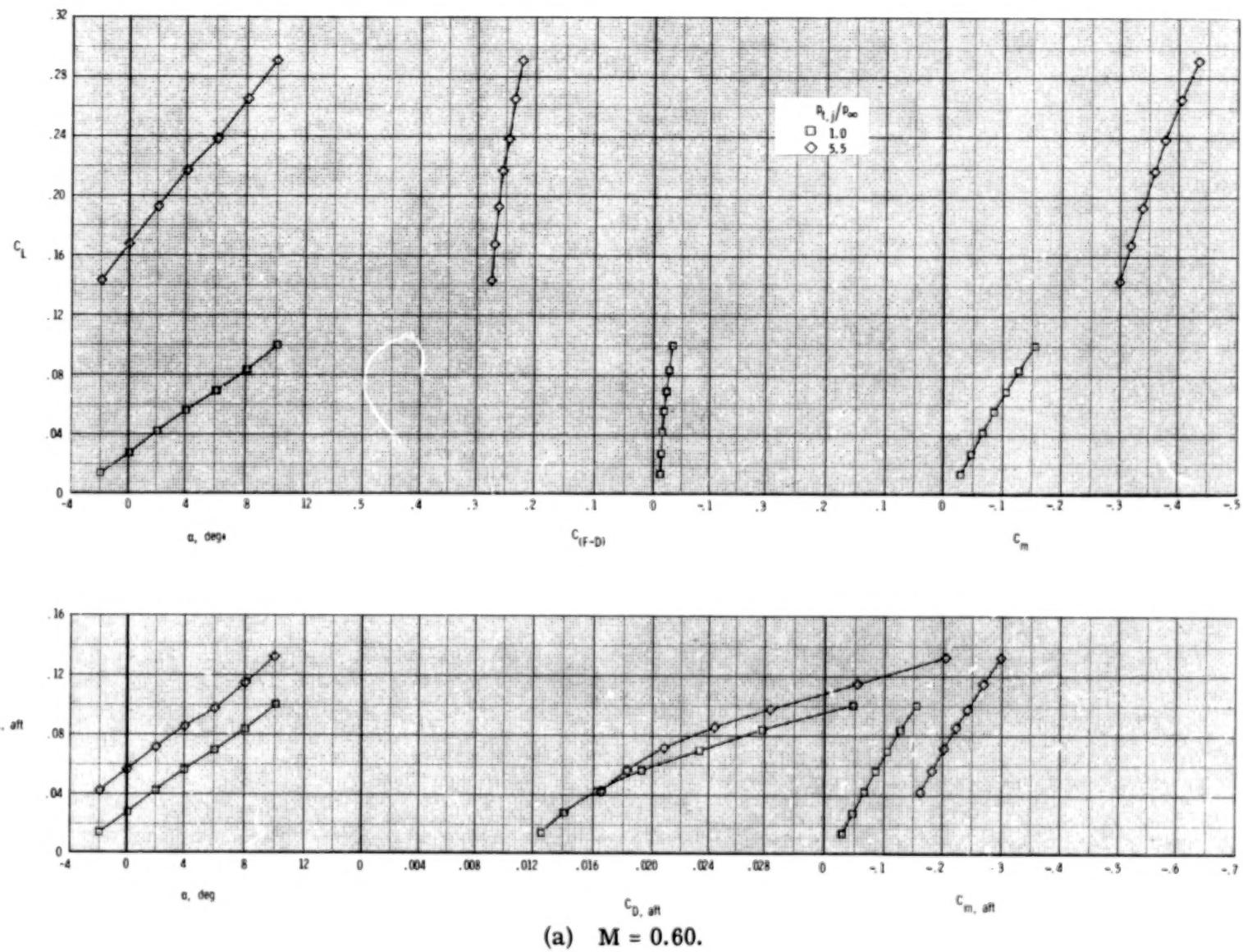
Figure 81.- Continued.

202



(c) $M = 1.20$.

Figure 81.- Concluded.



(a) $M = 0.60$.

Figure 82. - Longitudinal afterbody aerodynamic characteristics, wedge nozzle, A/B power.

$\delta_h = 0^\circ$; $\delta_v = 20^\circ$; straight sidewalls; $A_e/A_t = 1.20$.

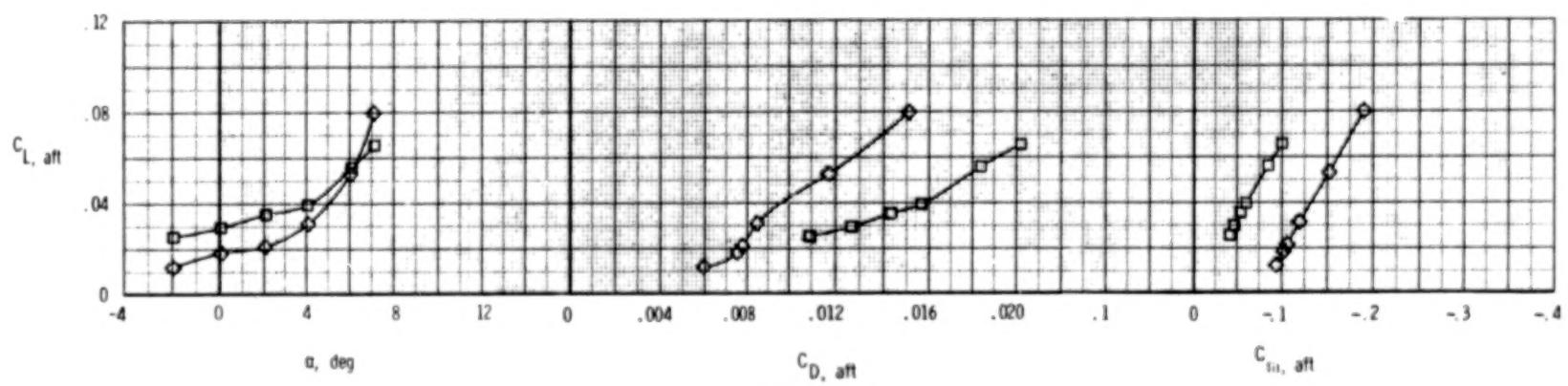
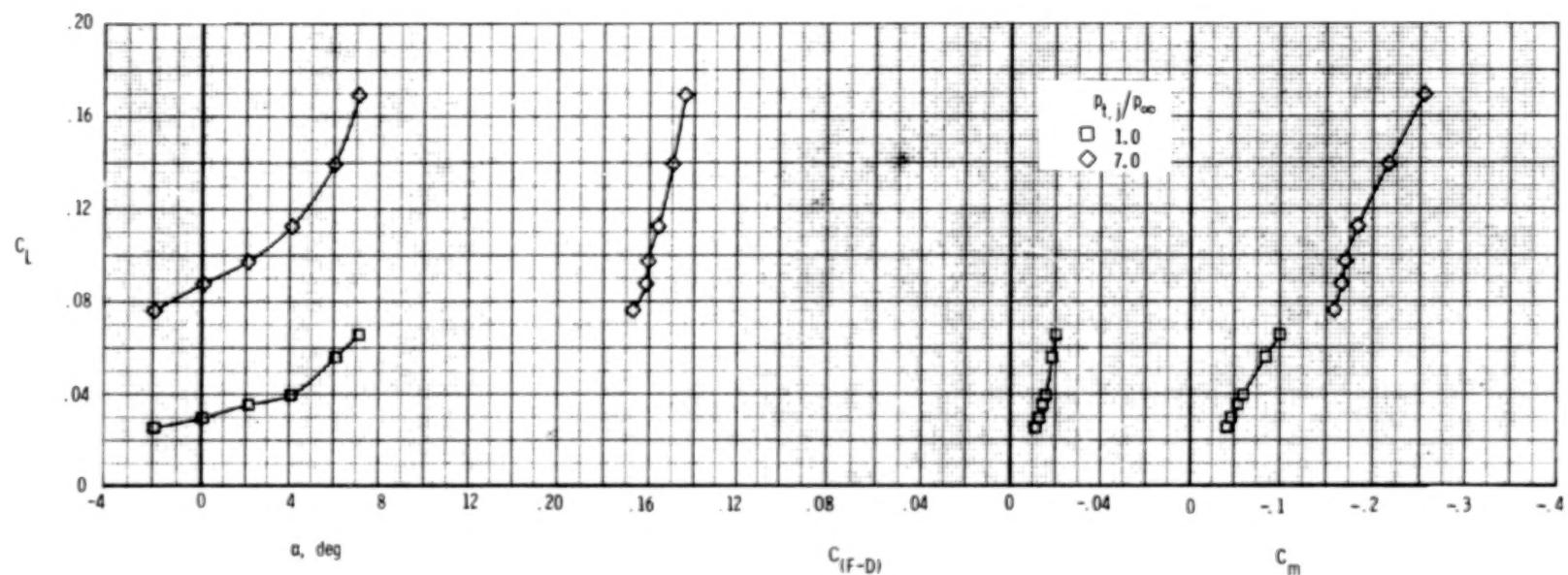
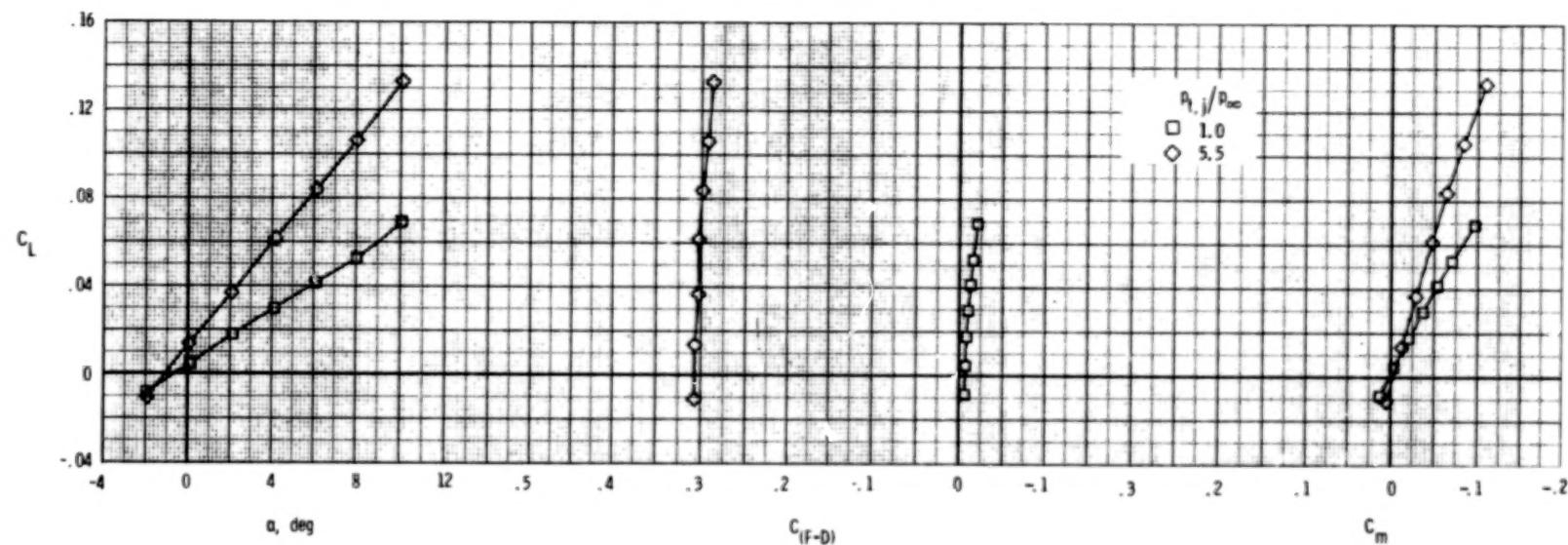
(b) $M = 0.90$.

Figure 82.- Concluded.



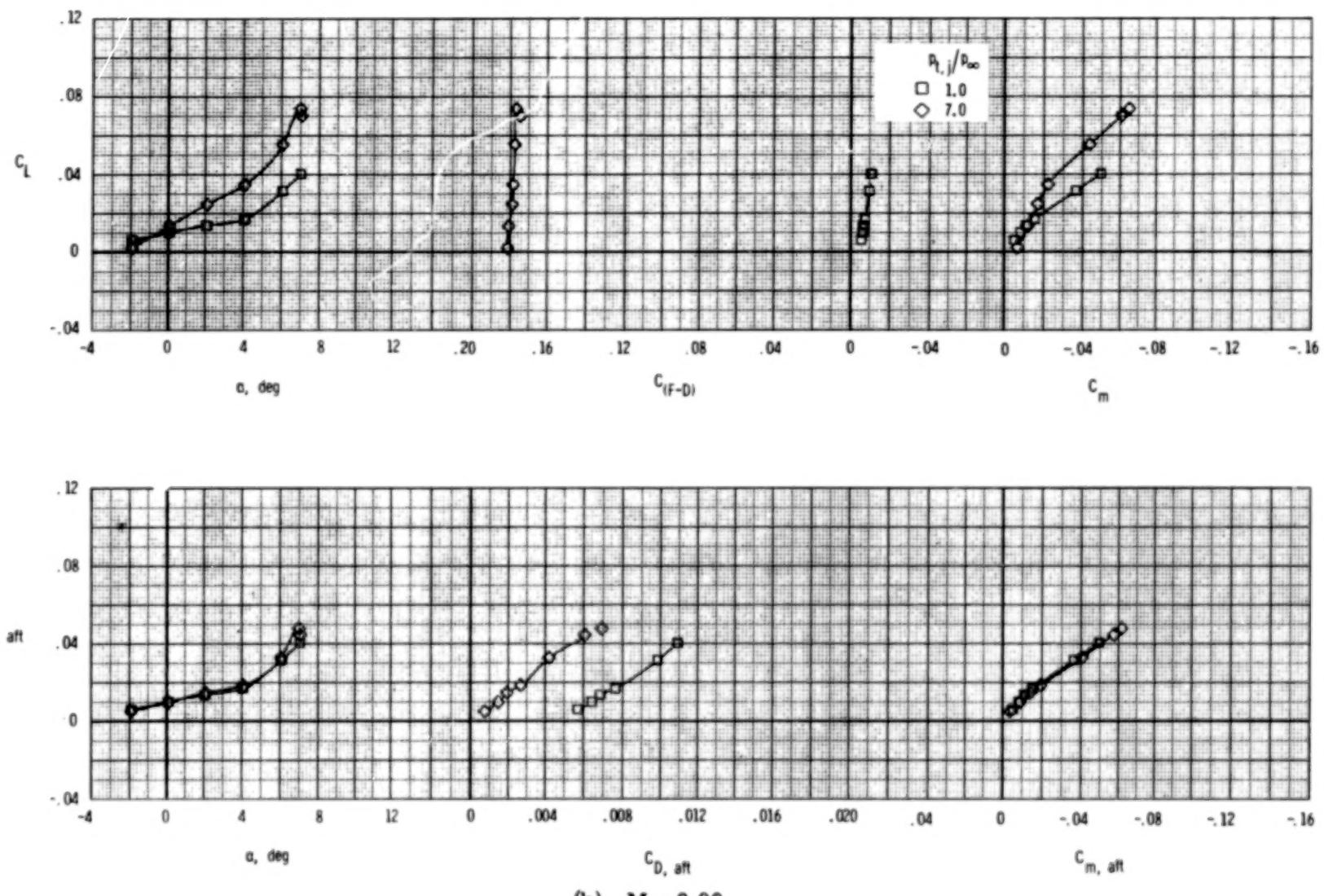
(a) $M = 0.60$.

Figure 83.- Longitudinal afterbody aerodynamic characteristics, wedge nozzle, A/B power.

$$\delta_h = 0^\circ; \quad \delta_v = 0^\circ; \quad A_e/A_t = 1.40.$$

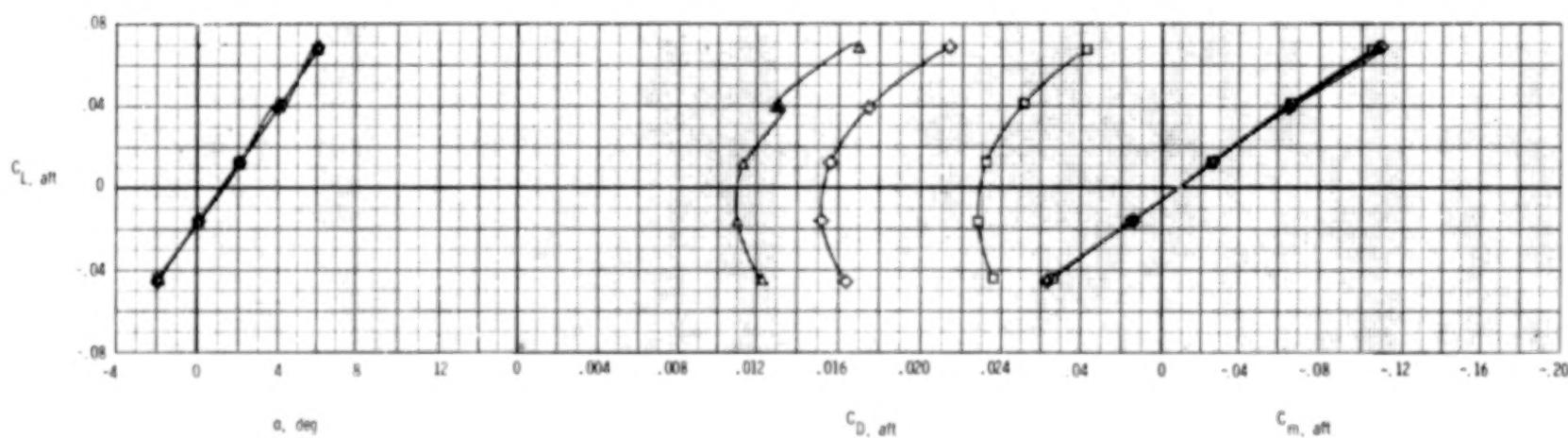
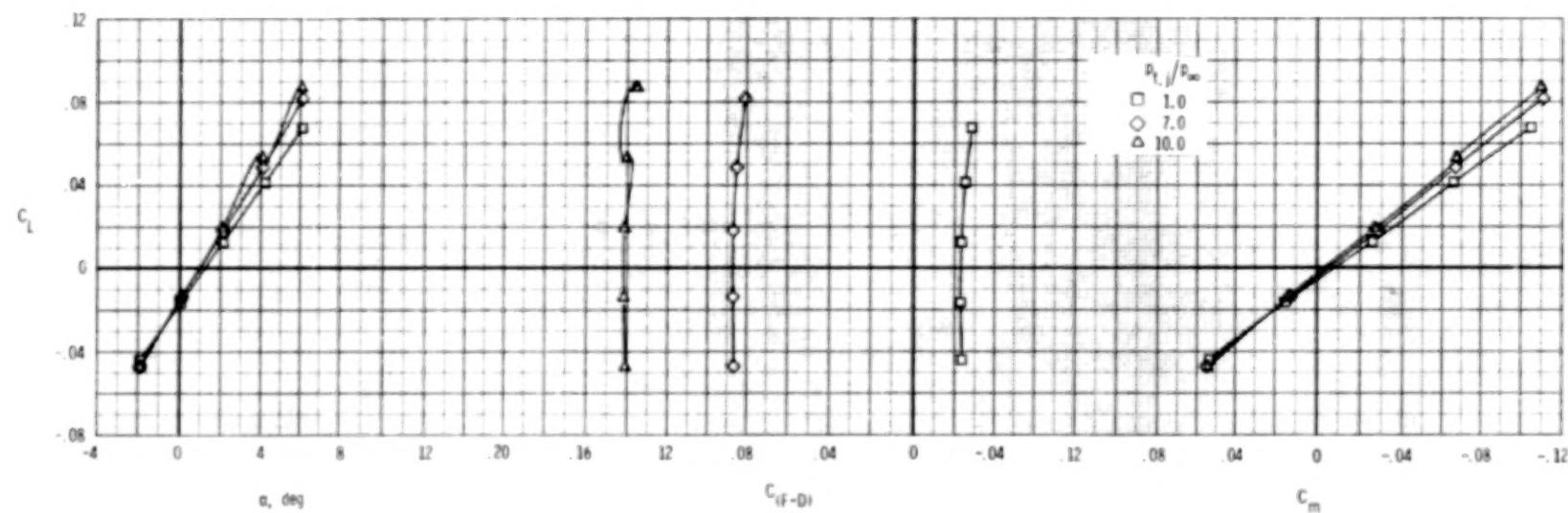
205

206



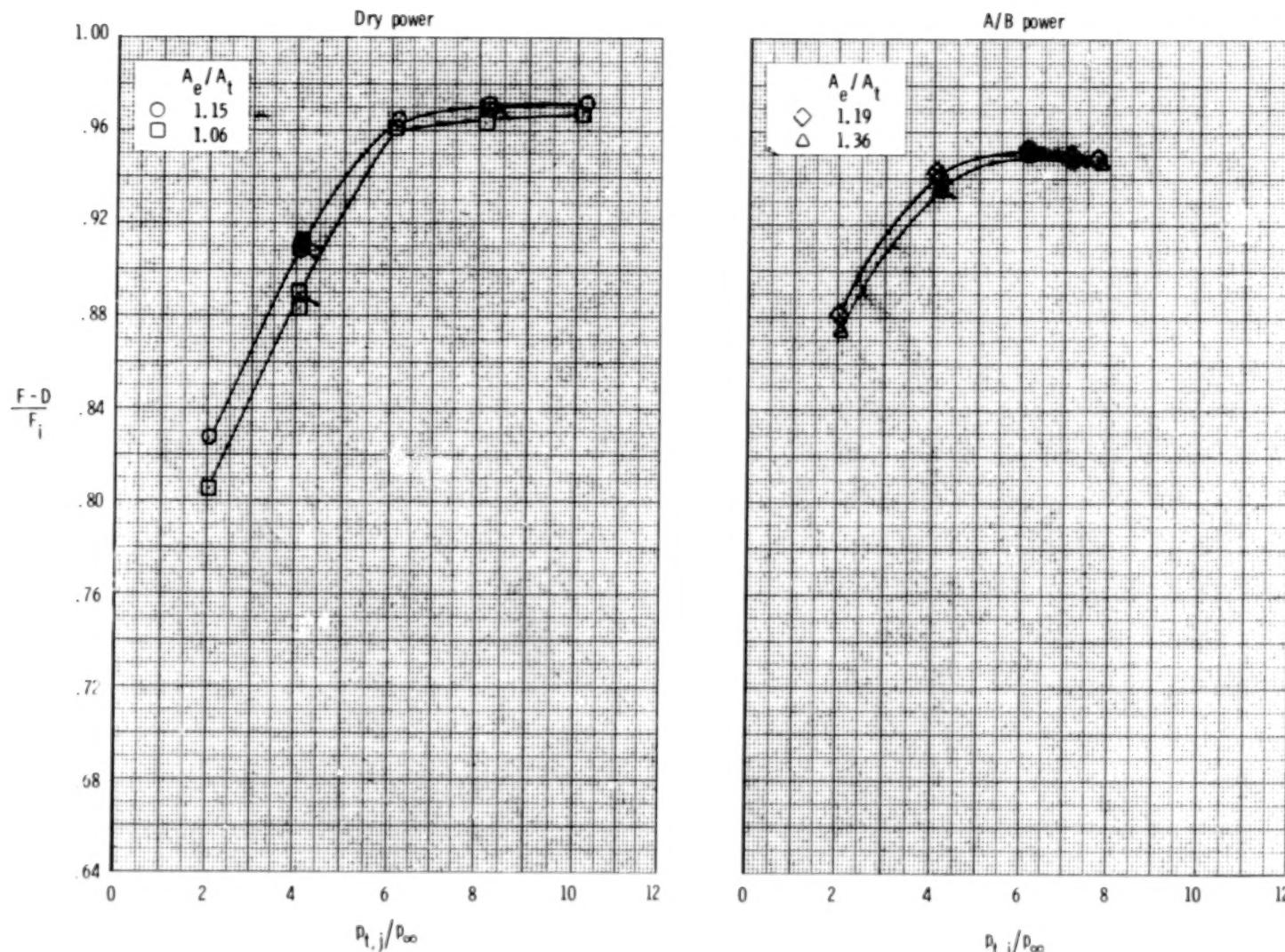
(b) $M = 0.90$.

Figure 83.- Continued.



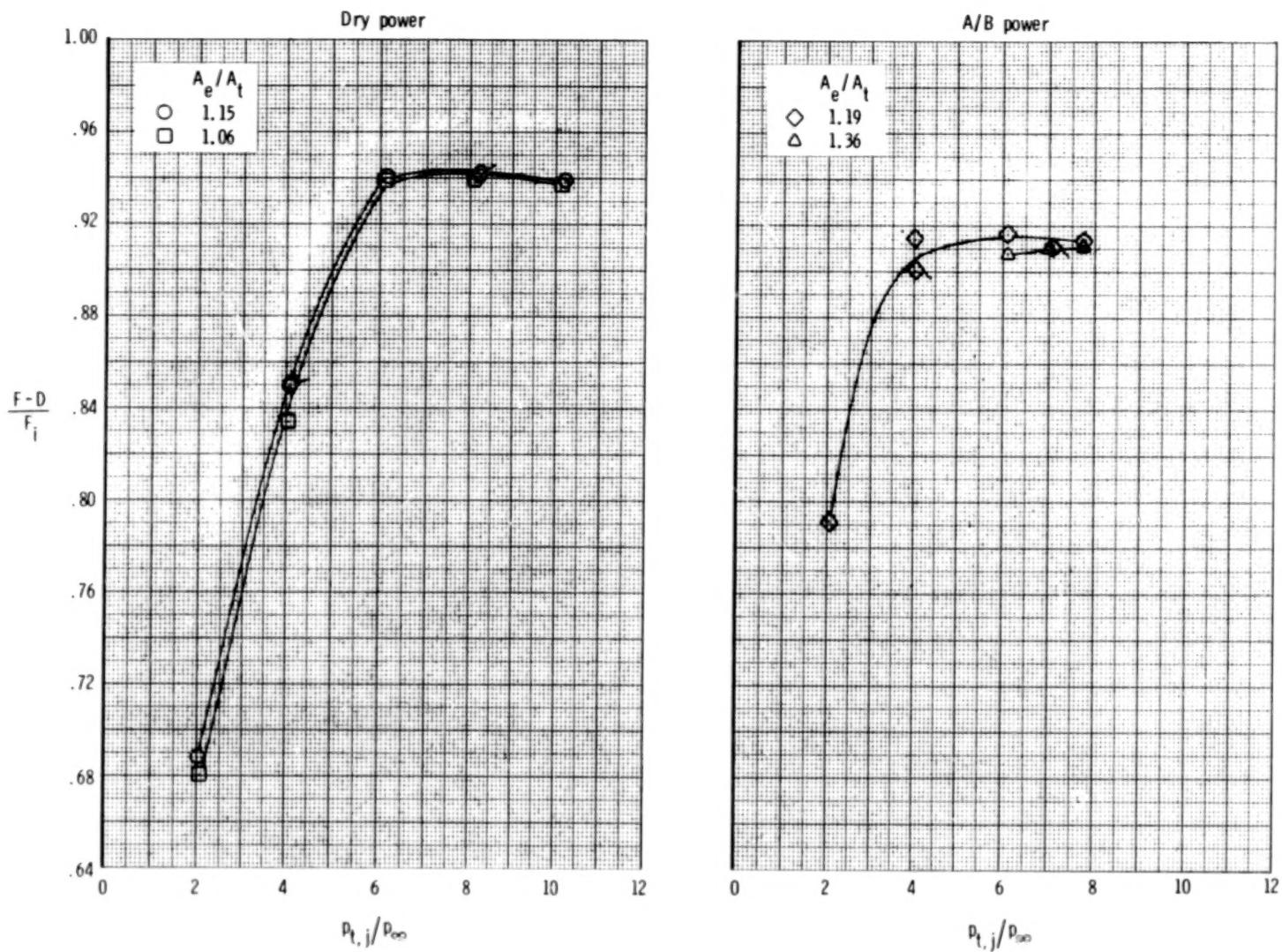
(c) $M = 1.20$.

Figure 83.- Concluded.



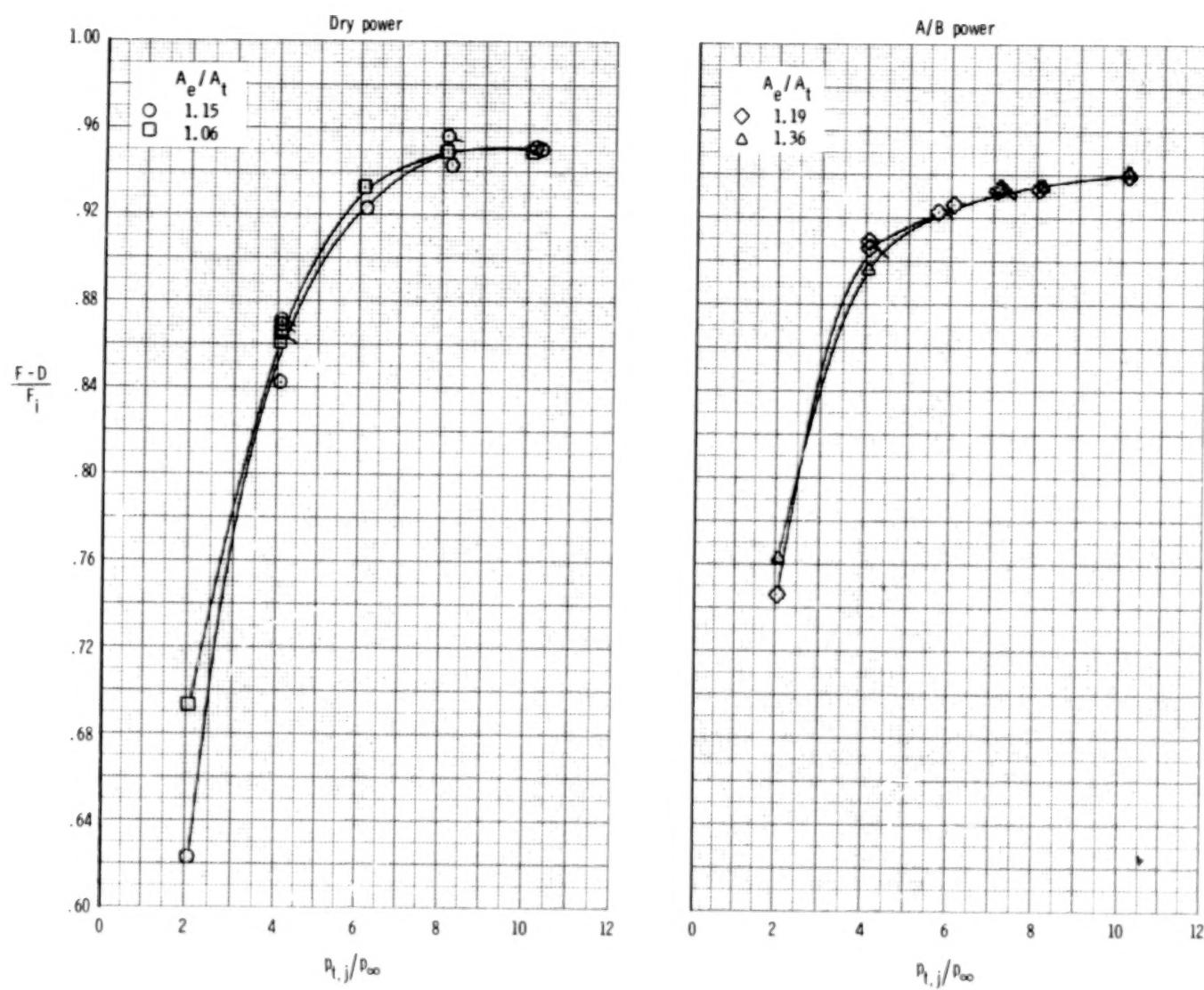
(a) $M = 0.60$; $\alpha \approx 0^\circ$.

Figure 84.- Effect of area ratio on afterbody performance, SERN nozzle. $\delta_h = 0^\circ$; $\delta_v = 0^\circ$.
Flagged symbols indicate repeat points.



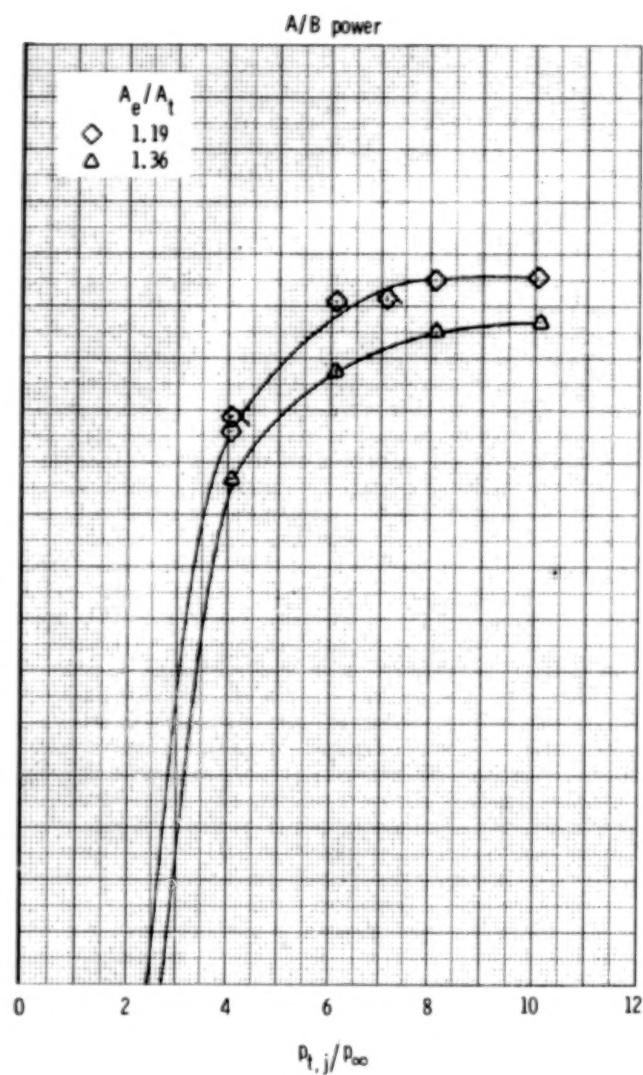
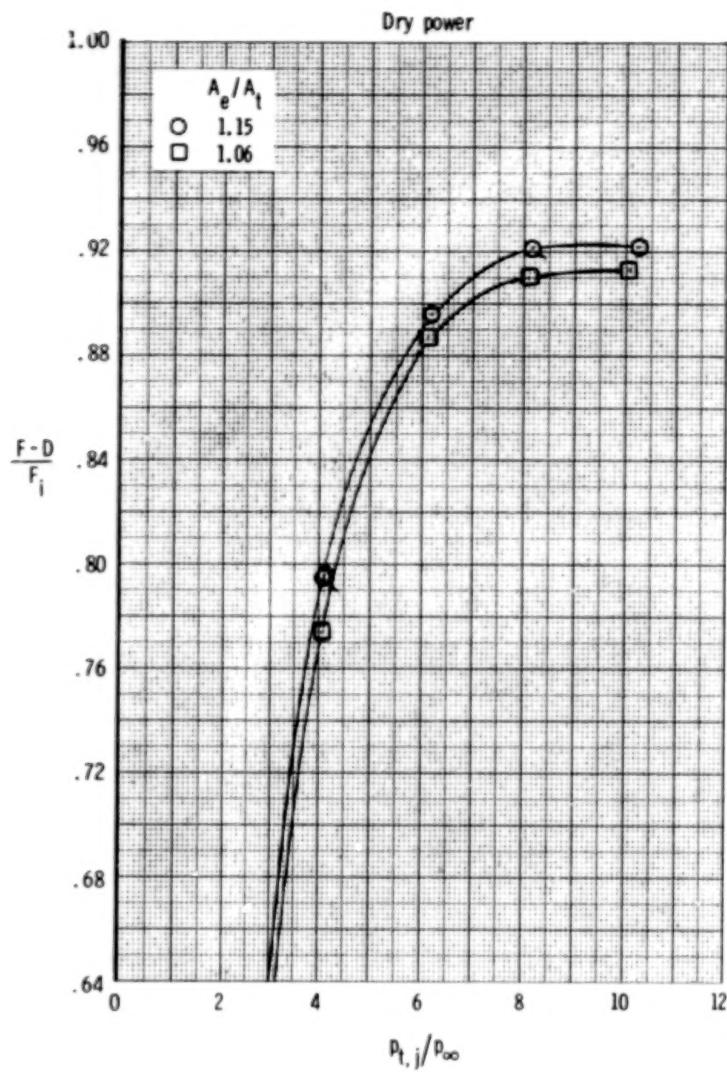
(b) $M = 0.60$; $\alpha \approx 6^0$.

Figure 84.- Continued.



(c) $M = 0.90$; $\alpha \approx 0^\circ$.

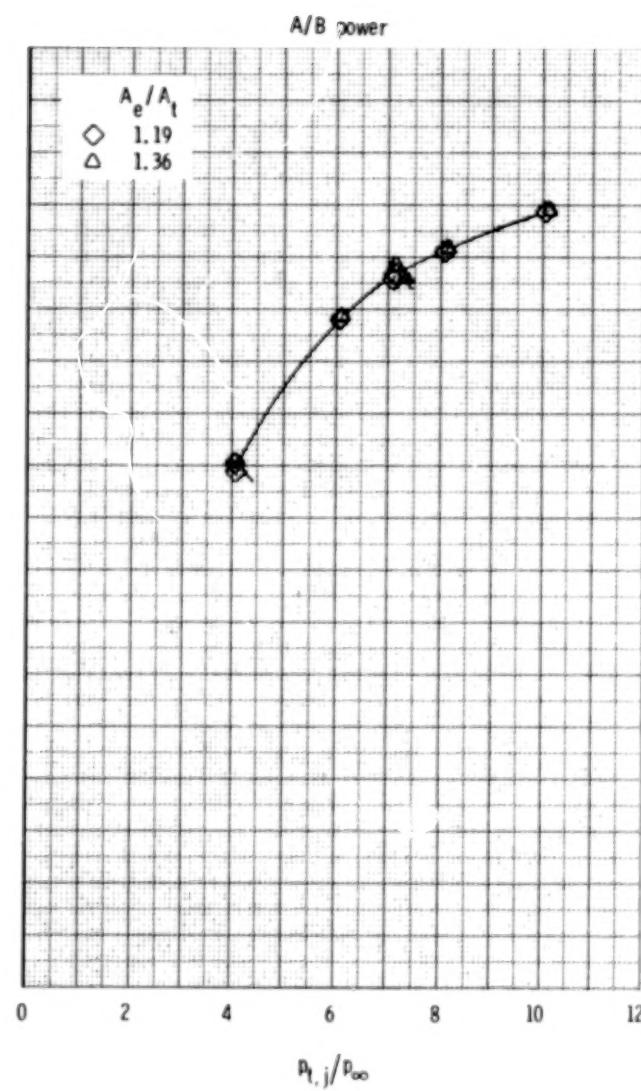
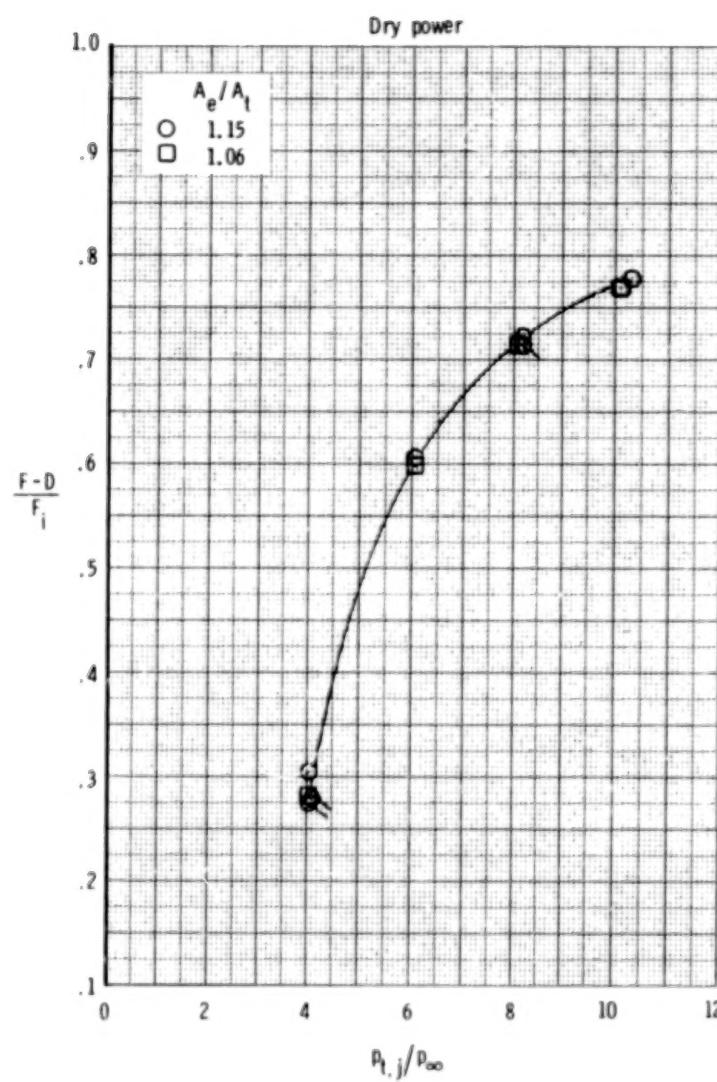
Figure 84.- Continued.



(d) $M = 0.90$; $\alpha \approx 6^\circ$.

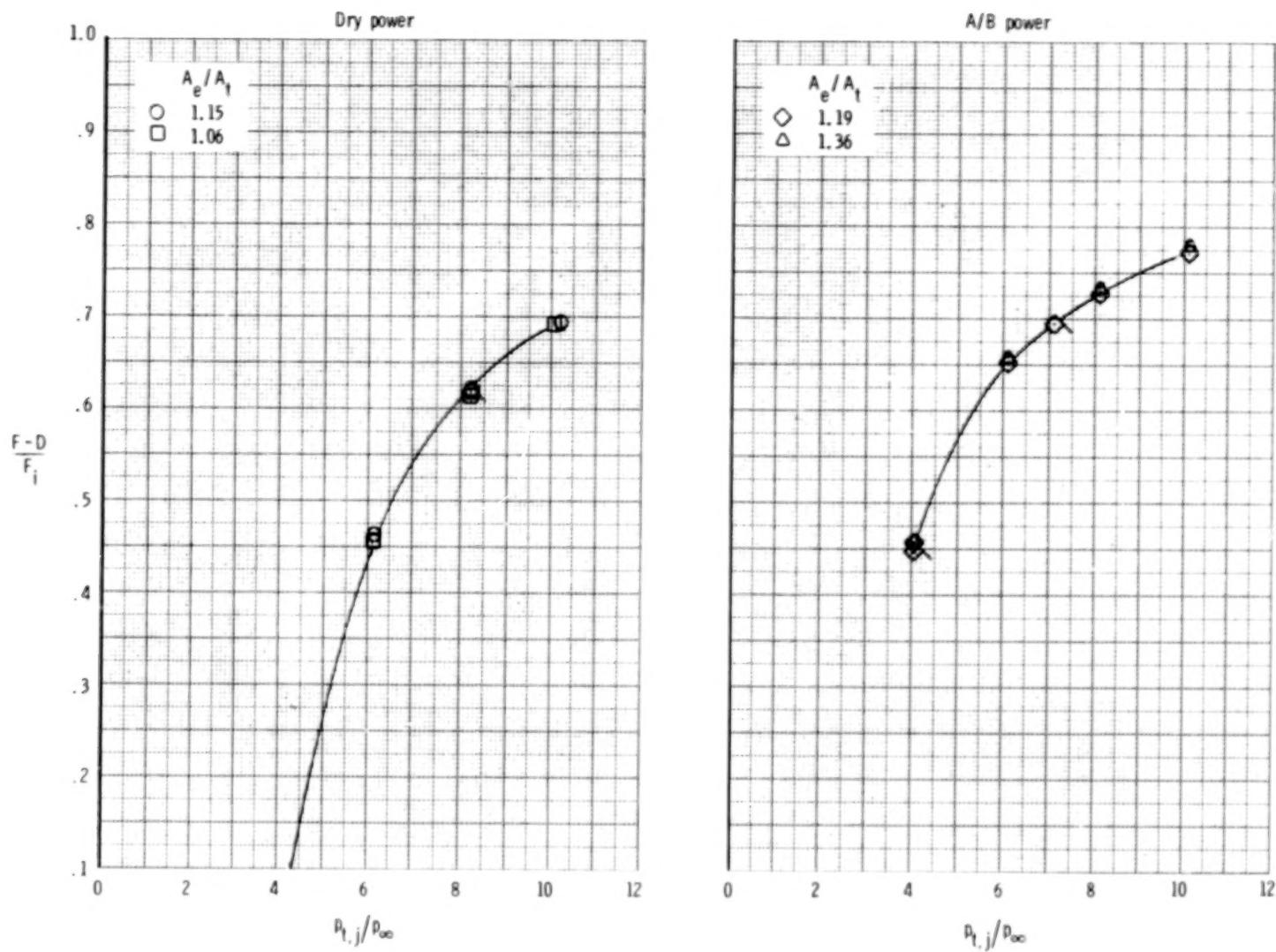
Figure 84.- Continued.

212



(e) $M = 1.20$; $\alpha \approx 0^\circ$.

Figure 84.- Continued.



(f) $M = 1.20$; $\alpha \approx 6^{\circ}$.

Figure 84.- Concluded.

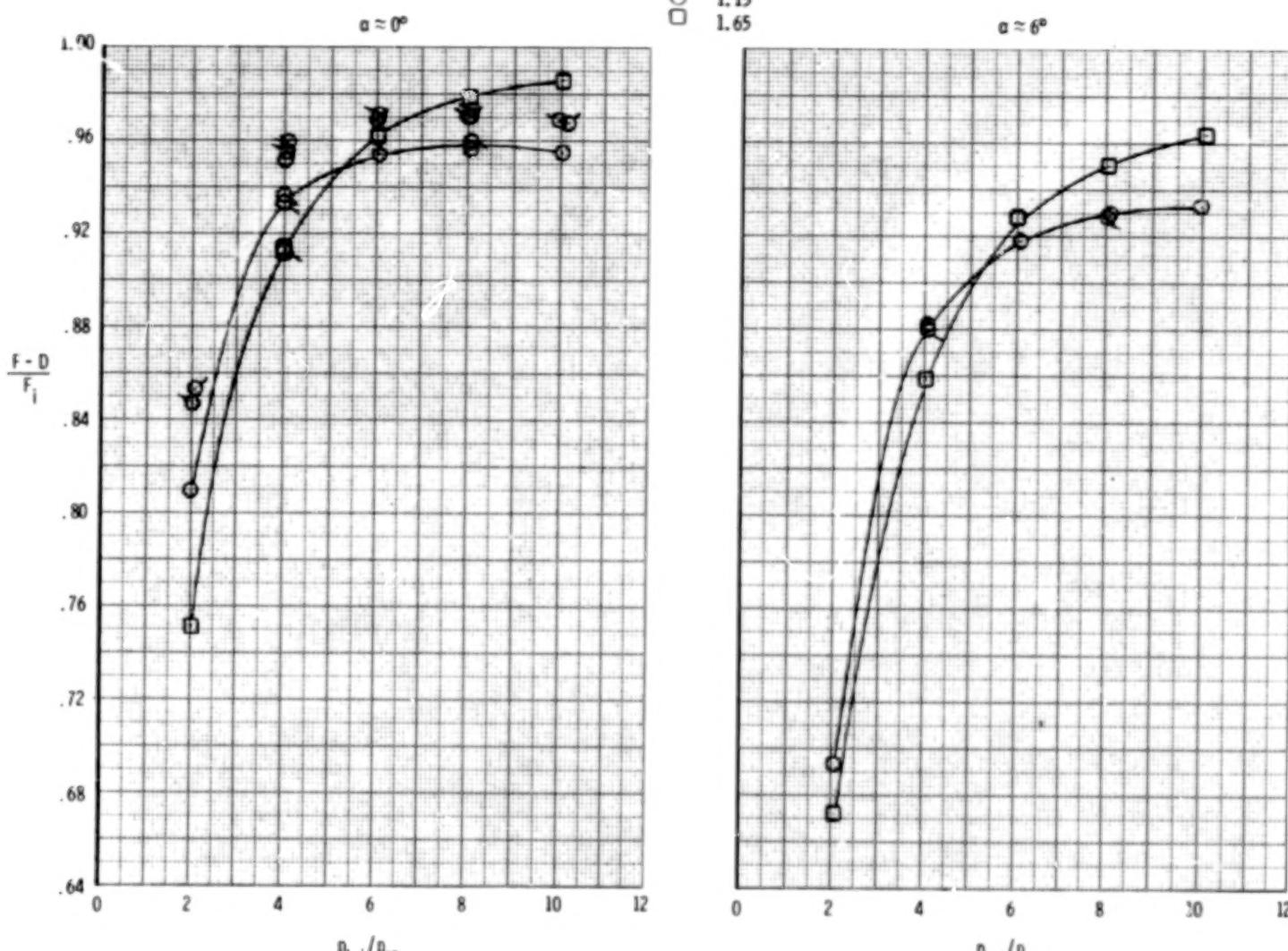
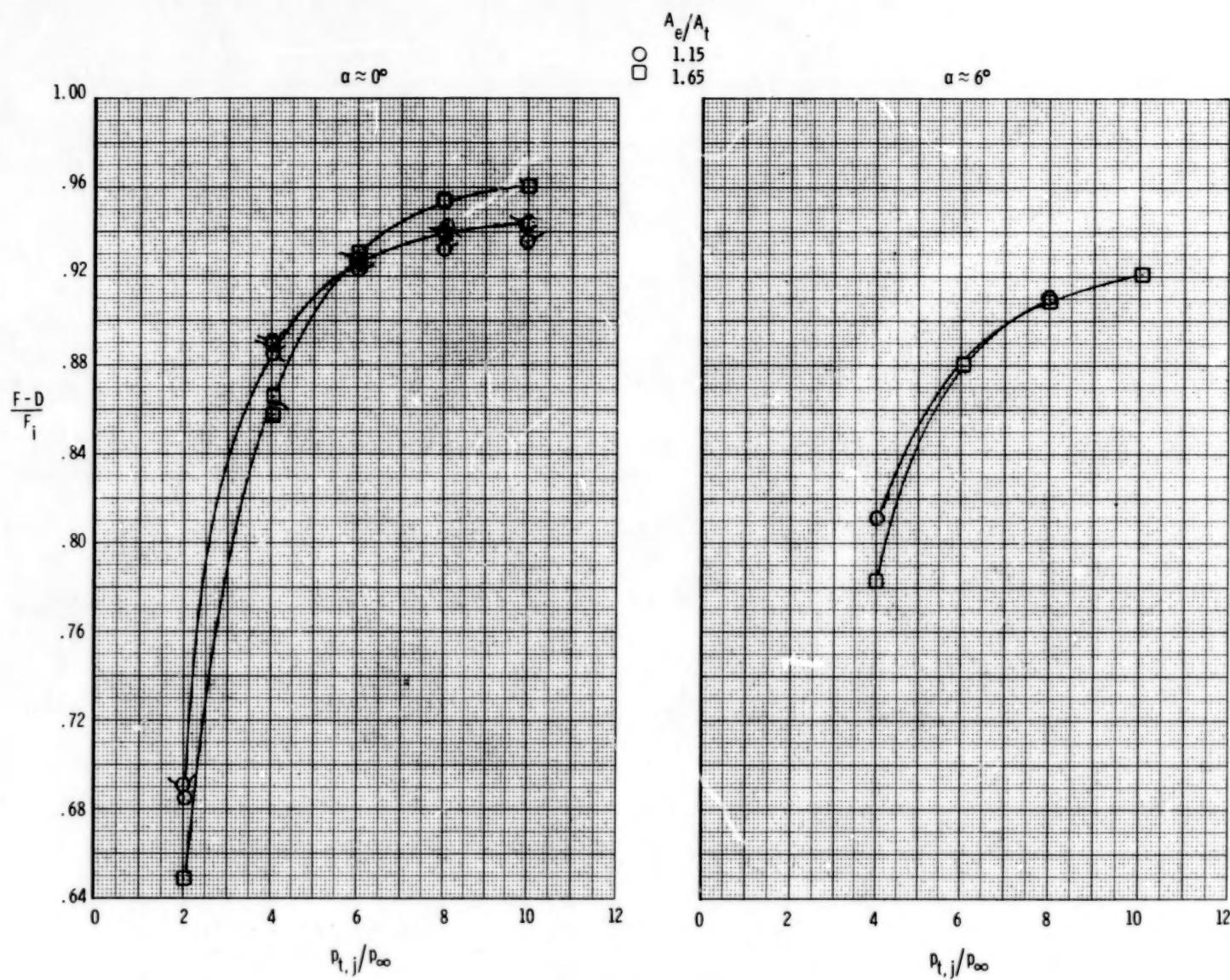
(a) $M = 0.60$.

Figure 85.- Effect of area ratio on afterbody performance, 2-D C-D nozzle, dry power. $\delta_h = 0^\circ$; $\delta_v = 0^\circ$.
 Flagged symbols indicate repeat points.



(b) $M = 0.90$.

Figure 85.- Continued.

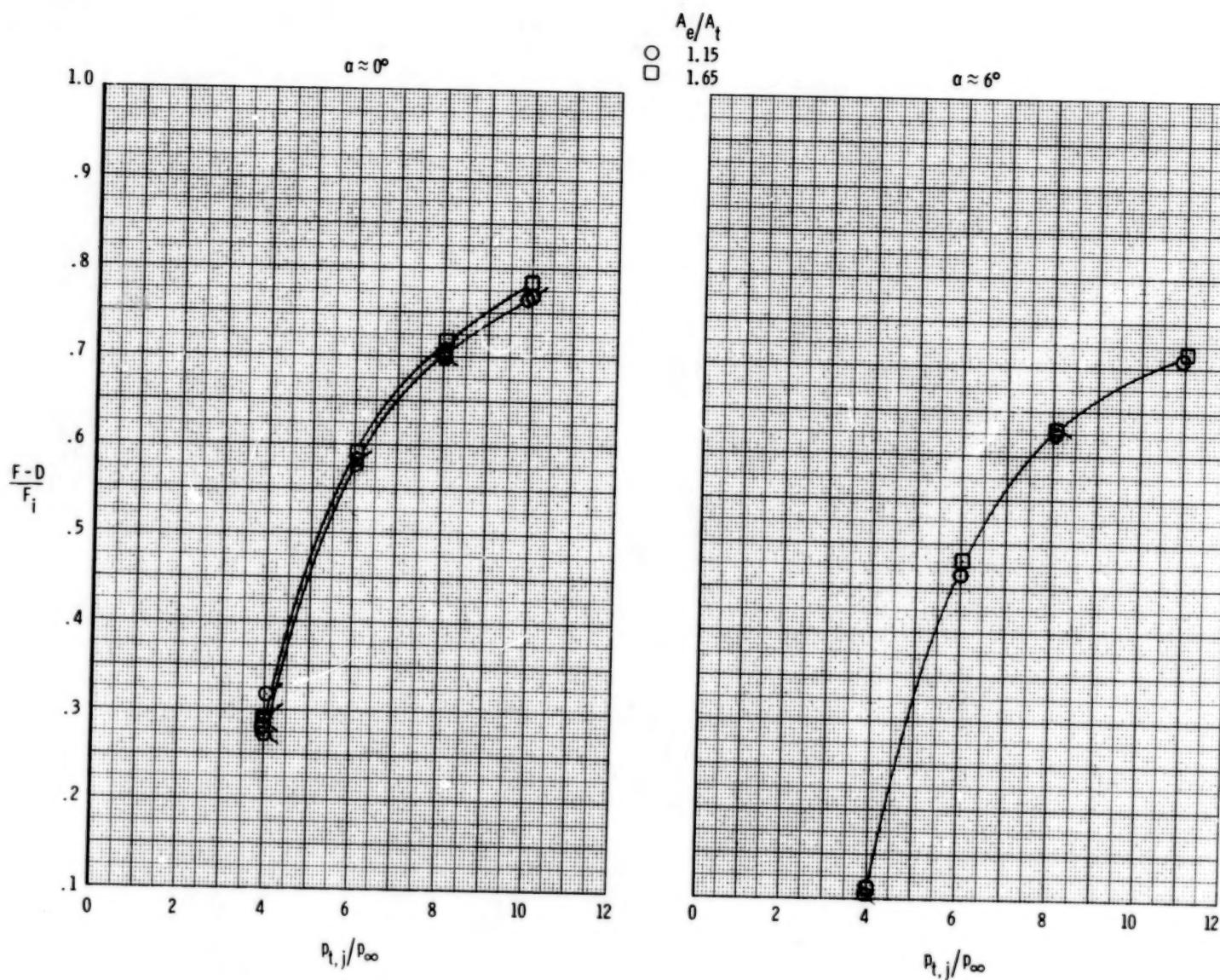
(c) $M = 1.20$.

Figure 85.- Concluded.

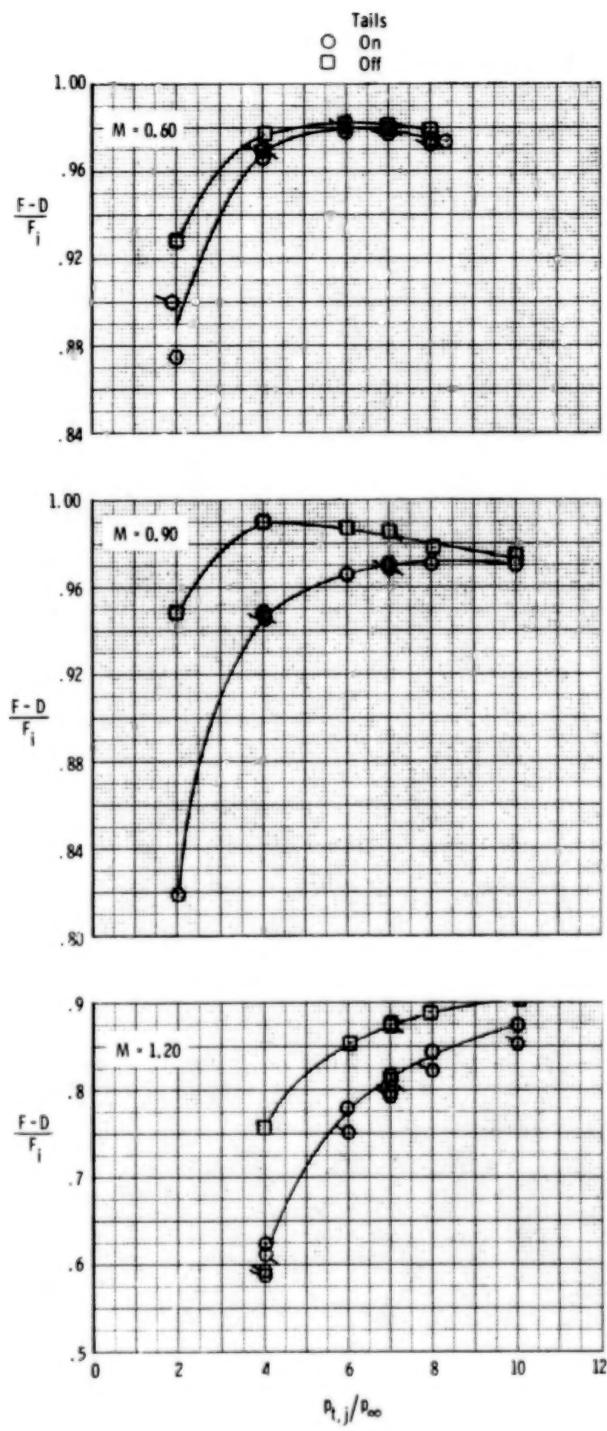
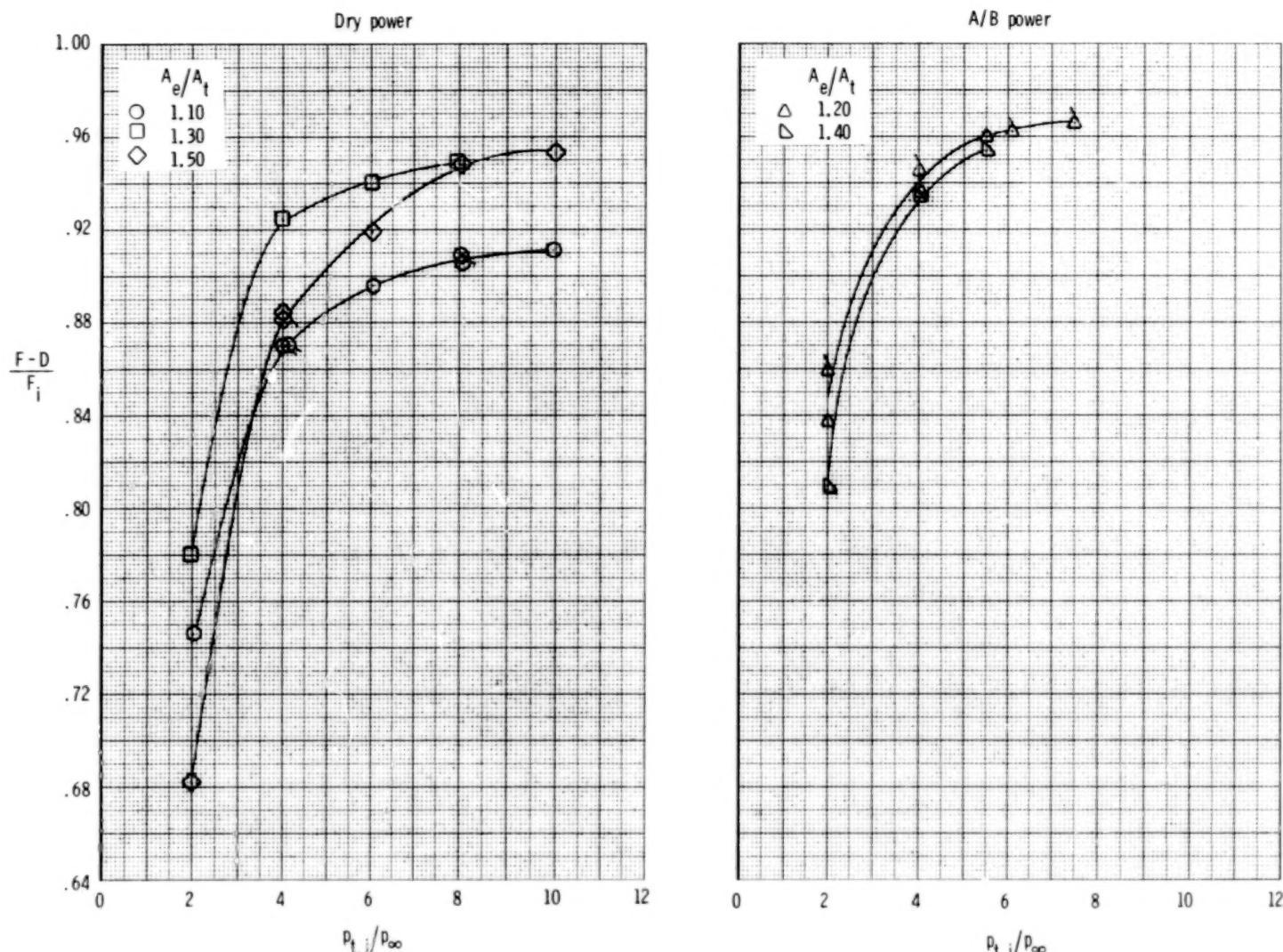
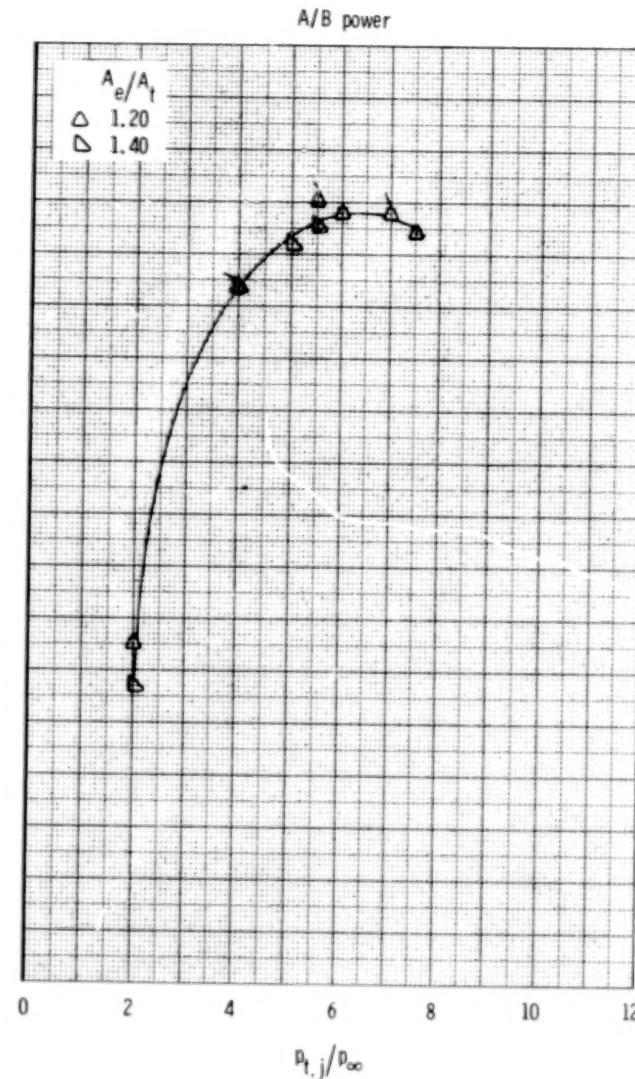
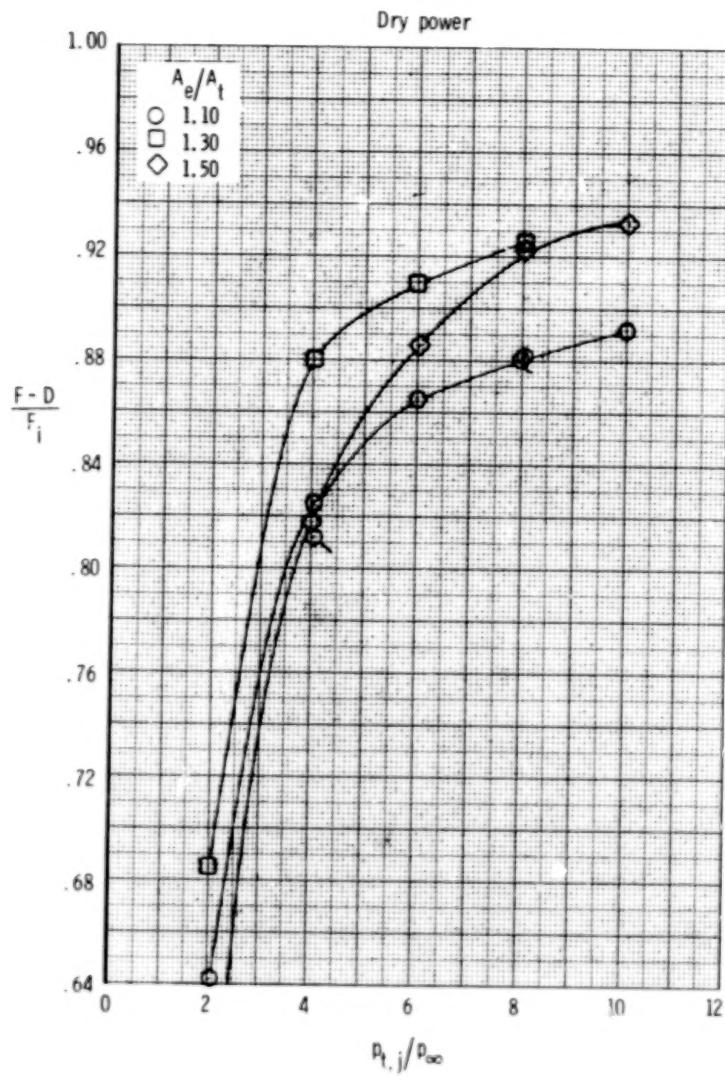


Figure 86.- Effect of tails on afterbody performance,
 2-D C-D nozzle, A/B power. $\delta_v = 0^\circ$; $\alpha \approx 0^\circ$.
 Flagged symbols indicate repeat points.



(a) $M = 0.60$; $\alpha \approx 0^0$.

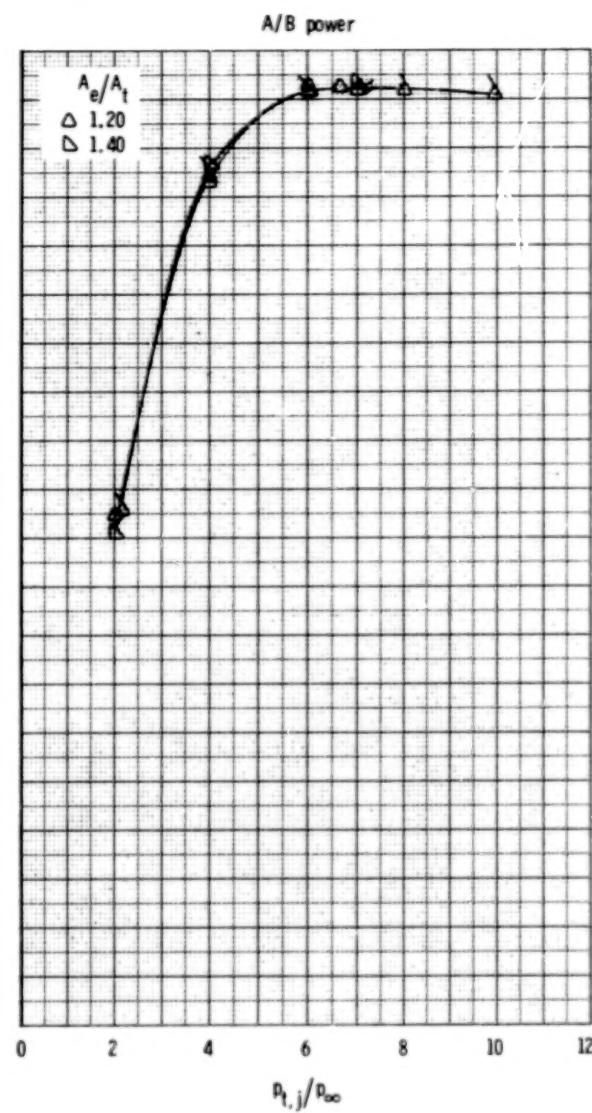
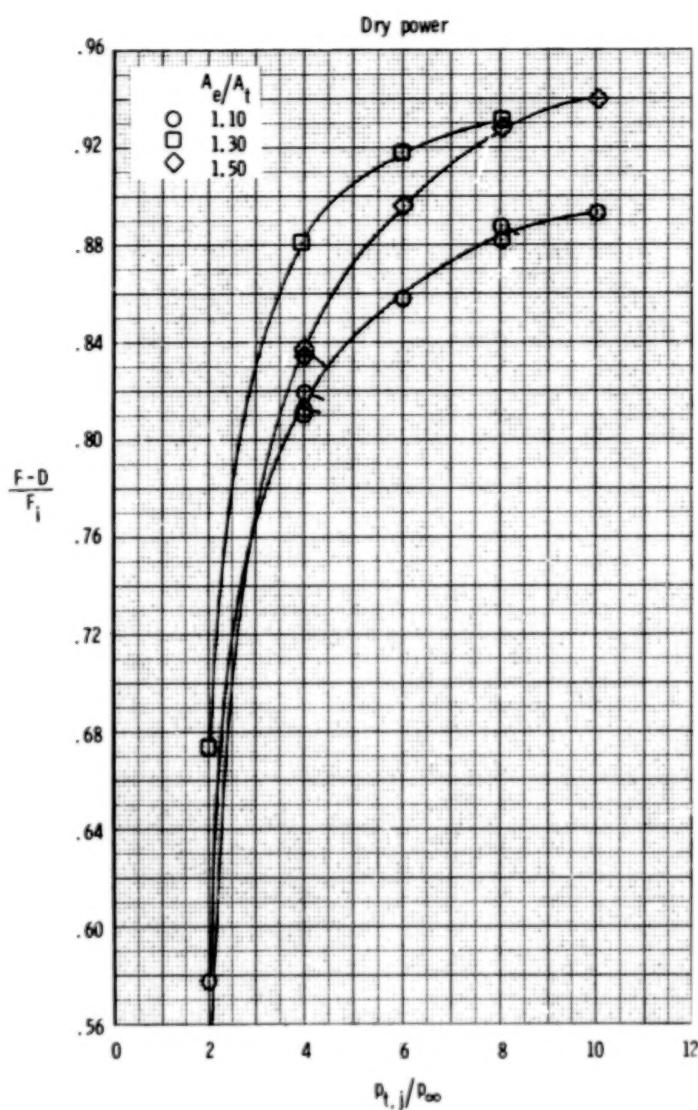
Figure 87. - Effect of area ratio on afterbody performance, wedge nozzle. $\delta_h = 0^0$; $\delta_v = 0^0$.
Flagged symbols indicate repeat points.



(b) $M = 0.60; \alpha \approx 6^\circ$.

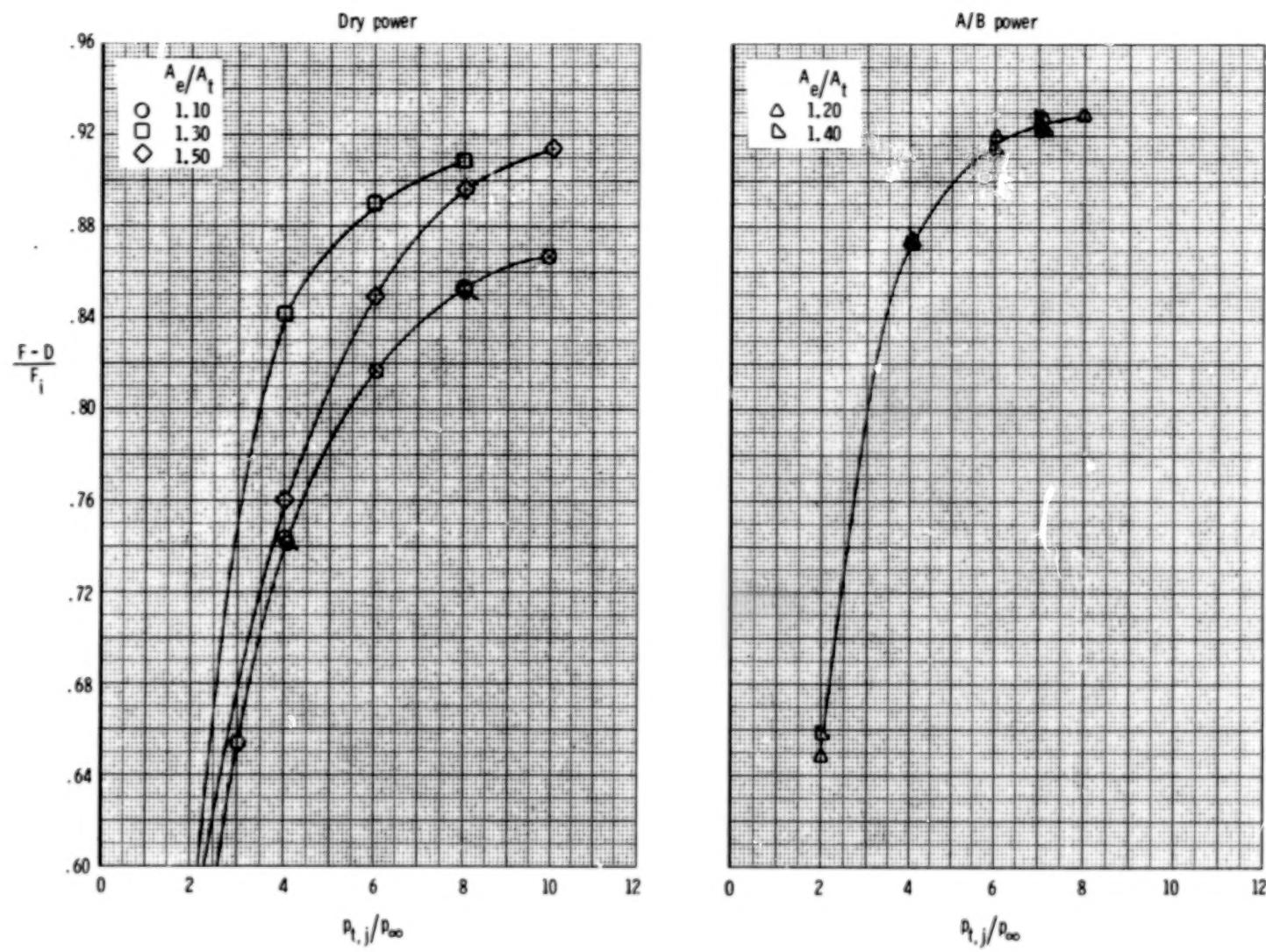
Figure 87.- Continued.

220



(c) $M = 0.90$; $\alpha \approx 0^\circ$.

Figure 87.- Continued.

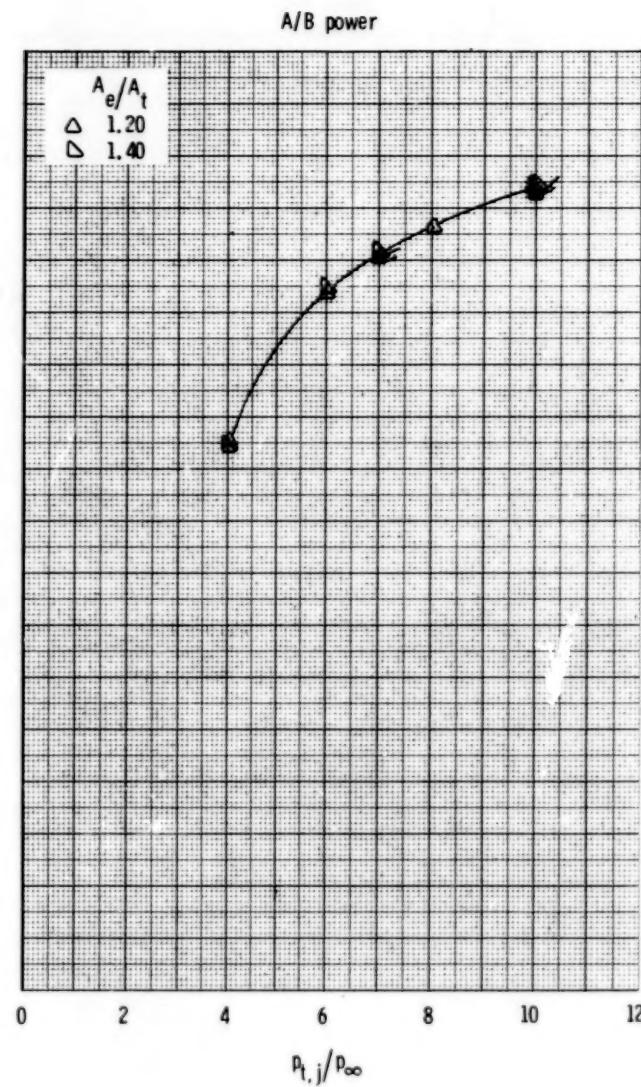
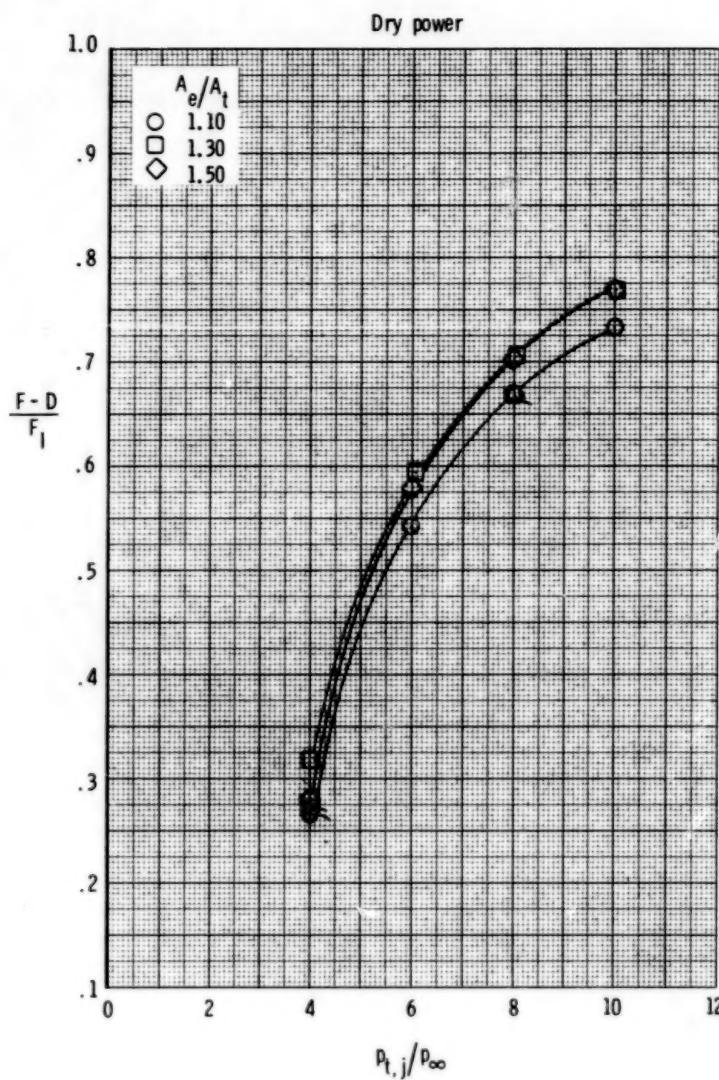


(d) $M = 0.90$; $\alpha = 6^\circ$.

Figure 87.- Continued.

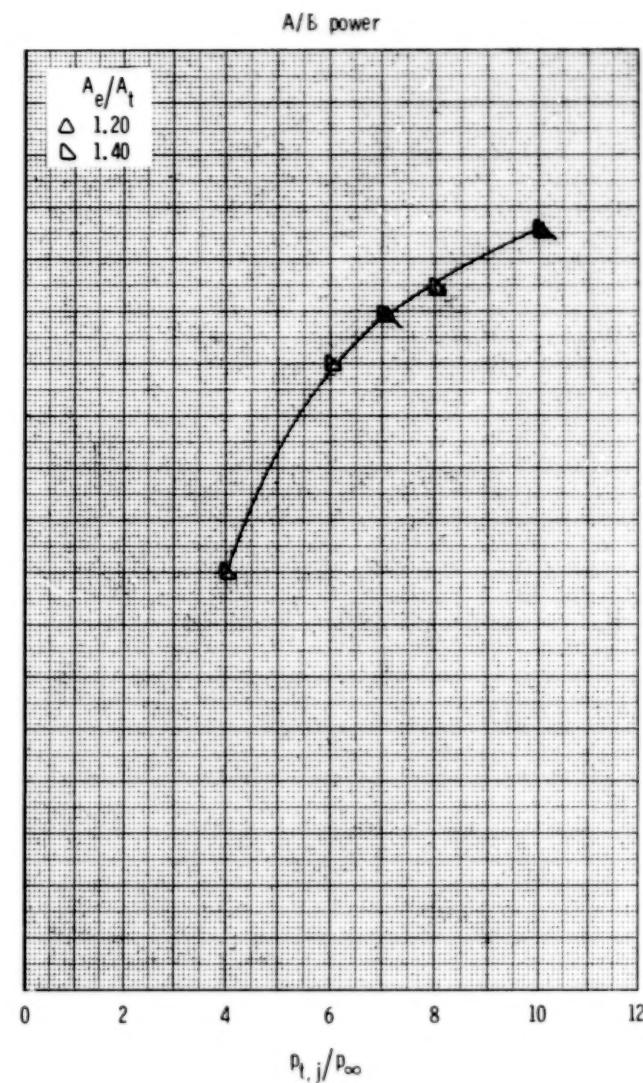
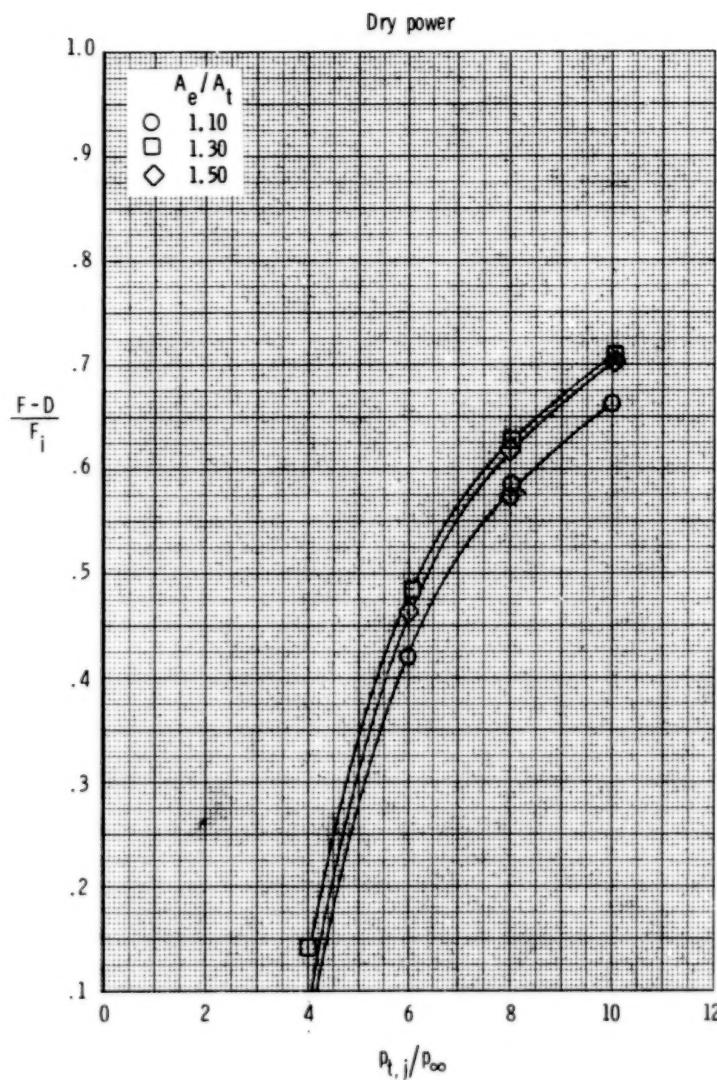
221

222



(e) $M = 1.20$; $\alpha \approx 0^\circ$.

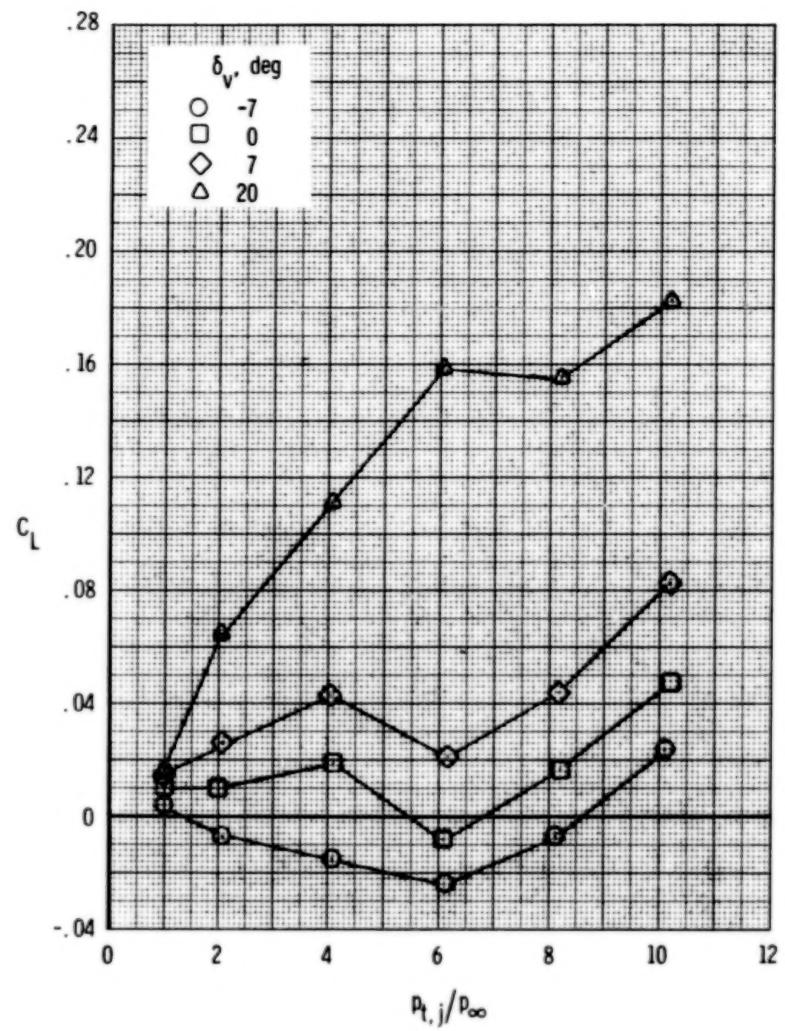
Figure 87.- Continued.



(f) $M = 1.20$; $\alpha \approx 6^0$.

Figure 87.- Concluded.

224



(a) $M = 0.60$.

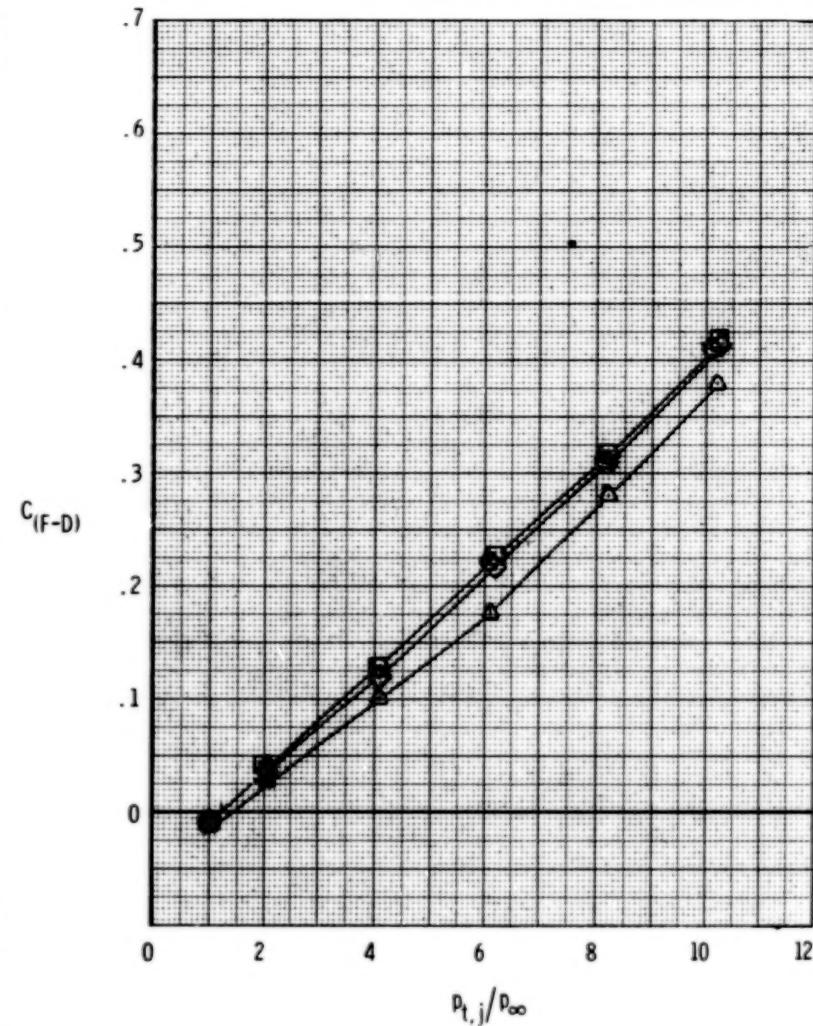
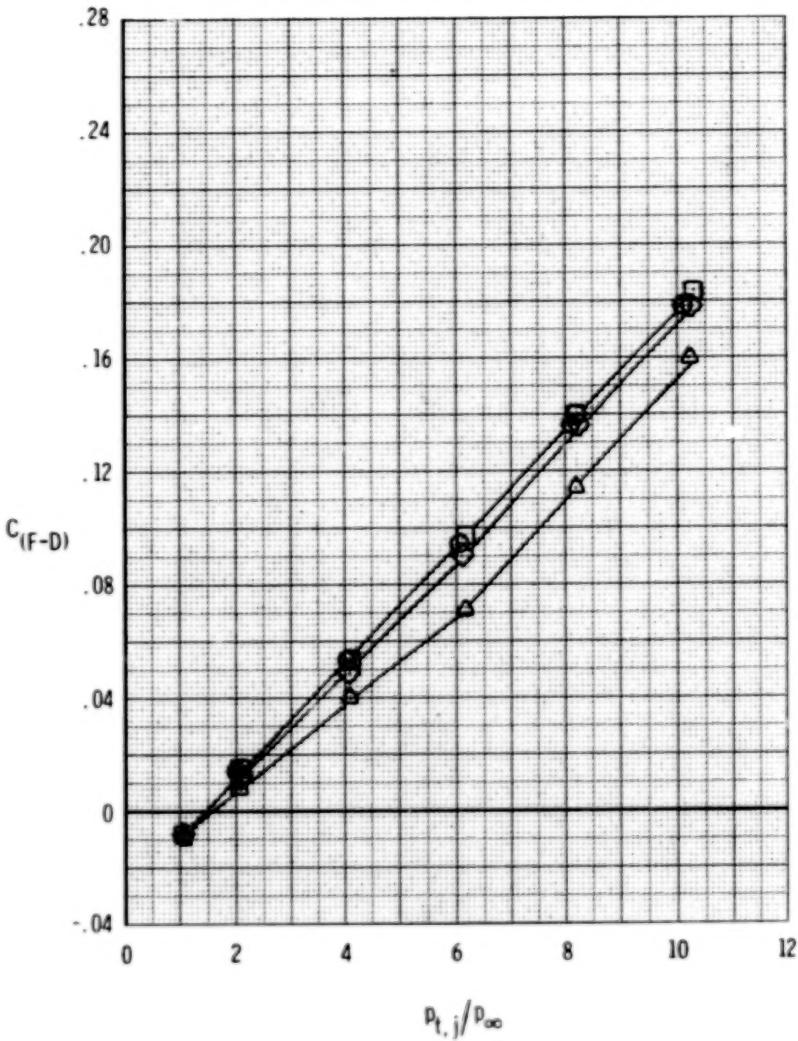
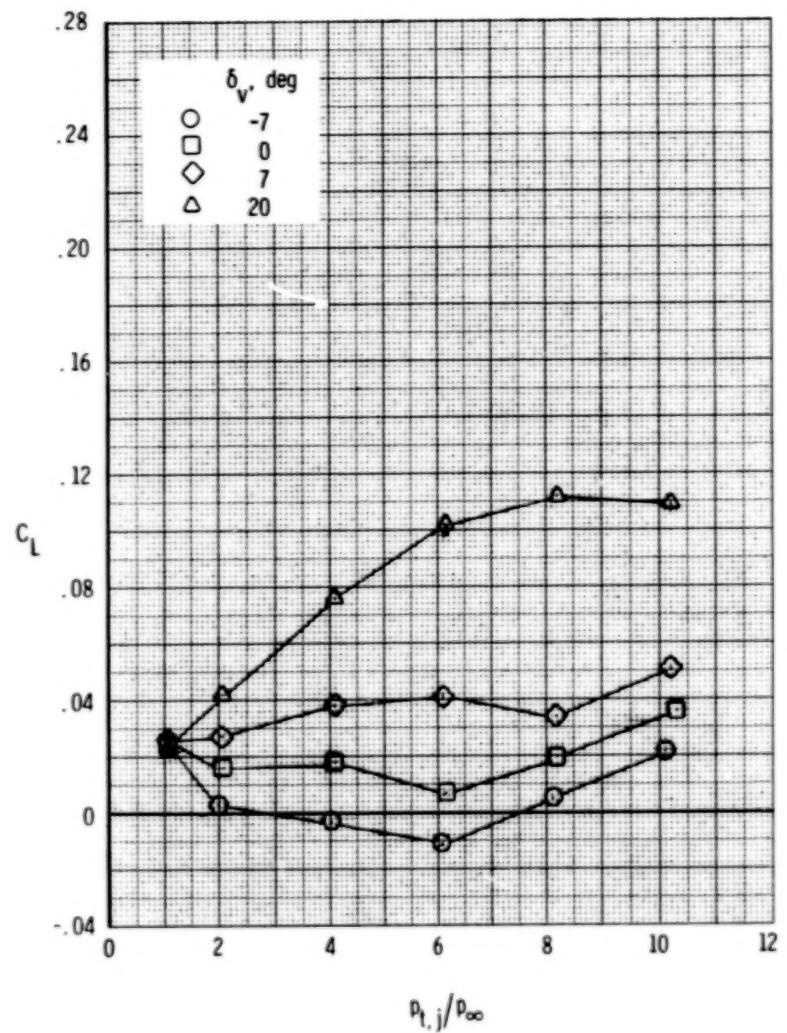


Figure 88.- Effect of vectoring on measured afterbody forces, SERN nozzle, dry power. $\delta_h = 0^0$; $\alpha = 0^0$.

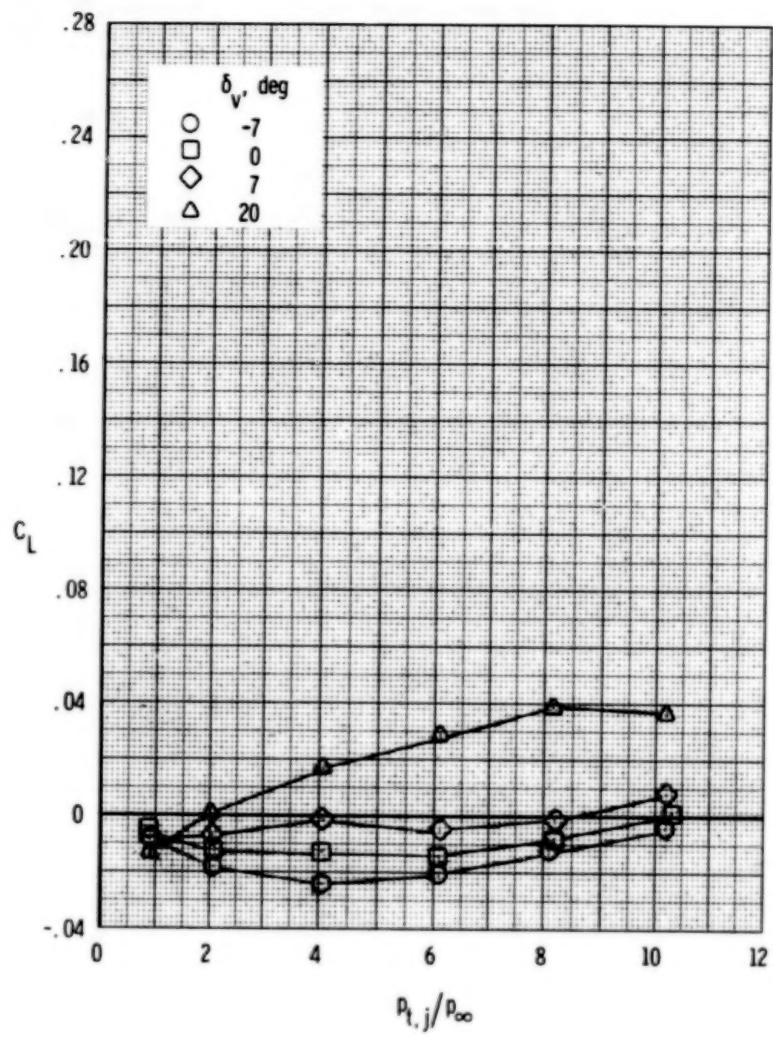


(b) $M = 0.90$.

Figure 88.- Continued.

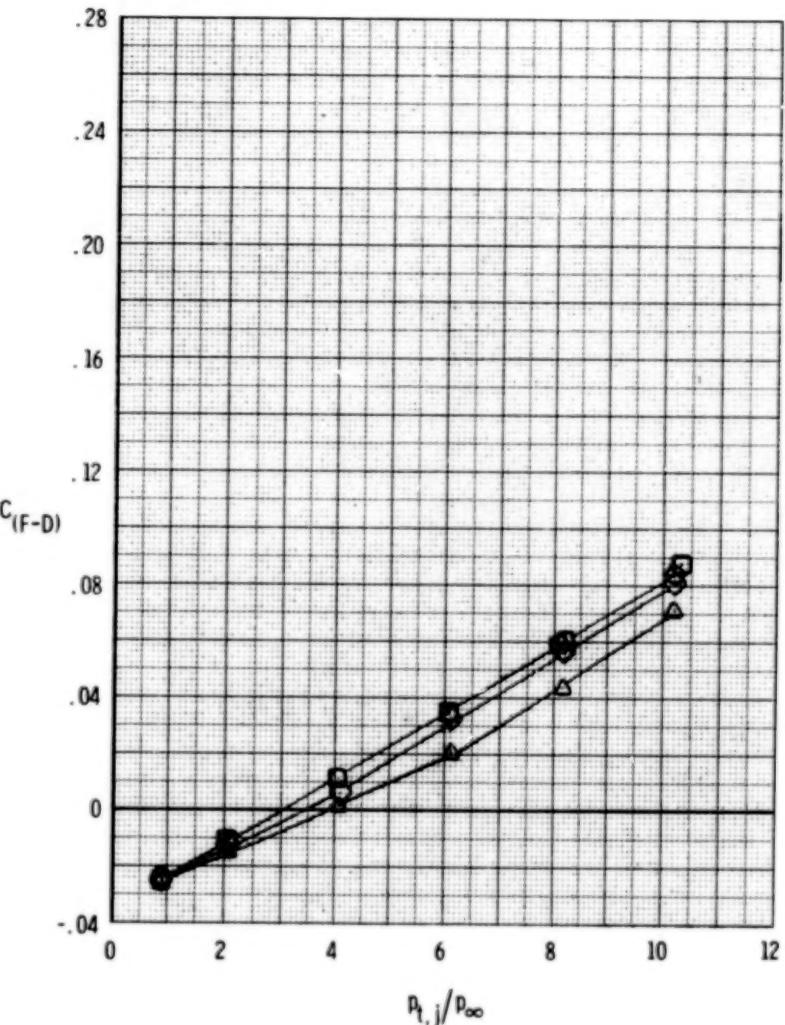
225

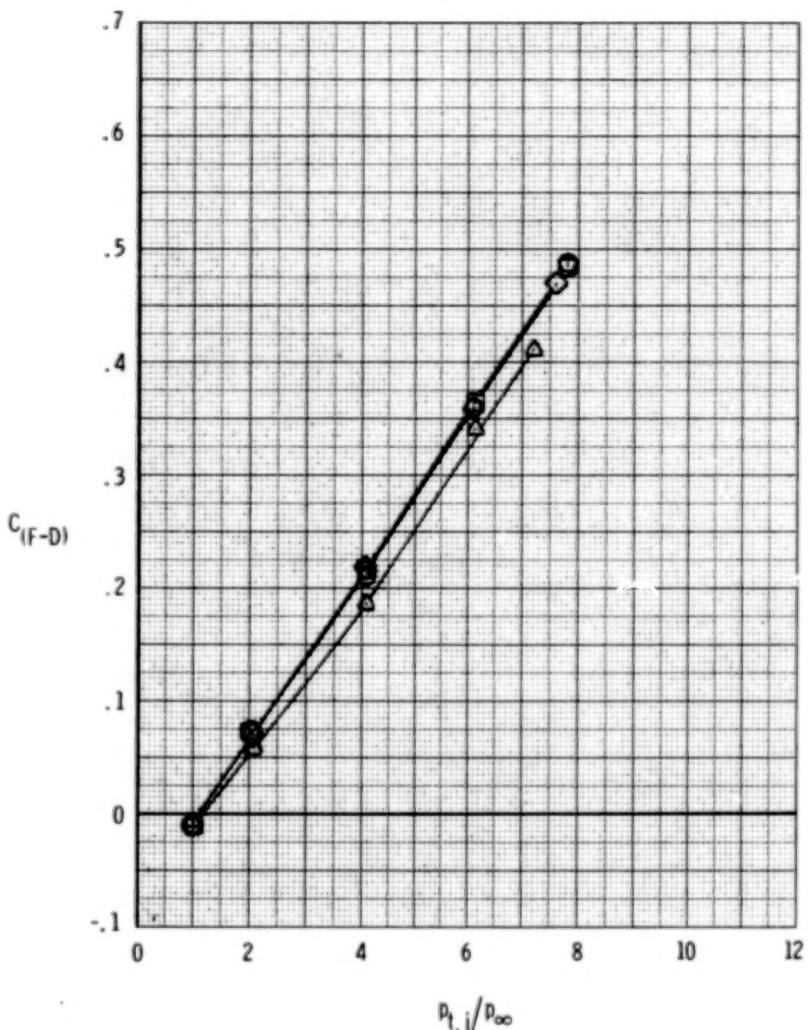
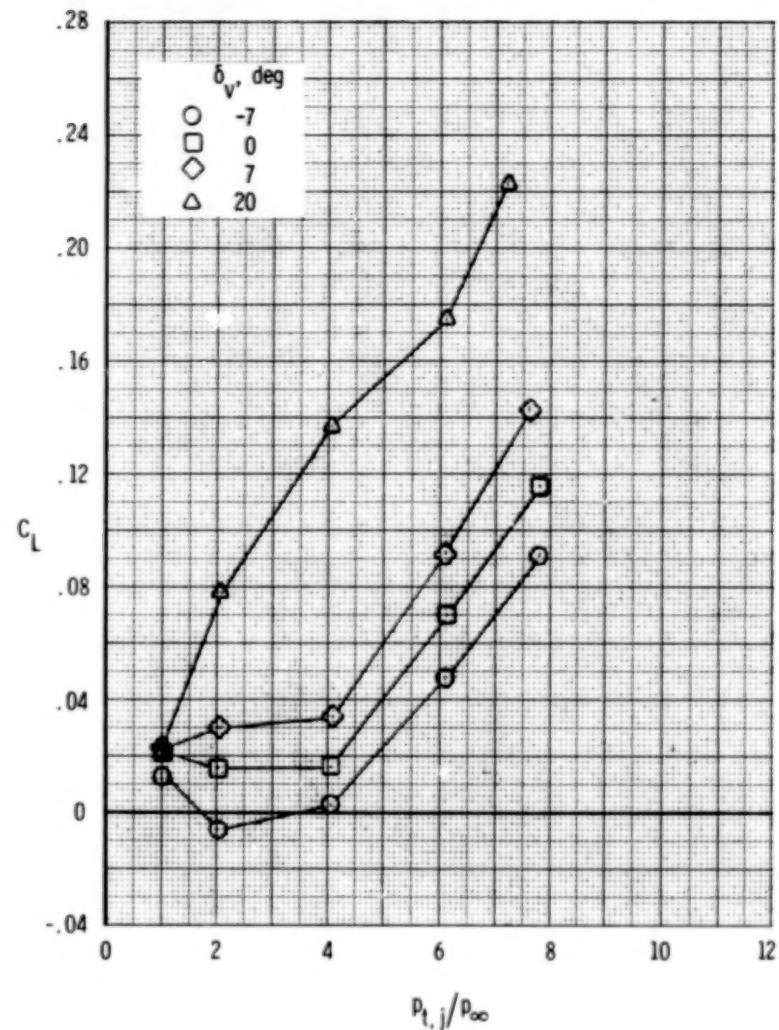
226



(c) $M = 1.20$.

Figure 88.- Concluded.





(a) $M = 0.60$.

Figure 89.- Effect of vectoring on measured afterbody forces, SERN nozzle, A/B power. $\delta_h = 0^{\circ}$; $\alpha = 0^{\circ}$.

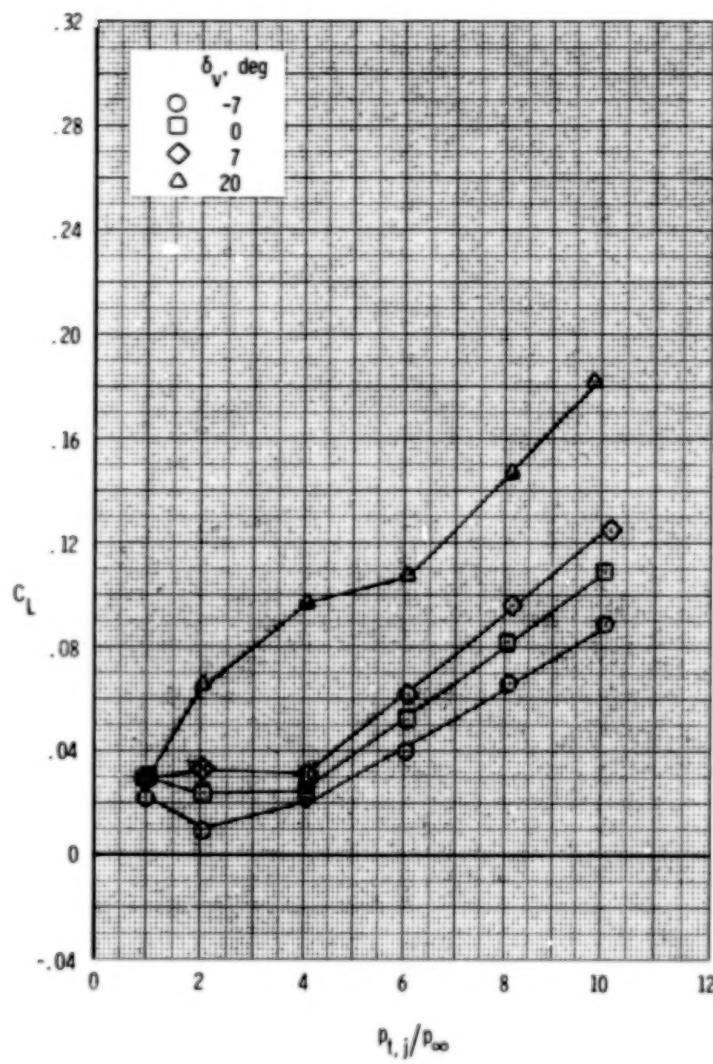
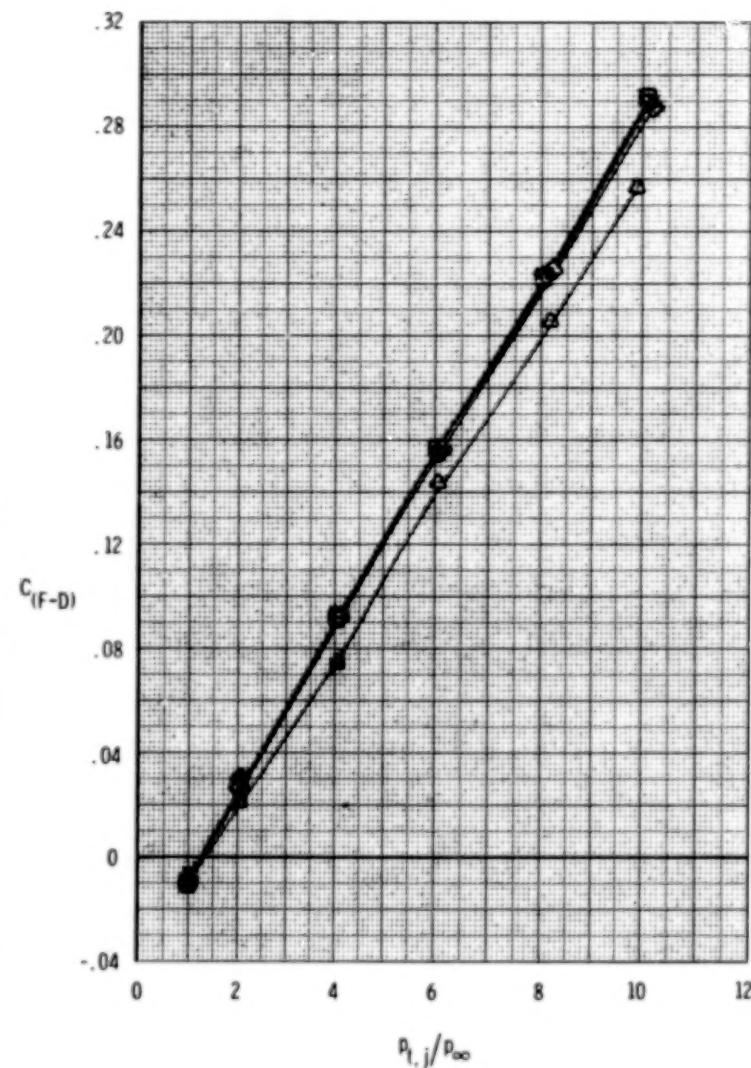
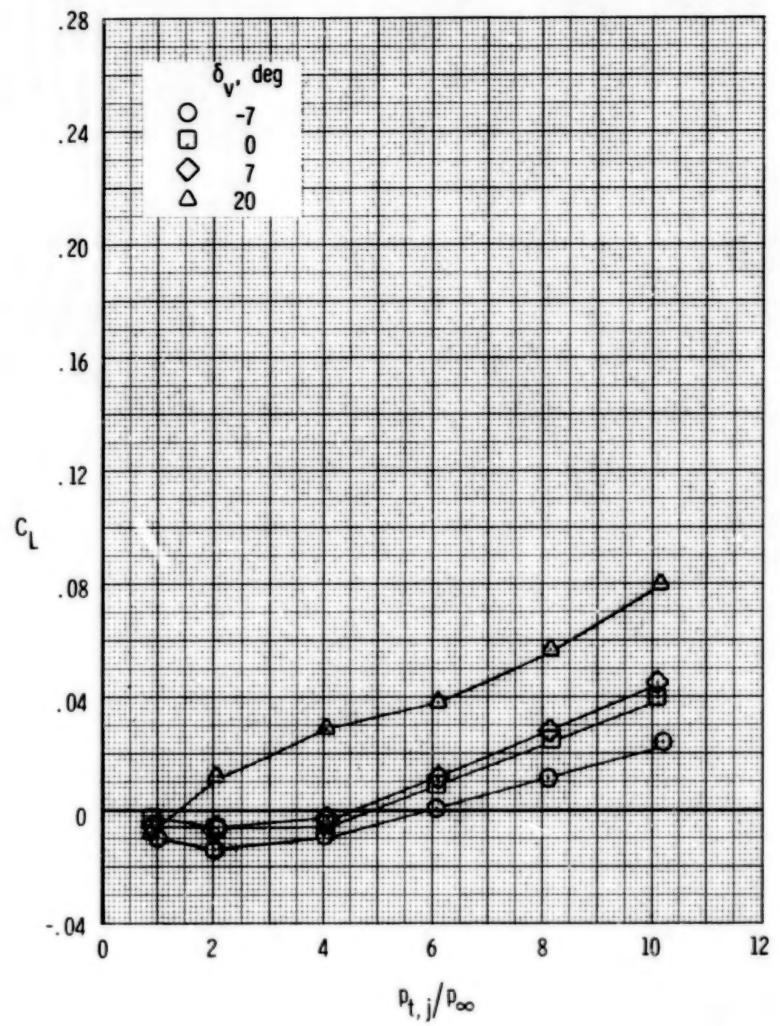
(b) $M = 0.90$.

Figure 89.- Continued.





(c) $M = 1.20.$

Figure 89.- Concluded.

229

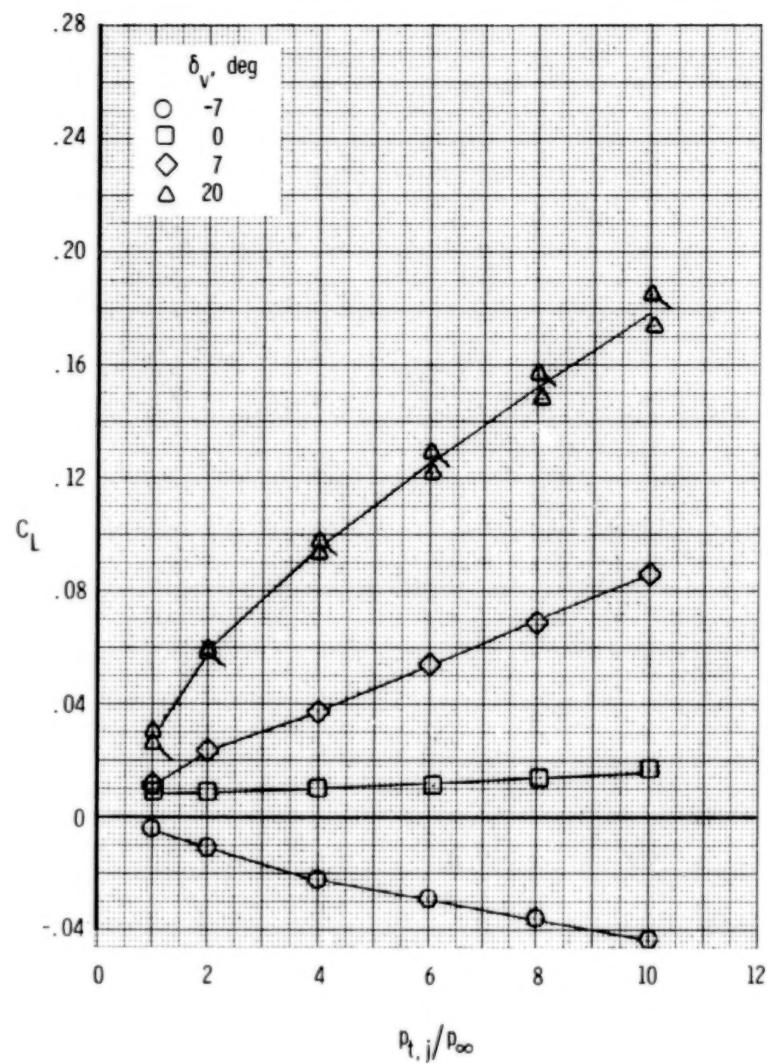
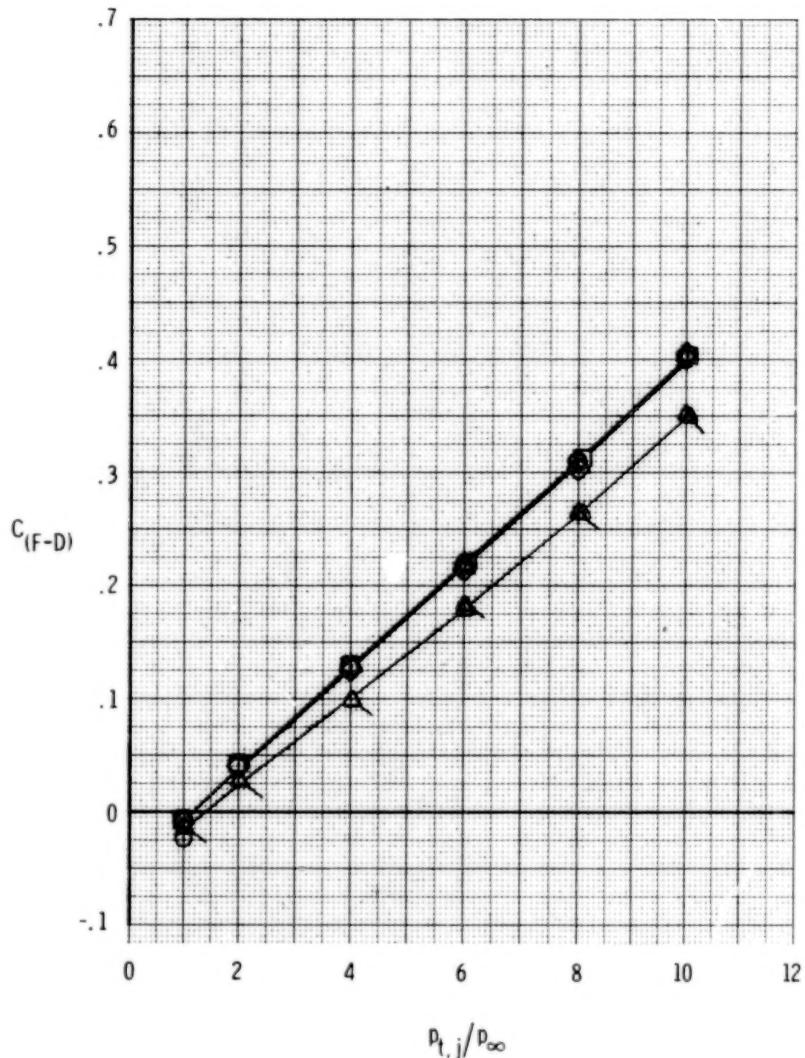
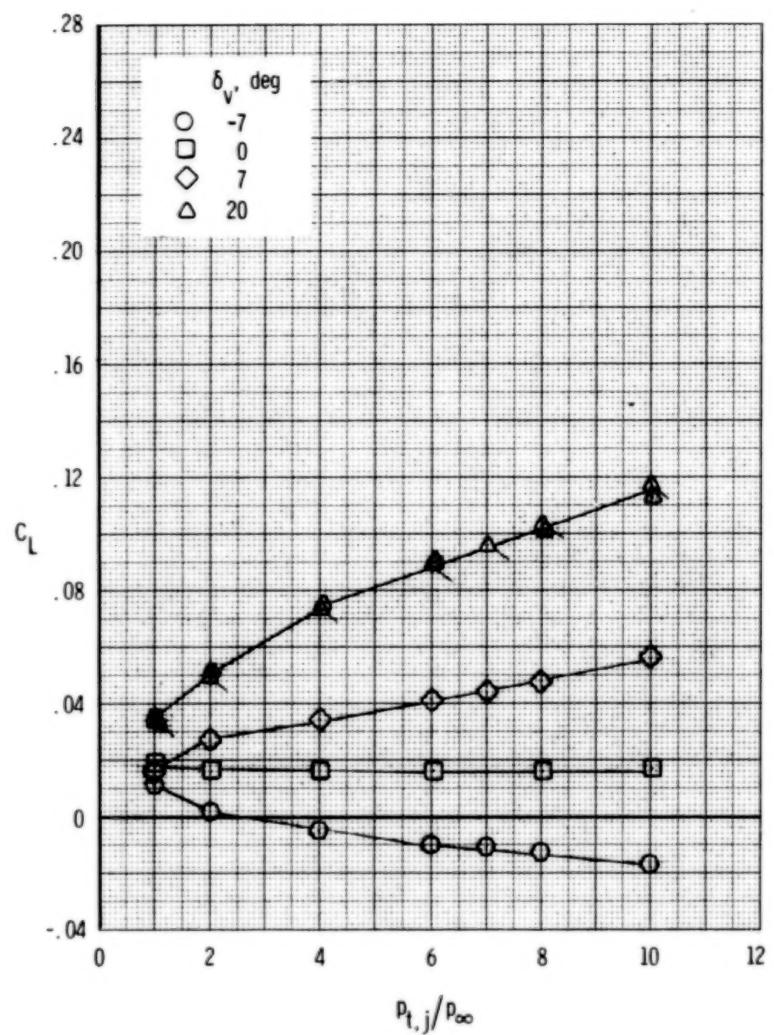
(a) $M = 0.60$.

Figure 90. - Effect of vectoring on measured afterbody forces, 2-D C-D nozzle, dry power. $\delta_h = 0^\circ$; $\alpha = 0^\circ$.
Flagged symbols indicate repeat points.



(b) $M = 0.90$.

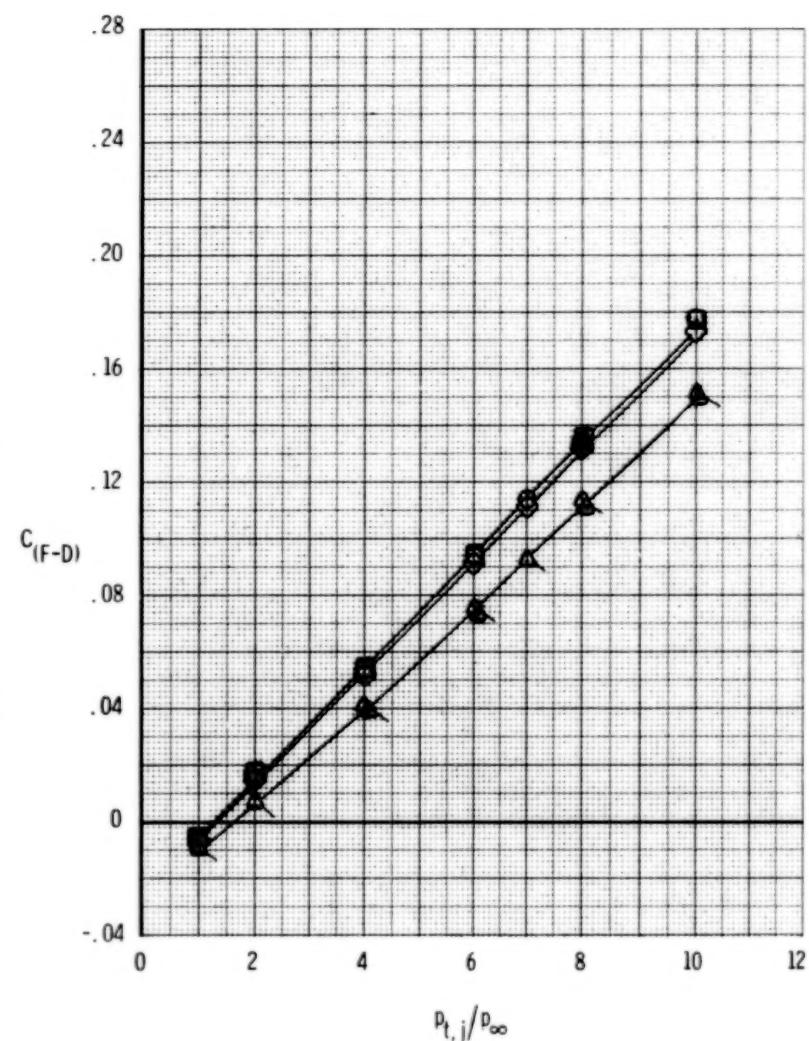
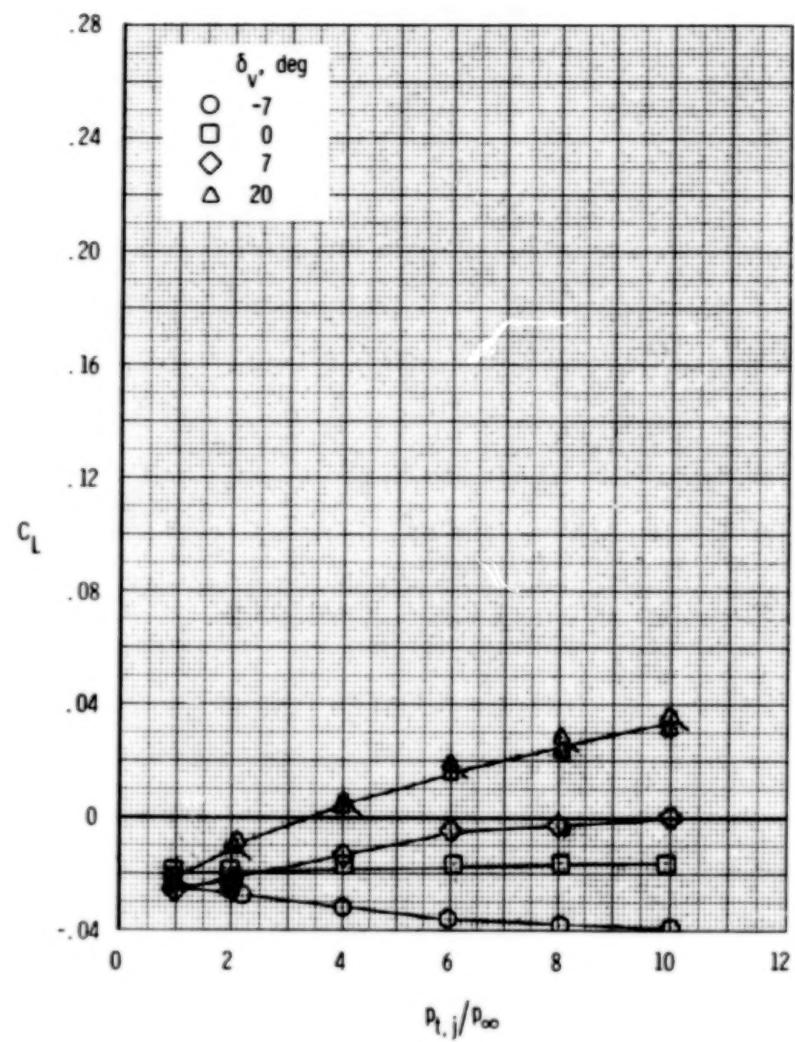


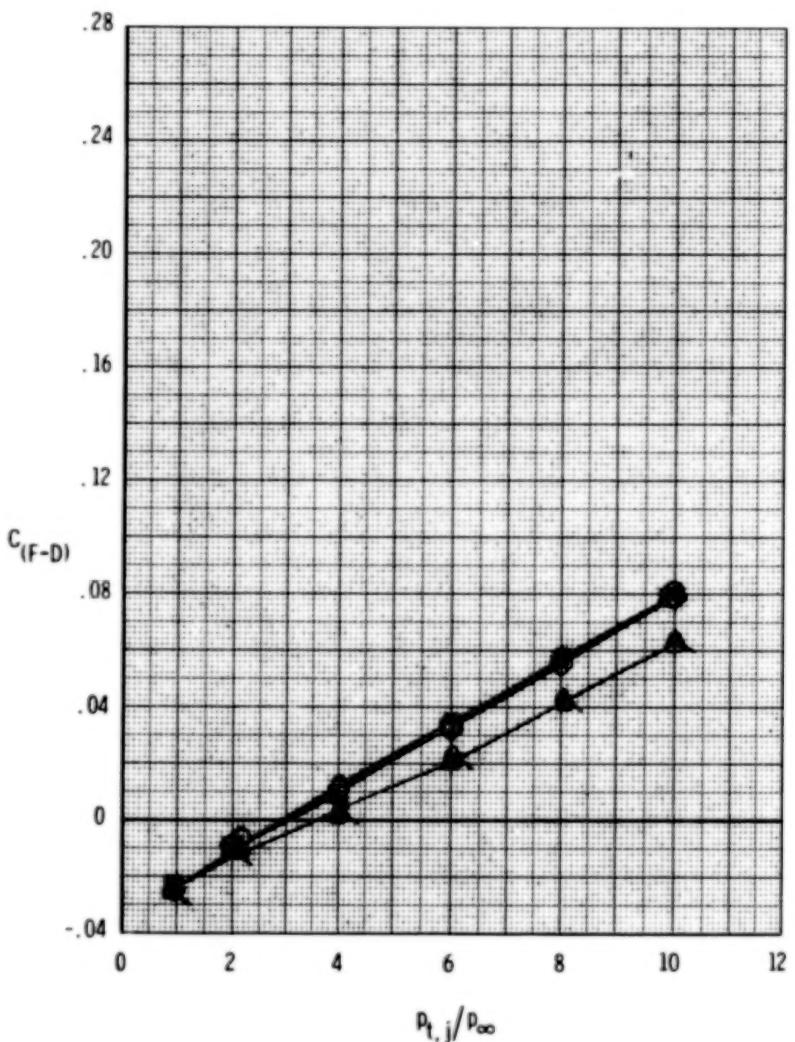
Figure 90.- Continued.

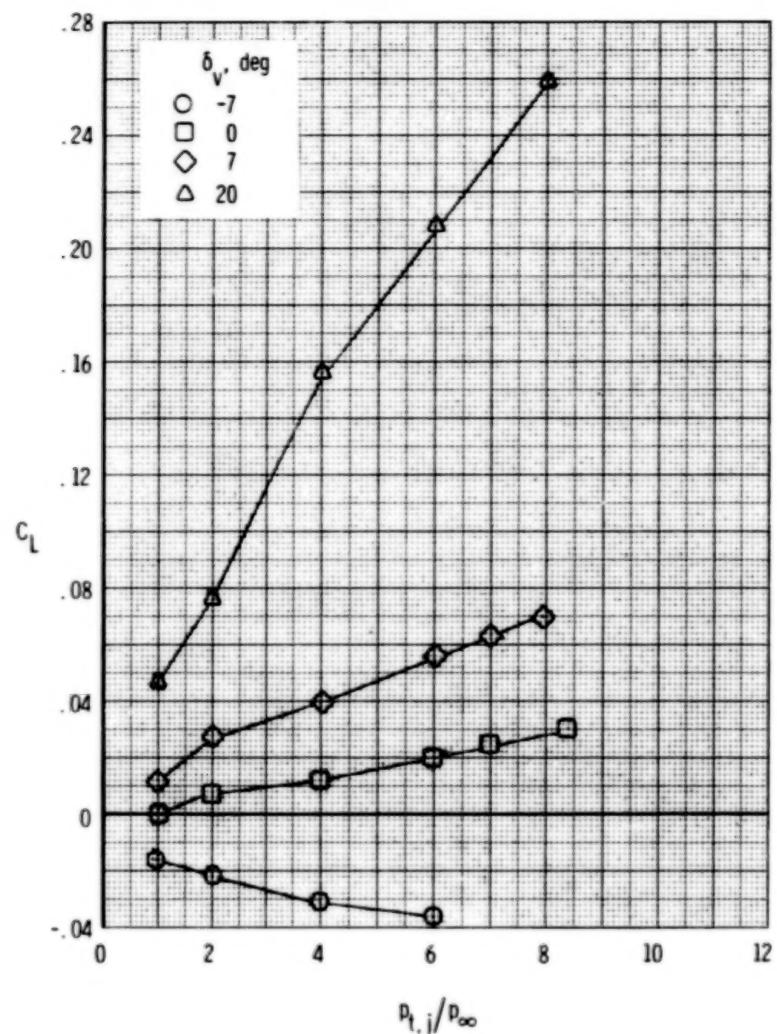
230



(c) $M = 1.20$.

Figure 90.- Concluded.





(a) $M = 0.60$.

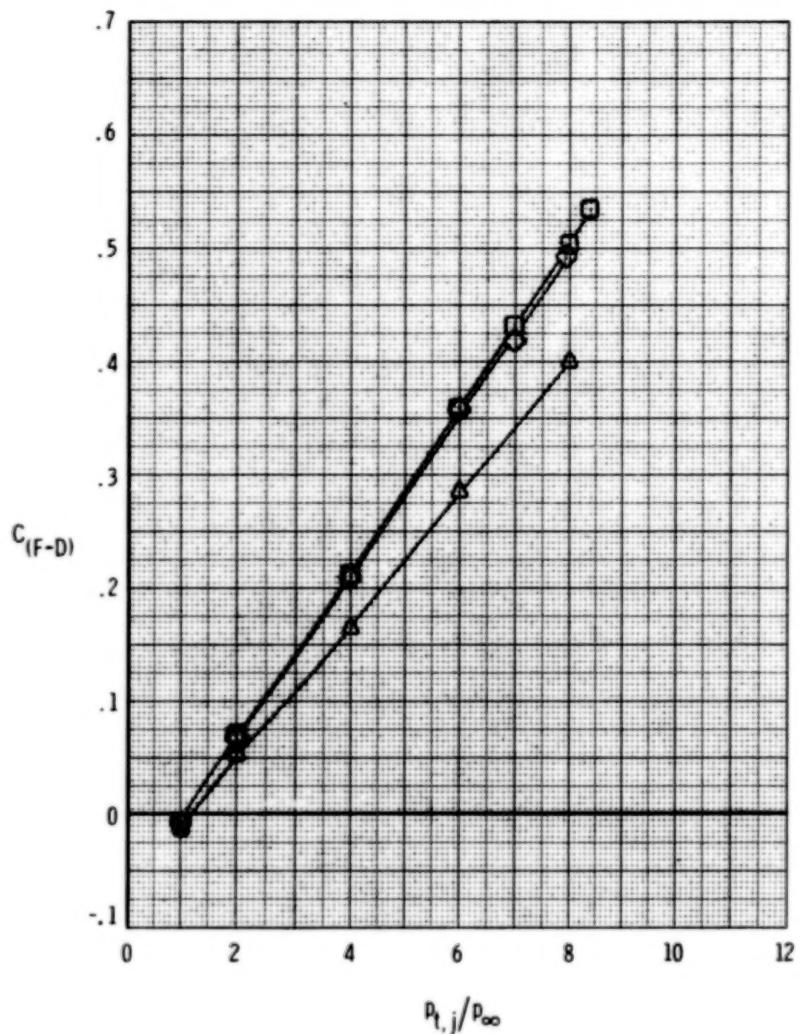
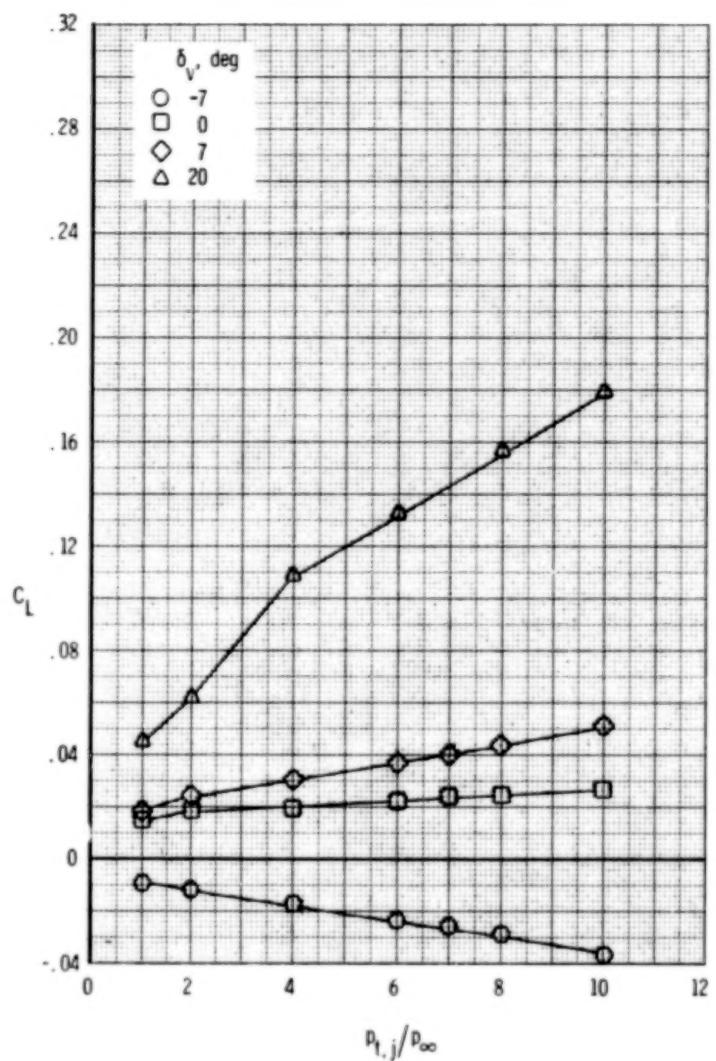


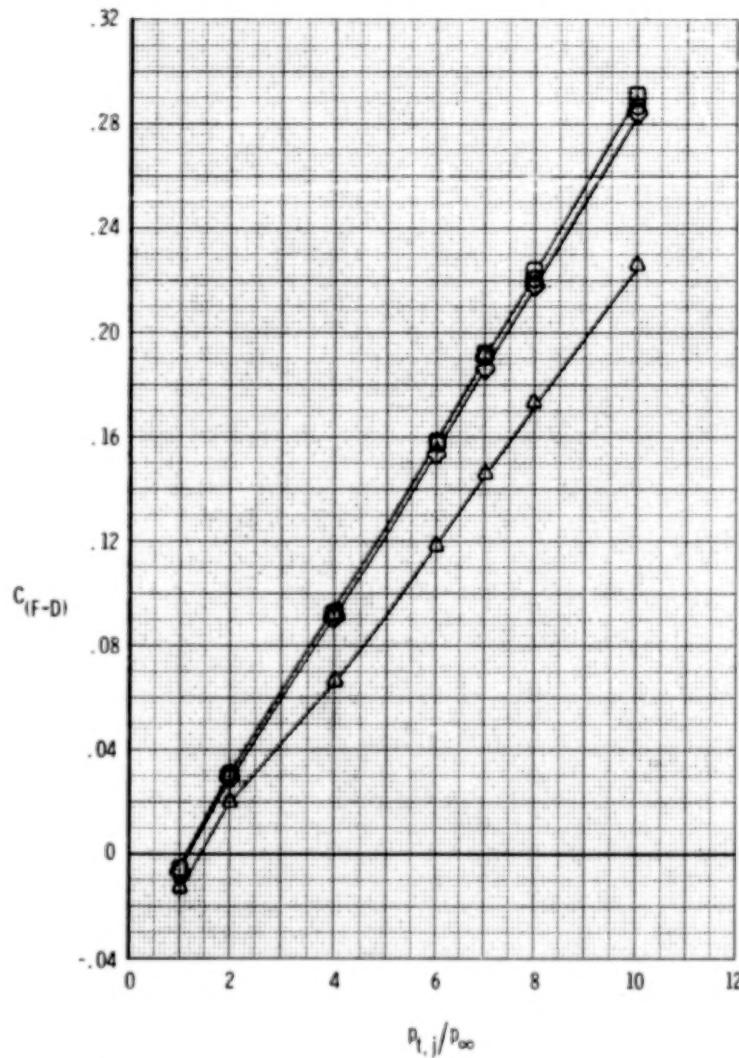
Figure 91.- Effect of vectoring on measured afterbody forces, 2-D C-D nozzle, A/B power. $\delta_h = 0^{\circ}$; $\alpha = 0^{\circ}$.

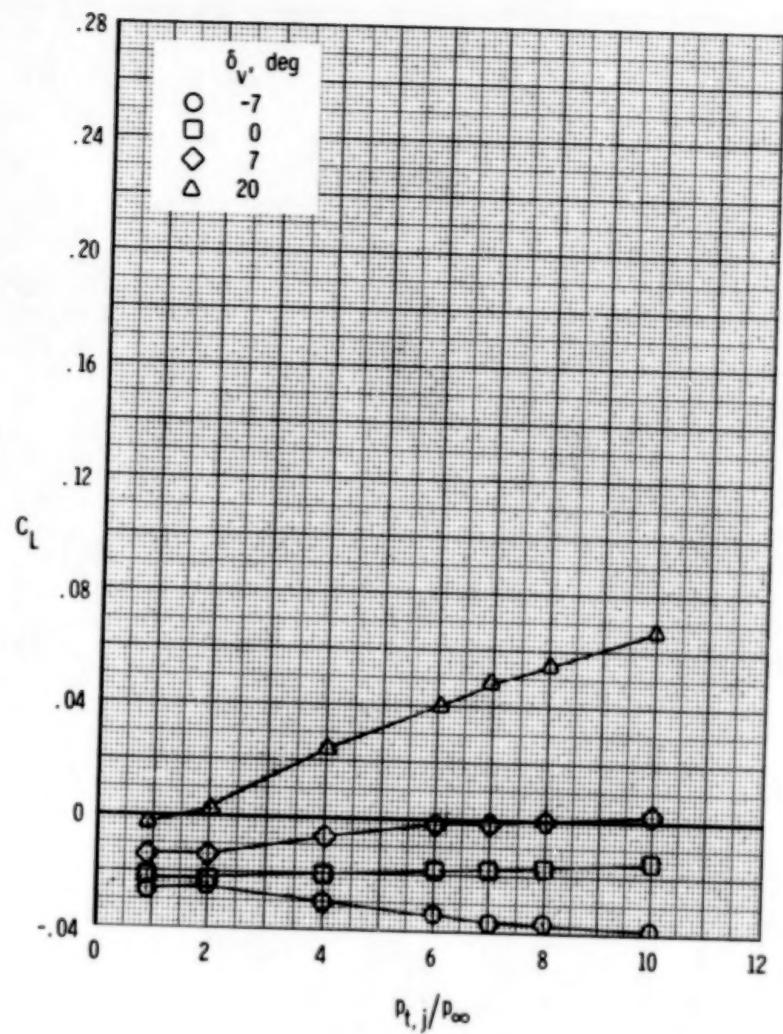
234



(b) $M = 0.90$.

Figure 91.- Continued.





(c) $M = 1.20$.

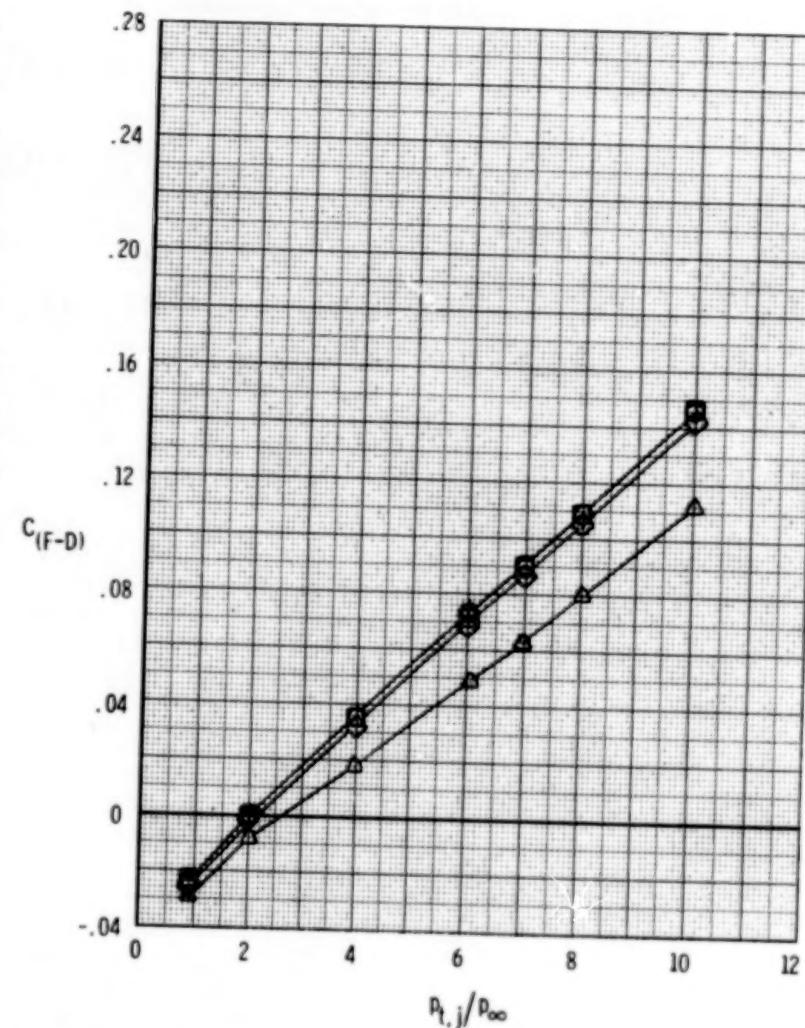
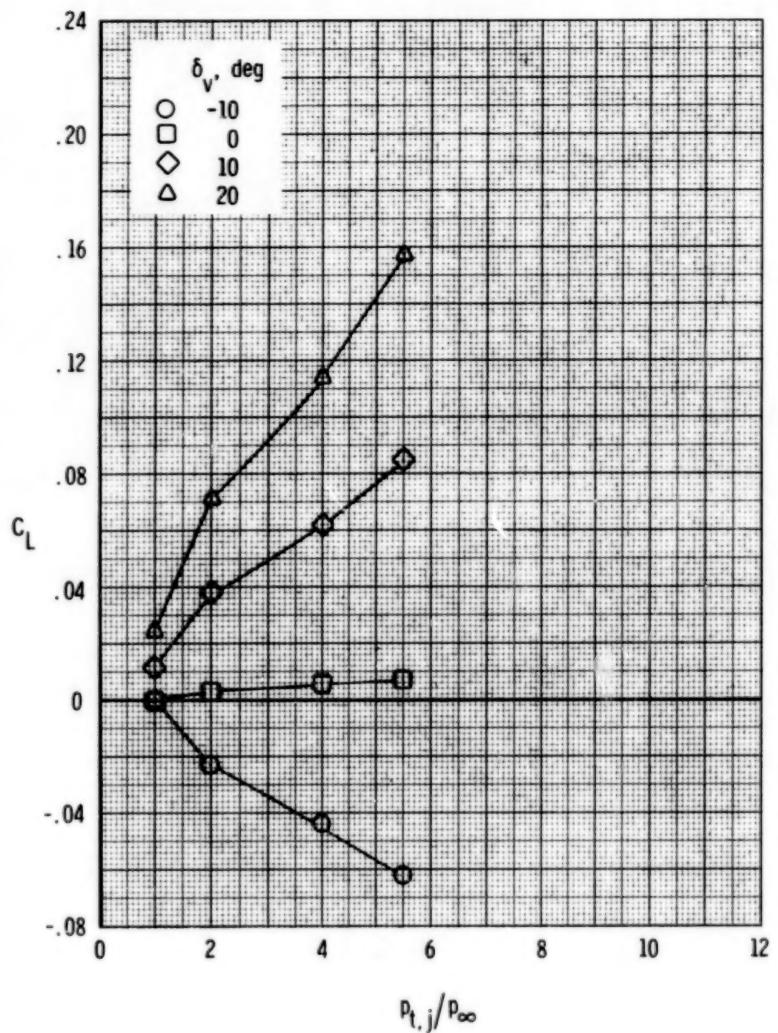
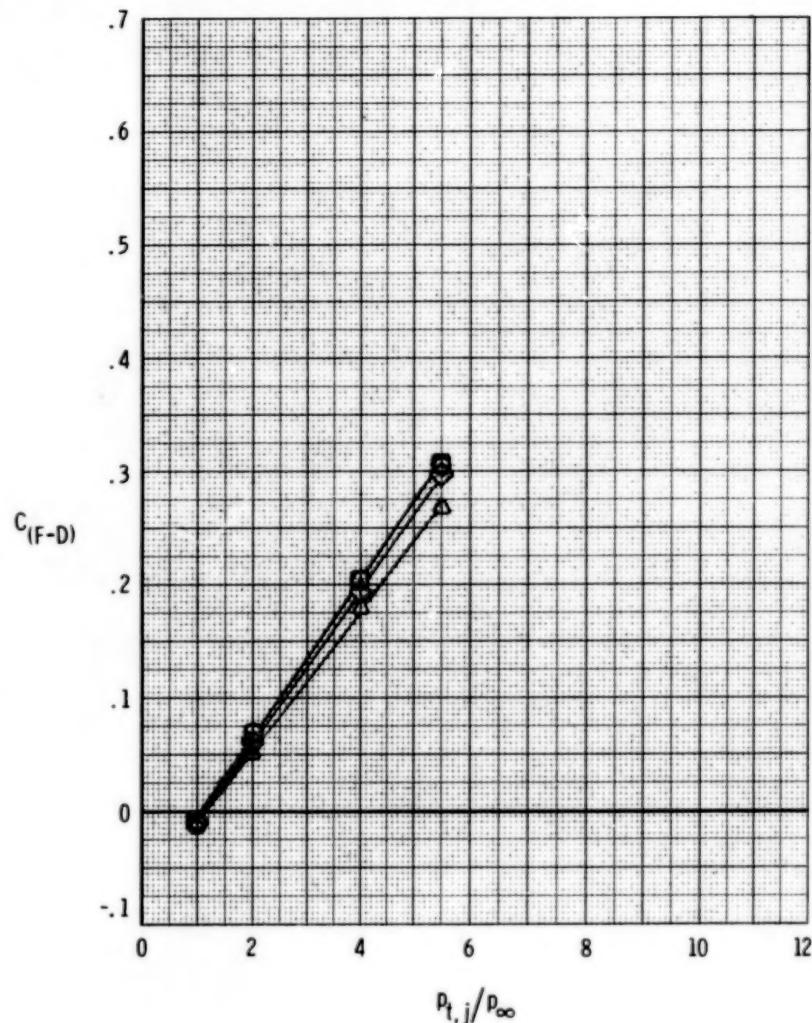
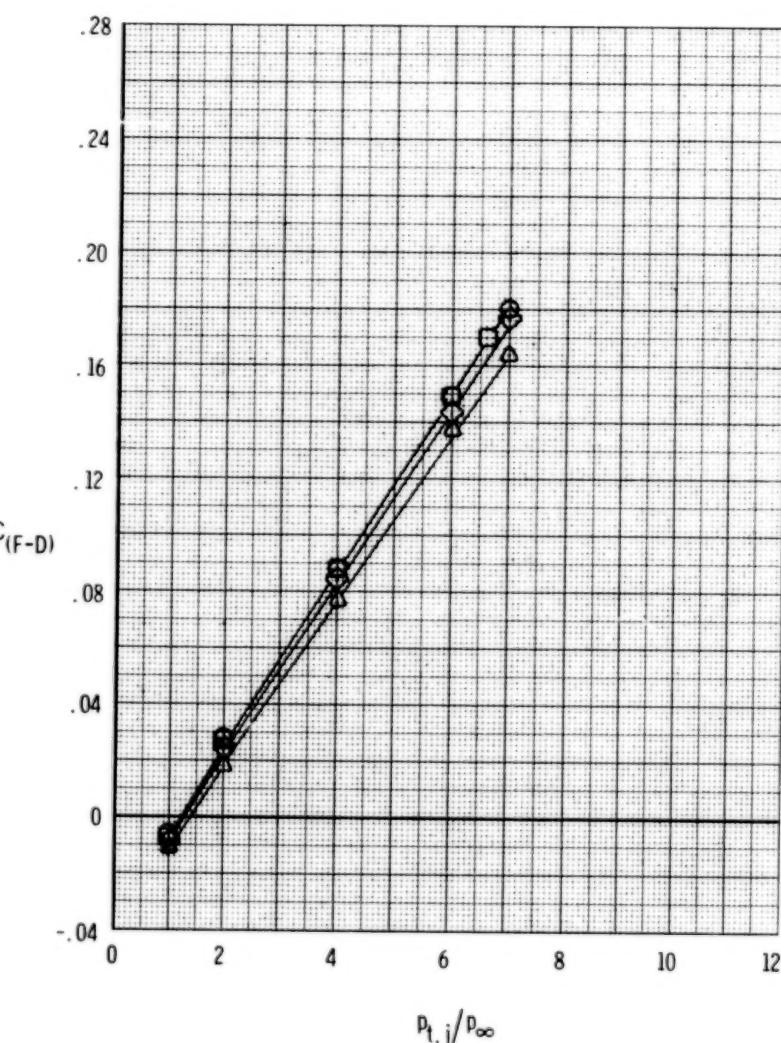
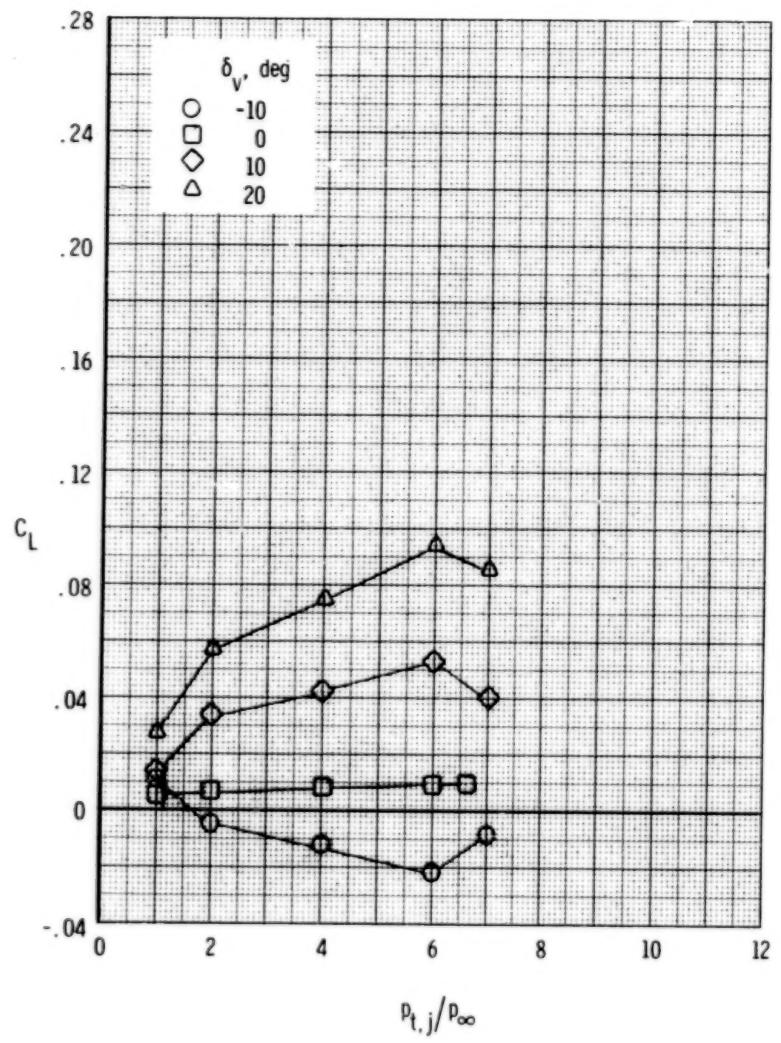


Figure 91.- Concluded.

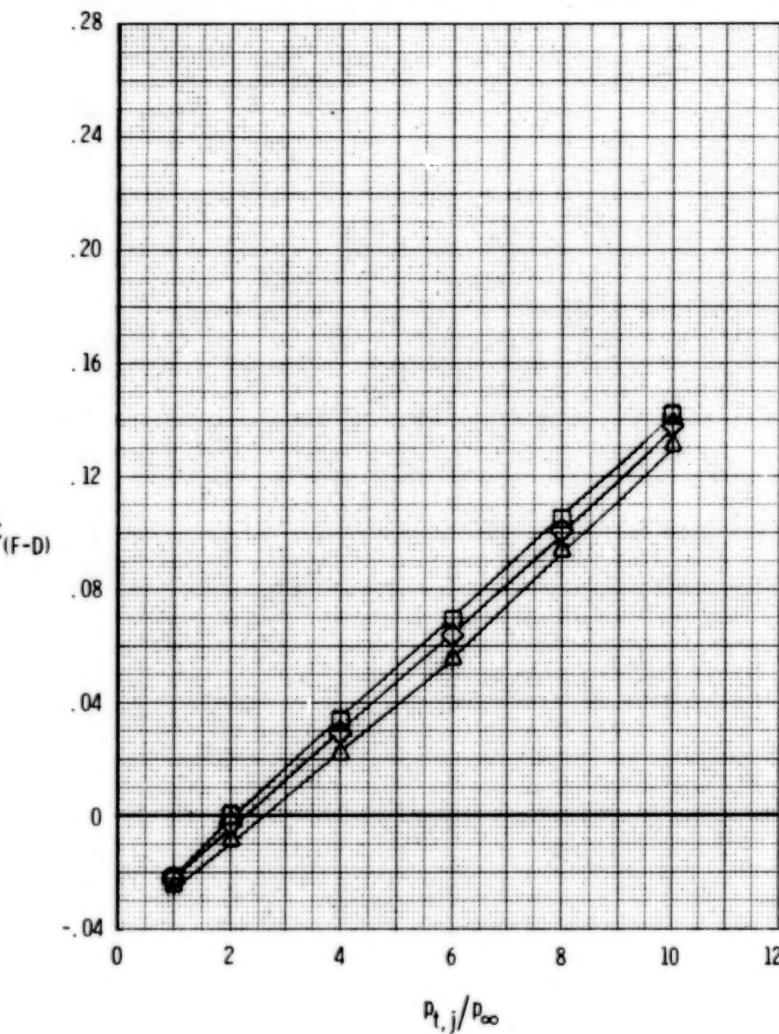
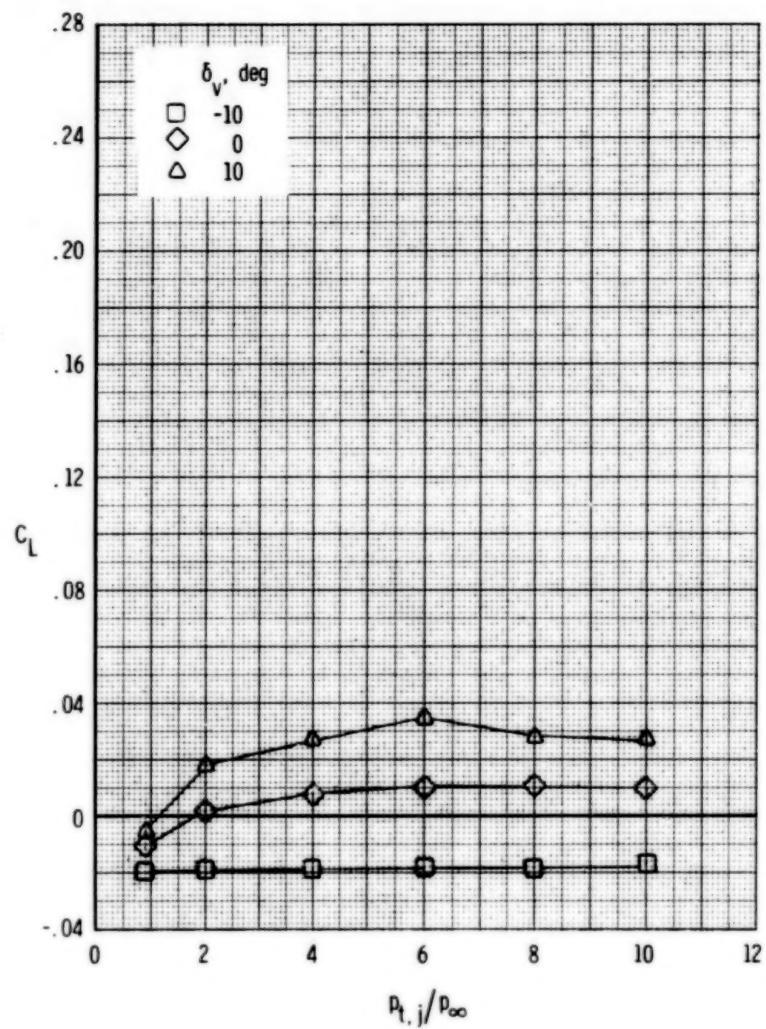
(a) $M = 0.60$.Figure 92. - Effect of vectoring on measured afterbody forces, wedge nozzle, A/B power. $\delta_h = 0^\circ$; $\alpha = 0^\circ$.



(b) $M = 0.90$.

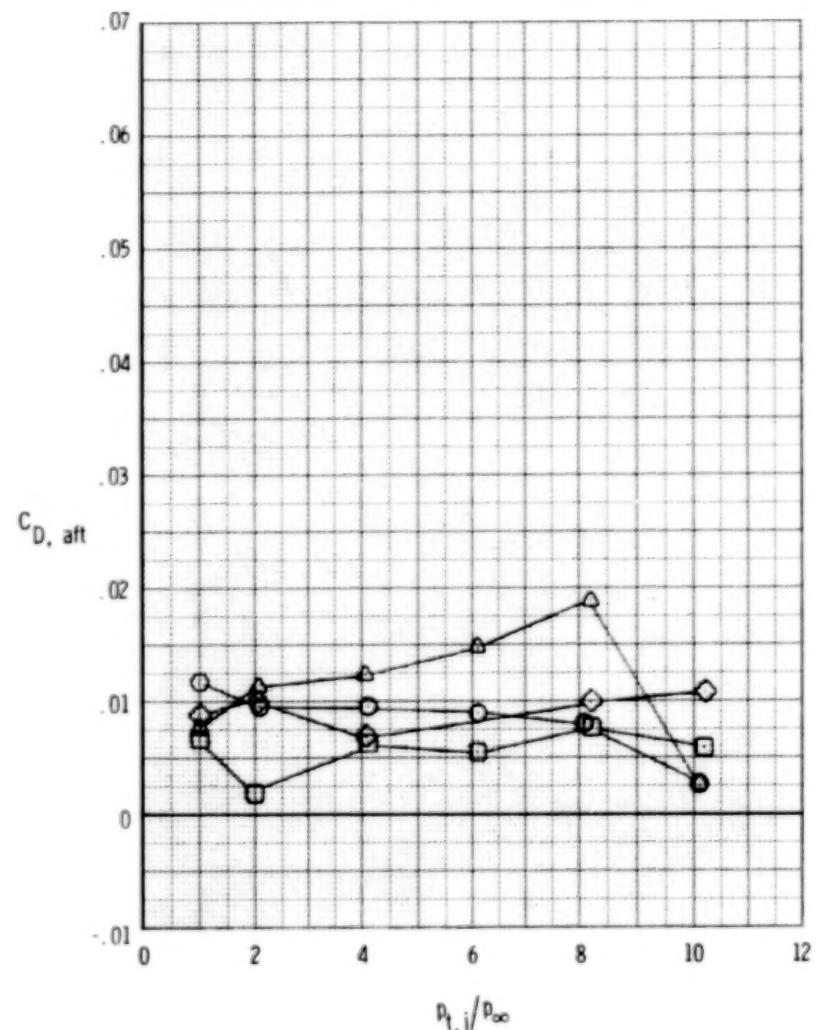
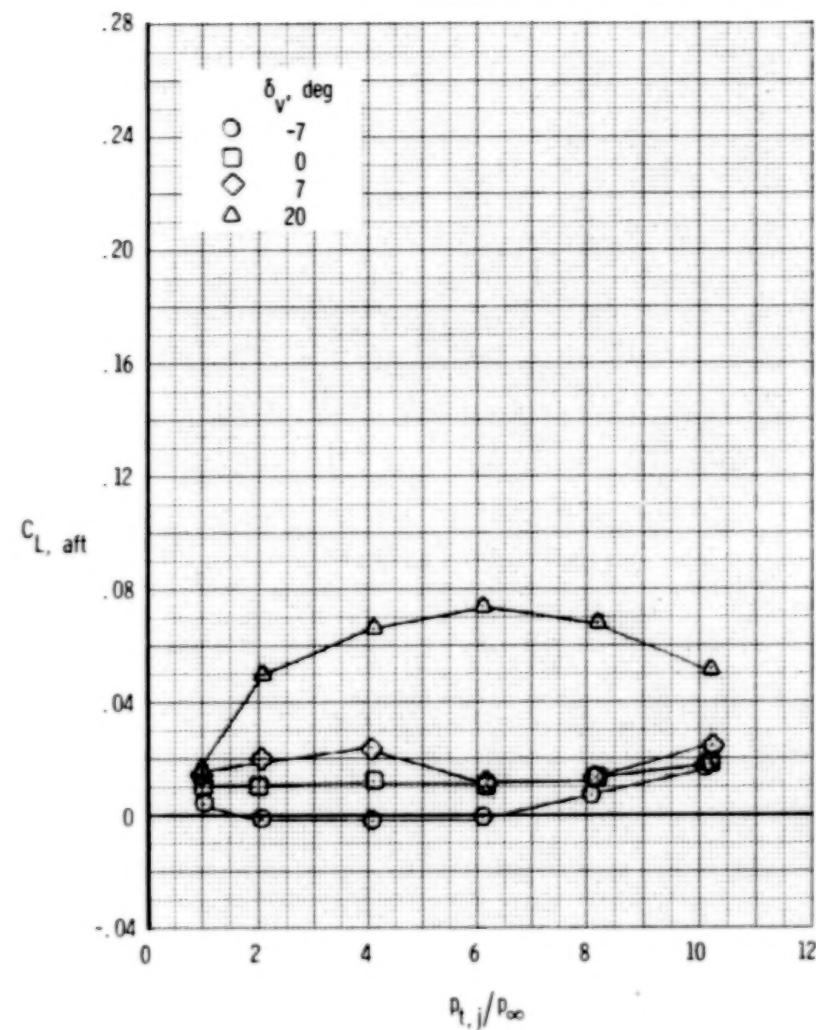
Figure 92.- Continued.

238



(c) $M = 1.20$.

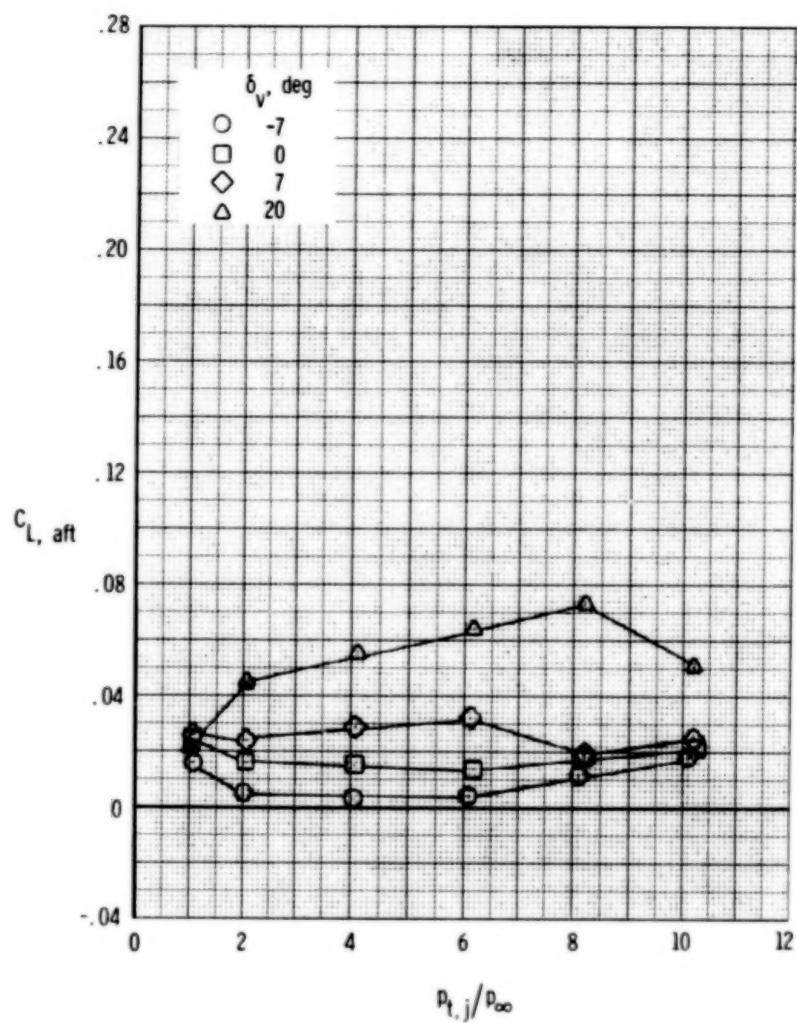
Figure 92.- Concluded.



(a) $M = 0.60$.

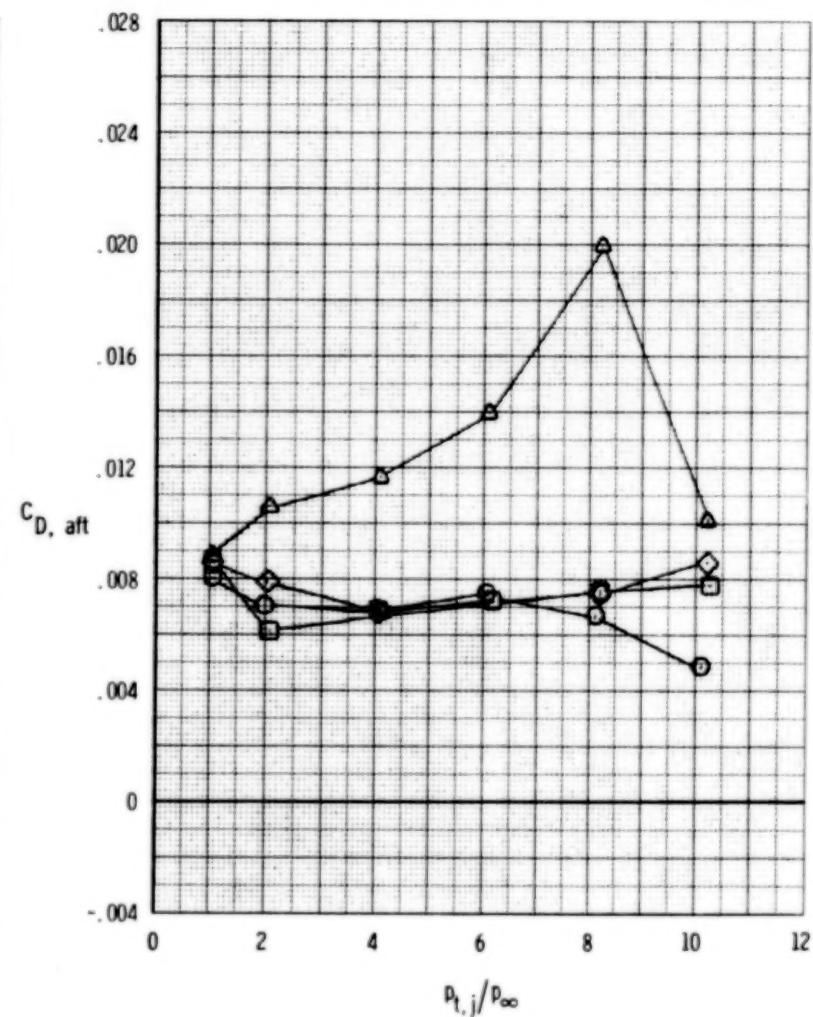
Figure 93.- Effect of vectoring on thrust-removed afterbody forces, SERN nozzle, dry power. $\delta_h = 0^\circ$; $\alpha = 0^\circ$.

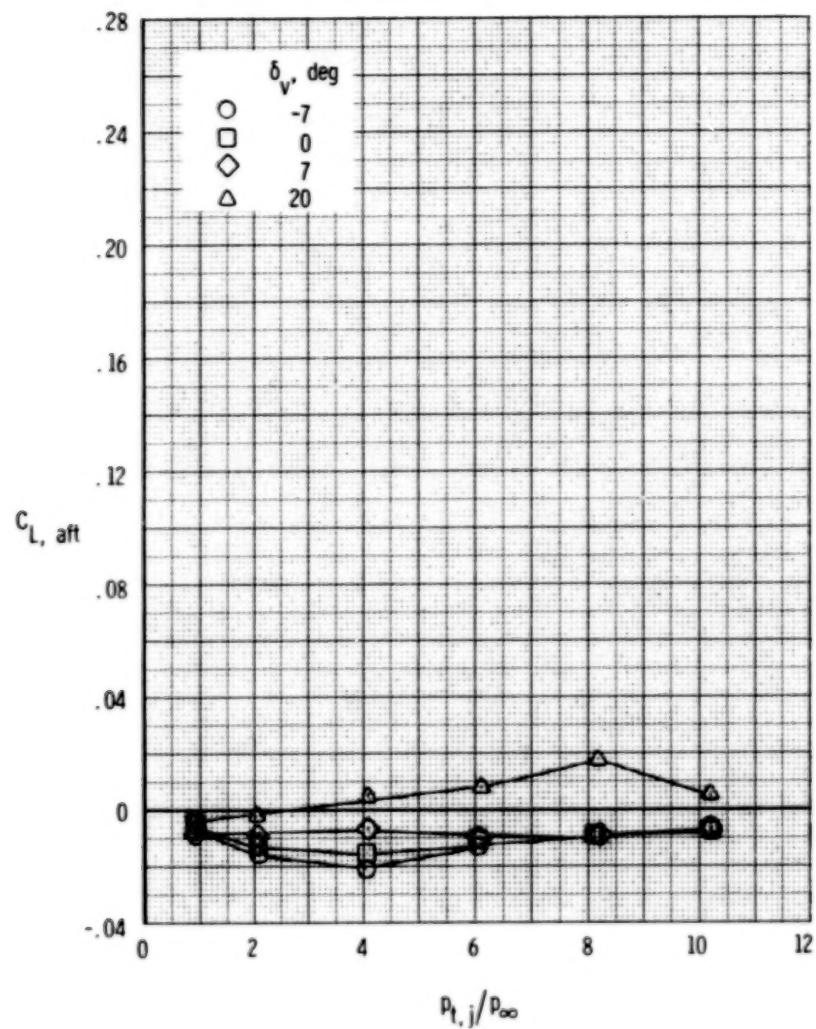
240



(b) $M = 0.90$.

Figure 93.- Continued.

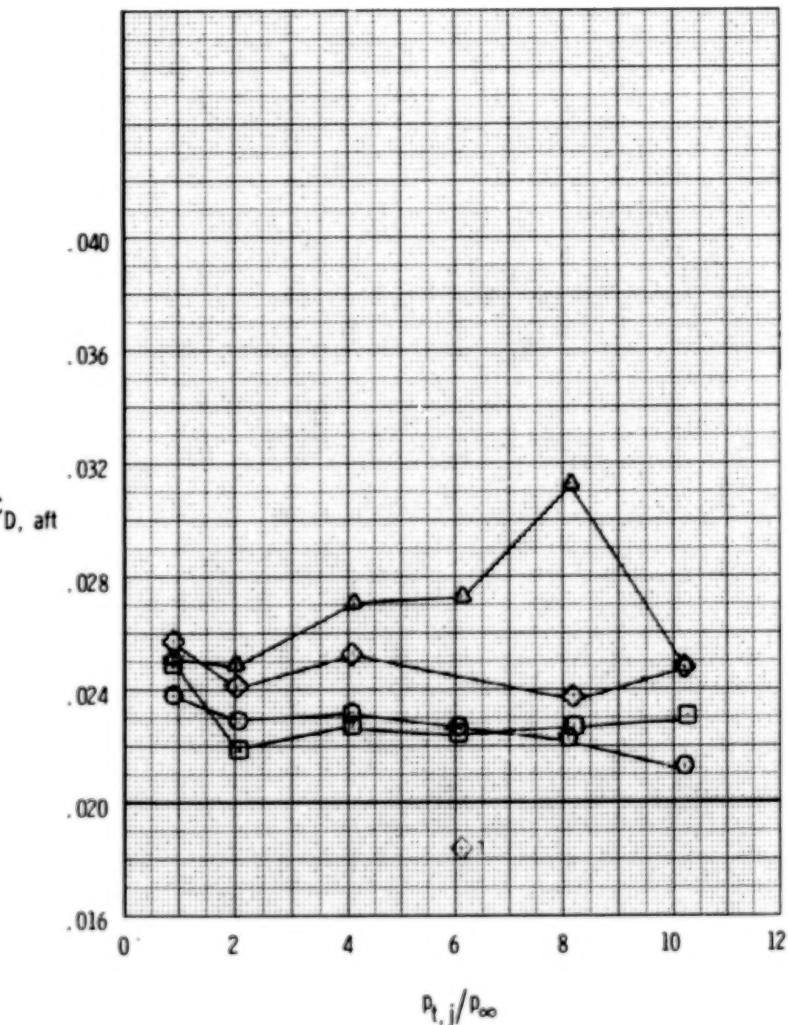




(c) $M = 1.20$.

Figure 93.- Concluded.

241



242

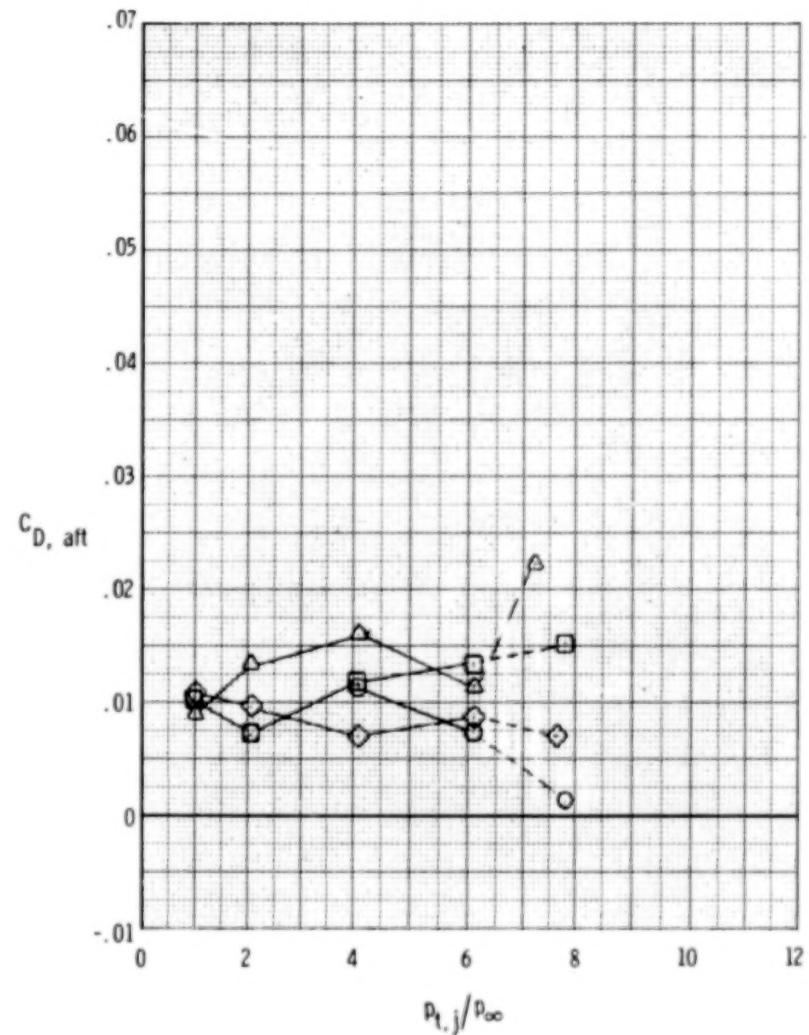
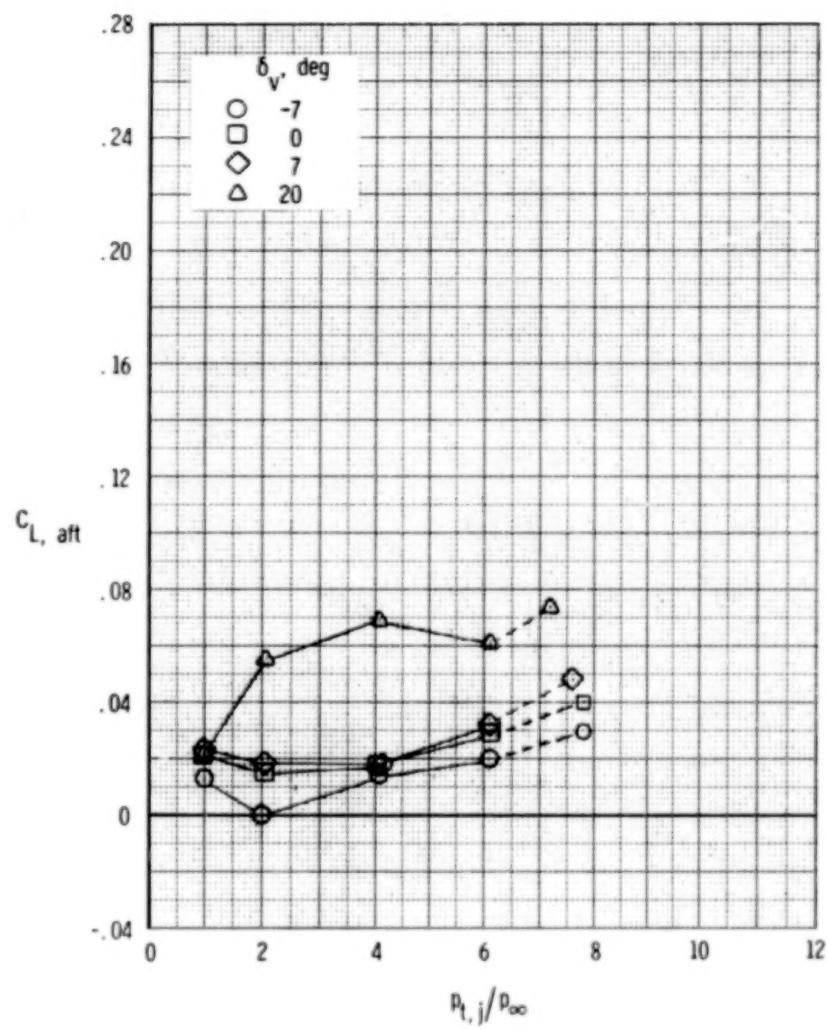
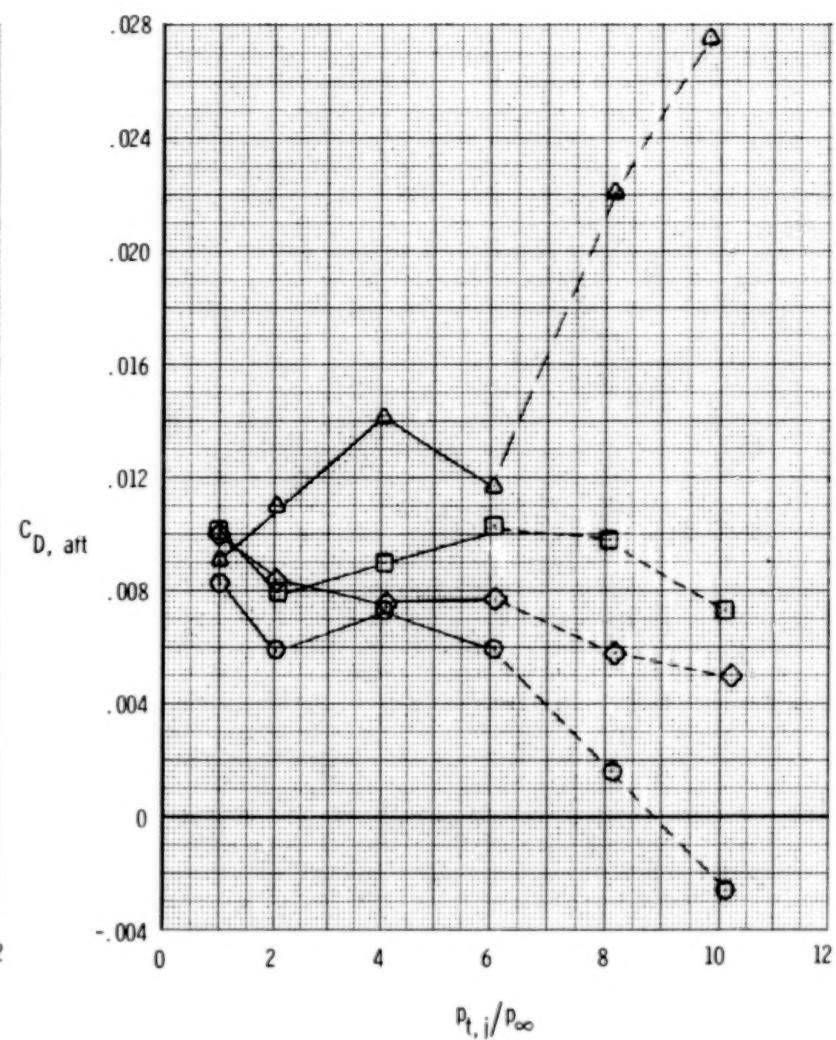
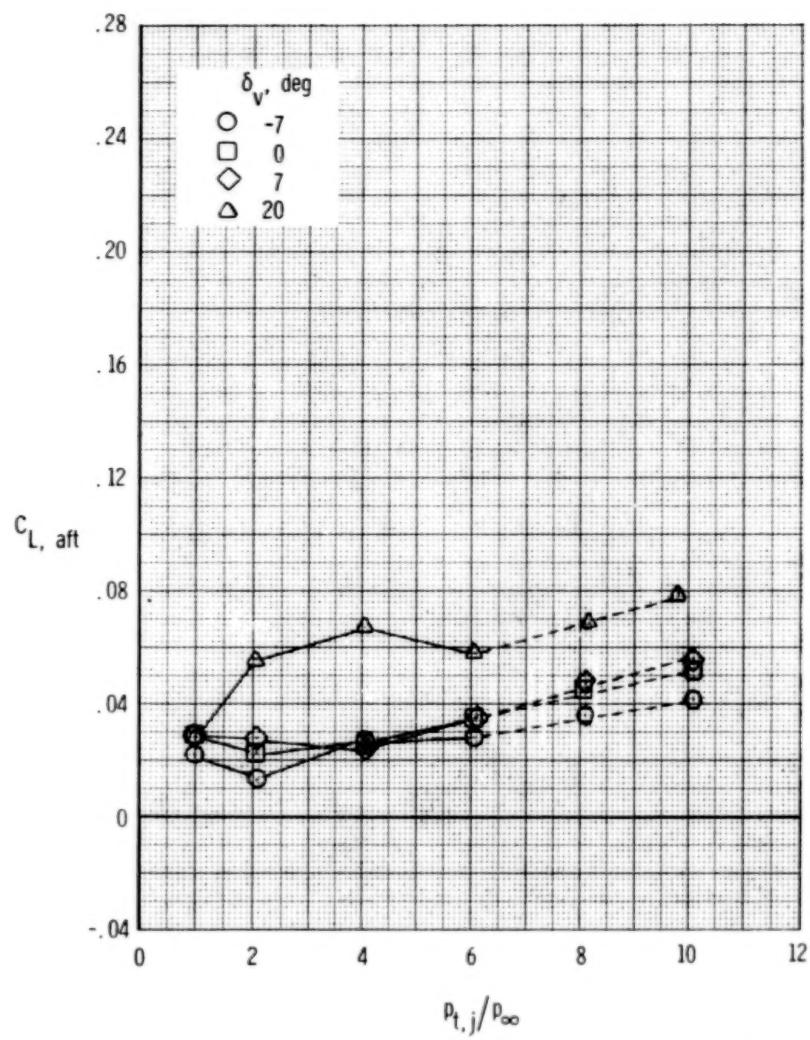
(a) $M = 0.60$.

Figure 94.- Effect of vectoring on thrust-removed afterbody forces, SERN nozzle, A/B power. $\delta_h = 0^0$; $\alpha = 0^0$.
 Dashed lines indicate data results from extrapolating static data.



(b) $M = 0.90$.

Figure 94.- Continued.

243

244

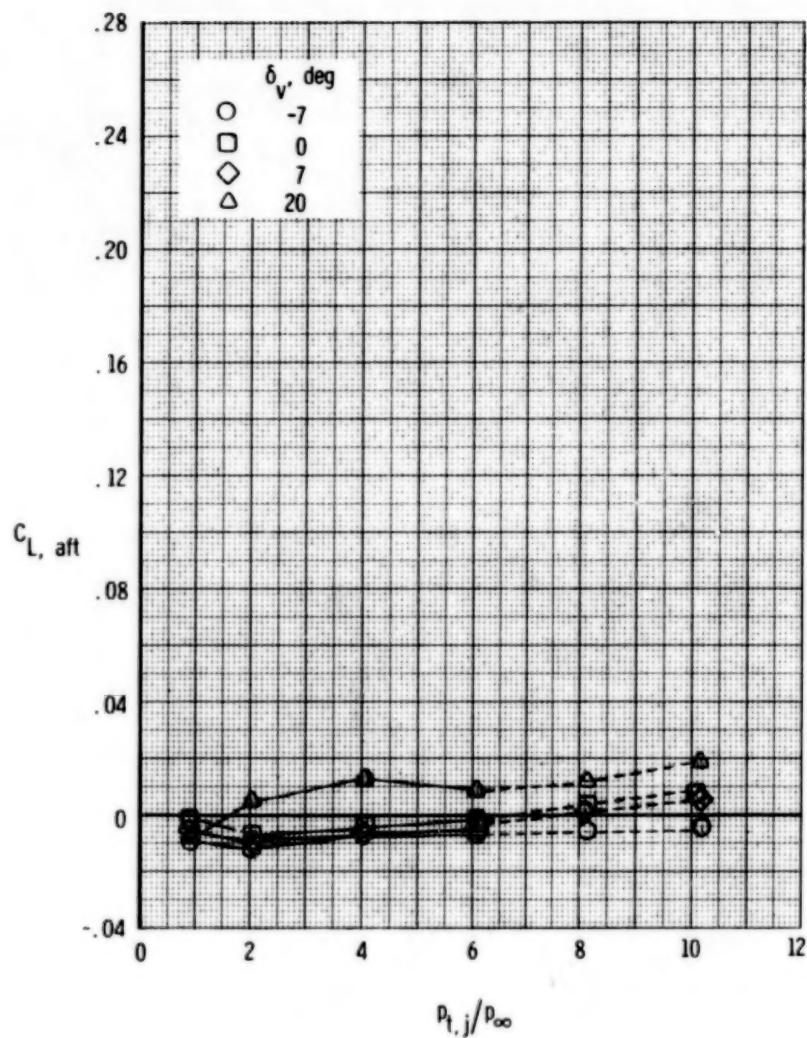
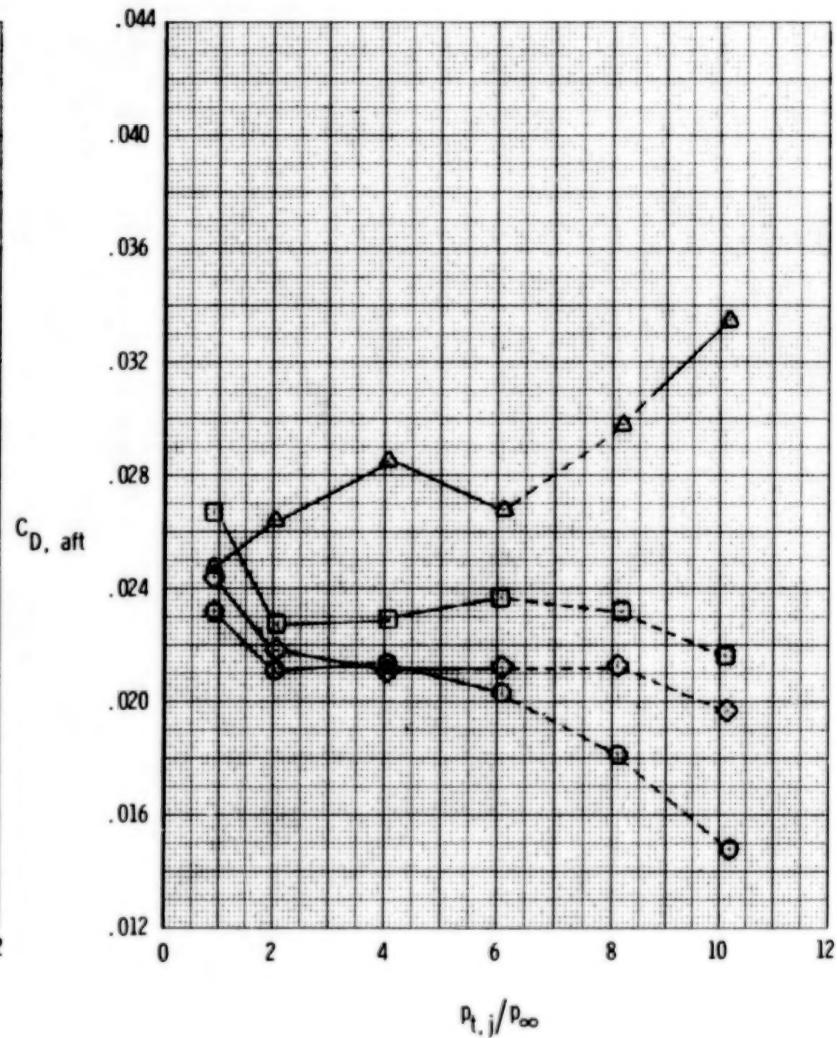
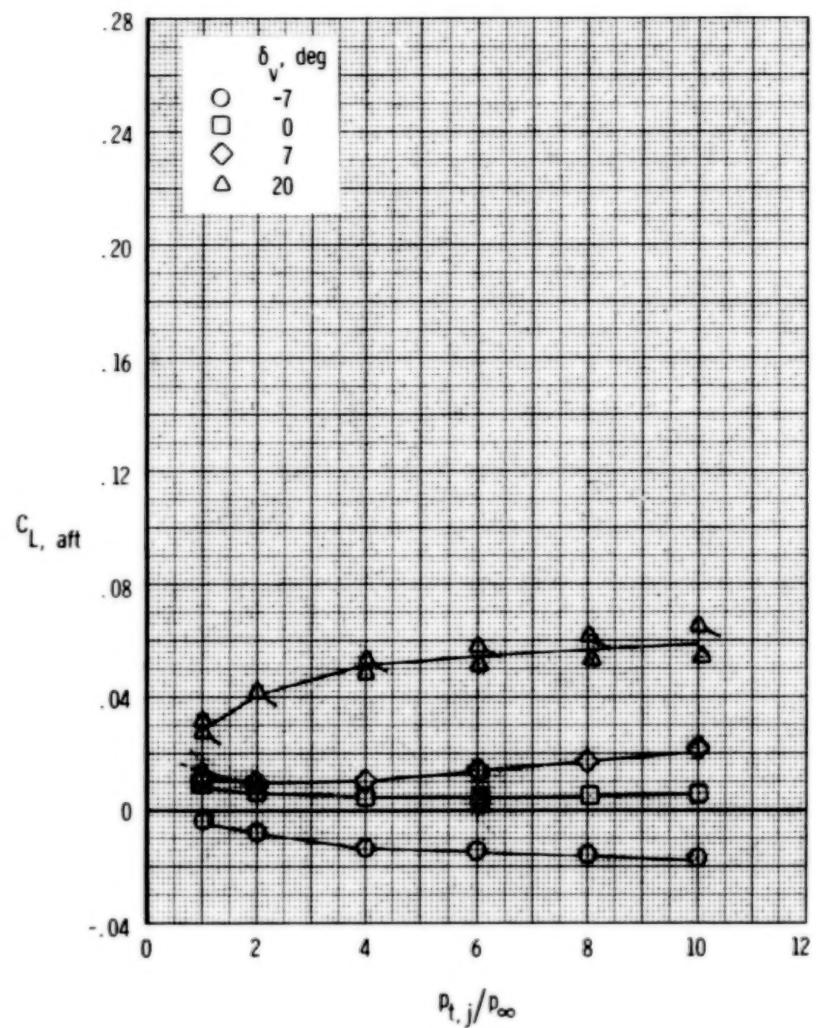
(c) $M = 1.20$.

Figure 94.- Concluded.





(a) $M = 0.60$.

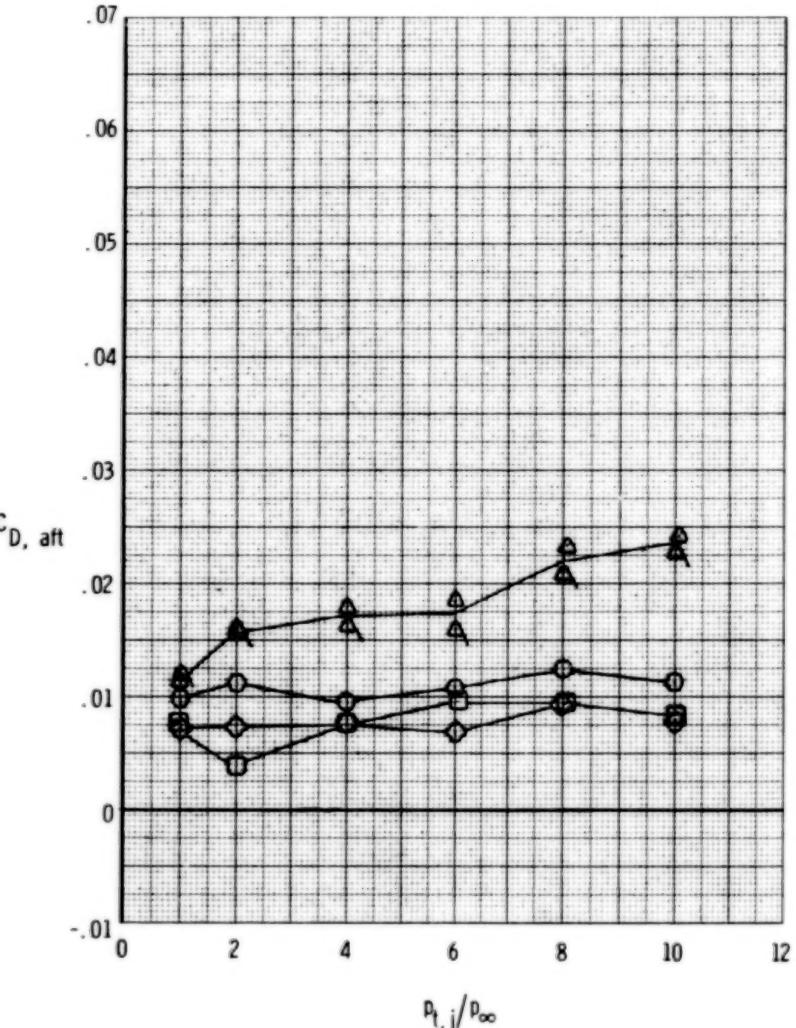


Figure 95.- Effect of vectoring on thrust-removed afterbody forces, 2-D C-D nozzle, dry power. $\delta_h = 0^{\circ}$; $\alpha = 0^{\circ}$.

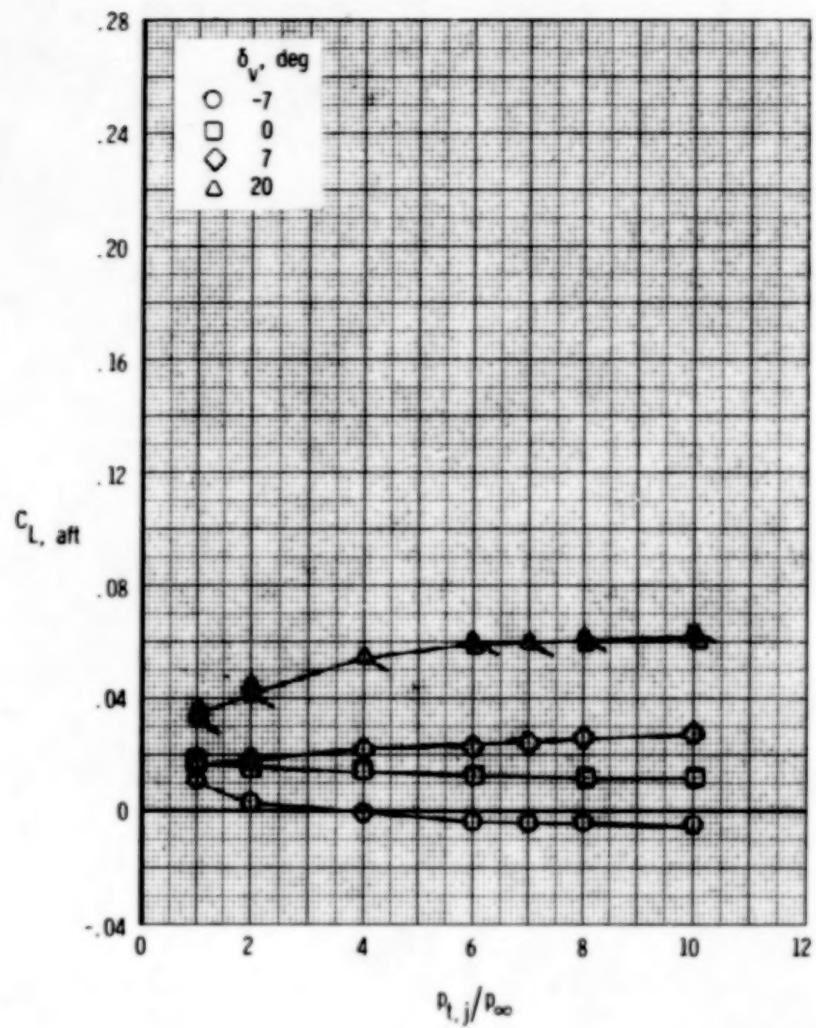
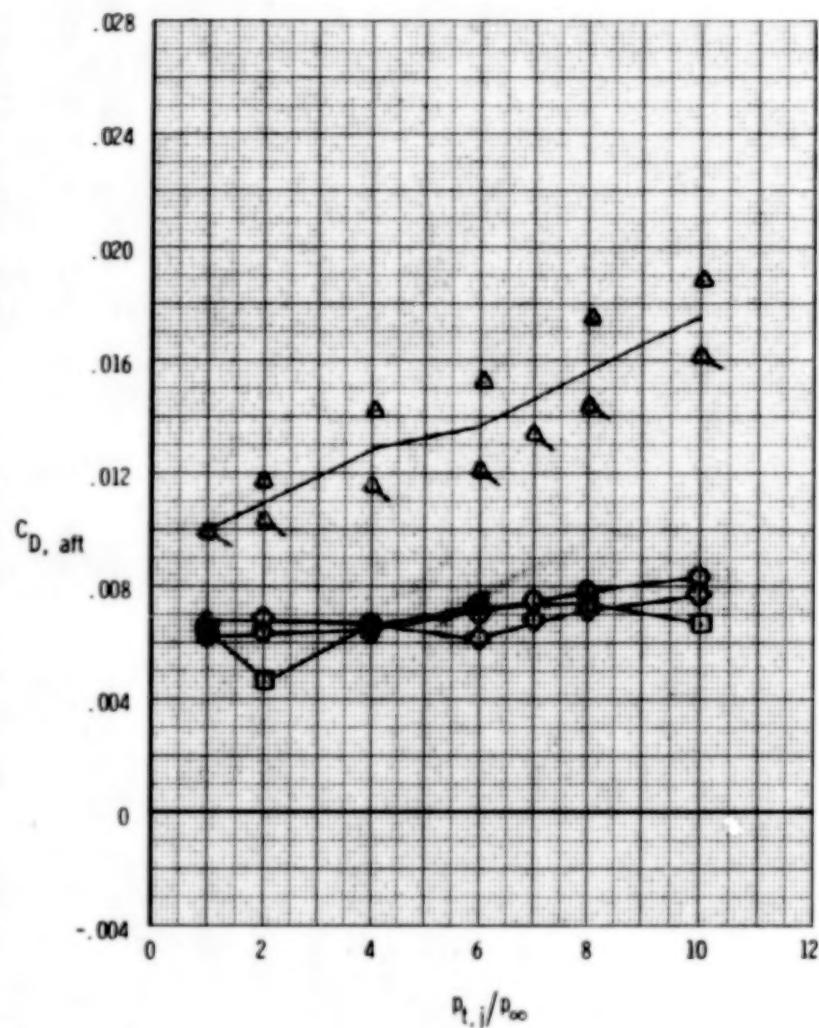
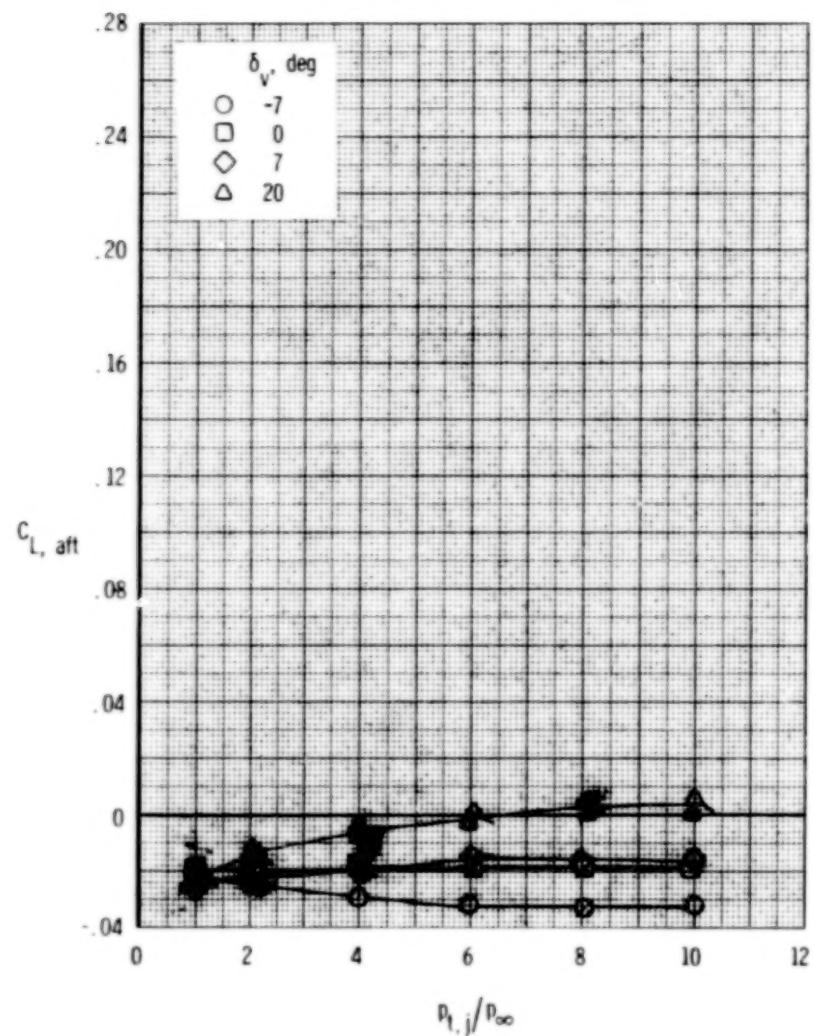
(b) $M = 0.90$.

Figure 95.- Continued.

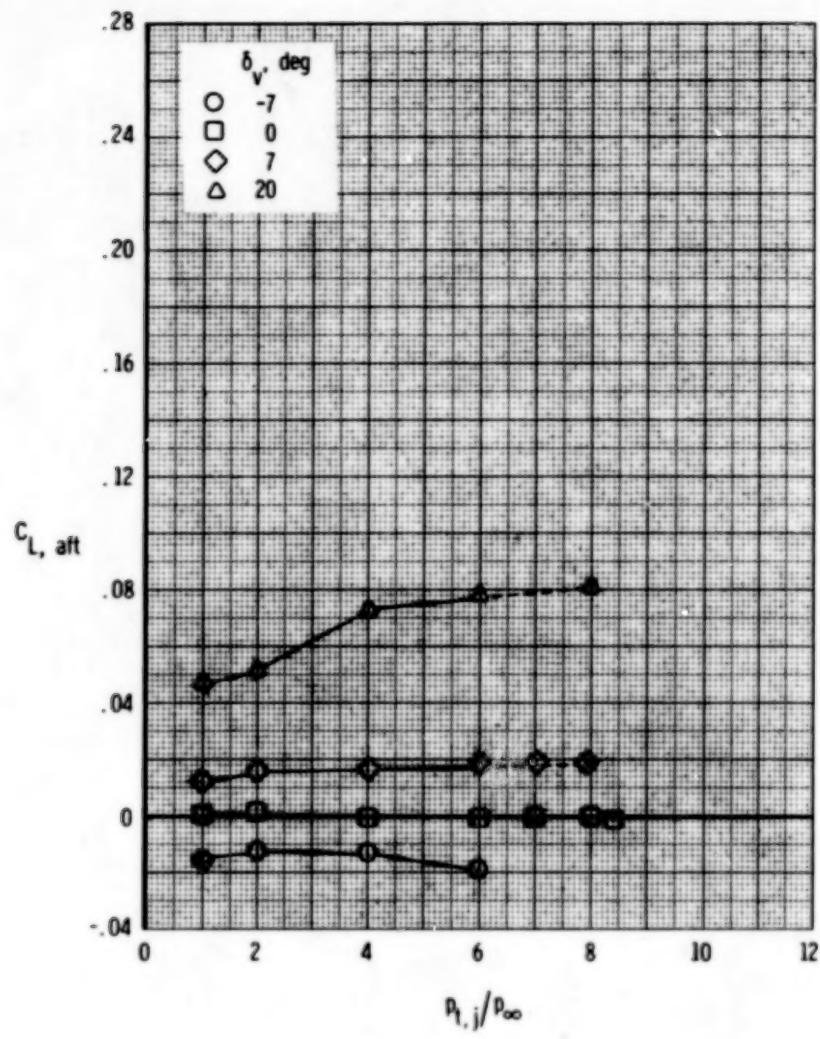




(c) $M = 1.20$.

Figure 95.- Concluded.

248



(a) $M = 0.60$.

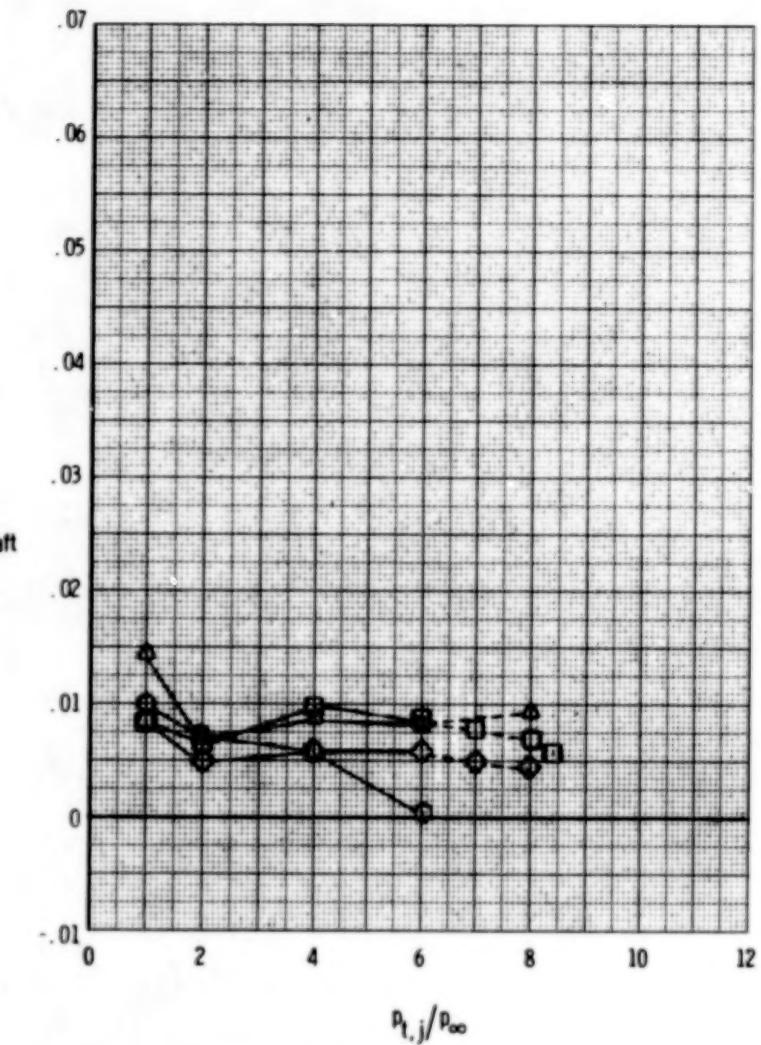
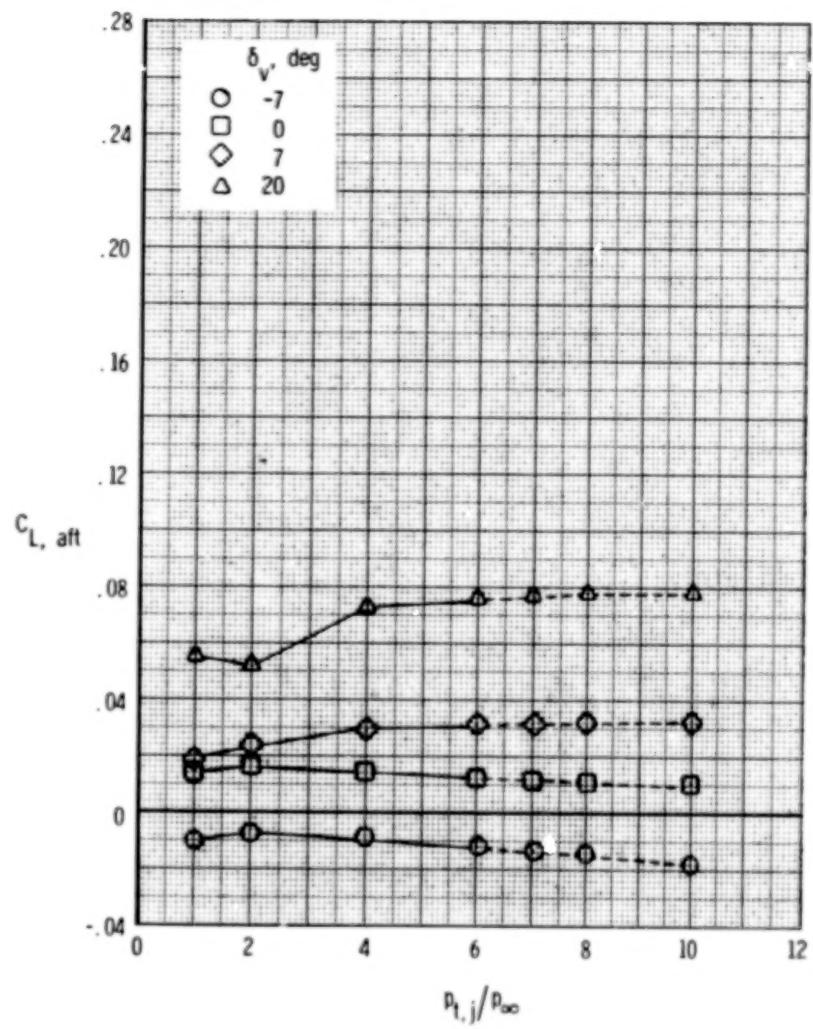


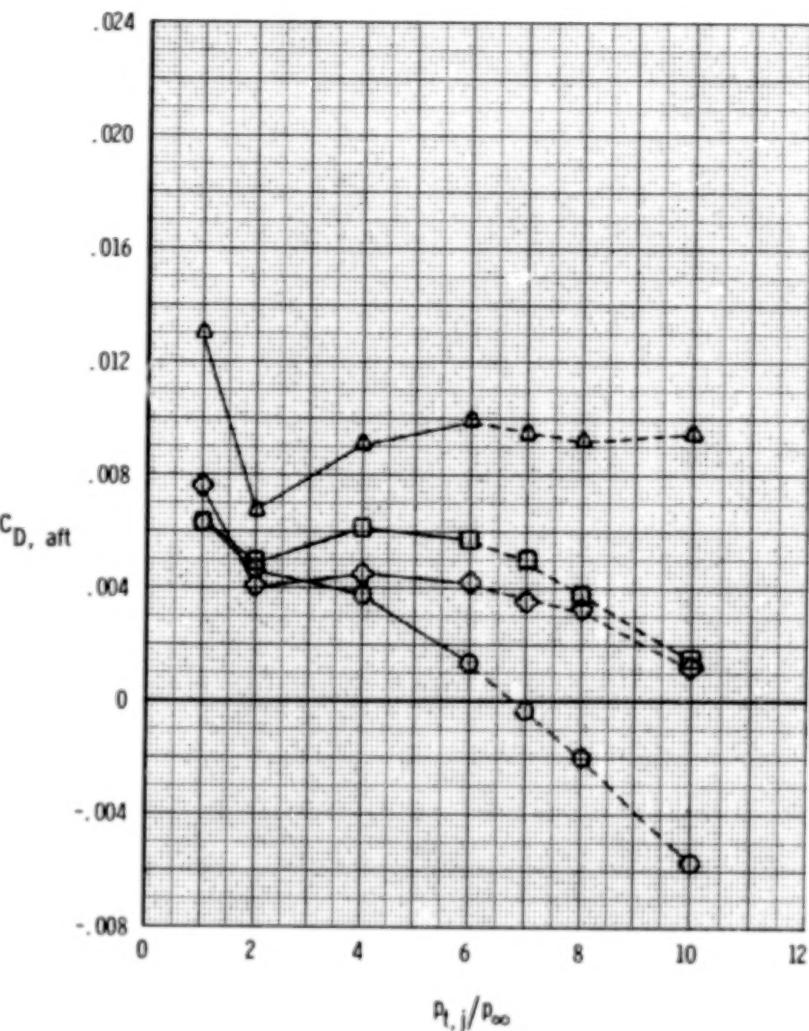
Figure 96.- Effect of vectoring on thrust-removed afterbody forces, 2-D C-D nozzle, A/B power. $\delta_h = 0^\circ$; $\alpha = 0^\circ$.



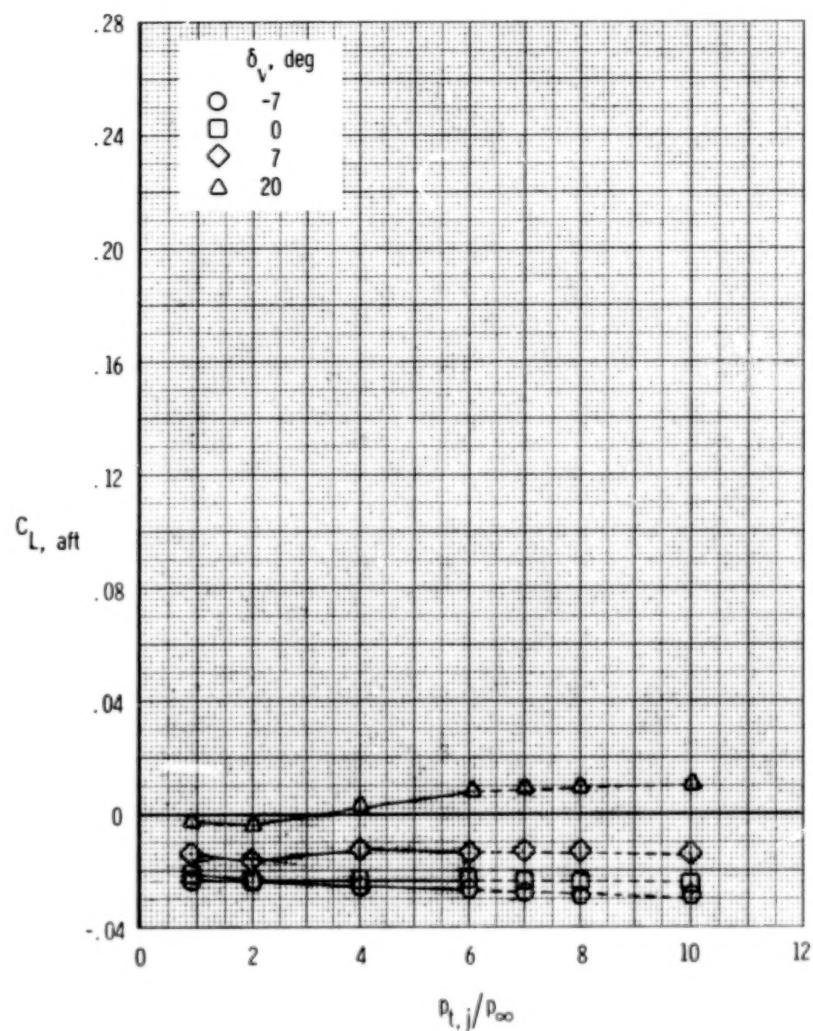
(b) $M = 0.90$.

Figure 96.- Continued.

249

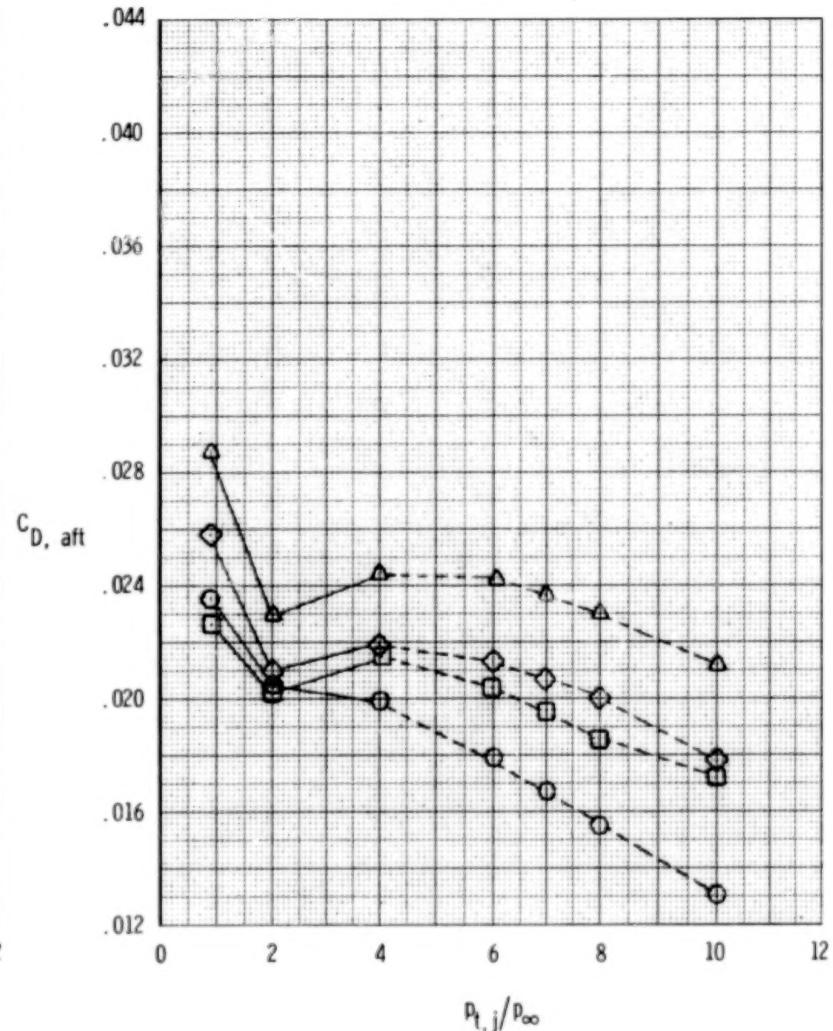


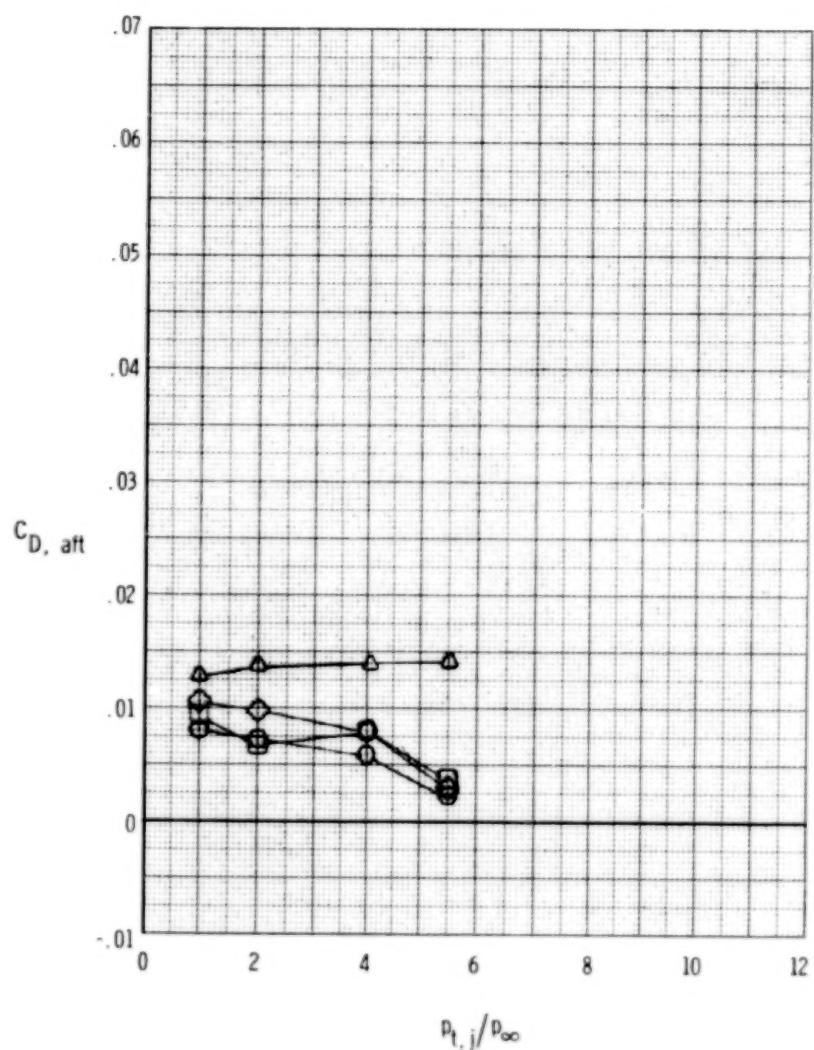
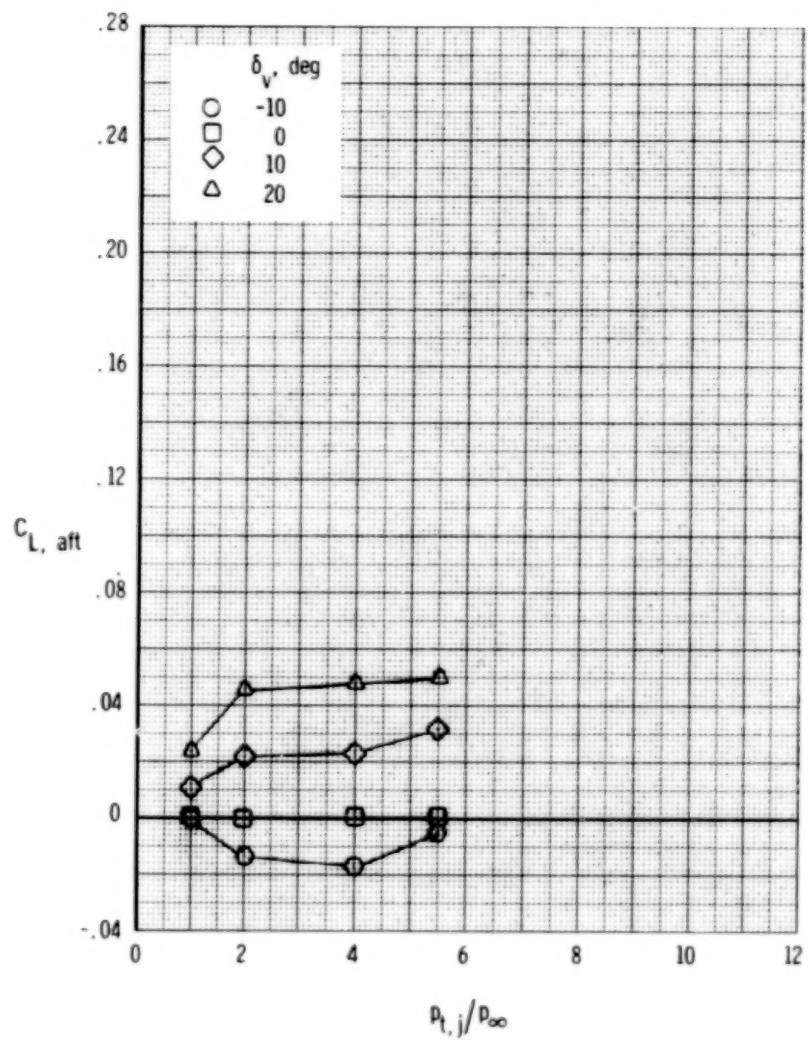
250



(c) $M = 1.20$.

Figure 96.- Concluded.





(a) $M = 0.60$.

Figure 97.- Effect of vectoring on thrust-removed afterbody forces, wedge nozzle, A/B power. $\delta_h = 0^\circ$; $\alpha = 0^\circ$.

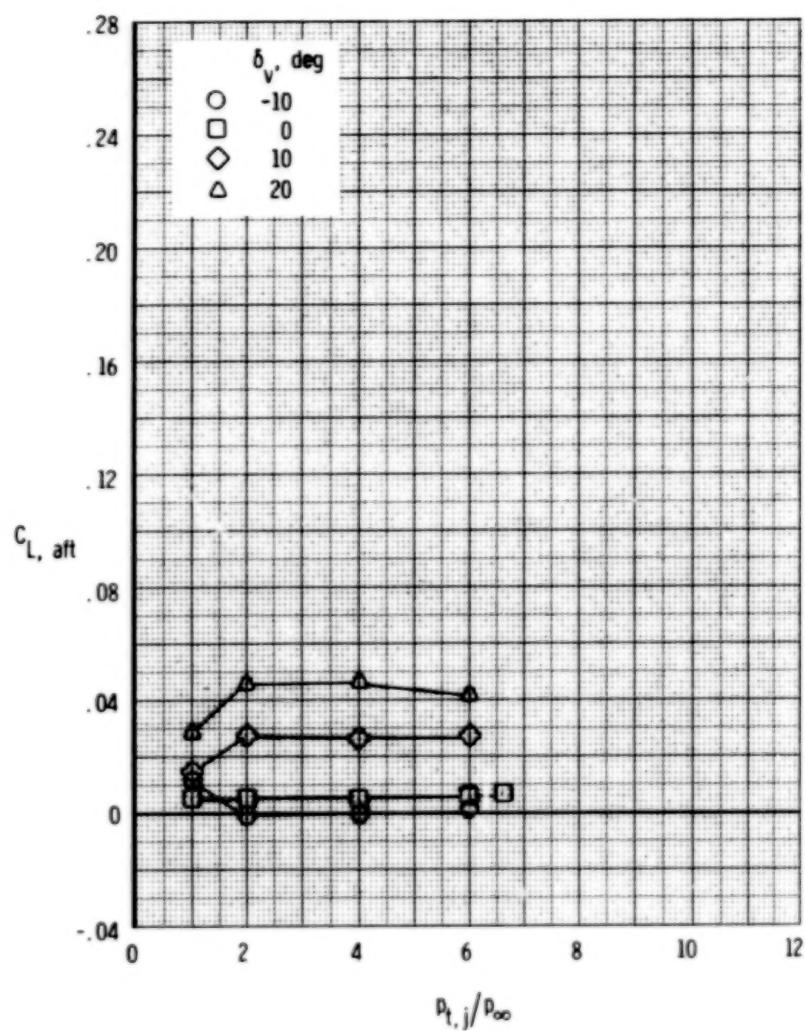
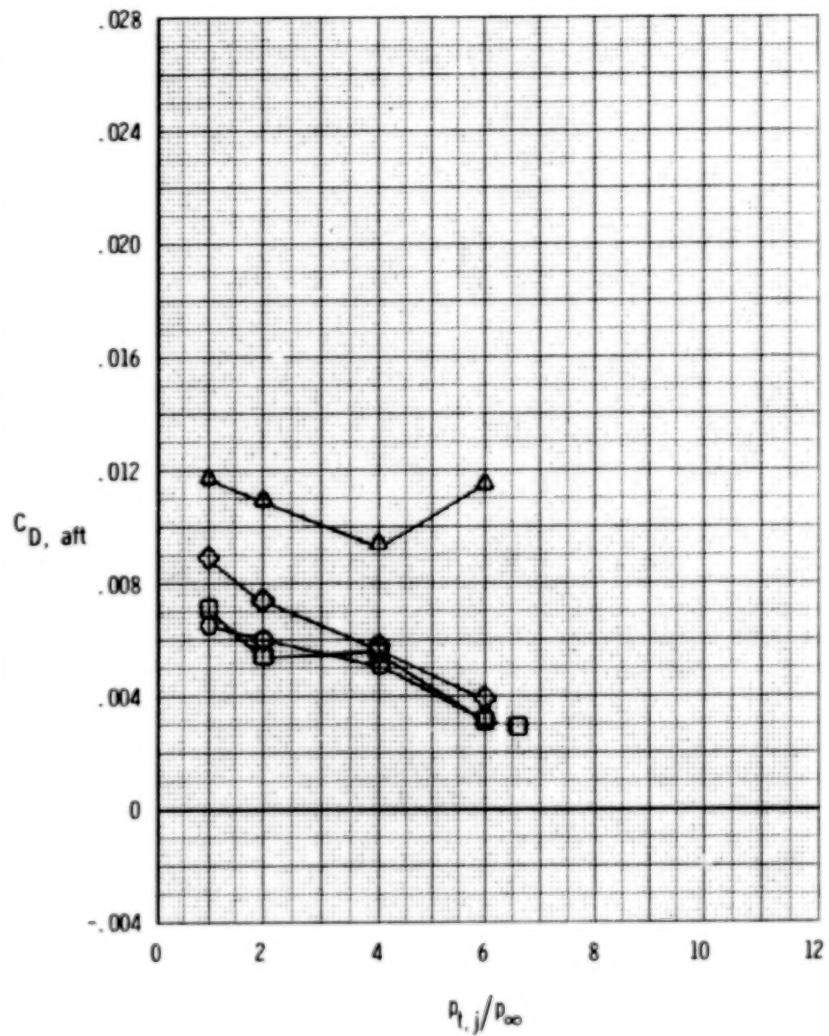
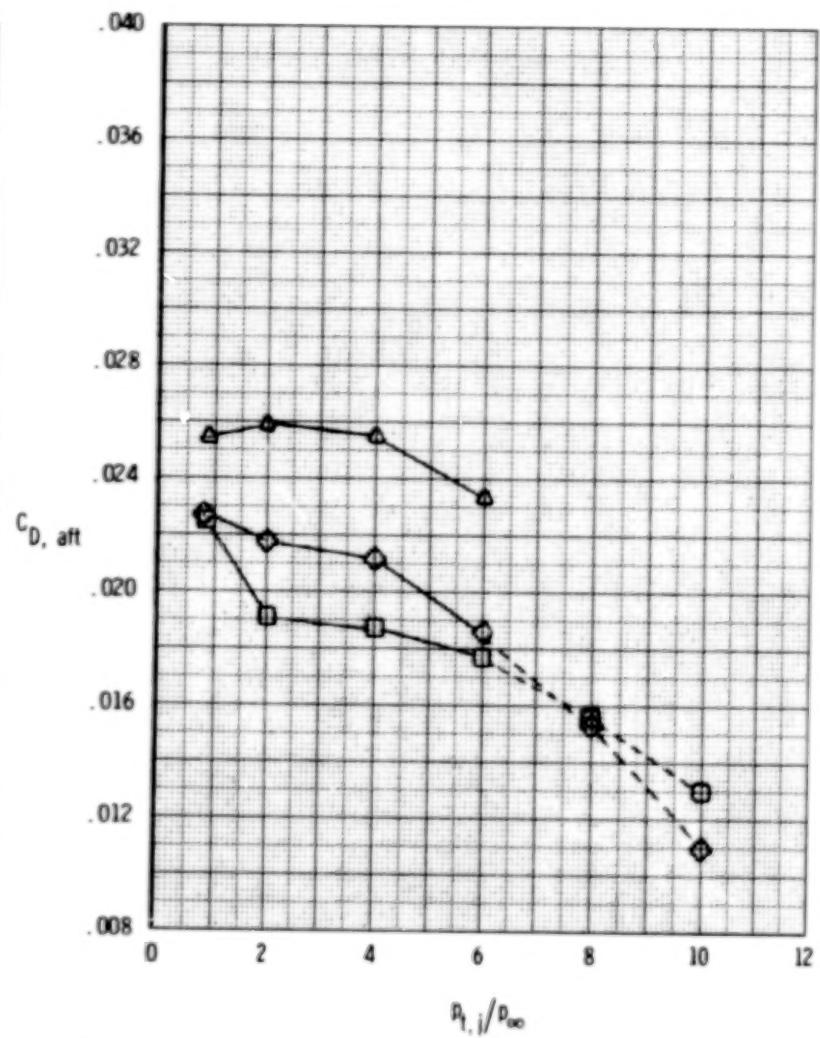
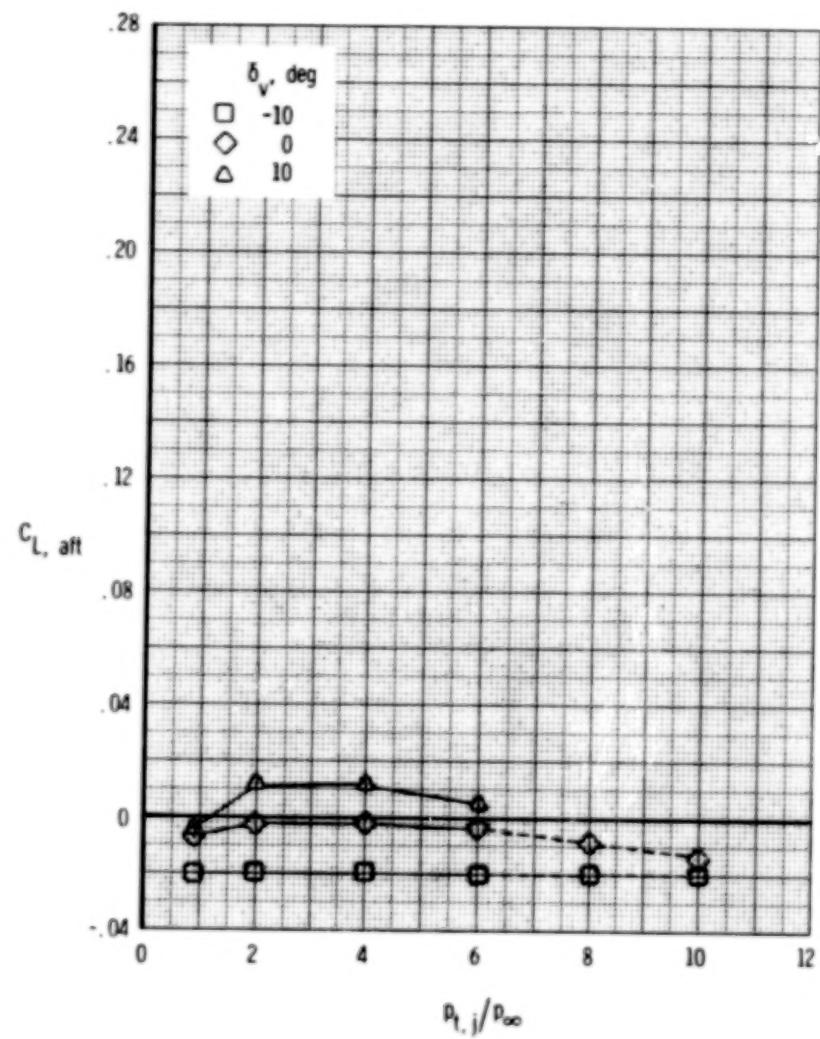
(b) $M = 0.90$.

Figure 97.- Continued.





(c) $M = 1.20.$

Figure 97.- Concluded.

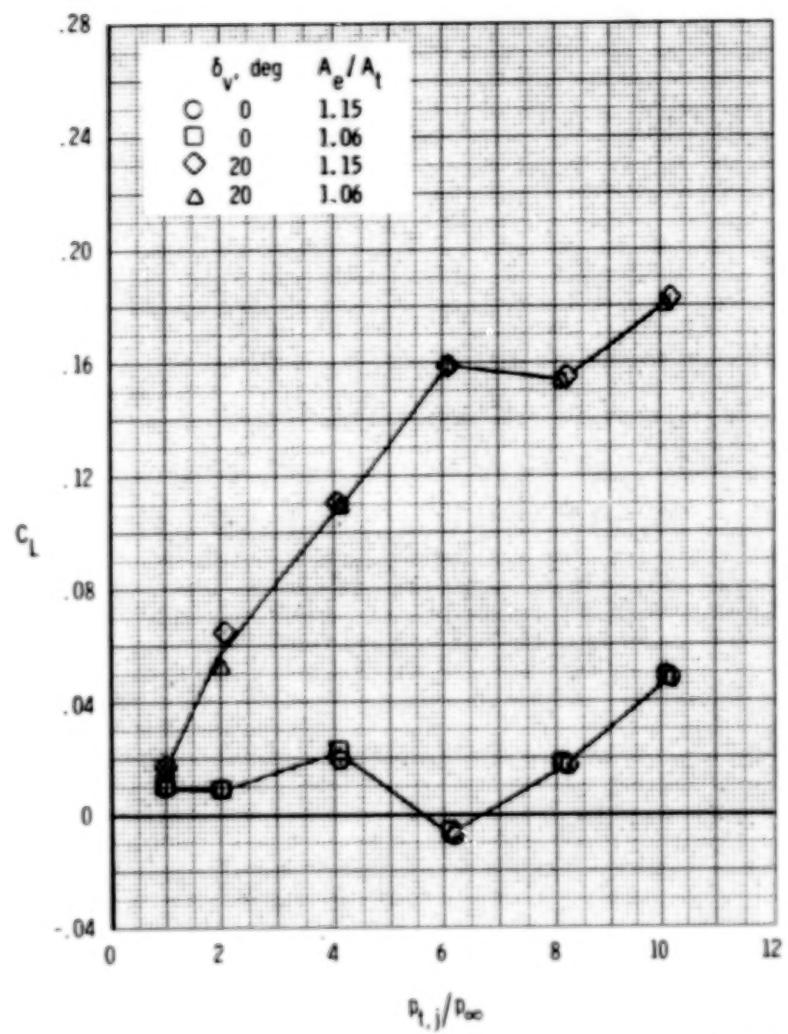
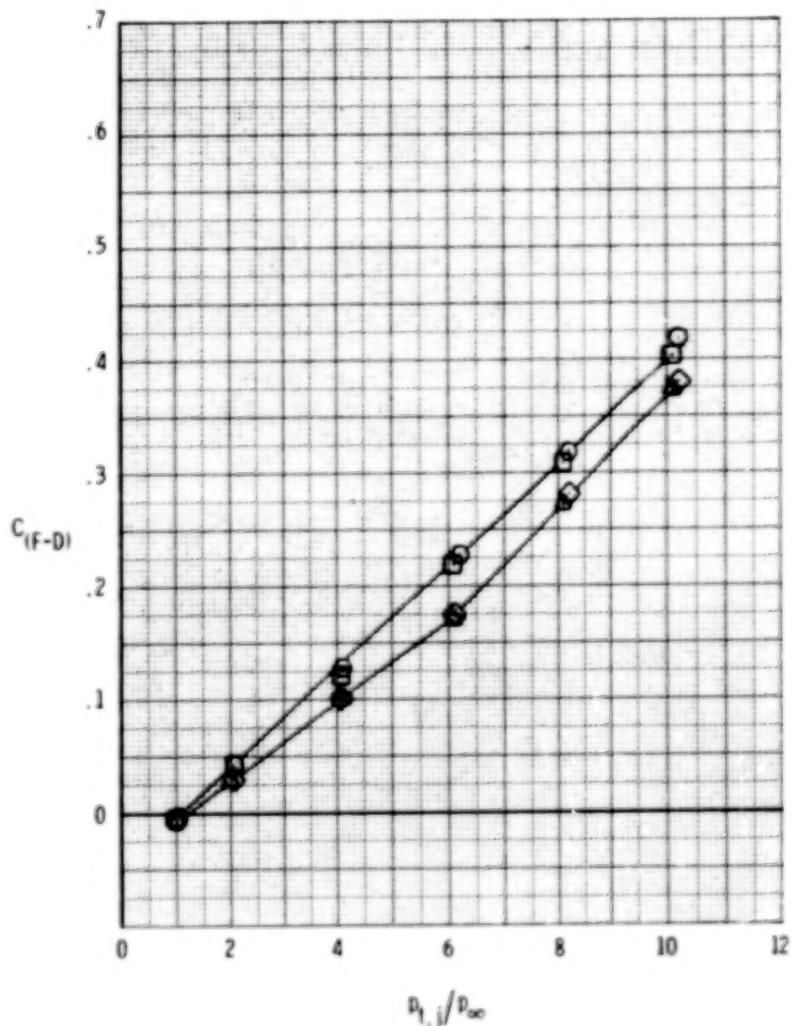
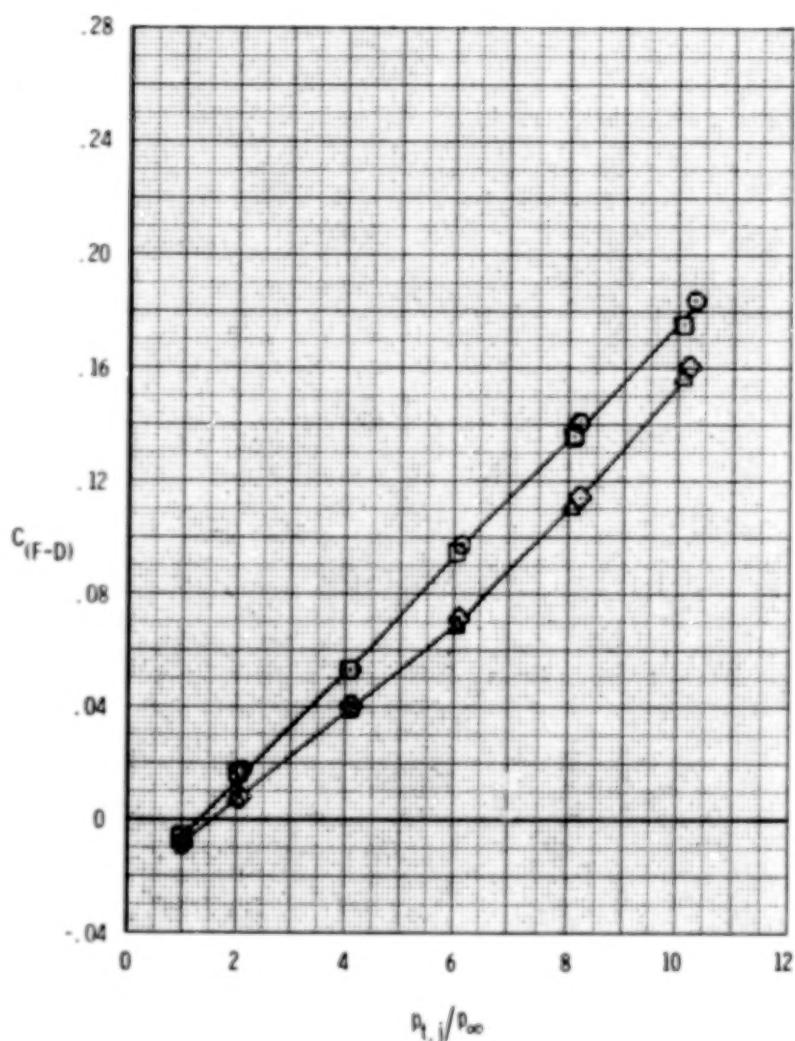
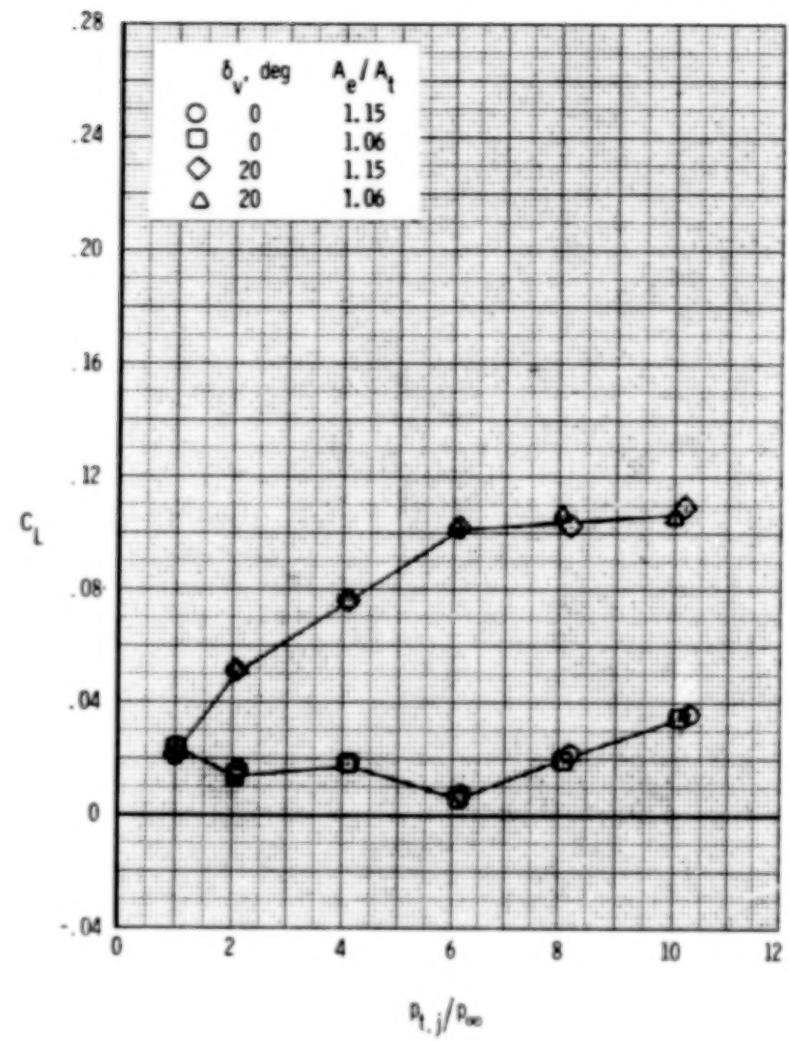
(a) $M = 0.60$.

Figure 98.- Effect of area ratio and vectoring on measured afterbody forces, SERN nozzle, dry power.
 $\delta_h = 0^\circ$; $\alpha = 0^\circ$.



(b) $M = 0.90$.

Figure 98.- Concluded.

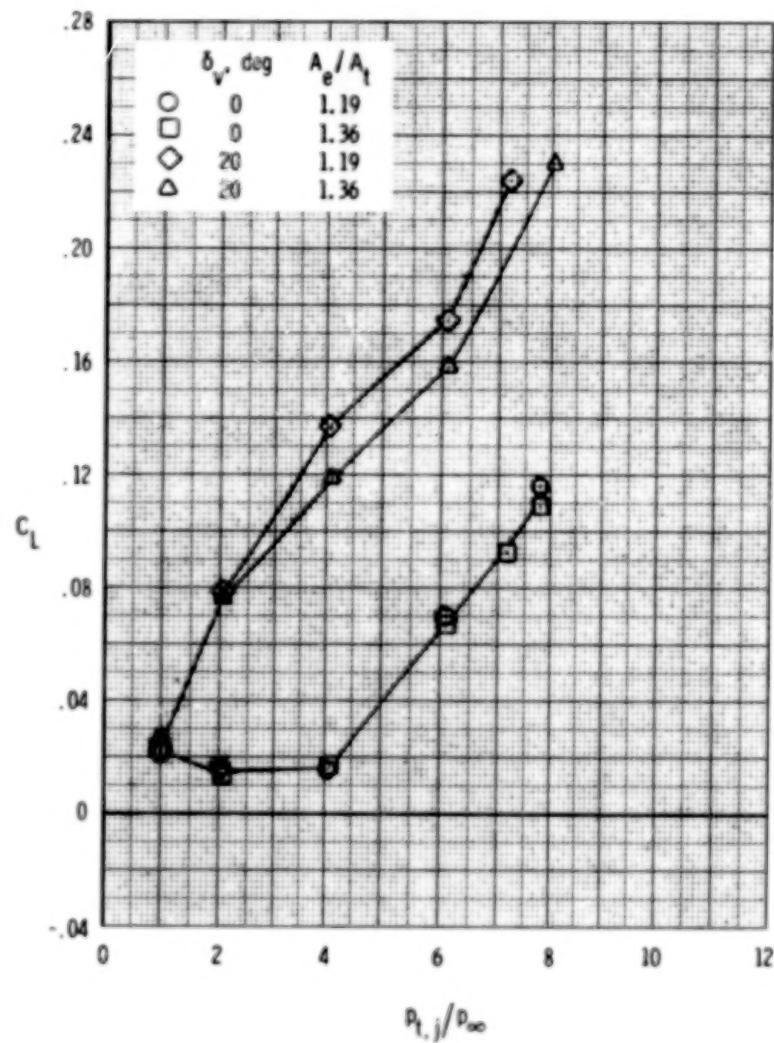
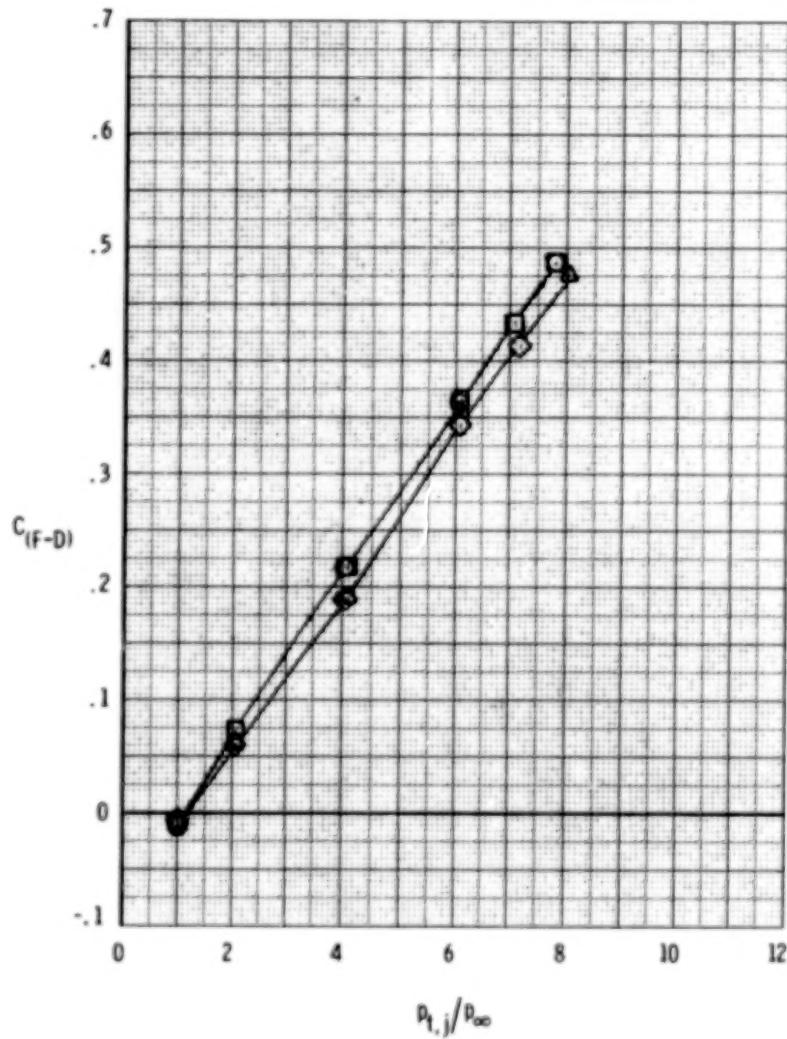
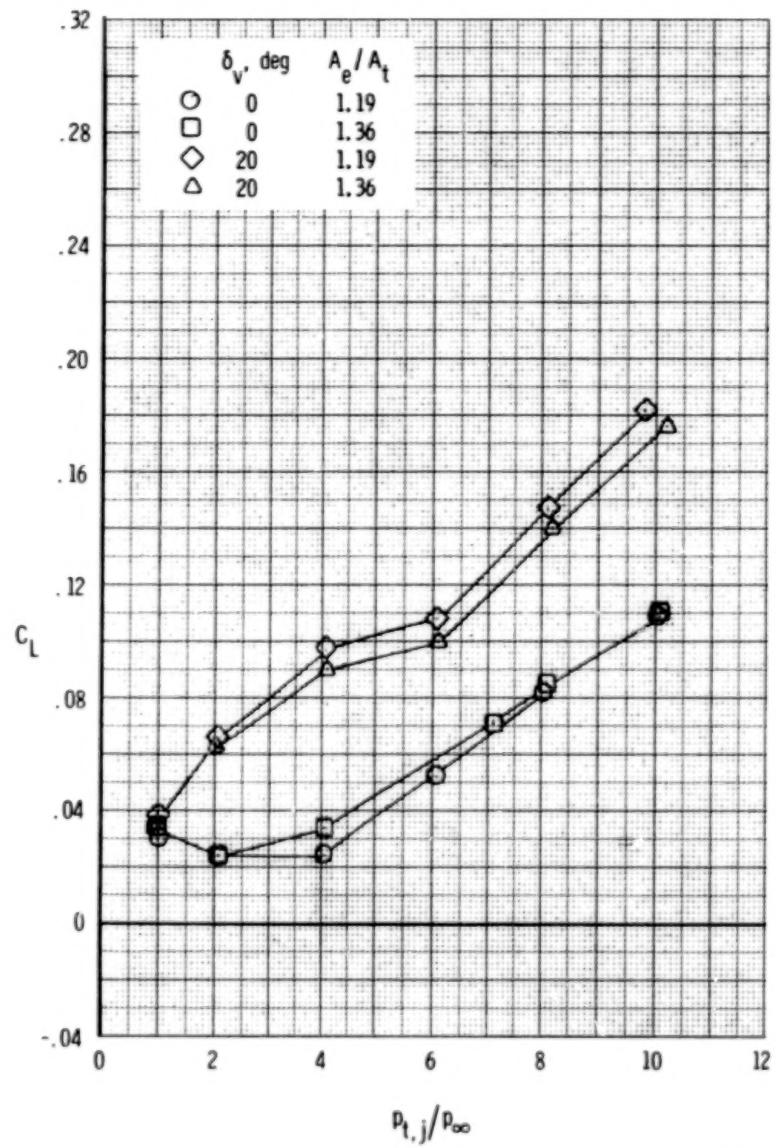
(a) $M = 0.60$.

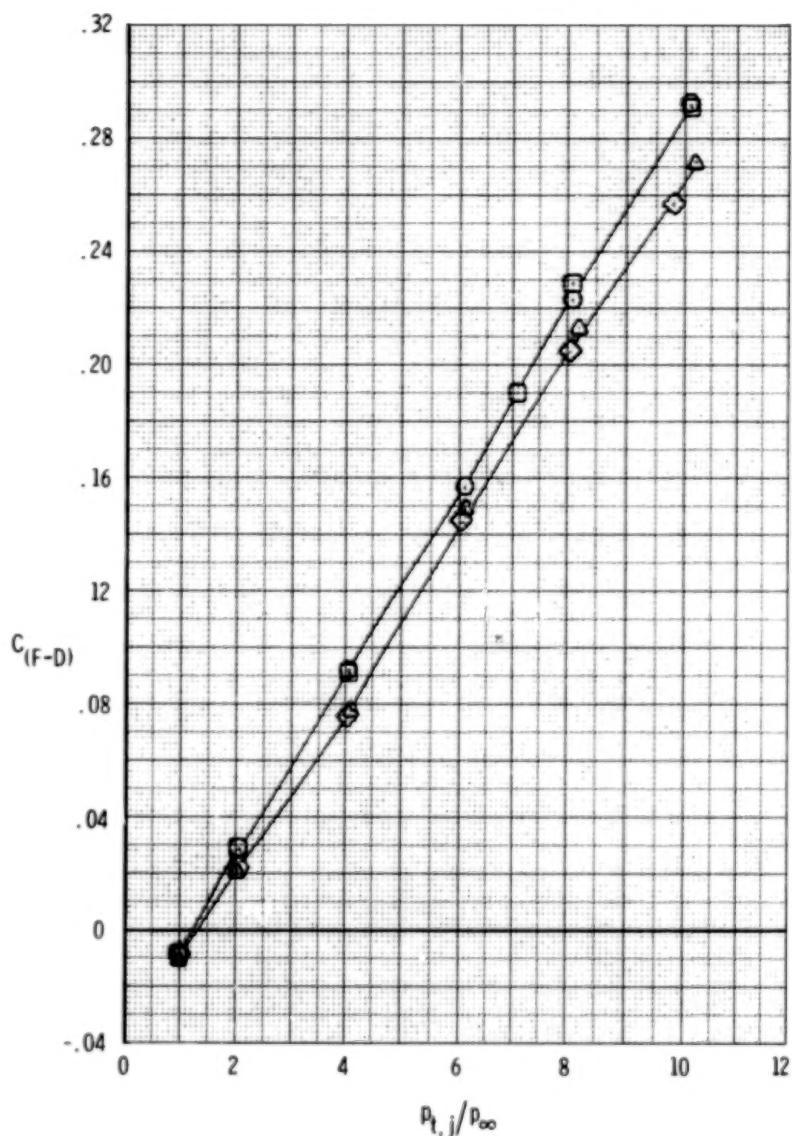
Figure 99. - Effect of area ratio and vectoring on measured afterbody forces, SERN nozzle, A/B power.

$$\delta_h = 0^\circ; \quad \alpha = 0^\circ.$$



(b) $M = 0.90$.

Figure 99.- Concluded.



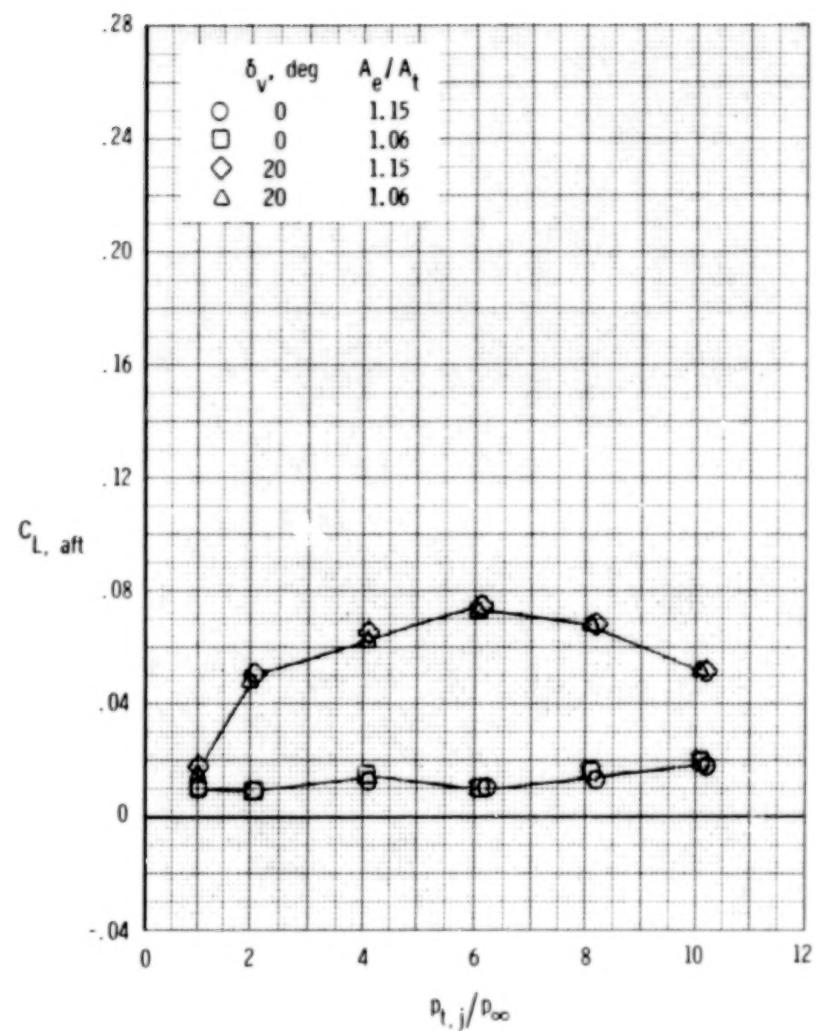
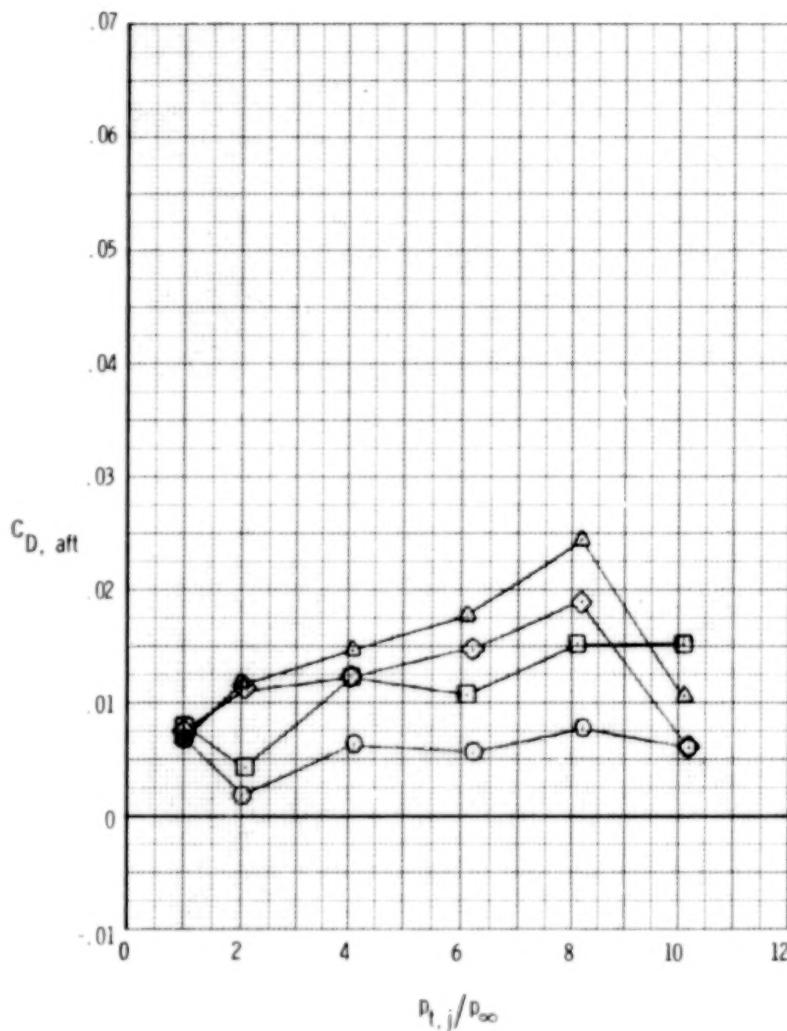
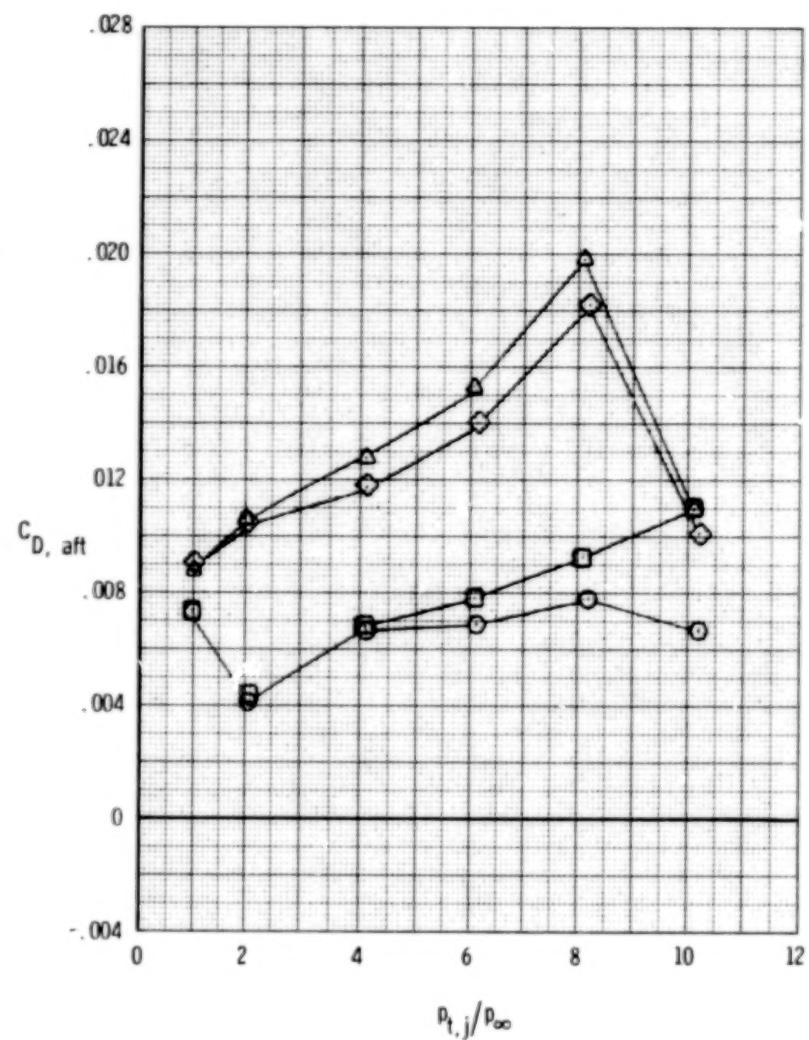
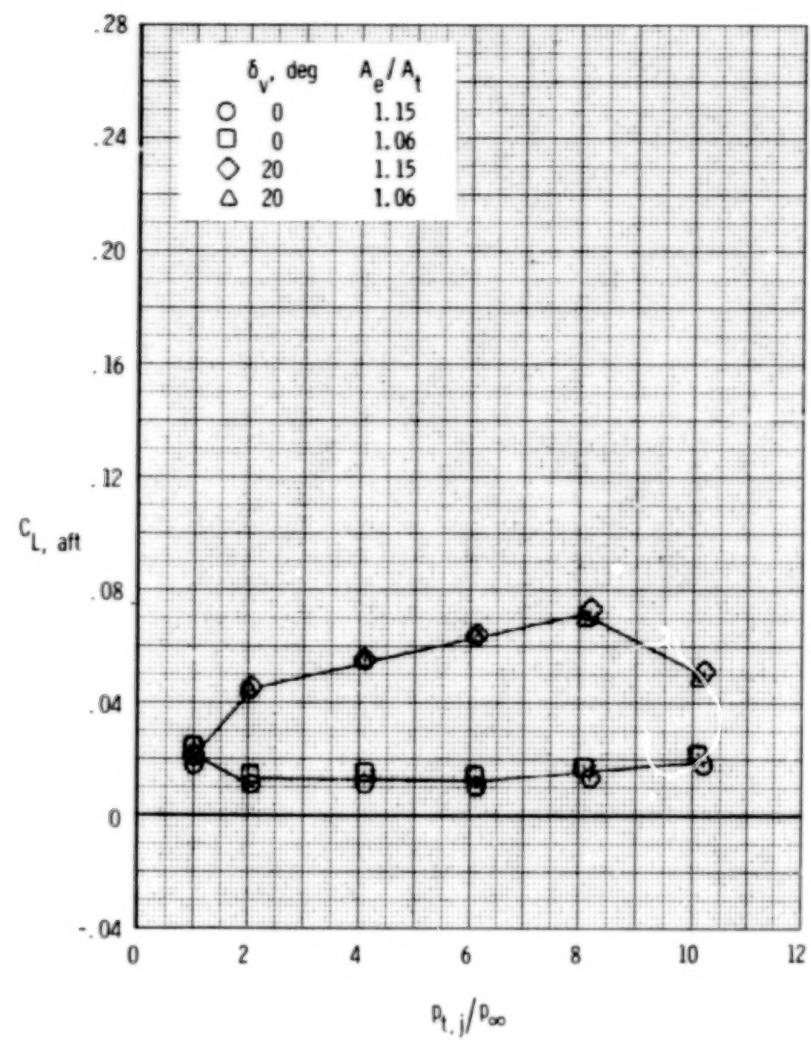
(a) $M = 0.60$.

Figure 100.- Effect of area ratio and vectoring on thrust-removed afterbody forces, SERN nozzle, dry power.

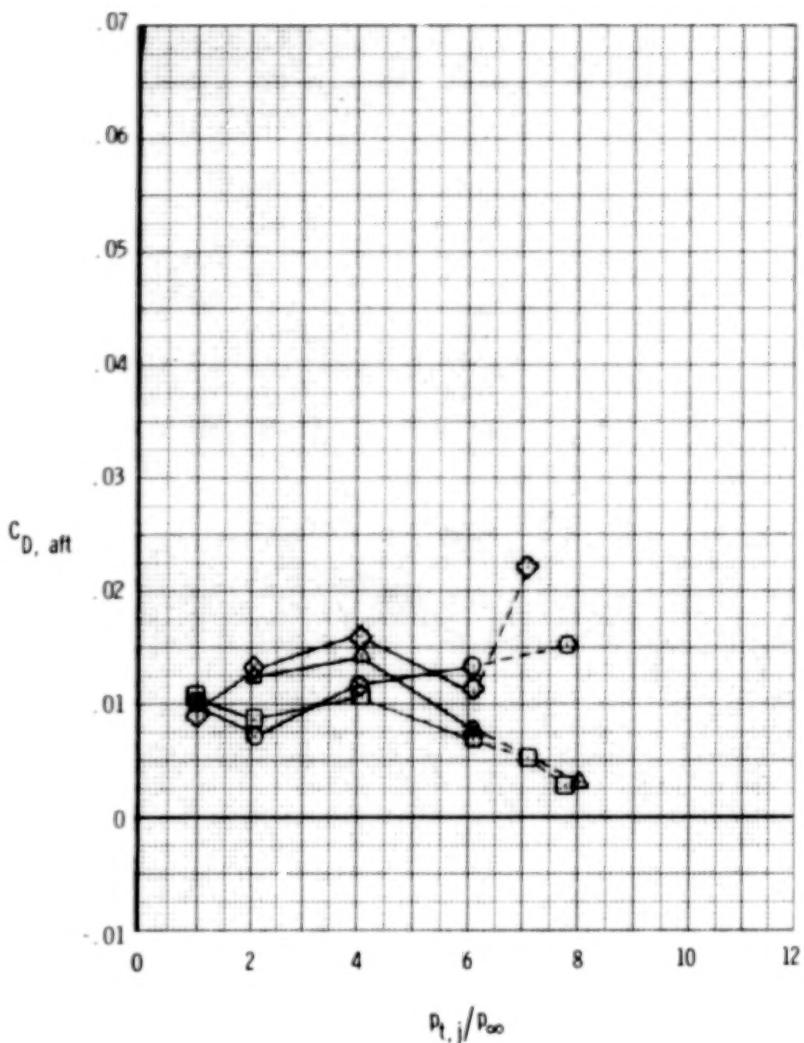
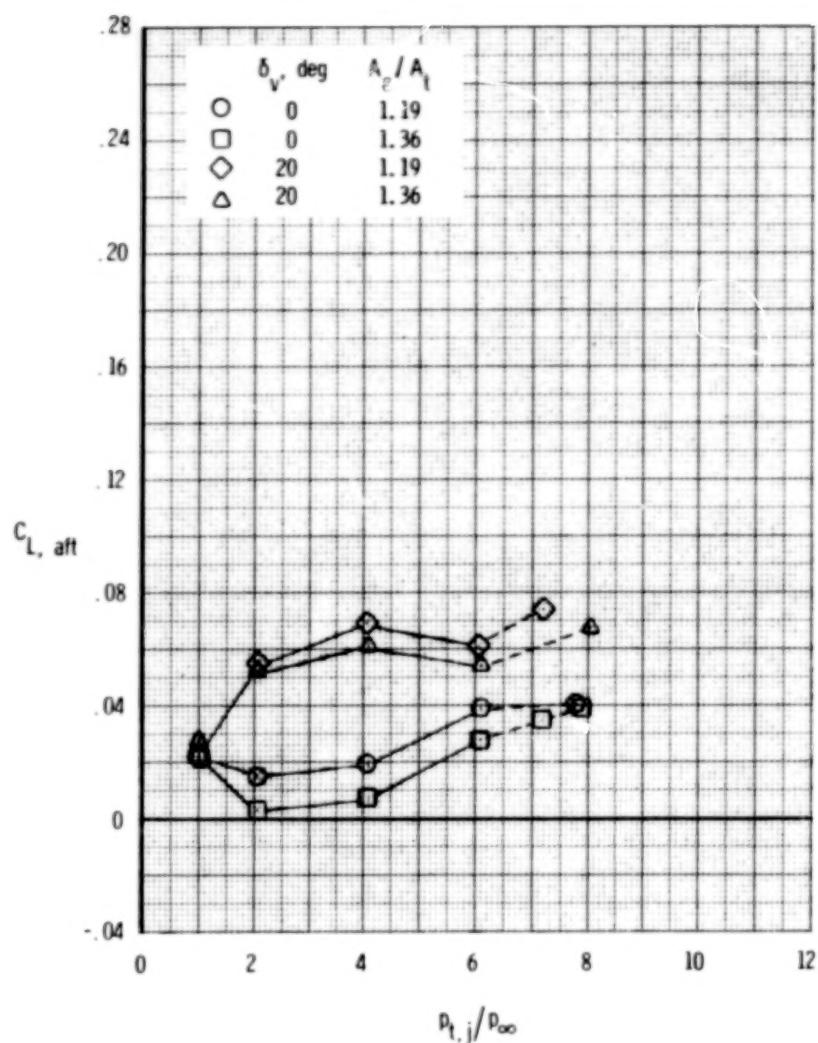
$$\delta_h = 0^\circ; \quad \alpha = 0^\circ.$$



(b) $M = 0.90$.

Figure 100.- Concluded.

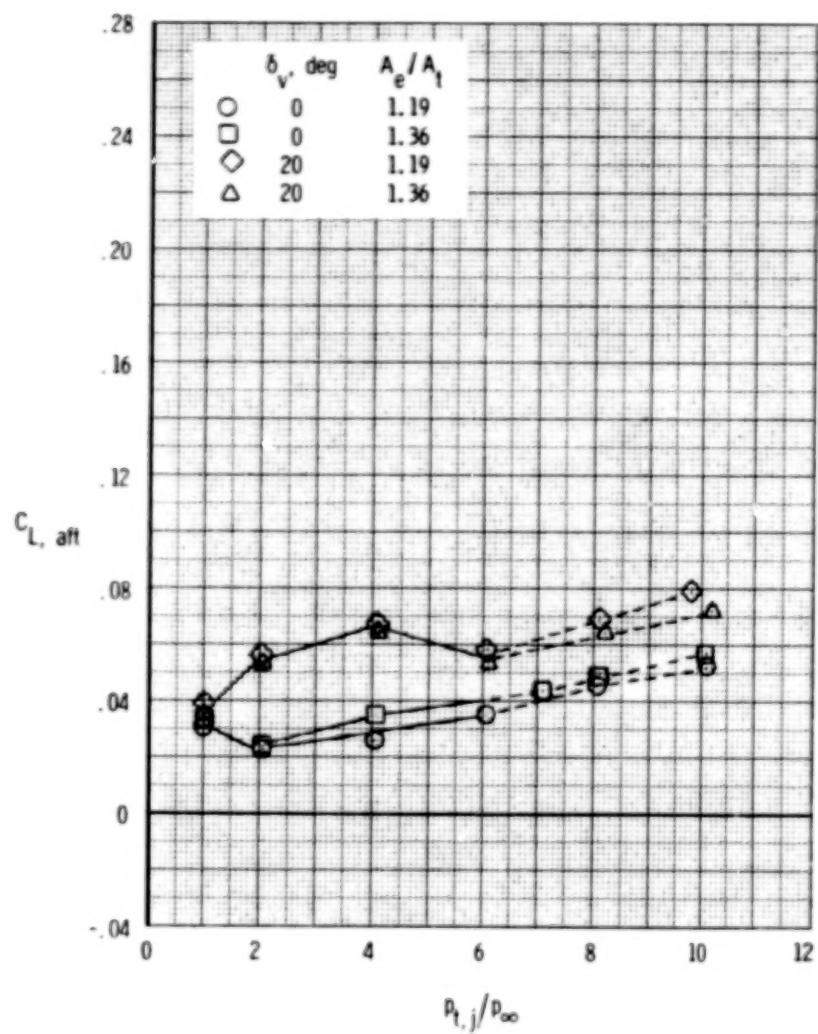
260



(a) $M = 0.60$.

Figure 101.- Effect of area ratio and vectoring on thrust-removed afterbody forces, SERN nozzle, A/B power.

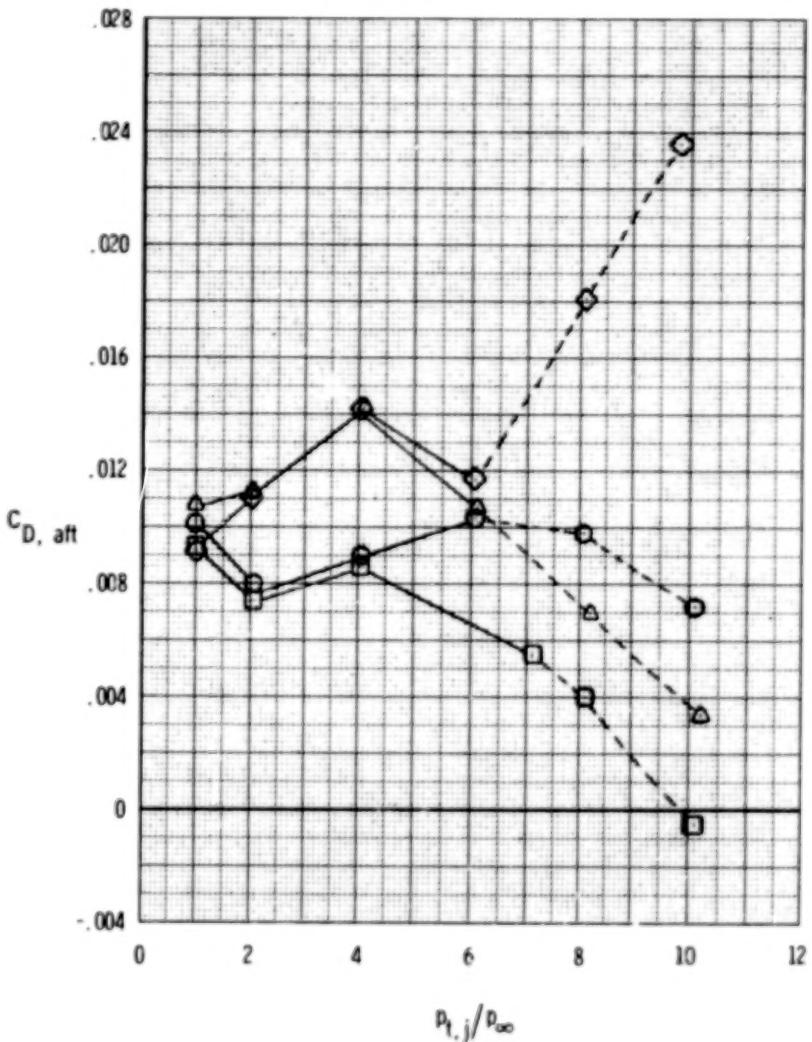
$\delta_h = 0^0$; $\alpha = 0^0$. Dashed lines indicate data results from extrapolating static data.



(b) $M = 0.90$.

Figure 101.- Concluded.

261



262

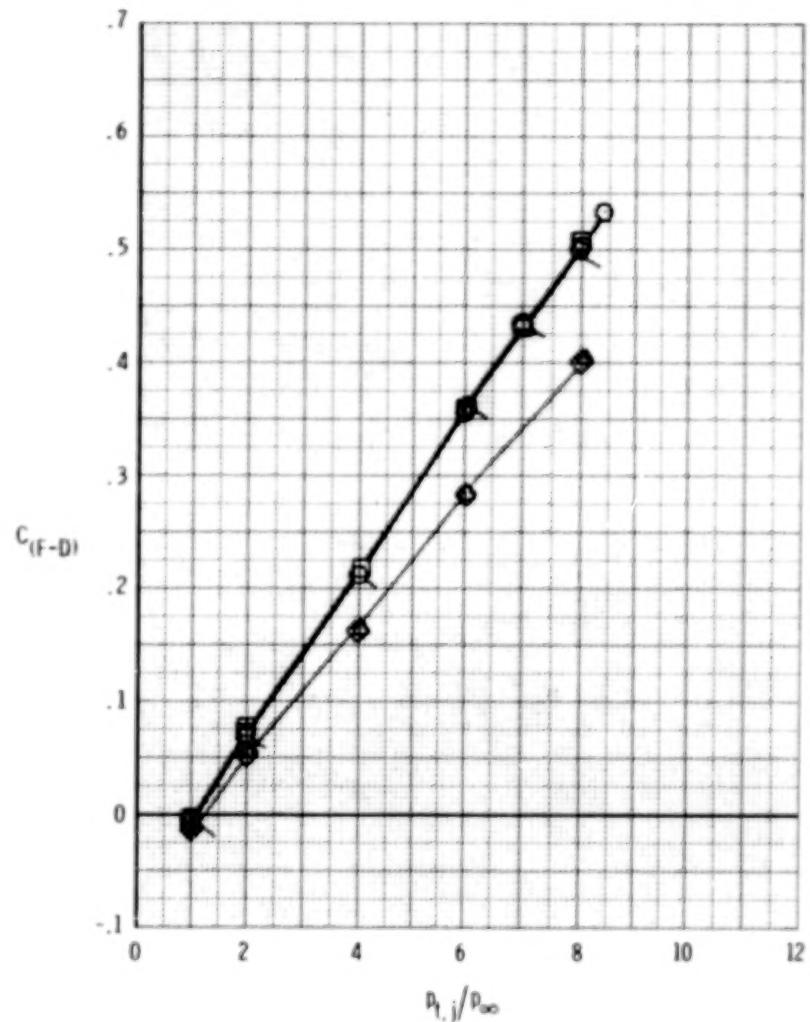
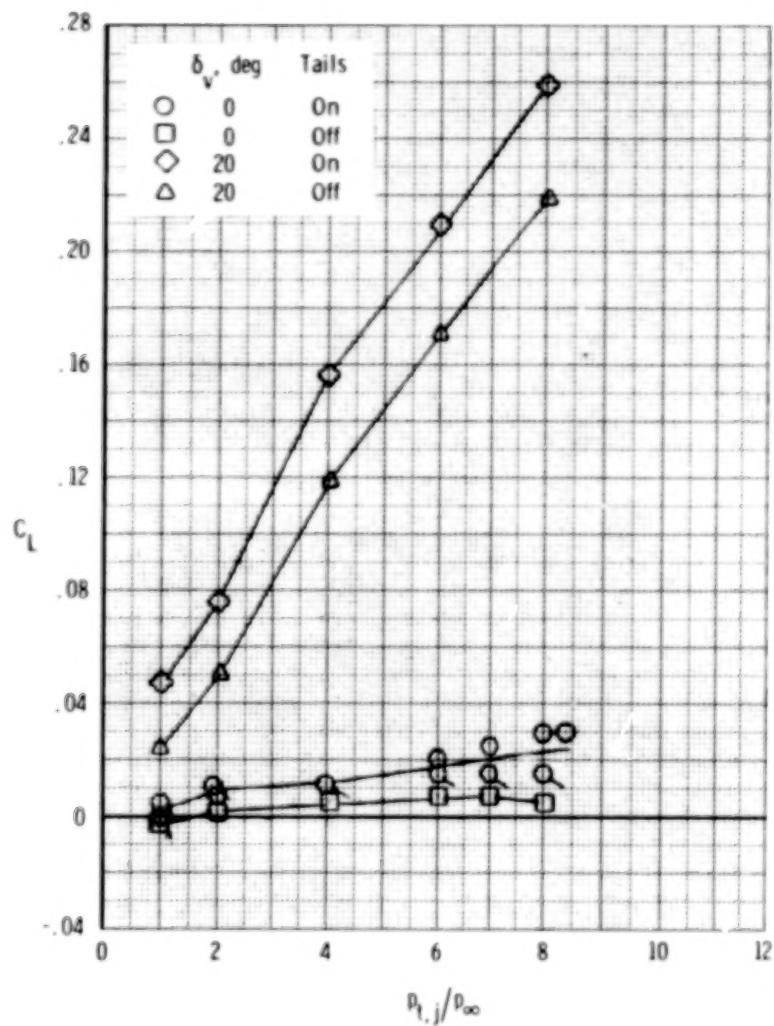
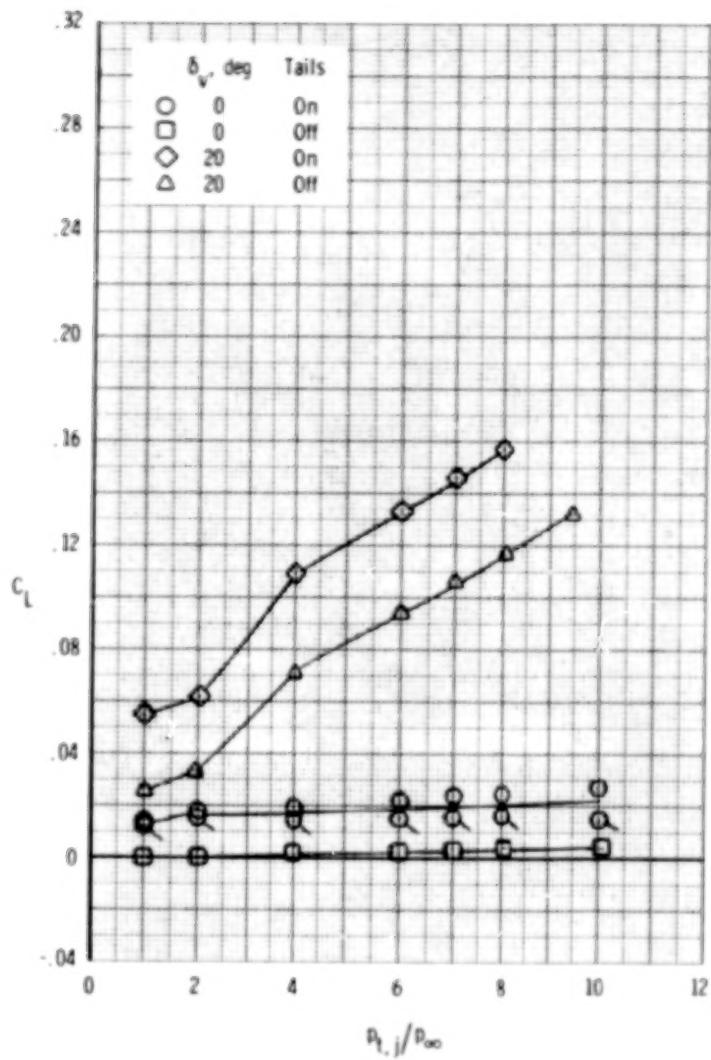
(a) $M = 0.60$.

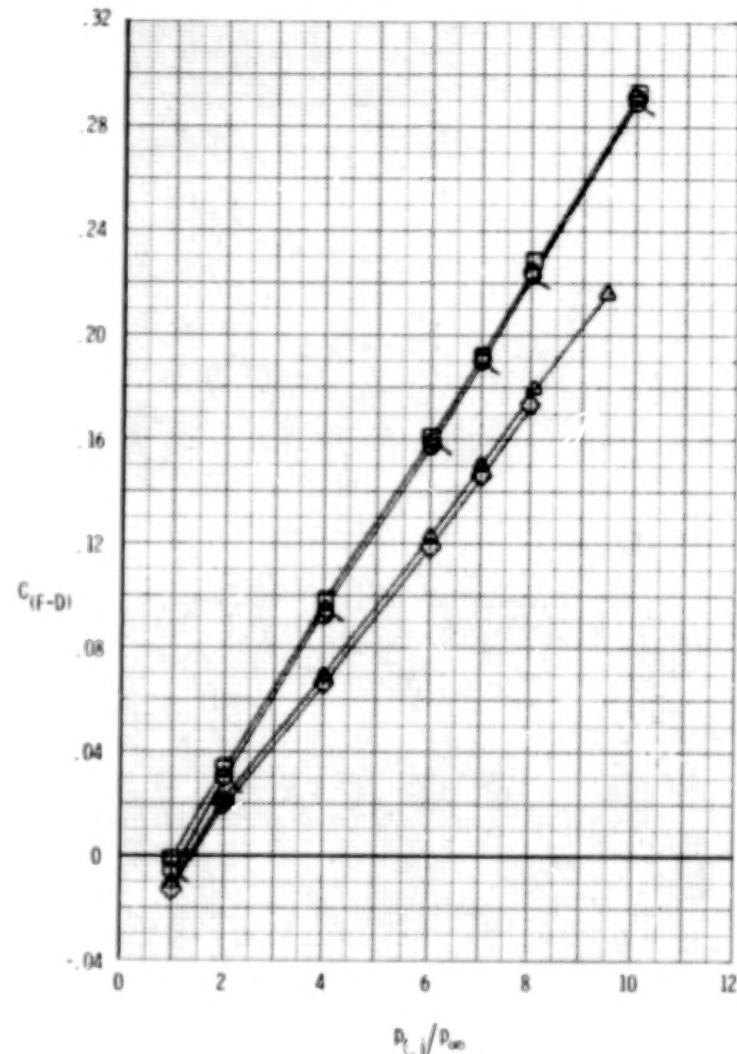
Figure 102.- Effect of tails and vectoring on measured afterbody forces, 2-D C-D nozzle, A/B power.
 $\delta_h = 0^{\circ}$; $\alpha = 0^{\circ}$. Flagged symbols indicate repeat points.



(b) $M = 0.90$.

Figure 102.- Continued.

263



INVESTIGATION OF AXISYMMETRIC AND NONAXISYMMETRIC
NOZZLES INSTALLED ON A 0.10-SCALE F-18 PROTOTYPE
AIRPLANE MODEL... NASA TECHNICAL PAPER 1638...
NAS 1.60:1638

JUN 1980
SUBTOPIC
NATIONAL AERONAUTICS AND SPACE ADM... JUNE 1980

60F 6
24X
SUBTOPIC
NATIONAL AERONAUTICS AND SPACE ADM... JUNE 1980

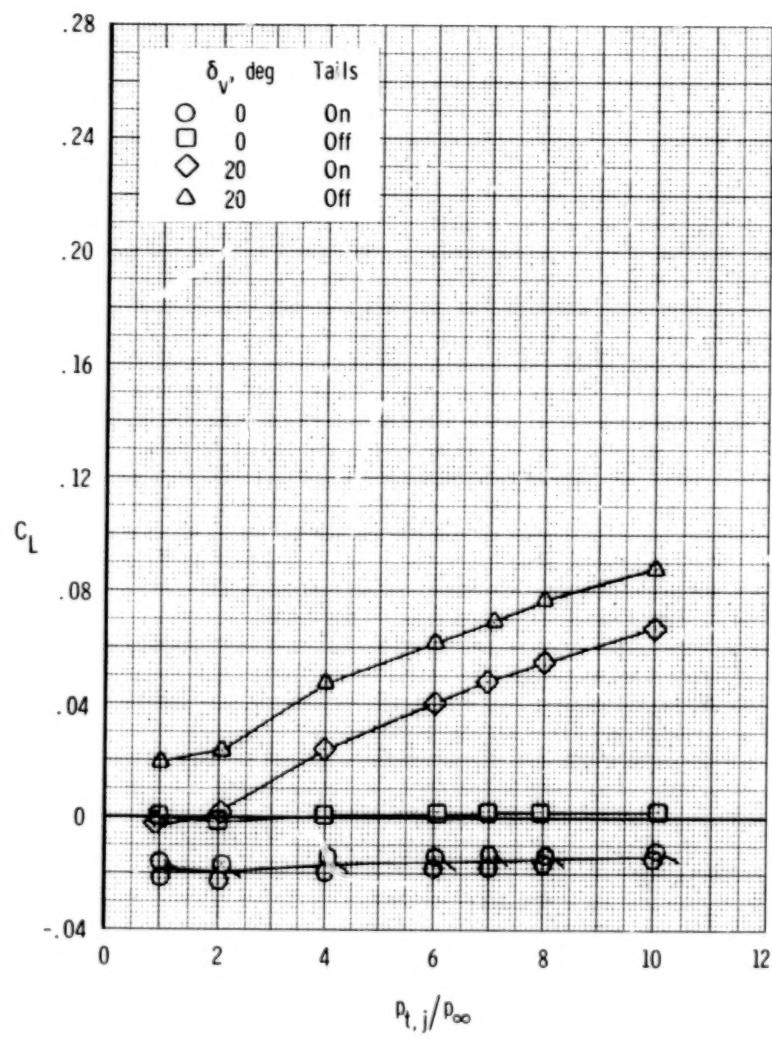
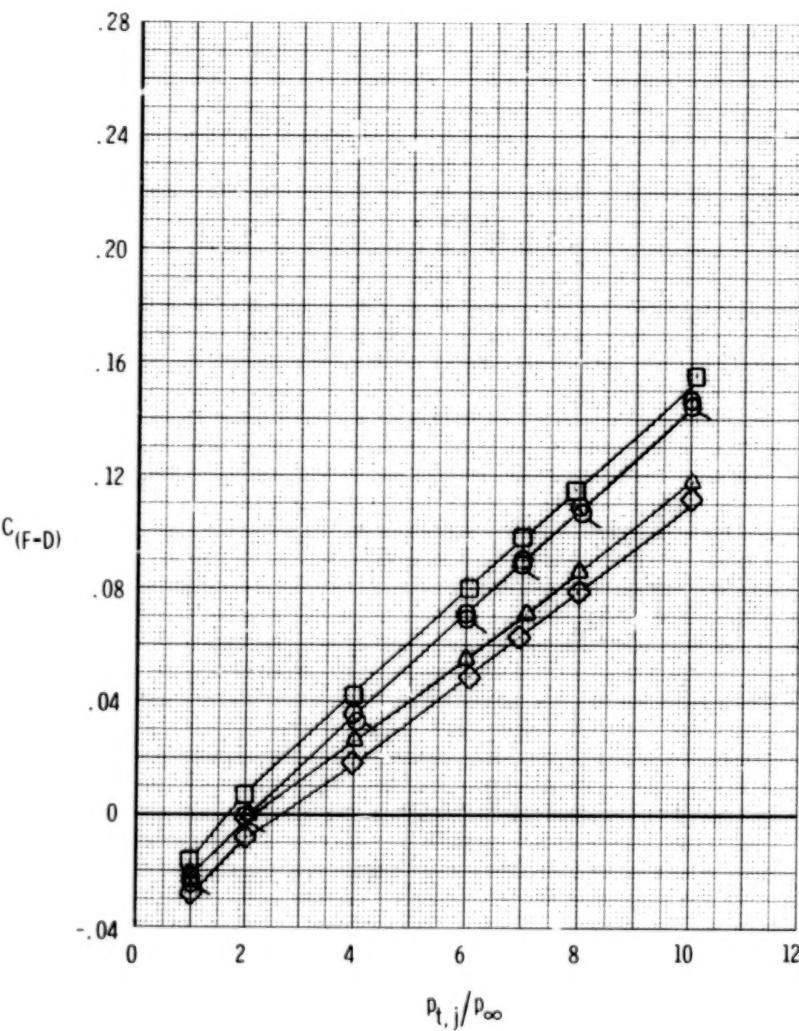
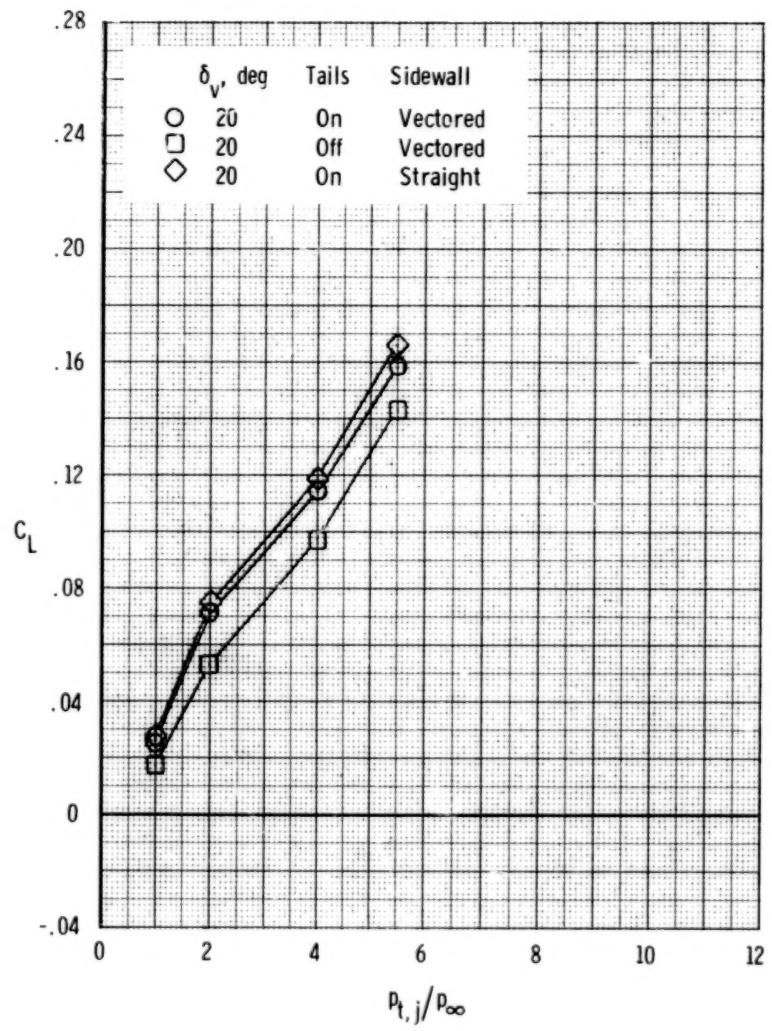
(c) $M = 1.20$.

Figure 102.- Concluded.





(a) $M = 0.60$.

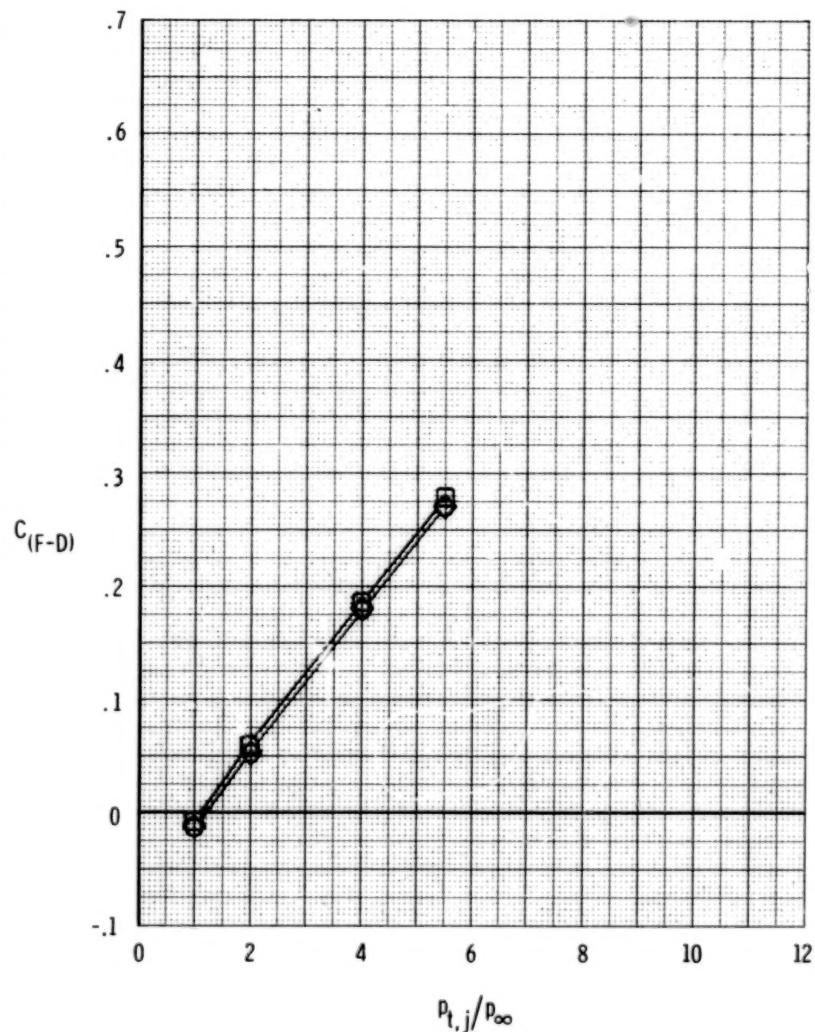
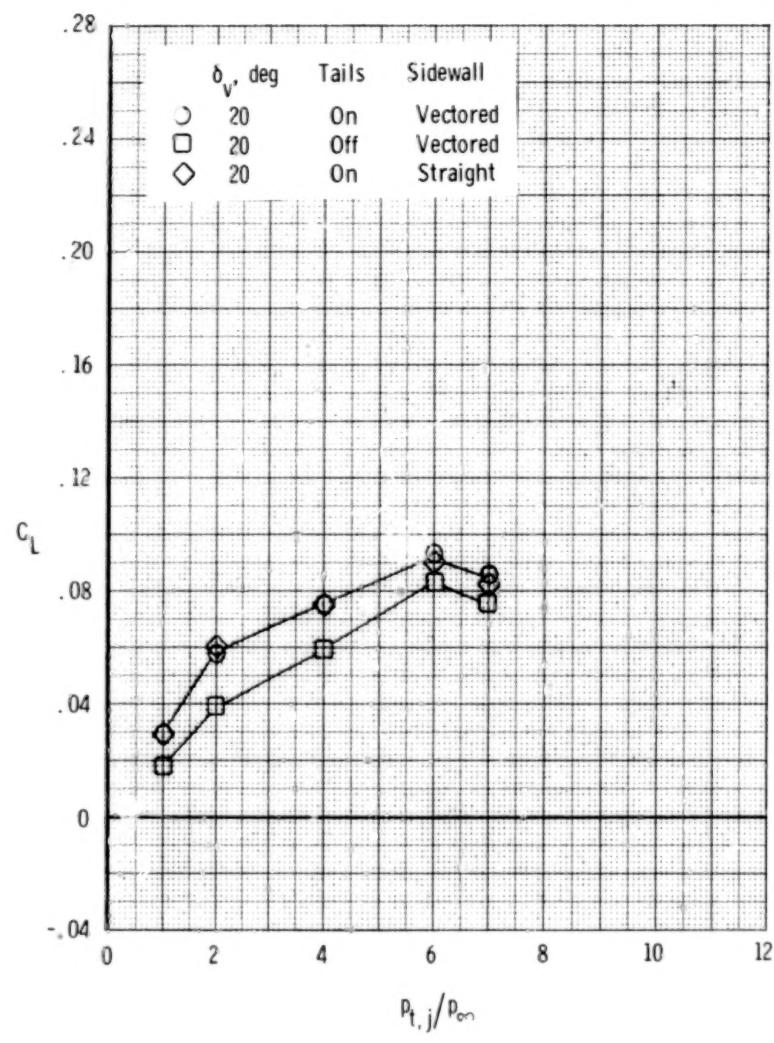


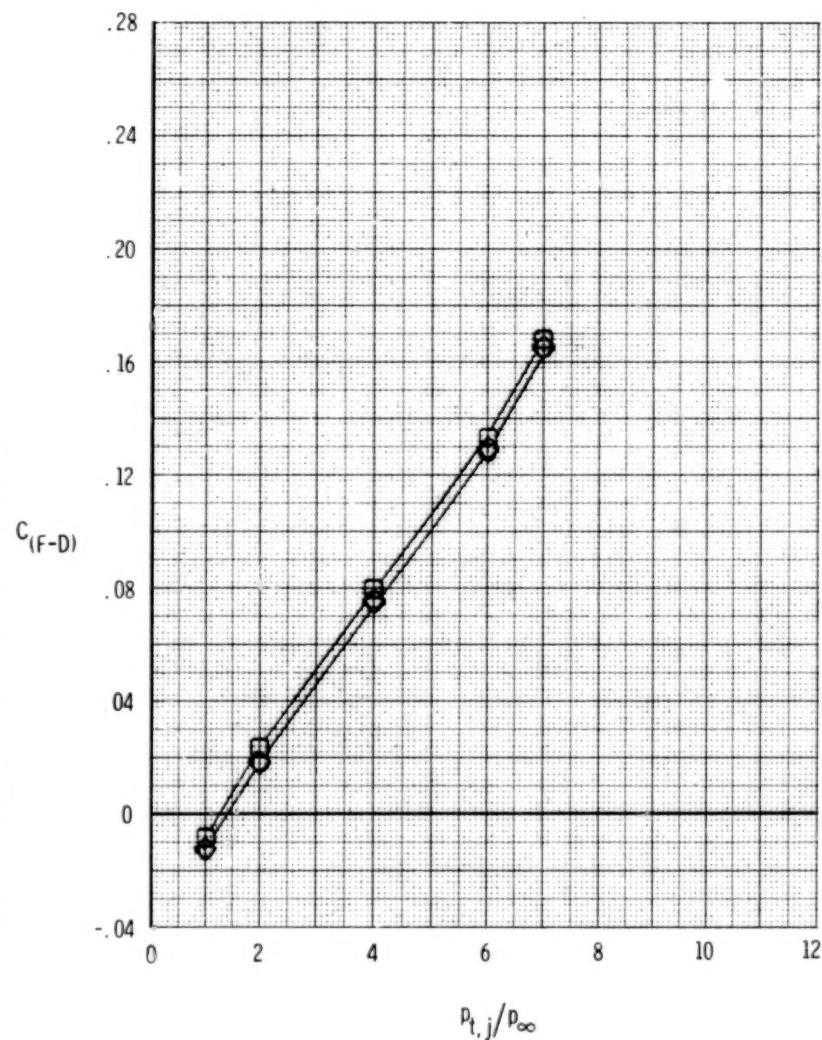
Figure 103.- Effect of tails and sidewall geometry on measured afterbody forces, wedge nozzle, A/B power.
 $\delta_h = 0^0$; $\alpha = 0^0$.

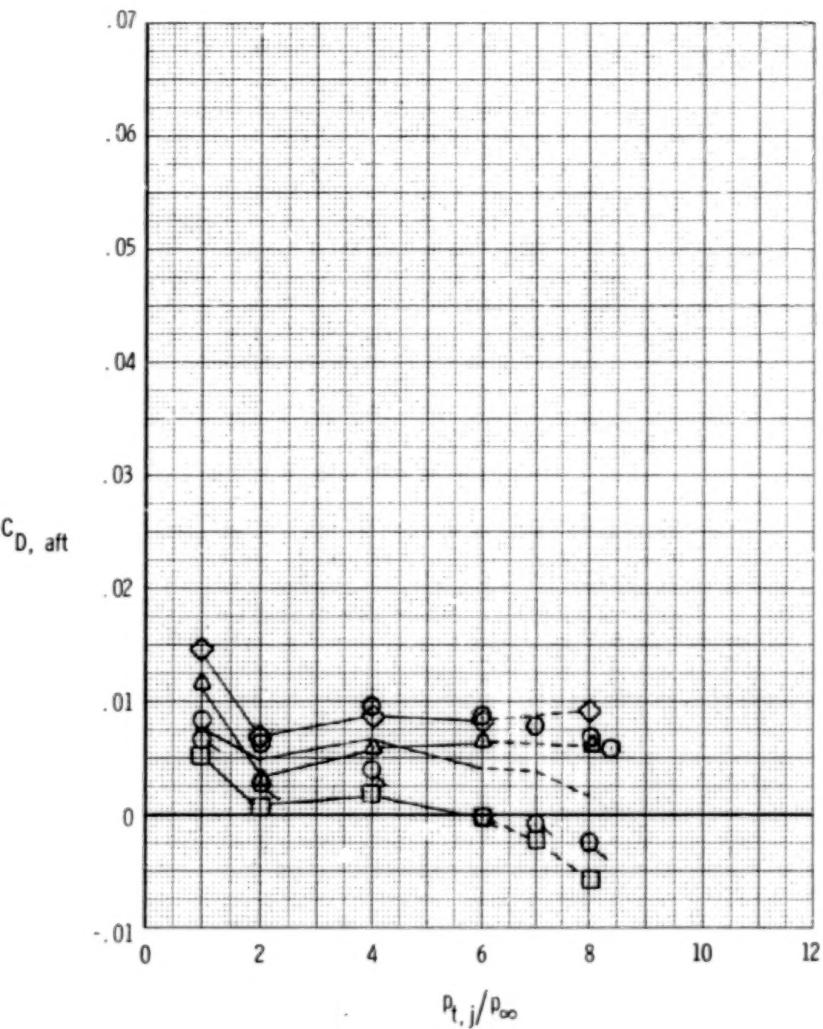
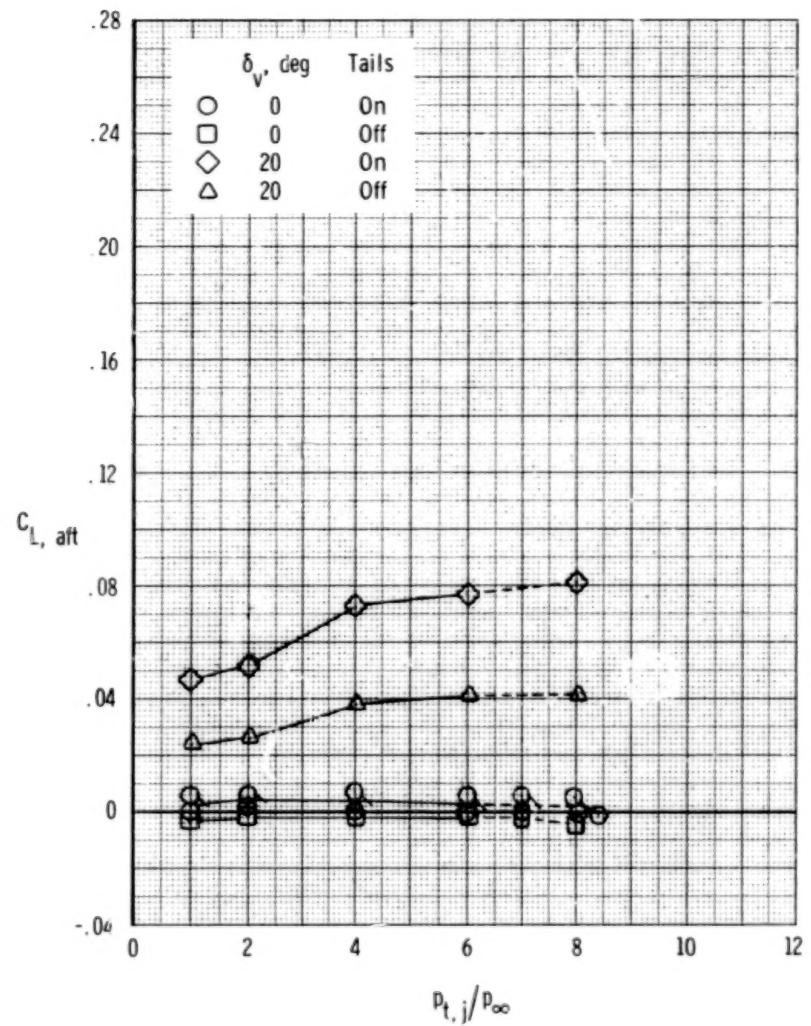
266



(b) $M = 0.90.$

Figure 103.- Concluded.





(a) $M = 0.60$.

Figure 104.- Effect of tails and vectoring on thrust-removed afterbody forces, 2-D C-D nozzle, A/B power.

$$\delta_h = 0^\circ; \quad \alpha = 0^\circ.$$

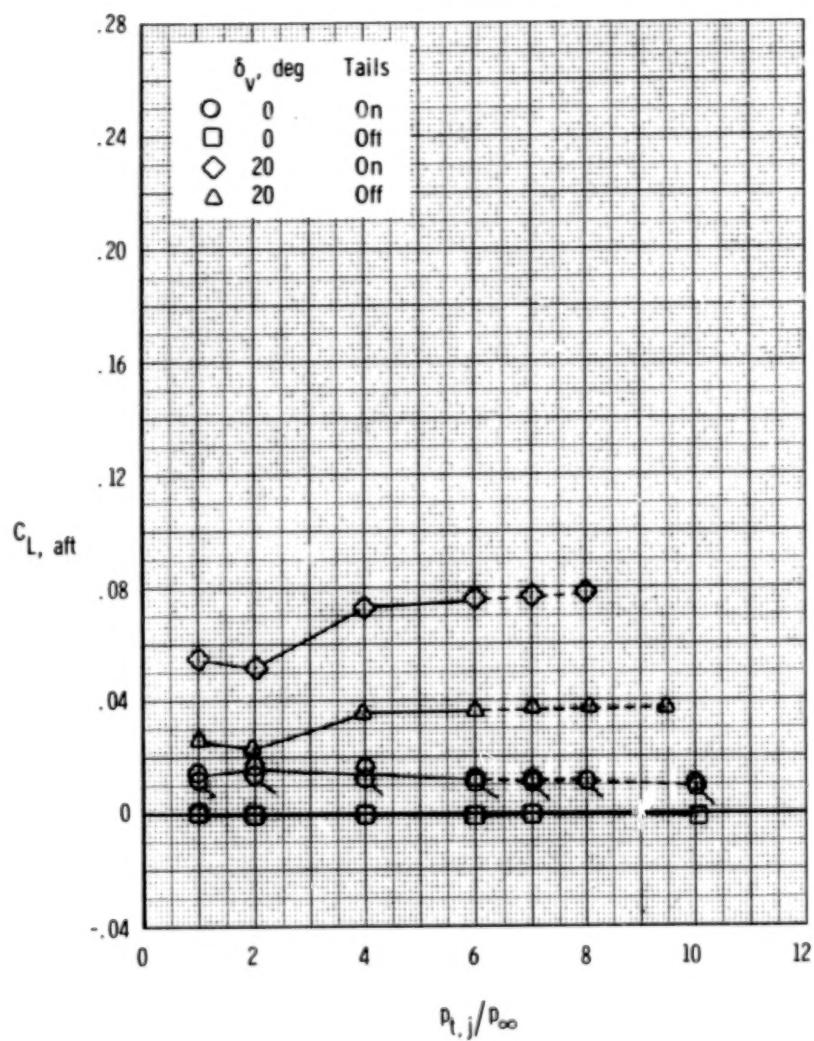
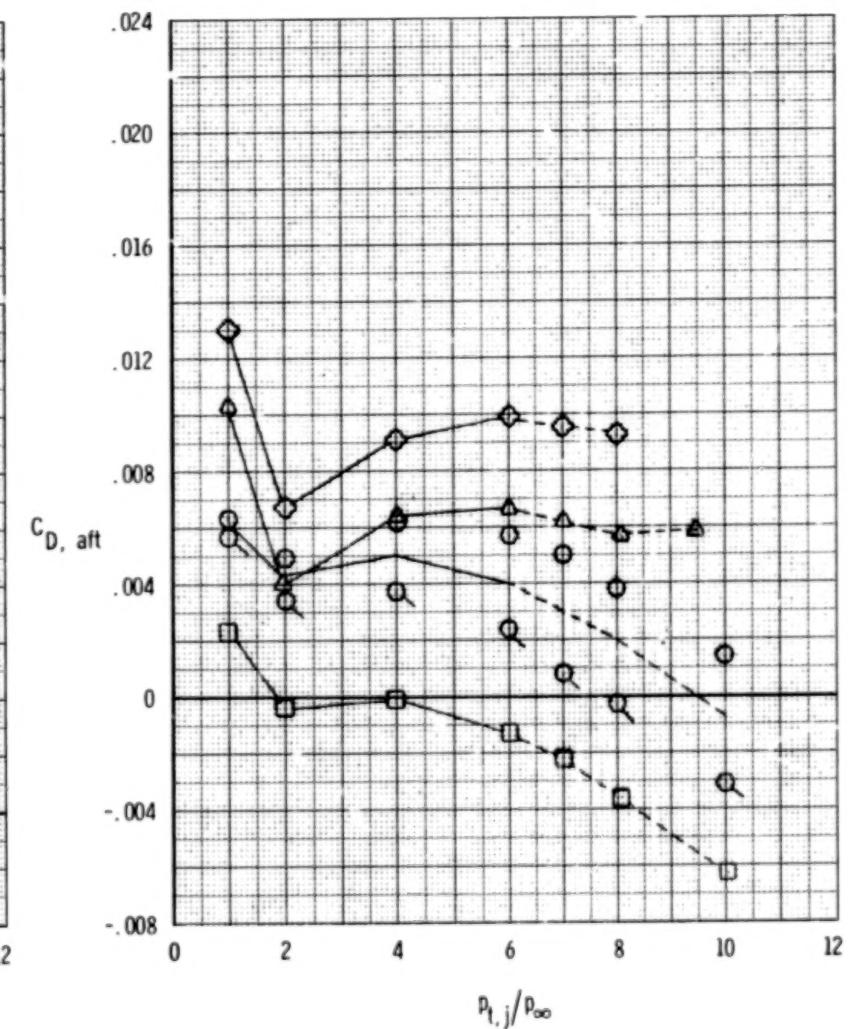
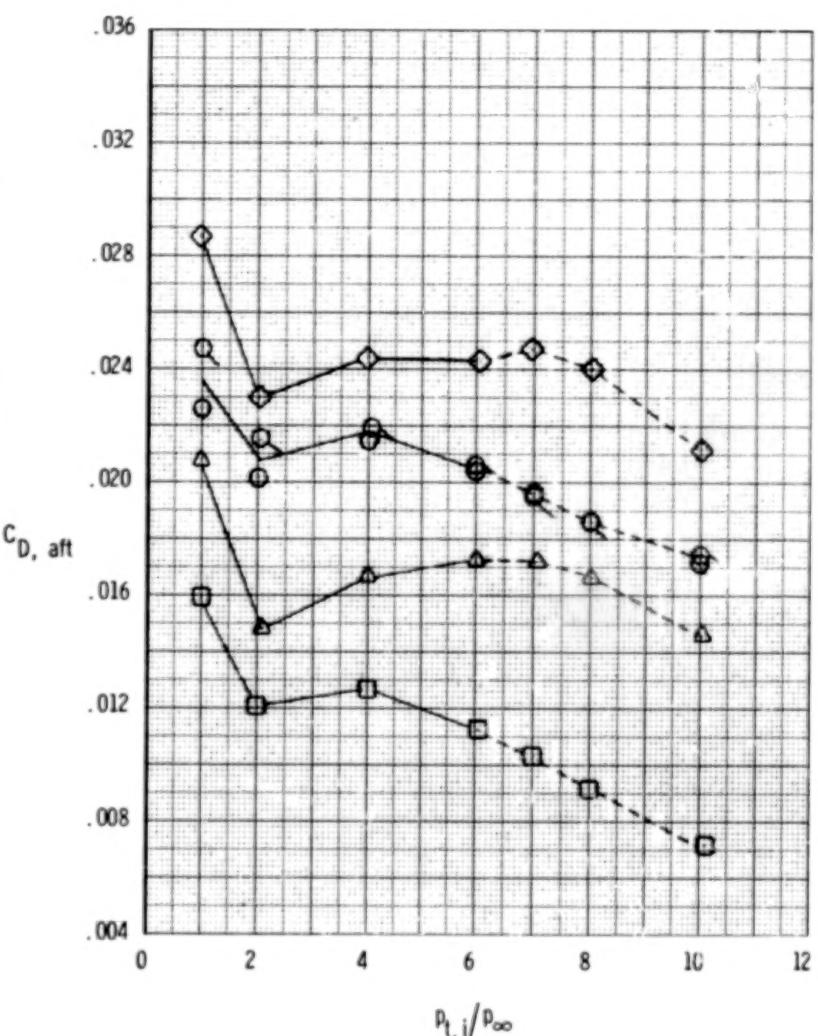
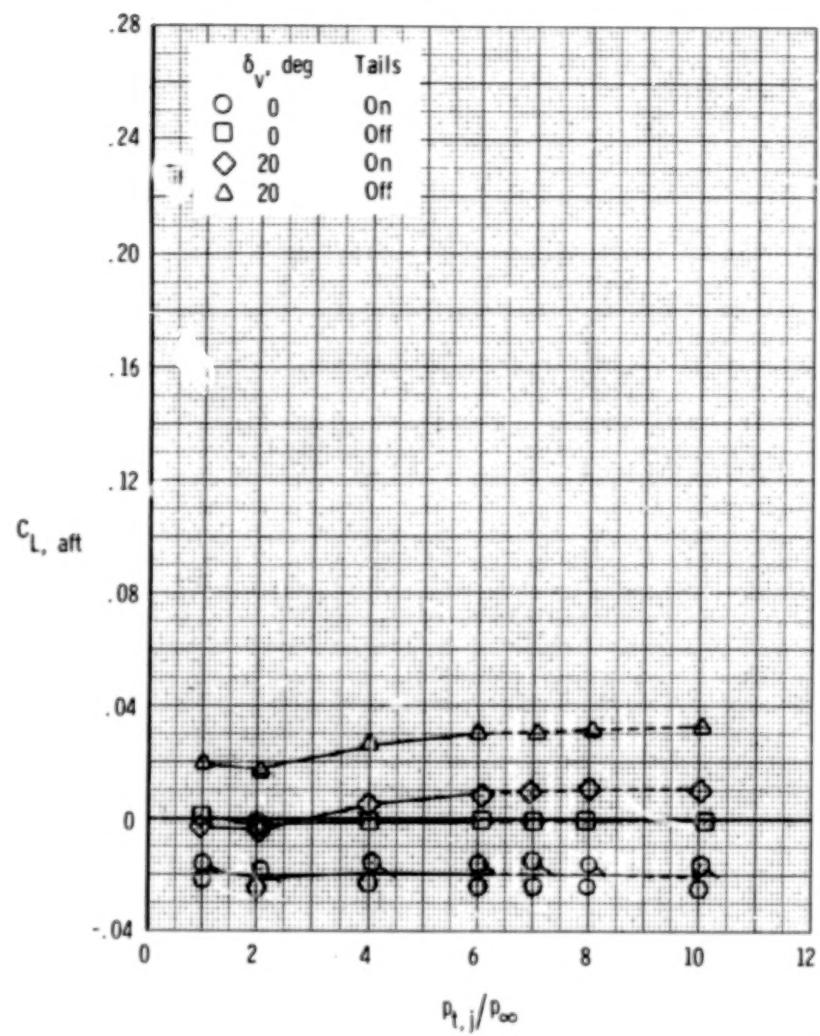
(b) $M = 0.90$.

Figure 104.- Continued.



(c) $M = 1.20$.

Figure 104.- Concluded.

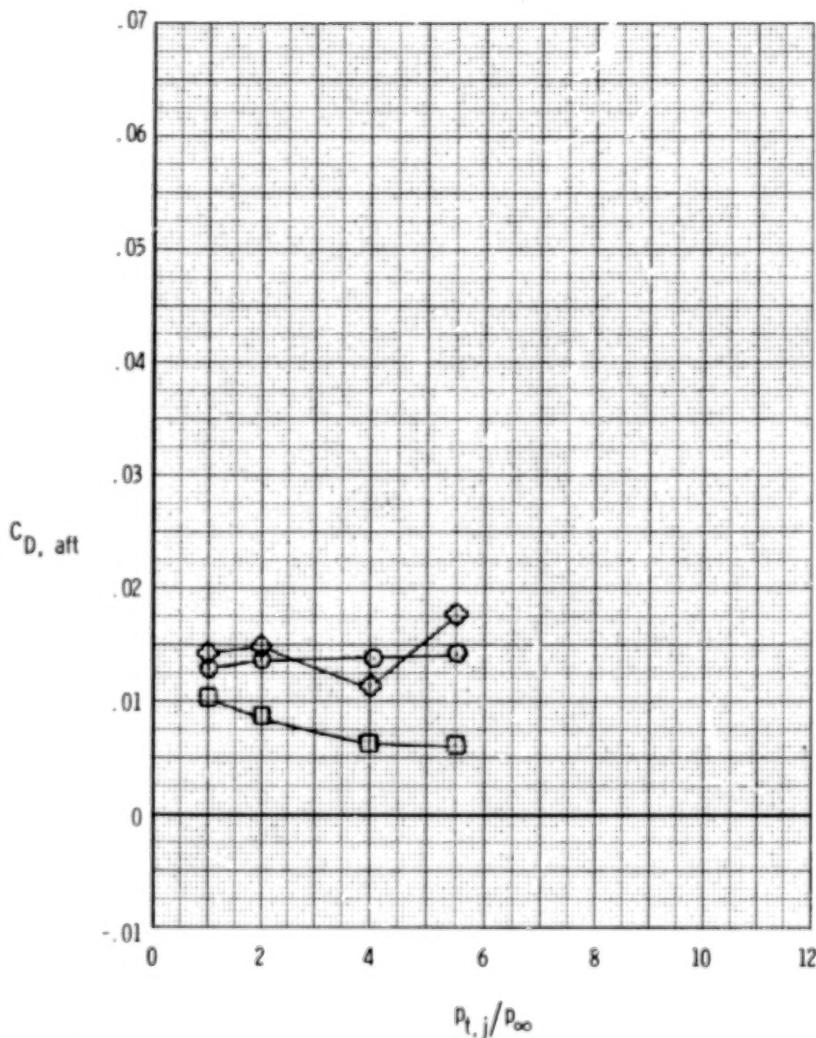
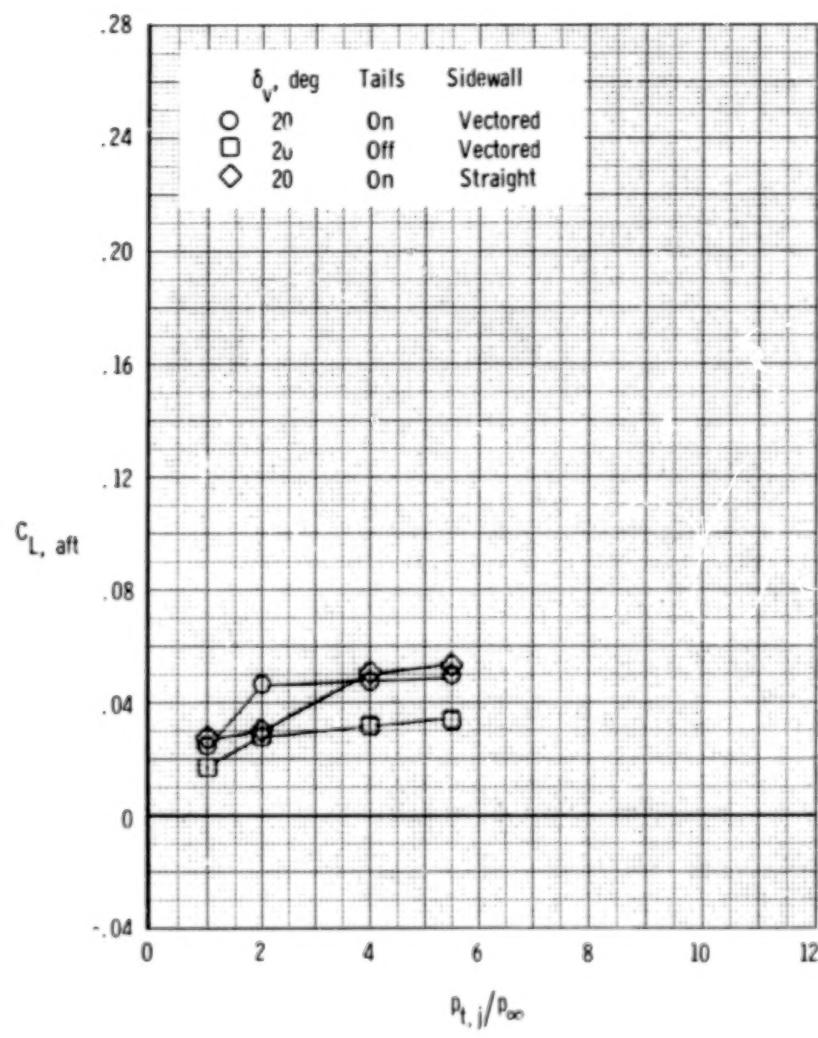
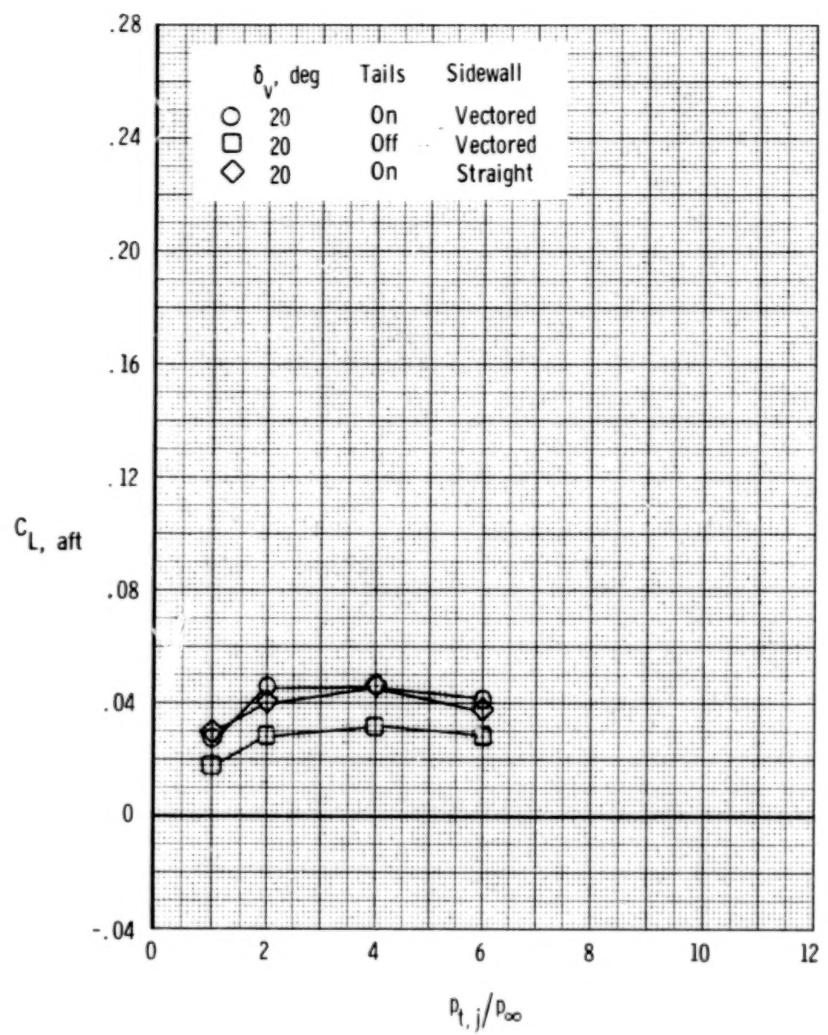
(a) $M = 0.60$.

Figure 105. - Effect of tails and sidewall geometry on thrust-removed afterbody forces, wedge nozzle, A/B power.
 $\delta_h = 0^\circ$; $\alpha = 0^\circ$.



(b) $M = 0.90$.

Figure 105.- Concluded.

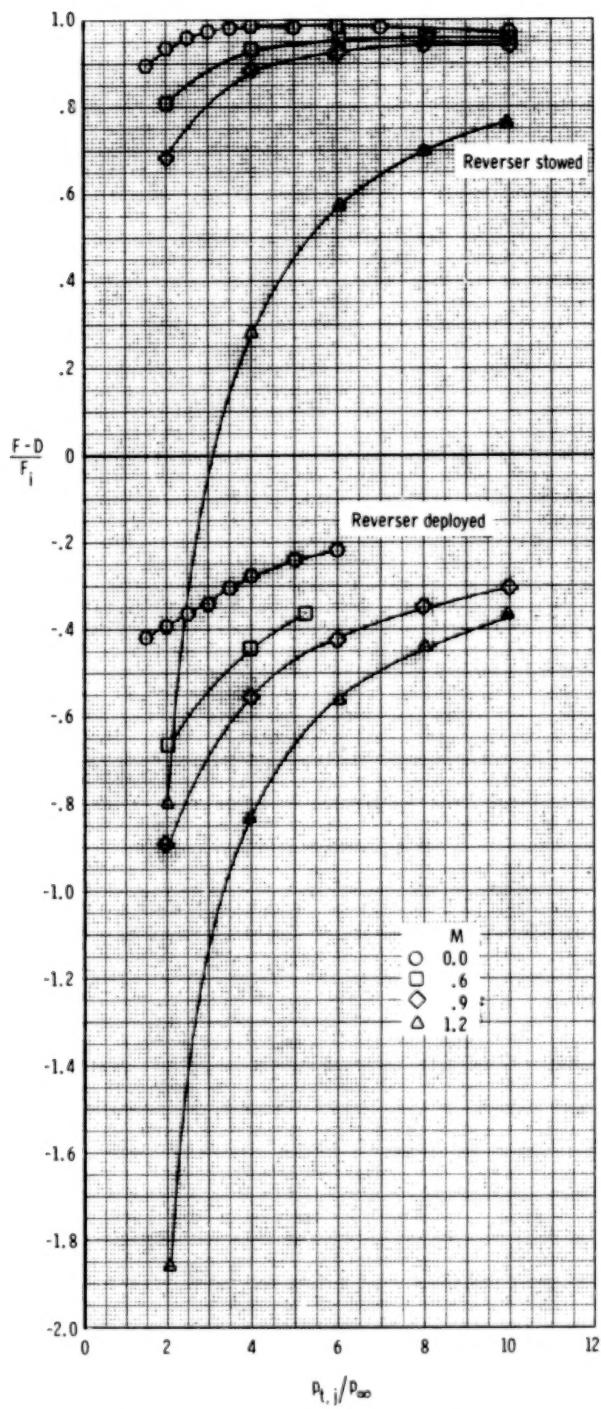


Figure 106.- Thrust reverser performance for the 2-D C-D nozzle, dry power. $\delta_h = 0^\circ$; $\alpha \approx 0^\circ$ except for reverser deployed at $M = 0.60$, $\alpha \approx 2^\circ$.

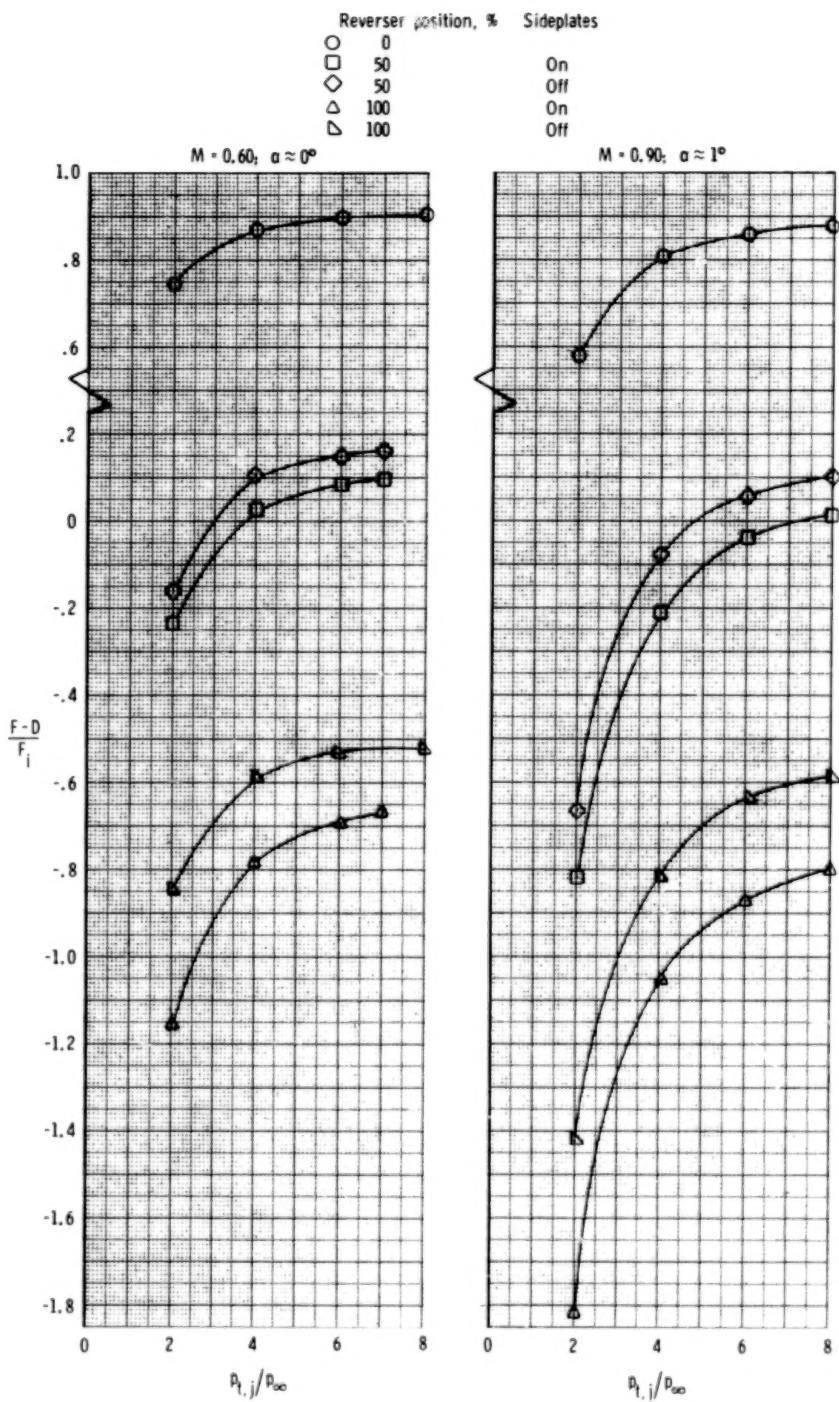


Figure 107. - Thrust reverser performance at various Mach numbers for the wedge nozzle, dry power. $\delta_h = 0^\circ$; $\alpha \approx 0^\circ$ except for reverser deployed at $M = 0.90$, $\alpha \approx 1^\circ$.

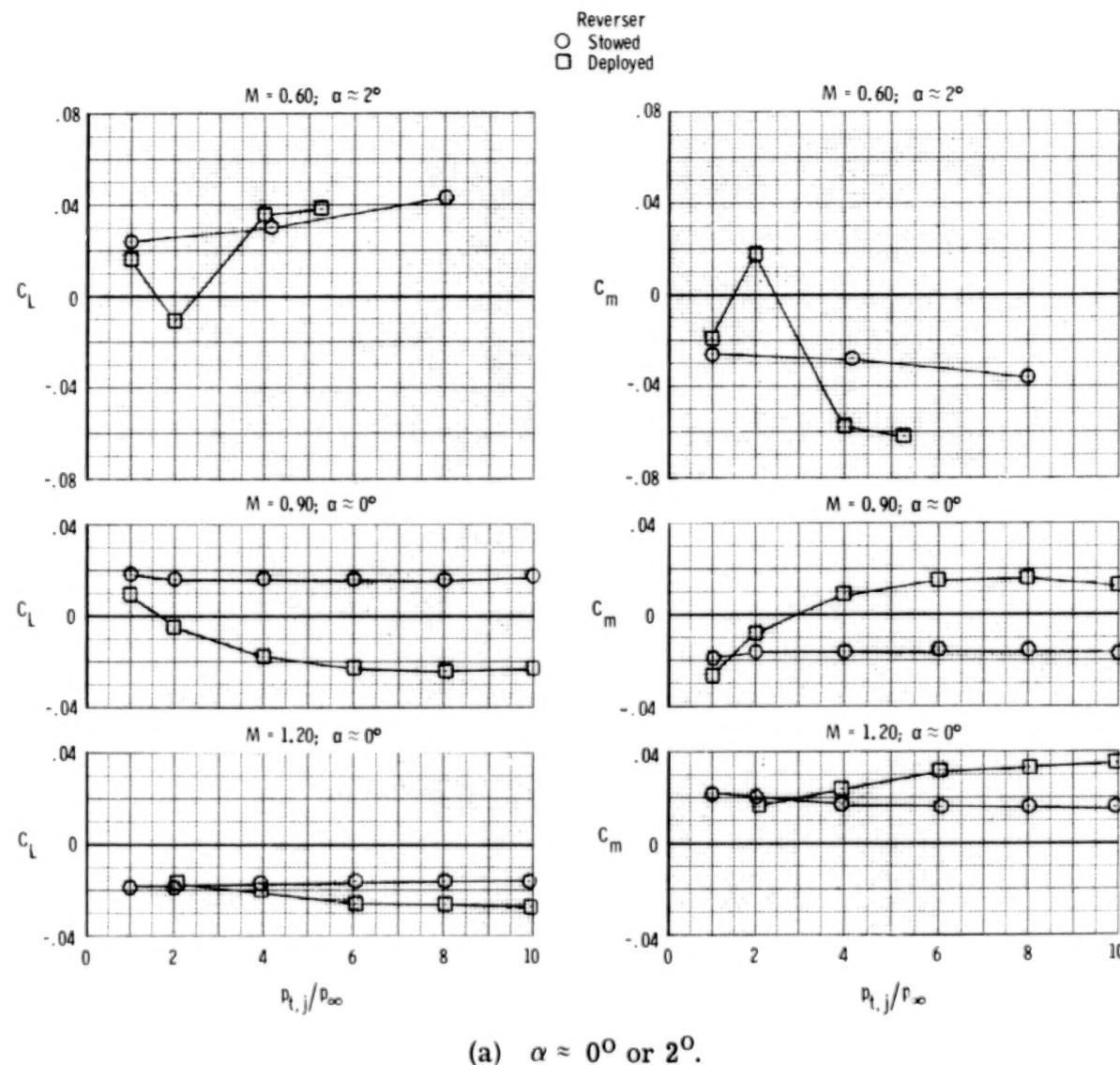


Figure 108.- Effect of thrust reversing on afterbody lift and pitching-moment characteristics, 2-D C-D nozzle, dry power. $\delta_h = 0^\circ$.

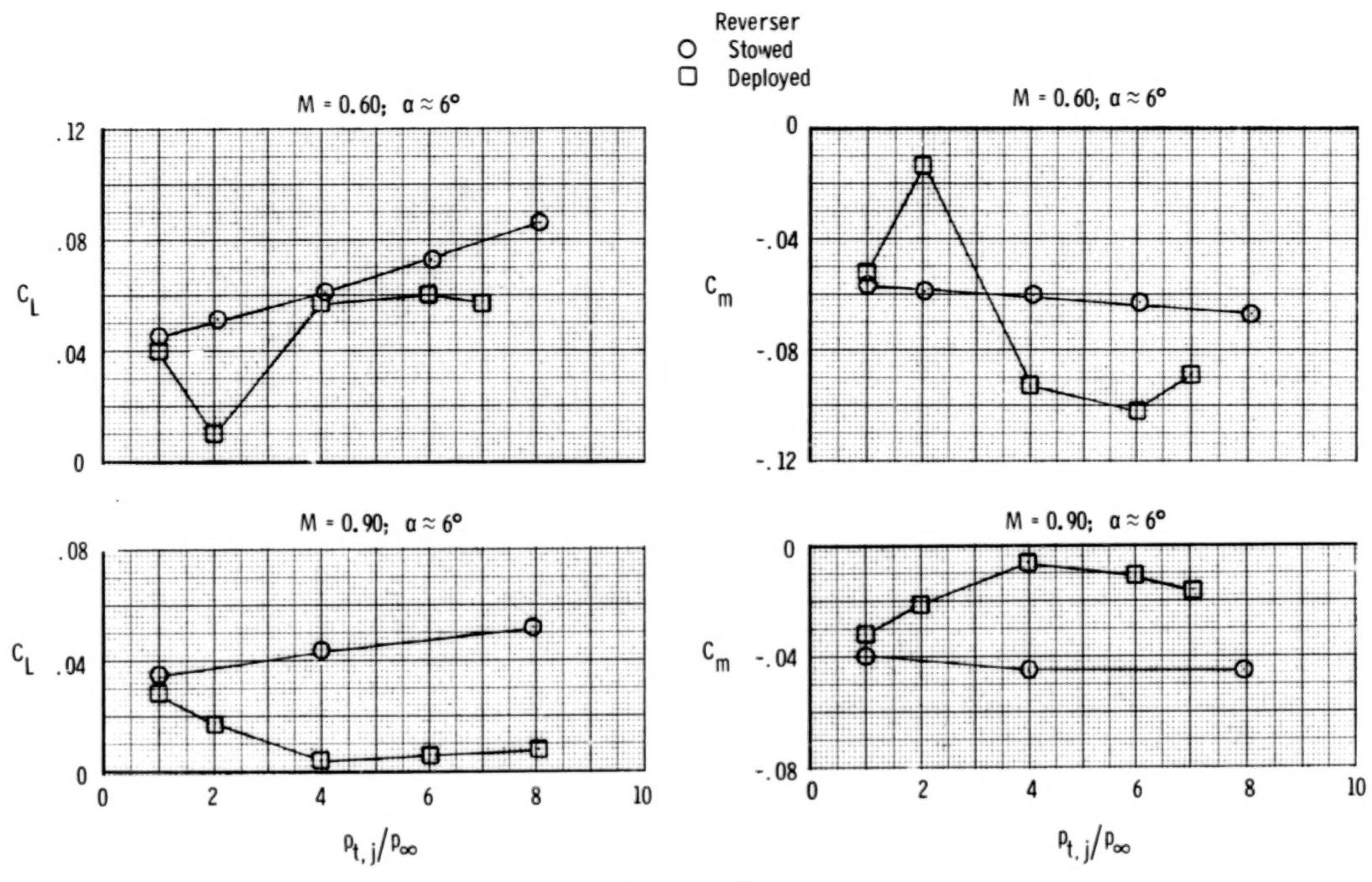
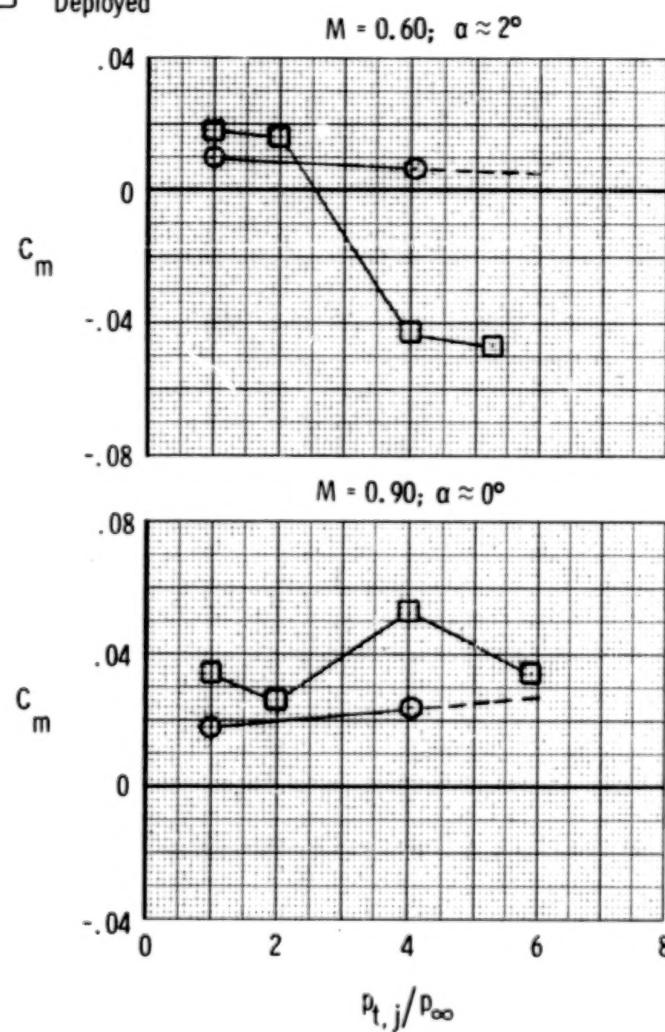
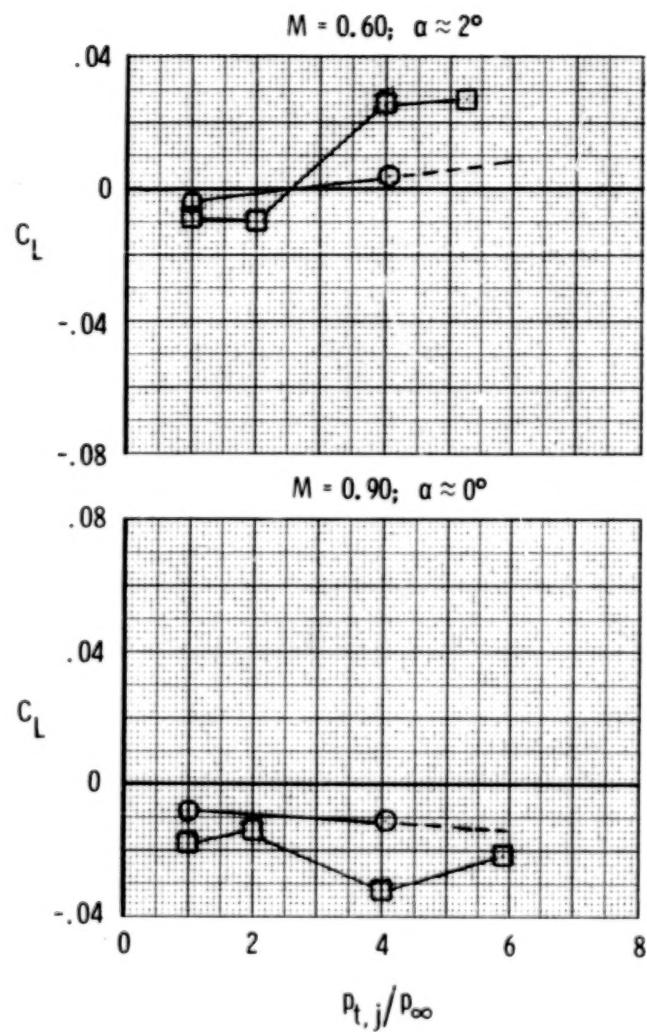


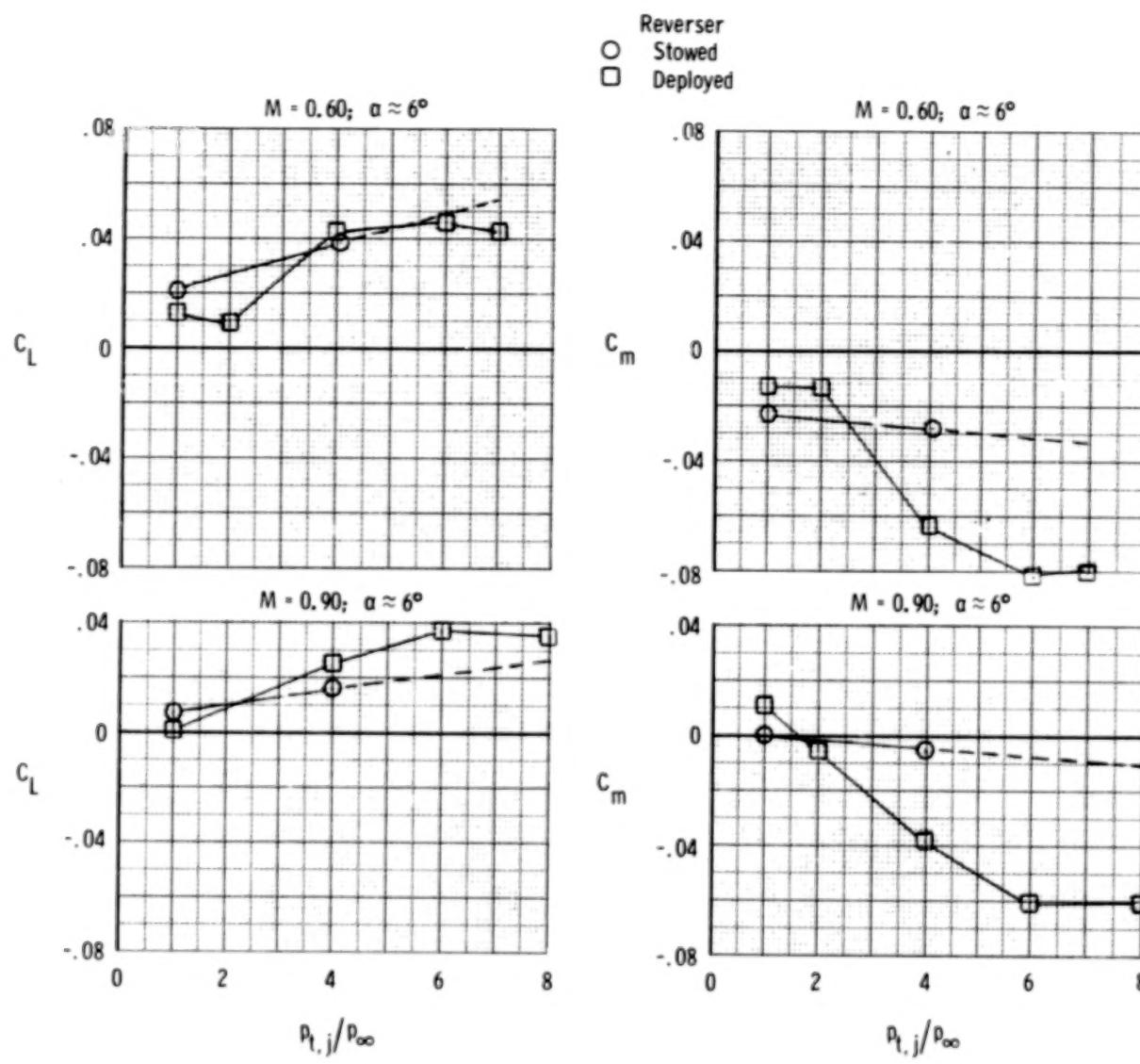
Figure 108.- Concluded.

276



(a) $\alpha \approx 0^\circ$ or 2° .

Figure 109.- Effect of thrust reversing on afterbody lift and pitching-moment characteristics, 2-D C-D nozzle, dry power. $\delta_h = -2^\circ$.



(b) $\alpha \approx 6^\circ$.

Figure 109.- Concluded.

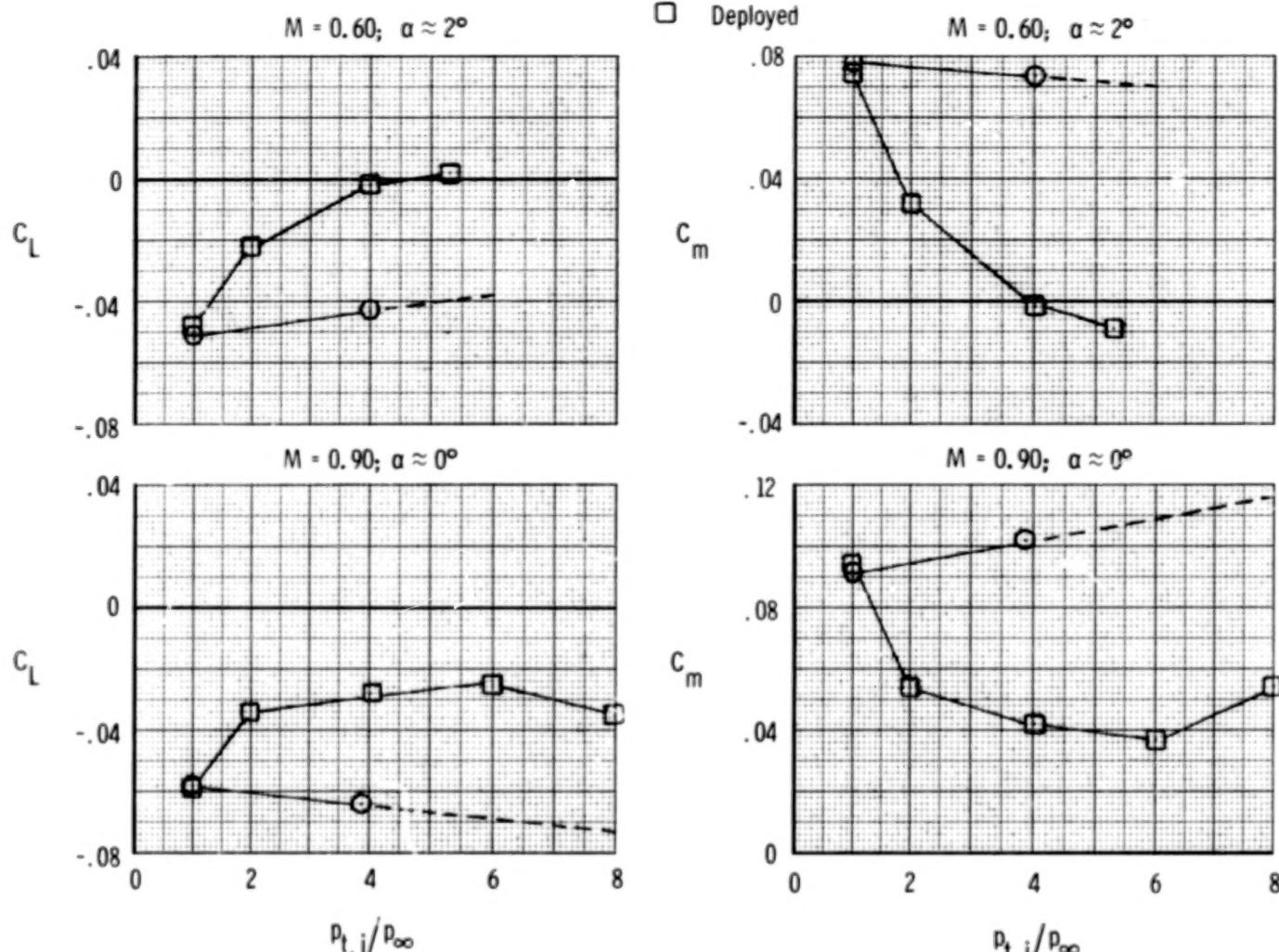
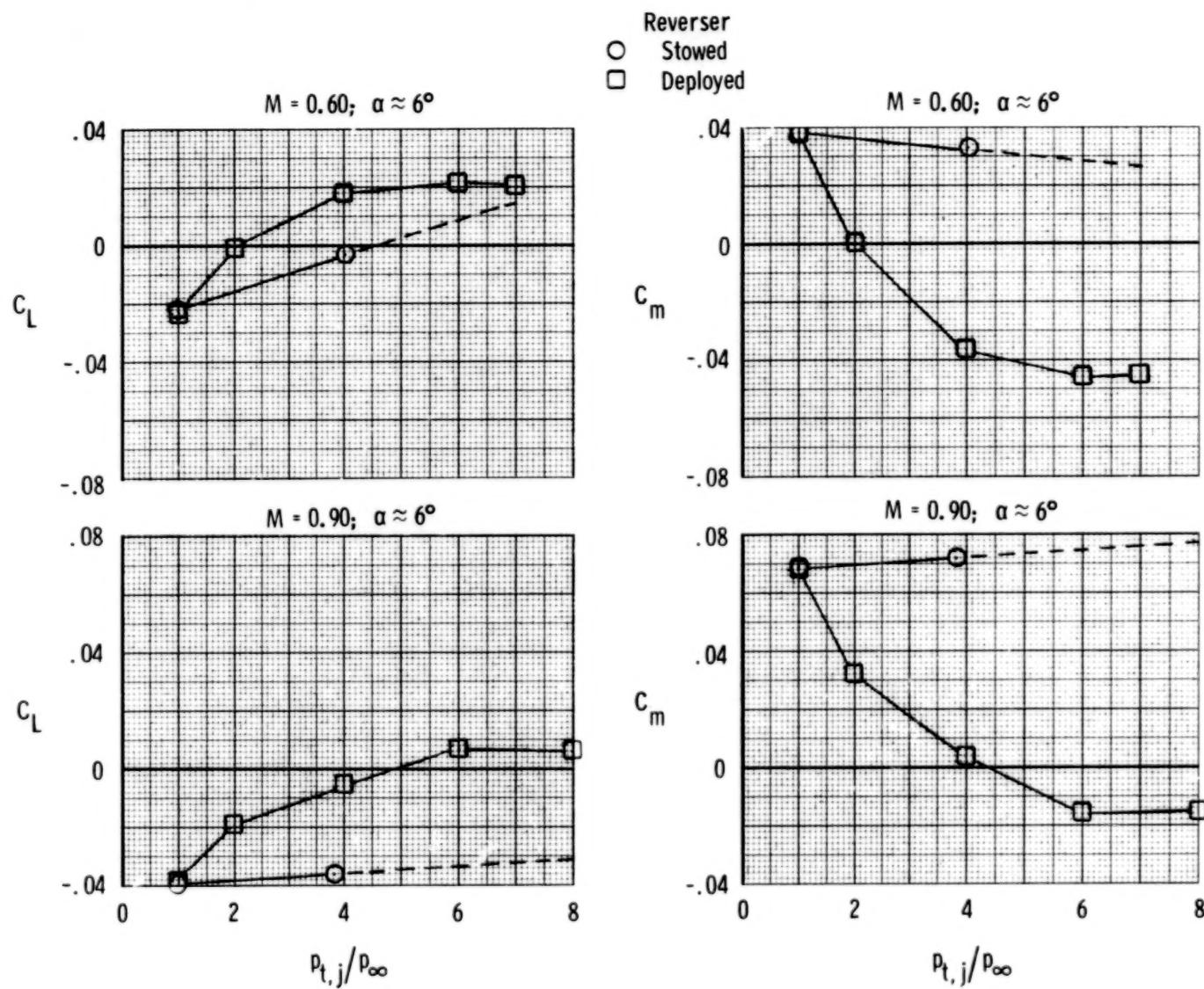
(a) $\alpha \approx 0^\circ$ or 2° .

Figure 110.- Effect of thrust reversing on afterbody lift and pitching-moment characteristics,
 2-D C-D nozzle, dry power. $\delta_h = -5^\circ$.



(b) $\alpha \approx 6^\circ$.

Figure 110.- Concluded.

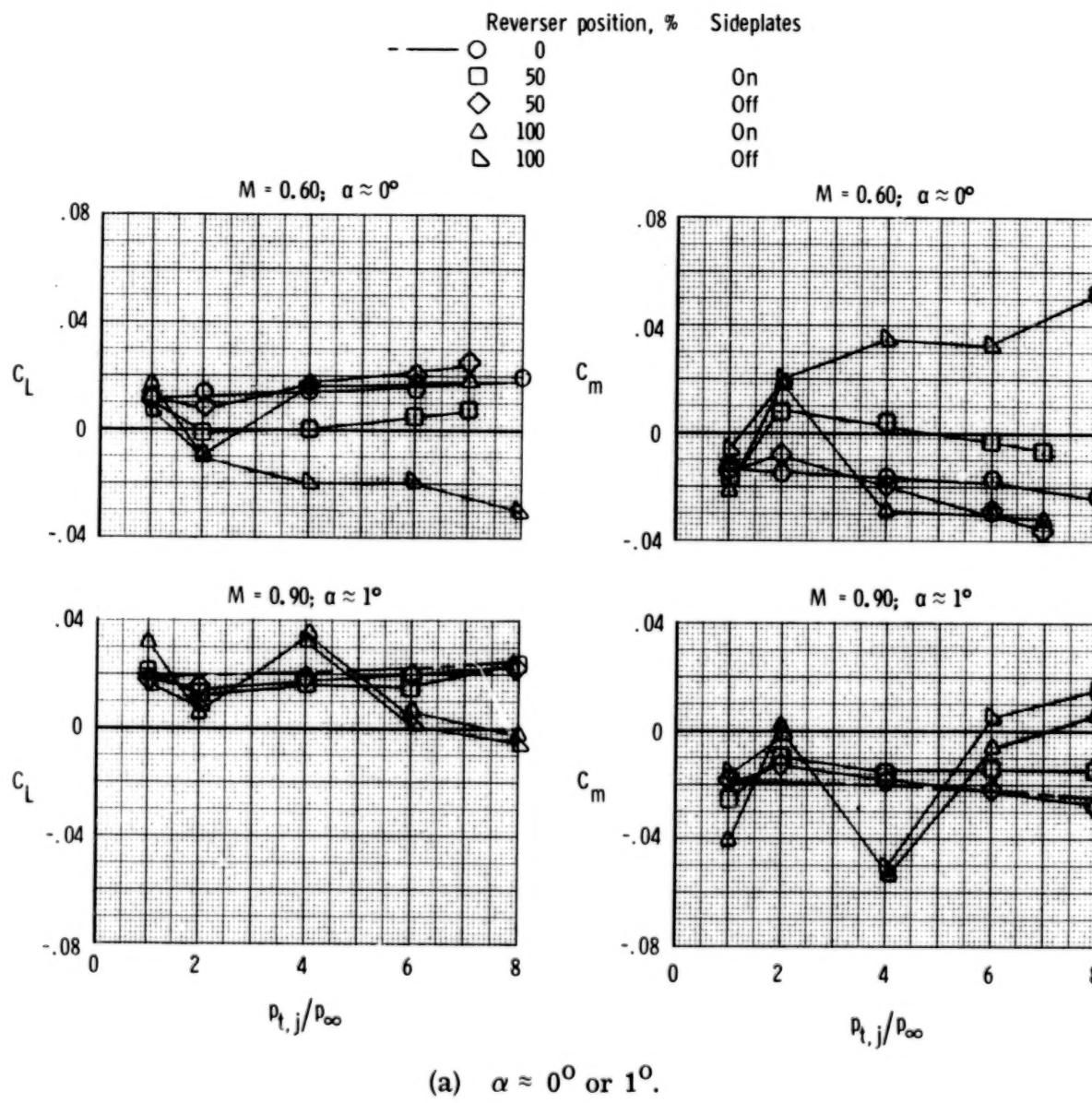
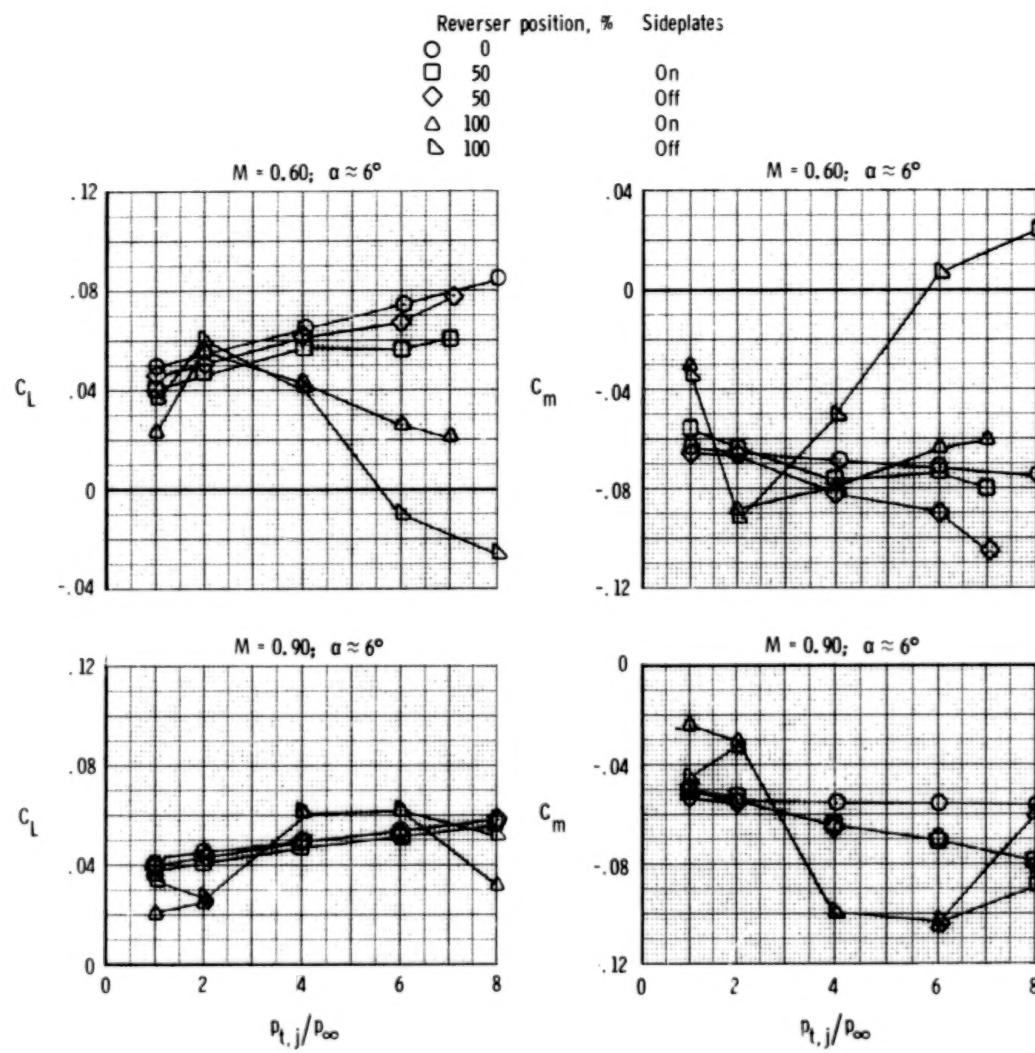


Figure 111.- Effect of thrust reversing on afterbody lift and pitching-moment characteristics, wedge nozzle, dry power. $\delta_h = 0^\circ$.



(b) $\alpha \approx 6^\circ$.

Figure 111.- Concluded.

282

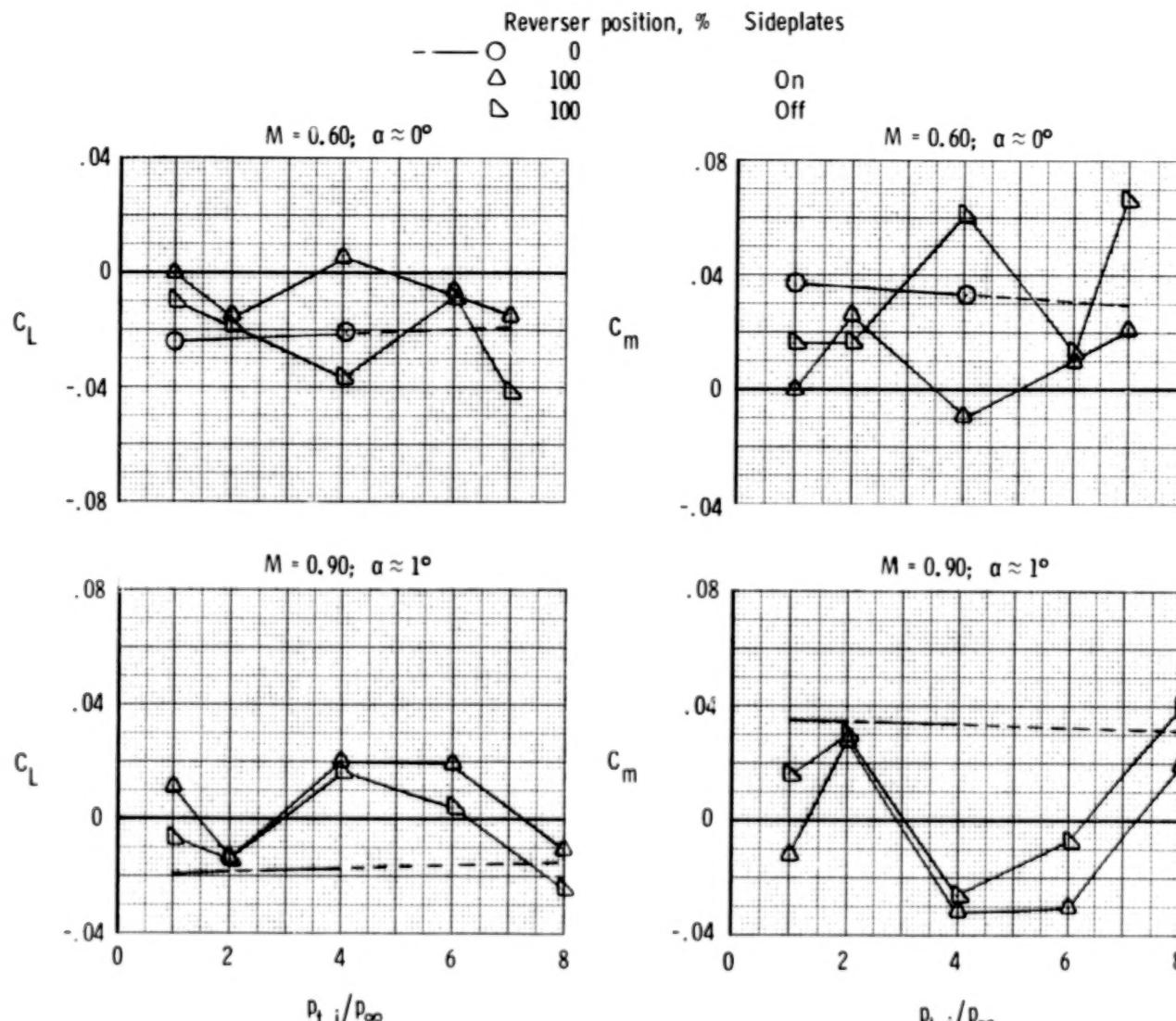
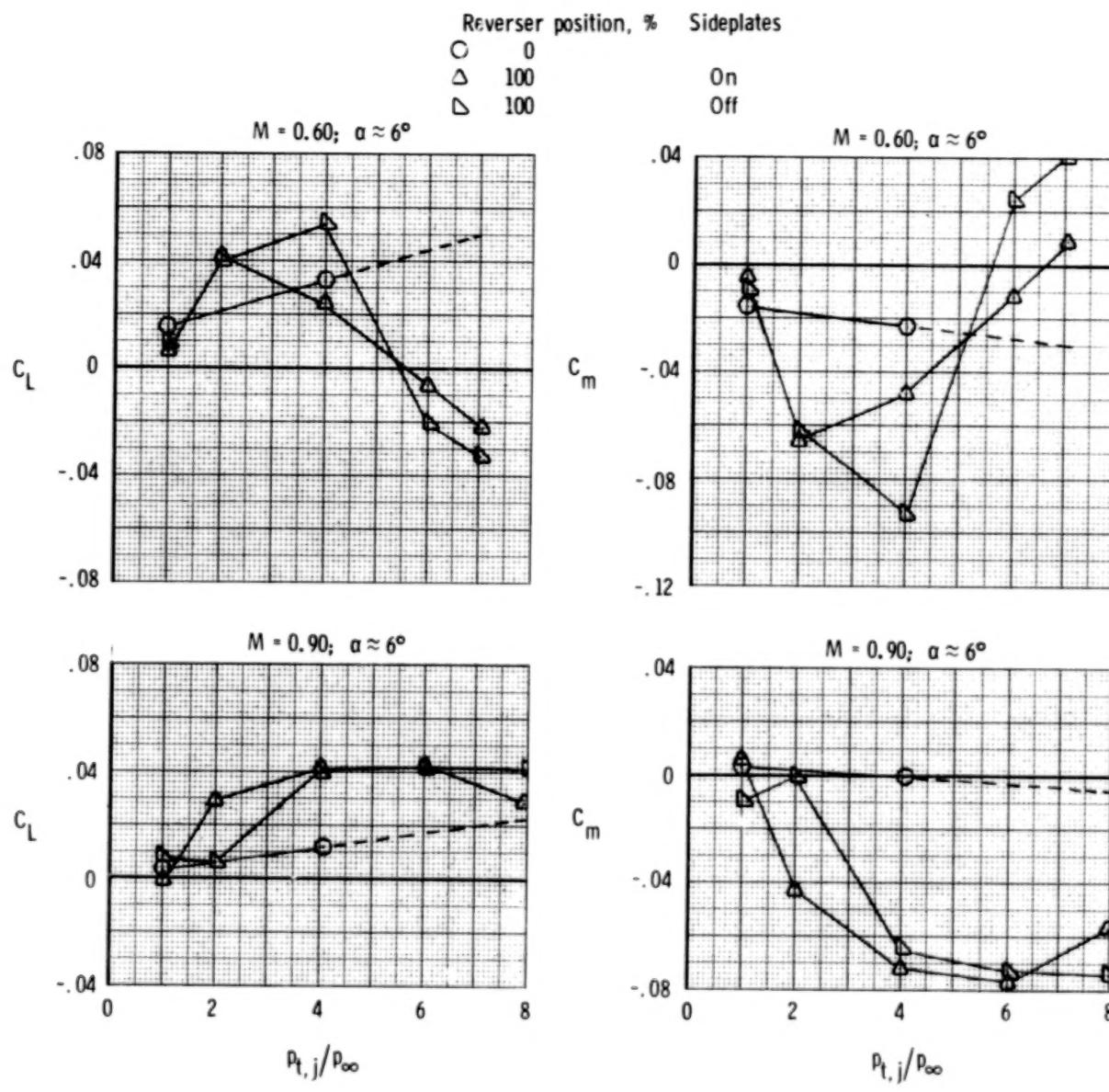
(a) $\alpha \approx 0^\circ$ or 1° .

Figure 112.- Effect of thrust reversing on afterbody lift and pitching-moment characteristics, wedge nozzle, dry power. $\delta_h = -2^\circ$.



(b) $\alpha \approx 6^\circ$.

Figure 112.- Concluded.

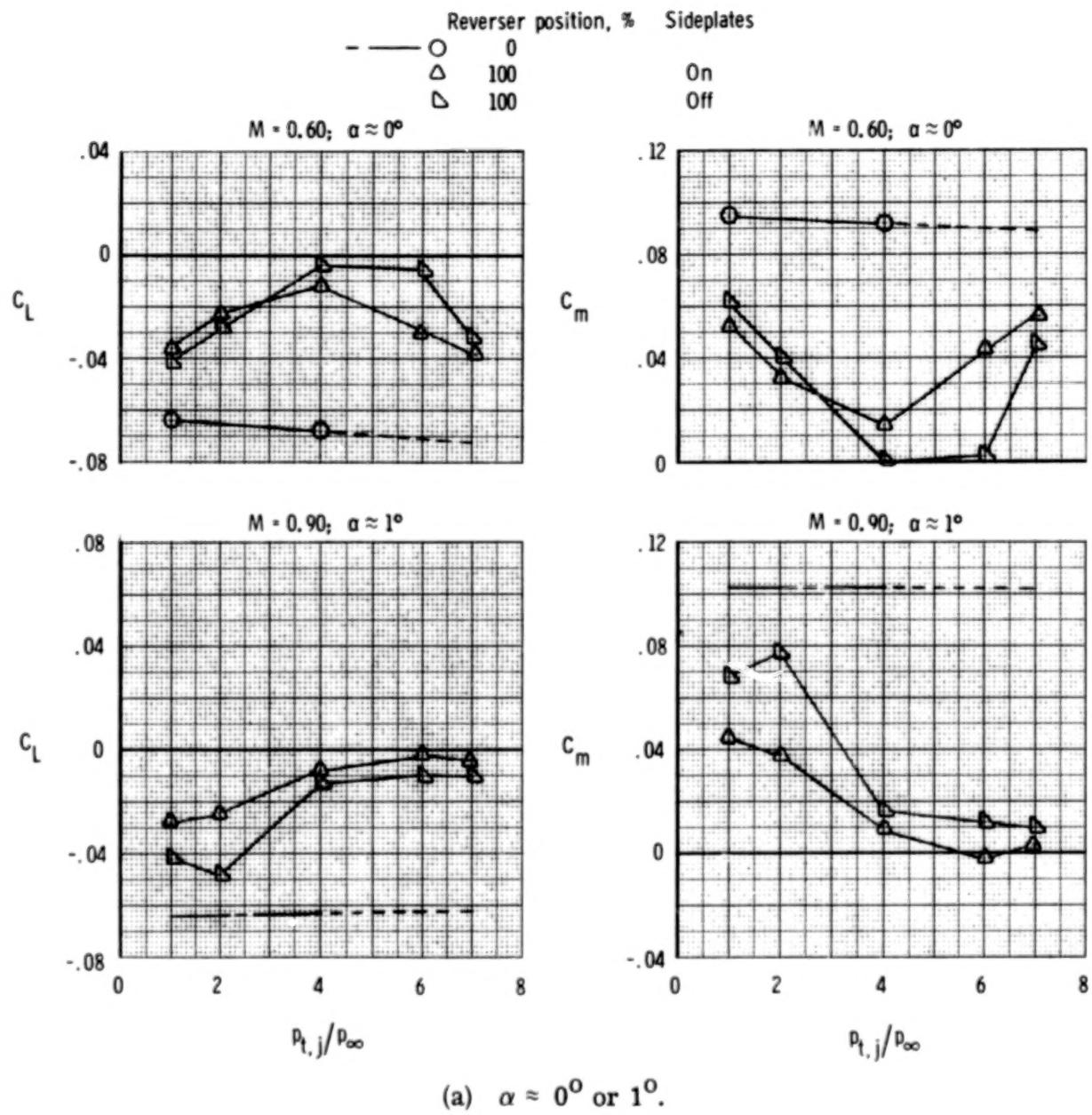


Figure 113.- Effect of thrust reversing on afterbody lift and pitching-moment characteristics, wedge nozzle. $\delta_h = -5^\circ$.

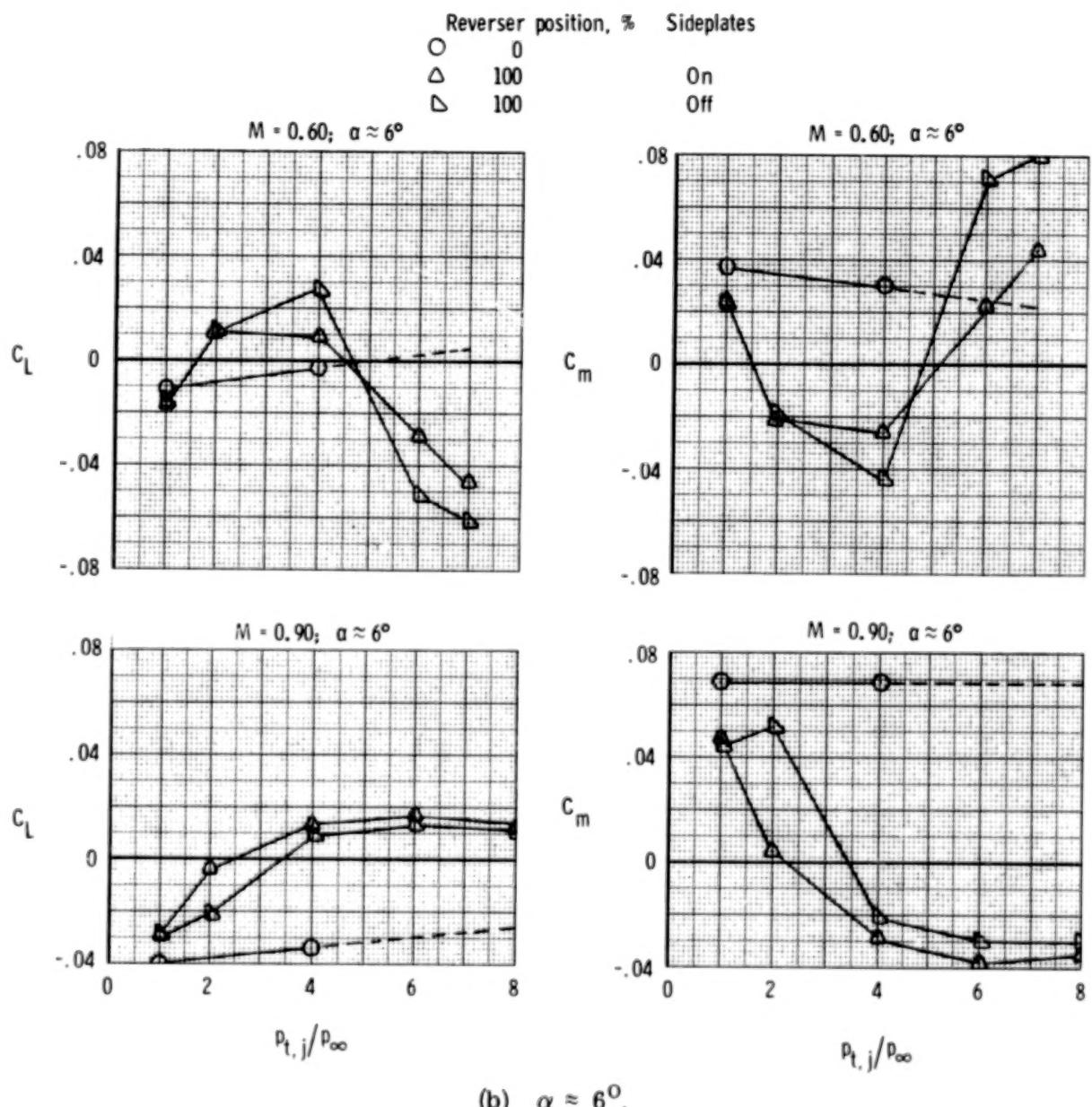


Figure 113.- Concluded.

286

Nozzle

- Axisymmetric
- - - Single expansion ramp
- - - 2-D C-D
- - - Wedge

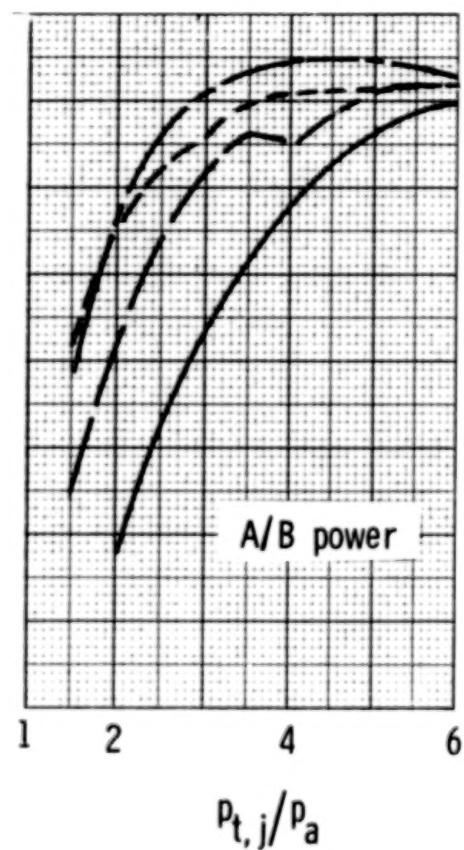
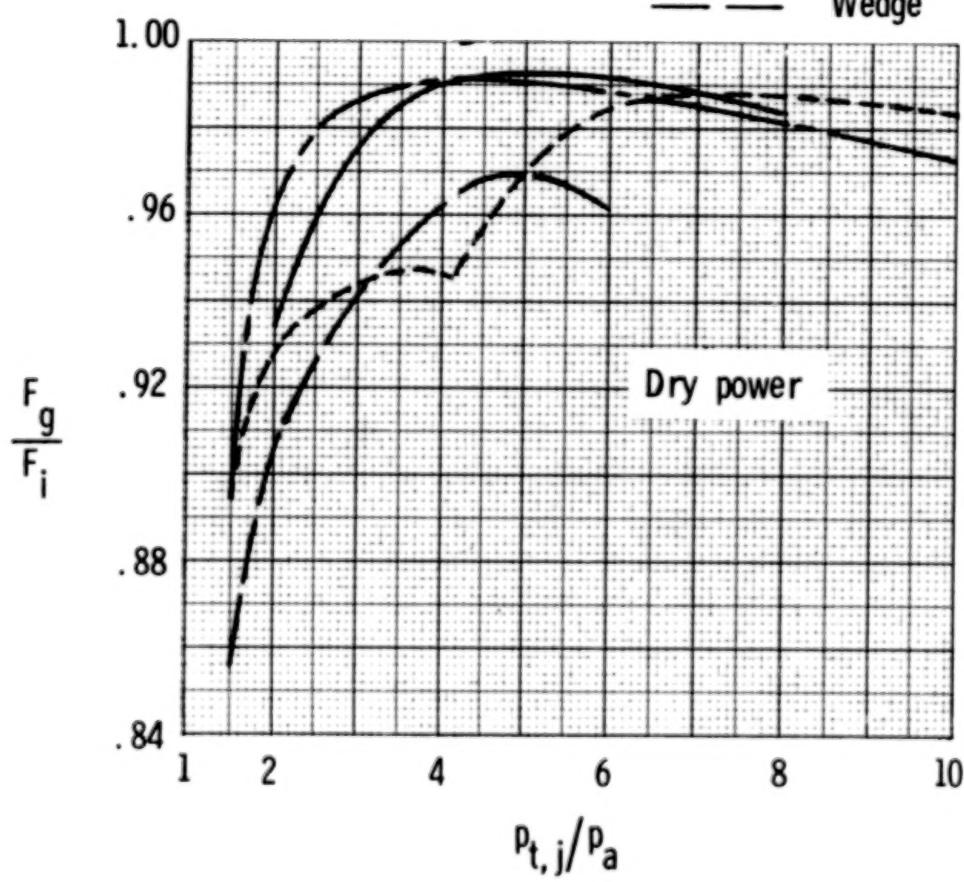
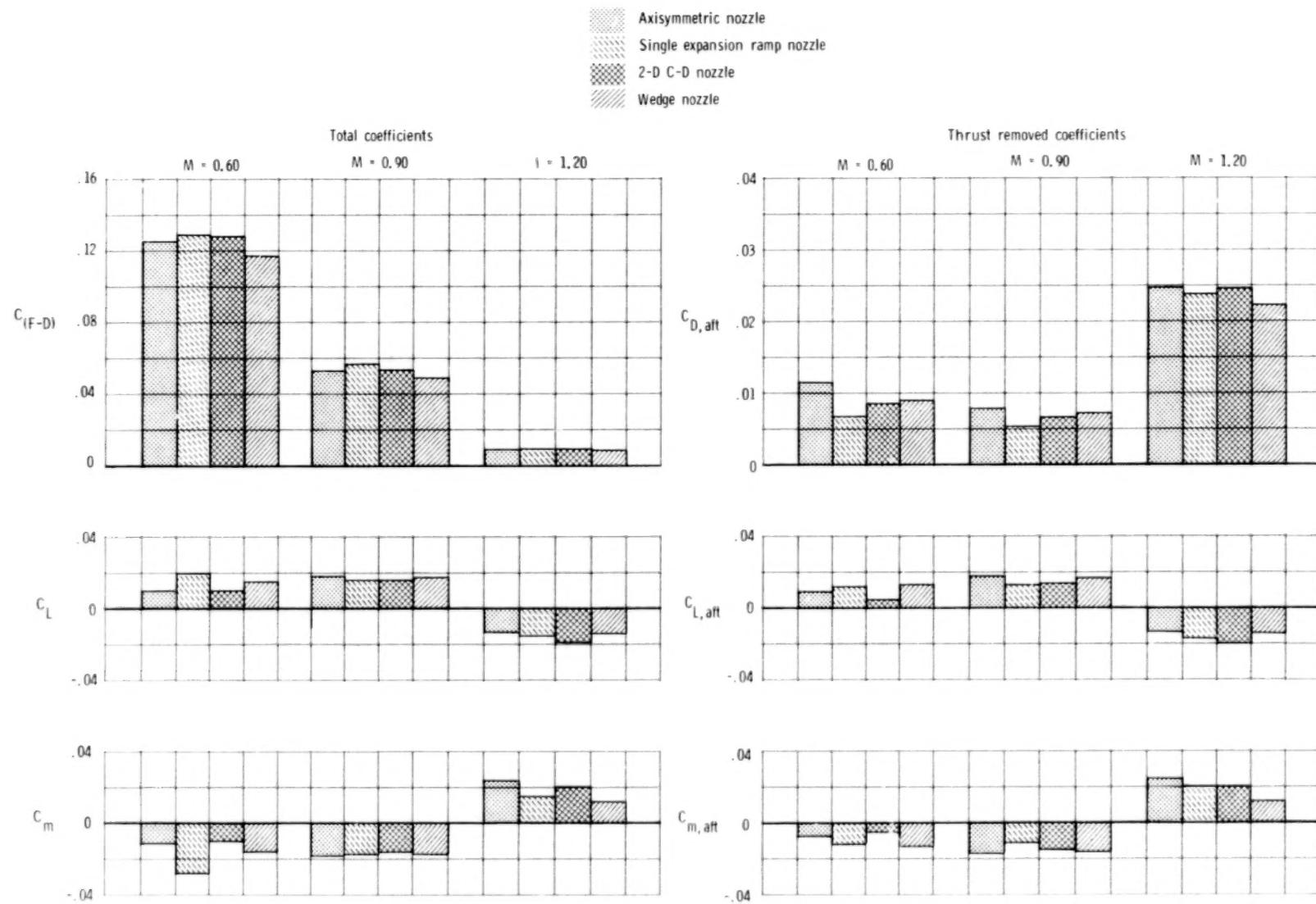


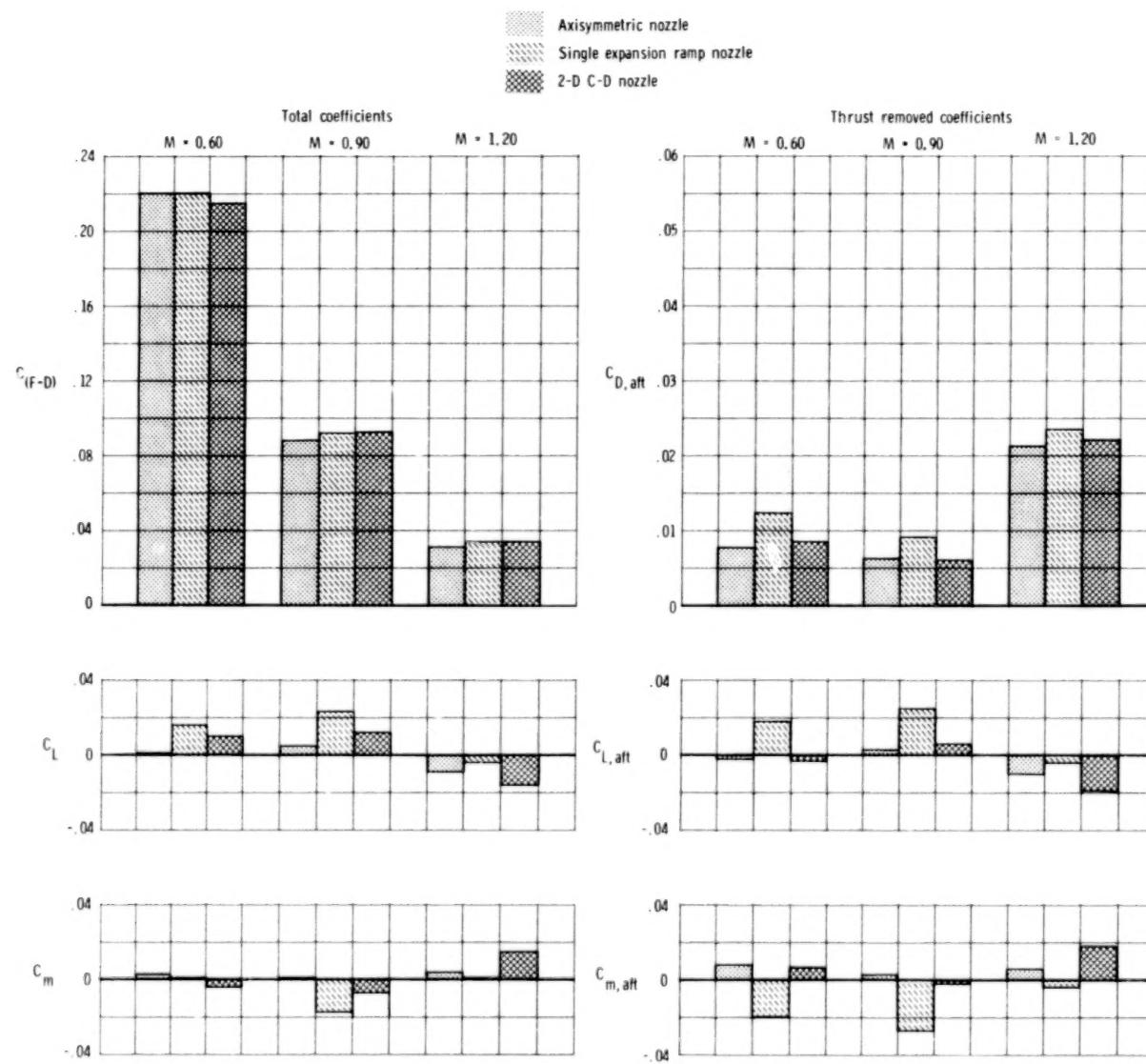
Figure 114.- Comparison of unvectored static nozzle performance.



(a) Dry power.

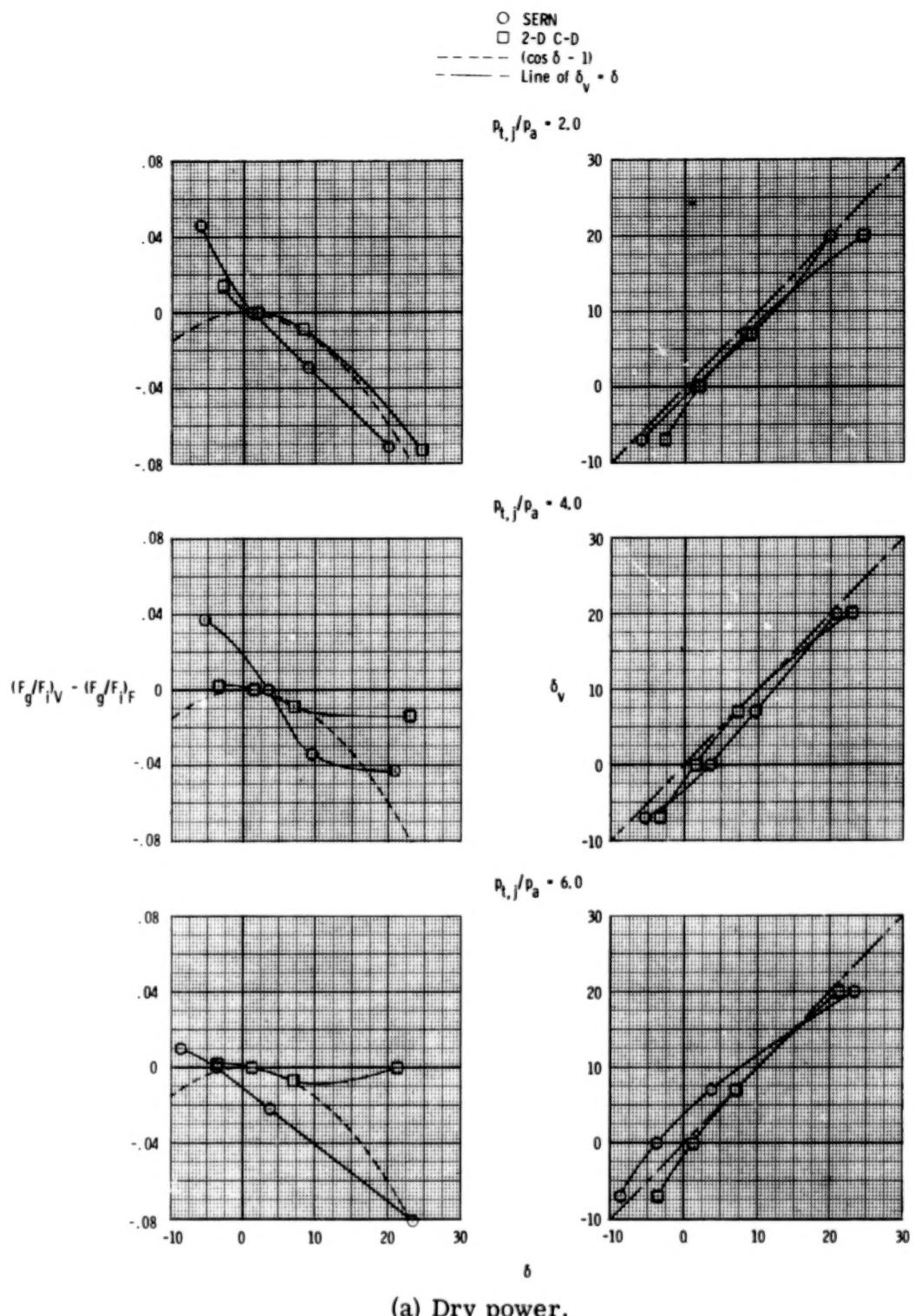
Figure 115.- Comparison of longitudinal aerodynamic characteristics.

$$p_{t,j}/p_{\infty} = 4.0; \quad \alpha = 0^{\circ}; \quad \delta_h = 0^{\circ}; \quad \delta_v = 0^{\circ}.$$



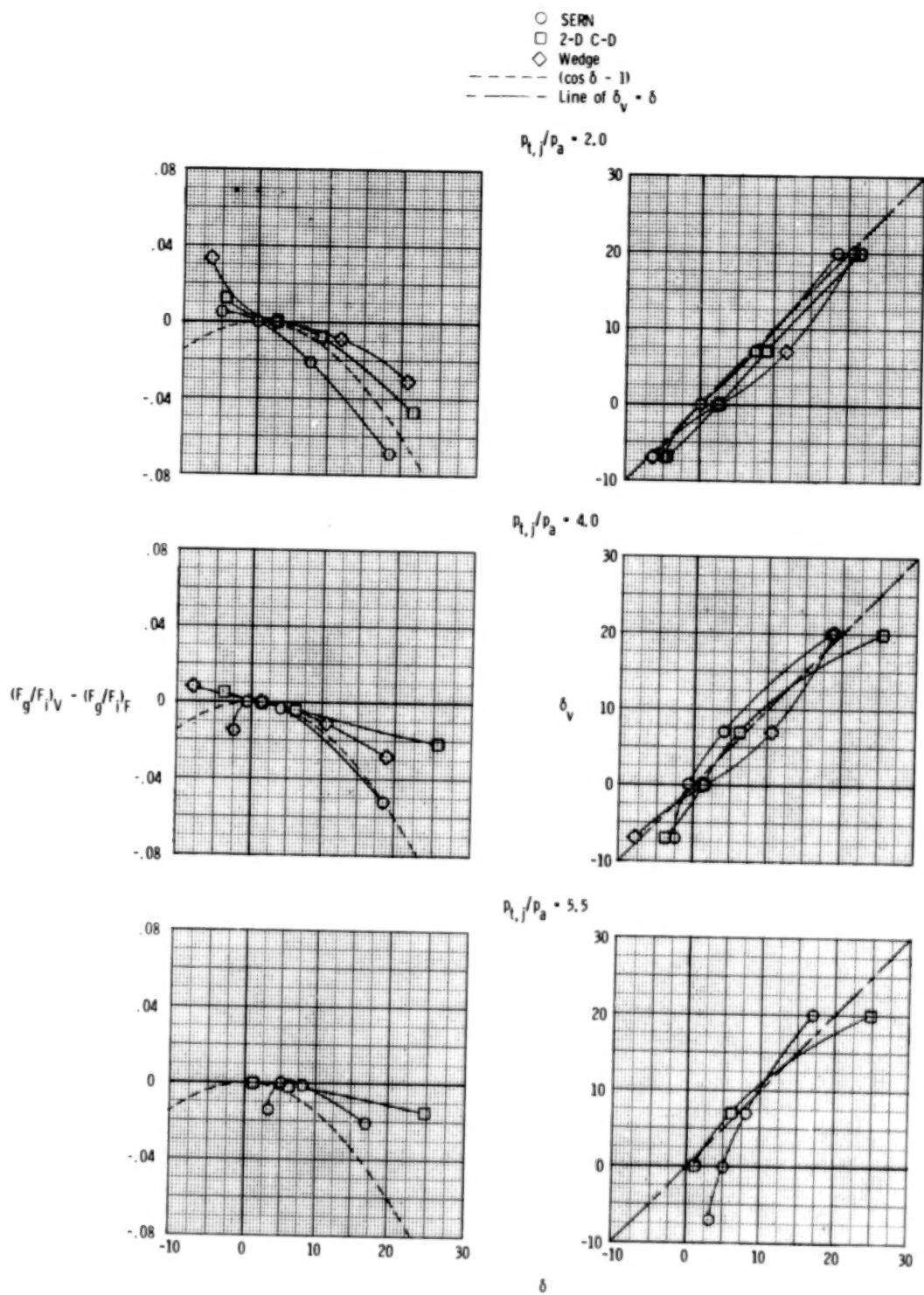
(b) A/B power.

Figure 115.- Concluded.



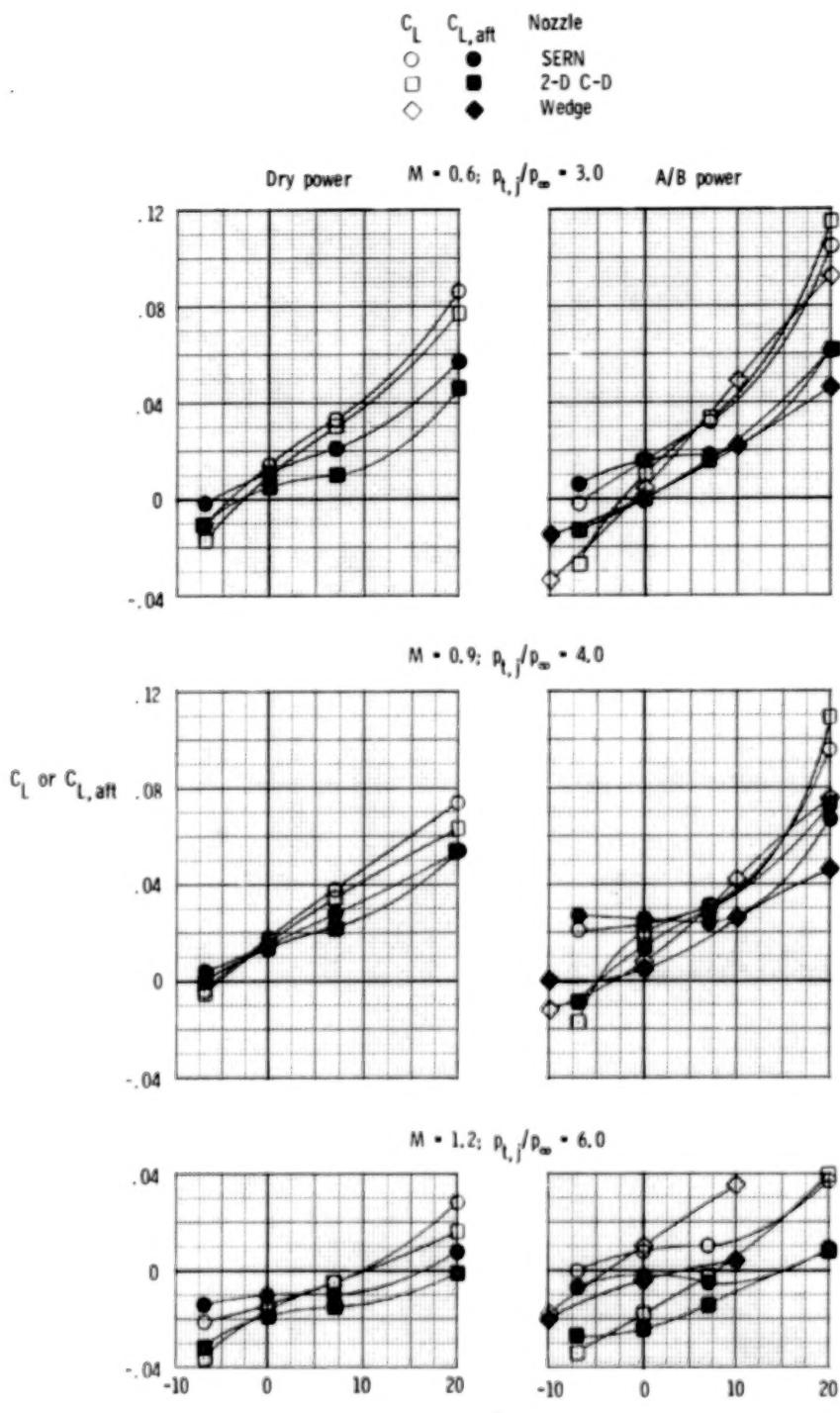
(a) Dry power.

Figure 116.- Comparison of vectored performance of nozzles at static conditions and several nozzle pressure ratios.



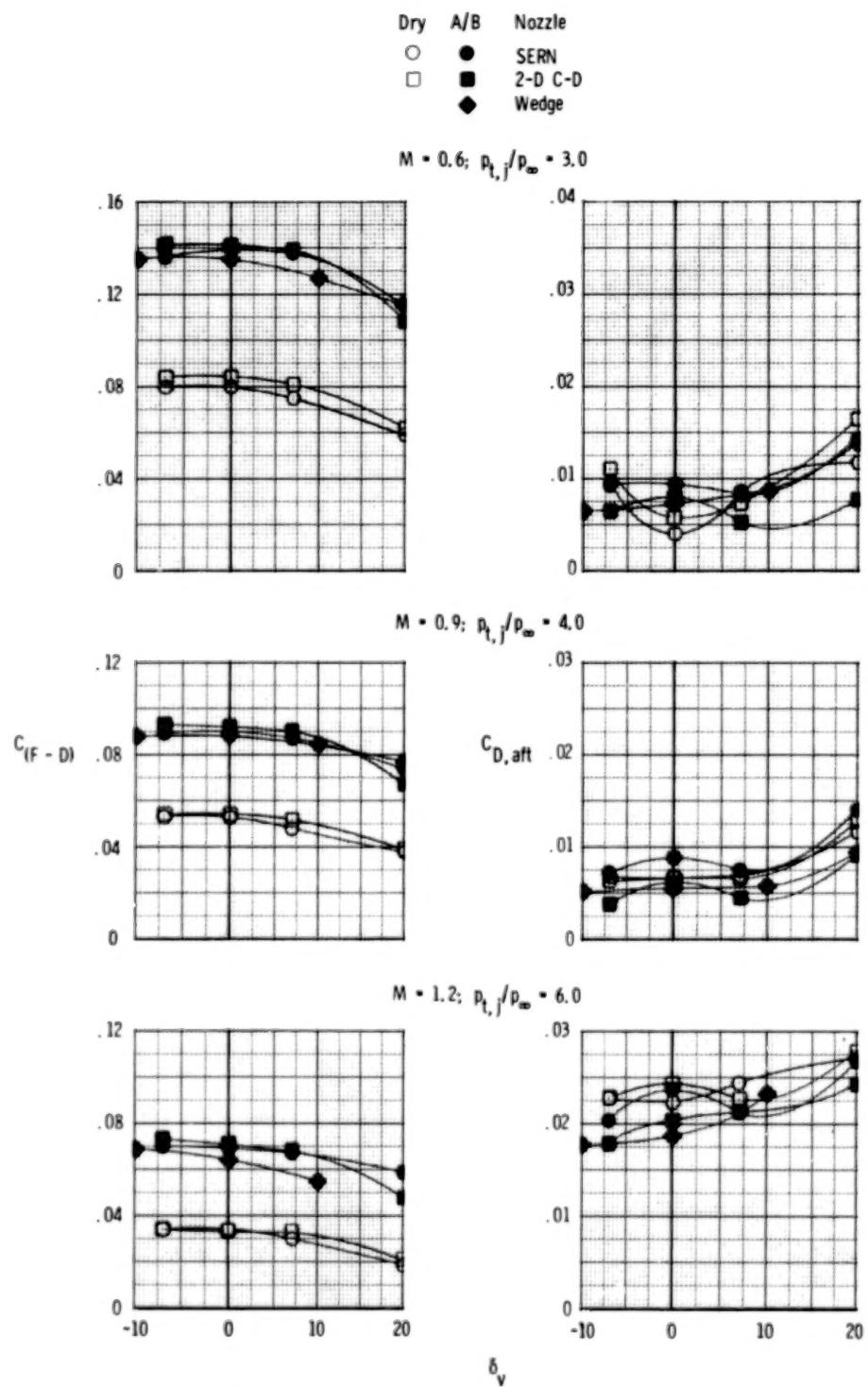
(b) A/B power.

Figure 116.- Concluded.



(a) Lift characteristics.

Figure 117. - Comparison of vectored thrust performance for nozzles at several Mach numbers and nozzle pressure ratios. $\alpha = 0^\circ$.



(b) Thrust and drag characteristics.

Figure 117.- Concluded.

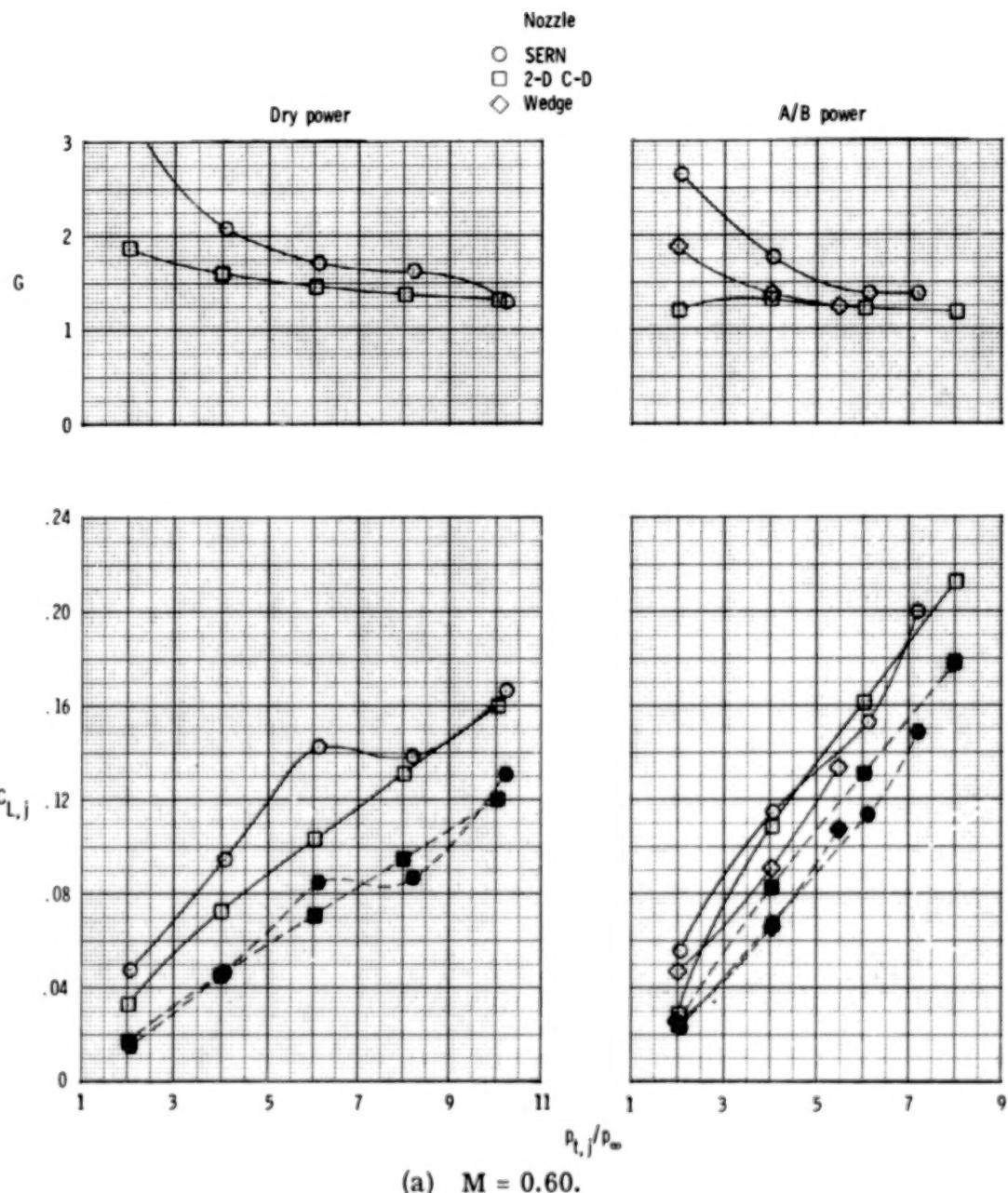


Figure 118.- Effect of thrust vectoring and nozzle pressure ratio on lift characteristics. $\delta_v = 20^0$; $\alpha = 0^0$. Solid symbols and dashed lines indicate jet lift coefficient $C_{L,j}$ computed from static resultant thrust vector angles.

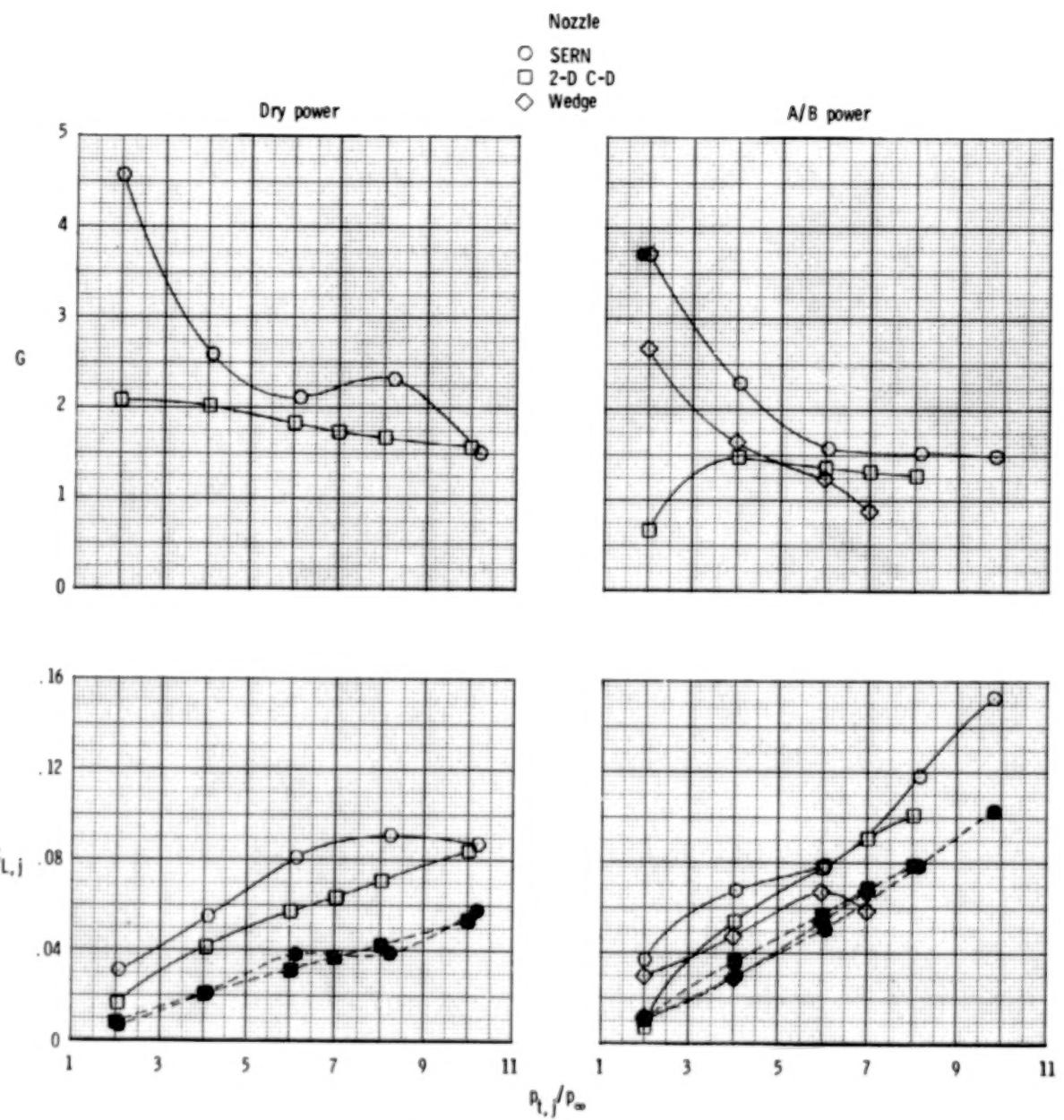
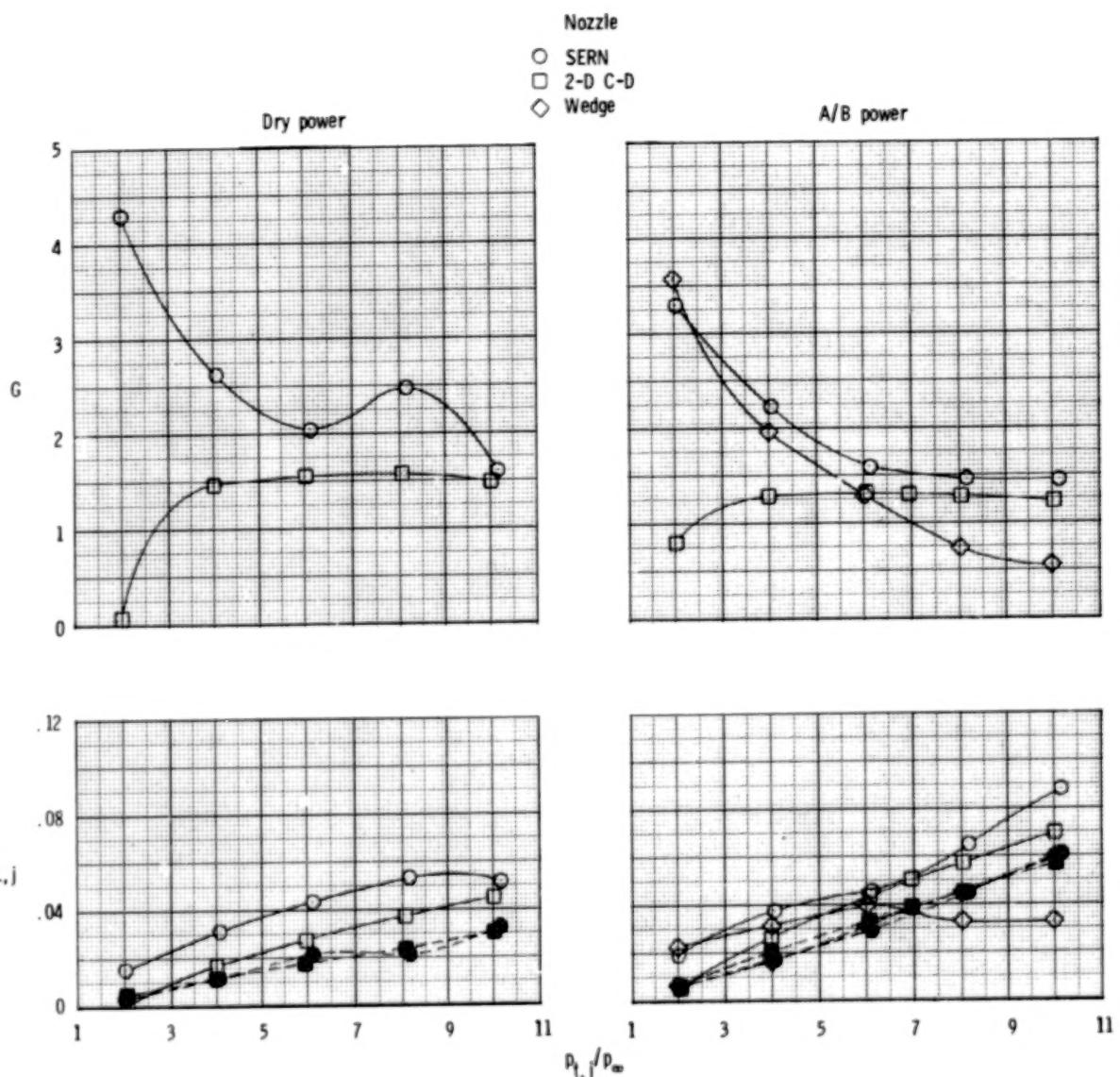


Figure 118.- Continued.



(c) $M = 1.20$.

Figure 118.- Concluded.

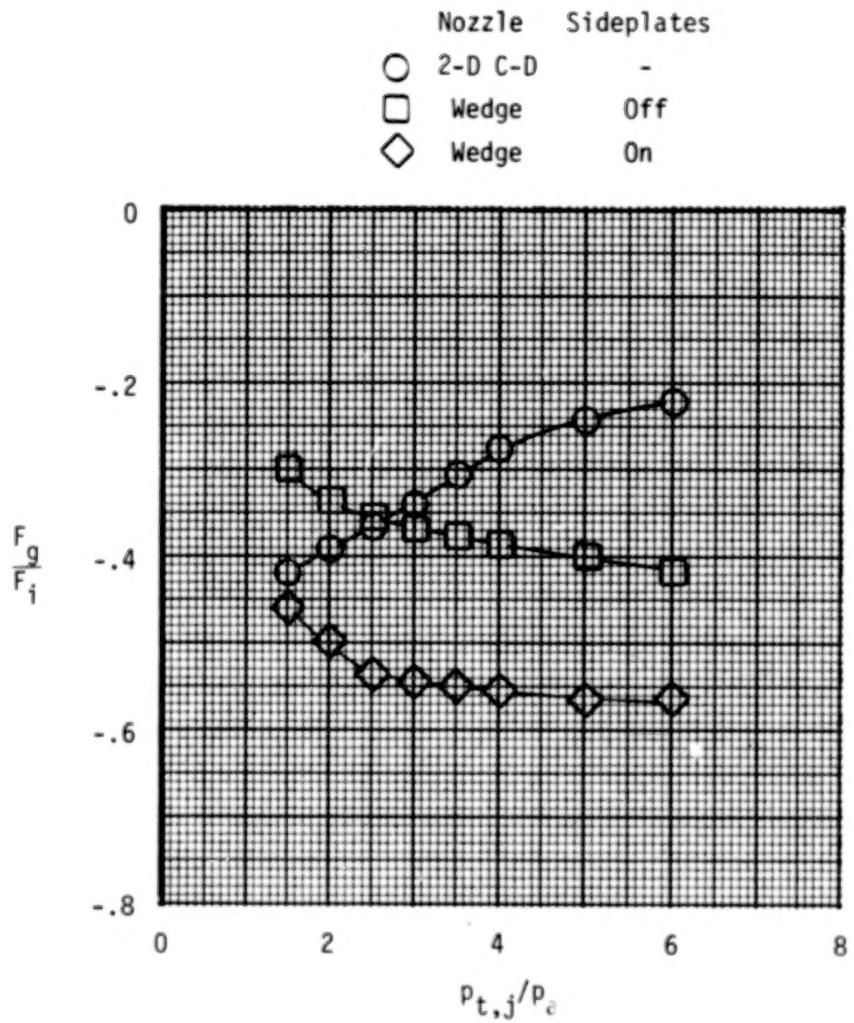


Figure 119.- Comparison of static reverse thrust performance for 2-D C-D and wedge nozzles. Dry power; 100-percent deployment.

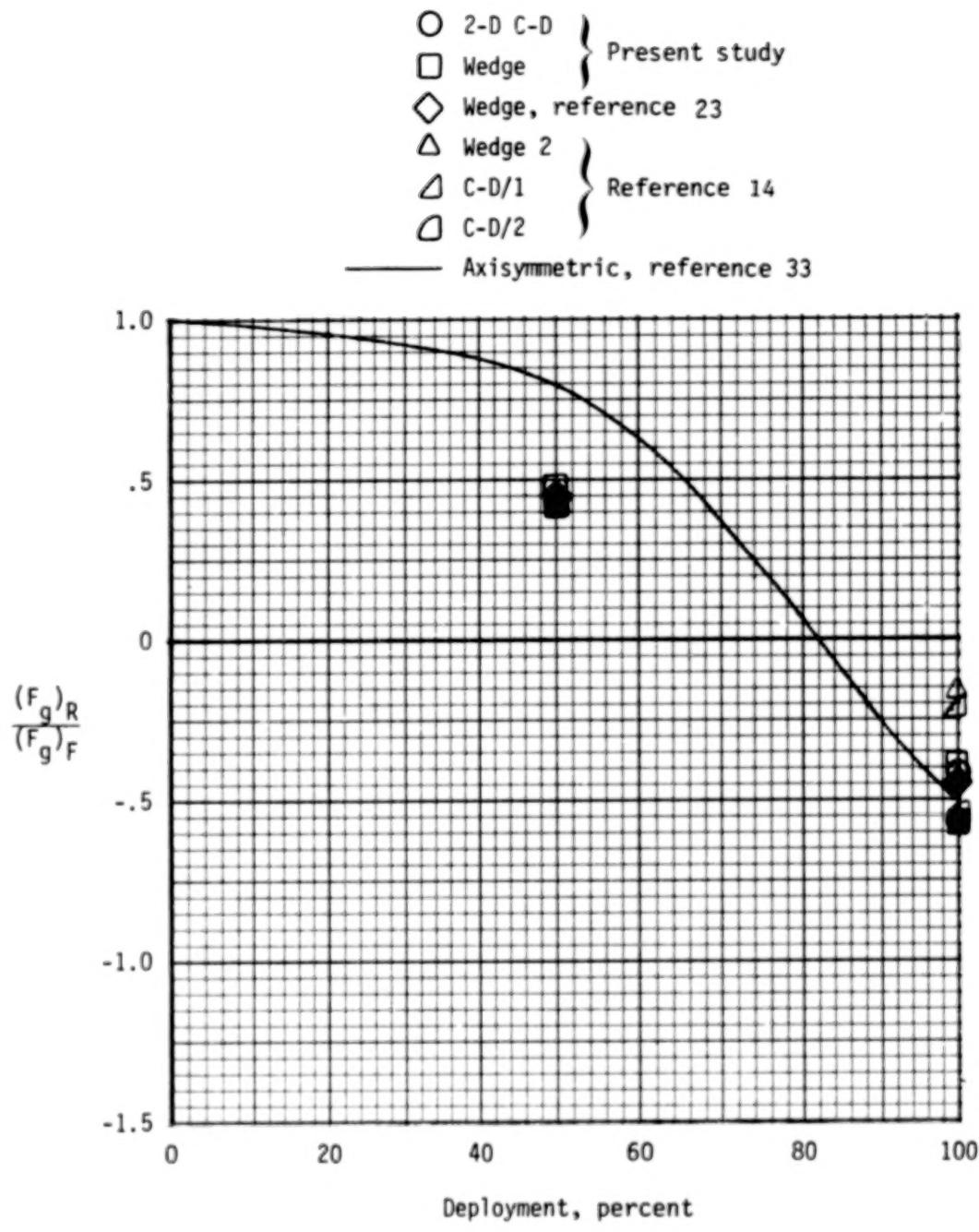
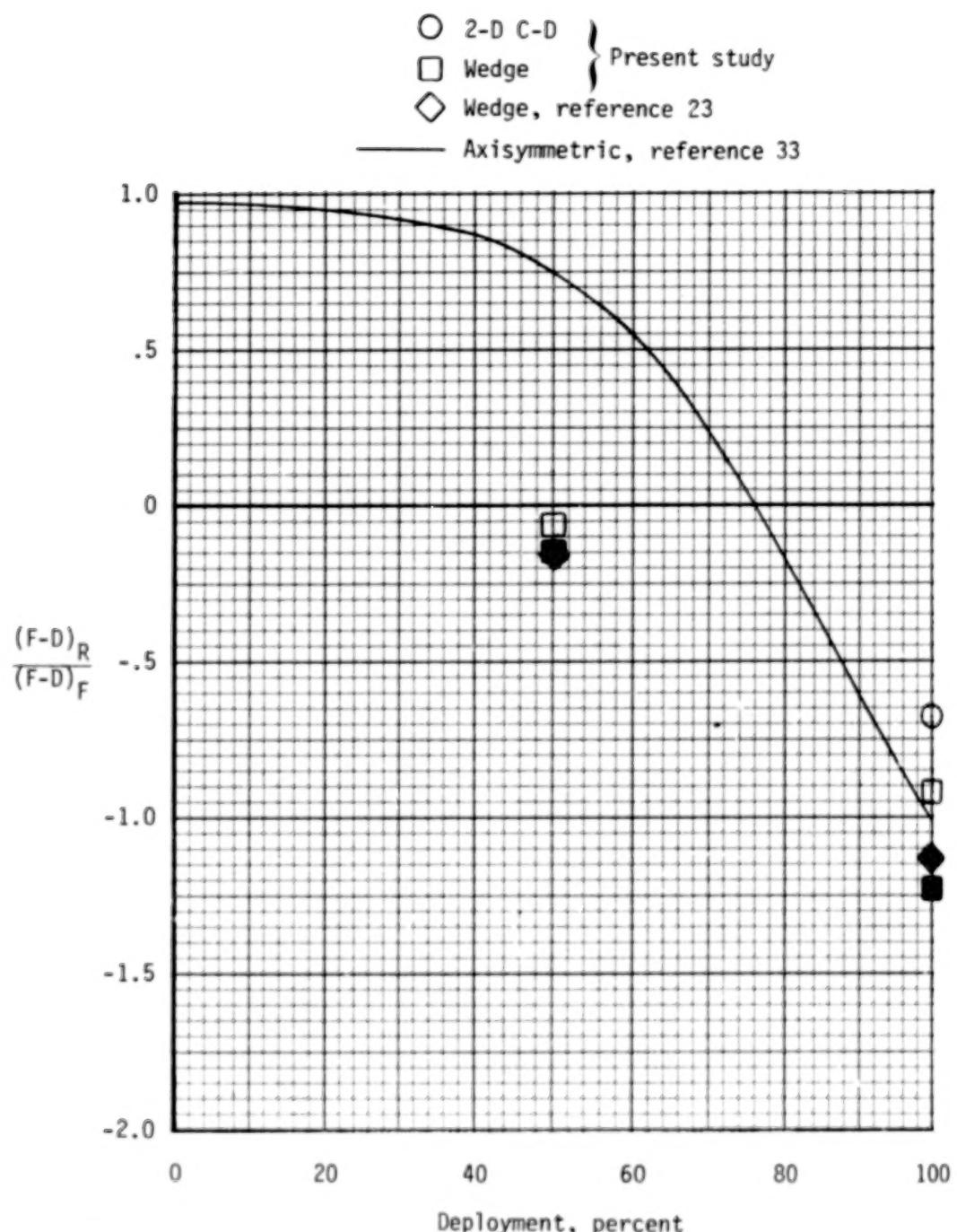
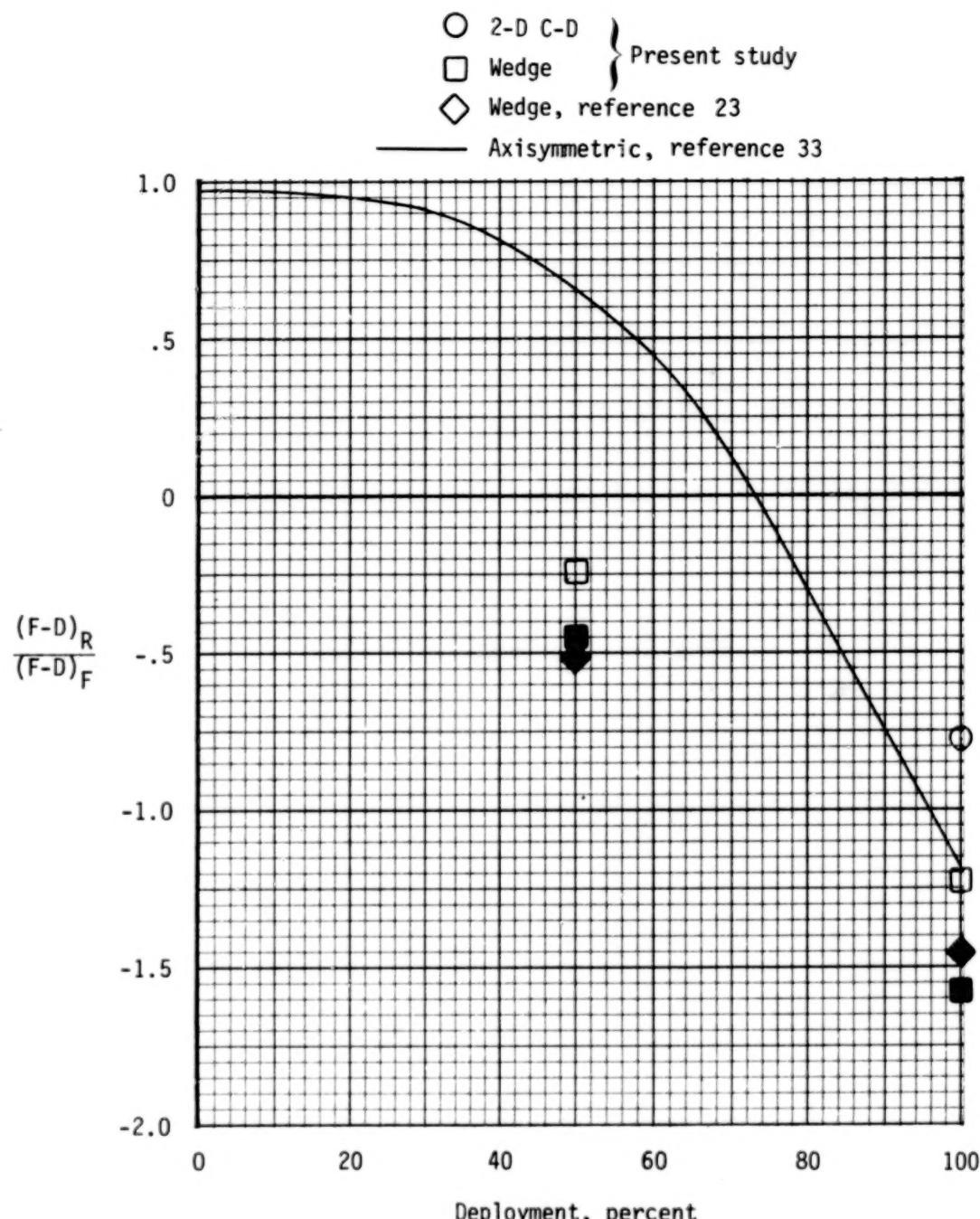


Figure 120.- Comparison of thrust reverser performance at several Mach numbers.
 Solid symbols indicate wedge nozzles with reverser panel sideplates.



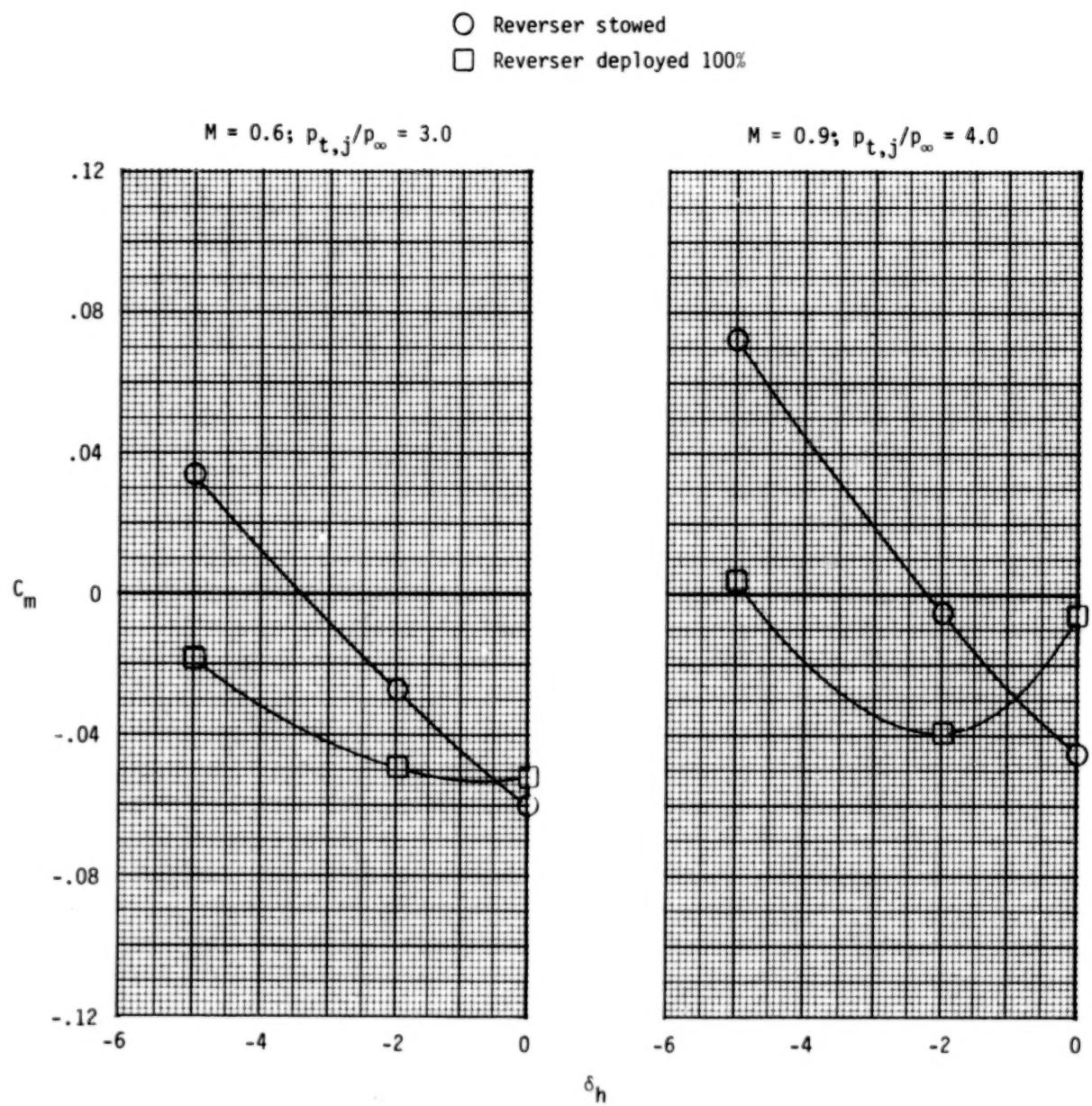
(b) $M = 0.6$; $p_{t,j}/p_{\infty} = 2.65$.

Figure 120.- Continued.



(c) $M = 0.9; p_{t,j}/p_{\infty} = 3.3.$

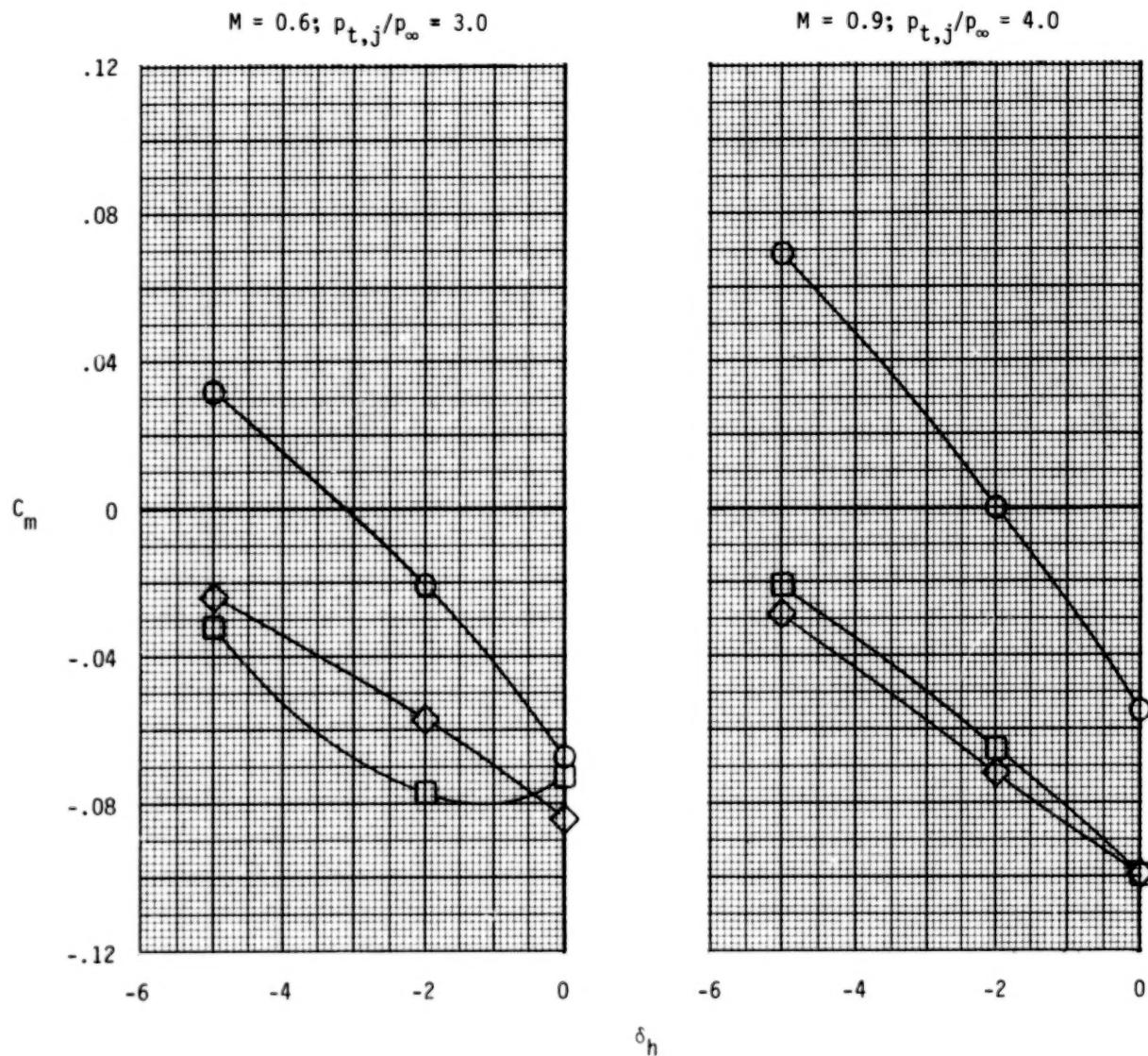
Figure 120.- Concluded.



(a) 2-D C-D nozzle; dry power.

Figure 121. - Effect of thrust reversing on horizontal-tail pitch effectiveness. $\alpha = 6^{\circ}$.

- Reverser stowed
- Reverser deployed 100%, sideplates off
- ◇ Reverser deployed 100%, sideplates on



(b) Wedge nozzle; dry power.

Figure 121.- Concluded.

1. Report No. NASA TP-1638	2. Government Accession No.	3. Recipient's Catalog No.	
4. Title and Subtitle INVESTIGATION OF AXISYMMETRIC AND NONAXISYMMETRIC NOZZLES INSTALLED ON A 0.10-SCALE F-18 PROTOTYPE AIRPLANE MODEL		5. Report Date June 1980	
7. Author(s) Francis J. Capone and Bobby L. Berrier		6. Performing Organization Code	
9. Performing Organization Name and Address NASA Langley Research Center Hampton, VA 23665		8. Performing Organization Report No. L-13401	
12. Sponsoring Agency Name and Address National Aeronautics and Space Administration Washington, DC 20546		10. Work Unit No. 505-43-23-01	
15. Supplementary Notes		11. Contract or Grant No.	
16. Abstract <p>An investigation was conducted in the Langley 16-Foot Transonic Tunnel to determine afterbody/nozzle longitudinal aerodynamic characteristics of three different two-dimensional nozzles and a base-line axisymmetric nozzle installed on a 0.10-scale model of the F-18 airplane. The effects of thrust vectoring and in-flight thrust reversing were also studied. Horizontal-tail deflections of 0°, -2°, and -5° were tested. Test data were obtained at static conditions and at Mach numbers from 0.60 to 1.20 over an angle-of-attack range from -2° to 10°. Nozzle pressure ratio was varied from jet off to about 10.</p>		13. Type of Report and Period Covered Technical Paper	
17. Key Words (Suggested by Author(s)) Nonaxisymmetric nozzles Two-dimensional nozzles Vectored thrust Reverse thrust		18. Distribution Statement Unclassified - Unlimited	
		Subject Category 02	
19. Security Classif. (of this report) Unclassified	20. Security Classif. (of this page) Unclassified	21. No. of Pages 301	22. Price* \$11.75

* For sale by the National Technical Information Service, Springfield, Virginia 22161

NASA-Langley, 1980

302

90 %

50 %